REVIEWS IN COMPUTATIONAL CHEMISTRY

Kenny B. Lipkowitz *Donald B. Boyd*

VOLUME 19

WILEY-VCH

Reviews in Computational Chemistry Volume 19

Reviews in Computational Chemistry Volume 19

Edited by

Kenny B. Lipkowitz, Raima Larter, and Thomas R. Cundari

Editor Emeritus

Donald B. Boyd

WILEY-VCH

Kenny B. Lipkowitz
Department of Chemistry
Ladd Hall 104
North Dakota State University
Fargo, North Dakota 58105-5516, USA
kenny.lipkowitz@chem.ndsu.nodak.edu

Thomas R. Cundari
Department of Chemistry
University of North Texas
Box 305070,
Denton, Texas 76203-5070, USA
tomc@unt.edu

Raima Larter
Division of Chemistry
National Science Foundation
4201 Wilson Boulevard
Arlington, Virginia 22230, USA
rlarter@nsf.gov

Donald B. Boyd
Department of Chemistry
Indiana University–Purdue University
at Indianapolis
402 North Blackford Street
Indianapolis, Indiana 46202-3274, USA
boyd@chem.iupui.edu

Published by John Wiley & Sons, Inc., Hoboken, New Jersey.
Published simultaneously in Canada.

ISBN 0-471-23585-7
ISSN 1069-3599

Printed in the United States of America

10 9 8 7 6 5 4 3 2 1

Preface

Ed Koch, former mayor of New York City, was fond of saying "How am I doing?" That's a question we asked ourselves recently. We have published over 100 chapters in this book series to date, and although we are confident that the material has been used heavily by the computational chemistry community at large, we have not been able to address Koch's question in a quantifiable way (other than from sales records). We can now answer the question of how we're doing; we're doing very well.

One indicator that can be used to assess the value of a book or journal is the impact factor of the Institute for Scientific Information Inc. (ISI). In a Sci-Bytes listing, journals were ranked by impact (http://in-cites.com/research/2002/august 19 2002-2.html). Three rankings were presented; they are tabulated below:

Rank	2001	1997–2001	1981–2001
1	*Chemical Reviews*	*Chemical Reviews*	*Chemical Reviews*
2	*Accounts of Chemical Research*	*Accounts of Chemical Research*	*Accounts of Chemical Research*
3	*Chemical Society Reviews*	*Chemical Society Reviews*	*Chemical Society Reviews*
4	*Angewandte Chemie International Edition*	*Journal of the American Chemical Society*	*Journal of the American Chemical Society*
5	*Journal of the American Chemical Society*	*Angewandte Chemie International Edition in English*	*Journal of Computational Chemistry*
6	*Topics in Current Chemistry*	*Topics in Current Chemistry*	*Topics in Current Chemistry*
7	*Chemistry—a European Journal*	*Chemische Berichte-Recueil*	*Chemistry International*
8	*Journal of Physical and Chemical Reference Data*	*Chemistry—a European Journal*	*Journal of the Chemical Society, Chemical Communications*
9	*Journal of Combinatorial Chemistry*	*Reviews in Computational Chemistry*	*Marine Chemistry*
10	*Reviews in Computational Chemistry*	*Chemical Research in Toxicology*	*Reviews of Chemical Intermediates*

In this table the citation impact of journals in a given field (in this case listed by Sci-Bytes as "general") are compared over three different time spans. The leftmost column ranks journals according to their "impact factors," as enumerated in the current edition of the ISI *Journal Citation Reports*. The 2001 impact factor was calculated by taking the number of all current citations to source items published in a journal over the previous 2 years and dividing it by the number of articles published in the journal during the same period. This is simply a ratio between citations and citable items published. The next two columns show impact over longer timespans of 5 and 21 years. These results were based on figures from the ISI *Journal Performance Indicators*. To generate the citations-per-paper impact scores, the total number of citations to a journal's published papers were divided by the total number of papers published in that particular journal.

Reviews in Computational Chemistry is ranked highly in the category of "general" journals, now making it among the top 10. We are pleased that the quality of the chapters has been high and that the community values these chapters enough to cite them as frequently as they have been.

Our goal over the years has been to provide tutorial-like reviews covering all aspects of computational chemistry. In this, our nineteenth volume, we present four chapters covering a range of topics that have as a theme macroscopic modeling. In Chapter 1, Professors Robert Q. Topper and David L. Freeman provide a short tutorial on Monte Carlo simulation techniques with their students Denise Bergin and Keirnan R. LaMarche. The emphasis of this tutorial is on calculating thermodynamic properties of systems at the atomic level. They begin their tutorial with the Metropolis method, the generalized Metropolis algorithm, and the Barker–Watts algorithm for molecular rotations. They provide insights along the way about random-number generation and practical matters concerning equilibration, error estimation, and heat capacities. Then they introduce the problem we all encounter: the inability to reach every possible state on the potential surface from every possible initial state. This, in turn, leads to quasiergodicity. Quasiergodic systems are insidious in that they usually appear to be ergodic. The authors point out this pitfall and in the next section of their tutorial describe methods available for overcoming quasiergodicity. Magnifying step sizes in a Metropolis walk (mag-walking), using the Shew–Mills subspace sampling method or the related "jump between wells" method of Still, can help overcome the ergodic problem, as can implementing umbrella sampling strategies and histogram methods. Another class of generally applicable Monte Carlo (MC) methods used to address quasiergodicity allows Metropolis walkers at different temperatures to exchange configurations with one another. J-walking, parallel tempering, and the use of Tsallis statistics are introduced and described. The authors end their tutorial by describing another class of methods used to remove sampling difficulties that is based on multicanonical ensembles. Throughout the chapter the strengths and weaknesses of methods used for

Monte Carlo simulations are delineated and pitfalls to avoid them are highlighted.

In Chapter 2, Professors David E. Smith and Tony Haymet provide a tutorial on computing hydrophobicity. The authors promulgate the opinion that one must seek to explain the set of verifiable experimental observations to fully understand hydrophobicity. Accordingly, rather than covering everything on this topic that has appeared in the literature, the authors treat only methods for which full details have been published. They begin their tutorial by explaining the basic simulation methods needed and point out, surprisingly, that hydrophobicity is relatively insensitive to the water potential used. An emphasis is placed on particle insertion methods, free-energy perturbation (FEP), and thermodynamic integration (TI) strategies. The authors explain that entropies of hydration and association are considered to be one of the primary signatures of hydrophobicity. Hydrophobic hydration is described in the next section of their review. Details about hydration structure, hydration free energy, entropy, and heat capacity are brought into sharp focus. The chapter ends with a description of computational techniques used to compute hydrophobic interactions, specifically, solvent-induced interactions between nonpolar solutes in water. A clear, concise exposé describing what is right and what is not right in the extant literature is presented in this chapter.

In Chapter 3, Lipeng Sun and Bill Hase review techniques for carrying out classical trajectory simulations within the Born–Oppenheimer (BO) approximation. They begin their chapter with a review of the basic theory in which equations of motion for the atoms involved in a chemical reaction are defined on a potential energy surface. Traditionally, this surface has been defined analytically, but with the increasing speed and computational power now available, it has become possible to use electronic structure theory directly in carrying out classical trajectory simulations with the equations of motion. Sun and Hase review the theoretical basis of the BO direct dynamics approach. This is followed by a discussion of integration techniques for the classical equations of motion and of algorithms for choosing initial conditions for ensembles of trajectories. They continue with a critique of the adequacy of classical mechanics in describing chemical processes that are, in reality, quantum-mechanical in nature. The importance of possible quantum effects is discussed. They conclude their chapter by giving several examples of application of the BO direct dynamics method of actual problems: cyclopropane stereomutation, $Cl^- + CH_3Cl$ barrier dynamics, $OH^- + CH_3F$ exit channel dynamics, and, finally, protonated glycine surface-induced dissociation.

The final chapter thoroughly discusses the theoretical underpinnings of the widely used Poisson–Boltzmann (PB) equation. During the 1990s there was a dramatic increase in the use of the PB equation that can be attributed to advances in computers, needs in biological chemistry, and a renewed interest in colloidal systems. Many computational chemists use the PB equation routinely in their research. But in spite of this usage, they are often completely

unaware of the theoretical underpinnings associated with the method. Dr. Gene Lamm presents us with a complete tutorial on the PB equation that covers and even extends the basic theoretical background. This chapter is not meant for the novice molecular modeler as are most chapters in this series, but instead it is directed toward the seasoned professional. The tutorial is divided into four parts, the first of which is a brief history of the PB equation and its derivation. In the second part the PB equation is applied to several model systems for which exact or approximate analytical solutions can be found. The author brings together in this, the largest part of the chapter, many examples for planar and curved systems scattered throughout the literature to demonstrate for the reader a coherence of purpose and application within the field. In the third part of the tutorial, numerical methods commonly used in applying the PB equation to systems more complicated than one-dimensional representations are provided. Most readers of this book series will be interested in this section of the chapter and are encouraged to skip to this section once they read about the Gouy–Chapman model. Here a brief description of finite-difference/finite element PB algorithms used in popular programs such as UHBD, DelPhi, APBS, and MEAD are explained. The fourth and final part of the chapter introduces topics of more advanced nature. This chapter sets the groundwork for a forthcoming chapter we intend to publish in a subsequent volume that will have as its focus the many uses and applications of the PB equation.

We invite our readers to visit the *Reviews in Computational Chemistry* Website at http://chem.iupui.edu/rcc/rcc/html. It includes the author and subject indexes, color graphics, errata, and other materials supplementing the chapters. We are delighted to report that the Google search engine (http://www.google.com/) ranks our Website among the top hits in a search on the term "computational chemistry." This search engine is becoming popular because it ranks hits in terms of their relevance and frequency of visits. Google also is very fast and appears to provide a quite complete and up-to-date picture of what information is available on the World Wide Web.

We are also pleased to note that our publisher plans to make our most recent volumes available in an online form through Wiley Interscience. Please check the Web (http://www.interscience.wiley.com/onlinebooks) or contact reference@wiley.com for the latest information. For readers who appreciate the permanence and convenience of bound books, these will, of course, continue.

We thank the authors of this and previous volumes for their excellent chapters.

Kenny B. Lipkowitz and Raima Larter
Indianapolis, Indiana
Thomas R. Cundari
Denton, Texas
January 2003

Contents

Contributors

Denise Bergin, Department of Chemistry, The Cooper Union for the Advancement of Science and Art, 51 Astor Place, New York, New York 10003, USA

David L. Freeman, Department of Chemistry, University of Rhode Island, Kingston, Rhode Island 02881, USA (Electronic mail: freeman@chm.uri.edu)

William L. Hase, Department of Chemistry and Department of Computer Science, Wayne State University, Detroit, Michigan 48202, USA (Electronic mail: wlh@cs.wayne.edu)

Anthony D. J. Haymet, Department of Chemistry, University of Houston, Houston, Texas 77204-5003, USA (Electronic mail: haymet@uh.edu)

Keirnan R. LaMarche, Department of Chemistry, The Cooper Union for the Advancement of Science and Art, 51 Astor Place, New York, New York 10003, USA

Gene Lamm, Department of Chemistry, University of Louisville, Louisville, Kentucky 40292, USA (Electronic mail: glamm@louisville.edu)

David E. Smith, Department of Chemistry and Biochemistry, New Mexico State University, Las Cruces, New Mexico 88003-8001, USA (Electronic mail: davsmith@nmsu.edu)

Lipeng Sun, Department of Chemistry and Department of Computer Science, Wayne State University, Detroit, Michigan 48202, USA (Electronic mail: lpsun@chem.wayne.edu)

Robert Q. Topper, Department of Chemistry, The Cooper Union for the Advancement of Science and Art, 51 Astor Place, New York, New York 10003, USA (Electronic mail: topper@magnum.cooper.edu)

Contributors to Previous Volumes*

Volume 1 (1990)

David Feller and **Ernest R. Davidson,**† Basis Sets for Ab Initio Molecular Orbital Calculations and Intermolecular Interactions.

James J. P. Stewart,‡ Semiempirical Molecular Orbital Methods.

Clifford E. Dykstra,¶ **Joseph D. Augspurger, Bernard Kirtman,** and **David J. Malik,** Properties of Molecules by Direct Calculation.

Ernest L. Plummer, The Application of Quantitative Design Strategies in Pesticide Design.

Peter C. Jurs, Chemometrics and Multivariate Analysis in Analytical Chemistry.

Yvonne C. Martin, Mark G. Bures, and **Peter Willett,** Searching Databases of Three-Dimensional Structures.

Paul G. Mezey, Molecular Surfaces.

Terry P. Lybrand,§ Computer Simulation of Biomolecular Systems Using Molecular Dynamics and Free Energy Perturbation Methods.

*Where appropriate and available, the current affiliation of the senior or corresponding author is given here as a convenience to our readers.

†Current address: Department of Chemistry, University of Washington, Seattle, Washington 98195 (Electronic mail: erdavid@u.washington.edu).

‡Current address: 15210 Paddington Circle, Colorado Springs, Colorado 80921-2512 (Electronic mail: jstewart@fai.com).

¶Current address: Department of Chemistry, Indiana University–Purdue University at Indianapolis, Indianapolis, Indiana 46202 (Electronic mail: dykstra@chem.iupui.edu).

§Current address: Department of Chemistry, Vanderbilt University, Nashville, Tennessee 37212 (Electronic mail: lybrand@structbio.vanderbilt.edu).

Donald B. Boyd, Aspects of Molecular Modeling.

Donald B. Boyd, Successes of Computer-Assisted Molecular Design.

Ernest R. Davidson, Perspectives on Ab Initio Calculations.

Volume 2 (1991)

Andrew R. Leach,* A Survey of Methods for Searching the Conformational Space of Small and Medium-Sized Molecules.

John M. Troyer and **Fred E. Cohen,** Simplified Models for Understanding and Predicting Protein Structure.

J. Phillip Bowen and **Norman L. Allinger,** Molecular Mechanics: The Art and Science of Parameterization.

Uri Dinur and **Arnold T. Hagler,** New Approaches to Empirical Force Fields.

Steve Scheiner,† Calculating the Properties of Hydrogen Bonds by Ab Initio Methods.

Donald E. Williams, Net Atomic Charge and Multipole Models for the Ab Initio Molecular Electric Potential.

Peter Politzer and **Jane S. Murray,** Molecular Electrostatic Potentials and Chemical Reactivity.

Michael C. Zerner, Semiempirical Molecular Orbital Methods.

Lowell H. Hall and **Lemont B. Kier,** The Molecular Connectivity Chi Indexes and Kappa Shape Indexes in Structure-Property Modeling.

I. B. Bersuker‡ and **A. S. Dimoglo,** The Electron-Topological Approach to the QSAR Problem.

Donald B. Boyd, The Computational Chemistry Literature.

---

*Current address: GlaxoSmithKline, Greenford, Middlesex, UB6 0HE, U.K. (Electronic mail: arl22958@ggr.co.uk).

†Current address: Department of Chemistry and Biochemistry, Utah State University, Logan, Utah 84322 (Electronic mail: scheiner@cc.usu.edu).

‡Current address: College of Pharmacy, The University of Texas, Austin, Texas 78712 (Electronic mail: bersuker@eeyore.cm.utexas.edu).

Volume 3 (1992)

Tamar Schlick, Optimization Methods in Computational Chemistry.

Harold A. Scheraga, Predicting Three-Dimensional Structures of Oligopeptides.

Andrew E. Torda and **Wilfred F. van Gunsteren,** Molecular Modeling Using NMR Data.

David F. V. Lewis, Computer-Assisted Methods in the Evaluation of Chemical Toxicity.

Volume 4 (1993)

Jerzy Cioslowski, Ab Initio Calculations on Large Molecules: Methodology and Applications.

Michael L. McKee and **Michael Page,** Computing Reaction Pathways on Molecular Potential Energy Surfaces.

Robert M. Whitnell and **Kent R. Wilson,** Computational Molecular Dynamics of Chemical Reactions in Solution.

Roger L. DeKock, Jeffry D. Madura, Frank Rioux, and **Joseph Casanova,** Computational Chemistry in the Undergraduate Curriculum.

Volume 5 (1994)

John D. Bolcer and **Robert B. Hermann,** The Development of Computational Chemistry in the United States.

Rodney J. Bartlett and **John F. Stanton,** Applications of Post-Hartree–Fock Methods: A Tutorial.

Steven M. Bachrach,* Population Analysis and Electron Densities from Quantum Mechanics.

---

*Current address: Department of Chemistry, Trinity University, San Antonio, Texas 78212 (Electronic mail: steven.bachrach@trinity.edu).

Jeffry D. Madura,* **Malcolm E. Davis, Michael K. Gilson, Rebecca C. Wade, Brock A. Luty,** and **J. Andrew McCammon,** Biological Applications of Electrostatic Calculations and Brownian Dynamics Simulations.

K. V. Damodaran and **Kenneth M. Merz Jr.,** Computer Simulation of Lipid Systems.

Jeffrey M. Blaney† and **J. Scott Dixon,** Distance Geometry in Molecular Modeling.

Lisa M. Balbes, S. Wayne Mascarella, and **Donald B. Boyd,** A Perspective of Modern Methods in Computer-Aided Drug Design.

Volume 6 (1995)

Christopher J. Cramer and **Donald G. Truhlar,** Continuum Solvation Models: Classical and Quantum Mechanical Implementations.

Clark R. Landis, Daniel M. Root, and **Thomas Cleveland,** Molecular Mechanics Force Fields for Modeling Inorganic and Organometallic Compounds.

Vassilios Galiatsatos, Computational Methods for Modeling Polymers: An Introduction.

Rick A. Kendall,‡ **Robert J. Harrison, Rik J. Littlefield,** and **Martyn F. Guest,** High Performance Computing in Computational Chemistry: Methods and Machines.

Donald B. Boyd, Molecular Modeling Software in Use: Publication Trends.

Eiji Ōsawa and **Kenny B. Lipkowitz,** Appendix: Published Force Field Parameters.

---

*Current address: Department of Chemistry and Biochemistry, Duquesne University, Pittsburgh, Pennsylvania 15282-1530 (Electronic mail: madura@duq.edu).

†Current address: Structural GenomiX, San Francisco, California (Electronic mail: jblaney@stromix.com).

‡Current address: Scalable Computing Laboratory, Ames Laboratory, Wilhelm Hall, Ames, Iowa 50011 (Electronic mail: rickyk@scl.ameslab.gov).

Volume 7 (1996)

Geoffrey M. Downs and **Peter Willett,** Similarity Searching in Databases of Chemical Structures.

Andrew C. Good* and **Jonathan S. Mason,** Three-Dimensional Structure Database Searches.

Jiali Gao,† Methods and Applications of Combined Quantum Mechanical and Molecular Mechanical Potentials.

Libero J. Bartolotti and **Ken Flurchick,** An Introduction to Density Functional Theory.

Alain St-Amant, Density Functional Methods in Biomolecular Modeling.

Danya Yang and **Arvi Rauk,** The A Priori Calculation of Vibrational Circular Dichroism Intensities.

Donald B. Boyd, Appendix: Compendium of Software for Molecular Modeling.

Volume 8 (1996)

Zdenek Slanina,‡ **Shyi-Long Lee,** and **Chin-hui Yu,** Computations in Treating Fullerenes and Carbon Aggregates.

Gernot Frenking, Iris Antes, Marlis Böhme, Stefan Dapprich, Andreas W. Ehlers, Volker Jonas, Arndt Neuhaus, Michael Otto, Ralf Stegmann, Achim Veldkamp, and **Sergei F. Vyboishchikov,** Pseudopotential Calculations of Transition Metal Compounds: Scope and Limitations.

Thomas R. Cundari, Michael T. Benson, M. Leigh Lutz, and **Shaun O. Sommerer,** Effective Core Potential Approaches to the Chemistry of the Heavier Elements.

---

*Current address: Bristol-Myers Squibb, 5 Research Parkway, P.O. Box 5100, Wallingford, Connecticut 06492-7660 (Electronic mail: andrew.good@bms.com).

†Current address: Depertment Chemistry, University of Minnesota, 207 Pleasant St. SE, Minneapolis, Minnesota 55455-0431 (Electronic mail: gao@chem.umn.edu).

‡Current address: Institute of Chemistry, Academia Sinica, Nankang, Taipei 11529, Taiwan, Republic of China (Electronic mail: zdenek@chem.sinica.edu.tw).

Jan Almlöf and **Odd Gropen,*** Relativistic Effects in Chemistry.

Donald B. Chesnut, The Ab Initio Computation of Nuclear Magnetic Resonance Chemical Shielding.

Volume 9 (1996)

James R. Damewood Jr., Peptide Mimetic Design with the Aid of Computational Chemistry.

T. P. Straatsma, Free Energy by Molecular Simulation.

Robert J. Woods, The Application of Molecular Modeling Techniques to the Determination of Oligosaccharide Solution Conformations.

Ingrid Pettersson and **Tommy Liljefors,** Molecular Mechanics Calculated Conformational Energies of Organic Molecules: A Comparison of Force Fields.

Gustavo A. Arteca, Molecular Shape Descriptors.

Volume 10 (1997)

Richard Judson,† Genetic Algorithms and Their Use in Chemistry.

Eric C. Martin, David C. Spellmeyer, Roger E. Critchlow Jr., and **Jeffrey M. Blaney,** Does Combinatorial Chemistry Obviate Computer-Aided Drug Design?

Robert Q. Topper, Visualizing Molecular Phase Space: Nonstatistical Effects in Reaction Dynamics.

Raima Larter and **Kenneth Showalter,** Computational Studies in Nonlinear Dynamics.

Stephen J. Smith and **Brian T. Sutcliffe,** The Development of Computational Chemistry in the United Kingdom.

---

*Address: Institute of Mathematical and Physical Sciences, University of Tromsø, N-9037 Tromsø, Norway (Electronic mail: oddg@chem.uit.no).

†Current address: Genaissance Pharmaceuticals, Five Science Park, New Haven, Connecticut 06511 (Electronic mail: r.judson@genaissance.com).

Volume 11 (1997)

Mark A. Murcko, Recent Advances in Ligand Design Methods.

David E. Clark,* **Christopher W. Murray,** and **Jin Li,** Current Issues in De Novo Molecular Design.

Tudor I. Oprea† and **Chris L. Waller,** Theoretical and Practical Aspects of Three-Dimensional Quantitative Structure–Activity Relationships.

Giovanni Greco, Ettore Novellino, and **Yvonne Connolly Martin,** Approaches to Three-Dimensional Quantitative Structure–Activity Relationships.

Pierre-Alain Carrupt, Bernard Testa, and **Patrick Gaillard,** Computational Approaches to Lipophilicity: Methods and Applications.

Ganesan Ravishanker, Pascal Auffinger, David R. Langley, Bhyravabhotla Jayaram, Matthew A. Young, and **David L. Beveridge,** Treatment of Counterions in Computer Simulations of DNA.

Donald B. Boyd, Appendix: Compendium of Software and Internet Tools for Computational Chemistry.

Volume 12 (1998)

Hagai Meirovitch,‡ Calculation of the Free Energy and the Entropy of Macromolecular Systems by Computer Simulation.

Ramzi Kutteh and **T. P. Straatsma,** Molecular Dynamics with General Holonomic Constraints and Application to Internal Coordinate Constraints.

John C. Shelley¶ and **Daniel R. Bérard,** Computer Simulation of Water Physisorption at Metal–Water Interfaces.

---

*Current address: Computer-Aided Drug Design, Argenta Discovery Ltd., c/o Aventis Pharma Ltd., Rainham Road South, Dagenham, Essex, RM10 7XS, United Kingdom (Electronic mail: david.clark@argentadiscovery.com).

†Current address: Office of Biocomputing, University of New Mexico School of Medicine, 915 Camino de Salud NE, Albuquerque, New Mexico 87131 (Electronic mail: toprea@salud.unm.edu).

‡Current address: Department of Molecular Genetics & Biochemistry, School of Medicine, University of Pittsburgh, Pittsburgh, Pennsylvania 15213 (Electronic mail: hagaim@pitt.edu).

¶Current address: Schrödinger, Inc., 1500 S.W. First Avenue, Suite 1180, Portland, Oregon 97201 (Electronic mail: jshelley@schrodinger.com).

Donald W. Brenner, Olga A. Shenderova, and **Denis A. Areshkin,** Quantum-Based Analytic Interatomic Forces and Materials Simulation.

Henry A. Kurtz and **Douglas S. Dudis,** Quantum Mechanical Methods for Predicting Nonlinear Optical Properties.

Chung F. Wong,* **Tom Thacher,** and **Herschel Rabitz,** Sensitivity Analysis in Biomolecular Simulation.

Paul Verwer and **Frank J. J. Leusen,** Computer Simulation to Predict Possible Crystal Polymorphs.

Jean-Louis Rivail and **Bernard Maigret,** Computational Chemistry in France: A Historical Survey.

Volume 13 (1999)

Thomas Bally and **Weston Thatcher Borden,** Calculations on Open-Shell Molecules: A Beginner's Guide.

Neil R. Kestner and **Jaime E. Combariza,** Basis Set Superposition Errors: Theory and Practice.

James B. Anderson, Quantum Monte Carlo: Atoms, Molecules, Clusters, Liquids, and Solids.

Anders Wallqvist† and **Raymond D. Mountain,** Molecular Models of Water: Derivation and Description.

James M. Briggs and **Jan Antosiewicz,** Simulation of pH-Dependent Properties of Proteins Using Mesoscopic Models.

Harold E. Helson, Structure Diagram Generation.

Volume 14 (2000)

Michelle Miller Francl and **Lisa Emily Chirlian,** The Pluses and Minuses of Mapping Atomic Charges to Electrostatic Potentials.

---

*Current addrress: Howard Hughes Medical Institute, School of Medicine, University of California at San Diego, 9500 Gilman Drive, La Jolla, California 92093-0365 (Electronic mail: c4wong@ucsd.edu).

†Current address: National Cancer Institute, P.O. Box B, Frederick, Maryland 21702 (Electronic mail: wallqvist@ncifcrt.gov).

T. Daniel Crawford* and **Henry F. Schaefer III,** An Introduction to Coupled Cluster Theory for Computational Chemists.

Bastiaan van de Graaf, Swie Lan Njo, and **Konstantin S. Smirnov,** Introduction to Zeolite Modeling.

Sarah L. Price, Toward More Accurate Model Intermolecular Potentials for Organic Molecules.

Christopher J. Mundy,† **Sundaram Balasubramanian, Ken Bagchi, Mark E. Tuckerman, Glenn J. Martyna,** and **Michael L. Klein,** Nonequilibrium Molecular Dynamics.

Donald B. Boyd and **Kenny B. Lipkowitz,** History of the Gordon Research Conferences on Computational Chemistry.

Mehran Jalaie and **Kenny B. Lipkowitz,** Appendix: Published Force Field Parameters for Molecular Mechanics, Molecular Dynamics, and Monte Carlo Simulations.

Volume 15 (2000)

F. Matthias Bickelhaupt and **Evert Jan Baerends,** Kohn–Sham Density Functional Theory: Predicting and Understanding Chemistry.

Michael A. Robb, Marco Garavelli, Massimo Olivucci, and **Fernando Bernardi,** A Computational Strategy for Organic Photochemistry.

Larry A. Curtiss, Paul C. Redfern, and **David J. Frurip,** Theoretical Methods for Computing Enthalpies of Formation of Gaseous Compounds.

Russell J. Boyd, The Development of Computational Chemistry in Canada.

Volume 16 (2000)

Richard A. Lewis, Stephen D. Pickett, and **David E. Clark,** Computer-Aided Molecular Diversity Analysis and Combinatorial Library Design.

Keith L. Peterson, Artificial Neural Networks and Their Use in Chemistry.

---

*Current address: Department of Chemistry, Virginia Polytechnic Institute and State University, Blacksburg, Virginia 24061-0212 (Electronic mail: crawdad@vt.edu).

†Current address: Computational Materials Science, L-371, Lawrence Livermore National Laboratory, Livermore, California 94550 (Electronic mail: mundy2@llnl.gov).

Jörg-Rüdiger Hill, Clive M. Freeman, and **Lalitha Subramanian,** Use of Force Fields in Materials Modeling.

M. Rami Reddy, Mark D. Erion, and **Atul Agarwal,** Free Energy Calculations: Use and Limitations in Predicting Ligand Binding Affinities.

Volume 17 (2001)

Ingo Muegge and **Matthias Rarey,** Small Molecule Docking and Scoring.

Lutz P. Ehrlich and **Rebecca C. Wade,** Protein–Protein Docking.

Christel M. Marian, Spin–Orbit Coupling in Molecules.

Lemont B. Kier, Chao-Kun Cheng, and **Paul G. Seybold,** Cellular Automata Models of Aqueous Solution Systems.

Kenny B. Lipkowitz and **Donald B. Boyd,** Appendix: Books Published on the Topics of Computational Chemistry.

Volume 18 (2002)

Geoff M. Downs and John M. Barnard, Clustering Methods and Their Uses in Computational Chemistry.

Hans-Joachim Böhm and **Martin Stahl,** The Use of Scoring Functions in Drug Discovery Applications.

Steven W. Rick and **Steven J. Stuart,** Potentials and Algorithms for Incorporating Polarizability in Computer Simulations.

Dmitry V. Matyushov and **Gregory A. Voth,** New Developments in the Theoretical Description of Charge-Transfer Reactions in Condensed Phases.

George R. Famini and **Leland Y. Wilson,** Linear Free Energy Relationships Using Quantum Mechanical Descriptors.

Sigrid D. Peyerimhoff, The Development of Computational Chemistry in Germany.

Donald B. Boyd and **Kenny B. Lipkowitz,** Appendix: Examination of the Employment Environment for Computational Chemistry.

CHAPTER 1

Computational Techniques and Strategies for Monte Carlo Thermodynamic Calculations, with Applications to Nanoclusters

Robert Q. Topper,[*] David L. Freeman,[†] Denise Bergin,[*] and Keirnan R. LaMarche[*]

[*]Department of Chemistry, The Cooper Union for the Advancement of Science and Art, 51 Astor Place, New York, New York 10003,[**] and [†]Department of Chemistry, University of Rhode Island, Kingston, Rhode Island 02881

[**]Present address: Department of Chemistry, Medical Technology, and Physics, Monmouth University, West Long Branch, New Jersey

INTRODUCTION

This chapter is written for the reader who would like to learn how Monte Carlo methods[1] are used to calculate thermodynamic properties of systems at the atomic level, or to determine which advanced Monte Carlo methods might work best in their particular application. There are a number of excellent books and review articles on Monte Carlo methods, which are generally focused on condensed phases, biomolecules or electronic structure theory.[2–13] The purpose of this chapter is to explain and illustrate some of the special techniques that we and our colleagues have found to be particularly

Reviews in Computational Chemistry, Volume 19
edited by Kenny B. Lipkowitz, Raima Larter, and Thomas R. Cundari
ISBN 0-471-23585-7

well suited for simulations of nanodimensional atomic and molecular clusters. We want to help scientists and engineers who are doing their first work in this area to get off on the right foot, and also provide a pedagogical chapter for those who are doing experimental work. By including examples of simulations of some simple, yet representative systems, we provide the reader with some data for direct comparison when writing their own code from scratch.

Although a number of Monte Carlo methods in current use will be reviewed, this chapter is not meant to be comprehensive in scope. Monte Carlo is a remarkably flexible class of numerical methods. So many versions of the basic algorithms have arisen that we believe a comprehensive review would be of limited pedagogical value. Instead, we intend to provide our readers with enough information and background to allow them to navigate successfully through the many different Monte Carlo techniques in the literature. This should help our readers use existing Monte Carlo codes knowledgably, adapt existing codes to their own purposes, or even write their own programs. We also provide a few general recommendations and guidelines for those who are just getting started with Monte Carlo methods in teaching or in research.

This chapter has been written with the goal of describing methods that are generally useful. However, many of our discussions focus on applications to atomic and molecular clusters (nanodimensional aggregates of a finite number of atoms and/or molecules).[14] We do this for two reasons:

1. A great deal of our own research has focused on such systems,[15] particularly the phase transitions and other structural transformations induced by changes in a cluster's temperature and size, keeping an eye on how various properties approach their bulk limits. The precise determination of thermodynamic properties (such as the heat capacity) of a cluster type as a function of temperature and size presents challenges that must be addressed when using Monte Carlo methods to study virtually any system. For example, analogous structural transitions can also occur in phenomena as disparate as the denaturation of proteins.[16,17] The modeling of these transitions presents similar computational challenges to those encountered in cluster studies.

2. Although cluster systems can present some unique challenges, their study is unencumbered by many of the technical issues regarding periodic boundary conditions that arise when solids, liquids, surface adsorbates, and solvated biomolecules and polymers are studied. These issues are addressed well elsewhere,[7,11,12] and can be thoroughly appreciated and mastered once a general background in Monte Carlo methods is obtained from this chapter.

It should be noted that "Monte Carlo" is a term used in many fields of science, engineering, statistics, and mathematics to mean entirely different things. The one (and only) thing that all Monte Carlo methods have in common is that they all use random numbers to help calculate something. What we mean by "Monte Carlo" in this chapter is the use of random-walk processes to draw samples from a desired probability function, thereby allowing one to

calculate integrals of the form $\int dq f(q)\,\rho(q)$. The quantity $\rho(q)$ is a normalized probability density function that spans the space of a many-dimensional variable q, and $f(q)$ is a function whose average is of thermodynamic importance and interest. This integral, as well as all other integrals in this chapter, should be understood to be a definite integral that spans the entire domain of q. Finally, we note that the inclusion of quantum effects through path-integral Monte Carlo methods is not discussed in this chapter. The reader interested in including quantum effects in Monte Carlo thermodynamic calculations is referred elsewhere.[15,18–22]

METROPOLIS MONTE CARLO

Monte Carlo simulations are widely used in the fields of chemistry, biology, physics, and engineering in order to determine the structural and thermodynamic properties of complex systems at the atomic level. Thermodynamic averages of molecular properties can be determined from Monte Carlo methods, as can minimum-energy structures. Let $\langle f \rangle$ represent the average value of some coordinate-dependent property $f(\boldsymbol{x})$, with $\boldsymbol{x}$ representing the $3N$ Cartesian coordinates needed to locate all of the N atoms. In the canonical ensemble (fixed N, V and T, with V the volume and T the absolute temperature), averages of molecular properties are given by an average of $f(\boldsymbol{x})$ over the Boltzmann distribution

$$\langle f \rangle = \frac{\int d\boldsymbol{x}\, f(\boldsymbol{x}) \exp[-\beta U(\boldsymbol{x})]}{\int d\boldsymbol{x} \exp[-\beta U(\boldsymbol{x})]} \qquad [1]$$

where $U(\boldsymbol{x})$ is the potential energy of the system, $\beta = 1/k_B T$, and k_B is the Boltzmann constant.[23] If one can compute the thermodynamic average of $f(\boldsymbol{x})$ it is then possible to calculate various thermodynamic properties. In the canonical ensemble it is most common to calculate E, the internal energy, and C_V, the constant-volume heat capacity (although other properties can be calculated as well). For example, if we average $U(\boldsymbol{x})$ over all possible configurations according to Eq. [1], then E and C_V are given by

$$E = \frac{3Nk_B T}{2} + \langle U \rangle \qquad [2]$$

$$C_V = \frac{3Nk_B}{2} + \frac{\langle U^2 \rangle - \langle U \rangle^2}{(k_B T^2)} \qquad [3]$$

The first term in each equation represents the contribution of kinetic energy, which is analytically integrable. In the harmonic (low-temperature) limit, E given by Eq. [2] will be a linear function of temperature and C_V from Eq. [3] will be constant, in accordance with the Equipartition Theorem.[10] For a small cluster of, say, 6 atoms, the integrals implicit in the calculation of Eqs. [1]

and [2] are already of such high dimension that they cannot be effectively computed using Simpson's rule or other basic quadrature methods.[2,24,25,26] For larger clusters, liquids, polymers or biological molecules the dimensionality is obviously much higher, and one typically resorts to either Monte Carlo, molecular dynamics, or other related algorithms.

To calculate the desired thermodynamic averages, it is necessary to have some method available for computation of the potential energy, either explicitly (in the form of a function representing the interaction potential as in molecular mechanics) or implicitly (in the form of direct quantum-mechanical calculations). Throughout this chapter we shall assume that U is known or can be computed as needed, although this computation is typically the most computationally expensive part of the procedure (because U may need to be computed many, many times). For this reason, all possible measures should be taken to assure the maximum efficiency of the method used in the computation of U.

Also, it should be noted that constraining potentials (which keep the cluster components from straying too far from a cluster's center of mass) are sometimes used.[27] At finite temperature, clusters have finite vapor pressures, and particular cluster sizes are typically unstable to evaporation. Introducing a constraining potential enables one to define clusters of desired sizes. Because the constraining potential is artificial, the dependence of calculated thermodynamic properties on the form and the radius of the constraining potential must be investigated on a case-by-case basis. Rather than diverting the discussion from our main focus (Monte Carlo methods), we refer the interested reader elsewhere for more details and references on the use of constraining potentials.[15,19]

Random-Number Generation: A Few Notes

Because generalized Metropolis Monte Carlo methods are based on "random" sampling from probability distribution functions, it is necessary to use a high-quality random-number generator algorithm to obtain reliable results. A review of such methods is beyond the scope of this chapter,[24,28] but a few general considerations merit discussion.

Random-number generators do not actually produce random numbers. Rather, they use an integer "seed" to initialize a particular "pseudorandom" sequence of real numbers that, taken as a group, have properties that leave them nearly indistinguishable from truly random numbers. These are conventionally floating-point numbers, distributed uniformly on the interval (0,1). If there is a correlation between seeds, a correlation may be introduced between the pseudorandom numbers produced by a particular generator. Thus, the generator should ideally be initialized only once (at the beginning of the random walk), and not re-initialized during the course of the walk. The seed should be supplied either by the user or generated arbitrarily by the program

using, say, the number of seconds since midnight (or some other arcane formula). One should be cautious about using the "built-in" random-number generator functions that come with a compiler for Monte Carlo integration work because some of them are known to be of very poor quality.[26] The reader should always be sure to consult the appropriate literature and obtain (and test) a high-quality random-number generator before attempting to write and debug a Monte Carlo program.

The Generalized Metropolis Monte Carlo Algorithm

The Metropolis Monte Carlo (MMC) algorithm is the single most widely used method for computing thermodynamic averages. It was originally developed by Metropolis et al. and used by them to simulate the freezing transition for a two-dimensional hard-sphere fluid.[1] However, Monte Carlo methods can be used to estimate the values of multidimensional integrals in whatever context they may arise.[29,30] Although Metropolis et al. did not present their algorithm as a general-utility method for numerical integration, it soon became apparent that it could be generalized and applied to a variety of situations. The core of the MMC algorithm is the way in which it draws samples from a desired probability distribution function. The basic strategies used in MMC can be generalized so as to apply to many kinds of probability functions and in combination with many kinds of sampling strategies. Some authors refer to the generalized MMC algorithm simply as "Metropolis sampling,"[31] while others have referred to it as the $M(RT)^2$ method[6] in honor of the five authors of the original paper (Metropolis, the Rosenbluths, and the Tellers).[1] We choose to call this the generalized Metropolis Monte Carlo (gMMC) method, and we will always use the term MMC to refer strictly to the combination of methods originally presented by Metropolis et al.[1]

In the literature of numerical analysis, gMMC is classified as an importance sampling technique.[6,24] Importance sampling methods generate configurations that are distributed according to a desired probability function rather than simply picking them at random from a uniform distribution. The probability function is chosen so as to obtain improved convergence of the properties of interest. gMMC is a special type of importance sampling method which asymptotically (i.e., in the limit that the number of configurations becomes large) generates states of a system according to the desired probability distribution.[6,9] This probability function is usually (but not always[6]) the actual probability distribution function for the physical system of interest. Nearly all statistical-mechanical applications of Monte Carlo techniques require the use of importance sampling, whether gMMC or another method is used (alternatively, "stratified sampling" is sometimes an effective approach[22,32]). gMMC is certainly the most widely used importance sampling method.

In the gMMC algorithm successive configurations of the system are generated to build up a special kind of random walk called a *Markov*

chain.[29,33,34] The random walk visits successive configurations, where each configuration's location depends on the configuration immediately preceding it in the chain. The gMMC algorithm establishes how this can be done so as to asymptotically generate a distribution of configurations corresponding to the probability density function of interest, which we denote as $\rho(\boldsymbol{q})$.

We define $K(\boldsymbol{q}_i \rightarrow \boldsymbol{q}_j)$ to be the conditional probability that a configuration at $\boldsymbol{q}_i$ will be brought to $\boldsymbol{q}_j$ in the next step of the random walk. This conditional probability is sometimes called the "transition rate." The probability of moving from $\boldsymbol{q}$ to $\boldsymbol{q}'$ (where $\boldsymbol{q}$ and $\boldsymbol{q}'$ are arbitrarily chosen configurations somewhere in the available domain) is therefore given by $P(\boldsymbol{q} \rightarrow \boldsymbol{q}')$:

$$P(\boldsymbol{q} \rightarrow \boldsymbol{q}') = K(\boldsymbol{q} \rightarrow \boldsymbol{q}')\,\rho(\boldsymbol{q}) \qquad [4]$$

For the system to evolve toward a unique limiting distribution, we must place a constraint on $P(\boldsymbol{q} \rightarrow \boldsymbol{q}')$. The gMMC algorithm achieves the desired limiting behavior by requiring that, on the average, a point is just as likely to move from $\boldsymbol{q}$ to $\boldsymbol{q}'$ as it is to move in the reverse direction, namely, that $P(\boldsymbol{q} \rightarrow \boldsymbol{q}') = P(\boldsymbol{q}' \rightarrow \boldsymbol{q})$. This likelihood can be achieved only if the walk is ergodic (an ergodic walk eventually visits all configurations when started from any given configuration) and if it is aperiodic (a situation in which no single number of steps will generate a return to the initial configuration). This latter requirement is known as the "detailed balance" or the "microscopic reversibility" condition:

$$K(\boldsymbol{q} \rightarrow \boldsymbol{q}')\,\rho(\boldsymbol{q}) = K(\boldsymbol{q}' \rightarrow \boldsymbol{q})\,\rho(\boldsymbol{q}') \qquad [5]$$

Satisfying the detailed balance condition ensures that the configurations generated by the gMMC algorithm will asymptotically be distributed according to $\rho(\boldsymbol{q})$.

The transition rate may be written as a product of a trial probability Π and an acceptance probability A

$$K(\boldsymbol{q}_i \rightarrow \boldsymbol{q}_j) = \Pi(\boldsymbol{q}_i \rightarrow \boldsymbol{q}_j)A(\boldsymbol{q}_i \rightarrow \boldsymbol{q}_j) \qquad [6]$$

where Π can be taken to be any normalized distribution that asymptotically spans the space of all possible configurations, and A is constructed so that Eq. [5] is satisfied for a particular choice of Π. The wonderful flexibility with which Π can be chosen is one of the reasons so many Monte Carlo methods are found in the literature. For example, Metropolis et al. used a uniform distribution of points about $\boldsymbol{x}_i$ to define the trial probability (we describe this in greater detail in the next section),[1] but a Gaussian distribution of points can also be used profitably in certain situations.[20] Many other distributions are possible and even desirable in different contexts.

From the detailed balance condition, it is straightforward to show that the ratio of acceptance probabilities, given by r, is

$$r = \frac{A(\boldsymbol{q}_i \rightarrow \boldsymbol{q}_j)}{A(\boldsymbol{q}_j \rightarrow \boldsymbol{q}_i)} = \frac{\Pi(\boldsymbol{q}_j \rightarrow \boldsymbol{q}_i)\,\rho(\boldsymbol{q}_j)}{\Pi(\boldsymbol{q}_i \rightarrow \boldsymbol{q}_j)\,\rho(\boldsymbol{q}_i)} \quad [7]$$

where $r \geq 0$. From this, it can be seen that a rejection method can be used to effectively define the acceptance probability, A:

$$A(\boldsymbol{q}_i \rightarrow \boldsymbol{q}_j) = \min(1, r) \quad [8]$$

Equation [8] is the heart of the gMMC algorithm.

In their original paper, Metropolis et al. considered systems represented within the canonical ensemble, for which the density is given by

$$\rho(\boldsymbol{q}_j) = \frac{\exp\left[-\beta U(\boldsymbol{q}_j)\right] J(\boldsymbol{q})}{Z(N, V, T)} \quad [9]$$

where $Z(N,V,T)$ is the configuration integral, given by

$$Z(N, V, T) = \int d\boldsymbol{q}\, \exp[-\beta U(\boldsymbol{q})]\, J(\boldsymbol{q}) \quad [10]$$

and $J(\boldsymbol{q})$ is the determinant of the Jacobian matrix defining a canonical transformation from Cartesian coordinates $\boldsymbol{x}$ to arbitrary coordinates $\boldsymbol{q}$ ($J(\boldsymbol{q}) = 1$ if Cartesian coordinates are used in the walk).[35] $J(\boldsymbol{q})$ must generally be included because all of the statistical-mechanical integrations are performed in Cartesian coordinates $\boldsymbol{x}$, in which the kinetic energy matrix is diagonal, and not in the arbitrary coordinates $\boldsymbol{q}$.[36] The ratio then becomes

$$r = \frac{\Pi\,(\boldsymbol{q}_j \rightarrow \boldsymbol{q}_i)}{\Pi\,(\boldsymbol{q}_i \rightarrow \boldsymbol{q}_j)} \exp\{-\beta \Delta U\} \frac{J(\boldsymbol{q}_j)}{J(\boldsymbol{q}_i)} \quad [11]$$

where $\Delta U = U(\boldsymbol{q}_j) - U(\boldsymbol{q}_i)$. If Cartesian coordinates $\boldsymbol{x}$ are used in the walk, then $J = 1$ and we need not evaluate the Jacobian at each step to determine the acceptance probability. Metropolis et al. further chose the trial probability to be uniform so that the ratio of the trial probabilities Π cancel in the numerator and denominator of Eq. (11). Then the acceptance probability is simply given by

$$A(x_i \rightarrow x_j) = \min\{1, \exp\{-\beta \Delta U\}\} \quad [12]$$

The implementation of this method is described in detail in the following section.

Metropolis Monte Carlo: The "Classic" Algorithm

Having established the preceding important framework, we now turn to the particulars of the original Metropolis Monte Carlo algorithm for sampling configurations from the canonical ensemble. As alluded to in the previous section, it is often most convenient to work in Cartesian coordinates for MMC calculations (with some exceptions discussed later). In this case, Eqs. [6]–[12] reduce to the algorithm described by the flowchart in Figure 1. First, an initial configuration of the system is established. The initial configuration can be generated randomly, although it is sometimes advantageous to start from an energy-minimized structure,[37] a crystalline lattice structure, or a structure obtained from experiment.

Next, a "trial move" is made to generate a new trial configuration, according to a rule that we call a "move strategy." The simple move strategy introduced by Metropolis et al.[1] is still the most widely used method. One

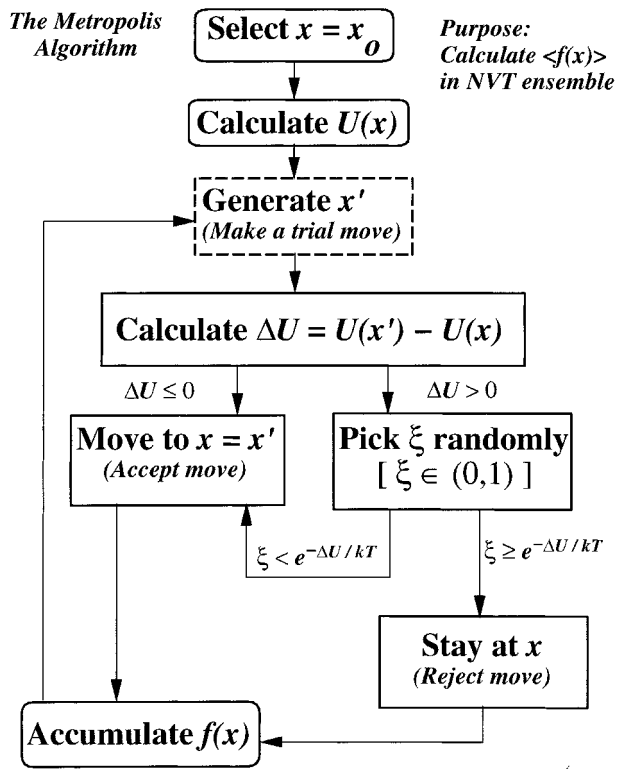

Figure 1 Flowchart of the "classic" Metropolis Monte Carlo algorithm for sampling in the canonical ensemble.[1] Note that samples of the property function $f(x)$ are always accumulated for averaging purposes, irrespective of whether a move is accepted or rejected.

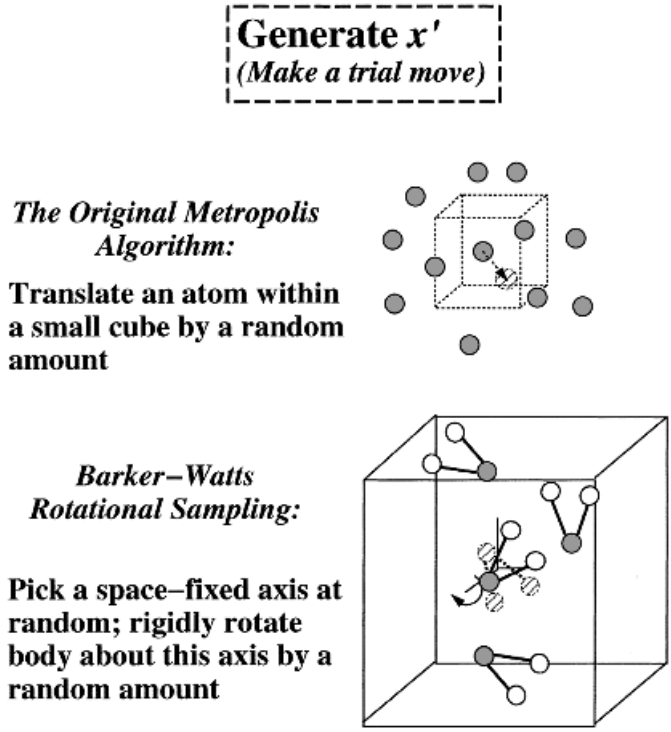

Figure 2 Single-particle Metropolis moves from the original MMC algorithm[1] and molecular rotation Barker–Watts moves[41] for generation of a trial Monte Carlo move.

preselects a maximum stepsize L and randomly moves each particle within a cube of length L centered on the atom's original position (see Figure 2). This procedure defines the Metropolis transition probability, Π_M. For a one-dimensional system moving along a single coordinate x:

$$\begin{aligned} \Pi_M &= \frac{1}{L}, \quad \frac{-L}{2} < x < \frac{L}{2} \\ &= 0 \qquad \text{elsewhere} \end{aligned} \tag{13}$$

The parameter L may have an optimum value for the particular type of atom of interest, as well as for the temperature and other variables studied. If L is too small, most moves will be accepted and a very large number of attempts will be required to move very far from the initial configuration. However, if L is too big very few trial moves will be accepted and again, the walker will require many steps to move away from the starting point. For this reason one generally chooses L so that between 30% and 70% of the moves are accepted (50% is a happy medium).[6,7] Each atom can be moved in sequence,

or an atom can be chosen randomly for each trial move, at the discretion of the programmer.

As noted previously, the Metropolis move strategy of "single-particle moves" is still the most widely used in the literature. The use of single-particle moves is often considered as being part and parcel of the Metropolis Monte Carlo method. However, a number of other move strategies in the canonical ensemble are possible, some of which are outlined later in this chapter. Metropolis Monte Carlo simulations in other ensembles require the use of other move strategies. For example, in the isothermal–isobaric ensemble (constant N,P,T), the volume and the configurations are perturbed.[7,13,38,39] In the grand canonical ensemble (constant chemical potential, V, and T) the number of particles N fluctuates, so a move may include randomly deleting or adding a particle.[11,13,39] The use of the Gibbs ensemble for phase equilibrium studies involves perturbations of volumes and configurations within each phase, as well as the transfer of particles between phases.[10,13,39,40] In all of these situations, suitable move strategies must be employed to ensure that detailed balance is satisfied for all variables involved.

Regardless how it is generated, the trial configuration does not automatically become the second step in the Markov chain. Within the canonical ensemble if the potential energy of the trial configuration is less than or equal to the potential energy of the previous configuration, that is, if $\Delta U \equiv U(\boldsymbol{x}') - U(\boldsymbol{x}) \leq 0$, the trial configuration is then "accepted." However, if $\Delta U > 0$ the trial move may still be conditionally accepted. A random number ζ between 0 and 1 is chosen and compared to $\exp(-\beta\Delta U)$. If ζ is less than or equal to $\exp(-\beta\Delta U)$ the trial move is accepted; otherwise, the trial configuration fails the "Boltzmann test," the move is "rejected," and the original configuration becomes the second step in the Markov chain (see Figure 1). The procedure is then repeated many times until equilibration is achieved (equilibration is defined in a later section). After equilibration, the procedure continues as before, but now the values of U and U^2 (and any other properties of interest, represented by f in Figure 1) are accumulated for each of the remaining n steps in the chain. Let n represent the number of samples used in computing the averages of U and U^2. The number of samples is chosen to be sufficiently large for convergence of $\langle U\rangle_n$ and $\langle U^2\rangle_n$, the n-point averages of U and U^2, to their true values $\langle U\rangle$ and $\langle U^2\rangle$. In the case of U,

$$\langle U\rangle = \lim_{n\to\infty} \langle U\rangle_n \qquad [14]$$

where

$$\langle U\rangle_n \equiv \frac{1}{n}\sum_{j=1}^{n} U(\boldsymbol{x}_j) \qquad [15]$$

Similar formulas hold for $\langle U^2 \rangle$ and $\langle U^2 \rangle_n$. It is important to emphasize that configurations are not excluded for averaging purposes simply because they have been most recently accepted or rejected. Both accepted and rejected configurations must be included in the average, or the potential energies will not be Boltzmann-distributed.

The Barker–Watts Algorithm for Molecular Rotations

The simplest way to generate trial configurations is to use single-particle moves, that is, to change the Cartesian coordinates of individual atoms according to the original MMC procedure presented by Metropolis et al. described in the preceding section.[1] For atomic clusters and liquids, this may be sufficient. However, single-particle moves alone are inefficient for molecular cluster systems, specifically clusters consisting of some finite number of molecules. For such systems it can be useful to also carry out Metropolis moves of each molecule's center of mass and to rotate each molecule within a cluster so as to efficiently generate all possible relative orientations. The Barker–Watts algorithm presented below is an example of such a "generalized Metropolis Monte Carlo" method. It is not limited to cluster systems, but is appropriate for any system for which rotational moves can be useful. Barker and Watts originally developed it for use in simulations of liquid water.[41]

In the Barker–Watts algorithm, a particular molecule is chosen either at random or systematically. One of the three Cartesian axes is selected at random and the molecule is rigidly rotated about the axis by a randomly chosen angle $\Delta\theta$ where $[-\Delta\theta_{MAX} \leq \Delta\theta \leq \Delta\theta_{MAX}]$, as shown in Figure 2. The Cartesian coordinates of each atom within the molecule after the trial move (x', y', z') are calculated from $\Delta\theta$ and the coordinates of that atom in the current configuration (x, y, z). For a rotation about the x axis, for example, the new coordinates would be given by

$$\begin{pmatrix} x' \\ y' \\ z' \end{pmatrix} = \begin{pmatrix} 1 & 0 & 0 \\ 0 & \cos\Delta\theta & \sin\Delta\theta \\ 0 & -\sin\Delta\theta & \cos\Delta\theta \end{pmatrix} \begin{pmatrix} x \\ y \\ z \end{pmatrix} \qquad [16]$$

with a similar expression for rotation about the y axis or the z axis. The new configuration's potential energy is calculated, and the move is accepted or rejected according to the Boltzmann probability. The transition probability is uniform in the chosen coordinate system for each trial move, in the same spirit as the original MMC algorithm.

Equilibration: Why Wait?

As a practical matter, one cannot immediately start accumulating U and U^2 for the computation of averages. The MMC algorithm does not instantly

sample configurations according to the Boltzmann distribution; the sampling is only guaranteed to be correct in the asymptotic limit of large n. It is therefore always necessary to allow the Markov walk to go through a large number of steps before beginning to accumulate samples to estimate U and U^2. This procedure is known as the "equilibration" of the walker.[6,7,10] The walker should undergo a sufficiently large number of iterations for there to be no "memory" of the system's initial configuration. The index value $j = 1$ in Eq. [15] refers to the first configuration after the system has equilibrated by cycling through n_{eq} steps; only states sampled after equilibration should be included in the average. n_{eq} is often referred to as the "equilibration period."

One way to estimate n_{eq} is to calculate the running averages of U and U^2 to make running estimates of E and C_V; these quantities are then plotted against m, the subtotal of all steps taken ($m < n$) at a few representative temperatures to determine when asymptotic, slowly varying behavior is attained.[7] Since E is given by Eq. [3], the running average of U may be plotted instead of E if desired. The running average of U is given by $\langle U \rangle_m$

$$\langle U \rangle_m \equiv \frac{1}{m} \sum_{j=1}^{m} U(\boldsymbol{x}_j) \qquad [17]$$

with a similar formula for $\langle U^2 \rangle_m$. These averages can then be used to form the running estimate of C_V. Alternatively, some authors have advocated the use of crystalline order parameters for this purpose in fluid simulations (but this is not generally practical for cluster simulations).[12] An example of a running-average equilibration study is shown in Figure 3 for a one-dimensional Lennard-Jones oscillator. The Lennard-Jones potential is given by

$$U(r) = 4\varepsilon \left[\left(\frac{\sigma}{r} \right)^{12} - \left(\frac{\sigma}{r} \right)^{6} \right] \qquad [18]$$

where r is the interparticle distance (varied uniformly during the walk according to Eq. [13]) and ε and σ are constants chosen appropriately to represent a particular system of interest (here we have chosen $\varepsilon/k_B = 124$ K and $\sigma = 0.3418$ nm, which would be appropriate for liquid argon[7]). Very low temperatures were considered and all calculations were initiated near the potential energy minimum, so it was not necessary to reject moves resulting in large interatomic separations. An imposed cutoff radius would be needed if higher temperatures were studied.[15,19]

In these plots the thermodynamic quantities go through some initial transient behavior, and then eventually settle down into small-amplitude oscillations. At this very low temperature both U and C_V settle down rapidly and they do so on similar "timescales." Typically, the running averages of U and C_V will not converge simultaneously. In fact C_V will usually be the slower of the two to converge, since its fluctuations arise from fluctuations of the

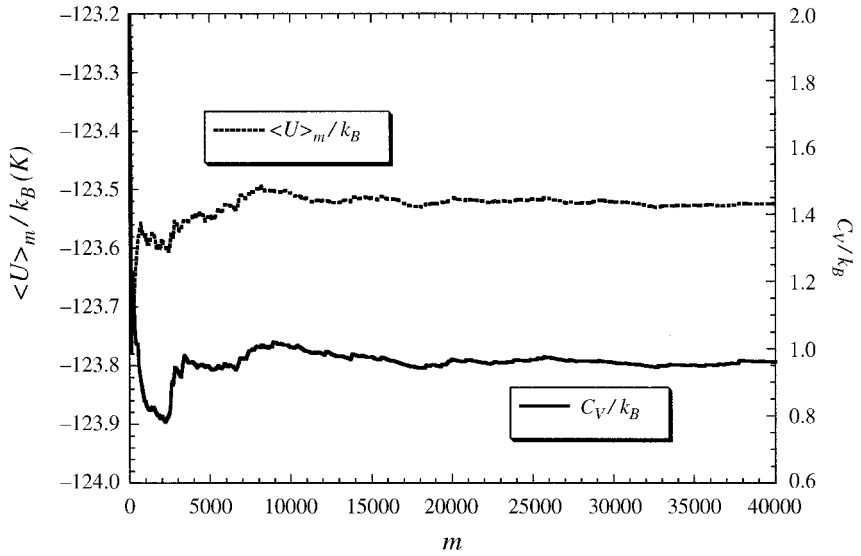

Figure 3 Cumulative values of $\langle U \rangle / k_B$ (dashed line) and C_V/k_B (solid line) for a Monte Carlo simulation of the one-dimensional Lennard-Jones oscillator (see text) at $T = 1$ K. Note that although C_V typically takes longer to equilibrate than does $\langle U \rangle$, there is no significant difference between the two for this simple system at this very low temperature.

potential energy (see Eq. [3]). By looking at these plots at representative temperatures, one chooses a conservative (but affordable) value of n_{eq}, for instance, 15,000 in the present example.

Note that if a different choice of initial conditions is used (e.g., starting from a lattice configuration rather than from a random one), n_{eq} might need to be adjusted (up or down). It is advisable to do a new equilibration study each time one substantially alters the way things are done, or when the system's properties become significantly different (e.g., when one moves substantially above or below a melting transition).

Error Estimation

It is expected that in the limit of large n, $\langle U \rangle_n$ will approach $\langle U \rangle$, that $\langle U^2 \rangle_n$ will approach $\langle U^2 \rangle$, and that both E and C_V will converge to their correct values. But what are the uncertainties in the calculated values of E and C_V? Because the Metropolis method is intrinsically based on the sampling of configurations from a probability distribution function, appropriate statistical error analysis methods can be applied. This fact alone is an improvement on most other numerical integration techniques, which typically lack such strict error bounds.

A significant correlation exists between successive configurations in the Markov walk.[42] In fact, some successive configurations are identical to one another (this happens when the walker rejects an uphill energy move). Because the configurations are correlated, the potential energies (and squared potential energies) that result from the sequence are likewise correlated. In practice, this makes the error analysis somewhat more complicated than it would otherwise be if the configurations were completely uncorrelated. Unfortunately, it is rarely possible to efficiently generate configurations in an uncorrelated manner; to do that, we would be restricted to potential energy functions for which the Boltzmann probability function is analytically integrable, with an integral that is analytically invertible.[5] Very few distribution functions have this property even in one dimension, although the Gaussian distribution function is one such exception.[43]

Fortunately, because there is so much randomness in the MMC algorithm, a configuration (A) spaced by n_{eq} iterations from another configuration (B) will have virtually no correlation with B. Even after equilibration there is a definite correlation length, which we can define qualitatively as the number of iterations required for the algorithm to "forget" where it was originally. We can take advantage of this to determine the errors of our estimates of E and C_V. It is worth noting that most of the following discussion can also be applied to "molecular dynamics" calculations, as well as virtually all algorithms used in molecular simulation work to calculate thermodynamic averages.

If the n samples were statistically independent of one another (which they are not), we could simply estimate σ_U, the error in $\langle U \rangle_n$, by using methods we all learned in our undergraduate laboratory courses.[44] Here we find that σ_U is not given by the standard error formula

$$\sigma_U \neq \sqrt{\frac{\langle U^2 \rangle_n - \langle U \rangle_n^2}{n-1}} \qquad [19]$$

and so one must work a little harder to assess the error. The following approach is effective for estimating the error. If Eq. [19] were an equality, σ_U would give the error at the 67% confidence level; multiplying σ_U by 2 would give a 95% confidence interval (there would be a 95% probability that $\langle U \rangle$ lies between $\langle U \rangle_n - 2\sigma_U$ and $\langle U \rangle_n + 2\sigma_U$). If the samples were uncorrelated, these error bars would be guaranteed to be accurate descriptors of the confidence interval in the limit of large n. A similar formula would hold for $\langle U^2 \rangle$.

However, in the case of a Markov process the variance is only the first (and largest) term in a series of terms, which must be added together. For a general property f, σ_f is given by

$$\sigma_f = \sqrt{\frac{\langle f^2 \rangle - \langle f \rangle^2}{n-1}} + \begin{pmatrix} \text{covariance terms due to the} \\ \text{correlations between } f \text{ values} \end{pmatrix} \qquad [20]$$

where n is the number of steps after equilibration. These covariance terms typically converge slowly; details for treating these kinds of problems can be found elsewhere.[45–48] Another commonly used method is "blocking."[7,12,49] For definiteness, let $n = 1{,}000{,}000$ samples. We divide these samples into $N_B = 100$ blocks of $s = 10{,}000$ samples each, with the first 10,000 samples in block 1, the second 10,000 samples in block 2, and so forth. Within the lth block we form estimates of $\langle U \rangle$ $[\langle U \rangle_s^{\{l\}}]$, and $\langle U^2 \rangle$ $[\langle U^2 \rangle_s^{\{l\}}]$. A list of 100 "block averages" for each property is thus established. The 100 block averages of each property are statistically independent of one another if s is substantially greater than the correlation length. This in turn means they can be analyzed as if they were 100 statistically independent objects. Considering the uncertainty in $\langle U \rangle_n$, we therefore have

$$\sigma_U = \sqrt{\frac{\mathrm{Var}\left[\langle U \rangle_s^{\{l\}}\right]}{N_B - 1}} \qquad [21]$$

where

$$\mathrm{Var}\left[\langle U \rangle_s^{\{l\}}\right] = \frac{1}{N_B} \sum_{l=1}^{N_B} \left[\langle U \rangle_s^{\{l\}} - \langle U \rangle_n\right]^2 \qquad [22]$$

with similar formulas defining σ_{U^2}. Note that σ_U decreases asymptotically as the inverse square root of the number of samples (even though only the number of blocks is explicit), and that $2\sigma_U$ defines the 95% confidence interval for $\langle U \rangle_n$. For published work we generally recommend that the 95% confidence level be reported. Since the thermodynamic energy E is given by Eq. [2] (which is linear in $\langle U \rangle$), Eqs. [21] and [22] also happen to give directly the error in E.

It should be noted that in practice the parameters s and N_B must generally be determined empirically by trial and error, until convergence of the error estimate is achieved at a single temperature. This is usually straightforward in practice, and the prior determination of the equilibration period makes this task considerably easier to achieve because the correlation length is likely to be less than or equal to the equilibration period.

Similar equations and considerations hold for the average of the squared potential energy, but the propagation of the error through Eq. [3] is somewhat more involved. It is simplest to compute N_B values of $(C_V)_s^{\{\ell\}}$, the heat capacity within each block, using Eq. [3], and then using Eq. [23] to obtain the standard error in C_V from the variance of the block heat capacities:

$$\sigma_{C_V} = \sqrt{\frac{\mathrm{Var}\left[(C_V)_s^{\{\ell\}}\right]}{N_B - 1}} \qquad [23]$$

Table 1 Convergence of Approximate 95% Confidence Level Error Estimates of a Metropolis Monte Carlo Estimate of $\langle U \rangle$ and C_V with Respect to the Number of Blocks Used for the One-Dimensional Lennard-Jones Oscillator at $T = 1$ K[a,b]

N_B	$\langle U \rangle / k_B$ (K)	$2\sigma_U$/abs($\langle$U$\rangle$)	C_V/k_B	$2\sigma_{C_V}/C_V$
2	−123.4958	3.3636×10^{-5}	1. 0044	0.0072
4	—	4.2259×10^{-5}	—	0.0109
5	—	1.8810×10^{-5}	—	0.0055
8	—	3.5502×10^{-5}	—	0.0118
10	—	3.3166×10^{-5}	—	0.0102
16	—	2.9819×10^{-5}	—	0.0106
20	—	2.8031×10^{-5}	—	0.0088
25	—	2.6449×10^{-5}	—	0.0093
32	—	2.6552×10^{-5}	—	0.0093
40	—	2.3754×10^{-5}	—	0.0076
50	—	2.2375×10^{-5}	—	0.0083
80	—	2.5355×10^{-5}	—	0.0087

[a]See Eq. [18] and accompanying text.
[b]All calculations given are for a single Metropolis Monte Carlo calculation in which 20,000 equilibration cycles were followed by 500,000 data collection cycles. The stepsize was 0.01 nm, which produced an acceptance ratio of approximately 50%.

In Table 1 we show how the error in the average potential energy and the error in C_V (at the 95% confidence level) depend upon the number of blocks in a sample of fixed size (500,000 samples after 20,000 equilibration cycles) for the one-dimensional Lennard-Jones oscillator at 1 K. As noted previously,

Table 2 Average Potential Energy, Heat Capacity, and Fractional 95% Confidence Level Statistical Errors for the One-Dimensional Lennard-Jones Oscillator[a,b]

$T(K)$	$\langle U \rangle / k_B(K)$	$2\sigma_U$/abs($\langle U \rangle$)	C_V/k_B	$2\sigma_{C_V}/C_V$
0.1	−123.9499	5×10^{-6}	0.999	0.01
0.5	−123.7495	2×10^{-5}	1.002	0.01
1.0	−123.4938	4×10^{-5}	1.008	0.01
1.5	−123.2367	5×10^{-5}	1.020	0.01
2.0	−122.9741	9×10^{-5}	1.022	0.02
2.5	−122.7207	8×10^{-5}	1.027	0.01
3.0	−122.4455	2×10^{-4}	1.043	0.02
3.5	−122.1789	2×10^{-4}	1.048	0.02
4.0	−121.6182	3×10^{-4}	1.053	0.02
4.5	−121.6182	3×10^{-4}	1.063	0.02
5.0	−121.3596	3×10^{-4}	1.060	0.02
5.5	−121.0521	4×10^{-4}	1.076	0.02
6.0	−120.7361	5×10^{-4}	1.100	0.03
6.5	−120.4725	5×10^{-4}	1.104	0.03

[a]See Eq. [18] and accompanying text.
[b]All calculations given are for Metropolis Monte Carlo calculations in which 20,000 equilibration cycles were followed by 500,000 data collection cycles. The stepsize was 0.01 nm, which produced an acceptance ratio of approximately 50%. Ten blocks were used to estimate the statistical errors.

the relative error in C_V is significantly larger than the error in E for the same value of n. This is because the heat capacity represents the mean-squared fluctuations of the energy, and its error is proportional to the root mean square (RMS) fluctuations of the energy's fluctuations. In some cases the blocking technique may fail to effectively "break" the correlations; in such a situation other methods may be employed to estimate the covariance directly.[44–48]

It is important to emphasize that different thermodynamic properties generally converge at different rates. Those rates also generally depend on the temperature and can be quite strong functions of temperature in certain cases (for example, when phase transitions are possible). Table 2 shows how the error in E and the error in C_V vary with temperature for the Lennard-Jones oscillator. For this simple system the temperature dependence of the error is weak, but the trend of gradual increases in the error is evident. Also note that the average potential energy is approximately a linear function of temperature at low temperatures with a slope equal to $k_B/2$ (Figure 4), and that the reduced heat capacity C_V/k_B approaches 1.0 as the temperature approaches zero (Figure 5), both in agreement with the Equipartition Theorem.[10]

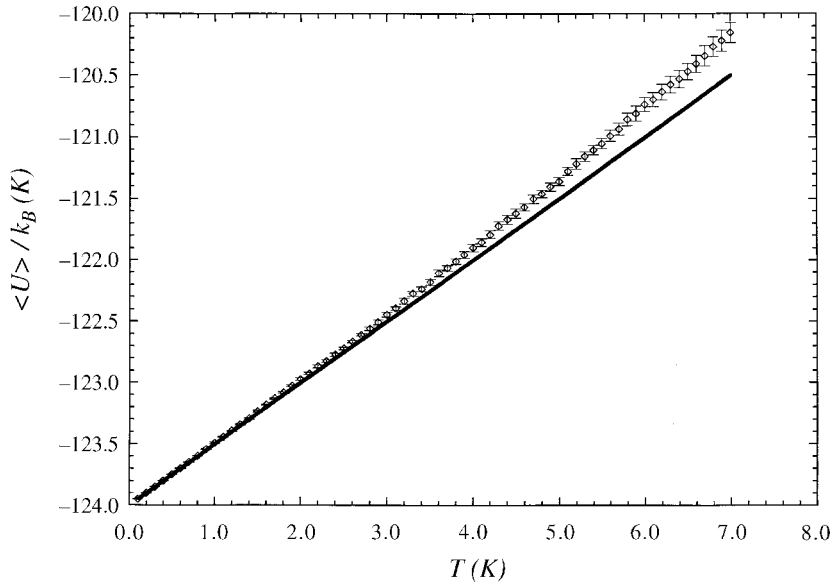

Figure 4 $\langle U \rangle / k_B$ as a function of temperature (diamonds) for the one-dimensional Lennard-Jones oscillator (see text). The Equipartition Theorem requires that the slope approach the harmonic limit ($= \frac{1}{2}$) as the temperature approaches zero (solid line).

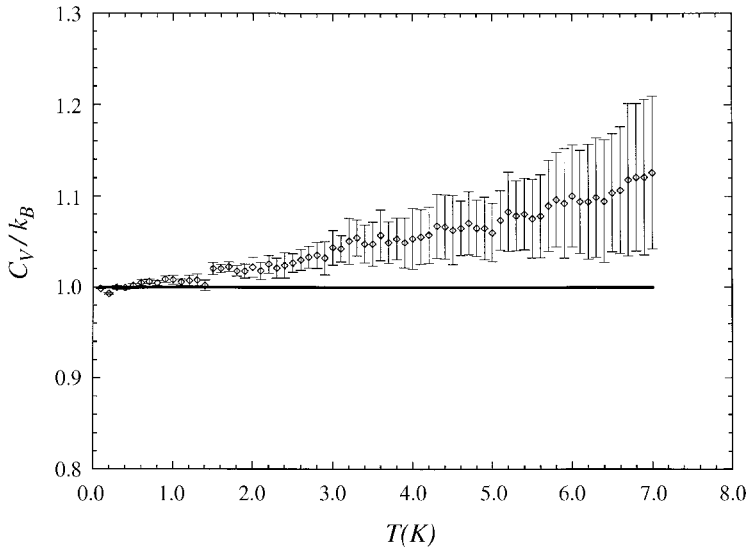

Figure 5 C_V/k_B as a function of temperature for the one-dimensional Lennard-Jones oscillator (see text). The Equipartition Theorem requires that the ratio of the heat capacity to k_B approach the harmonic limit (= 1) as the temperature approaches zero (solid line).

QUASI-ERGODICITY: AN INSIDIOUS PROBLEM

While the methods discussed thus far are sufficiently powerful to allow the simulation of many complex phenomena, there are circumstances where their direct implementation must be modified for efficient sampling. In many important cases the direct application of the preceding strategies with a (necessarily) finite set of points can give misleading or incorrect results.

In Monte Carlo computations of thermodynamic properties, it is often desirable that the sampling be ergodic.[50] In the present context, we define an ergodic random walk as one that can eventually reach every possible state from every possible initial state. A simulation that samples ergodically is typically characterized by low asymptotic variance and by rapid convergence. However, for systems for which there are wells in the potential energy surface that are separated by high barriers, sampling that is confined to a subset of the wells becomes problematic. This type of sampling is termed *quasi-ergodic sampling*.[15,51] When a system is quasi-ergodic it usually appears to be ergodic, exhibiting low asymptotic variance and rapid convergence, thus making quasi-ergodicity particularly difficult to detect. This problem is not unique to Monte Carlo methods, but is also a feature of molecular dynamics calculations and virtually all other molecular simulation methods.

Cluster melting simulations are situations in which special effort must be taken to ensure ergodic sampling. The melting transitions typically occur over a range of temperatures, and clusters can often coexist in solid-like and liquid-like forms (or in several solidlike forms) within this range. The large energy barriers characteristic of "magic number clusters" lead to quasi-ergodic sampling.[15]

To illustrate the kinds of problems to which we refer, we make use of a classical double-well potential that has proved to be useful[52] for the study of quasi-ergodicity:

$$U(x) = \frac{3x^4}{2a+1} + \frac{4(a-1)x^3}{2a+1} - \frac{6ax^2}{2a+1} + 1 \qquad [24]$$

This potential has a minimum of zero energy at $x = 1$, a second minimum of variable energy at $x = -a$ and a barrier of unit height separating the minima at $x = 0$. For $0 \leq a \leq 1$ it is useful to define the relative well depth by

$$\gamma = \frac{U(0) - U(-a)}{U(0) - U(1)} = a^3 \frac{a+2}{2a+1} \qquad [25]$$

For the case $\gamma = 0.9$ ($a = 0.961261$), $U(x)$ is shown in Figure 6. This model potential has many features generic to molecular potential surfaces, in particular

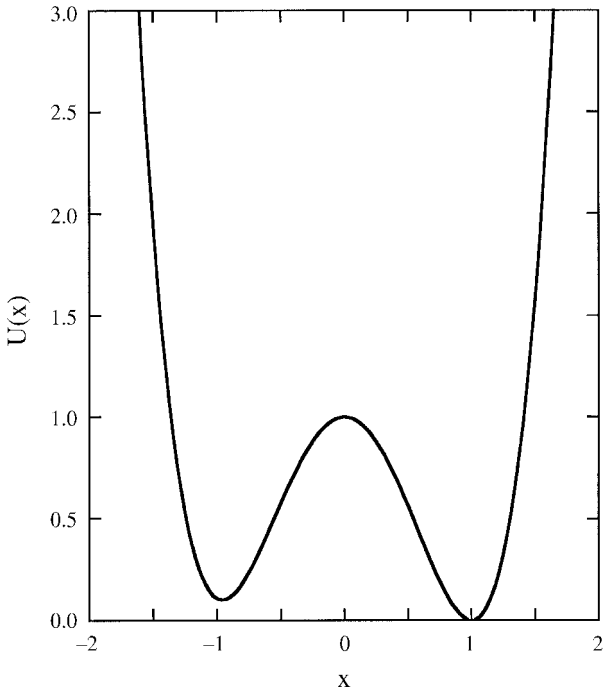

Figure 6 Asymmetric double-well potential $U(x)$ with $\gamma = 0.9$ (see Eqs. [24,25]).

the multiple minima separated by energy barriers. In general we might not know the locations and depths of the minima nor the heights or locations of the barriers that separate the minima on a potential surface. In thinking about the potential shown in Figure 6 it is helpful to imagine what happens in a simulation if the actual structure of the potential surface is not known in advance.

In a Metropolis Monte Carlo calculation, the simulation must be initiated at some configuration. We imagine the result of some random process initiating the walk in the highest-energy well (on the left side in Figure 6). At the lowest temperatures a finite Monte Carlo walk may never leave this well. Thermodynamic properties calculated from such a walk would appear reasonable with the statistical fluctuations in the computed values falling, as expected, with the number of points included. However, such computed thermodynamic properties would reflect contributions only from the left well and thereby be incorrect having ignored the contributions from the lower energy potential minimum. At somewhat higher simulation temperatures, a finite Metropolis Monte Carlo walk may visit both wells, hopping between the wells infrequently. The infrequency implies contributions from the two wells may not be properly weighted, and the resulting calculated thermodynamic property may still be incorrect. Contrary to the situation at low temperatures, the fluctuations of calculated properties at intermediate temperatures may not decrease properly with increasing Monte Carlo points, a behavior that is indicative of a problem in attaining an ergodic result. At sufficiently high temperatures, a Metropolis Monte Carlo walk can be expected to execute transitions over the barrier with sufficient frequency that a correct and well-behaved result follows.

We illustrate the behavior discussed in the previous paragraph with a simulation of the heat capacity associated with an assembly of one-dimensional particles subject to the potential energy expressed in Eq. [24]. We choose to examine the heat capacity because, as a fluctuation quantity, it is particularly sensitive to sampling errors. In Figure 7 we present the computed heat capacity of the double-well potential as a function of temperature. The solid dark line represents the exact results obtained from one-dimensional numerical quadrature. The dotted line with error bars marked "Metropolis" represents MMC data. The MMC calculations were initiated from the leftmost (highest-energy) well represented in Figure 6, and the simulation consists of 10^8 Metropolis Monte Carlo points. The Metropolis box size for the simulation was chosen so that approximately 50% of the attempted Metropolis moves are accepted. At the lowest temperatures both the exact and simulated results agree with the value anticipated from the Equipartition Theorem. However, the exact result rises at low temperatures owing to fluctuations between the two potential wells. The simulated MMC results remain flat because at low temperatures hops between the wells are not observed for a finite set of

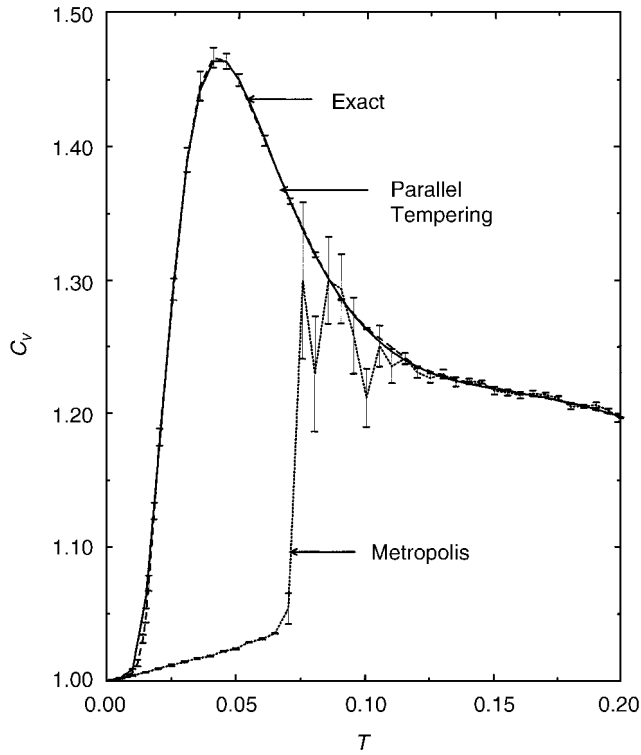

Figure 7 C_V as a function of T for the asymmetric double-well potential shown in Figure 6. The "exact" result (solid line) is obtained by direct integration of the Boltzmann average. "Metropolis" Monte Carlo results (dotted line) are seen to be in sharp disagreement with the exact result until temperatures are sampled that are well above the transition temperature for motion between the two potential energy wells. Parallel tempering Monte Carlo results (dashed line) are in all cases within the 95% confidence interval of the exact result.

Monte Carlo points. As the temperature is increased beyond the heat capacity maximum in the exact result, the MMC simulated points begin to rise but they are in poor agreement with the exact data. Additionally, the calculated error bars increase, but are artificially large in this calculation and do not accurately reflect the true asymptotic fluctuations of the heat capacity. Finally, at the highest calculated temperatures, both the Metropolis Monte Carlo and exact data are in agreement.

Several methods have been developed to remove such difficulties from MMC simulations. One obvious but not very useful method is to include more Metropolis Monte Carlo points. In the limit of an infinite simulation

adding more points is guaranteed to work, but in many cases this is impractical. Another approach, which does work for the present one-dimensional example problem, is to simply extend the original Metropolis scheme. In the Metropolis method one usually chooses a single maximum displacement for each Monte Carlo attempted move (the Metropolis step size). As in the example displayed in Figure 7, the step size is selected so that approximately 50% of the attempted moves are accepted. A simple modification to this procedure is to include two stepsizes. The first, used for most moves, has a size chosen to meet the usual 50% criterion. The second maximum stepsize is chosen to be two units of distance in length (the distance between the two minima in Figure 6). By using this magnified stepsize for a portion of the moves, the barrier between the wells is overcome even at low temperatures. It is not difficult to verify that the occasional inclusion of a magnified stepsize, which we call "mag-walking," satisfies detailed balance.[52]

Mag-walking is sufficiently simple that it can be useful for some many-particle applications where the locations of the barriers between the minima are known in advance. Unfortunately this simple extension, based on two (or more) maximum stepsizes, fails for many important applications of Monte Carlo to interacting many-particle systems. For many-body applications the potential minima are generally separated not just by a distance but also by one or more curvilinear directions. To move from one potential well to another in a many-particle application, specifying the distance between the wells is insufficient. Because the locations of the wells are seldom known in advance, more sophisticated approaches are usually necessary.

From the previous discussion, we see that the problem of adequately sampling a potential energy surface can often be solved with a strategy having two distinct parts. The first part concerns locating the relevant potential minima in the energy surface along with the transition state barriers that separate those minima. The second part concerns the development of a strategy to sample the important minima with the correct statistics. Simulation methods based on this two-part separation strategy have limited utility in cluster studies because the number of minima on a potential surface grows extremely rapidly with the size of the system studied (at a rate believed to be exponential). For example, a cluster of 13 atoms interacting via Lennard-Jones forces is known to have more than 1500 minima,[53] while nanodimensional Lennard-Jones clusters containing 147 atoms are believed to have about 10^{60} minima.[54] It is clearly impossible to enumerate all the minima for the latter cluster, even if a practical procedure were available to sample all such minima. Of course, we are really concerned with only those minima that are actually accessible with a reasonable probability at a given temperature, but the number of such minima can also be unreasonably large. The most successful approaches to proper sampling of complex potential surfaces involve methods that solve both parts in a single step.

OVERCOMING QUASI-ERGODICITY

Mag-Walking

As mentioned previously, the simplest method for addressing quasi-ergodicity is to occasionally magnify the stepsize in a Metropolis walk.[52] A probability P_m is specified, and a magnified stepsize is used if P_m is greater than or equal to a random number ξ. The probability that a magnified move is accepted is the same as that for a regular move. For example, if P_m is chosen to be 0.1 then magnified steps are possible 10% of the time.

This very simple method has a chance of being effective only when the magnified stepsize corresponds to a displacement that is known to carry a molecule from one conformation to another. For example, we have found mag-walking to be useful in certain contexts when applied to Barker–Watts rotational moves; $\Delta\theta_{MAX}$ may be equal to one radian for a regular rotational step, and π radians for a magnified step. We have used this method successfully in simulations of order–disorder transitions in solid ammonium chloride,[55] and in some preliminary investigations of cationic ammonium chloride clusters.[56] However, because one does not usually know a priori what kind of displacement will tend to generate new conformers, mag-walking is of limited utility.

Subspace Sampling

The subspace sampling method developed by Shew and Mills uses transitions among subspaces of the configuration space to overcome quasi-ergodicity.[57] Configuration space is divided into subspaces based on the potential energy surface. For example, for a double-well potential each well would be a subspace defined by the location of the local maximum separating the two wells (subspaces A and B hereafter). A transfer probability P_{AB} is specified and a transfer of the system from configuration i in subspace A to configuration j in subspace B is attempted if P_{AB} is greater than a random number ξ. The transfer is accepted by the probability $A(\boldsymbol{q}_{i,A} \rightarrow \boldsymbol{q}_{j,B})$,

$$A(\boldsymbol{q}_{i,A} \rightarrow \boldsymbol{q}_{j,B}) = c\frac{V_B}{V} \qquad \text{if } U(\boldsymbol{q}_{i,A}) < U(\boldsymbol{q}_{j,B})$$

$$= c\frac{V_B}{V}\exp[-\beta(U(\boldsymbol{q}_{i,A}) - U(\boldsymbol{q}_{j,B}))] \qquad \text{if } U(\boldsymbol{q}_{i,A}) > U(\boldsymbol{q}_{j,B}) \quad [26]$$

where V is the total volume, V_B is the volume occupied by subspace B and c is an empirically chosen constant. As in mag-walking, the subspace sampling

method requires prior knowledge of the potential energy surface to divide configuration space into subspaces. Moreover, the determination of each subspace's volume is only possible when definite rectilinear or spherical boundaries can be drawn which separate and enclose all the subspaces (in which case the volume calculations are trivial). Identifying definite boundaries that correctly separate the relevant subspaces can be challenging. Subspace sampling is therefore generally practical only for low-dimensional systems.

Jump Between Wells Method

The jump between wells (JBW) method developed by Senderowitz, Guarnieri, and Still[58] involves repeated sampling from known low energy conformers to generate a Markov chain. Each trial move is based on the transformation of one low-energy conformer to another and subsequent perturbation of the selected conformer. This method has been shown to work well for relatively small organic molecules, but because it requires knowledge of all low energy conformers, it may not be practical for larger molecules. This limitation applies especially to atomic and molecular clusters, since the location of all low energy conformers may itself be a significant computational challenge.

Atom-Exchange Method

The atom-exchange method was developed by Tsai, Abraham, and Pound[59] to speed barrier crossing in binary (two types of atoms) alloy cluster simulations. During the Metropolis walk two different types of atoms are periodically chosen, and their positions are exchanged. The exchange is accepted or rejected by the standard Metropolis acceptance probability. The utility of this method is naturally limited to systems of this particular type, namely, binary atomic clusters and liquids.

Histogram Methods

The single histogram method[17,60] involves constructing a histogram of energies $h(U)$ that are obtained at an elevated sampling temperature T_s, with $T_s > T$. For continuous systems a large number of bins should be set up to discretize the energy. Because the probability distribution function is known, it can be used to calculate ensemble averages at any temperature T

$$\langle f \rangle = \frac{\sum_U f(U)\, h(U)\, \exp[-U(\beta - \beta_s)]}{\sum_U h(U)\, \exp[-U(\beta - \beta_s)]} \qquad [27]$$

where β_s is $1/k_B T_s$. It is not necessary to actually save the histogram of energies if the summations are carried out over configurations instead of energies:[61]

$$\langle f \rangle = \frac{\sum_i (f(\boldsymbol{x}_i)/\{\exp[-\beta_s U(\boldsymbol{x}_i)]\}) \exp[-\beta U(\boldsymbol{x}_i)]}{\sum_i (1/\{\exp[-\beta_s U(\boldsymbol{x}_i)]\}) \exp[-\beta U(\boldsymbol{x}_i)]} \quad [28]$$

In addition to improving the simulation efficiency, the single-histogram method is designed to alleviate quasi-ergodicity by increasing the effective sampling temperature. The square of the error is proportional to the number of entries in the histogram, so the accuracy is greatest where $h(U)$ is largest and the error is greatest at the wings of the histogram.[62] Thus the limitation of this method is that it may not be accurate for temperatures far below the sampling temperature T_s, whereas T_s must be much higher than T for many cases to overcome quasi-ergodicity.

The accuracy of the histogram method can be improved and its limitations largely overcome by combining multiple histograms with overlapping temperature ranges.[60,63] The density is estimated from a linear combination of the estimates from multiple histograms $h_i(U)$ measured at temperatures T_i. The weight assigned to each estimate is optimized to reduce error through an iterative procedure. The simulated annealing–optimal histogram method takes a different approach wherein simulations at various temperatures are used to generate optimized sampling of energy bins.[17] A more detailed discussion is beyond the scope of this chapter.

Umbrella Sampling

Umbrella sampling is a technique that facilitates barrier crossing by introducing an artificial bias potential, called the "umbrella potential."[4] The umbrella potential optimally biases the sampling toward important regions of configuration space that might otherwise be rarely visited. The probability distribution of the physical system can then be extracted from the probability distribution of the unphysical system. The probability distributions are often analyzed along a "reaction coordinate" ζ, which can be one- or multidimensional and is expressed as a function of the coordinates of the system.[64] The reaction coordinate is often taken to be a distance or angle, or a linear combination of distances or angles.

A modified potential energy function $U_{\text{mod}} = U + E_u(\zeta)$ is constructed, where U is the true potential energy of the system and $E_u(\zeta)$ is the umbrella sampling potential [note that $\zeta = \zeta(\boldsymbol{q})$ in general]. The Boltzmann average of any property f can be computed by using $U_{\text{mod}} = U + E_u$ in place of U in the Metropolis algorithm and calculating the average as

$$\langle f \rangle = \frac{\langle f \exp(\beta E_u) \rangle_{U_{\text{mod}}}}{\langle \exp(\beta E_u) \rangle_{U_{\text{mod}}}} \quad [29]$$

where $\langle B \rangle_{U_{\text{mod}}}$ is the average of B taken using the modified potential function in a Markov walk where moves are accepted or rejected with probability

$$\min\{\, 1, e^{-\beta \Delta U_{\text{mod}}} \}$$

The efficiency of the method depends on the choice of umbrella potential. The limitation of the umbrella sampling method is that the umbrella potential must be appropriately chosen for each system of interest. There are many methods of calculating an appropriate umbrella potential depending on the goals of the simulation.[65] A number of procedures have been developed to automatically and iteratively calculate an umbrella potential for certain types of situations.[66–70] We will also see in a later section that umbrella sampling is used within the multicanonical ensemble. Finally, Valleau has recently reviewed the thermodynamic-scaling Monte Carlo method, which uses umbrella sampling to guide a system between thermodynamic states.[71]

J-WALKING, PARALLEL TEMPERING, AND RELATED METHODS

There is a class of generally applicable Monte Carlo methods that have been developed to address the problem of quasi-ergodicity. These methods involve allowing Metropolis walkers at different temperatures to either "jump" to one another or exchange configurations with one another. These methods generally result in greatly improved sampling, and they are based on two key concepts: (1) at temperatures that are sufficiently high to overcome the barriers between basins on the potential surface, Metropolis Monte Carlo methods are free of serious sampling problems; and (2) the particle density at high (but not infinite) temperatures has a form that reflects the structure of the underlying potential energy surface. Figure 8 illustrates this latter point.

The heavy solid line in Figure 8 represents the double-well potential, redrawn from Figure 6. The light solid line in Figure 8 is the particle density $\exp[-\beta U(x)]$ for $\beta = 1$ and the dashed line is the particle density for $\beta = 5$. The low temperature particle density ($\beta = 5$) is nearly zero in the barrier region near $x = 0$, signaling difficulties in accessing both potential wells in a Metropolis Monte Carlo calculation. At higher temperatures ($\beta = 1$) there is significant particle density in the barrier region, and Metropolis Monte Carlo simulations at such temperatures do not suffer from the sampling problems discussed here. Furthermore, the particle density for $\beta = 1$ reflects the structure of the underlying potential energy surface. The maxima in the particle density are located at the same places as the potential energy minima, with the deeper well associated with the largest particle density. It is desirable to exploit the information contained in the particle density at high temperatures,

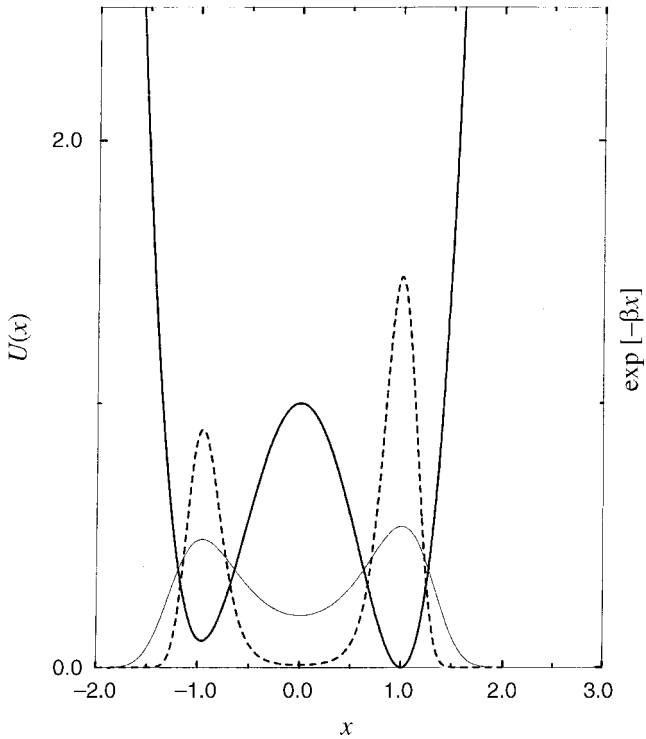

Figure 8 Boltzmann particle densities $\exp[-\beta U(x)]$ at $\beta = 1$ (light, solid line) and $\beta = 5$ (dashed line) for the asymmetric double-well potential $U(x)$ with $\gamma = 0.9$, which is also shown (dark, solid line; see Figure 6).

which is easily generated from a Metropolis calculation, to enable an ergodic simulation at low temperatures where the problems are more serious.

J-Walking

The first method to have been developed using the concepts discussed in the previous paragraph is called J-walking, or alternatively, jump-walking.[52] In the J-walking method a Metropolis calculation is performed at a temperature sufficiently high to avoid ergodic sampling problems. A Monte Carlo walk is then performed at a low temperature that periodically makes moves to the configurations determined by the high-temperature walk. The configurations can be taken from either a walk carried out simultaneously (often called *tandem J-walking*) or configurations that have been stored from a previous high-temperature walk. In the low temperature simulation, where achieving ergodic sampling is problematic, moves are made periodically to the configurations from the high-temperature walk (see Figure 9). Attempts to jump to these

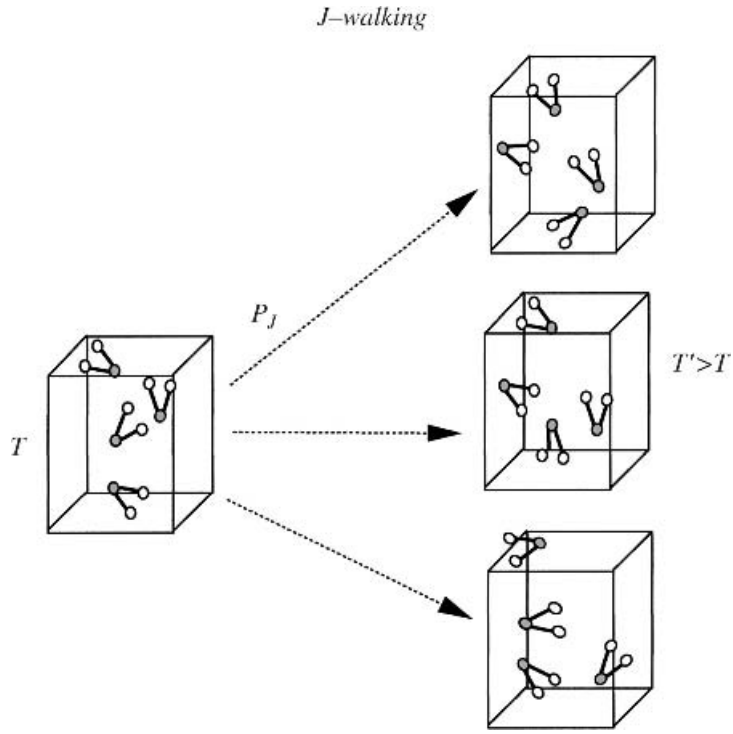

Figure 9 Schematic illustration of J-walking. A Monte Carlo walk at temperature T occasionally "jumps" to a configuration selected (not necessarily sequentially) from a configuration generated by a Monte Carlo walk at a higher temperature T'.

high-temperature configurations are accepted or rejected in a fashion that satisfies the detailed balance relation given in Eq. [5]. Recall that the transition rate may be written as a product of a trial probability Π and an acceptance probability A

$$K(\boldsymbol{x}_i \rightarrow \boldsymbol{x}_j) = \Pi(\boldsymbol{x}_i \rightarrow \boldsymbol{x}_j)A(\boldsymbol{x}_i \rightarrow \boldsymbol{x}_j) \qquad [30]$$

where Π can be taken to be any normalized distribution and A is constructed so that Eq. [30] is satisfied. For example, in Metropolis Monte Carlo the trial probability is usually taken to be a uniform distribution of points about the starting point of width L, as discussed previously. In J-walking the trial probability is taken to be that of the high-temperature configurations, which for classical canonical simulations takes the form

$$\Pi(\boldsymbol{x}_i \rightarrow \boldsymbol{x}_j) = Z_J^{-1} \exp[-\beta_J U(\boldsymbol{x}_i)] \qquad [31]$$

where Z_J is a normalization factor, $\beta_J = 1/k_B T_J$ and T_J is the temperature used to generate the high-temperature configurations. An acceptance probability ensuring satisfaction of detailed balance is given by

$$A(\boldsymbol{x}_i \rightarrow \boldsymbol{x}_j) = \min\left(1, \frac{\rho(\boldsymbol{x}_j)\,\Pi(\boldsymbol{x}_j \rightarrow \boldsymbol{x}_i)}{\rho(\boldsymbol{x}_i)\,\Pi(\boldsymbol{x}_i \rightarrow \boldsymbol{x}_j)}\right) \qquad [32]$$

which, for jumps to the high-temperature configurations in a classical canonical simulation, takes the form

$$A(\boldsymbol{x}_i \rightarrow \boldsymbol{x}_j) = \min(1, \exp(-\Delta\beta\Delta U)) \qquad [33]$$

where $\Delta\beta = \beta - \beta_J$ and $\Delta U = U(\boldsymbol{x}_j) - U(\boldsymbol{x}_i)$. Again, $\beta = 1/k_B T$, where T is the temperature of interest (associated with the low-temperature walk) and β_J is the inverse temperature used to generate the high-temperature external distribution.

The barriers that separate potential wells and make sampling difficult at low temperatures are overcome by jumping periodically to the high-temperature configurations. In this J-walking procedure detailed balance is satisfied to the extent that the configurations in the high-temperature walk are an exact representation of the actual high-temperature probability function (Eq. [31]). Such an exact representation of the actual probability function is possible only in the limit of an infinite external distribution, or when jumps to the tandem distribution are taken after an infinite number of steps. Systematic errors are difficult to remove in the tandem method, so most published applications have used external distributions. In practice a large (but necessarily finite) high-temperature distribution is generated. In the low-temperature simulation most Monte Carlo moves are generated using the Metropolis method with moves to the external high-temperature distribution at some prescribed frequency. In most applications these jump attempts are made about 10% of the simulation time, although higher jump attempt rates have been shown to be optimal in some cases.[72] To ensure that the distribution is sufficiently large (so as to be an accurate representation of the true high-temperature probability function), the distribution size must be larger than the number of jumps attempted in a simulation.

When using finite high-temperature external distributions, another issue arises when applying Eq. [33], because this equation assumes the exact probability is used. This issue is the origin of tandem J-walking problems. When generating the external high-temperature distribution using the Metropolis method, it is important to not store every configuration from that Metropolis walk. As noted previously, configurations generated using a Metropolis walk are correlated,[6] and the correlations can introduce systematic errors when moves are accepted and rejected on the basis of the criterion of Eq. [33]. To avoid these systematic errors it is necessary to store configurations from a

high-temperature Metropolis walk only after a sufficient number of Monte Carlo steps have been taken to break the correlations.

There is a final issue in J-walking that occurs in related simulation methods as well. If the difference in temperature between that used to generate the jumping distribution T_J and the temperature of interest T is sufficiently large, the probability that an attempted jump is accepted can become vanishingly small. When (effectively) no attempted jumps are accepted, the J-walking algorithm is equivalent to a Metropolis walk. Rather than jumping from temperature T to the distribution generated at temperature T_J, a series of temperatures are chosen between T and T_J, and configurations are stored at each of the series of temperatures to circumvent this problem. The temperatures are chosen to be sufficiently close to each other so that jump attempts between adjacent temperatures are accepted with reasonable probability (e.g., at least 10%). J-walking between adjacent temperatures is used to ensure ergodic distributions at each temperature.

To decrease the size of the external distributions needed in J-walking, an alternative method known as "smart walking" has been developed.[73] In smart walking, the energy of each high-temperature configuration is minimized before a jump is attempted. However, smart walking does not satisfy detailed balance.[74] A new technique called "smart darting" has recently been developed that modifies the smart-walking procedure by including the use of "darts," which are displacement vectors connecting the minimum-energy configurations.[74] Smart darting satisfies detailed balance, and it has been applied successfully to calculations of an 8-atom Lennard-Jones cluster and also for the alanine dipeptide.

While J-walking has proved to be useful for many applications,[75–82] the need for a series of large external distributions limits its application to many-body systems having modest numbers of particles. The needed configurations for J-walking can require a prohibitively large portion of both computer memory and disk space. In the next section we describe another approach that obviates the need for external distributions.

Parallel Tempering

Like J-walking, parallel tempering[83–90] addresses sampling problems by using information about the underlying potential surface obtained from a high-temperature walk where sampling is not problematic to ensure proper sampling by a lower-temperature simulation. While high-temperature configurations are fed to a low-temperature walk in J-walking, parallel tempering uses configurations that are exchanged between the high- and low-temperature walkers (see Figure 10).

To understand the basis of parallel tempering, we let

$$\rho_2(\boldsymbol{x}, \boldsymbol{x}') = F^{-1} \exp[-\beta U(\boldsymbol{x})] \exp[-\beta_J U(\boldsymbol{x}')] \qquad [34]$$

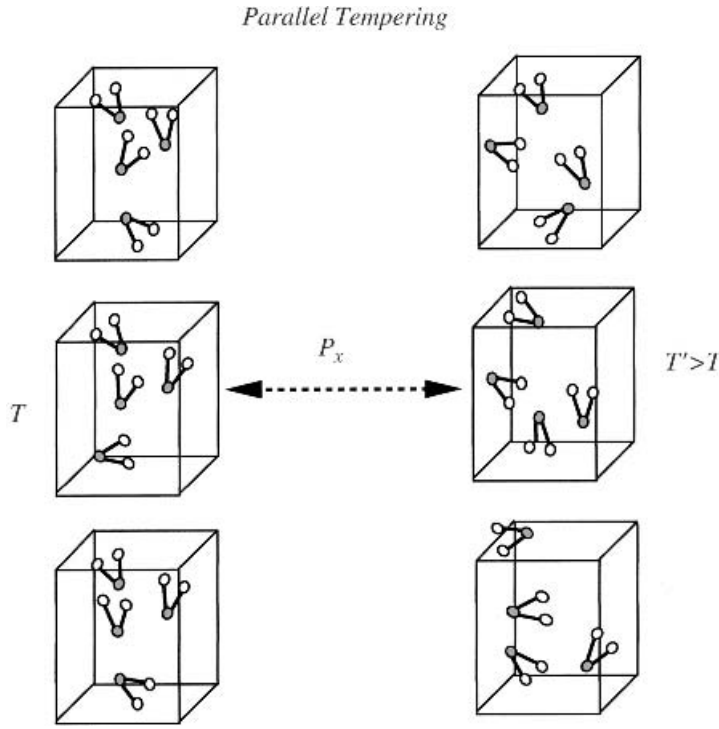

Figure 10 Schematic illustration of parallel tempering. Two Monte Carlo walks at two different temperatures (T and T' with $T' > T$) are executed in parallel, and occasionally the two walks exchange configurations with one another.

be the joint probability density that the low-temperature walker is at configuration $\boldsymbol{x}$ and the high-temperature walker is at configuration $\boldsymbol{x}'$. The detailed balance condition for exchanging configurations between the two walkers is given by

$$\rho_2(\boldsymbol{x}, \boldsymbol{x}')K(\boldsymbol{x} \to \boldsymbol{x}', \boldsymbol{x}' \to \boldsymbol{x}) = \rho_2(\boldsymbol{x}', \boldsymbol{x})K(\boldsymbol{x}' \to \boldsymbol{x}, \boldsymbol{x} \to \boldsymbol{x}') \qquad [35]$$

By solving for the ratio of the conditional transition probabilities

$$\frac{K(\boldsymbol{x} \to \boldsymbol{x}', \boldsymbol{x}' \to \boldsymbol{x})}{K(\boldsymbol{x}' \to \boldsymbol{x}, \boldsymbol{x} \to \boldsymbol{x}')} = \exp\{-(\beta - \beta_J)[U(\boldsymbol{x}') - U(\boldsymbol{x})]\} \qquad [36]$$

it is evident that if exchanges are accepted with the same probability as the acceptance criterion used in J-walking (see Eq. [33]), detailed balance is satisfied.

Like the Metropolis method, and unlike J-walking (which satisfies detailed balance only in the limit that the external distributions required are of infinite size), the parallel tempering approach satisfies detailed balance once the random walk has reached the asymptotic limit. Consequently, no external distributions are required, and parallel tempering can be organized in the same simple fashion as tandem J-walking. The simple organization implies that parallel tempering can be applied to large scale problems.

We illustrate an application of the parallel tempering method again using the double-well potential represented in Eq. [24]. The data have been generated using 28 temperatures roughly equally spaced between $T = 0.002$ and $T = 0.2$ in reduced units. Including a series of temperatures in the simulation ensures adequate acceptance of exchange attempts between adjacent temperatures. As in a J-walking simulation, if the gaps in temperature between adjacent temperatures are too large, exchanges can be accepted too infrequently for parallel tempering to provide an improvement over Metropolis simulations. Each temperature point plotted in Figure 7 is the result of 10^7 equilibration moves followed by 10^8 Monte Carlo points with the accumulation of data. Both the equilibration and Metropolis moves with the accumulation of data used box sizes satisfying the usual 50% acceptance criterion, and parallel tempering exchanges were attempted with a 10% probability. The parallel tempering data in Figure 7, displayed with the dashed line that is labeled "parallel tempering," are essentially indistinguishable from the exact results. Results using the J-walking method would be essentially identical to the parallel tempering data, but the J-walking results require significantly more effort to obtain.

Jumping to Tsallis Distributions

Both J-walking and parallel tempering depend on: (1) a set of configurations generated ergodically at a high temperature and (2) attempted moves to those configurations in a manner that satisfies detailed balance. The use of temperature as a parameter to generate ergodic configurations is not required. Instead, jumping approaches can be developed that use configurations generated in any fashion that are simultaneously ergodic and overcome energy barriers in the potential surface. Tsallis statistics[91] have been used to generate such ergodic configurations. Tsallis distributions are based on the probability function

$$\rho_q(\boldsymbol{x}) = N_q^{-1}[1 - (1 - q)\beta U(\boldsymbol{x})]^{1/(1-q)} \qquad [37]$$

where q is a parameter whose value is optimized for the system of interest. N_q is a normalization defined so that

$$N_q = \int d\boldsymbol{x}\,[1 - (1 - q)\beta U(\boldsymbol{x})]^{1/(1-q)} \qquad [38]$$

The Tsallis probability distribution is equivalent to the classical Boltzmann distribution in the limit $q \to 1$. As shown numerically elsewhere,[92] for $q > 1$ the Tsallis distribution broadens, overcoming energy barriers, and like high-temperature Boltzmann particle densities, the Tsallis distribution has maxima at the coordinates of potential minima. The Tsallis distribution can be used like high-temperature Boltzmann distributions if Tsallis configurations are accepted or rejected with probability

$$\min\left\{1,\ e^{-\beta\Delta U}\left[\frac{\rho_q(\boldsymbol{x})}{\rho_q(\boldsymbol{x}')}\right]^q\right\}$$

Successful applications of jumps to Tsallis distributions have included cluster systems.[92]

Applications to Microcanonical Simulations

Monte Carlo methods can also be applied to systems in the microcanonical ensemble,[7,10] and the techniques just described can be extended to this ensemble as well. For a cluster of N atoms with the same mass m, microcanonical averages of observables are obtained by calculating statistical expectations using the density function

$$\rho_E(\boldsymbol{x}) = \frac{\left(2\pi m/h^2\right)^{3N/2}\{1/[N!\,\Gamma(3N/2)]\}}{\Omega(E)}\,\Theta[E - U(\boldsymbol{x})]\,[E - U(\boldsymbol{x})]^{(3N/2)-1} \qquad [39]$$

where $\Gamma(y)$ is the gamma function, $\Theta(y)$ is the Heaviside (step) function and Ω(E) is the classical density of states[93]

$$\Omega(E) = \frac{1}{h^{3N}N!}\int d\boldsymbol{x}\,d\boldsymbol{p}\,\delta[E - H(\boldsymbol{x},\boldsymbol{p})] \qquad [40]$$

where $\boldsymbol{p}$ is the linear momentum vector, H the classical Hamiltonian, and $\delta[y]$ the Dirac delta function.[35] For example, the average kinetic energy K of a system can be obtained from the expression

$$\langle K\rangle = \frac{\int d\boldsymbol{x}\,\Theta(E-U)\,(E-U)^{(3N/2)-1}(E-U)}{\int d\boldsymbol{x}\,\Theta(E-U)\,(E-U)^{(3N/2)-1}} = \langle (E-U)\rangle \qquad [41]$$

Either parallel tempering[94,95] or J-walking[82] in the microcanonical ensemble consists of taking configurations from a walk at high energy E_h, rather than

from a high temperature. Exchanges or jumps are accepted or rejected with probability

$$\min\left\{1, \frac{\rho_E(\boldsymbol{x}')\rho_{E_b}(\boldsymbol{x})}{\rho_E(\boldsymbol{x})\rho_{E_b}(\boldsymbol{x}')}\right\}$$

Microcanonical parallel tempering has been extended to the molecular dynamics ensemble by introducing the appropriate center of mass and angular momentum constraints, the details of which can be found elsewhere.[94]

MULTICANONICAL ENSEMBLE / ENTROPY SAMPLING

Another class of methods that has been used to remove sampling difficulties is based on what is often called the *multicanonical ensemble*.[96] These methods have also been called "entropy sampling" methods,[97] for reasons that are made clear below.[98] It is easiest to understand the multicanonical methods by considering the full classical canonical coordinate–momentum distribution

$$\rho(\boldsymbol{x}, \boldsymbol{p}) = M^{-1} \exp[-\beta H(\boldsymbol{x}, \boldsymbol{p})] \qquad [42]$$

where M is a normalization factor. The canonical density can also be expressed as a function of the total energy E rather than the coordinates and momenta

$$\rho(\beta, E) = M^{-1}\Omega(E) \exp[-\beta E] \qquad [43]$$

As is discussed in many elementary treatments of statistical mechanics, $\Omega(E)$ is a rapidly increasing function of the energy.[99] Owing to the decay of the exponential factor in Eq. [42], $\rho(\beta, E)$ is a sharp Gaussian distribution, and is peaked about the mean energy associated with the inverse temperature β.

For a Metropolis walk using Eq. [42] the energy of each configuration generated can be tabulated to generate $\Omega(E)$. The sorting of configurations into energy bins is the basis of histogram sampling methods,[17,60,100,101] which (as mentioned previously) are beyond the scope of this chapter. Accurate estimates of $\Omega(E)$ can be achieved only for energies about the average energy of the temperature used to generate the density of states. Consequently, to generate $\Omega(E)$ accurately, calculations must be performed at a series of temperatures. The normalization for each energy distribution so generated must be chosen carefully such that the distributions created for each temperature match. The subtleties associated with this procedure are also beyond the scope of this chapter; for the purposes of this section, we only remark that $\Omega(E)$ can be constructed using a canonical Boltzmann Monte Carlo walk.[17]

Earlier we made clear that Monte Carlo walks can become trapped in regions of space owing to energy barriers that separate the disconnected configurations. In multicanonical methods the energy barriers are overcome by performing a walk in a space with a uniform energy distribution. The energy distribution is defined by the relation

$$\rho_M(E) = M^{-1}\Omega(E)w(E) = \bar{\kappa} \tag{44}$$

where $\bar{\kappa}$ is a constant. We then sample with respect to the distribution

$$w(E) = \frac{\kappa}{\Omega(E)} \tag{45}$$

where $\kappa = \bar{\kappa}M$. It is of interest to write

$$\begin{aligned} \ln w(E) &= \ln \kappa - \frac{k_B}{k_B} \ln \Omega(E) \\ w(E) &= K \exp[-k_B \ln \Omega(E)] \end{aligned} \tag{46}$$

where K is a constant. Using the standard microcanonical expression for the entropy $S = k_B \ln \Omega$,[99] w becomes

$$w(E) = K \exp[-S(E)] \tag{47}$$

Because of expression Eq. [47], multicanonical sampling is often called "entropy sampling."

To calculate canonical averages of an observable $f(\boldsymbol{x}, \boldsymbol{p})$ using the entropy distribution (Eq. [47]), we can implement umbrella sampling methods

$$\langle f \rangle = \frac{\int d\boldsymbol{x}\, d\boldsymbol{p}\, f(\boldsymbol{x}, \boldsymbol{p}) \exp(-\beta H)}{\int d\boldsymbol{x}\, d\boldsymbol{p}\, \exp(-\beta H)} \tag{48}$$

$$= \frac{\left\langle f(\boldsymbol{x}, \boldsymbol{p}) \frac{\exp(-\beta H)}{w} \right\rangle_S}{\left\langle \frac{\exp(-\beta H)}{w} \right\rangle_S} \tag{49}$$

where the subscript S below each average in Eq. [49] implies sampling with respect to the distribution w.

J-walking ideas have also been used in multicanonical approaches[102] as an alternative to calculating expectation values using Eq. [49]. In the multicanonical J-walking approach, periodic jumps are made to the distribution of configurations associated with the entropy distribution w rather than periodic jumps to a set of high-temperature ergodic configurations. To satisfy detailed balance, such jumps are accepted with probability

$$\min\left\{ 1, \frac{\exp[-\beta H(\boldsymbol{x}', \boldsymbol{p}')]\, w[H(\boldsymbol{x}, \boldsymbol{p})]}{\exp[-\beta H(\boldsymbol{x}, \boldsymbol{p})]\, w[H(\boldsymbol{x}', \boldsymbol{p}')]} \right\}$$

From an operational point of view, an important issue when using multicanonical methods is the generation of the multicanonical weight w. Because w is not in general known analytically, w must be generated numerically. Some of the most successful methods for generating w are based on iterative methods, the discussion of which can be found elsewhere.[103] These iterative procedures suffer from oscillatory convergence characteristics, but these convergence problems have been solved using other J-walking based approaches.[104] In practice, the generated multicanonical weights are accurately described at intermediate energies but often provide poor representations at low energies. Consequently, multicanonical methods can be deficient for systems having important low temperature structures that are difficult to access.[88]

CONCLUSIONS

As you perhaps may have noticed, many Monte Carlo methods can be found in the literature. We have not described all of the Monte Carlo methods developed to date. Indeed, new methods are being developed every day, and methods better than those that now exist can be expected to appear in the future. Nonetheless we can make a few definite recommendations to the readers interested in writing their own Monte Carlo programs (especially for studying atomic and molecular clusters) based on existing methodology.

First, it is often useful to study a simple potential such as that given in Eq. [29], and use it as a *minimal* proving ground for testing and implementation of new Monte Carlo algorithms. Such potentials contain some (but not all) of the features of more realistic and complex problems. However, some methods will work well for an asymmetric double-well potential but fail when applied to more complex systems. We therefore warn the reader: let the buyer of a "foolproof" Monte Carlo algorithm beware!

Second, it is advisable to carry out ordinary Metropolis Monte Carlo calculations using Metropolis sampling[1] (with Barker–Watts rotational sampling[41] and center-of-mass moves in addition to single-particle moves if the cluster contains molecules) as a function of temperature before moving to more complex methods. This will help identify the temperature range of greatest importance and indicate how high the temperature must be for quasi-ergodic sampling problems to be avoided. This information can then be used in parallel tempering, J-walking, and other calculations.

Parallel tempering works, and works well in a wide variety of contexts (although the reader should be warned that we are even now finding particularly nasty examples where even parallel tempering converges at an unacceptably slow rate). In our experience, parallel tempering is much simpler to

implement than many of the alternatives. Thus, our final recommendation is that parallel tempering is strongly recommended whenever quasi-ergodicity problems are possible. Parallel tempering can be extremely useful in Monte Carlo studies of atomic and molecular clusters. It also can be used to excellent effect in molecular dynamics simulations, and thus it constitutes an extremely general and powerful technique. We are hopeful that the reader who uses this chapter as a starting point to develop new and improved Monte Carlo methods will find the work as rewarding and interesting as we have.

ACKNOWLEDGMENTS

We are grateful for the efforts of all of our colleagues and students who have helped us understand and use the Monte Carlo method, and other stochastic methods, in our studies of clusters and condensed phases. Our sincere thanks to Sarah Kopel-Fink for assisting with some of the calculations presented here, and to Gayle G. Topper for her help with the literature search. RQT and KRL's work on this chapter was supported in part by the Petroleum Research Fund of the American Chemical Society under grant PRF 33601-B6. DLF's work on this chapter has been supported in part by NSF grant CHE-0095053. DB acknowledges fellowship support from the Enders Memorial Fund, as well from as the Supercomputer Research Institute (SCRI) at Florida State University for a travel grant to attend the 1999 SCRI Monte Carlo Workshop.

REFERENCES

1. N. Metropolis, A. W. Rosenbluth, M. N. Rosenbuth, A. H. Teller, and E. Teller, *J. Chem. Phys.,* **21,** 1087 (1953). Equation of State Calculations by Fast Computing Machines.
2. J. M. Hammersley and D. C. Handscomb, *Monte Carlo Methods,* Methuen, London, 1964.
3. J. P. Valleau and S. G. Whittington, in *Statistical Mechanics Part A: Equilibrium Techniques,* B. J. Berne, Ed., Plenum Press, New York, 1977, pp. 137–168. A Guide to Monte Carlo for Statistical Mechanics: 1. Highways.
4. J. P. Valleau and G. M. Torrie, in *Statistical Mechanics Part A: Equilibrium Techniques*; B. J. Berne, Ed., Plenum Press, New York, 1977, pp. 169–191. A Guide to Monte Carlo for Statistical Mechanics: 2. Byways.
5. K. Binder, in *Monte Carlo Methods in Statistical Physics,* K. Binder. Ed., Springer-Verlag, Berlin, 1979, pp. 1–45. Introduction: Theory and "Technical" Aspects of Monte Carlo Simulations.
6. M. H. Kalos and P. A. Whitlock, *Monte Carlo Methods,* Wiley, New York, 1986.
7. M. P. Allen and D. J. Tildesley, *Computer Simulation of Liquids,* Clarendon Press, Oxford, 1992.
8. J. M. Lluch, M. Moreno, and J. Bertran, in *Computational Chemistry: Structure, Interaction, and Reactivity*; S. Fraga, Ed., Elsevier Science Publishers, Amsterdam, 1992, p. 311. Monte Carlo Simulations for Solutions.
9. D. J. Tildesley, *NATO ASI Ser., Ser. C* (*Computer Simulations in Chemical Physics*) **397,** 1 (1993). The Monte Carlo Method.
10. R. L. Rowley, *Statistical Mechanics for Thermophysical Property Calculations,* PTR Prentice-Hall, Englewood Cliffs, NJ, 1994.
11. D. Frenkel and B. Smit, *Understanding Molecular Simulation: From Algorithms to Applications,* Academic Press, San Diego, 1996.

12. A. R. Leach, *Molecular Modelling: Principles and Applications,* Longman, London, 1996.
13. J. I. Siepmann, *Adv. Chem. Phys.,* **105,** 1–12 (1999). An Introduction to the Monte Carlo Method for Particle Simulations.
14. G. Benedek, T. P. Martin, and G. Pacchioni, Eds., *Elemental and Molecular Clusters: Proc. 13th International School,* Springer-Verlag, Berlin, 1988.
15. D. L. Freeman and J. D. Doll, *Ann. Rev. Phys. Chem.,* **47,** 43–80 (1996). Computational Studies of Clusters: Methods and Results.
16. D. Eisenberg and D. Crothers, *Physical Chemistry with Applications to the Life Sciences,* Benjamin/Cummings, Menlo Park, CA, 1979.
17. D. M. Ferguson and D. G. Garrett, *Adv. Chem. Phys.,* **105,** 311 (1999). Simulated Annealing—Optimal Histogram Methods.
18. B. J. Berne and D. Thirumalai, *Ann. Rev. Phys. Chem.,* **37,** 401–424 (1986). On the Simulation of Quantum Systems: Path Integral Methods.
19. D. L. Freeman and J. D. Doll, *Adv. Chem. Phys.,* **70B,** 139 (1988). The Quantum Mechanics of Clusters.
20. J. D. Doll, D. L. Freeman, and T. L. Beck, *Adv. Chem. Phys.,* **78,** 61–128 (1990). Equilibrium and Dynamical Fourier Path Integral Methods.
21. G. A. Voth, *Adv. Chem. Phys.,* **93,** 135–218 (1996). Path Integral Centroid Methods in Quantum Statistical Mechanics and Dynamics.
22. R. Q. Topper, *Adv. Chem. Phys.,* **105,** 117–170 (1999). Adaptive Path-Integral Monte Carlo Methods for Accurate Computation of Molecular Thermodynamic Properties.
23. J. W. Gibbs, *Elementary Principles in Statistical Mechanics,* Yale Univ. Press, New Haven, CT, 1902.
24. J. H. Halton, *SIAM Rev.,* **12,** 1 (1970). A Retrospective and Prospective Survey of the Monte Carlo Method.
25. F. James, *Rep. Prog. Phys.,* **43,** 73 (1980). Monte Carlo Theory and Practice.
26. W. H. Press, S. A. Teukolsky, W. T. Vetterling, and B. P. Flannery, *Numerical Recipes in FORTRAN: The Art of Scientific Computing,* 2nd ed., Cambridge Univ. Press, Cambridge UK, 1992.
27. J. K. Lee, J. A. Barker, and F. F. Abraham, *J. Chem. Phys.,* **58,** 3166 (1973). Theory and Monte Carlo Simulation of Physical Clusters in the Imperfect Vapor.
28. A. Srinivasan, D. M. Ceperley, and M. Mascagni, *Adv. Chem. Phys.,* **105,** 13–36 (1999). Random Number Generators for Parallel Applications.
29. R. W. Wilde and S. Singh, *Statistical Mechanics: Fundamentals and Modern Applications,* Wiley, New York, 1998.
30. W. L. McMillan, *Phys. Rev.,* **138,** 442 (1965). Ground State of Liquid ^{4}He.
31. J. B. Anderson, in *Reviews in Computational Chemistry,* K. B. Lipkowitz and D. B. Boyd, Eds., Wiley-VCH, New York, 1999, Vol. 13, pp. 133–182. Quantum Monte Carlo: Atoms, Molecules, Clusters, Liquids, and Solids.
32. A. Riganelli, W. Wang, and A. J. C. Varandas, *J. Phys. Chem. A,* **103,** 8303 (1999). Monte Carlo Approach to Internal Partition Functions for Van der Waals Molecules.
33. U. Grenander, *Ark. Matemat.,* **1,** 195 (1950). Stochastic Processes and Statistical Inference.
34. W. K. Hastings, *Biometrika,* **5,** 97 (1970). Monte Carlo Sampling Methods Using Markov Chains and Their Applications.
35. H. Goldstein, *Classical Mechanics,* 2nd ed., Addison-Wesley, Reading MA, 1980.
36. D. A. McQuarrie, *Statistical Mechanics,* HarperCollins, New York, 1976.
37. D. D. Frantz, D. L. Freeman, and J. D. Doll, *J. Chem. Phys.,* **93,** 2769 (1990). Reducing Quasi-Ergodic Behavior in Monte Carlo Simulations by J-Walking: Applications to Atomic Clusters.

38. I. R. McDonald, *Molec. Phys.,* **23,** 41 (1972). NpT-Ensemble Monte Carlo Calculations for Binary Liquid Mixtures.

39. J. I. Siepmann, *Adv. Chem. Phys.,* **105,** 443 (1999). Monte Carlo Methods for Simulating Phase Equilibria of Complex Fluids.

40. A. Z. Panagiotopoulos, *Molec. Phys.,* **61,** 813 (1987). Direct Determination of Phase Coexistence Properties of Fluids by Monte Carlo Simulation in a New Ensemble.

41. J. A. Barker and R. O. Watts, *Chem. Phys. Lett.,* **3,** 144 (1969). Structure of Water: A Monte Carlo Calculation.

42. W. J. Dixon, *Ann. Math. Stat.,* **15,** 119 (1944). Further Contributions to the Problem of Serial Correlation.

43. G. E. P. Box and M. E. Müller, *Ann. Math. Statist.,* **29,** 610 (1958). A Note on the Generation of Random Normal Deviates.

44. J. R. Taylor, *An Introduction to Error Analysis: The Study of Uncertainties in Physical Measurements,* University Science, Mill Valley, CA, 1982.

45. E. B. Smith and B. H. Wells, *Molec. Phys.,* **53,** 701 (1984). Estimating Errors in Molecular Simulation Calculations.

46. T. P. Straatsma, H. J. C. Berendsen, and A. J. Stam, *Molec. Phys.,* **57,** 89 (1986). Estimation of Statistical Errors in Molecular Simulation Calculations.

47. R. Q. Topper and D. G. Truhlar, *J. Chem. Phys.,* **97,** 3647 (1992). Quantum Free-Energy Calculations: Optimized Fourier Path-Integral Monte Carlo Computation of Coupled Vibrational Partition Functions.

48. J. D. Doll and D. L. Freeman, *Chem. Phys. Lett.,* **227,** 436 (1994). Decisions, Decisions: Noise and Its Effect on Integral Monte Carlo Algorithms.

49. J. M. Haile, *Molecular Dynamics Simulation: Elementary Methods,* Wiley, New York, 1992.

50. R. W. Wilde and S. Singh, *Statistical Mechanics: Fundamentals and Modern Applications,* Wiley, New York, 1998.

51. J. I. Siepmann and I. R. McDonald, *Molec. Phys.,* **75,** 255 (1992). Monte Carlo Simulations of Mixed Monolayers.

52. D. D. Frantz, D. L. Freeman, and J. D. Doll, *J. Chem. Phys.,* **93,** 2769 (1990). Reducing Quasi-Ergodic Behavior in Monte Carlo Simulations by J-Walking: Applications to Atomic Clusters.

53. D. B. Faken, A. F. Voter, D. L. Freeman, and J. D. Doll, *J. Phys. Chem.,* **103,** 9521 (1999). Dimensional Strategies and the Minimization Problem: Barrier-Avoiding Algorithms.

54. D. J. Wales and J. P. K. Doye, *J. Phys. Chem.,* **101,** 5111 (1997). Global Optimization by Basin-Hopping and the Lowest Energy Structures of Lennard-Jones Clusters Containing up to 110 Atoms.

55. R. Q. Topper and D. L. Freeman, *Los Alamos Chemical Physics Preprint Database,* #9403002, http://xxx.lanl.gov/archive/physics (1994). Monte Carlo Studies of the Orientational Order-Disorder Phase Transition in Solid Ammonium Chloride.

56. D. Bergin, P. Sweeney, S. Fink, and R. Q. Topper, work in progress.

57. C.-Y. Shew and P. Mills, *J. Phys. Chem.,* **97,** 13824 (1993). A Monte Carlo Method to Simulate Systems with Barriers: Subspace Sampling.

58. H. Senderowitz, F. Guarnieri, and W. C. Still, *J. Am. Chem. Soc.,* **117,** 8211 (1995). A Smart Monte-Carlo Technique for Free-Energy Simulations of Multiconformational Molecules: Direct Calculations of the Conformational Populations of Organic Molecules.

59. N.-H. Tsai, F. F. Abraham, and G. M. Pound, *Surf. Sci.,* **77,** 465 (1978). The Structure and Thermodynamics of Binary Microclusters: A Monte Carlo Simulation.

60. A. M. Ferrenberg and R. H. Swendsen, *Phys. Rev. Lett.,* **61,** 2635 (1988). New Monte Carlo Technique for Studying Phase Transitions.

61. C. J. Tsai and K. D. Jordan, *J. Chem. Phys.,* **99,** 6957 (1993). Use of the Histogram and Jump-Walking Methods for Overcoming Slow Barrier Crossing Behavior in Monte Carlo Simulations: Applications to the Phase Transitions in the $(Ar)_{13}$ and $(H_2O)_8$ Clusters.
62. R. H. Swendsen, *Physica A,* **194,** 53 (1993). Modern Methods of Analyzing Monte Carlo Computer Simulations.
63. P. Labastie and R. L. Whetten, *Phys. Rev. Lett.,* **65,** 1567 (1990). Statistical Thermodynamics of the Cluster Solid-Liquid Transition.
64. O. Engkvist and G. Karlström, *Chem. Phys.,* **63,** 213 (1996). A Method to Calculate the Probability Distribution for Systems with Large Energy Barriers.
65. T. C. Beutler and W. F. van Gunsteren, *J. Chem. Phys.,* **100,** 1492 (1994). The Computation of a Potential of Mean Force: Choice of the Biasing Potential in the Umbrella Sampling Technique.
66. M. Mezei, *J. Comput. Phys.,* **68,** 237 (1987). Adaptive Umbrella Sampling: Self-Consistent Determination of the Non-Boltzmann Bias.
67. J. E. Hunter III and W. P. Reinhardt, *J. Chem. Phys.,* **103,** 8627 (1995). Finite-Size-Scaling Behavior of the Free-Energy Barrier between Coexisting Phases—Determination of the Critical Temperature and Interfacial Tension of the Lennard-Jones Fluid.
68. R. W. W. Hooft, B. P. van Eijck, and J. Kroon, *J. Chem. Phys.,* **97,** 6690 (1992). An Adaptive Umbrella Sampling Procedure in Conformational Analysis Using Molecular Dynamics and Its Application to Glycol.
69. C. Bartels and M. Karplus, *J. Comput. Chem.,* **18,** 1450 (1997). Multidimensional Adaptive Umbrella Sampling: Applications to Main Chain and Side Chain Peptide Conformations.
70. C. Bartels and M. Karplus, *J. Phys. Chem. B,* **102,** 865 (1998). Probability Distributions for Complex Systems: Adaptive Umbrella Sampling of the Potential Energy.
71. J. P. Valleau, *Adv. Chem. Phys.,* **105,** 369 (1999). Thermodynamic-Scaling Methods in Monte Carlo and Their Application to Phase Equilibria.
72. M. Eleftheriou, D. Kim, J. D. Doll, and D. L. Freeman, *Chem. Phys. Lett.,* **276,** 353 (1997). Information Theory and the Optimization of Monte Carlo Simulations.
73. R. Zhou and B. J. Berne, *J. Chem. Phys.,* **107,** 9185 (1997). Smart Walking: A New Method for Boltzmann Sampling of Protein Conformations.
74. I. Andricioaei, J. E. Straub, and A. F. Voter, *J. Chem. Phys.,* **114,** 6994 (2001). Smart Darting Monte Carlo.
75. M. A. Strozak, G. E. Lopez, and D. L. Freeman, *J. Chem. Phys.,* **97,** 4445 (1992). Gibbs Free-Energy Changes for the Growth of Argon Clusters Adsorbed on Graphite.
76. G. E. Lopez and D. L. Freeman, *J. Chem. Phys.,* **98,** 1428 (1993). A Study of Low Temperature Heat Capacity Anomalies in Bimetallic Alloy Clusters Using J-Walking Monte Carlo Methods.
77. D. D. Frantz, *J. Chem. Phys.,* **102,** 3747 (1995). Magic Numbers for Classical Lennard-Jones Cluster Heat-Capacities.
78. C. J. Tsai and K. D. Jordan, *J. Chem. Phys.,* **99,** 6957 (1993). Use of the Histogram and Jump-Walking Methods for Overcoming Slow Barrier Crossing Behavior in Monte Carlo Simulations: Applications to the Phase Transitions in the $(Ar)_{13}$ and $(H_2O)_8$ Clusters.
79. A. Matro, D. L. Freeman, and R. Q. Topper, *J. Chem. Phys.,* **104,** 8690 (1996). Computational Study of the Structures and Thermodynamic Properties of Ammonium Chloride Clusters Using a Parallel Jump-Walking Approach.
80. A. J. Acevedo, L. M. Caballero, and G. E. Lopez, *J. Chem. Phys.,* **106,** 7257 (1997). Phase Transitions in Molecular Clusters.
81. N. Y. Matos and G. E. Lopez, *J. Chem. Phys.,* **109,** 1141 (1998). Classical Monte Carlo Study of Phase Transitions in Rare-Gas Clusters Adsorbed on Model Surfaces.
82. E. Curotto, D. L. Freeman, and J. D. Doll, *J. Chem. Phys.,* **109,** 1643 (1998). A J-Walking Algorithm for Microcanonical Simulations: Applications to Lennard-Jones Clusters.

83. E. Marinari and G. Parisi, *Europhys. Lett.,* **19,** 451 (1992). Simulated Tempering: A New Monte Carlo Scheme.

84. C. J. Geyer and E. A. Thompson, *J. Am. Stat. Assoc.,* **90,** 909 (1995). Annealing Markov-Chain Monte-Carlo with Applications to Ancestral Inference.

85. M. C. Tesi, E. J. Janse van Rensburg, E. Orlandini, and S. G. Whittington, *J. Stat. Phys.,* **82,** 155 (1996). Monte Carlo Study of the Interacting Self-Avoiding Walk Model in Three Dimensions.

86. M. Falcioni and M. W. Deem, *J. Chem. Phys.,* **110,** 1754 (1999). A Biased Monte Carlo Scheme for Zeolite Structure Solution.

87. Q. Yan and J. J. de Pablo, *J. Chem. Phys.,* **111,** 9509 (1999). Hyper-Parallel Tempering Monte Carlo: Application to the Lennard-Jones Fluid and the Restricted Primitive Model.

88. J. P. Neirotti, F. Calvo, D. L. Freeman, and J. D. Doll, *J. Chem. Phys.,* **112,** 10340 (2000). Phase Changes in 38-Atom Lennard-Jones Clusters. I. A Parallel Tempering Study in the Canonical Ensemble.

89. M. R. Ghayal and E. Curotto, *J. Chem. Phys.,* **113,** 4298 (2000). The Melting of Ar_{54}–HF: A Canonical Parallel Tempering Simulation.

90. D. D. Frantz, *J. Chem. Phys.,* **115,** 6136 (2001). Magic Number Behavior for Heat Capacities of Medium-Sized Classical Lennard-Jones Clusters.

91. C. Tsallis, *J. Stat. Phys.,* **52,** 479 (1988). Possible Generalization of Boltzmann-Gibbs Statistics.

92. I. Andricioaei and J. E. Straub, *J. Chem. Phys.,* **107,** 9117 (1997). On Monte Carlo and Molecular Dynamics Methods Inspired by Tsallis Statistics: Methodology, Optimization, and Application to Atomic Clusters.

93. J. I. Steinfeld, J. S. Francisco, and W. L. Hase, *Chemical Kinetics and Dynamics,* Prentice-Hall, Englewood Cliffs NJ, 1989.

94. F. Calvo, J. P. Neirotti, D. L. Freeman, and J. D. Doll, *J. Chem. Phys.,* **112,** 10350 (2000). Phase Changes in 38-Atom Lennard-Jones Clusters. II. A Parallel Tempering Study of Equilibrium and Dynamic Properties in the Molecular Dynamics and Microcanonical Ensembles.

95. E. Curotto, *J. Chem. Phys.,* **114,** 4533 (2001). The HF Stretch Red Shift as a Function of Internal Energy in Ar_n – HF ($n = 12,54$): Comparisons in the Microcanonical Ensemble.

96. B. A. Berg and T. Neuhaus, *Phys. Lett. B,* **267,** 249 (1991). Multicanonical Algorithms for First Order Phase Transitions.

97. J. Lee, *Phys. Rev. Lett.,* **71,** 211 (1993). New Monte Carlo Algorithm: Entropic Sampling.

98. B. A. Berg, U. H. E. Hansmann, and Y. Okamoto, *J. Phys. Chem.,* **99,** 2236 (1995). Comment on "Monte Carlo Simulation of a First-order Transition for Protein Folding."

99. R. S. Berry, S. A. Rice, and J. Ross, *Matter in Equilibrium: Statistical Mechanics and Thermodynamics,* 2nd ed., Oxford Univ. Press, New York, 2002.

100. R. H. Swendsen and J. S. Wang, *Phys. Rev. Lett.,* **58,** 86 (1987). Nonuniversal Critical Dynamics in Monte Carlo Simulations.

101. P. Labastie and R. L. Whetten, *Phys. Rev. Lett.,* **65,** 1567 (1990). Statistical Thermodynamics of the Cluster Solid-Liquid Transition.

102. H. Xu and B. J. Berne, *J. Chem. Phys.,* **110,** 10299 (1999). Multicanonical Jump Walking: A Method for Efficiently Sampling Rough Energy Landscapes.

103. Y. Okamoto and U. H. E. Hansmann, *J. Phys. Chem.,* **99,** 11276 (1995). Thermodynamics of Helix-Coil Transitions Studied by Multicanonical Algorithms.

104. M-H. Hao and H. A. Scheraga, *J. Phys. Chem.,* **98,** 9882 (1994). Statistical Thermodynamics of Protein-Folding Sequence Dependence.

CHAPTER 2

Computing Hydrophobicity

David E. Smith* and A. D. J. Haymet†

Department of Chemistry and Biochemistry, New Mexico State University, Las Cruces, New Mexico 88003-8001 and Department of Chemistry, University of Houston, Houston, Texas 77204-5003
**Author for correspondence*
†Present address: CSIRO Marine Research, GPO Box 1538 Hobart, TAS 7001 Australia

INTRODUCTION

We provide here a tutorial on how to compute hydrophobicity. *Hydrophobicity*, which in literal Greek translation means water hating or loathing, is often the "concept of last resort" when trying to explain complex association and assembly phenomena in biology and biophysics.[1] We are fond of speculating on the SI unit of such hate or loathing.[2]

Many papers claim to discuss hydrophobicity. Regrettably, many present comparisons with neither laboratory experiments nor with computer experiments. The days of such papers having any value are—in our opinion—far in the past. We argue that a respect for the experimental data is essential, that one must seek to explain the set of verifiable experimental observations in order to fully understand hydrophobicity. This rigorous, thermodynamic, factual, and experimental approach to hydrophobicity is the antithesis of the "opinions" so clearly and insightfully summarized a decade ago by Blokzijl

Reviews in Computational Chemistry, Volume 19
edited by Kenny B. Lipkowitz, Raima Larter, and Thomas R. Cundari
ISBN 0-471-23585-7

and Engberts.[3] A number of recent, important, advanced reviews in the same vein now exist.[4,5]

This chapter summarizes the methods used to calculate hydrophobicity on a computer. It is important to state here what the chapter does and does not do. It treats only methods for which full details have been published in the literature. It treats work that is therefore refutable by appealing directly to real experiments or, for certain simplified models, to computer experiments of known or knowable accuracy. To make a manageable chapter covering computational approaches for which all details have been published, we omit those concepts that have been summarized in clear and elegant fashion,[5] like the "maximal entropy" method of Hummer and co-workers.[6,7]

Our approach to "computing hydrophobicity" is to work from experimental data and move toward simplified explanations, omitting models and theories that have already been disproved by experiment. This approach is illustrated with the elegant experiment of Hare and Sorensen,[8,9] who for the first time put a solid experimental foundation under the otherwise obtuse expression "the degree of hydrogen bonding" in pure liquid water. These authors presented Raman spectroscopic measurements on the OH stretch region of pure water (2900–3800 cm^{-1}) covering the remarkable range of temperatures from -33 to $+80°C$. They provided an unambiguous interpretation (albeit one not without controversy) of the behavior of two Raman peaks that grow and decay as a function of temperature change. Their data are reproduced in Figure 1. They associated these two peaks with (perhaps collective) "intact" and "broken" hydrogen bonds, which leads naturally to a simplified "two state" description of the degree of hydrogen-bonding in water and supercooled water. The parameters extracted from their measurements were shown by Silverstein, Haymet, and Dill[10] 10 years later to be consistent with the independently measured heat capacity of water, whereas six or seven other *different* experimental definitions of the degree of H bonding were inconsistent with the thermodynamic data. This experimental data with a seemingly oversimplified model thus yielded a neat and easy-to-explain connection between the concepts of hydrogen-bonding and hydrophobicity!

Additional experimental data of direct relevance to this chapter are the many thermodynamic measurements of gas solubility. An extensive set of experimental measurements below water's normal boiling point have been compiled and reviewed by Wilhelm, Battino, and Wilcock.[11] Solubility data at higher temperatures are available from a more recent article by Fernández Prini and Crovetto.[12] Gas solubilities are often tabulated in terms of the Ostwald solubility coefficient

$$L = \frac{\rho_2^l}{\rho_2^g} \qquad [1]$$

where ρ_2^l and ρ_2^g are the gas density in the liquid and vapor phases, respectively. The nonideal portion of the free energy of solvation, also called the

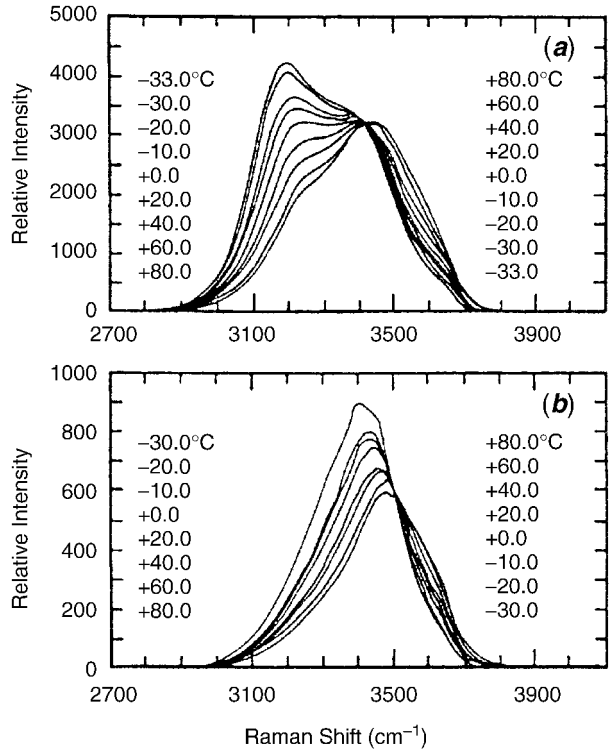

Figure 1 Raman data in the OH stretch region of water at temperatures ranging from −33 to +80°C (from Hare and Sorensen[8]). Data for scattered light with vertical and horizontal polarization are displayed in (*a*) and (*b*), respectively, and are normalized using a method described by the authors.

excess chemical potential (μ^{ex}), is directly related to L via

$$\mu^{ex} = -RT \ln L \qquad [2]$$

Plots of μ^{ex} versus temperature for neon and methane gases in water are displayed in Figure 2. The solubility of these gases in water is very small, as indicated by the large positive values of μ^{ex}. The positive slope and negative curvature of each plot reveal a large negative entropy and a large positive heat capacity of solvation, respectively. Near room temperature, the low solubility of nonpolar gases is due entirely to this unfavorable entropy of hydration. As the temperature increases, however, the heat capacity leads to a reversal in the role of entropy and enthalpy. The entropy and heat capacity of hydration together provide clear thermodynamic signatures for hydrophobicity. Understanding the origin of these signatures has been a primary goal of

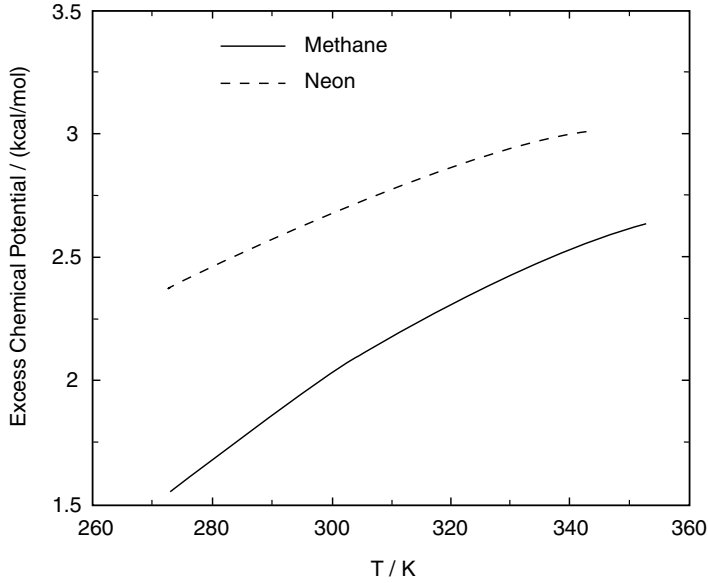

Figure 2 Excess chemical potentials (μ^{ex}) for methane and neon gases plotted as a function of temperature (data taken from Ref. 11). The positive slope and negative curvature of each function indicate a negative entropy and a positive heat capacity of hydration, respectively.

hydrophobicity research for decades and constitutes a main focus of what follows in this tutorial.

The chapter contains three main sections. In the first, we present a detailed but not exhaustive survey of simulation methods for the calculation of free energy, entropy, and heat capacity. This is followed by a section that discusses results from several hydrophobic hydration and hydrophobic interaction simulations. These applications are then used in the last section of this chapter to illustrate the simulation methods and to highlight several important conceptual developments in the theory of hydrophobicity.

SIMULATION METHODS

Molecular dynamics (MD) and Monte Carlo (MC) simulation techniques have been used now for decades to characterize aqueous solutions. The most basic elements that underlie these techniques, such as numerical integration algorithms and the Metropolis method, are discussed thoroughly elsewhere,[13,14] so they are not included here. Our intention here is to survey methods used for determining the thermodynamic and structural quantities most closely tied to hydrophobicity.

One might anticipate that quantitative aspects of hydrophobicity would be sensitive to details of the water model used in a simulation. This may seem troubling given the dozens of popular water models discussed in the literature. However, there is little evidence that subtle changes in water interaction potentials have any qualitative effect on the nature of hydrophobicity, as illustrated by the finding that a two-dimensional model for water reproduces all the thermodynamic signatures usually associated with hydrophobicity.[15] Accordingly, water model details are omitted from the ensuing discussion.

Most of the applications discussed below involve atomic solutes with either hard-sphere (HS) or Lennard-Jones (LJ) solute–water interaction potentials. The potential energy of a HS is infinite if the solute–oxygen distance is less than the sum of the solute and water HS radii and zero otherwise. An effective HS radius is assigned to water in some reasonable fashion.[16] The solute–water LJ interaction has the form

$$U_{\mathrm{LJ}}(r) = 4\epsilon\left[\left(\frac{\sigma}{r}\right)^{12} - \left(\frac{\sigma}{r}\right)^{6}\right] \qquad [3]$$

where σ and ϵ are size and well-depth parameters, respectively. The Weeks–Chandler–Andersen[17] (WCA) interaction potential provides a useful representation of the repulsive part of the LJ function, and is given by

$$U_{\mathrm{WCA}}(r) = U_{\mathrm{LJ}}(r) + \epsilon \qquad r < 2^{1/6}\sigma \qquad [4]$$

$$U_{\mathrm{WCA}}(r) = 0 \qquad r \geq 2^{1/6}\sigma \qquad [5]$$

A plot of the LJ and WCA potentials is displayed in Figure 3. Simple solutions modeled with these solute-water potentials capture a wide range of hydrophobic behavior without the complications inherent in biochemical systems.

Statistical Mechanics and Thermodynamics

Computer simulations of hydrophobicity usually involve the measurement of thermodynamic properties because the most basic signatures of hydrophobic phenomena are thermodynamic in nature. In this section, we briefly review the relationships between the classical partition function and various thermodynamic quantities. These relationships provide the basis for most of the simulation methods described subsequently.

A system of N particles under thermodynamic constraints of constant volume and temperature is described by the canonical ensemble partition function Q. In the classical limit for a three-dimensional system Q is given by

$$Q = \frac{1}{N!h^{3N}}\int d\mathbf{r}^N d\mathbf{p}^N \exp[-\beta\mathcal{H}(\mathbf{r}^N, \mathbf{p}^N)] \qquad [6]$$

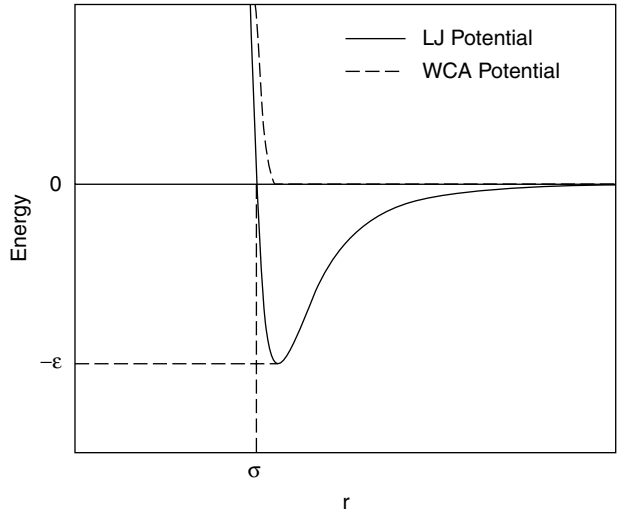

Figure 3 Plot of the LJ and WCA interaction potentials. The LJ potential energy crosses zero at $r = \sigma$ and has a minimum energy of $-\epsilon$. The WCA potential has the same shape as the repulsive part of the LJ potential, but is shifted up in energy by ϵ.

where $\mathcal{H}(\mathbf{r}^N, \mathbf{p}^N)$ is the N-particle Hamiltonian. The variable β equals $1/k_B T$, where k_B is the Boltzmann constant. Separating out the momentum terms yields the "configurational" partition function, Z_N, with

$$Z_N = \int d\mathbf{r}^N \exp[-\beta \mathcal{U}(\mathbf{r}^N)] \qquad [7]$$

The configurational energy of the system $\mathcal{U}(\mathbf{r}^N)$ is calculated directly from the assumed interaction potentials and the particle positions in a computer simulation. The Helmholtz free energy A, energy E, and entropy S are given in terms of Q by

$$A = -k_B T \ln Q \qquad [8]$$

and

$$E = k_B T^2 \left(\frac{\partial \ln Q}{\partial T} \right)_{N,V} \qquad [9]$$

and

$$S = k_B T \left(\frac{\partial \ln Q}{\partial T} \right)_{N,V} + k_B \ln Q \qquad [10]$$

Simulations are commonly used to determine the excess parts of these thermodynamic variables. The excess Helmholtz free energy is given in terms of Z_N as

$$A^{\text{ex}} = -k_B T \ln \frac{Z_N}{V^N} \qquad [11]$$

Similar expressions are easily derived for for S^{ex} and E^{ex}.

Generally, a full evaluation of the partition function for a system is impossible. Computer simulations rely instead on calculating averages, expressed in terms of the configurational partition function as

$$\langle X \rangle = \frac{1}{Z_N} \int d\mathbf{r}^N X(\mathbf{r}^N) \exp[-\beta U(\mathbf{r}^N)] \qquad [12]$$

where X is any observable quantity.

Expressions similar to those given above may be derived easily from partition functions in other ensembles.[13,14] The choice of ensemble is very important in calculations of hydration entropy, enthalpy, and heat capacity, as discussed below. Many other quantities, including all free energies, are ensemble invariant, with the choice of ensemble affecting only system size dependence. For simplicity, the discussion here is therefore limited to the canonical ensemble except in such cases where a true ensemble dependence exists.

Particle Insertion Methods

The test particle method of Widom[18,19] and related particle insertion schemes reviewed recently by Kofke and Cummings[20] have been used extensively to investigate the hydration of small nonpolar molecules. Widom's approach to this problem involves performing NVT-ensemble simulations of pure water. A variety of solution properties may be investigated by measuring the energy of solute molecules randomly inserted into the pure solvent. These "test particles" probe the system but do not affect the solvent trajectories. The excess chemical potential of a solute molecule is thus calculated as

$$\mu^{\text{ex}} = -k_B T \ln \langle e^{-\beta \Phi} \rangle_N \qquad [13]$$

where the test particle energy Φ is the change in the total energy on addition of the test particle. The brackets indicate an average over pure solvent configurations, each containing N molecules.

The derivation of this relationship from the canonical ensemble partition function is straightforward. It is given here to illustrate the type of partition function manipulations commonly used in developing simulation expressions for thermodynamic quantities. The excess chemical potential is defined as the Helmholtz free energy difference between two $(N+1)$-particle systems, one

with a full solute particle and the second with a noninteracting, ideal-gas solute particle:

$$\mu^{ex} = A_{N+1} - A_{N+id} = A^{ex}_{N+1} - A^{ex}_{N} \quad [14]$$

The second equality follows since the ideal parts of each system's partition function are equivalent. Substituting Eq. [11] into this expression and rearranging yields

$$\mu^{ex} = -k_B T \ln \frac{Z_{N+1}}{V Z_N} \quad [15]$$

Evaluating the ratio using Eqs. [7] and [12] gives

$$\mu^{ex} = -k_B T \ln \frac{\int dr_s \left\langle e^{-\beta\Phi(r_s)} \right\rangle}{V} \quad [16]$$

where r_s is the solute particle position. Widom's formula follows directly by noting that, for a spatially homogeneous system, $\left\langle e^{-\beta\Phi(r_s)} \right\rangle$ does not depend on r_s. The integral in the numerator therefore yields a volume term that cancels the V in the denominator.

While formally exact, Widom's formula is of practical use only for small solutes up to around the size of methane or xenon. This limitation exists because the value of $\left\langle e^{-\beta\Phi} \right\rangle$ is dominated by relatively few low-energy insertions where there is little or no overlap between the solute and solvent molecules. Sampling of these low energy states requires the spontaneous formation of solute-sized cavities in the solvent, an event that is common for very small solutes but becomes exceedingly rare as solute size increases.

In addition to solute excess chemical potentials, test particle methods may be used to determine a variety of solution properties via Eq. [17]:

$$\langle A \rangle_{solution} = \frac{\left\langle A e^{-\beta\Phi} \right\rangle_N}{\left\langle e^{-\beta\Phi} \right\rangle_N} \quad [17]$$

where A is the value of an observable quantity. The averages on the right-hand side are again taken over pure solvent configurations. Among its many uses, this expression may be used to calculate solute–solvent[21] and solute–solute[19,22] radial distribution functions, with the latter requiring the simultaneous insertion of pairs of test particles. This is discussed further in the section on potential of mean force calculations.

Alternative test particle expressions for use in *NPT*- and *NVE*-ensemble simulations have also been derived, with relevant expressions given in Frenkel and Smit.[14] Local density fluctuations play an important role in generating solvent configurations that are favorable for solute insertion. When the length

scale of density fluctuations is large relative to the simulation box length, either due to small system size or being in the vicinity of a critical point, a constant pressure approach is required. The *NVE*-ensemble expression is useful for conventional (microcanonical) MD simulations.

For hard-sphere solutes, the test particle energy Φ has only two possible values, infinity or zero, depending on whether the solute overlaps with a solvent molecule. In this case, Eq. [13] becomes

$$\mu^{ex} = -k_B T \ln p_0 \qquad [18]$$

where p_0 is the probability that there are no solvent molecules within the overlap distance of the test particle. The probability of insertion of a hard-sphere solute is equivalent to the probability of finding a spontaneously formed cavity of the appropriate size in the pure solvent. Analysis of cavity statistics in liquids or near solutes provides a simple yet powerful approach for analysis of hydrophobicity.[23–25] The information theory (IT) of hydrophobicity, reviewed by Pratt,[5] provides a means for predicting the value of p_0 for larger solutes.

A key strength of the test particle approach is that quantities may be evaluated simultaneously for a wide range of solutes from a single pure water simulation. This is particularly useful for evaluation of theoretical models of hydrophobic hydration as a function of either solute size or the strength of solute–solvent attractions. Nevertheless, the test particle approach is severely limited in its applicable size range. Treatment of larger solutes requires use of thermodynamic integration or free-energy perturbation methods, of which the test particle approach is a special case. These methods are discussed below. The overlapping distribution method[20,26,27] is closely related to Widom's test particle method. The approach involves two simulations, one of pure water as before and one with a single solute particle present. It is easy to show that the chemical potential may be determined not only by the insertion formula in Eq. [13] but also by a deletion formula

$$\mu^{ex} = k_B T \ln \langle e^{\beta\Phi} \rangle_{N+1} \qquad [19]$$

where the $N+1$ subscript indicates that the average is calculated from the solute–water system. As before, Φ is the difference in energy between the systems with and without the solute molecule included, although it is now calculated via a deletion process. Equation [19] is of little direct value in calculating the chemical potential since pure solvent configurations are improperly sampled in the $N+1$ molecule simulation.[20] Nevertheless, the information contained in the simulation may be used effectively as follows. Probability distribution functions $p_N(\Phi)$ and $p_{N+1}(\Phi)$ for the solute particle energy are calculated from the N and $N+1$ molecule simulations, respectively. The information contained in $p_N(\Phi)$ may be used to determine μ^{ex} using

Eq. [13]. These two functions have different ranges but are similar in form in regions of equal Φ, where the phase spaces of the two systems overlap. It can be shown that the excess chemical potential is related to these distribution functions by

$$\mu^{ex} = \ln[p_{N+1}(\Phi)] + \Phi - \ln[p_N(\Phi)] \quad [20]$$

This approach may yield a result for μ^{ex} that is superior to the simple test particle result if the overlap in the two distribution functions is significant. Contrarily, if the distributions do not overlap significantly, it is difficult to extract a reliable result from either the test particle or overlapping distribution formulae, and an alternative approach like thermodynamic integration or the staged insertion method is favored.

Particle insertion methods may also be used in spatially inhomogeneous systems. In this case, the spatial variation in the excess chemical potential is directly related to the potential of mean force for the solute molecule. The calculation is more computationally intensive because the test particle insertion energy Φ must be determined as a function of its position. The potential of mean force, $w(r)$, is then given by

$$w(\mathbf{r}) = -k_B T \ln\langle e^{-\beta\Phi(\mathbf{r})}\rangle_N \quad [21]$$

where N now refers to all particles in the system except the test particles. A similar expression gives the potential of mean force for a hard sphere or cavity:

$$w(\mathbf{r}) = -k_B T \ln p_0(\mathbf{r}) \quad [22]$$

These equations may provide a fruitful approach for analyzing the spatial variation of hydrophobicity in complicated biological systems.

Perturbation Methods

The test particle method is a special case of a more general free-energy perturbation (FEP) technique. The free-energy difference between a reference state (0) and a perturbed state (1) is given by

$$\Delta A = A_1 - A_0 = -k_B T \ln\left\langle e^{-\beta\Delta U}\right\rangle_0 \quad [23]$$

where $\Delta U = U_1 - U_0$ and the 0 subscript indicates that the average is taken over the unperturbed system configurations. The expression is exact, but statistically reliable results are obtained only for relatively small perturbations. Widom's test particle expression is recovered when the reference and perturbed states differ only by the absence and presence of a solute molecule,

respectively. The derivation of this expression is therefore similar to that given for Eq. [13]. The difference between states 0 and 1 in Eq. [23] may take on a wide variety of forms, including movement along simple or complex structural coordinates, simple or complex reaction coordinates, or creation/annihilation/mutation coordinates.[28] The method is also applicable to calculation of potentials of mean force between nonpolar solutes and between nonpolar solutes and interfaces. When particle insertion methods fail due to large solute size, an efficient alternative is the staged insertion method in which the overall insertion process is broken into multiple steps, with the perturbation method used to determine the free-energy change for each step.[20] The path between initial and final states is specified using a coupling parameter λ, with the choice of λ path impacting simulation efficiency. A common rule of thumb has been to follow a path with roughly equal free-energy change in each step. This led Pearlman and Kollman to develop a "dynamically modified windows" method in which the λ stepsize is adjusted as the simulation proceeds.[29] More recently, Lu and Kofke have argued that the optimal path is essentially one with equal entropy differences in each stage rather than free-energy differences.[30] Unfortunately, entropy changes are difficult or impossible to assess a priori.

Reversing the roles of the reference and perturbed states in Eq. [23] yields an alternative expression:

$$\Delta A = A_1 - A_0 = k_B T \ln\left\langle e^{\beta \Delta U} \right\rangle_1 \qquad [24]$$

The symmetry of these two equations implies that the calculation of free-energy differences can be done in both "forward" and "reverse" directions. However, while the two expressions are both exact, they are not equally reliable. Phase space considerations indicate that free-energy perturbation methods are best applied in the direction of decreasing entropy.[30–32] In other words, the accessible regions of phase space for the perturbed system should lie completely within the accessible regions of phase space for the reference system. This principle calls into question the common practice of averaging results from forward and reverse free-energy simulations. In the event of significant hysteresis, the results obtained in the direction of decreasing entropy are more reliable.

Thermodynamic Integration

Thermodynamic integration (TI) provides another related method for determining free energy differences in simulations.[14,28] The approach involves calculation of a free energy difference through integration,

$$\Delta A = A_1 - A_0 = \int_0^1 \left(\frac{\partial A(\lambda)}{\partial \lambda} \right)_{N,V,T} d\lambda \qquad [25]$$

where λ is a coupling parameter defined such that when $\lambda = 0$ the system is in its desired initial state and when $\lambda = 1$ the system is in its desired final state. As with the perturbation methods, free-energy differences may be calculated along a wide variety of coordinates. Substituting Eq. [8] into the integrand and evaluating the partial derivative yields

$$\left(\frac{\partial A(\lambda)}{\partial \lambda}\right)_{N,V,T} = \frac{\int d\mathbf{r}^N (\partial U(\mathbf{r}^N, \lambda)/\partial \lambda) \exp[-\beta U(\mathbf{r}^N, \lambda)]}{\int d\mathbf{r}^N \exp[-\beta U(\mathbf{r}^N, \lambda)]} \quad [26]$$

$$= \left\langle \frac{\partial U(\lambda)}{\partial \lambda} \right\rangle_{\lambda} \quad [27]$$

The TI approach therefore consists of performing a series of simulations with λ varying from 0 to 1, with $\partial U(\lambda)/\partial \lambda$ evaluated for each value of λ. The integration in Eq. [25] is then performed numerically to yield the desired free-energy difference. As with FEP calculations, some care is required in choosing an appropriate λ path. Both TI and multistep FEP calculations can be performed simultaneously as λ is varied from 0 to 1, and often yield nearly equivalent results. The TI method is illustrated through a calculation of the methane-methane potential of mean force in water, displayed in Figure 4.

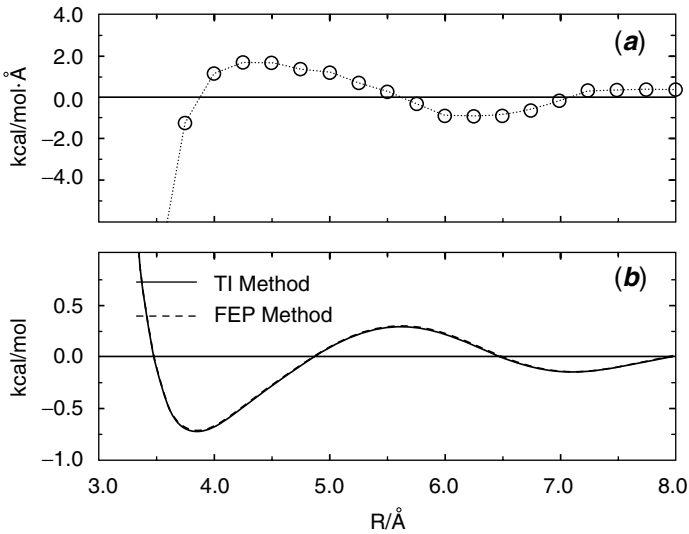

Figure 4 Mean force (*a*) and potential of mean force (*b*) between two methane molecules in water, from Smith and Haymet.[45] The potential of mean force is calculated by thermodynamic integration (TI) of the mean force and also from the free-energy perturbation (FEP) method. TI and FEP quantities were calculated simultaneously from the same simulations, with nearly identical results. Maxima and minima in the potential of mean force correspond to separations where the mean force is zero.

The coupling parameter in this calculation is proportional to the solute–solute distance. The top graph shows the mean force between the methane molecules, equivalent to the average in Eq. [27]. Integration of the mean force as in Eq. [25] yields the potential of mean force, $\Delta A(r)$. Results for an FEP calculation are also displayed in the figure with nearly exact agreement observed between the TI and FEP calculations.

The "slow growth" method developed by Straatsma, Berendsen, and Postma[33] is an interesting variant of the TI method. In slow growth, λ is varied continuously with each step during the simulation. The free-energy change is still evaluated by numerical integration of Eq. [34], but the average in the integrand is now "evaluated" over a single simulation step. The method should be reliable as long as the variation of λ is slow relative to the system relaxation time, such that a quasiequilibrium is constantly maintained. A lack of hysteresis in forward and reverse slow-growth calculations is used to evaluate this condition.

Free Energy and Structure

A simple and effective approach to determining free energies of hydrophobic interactions makes use of the relationship

$$\Delta A(r) = -k_B T \ln g(r) \qquad [28]$$

where $g(r)$ is the solute–solute radial distribution function. Radial distribution functions are routinely calculated during the course of most computer simulations, so this method is particularly convenient to implement. The disadvantage is that the method is computationally tractable only for ≈ 1 mol/L solute concentrations, well above the experimental solubilities of nonpolar solutes. Nevertheless, qualitative aspects of hydrophobicity are probably not sensitive to solute concentrations in this range, and this approach has been commonly used in hydrophobicity investigations.[34–36]

The relationship in Eq. [28] can be used for a single solute pair if simulations are performed using the umbrella sampling technique.[37] In this method, the solute–solute distance is constrained to lie within a small window, allowing for the efficient calculation of $g(r)$ over that restricted distance range. The effect of the constraint is subtracted from the calculated $w(r)$ after the fact. Results from several overlapping windows may be combined to yield the full potential of mean force.

Entropy and Energy

Entropies of hydration and association are considered to be one of the primary signatures of hydrophobicity. The goal of many simulations is therefore the decomposition of calculated free energies into their entropic and

energetic (or enthalpic) parts. This process is much more demanding computationally than free-energy calculations, but has become feasible since the early 1990s. Several complementary approaches to the free-energy decomposition have been developed, each involving calculation of either the energy or the entropy, with the other being determined from Eq. [29]:

$$\Delta A = \Delta E - T\Delta S \qquad [29]$$

Results of entropy and energy calculations are strongly ensemble-dependent,[38–40] a fact not always appreciated in the literature. In particular, it can be shown readily that the difference between the constant-pressure solvation energy $(\Delta E)_P$ and the constant volume solvation energy $(\Delta E)_V$ is given by

$$(\Delta E)_P - (\Delta E)_V = \Delta V\left(\frac{T\alpha}{\kappa} - P\right) \qquad [30]$$

where ΔV is the partial molar volume of the solute, α is the thermal expansion coefficient, and κ is the isothermal compressibility. The term on the right-hand side of this expression is generally significant even if $\Delta(PV)$ (the difference between the energy and enthalpy) is negligible.[41,42]

The simplest approach to free-energy decomposition involves calculating the energy difference directly:

$$\Delta E = \langle U_1\rangle_1 - \langle U_0\rangle_0 \qquad [31]$$

This method is plagued by large uncertainties in calculated configurational energies that grow with system size. Nevertheless, it has been used successfully, most recently by Durell and Wallqvist to investigate the hydrophobic hydration of krypton.[43]

The energy change can also be evaluated using a perturbation expression for ΔE:[21,44,45]

$$\Delta E = \frac{\langle U_1 \exp(-\beta\Delta U)\rangle_0}{\langle \exp(-\beta\Delta U)\rangle_0} - \langle U_0\rangle_0 \qquad [32]$$

Fluctuations in the configurational energy calculated using this method are again wide and grow with system size, but are correlated in each separate average. The resulting cancellation in noise may lead to an improvement in the efficiency of the method when compared to Eq. [31]. In test particle investigations of hydrophobic hydration, Eq. [32] is sometimes written in an alternative form in order to reveal the magnitude of the solvent reorganization energy:

$$\Delta E = \frac{\langle \Delta U \exp(-\beta\Delta U)\rangle_0}{\langle \exp(-\beta\Delta U)\rangle_0} + \frac{\langle \delta U_{ww} \exp(-\beta\Delta U)\rangle_0}{\langle \exp(-\beta\Delta U)\rangle_0} \qquad [33]$$

Here $\delta U_{ww} = U_0 - \langle U \rangle_0$ is the instantaneous deviation of solvent energy from its average value. The first term in this expression gives the average solute–solvent energy, and is sometimes incorrectly equated with the full solvation energy, ΔE. The second term yields the solvent reorganization energy, and is related directly to the classic iceberg hypothesis discussed in the hydrophobic hydration section below. While the first term may be calculated precisely, the second term's uncertainty is large and grows with system size.

It is possible to derive a formula for the entropy that is analogous to the previously described TI expression for the free energy:[44,45]

$$-T\Delta S = \frac{1}{k_B T}\int_0^1 d\lambda \left[\left\langle U(\lambda)\frac{\partial U(\lambda)}{\partial \lambda}\right\rangle_\lambda - \langle U(\lambda)\rangle \left\langle \frac{\partial U(\lambda)}{\partial \lambda}\right\rangle_\lambda \right] \qquad [34]$$

This expression allows for a free-energy decomposition from a single-free energy simulation, and it gives results essentially equivalent to those obtained from Eq. [32], including divergence with system size.

All of the methods for free energy decomposition described above suffer from the similar drawback of large statistical uncertainty that grows with system size. An alternative approach that avoids this problem begins with the entropy relationship:

$$\left(\frac{\partial \Delta A}{\partial T}\right)_{N,V} = -\Delta S \qquad [35]$$

The partial derivative may be evaluated numerically from the values of the free energies calculated at two or more temperatures. This finite-difference approach has the disadvantage of requiring multiple simulations but can be quite efficient if a large spread in temperatures is used. Care must be taken in cases where there is substantial curvature in the temperature dependence of the free energy, specifically when the heat capacity is large. This situation is common when treating hydrophobic effects, but can be dealt with effectively by using an algorithm that brackets the desired temperature:

$$-\Delta S = \frac{\Delta A(T + \Delta T) - \Delta A(T - \Delta T)}{2\Delta T} \qquad [36]$$

Values of ΔT in the range of 10–50 K are reasonable, limited by the convergence of ΔA at low temperature. More recently, it has become common to calculate free energies at many points over wide temperature ranges.[15,46–49] In this case, evaluation of entropy may be performed by first fitting the free energy to a function and then evaluating the derivative in Eq. [35] analytically.

The value of the entropy calculated from the finite-difference expression depends on how the system's volume varies with temperature. To facilitate

comparison with experiment, the volume is usually adjusted either to keep the pressure constant, or to track the liquid density along the liquid–vapor coexistence curve. These two strategies yield nearly identical results below the normal boiling point. In contrast Eqs. [32] and [34] give dramatically different results, a consequence of imposing a constant volume constraint. The finite-difference approach is therefore preferred when comparison with experimental entropies is being made.

Heat Capacity

Explaining heat capacities associated with hydrophobic hydration or hydrophobic interactions is essential to validating any model of hydrophobicity. One approach to calculating heat capacities takes advantage of the relationship between free energy and heat capacity:

$$\Delta C_V = -T\left(\frac{\partial^2 \Delta A}{\partial T^2}\right)_{V,N} = T\left(\frac{\partial \Delta S}{\partial T}\right)_{V,N} \qquad [37]$$

The second derivative in this expression may be evaluated by taking analytical derivatives of a function fit to temperature-dependent free-energy data or, through a finite difference algorithm, as in Eq. [38]:

$$\Delta C_V = -T\frac{\Delta A(T+\Delta T) - 2\Delta A(T) + \Delta A(T-\Delta T)}{\Delta T^2} \qquad [38]$$

While these expressions are simple, determination of heat capacities is so computationally intensive that very few such calculations have been reported to date.

HYDROPHOBIC HYDRATION

The origin of hydrophobicity, in even the most complicated biological systems, is due to the unique solvation properties of water. As a result, simulations of hydrophobic hydration are arguably among the most important computational investigations related to hydrophobicity. The systems studied to date have often been simple, such as noble gases in water, but in spite of this simplicity the observed behavior is surprisingly rich and complex.

Several key issues have been addressed in these published simulations, but the one receiving most attention involves the structural origin of the entropy of hydrophobic hydration. The classic perspective on this issue, originally put forth by Frank and Evans as the ''iceberg'' hypothesis,[50] involves an ordering of water molecules in the hydration shell of the nonpolar solute.

While still widely accepted in some form, this perspective has been criticized (often in favor of a view that water's small size determines its unique behavior).[51,52] More recently, simulations have been used to probe issues related to the heat capacity of solvation. A large heat capacity leads to enthalpy-dominated hydration thermodynamics at high temperatures and also to a high-temperature convergence of solvation entropies for various-sized solutes.

This section includes a survey of several representative investigations of the hydrophobic hydration of simple atomic solutes and methane, with methane modeled as a spherical solute. A thorough review of early work in this area has been presented by Blokzijl and Engberts,[3] but more recent reviews are also available.[5,53] We present these studies in order of increasing complexity of the calculations, beginning with simple structural results, followed by calculations of hydration free energy, entropy, and energy (enthalpy), and ending with heat capacity. The section concludes with a brief survey of simulation results for water "mimics"—spherically symmetric solvents designed to reproduce water's density and molecular size but without hydrogen bonding and the associated orientational structure.

Structure

Much of the early work on hydrophobic hydration of atomic solutes involved hydration structure. Results of many investigations are surprisingly similar given the wide range of interaction potentials used. Around small solutes, water is remarkably adept at maintaining its hydrogen bond network by orienting its O—H bonds in a direction tangential to the surface of the solute.[21,54–58] This tangential orientation is revealed by the overlap of the first peaks in solute-oxygen and solute-hydrogen radial distribution functions and in orientational correlation functions for first shell waters. Further analysis of the solvation structure has, in some instances, revealed a resemblance to clathrate–hydrate cage structures, a picture consistent with the "iceberg" hypothesis.[50] Several studies have also indicated that hydrogen bond strengths are increased slightly in the first hydration shell of nonpolar solutes. Dynamical studies indicate that both translational and rotational mobility of water molecules in the first solvation shell are reduced somewhat compared to bulk water values, but those studies still clearly reveal liquid rather than solid like behavior.[59] In this sense the "iceberg" term for the solvation shell is misleading and is no longer widely used.

In contrast to its behavior around small solutes, water is unable to maintain a complete hydrogen bonding network around large solutes or near hydrophobic interfaces. Two investigations of the transition region between small solutes and interfaces have been reported recently.[49,60] Using the two-dimensional "Mercedes Benz" (MB) model of water, Southall and Dill observed that at low temperatures water molecules around a small solute are moderately effective at maintaining the three hydrogen bonds typical of

the bulk 2D structure. Orientational correlation functions indicate that the water's hydrogen bonding arms typically straddle the small solute. As the solute size is increased, however, the extent of hydrogen bonding in the first solvation shell is reduced gradually. For a flat nonpolar interface, a nearly complete sacrifice of one hydrogen bond was observed for MB water molecules next to the surface. These features are clearly displayed in Figure 5, taken from a recent review by Southall, Dill, and Haymet.[53]

Ashbaugh and Paulaitis recently reported a thorough analysis of the hydration structure around large solutes comprised of frozen clusters of "methane" spheres.[60] Their analysis was given in terms of proximal radial

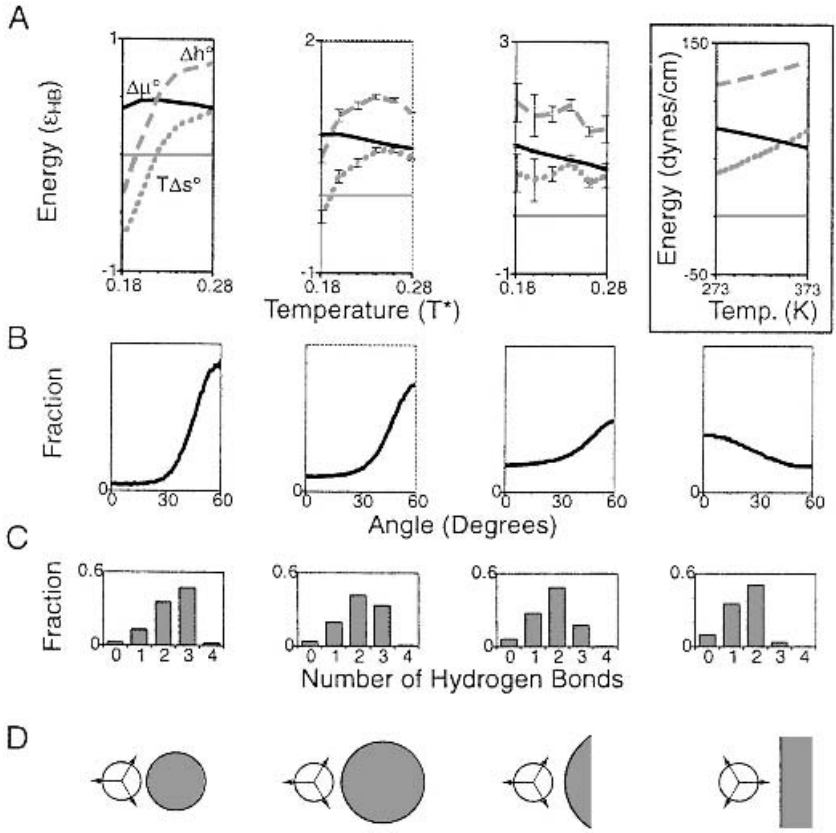

Figure 5 Solute size dependence of hydrophobicity for the 2D MB model (from Southall and Dill[53]): (*a*) transfer thermodynamics and experimental surface tension of water (inset box); (*b*) angular orientations of first-shell waters; (*c*) histograms of the numbers of hydrogen bonds among first-shell waters; (*d*) the most probable structure of a water adjacent to a hydrophobic solute for a series of solutes. Solute size increases to the right for the first three columns, with the fourth column corresponding to a nonpolar interface.

distribution functions (RDFs) in which each solvent atom is assigned only to its nearest-neighbor solute sphere. Perhaps surprisingly, solute–oxygen proximal RDFs change only slightly with solute cluster size, while solute-hydrogen proximal RDFs broaden and shift outward somewhat, indicative of a breakage of water structure around the larger solutes.

Hydration Free Energy

There exist numerous calculations of hydration free energies of atomic solutes at room temperature, only a few of which are referenced here.[21,25,46,48,56,61,62] Good qualitative agreement is found among most calculations on similar solutes regardless of the water model or the free-energy method used. The test particle method is the most popular approach for treating small solutes, although multistep FEP and TI methods have also been used (for larger particles, these latter methods are required).

Jorgensen, Blake, and Buckner[61] reported a staged FEP calculation of the hydration free energy of methane, which was treated as a Lennard-Jones (LJ) sphere. The size (σ) and well depth (ϵ) LJ parameters were each scaled linearly with the coupling parameter lambda:

$$\sigma(\lambda) = \lambda\sigma \qquad [39]$$

and

$$\epsilon(\lambda) = \lambda\epsilon \qquad [40]$$

Simulations were run at 11 values of λ ranging from 0 to 1 with a 0.1 stepsize. Incremental free-energy changes were calculated in both the forward and reverse directions. Their results are displayed in Figure 6, where the free energy change is noted to be nonlinear with respect to λ, rising steeply near $\lambda = 1$. Additional calculations (not shown) were therefore performed at $\lambda = 0.85$ and $\lambda = 0.95$ to improve the statistical uncertainty. With these additional points, the average of forward and reverse direction results yielded a "best value" of 2.27 ± 0.3 kcal/mol for the hydration free energy, in good agreement with the experimental value of 1.93 kcal/mol.[38] Recall that results for particle insertion are often superior to those for particle deletion and that averaging of forward and reverse results may therefore not be justified.[31,32]

Arthur and Haymet's calculation of the hydration free energy of methane illustrates how various simulation pathways are possible in the staged FEP approach.[62] In their work, λ was used to scale the full methane–water interaction potential rather than the size and well-depth parameters separately. Results displayed in Figure 7 show a very different λ dependence for the free energy compared to the results of Figure 6, yet the final answer (1.92 ± 0.72 kcal/mol) is still in good agreement with the experimental value. Their calculation was performed only in the more reliable insertion direction.

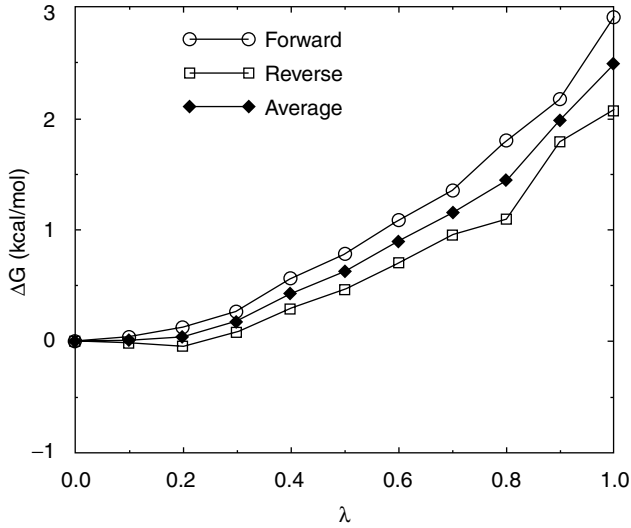

Figure 6 Free energy of particle insertion for methane calculated using a staged FEP method; the free-energy change is shown for both the forward ($\lambda = 0 \rightarrow 1$) and reverse ($\lambda = 1 \rightarrow 0$) processes and for the average (data taken from Jorgensen, Blake, and Buckner.[61]).

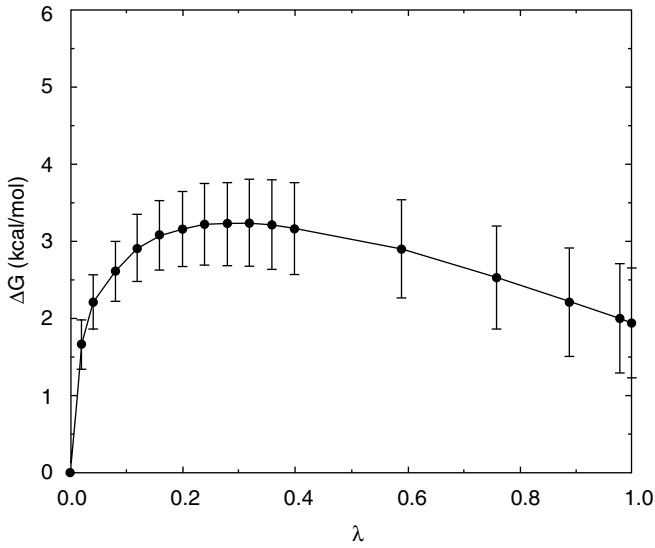

Figure 7 The free energy of solvation of methane calculated using the staged insertion method of Kofke and Cummings.[20] Each point represents the cumulative free energy calculated from all stages up to the value of the coupling parameter λ. Taken from Arthur and Haymet.[62]

Durell and Wallqvist recently evaluated krypton hydration free energies using the TI method.[43] Particle creation or annihilation using the TI approach requires some care so as to avoid a divergent integrand in Eq. [27].[63] For the LJ potential, the exponent on λ must be ≥ 4 for the integrand to be bounded. Durell and Wallqvist calculated μ^{ex} along four different paths, three of which were polynomial paths suggested by Resat and Mezei,[64] while the fourth involved a separation-shifted path proposed by Zacharias, Straatsma, and McCammon.[65] Each path yields a unique λ dependence of the integrand in Eq. [27]. Nevertheless, the integrals in each of the four cases give nearly identical μ^{ex} values (1.0–1.1 kcal/mol) and uncertainties ($\pm$0.6–0.7 kcal/mol), with the calculated chemical potentials all being somewhat lower than the experimental value of 1.68 kcal/mol. While the choice of TI path is important, particularly near $\lambda = 0$, a variety of paths can provide comparable and reliable free energies.

Interpretation of solvation free energies for different gases, along the noble gas series for example, is complicated by the simultaneous variation of both size and well depth parameters. Some recent studies have therefore attempted to establish trends in solvation free energy in which these two properties are isolated. For example, Arthur and Haymet[62] used the TI method to create a three-dimensional free-energy surface for a LJ solute in their central force model 1 (CF1) over a size range of 0–5 Å and a well-depth range of 0.1–0.5 kcal/mol. That surface is displayed in Figure 8. It was found that the free energy increases sharply with σ for values greater than $\sim$3 Å, while the variation with ϵ is smaller and essentially linear.

In a related study, Garde et al. used a test-particle approach to perform a systematic comparison of hydration free energies for nine different LJ particles along with their WCA and HS equivalents.[48] Their results indicate that the attractive part of the LJ solute–water potential is very well modeled as a perturbation of the WCA result. The excess chemical potential was calculated

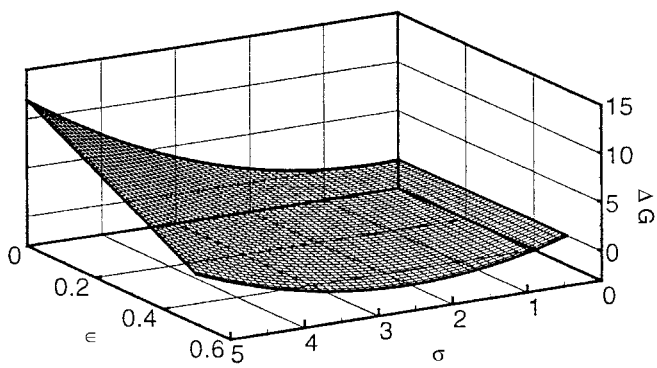

Figure 8 Hydration free energy as a function of solute–water size [σ/Å] and well depth [ϵ/(kcal mol^{-1})] parameters (taken from Arthur and Haymet[62]).

using the test particle method as a function of temperature for four LJ solutes differing only in their ϵ parameters. These values were compared with excess chemical potentials estimated from

$$\mu_{LJ}^{ex} \approx \mu_{WCA}^{ex} + \langle U_{att} \rangle_{WCA} \quad [41]$$

where the last term is the average solute-water energy of attraction for the LJ particle calculated from the WCA simulation. Specifically, we obtain

$$U_{att}(r) = U_{LJ}(r) - U_{WCA}(r) \quad [42]$$

Agreement between μ_{LJ}^{ex} calculated from the test particle method and from Eq. [41] was nearly exact. Garde et al. also found that the contribution of the attractive part of the solute–water interaction energy to μ^{ex} is reasonably well represented by even a very crude model and that this contribution shows little temperature dependence. These observations suggest that purely repulsive models capture many of the essential features of hydrophobicity for small solute molecules. Note, however, that this conclusion does not hold for large solutes or for interfaces.[60,66]

Wallqvist and Berne used an FEP method to determine hydration free energies for hard-sphere cavities as a function of both size and shape.[67] They observed a nearly linear relationship between solute surface area and hydration free energy for both spherical and ellipsoidal cavities. The hydration free energy also exhibited a significant dependence on solute curvature.[67]

Hydration Entropy and Energy

In their study of krypton hydration, Durell and Wallqvist also reported a calculation of the enthalpy of hydration evaluated by the direct method of Eq. [31].[43] Both constant volume and constant pressure enthalpies were determined by varying the volume of the krypton solution. Their results are displayed in Table 1. The enthalpy of hydration in the constant volume case (-6.3 ± 1.3 kcal/mol) is significantly more exothermic than in the constant pressure case (-3.4 ± 1.3 kcal/mol). The latter number agrees very well with the experimental value of -3.3 kcal/mol, also obtained at constant pressure. The calculated enthalpies of solvation were decomposed into solute–water and water–water (solvent reorganization) terms. The solute-water contribution is comparable and favorable (-5.4 kcal/mol) in both the constant volume and constant pressure calculations. The solvent reorganization term, in contrast, shows a large ensemble dependence. In the constant-pressure case, the solvent reorganization term has a value of $+2.0 \pm 1.3$ kcal/mol. The overall favorable enthalpy of hydration of krypton at constant pressure therefore results from the solute–water attractions rather than from a

Table 1 Solvation Thermodynamics for Krypton in TIPS3P Water and an LJ Mimic, at $T = 300$ K[a,b]

	ΔG (kcal/mol)	ΔH (kcal/mol)	ΔS (cal/mol · K)
TIPS3P water			
Constant V	1.1 (0.6)	−6.3 (1.3)	−25 (5)
Constant P	1.1 (0.6)	−3.4 (1.3)	−15 (5)
LJ water			
Constant V	−0.2 (0.4)	−6.4 (0.5)	−21 (3)
Constant P	−0.2 (0.4)	−3.4 (0.5)	−10 (3)

[a]All simulations were performed at constant volume, with the constant P and constant V labels referring to the change in system volume on addition of the solute.
[b]Values in parentheses are the statistical uncertainty (2σ).
Source: From Durell and Wallqvist.[43]

stabilization of the hydrogen bond network. This is in apparent conflict with solvent ordering predicted by the ''iceberg'' hypothesis.

Tomás-Oliveira and Wodak used a test particle approach and Eq. [32] to investigate the free energy, energy, and enthalpy of solvation of small cavities as a function of size in both water and hexane.[68] The test particle approach allows for determination of thermodynamic quantities as a function of cavity size from a single simulation. Their results illustrate the importance of solvation entropy when determining solvation free energies near room temperature.

Several studies of the temperature dependence of hydration free energies or (equivalently) solubilities have been reported.[15,46–49,56] Entropies and enthalpies of hydration can, of course, be extracted from these data using methods described above. The earliest study by Swope and Andersen,[56] albeit restricted in scope due to limited computational resources, still revealed the expected trends for Ar, Kr, and Xe solutes. In particular, the solubility decreased with temperature near room temperature and showed a positive curvature in a plot of solubility versus T. This behavior was not reproduced for He nor for Ne.

The more recent study by Guillot and Guissani[46] successfully reproduced experimental solubility data for the noble gases (Ne through Xe) and for methane along the saturation curve with temperatures ranging between room temperature and the critical point for the water model they used. In addition, they observed solvation free-energy maxima for all solutes at ~400 K. The finite difference method therefore yields hydration entropies near zero at this temperature, in good agreement with experimental predictions. Guillot and Guissani also decomposed their calculated values of μ^{ex} into entropic and energetic terms using Eq. [32]. The constant-volume values of $-T\Delta S$ are large and positive for all temperatures, in contrast to the finite-difference result. This illustrates very clearly the ensemble dependence of the

hydration entropy, and it reinforces the conclusion that proper interpretation of hydration entropies requires considerable care.[69]

Garde et al. used a test particle approach to determine the temperature dependence of μ^{ex} for hard spheres with sizes comparable to Ne, Ar, methane, and Xe.[70] Results were compared to information theory predictions and used to locate an entropy convergence temperature of ~400 K. Silverstein, Haymet and Dill studied hydration thermodynamics of a small nonpolar solute in two-dimensional MB water as a function of temperature. The computational advantages of the two-dimensional model are most dramatically evident in this study. The calculated hydration free energies were decomposed to yield precise entropy and enthalpy contributions that in turn were used to generate a temperature-dependent heat capacity of hydration. The enthalpy and entropy terms are fully consistent with the behavior of three-dimensional models. The heat capacity of solvation is large, as expected in hydrophobic hydration, and shows a temperature dependence that is qualitatively consistent with a Muller's two-state model[71] for hydrogen bonding in water.[10] This model's profound prediction of a turnover in the heat capacity of solvation in supercooled water has yet to be tested either experimentally or in three-dimensional water model simulations.

Southall and Dill identified an interesting solute size dependence for hydration thermodynamics in the 2D MB water model,[49] illustrated in Figure 5. For small solutes at low temperature the hydration free energy is unfavorable due to a large, negative entropy of hydration, as expected. As the solute size is increased, however, the entropy and energy contributions to the free energy both increase, leading to a change in sign of both terms. For larger solutes, the unfavorable hydration free energy is dominated by an unfavorable energy term. The thermodynamic changes with solute size correlate well with the structural changes discussed above. It is unclear whether the behavior of the 2D MB model is general, however. For example, Wallqvist and Berne calculated the free energy and entropy of hydration of spherical cavities and found that both the free energy and the entropy of hydration increase steadily with cavity radius.[72]

Hydration Heat Capacity

As noted in the Simulation Methods section, calculation of heat capacity is computationally demanding and there are few examples of such investigations in the literature. Silverstein, Haymet and Dill[10] determined the heat capacity of solvation of a nonpolar solute in the 2D MB water model using Eq. [37]. Their results are presented in Figure 9. The heat capacity is positive and decreases with temperature at higher temperatures, an observation that is in qualitative agreement with experimental hydration heat capacities. The turnover in the heat capacity at low temperatures has not yet been confirmed experimentally because such measurements have not been performed much

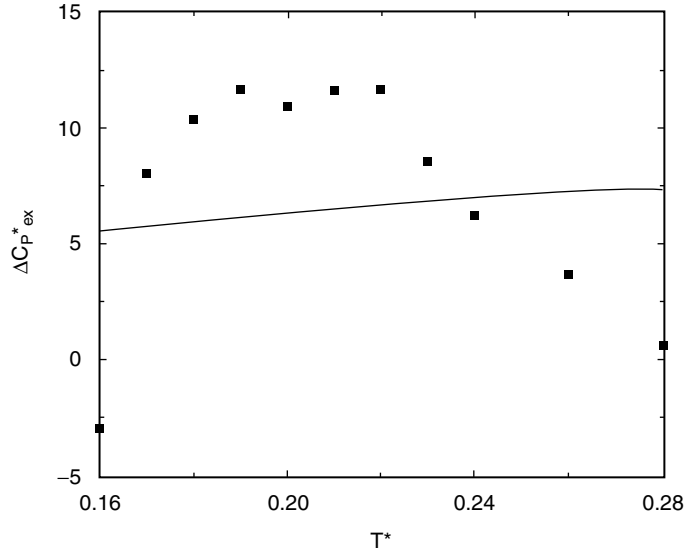

Figure 9 Constant pressure excess heat capacity of solvation as a function of reduced temperature (T^*, defined in Ref. 15) for a nonpolar solute in 2D MB water. Simulation data (symbols) are from Silverstein, Haymet, and Dill,[15] while the solid line is the result of an information theory approximation as given by Arthur and Haymet.[82] Taken from Arthur and Haymet.[82]

below room temperature. Heat capacity calculations will certainly become more common as computational resources continue to increase.

Water Mimics

Several publications have reported direct comparisons of the solvation properties of water with atomic liquids that have been designed to reproduce the density and molecular size of water.[24,25,43] The rationale behind some of these investigations is to test the hypothesis that the unfavorable entropy of hydration has its origin in the hydrogen bonding structure of water around nonpolar solutes. If atomic liquids with no hydrogen bonding capability can mimic water's solvation properties, credibility is given to the competing "small size" hypothesis put forth by Lee.[52] Madan and Lee (ML) measured cavity formation free energies as a function of cavity radius in water and in two LJ solvents.[25] Calculated free energies were nearly equal in water and in its closest LJ mimic ($\sigma = 2.8$), suggesting that hydrogen bonding plays only a small role in solvation free energies. Durell and Wallqvist subsequently published a similar comparison using a LJ model that, unlike the ML study, also matched the pressure of water at 300 K.[43] They calculated the free energy, enthalpy, and entropy of solvation for krypton in both LJ and water solvents (see

Table 1). The computed solvation free energy is 1.3 kcal/mol smaller in the LJ solvent, a difference traced to entropic contributions to the free energy. Solvation is entropically unfavorable in both solvents, but more so in water. These results are consistent with water hydrogen bonding playing an important, but not exclusive, role in hydrophobicity.

While these results are interesting, comparison between water and its mimics is of limited use for investigating the full range of hydrophobic effects. Any spherically symmetric water mimic should be effective in reproducing water properties only near the thermodynamic state point for which it is parameterized. Pratt and co-workers showed that many features of hydrophobicity are linked closely to the equation of state for water.[5] From this perspective, it is not surprising that simple solvents designed to mimic water at a particular state point behave similarly to water regardless of the presence or absence of hydrogen bonding. Such solvents will, however, generally fail to reproduce the water equation of state over a wide range of conditions.

HYDROPHOBIC INTERACTIONS

The term "hydrophobic interaction" refers to the *solvent-induced* interaction between nonpolar solutes in water. While experimental information on hydrophobic hydration is readily available, comparable information is nearly nonexistent for hydrophobic interactions, particularly for simple systems where interpretation of data would be unambiguous. This is due to the very low solubility of nonpolar solutes in water. Computational investigations have therefore been used extensively to investigate the nature of hydrophobic interactions. Early calculations in this area dealt primarily with the free energy of association, or potential of mean force (PMF), between pairs of nonpolar solutes in water, and have been reviewed by Blokzijl and Engberts.[3] More recent calculations have included evaluations of the entropy and heat capacity of association.

As discussed in the methods section, computational techniques used to study hydrophobic interactions are similar to those used for hydrophobic hydration. Most commonly, TI and FEP methods have been adapted to yield a PMF by equating the coupling parameter λ or the perturbation coordinate, respectively, to the radial distance between two solute particles. The application of a test particle approach or of Eq. [28] is also possible. Methods for decomposition of the free energy of association into its entropic and energetic (enthalpic) parts are equivalent to those discussed above, as are techniques for determining the heat capacity.

Models of hydrophobic hydration including the "iceberg" hypothesis and its more modern variants have led to several qualitative predictions for pairwise hydrophobic interactions. The first and simplest prediction based on free-energy arguments is that nonpolar solutes should tend to associate

together in water, thus reducing the total solvent accessible surface area. Furthermore, if the negative entropy of hydration for nonpolar solutes is associated with solvent ordering, then the reduction in surface area on association should be accompanied by an increase in the entropy. This yields an entropic driving force for pairwise solute association. Similar arguments suggest that the heat capacity of association should be negative.

Free Energy of Association

A surprising result that emerged from the earlier work on hydrophobic interactions is that there is little or no tendency for nonpolar solute association at low concentration. For example, simulation results led Watanabe and Andersen to discuss the ''hydrophobic repulsion'' between krypton atoms in water.[73] Calculated PMFs have typically supported a similar conclusion (discussed below). Aggregation of methane in water was observed to occur at higher concentrations,[74] suggesting that there may be cooperative aspects to the solute aggregation process. This conflicts, however, with results from Shimizu and Chan who explicitly observed anticooperativity in three-body hydrophobic interactions.[75]

Smith and Haymet reported a calculation of the free energy, energy, and entropy of association for methane in water.[45] Their free-energy results (displayed in Figure 10) were calculated using the TI method and are typical

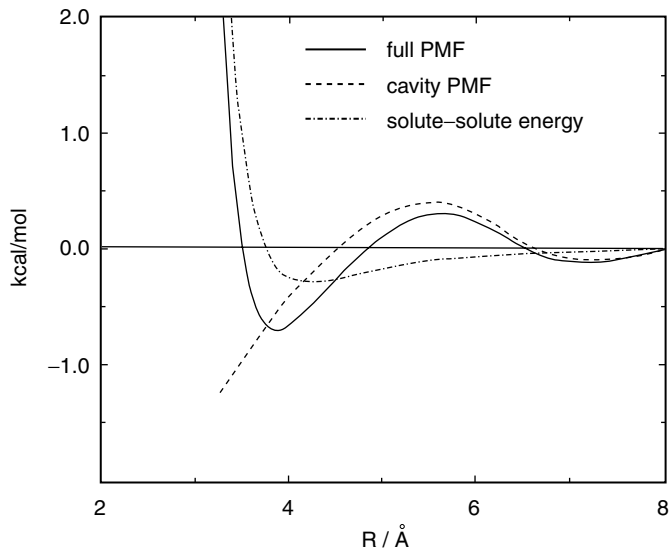

Figure 10 Methane–methane potential of mean force (PMF) using data from Smith and Haymet.[45] The cavity PMF is the solvent-induced part of the PMF and is calculated from the difference between the full PMF and the methane–methane potential energy.

of PMFs reported in the literature. There is a clear contact pair minimum at ~4 Å, a subtle solvent separated minimum at ~7 Å, with a significant barrier in between. The solvent-induced contribution to the PMF, generated by subtracting the direct methane–methane interaction from the PMF, is also displayed in the figure. Solvent effects stabilize the contact pair minimum but they are destabilizing in the barrier region. The overall solvent-induced contribution to methane association may be calculated from the second osmotic virial coefficient

$$B_2 = -2\pi \int_0^\infty [\exp(-\beta w(r)) - 1] r^2 dr \qquad [43]$$

where $w(r)$ is the potential of mean force and $\beta = 1/k_B T$. Numerical integration of the PMF in Figure 10 gives a value for B_2 of -44 Å^3 compared with a value of -65 Å^3 calculated for the direct methane–methane interaction. This comparison indicates that the solvent makes a net repulsive contribution to the PMF even though the contact methane pair at ~4 Å is stabilized relative to the direct interaction. Lüdemann et al. obtained similar results at 300 K for a somewhat different methane model.[76]

Nonpolar solute PMFs have also been calculated using test particle methods. Forsman and Jönsson calculated PMFs for neon and for various hard-sphere solutes in water by a method where pairs of test particles were inserted into a pure water system.[22] It is unclear whether this method is computationally feasible for larger solutes. Shimizu and Chan used both FEP and test particle methods to calculate methane–methane PMFs.[77] Their test particle method involved simulations of an aqueous system containing one explicit solute atom. The test particle insertion free energies were calculated as a function of distance from the explicit solute. Good agreement for the two independent approaches was reported. The advantage of the test particle method is most evident from their subsequent study of many-body effects in hydrophobic interactions where a broad range of three-body configurations were studied simultaneously by inserting test particles near a dimer of fixed geometry.[75]

Entropy and Energy of Association

Numerous studies have been designed to reveal the entropy and energy of hydrophobic interactions. The simplest approach used in these studies is to investigate the temperature dependence of aggregation in finite-concentration solutions. Skipper reported the first such calculation on methane solutions.[34] He observed that aggregation became more favorable as T was increased, indicating that the process is endothermic. Interpretation of this type of study is obfuscated by the contribution of many-body solute–solute effects, however. Smith and co-workers reported the first calculations of the entropy and the

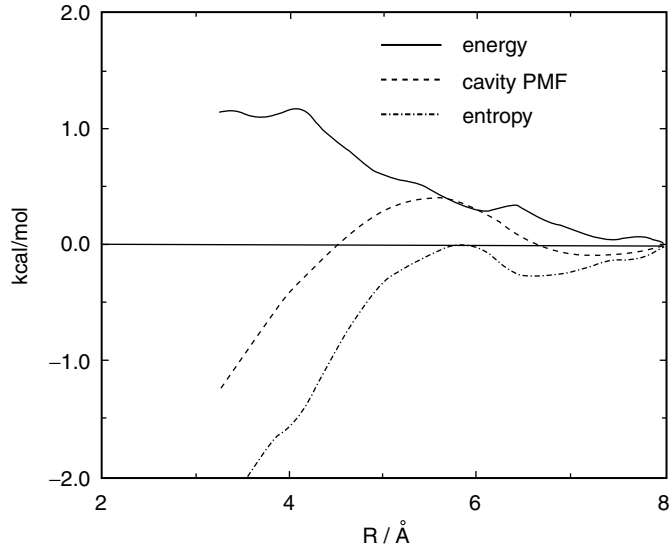

Figure 11 Methane–methane cavity PMF (as in Figure 10) along with its energetic (ΔE) and entropic ($-T\Delta S$) contributions (data from Smith and Haymet[45]).

energy of pairwise hydrophobic interactions.[44,45] Their calculations were performed using the direct (Eq. [31]), TI (Eq. [34]), and finite-difference (Eq. [36]) methods, all giving comparable results; the finite-difference approach was slightly more efficient. The computed free energy [$\Delta A(r)$, presented as the cavity PMF], energy [$\Delta E(r)$], and entropy [$-T\Delta S(r)$] of association are displayed in Figure 11. For clarity, the direct methane-methane interaction has been subtracted from the free energy and energy. The entropy of association was found to be strongly attractive at short separations, in agreement with the qualitative predictions discussed above. The energy of association was slightly repulsive in the same region.

The calculations by Skipper and by Smith and co-workers were all performed under conditions of constant volume, but the question as to their applicability under a constant-pressure constraint has been raised. Dang calculated the temperature dependence of methane-methane PMFs at both constant volume and constant pressure.[78] At constant volume, the PMF showed a contact pair stabilization as the temperature was increased from 300 to 330 K, in agreement with the results of Smith and co-workers. Raising the temperature at constant pressure led to little change in the PMF, implying that the constant pressure entropy of association is small. Rick and Berne performed a similar calculation at constant pressure using the umbrella sampling technique.[79] Their results contradicted Dang's, indicating an entropic driving force for association 3 times larger than found in constant volume simulations.

More recent constant pressure simulations[77,36] generally agree with results from Smith and co-workers, however, suggesting that pressure effects do not change the qualitative conclusions from entropy of association calculations.

Heat Capacity of Association

Calculations of the heat capacity of association for nonpolar solutes in water have been published. The earliest study, by Lüdemann and co-workers, does not explicitly report heat capacities of association but gives instead temperature-dependent entropies and enthalpies of association from which qualitative heat capacities can be extracted.[76] They performed a series of constant volume simulations of the methane–methane PMF at temperatures ranging from 250 to 500 K. A finite-difference approach was then used to determine the entropic and energetic contributions to the free energy. Results near room temperature are in good agreement with those from Smith and co-workers discussed above. As the temperature was increased, the favorable entropy of association disappeared and was replaced by an energetic attraction. The results indicate that the constant volume heat capacity of association is negative, in agreement with the qualitative prediction given above.

Subsequent simulations by Rick[80] and by Shimizu and Chan[77,81] attempted to evaluate the constant-pressure heat capacity of association, with conflicting results. Rick used a finite-difference method with PMF simulations of methane in water to evaluate the entropy and heat capacity of association at three temperatures ranging within 283–313 K. The heat capacity of association was found to be very large and negative for all solute pair separations within 7 Å. Shimizu and Chan also used a finite-difference approach to determine the entropy and heat capacities of association from PMFs at temperatures of 278–388 K. Their entropies of association were in qualitative agreement with several other calculations including Rick's. In contrast to Rick, however, they observed a small, positive heat capacity of association for the contact pair around 4 Å separation, and a larger, positive heat capacity in the barrier region around 6 Å. A positive heat capacity of association is interesting because it disagrees qualitatively with solvent accessible surface area predictions. It is to be noted that the temperature range for these two studies is somewhat different; the apparent conflict, while possibly related to the difficulty of heat capacity calculations, might also indicate a temperature dependent heat capacity.

Pressure Dependence of Hydrophobic Interactions

Pressure-induced denaturation of proteins and related problems are possibly linked to hydrophobicity. As a result, there has been considerable interest in studying the pressure dependence of hydrophobic interactions, highlighted by two studies. The first, by Rick, involved calculation of the pairwise

methane–methane PMF in water at pressures ranging from 1 atm to 7 kbar.[80] He observed that increasing the pressure stabilizes the solvent separated methane pair while having relatively little effect on the contact pair. In addition, he observed a significant pressure dependence on the entropy of association, with the favorable entropy of association at 1 atm pressure essentially eliminated at 7 kbar. Ghosh and co-workers investigated an aqueous methane solution with pressures ranging from 1 to 8000 atm.[36] Their system consisted of 10 methane and 508 water molecules. PMFs were calculated using Eq. [28], and their results were in good agreement with Rick's despite the potential problems arising from possible many-body solute effects. The solvent separated methane pair was stabilized significantly with increasing pressure, and there was an associated increase in the barrier height between contact and solvent separated configurations. Increasing the pressure was also found to reduce the magnitude of the entropic driving force for association. In a previous study, Ghosh and co-workers showed that increasing the pressure has a dramatic effect on solute aggregation for large ($\sigma = 5$ Å) solutes.[35] At low pressures, the solutes clearly formed an aggregate, but at high pressures the solutes did not aggregate but instead preferred solvent separated configurations. This finding has possible implications for the mechanism of protein denaturation at high pressures.

OUTLOOK

Our tutorial review of ''computing hydrophobicity'' is now completed. At the time of writing, debate over the origins of hydrophobicity continues in the literature, some in the absence of experimental data (i.e., lacking relevance). As the power of computers continues to expand, it is highly likely that the molecule-level understanding of hydrophobicity and the simple concepts needed to explain it will be developed via computer simulations. Applications of these simulations to combinations of hydrophobicity and hydrophilic effects, so important in biology, will also increase dramatically in the near future.

ACKNOWLEDGMENTS

ADJH acknowledges gratefully support from the Welch Foundation grant E-1429.

REFERENCES

1. A. Ben-Naim, *Hydrophobic Interactions*, Plenum Press, New York, 1980.
2. A. D. J. Haymet, *Curr. Biol.*, **9**, R81 (1999). Hydrophobicity—Quick Guide.
3. W. Blokzijl and J. B. F. N. Engberts, *Angew. Chem., Int. Ed. Engl.*, **32**, 1545 (1993). Hydrophobic Effects. Opinions and Facts.

4. L. R. Pratt and A. Pohorille, *Chem. Rev.,* **102,** 2671 (2002). Hydrophobic Effects and Modeling of Biophysical Aqueous Solution Interfaces.
5. L. R. Pratt, *Annu. Rev. Phys. Chem.,* **53,** 409 (2002). Molecular Theory of Hydrophobic Effects: "She is Too Mean to Have Her Name Repeated."
6. G. Hummer, S. Garde, A. E. García, A. Pohorille, and L. R. Pratt, *Proc. Natl. Acad. Sci.,* (*USA*) **93,** 8951 (1996). An Information Theory Model of Hydrophobic Interactions.
7. G. Hummer, S. Garde, A. E. García, M. E. Paulaitis, and L. R. Pratt, *J. Phys. Chem. B,* **102,** 10469 (1998). Hydrophobic Effects on a Molecular Scale.
8. D. E. Hare and C. M. Sorensen, *J. Chem. Phys.,* **93,** 25 (1990). Raman Spectroscopic Study of Bulk Water Supercooled to −33°C.
9. D. E. Hare and C. M. Sorensen, *J. Chem. Phys.,* **93,** 6954 (1990). Raman Spectroscopic Study of Dilute HOD in Liquid H_2O in the Temperature Range −31.5 to 160°C.
10. K. A. T. Silverstein, A. D. J. Haymet, and K. A. Dill, *J. Am. Chem. Soc.,* **122,** 8037 (2000). The Strength of Hydrogen Bonds in Liquid Water and Around Nonpolar Solutes.
11. E. Wilhelm, R. Battino, and R. J. Wilcock, *Chem. Rev.,* **77,** 219 (1977). Low-Pressure Solubility of Gases in Liquid Water.
12. R. Fernández Prini and R. Crovetto, *J. Phys. Chem. Ref. Data,* **18,** 1231 (1989). Evaluation of Data on Solubility of Simple Apolar Gases in Light and Heavy Water at High Temperature.
13. M. P. Allen and D. J. Tildesley, *Computer Simulation of Liquids,* Oxford Univ. Press, Oxford, UK, 1987.
14. D. Frenkel and B. Smit, *Understanding Molecular Simulation*, Academic Press, New York, 1996.
15. K. A. T. Silverstein, A. D. J. Haymet, and K. A. Dill, *J. Am. Chem. Soc.,* **120,** 3166 (1998). A Simple Model of Water and the Hydrophobic Effect.
16. J. P. Hansen and I. R. McDonald, *Theory of Simple Liquids*, Academic Press, London, 1986.
17. J. D. Weeks, D. Chandler, and H. C. Andersen, *J. Chem. Phys.,* **54,** 5237 (1971). Role of Repulsive Forces in Forming the Equilibrium Structure of Simple Liquids.
18. B. Widom, *J. Chem. Phys.,* **39,** 2808 (1963). Some Topics in the Theory of Fluids.
19. B. Widom, *J. Phys. Chem.,* **86,** 869 (1982). Potential-Distribution Theory and the Statistical Mechanics of Fluids.
20. D. A. Kofke and P. T. Cummings, *Molec. Phys.,* **92,** 973 (1997). Quantitative Comparison and Optimization of Methods for Evaluating the Chemical Potential by Molecular Simulation.
21. B. Guillot, Y. Guissani, and S. Bratos, *J. Chem. Phys.,* **95,** 3643 (1991). A Computer Simulation Study of Hydrophobic Hydration of Rare Gases and of Methane. I. Thermodynamic and Structural Properties.
22. J. Forsman and B. Jönsson, *J. Chem. Phys.,* **101,** 5116 (1994). Monte Carlo Simulations of Hydrophobic Interactions: A Test Particle Approach.
23. A. Pohorille and L. R. Pratt, *J. Am. Chem. Soc.,* **112,** 5066 (1990). Cavities in Molecular Liquids and the Theory of Hydrophobic Solubilities.
24. L. R. Pratt and A. Pohorille, *Proc. Natl. Acad. Sci.* (*USA*), **89,** 2995 (1992). Theory of Hydrophobicity: Transient Cavities in Molecular Liquids.
25. B. Madan and B. Lee, *Biophys. Chem.,* **51,** 279 (1994). Role of Hydrogen Bonds in Hydrophobicity: The Free Energy of Cavity Formation in Water Models With and Without the Hydrogen Bonds.
26. C. H. Bennett, *J. Comput. Phys.,* **22,** 245 (1976). Efficient Estimation of Free Energy Differences from Monte Carlo Data.
27. K. S. Shing and K. E. Gubbins, *Molec. Phys.,* **46,** 1109 (1982). The Chemical Potential in Dense Fluids and Fluid Mixtures via Computer Simulation.
28. M. Mezei and D. L. Beveridge, *Ann. NY Acad. Sci.,* **482,** 1 (1986). Free Energy Simulations.

29. D. A. Pearlman and P. A. Kollman, *J. Chem. Phys.,* **90,** 2460 (1989). A New Method for Carrying out Free Energy Perturbation Calculations: Dynamically Modified Windows.
30. N. Lu and D. A. Kofke, *J. Chem. Phys.,* **111,** 4414 (1999). Optimal Intermediates in Staged Free Energy Calculations.
31. N. Lu and D. A. Kofke, *J. Chem. Phys.,* **114,** 7303 (2001). Accuracy of Free-Energy Perturbation Calculations in Molecular Simulation. I. Modeling.
32. N. Lu and D. A. Kofke, *J. Chem. Phys.,* **115,** 6866 (2001). Accuracy of Free-Energy Perturbation Calculations in Molecular Simulation. I. Heuristics.
33. T. P. Straatsma, H. J. C. Berendsen, and J. P. M. Postma, *J. Chem. Phys.,* **85,** 6720 (1986). Free Energy of Hydrophobic Hydration: A Molecular Dynamics Study of Noble Gases in Water.
34. N. T. Skipper, *Chem. Phys. Lett.,* **207,** 424 (1993). Computer Simulation of Methane-Water Solutions. Evidence for a Temperature-Dependent Hydrophobic Attraction.
35. T. Ghosh, A. E. García, and S. Garde, *J. Am. Chem. Soc.,* **123,** 10997 (2001). Molecular Dynamics Simulations of Pressure Effects on Hydrophobic Interactions.
36. T. Ghosh, A. E. García, and S. Garde, *J. Chem. Phys.,* **123,** 2480 (2002). Enthalpy and Entropy Contributions to the Pressure Dependence of Hydrophobic Interactions.
37. G. M. Torrie and J. P. Valleau, *J. Comput. Phys.,* **23,** 187 (1977). Nonphysical Sampling Distributions in Monte Carlo Free-Energy Estimation: Umbrella Sampling.
38. A. Ben-Naim and Y. Marcus, *J. Chem. Phys.,* **81,** 2016 (1984). Solvation Thermodynamics of Nonionic Solutes.
39. H. Qian and J. J. Hopfield, *J. Chem. Phys.,* **105,** 9292 (1996). Enthalpy-Entropy Compensation: Perturbation and Relaxation in Thermodynamic Systems.
40. R. M. Levy and E. Gallicchio, *Annu. Rev. Phys. Chem.,* **49,** 531 (1998). Computer Simulations with Explicit Solvent: Recent Progress in the Thermodynamic Decomposition of Free Energies and in Modeling Electrostatic Effects.
41. N. Matubayasi, L. H. Reed, and R. M. Levy, *J. Phys. Chem.,* **98,** 10640 (1994). Thermodynamics of the Hydration Shell. I. Excess Energy of a Hydrophobic Solute.
42. E. Gallicchio, M. M. Kubo, and R. M. Levy, *J. Am. Chem. Soc.,* **120,** 4526 (1998). Entropy-Enthalpy Compensation in Solvation and Ligand Binding Revisited.
43. S. R. Durell and A. Wallqvist, *Biophys. J.,* **71,** 1695 (1996). Atomic-Scale Analysis of the Solvation Thermodynamics of Hydrophobic Hydration.
44. D. E. Smith, L. Zhang, and A. D. J. Haymet, *J. Am. Chem. Soc.,* **114,** 5875 (1992). Entropy of Association of Methane in Water: A New Molecular Dynamics Computer Simulation.
45. D. E. Smith and A. D. J. Haymet, *J. Chem. Phys.,* **98,** 6445 (1993). Free Energy, Entropy, and Internal Energy of Hydrophobic Interactions: Computer Simulations.
46. B. Guillot and Y. Guissani, *J. Chem. Phys.,* **99,** 8075 (1993). A Computer Simulation Study of the Temperature Dependence of the Hydrophobic Hydration.
47. S. Garde, G. Hummer, A. E. García, L. R. Pratt, and M. E. Paulaitis, *Phys. Rev. E,* **53,** R4310 (1996). Hydrophobic Hydration: Inhomogeneous Water Structure Near Nonpolar Molecular Solutes.
48. S. Garde, A. E. García, L. R. Pratt, and G. Hummer, *Biophys. Chem.,* **78,** 21 (1999). Temperature Dependence of the Solubility of Non-Polar Gases in Water.
49. N. T. Southall and K. A. Dill, *J. Phys. Chem. B,* **104,** 1326 (2000). The Mechanism of Hydrophobic Solvation Depends upon Solute Radius.
50. H. S. Frank and M. W. Evans, *J. Chem. Phys.,* **13,** 507 (1945). Free Volume and Entropy in Condensed Systems. III. Entropy in Binary Liquid Mixtures; Partial Molal Entropy in Dilute Solutions; Structure and Thermodyanmics in Aqueous Electrolytes.
51. M. Lucas, *J. Phys. Chem.,* **80,** 359 (1976). Size Effect in Transfer of Nonpolar Solutes from Gas or Solvent to Another Solvent with a View on Hydrophobic Behavior.
52. B. Lee, *Biopolymers,* **24,** 813 (1985). The Physical Origin of the Low Solubility of Nonpolar Solutes in Water.

53. N. T. Southall, K. A. Dill, and A. D. J. Haymet, *J. Phys. Chem. B,* **106,** 521 (2002). A View of the Hydrophobic Effect.

54. A. Geiger, A. Rahman, and F. H. Stillinger, *J. Chem. Phys.,* **70,** 263 (1979). Molecular Dynamics Study of the Hydration of Lennard-Jones Solutes.

55. C. Y. Lee, J. A. McCammon, and P. J. Rossky, *J. Chem. Phys.,* **80,** 4448 (1984). The Structure of Liquid Water at an Extended Hydrophobic Surface.

56. W. C. Swope and H. C. Andersen, *J. Phys. Chem.,* **88,** 6548 (1984). A Molecular Dynamics Method for Calculating the Solubility of Gases in Liquids and the Hydrophobic Hydration of Inert-Gas Atoms in Aqueous Solution.

57. A. Wallqvist and B. J. Berne, *Chem. Phys. Lett.,* **145,** 26 (1988). Hydrophobic Interaction between a Methane Molecule and a Paraffin Wall in Liquid Water.

58. Y.-K. Cheng and P. J. Rossky, *Nature,* **392,** 696 (1998). Surface Topography Dependence of Biomolecular Hydrophobic Hydration.

59. D. A. Zichi and P. J. Rossky, *J. Chem. Phys.,* **84,** 2814 (1986). Solvent Molecular Dynamics in Regions of Hydrophobic Hydration.

60. H. S. Ashbaugh and M. E. Paulaitis, *J. Am. Chem. Soc.,* **123,** 10721 (2001). Effect of Solute Size and Solute-Water Attractive Interactions on Hydration Water Structure Around Hydrophobic Solutes.

61. W. L. Jorgensen, J. F. Blake, and J. K. Buckner, *Chem. Phys.,* **129,** 193 (1989). Free Energy of TIP4P Water and the Free Energies of Hydration of CH_4 and Cl^- from Statistical Perturbation Theory.

62. J. W. Arthur and A. D. J. Haymet, *J. Chem. Phys.,* **109,** 7991 (1998). Solubility of Nonpolar Solutes in Water: Computer Simulations Using the CF1 Central Force Model.

63. T. Simonson, *Molec. Phys.,* **80,** 441 (1993). Free Energy of Particle Insertion: An Exact Analysis of the Origin Singularity for Simple Liquids.

64. H. Resat and M. Mezei, *J. Chem. Phys.,* **99,** 6052 (1993). Studies on Free Energy Calculations. I. Thermodynamic Integration Using a Polynomial Path.

65. M. Zacharias, T. P. Straatsma, and J. A. McCammon, *J. Chem. Phys.,* **100,** 9025 (1994). Separation-Shifted Scaling, a New Scaling Method for Lennard-Jones Interactions in Thermodynamic Integration.

66. A. Wallqvist, E. Gallicchio, and R. M. Levy, *J. Phys. Chem. B,* **105,** 6745 (2001). A Model for Studying Drying at Hydrophobic Interfaces: Structural and Thermodynamic Properties.

67. A. Wallqvist and B. J. Berne, *J. Phys. Chem.,* **99,** 2893 (1995). Computer-Simulation of Hydrophobic Hydration Forces on Stacked Plates at Short-Range.

68. I. Tomás-Oliveira and S. J. Wodak, *J. Chem. Phys.,* **111,** 8576 (1999). Thermodynamics of Cavity Formation in Water and n-hexane Using the Widom Particle Insertion Method.

69. B. Guillot and Y. Guissani, *Molec. Phys.,* **79,** 53 (1993). Temperature Dependence of the Solubility of Non-Polar Gases in Liquids.

70. S. Garde, G. Hummer, A. E. García, M. E. Paulaitis, and L. R. Pratt, *Phys. Rev. Lett.,* **77,** 4966 (1996). Origin of Entropy Convergence in Hydrophobic Hydration and Protein Folding.

71. N. Muller, *Acc. Chem. Res.,* **23,** 23 (1990). Search for a Realistic View of Hydrophobic Effects.

72. A. Wallqvist and B. J. Berne, *J. Phys. Chem.,* **99,** 2885 (1995). Molecular Dynamics Study of the Dependence of Water Solvation Free Energy on Solute Curvature and Surface Area.

73. K. Watanabe and H. C. Andersen, *J. Phys. Chem.,* **90,** 795 (1986). Molecular Dynamics Study of the Hydrophobic Interaction in Aqueous Solutions of Krypton.

74. A. Wallqvist, *J. Phys. Chem.,* **95,** 8921 (1991). Molecular Dynamics Study of a Hydrophobic Aggregate in an Aqueous Solution of Methane.

75. S. Shimizu and H. S. Chan, *J. Chem. Phys.,* **115,** 1414 (2001). Anti-Cooperativity in Hydrophobic Interactions: A Simulation Study of Spatial Dependence of Three-Body Effects and Beyond.

76. S. Lüdemann, R. Abseher, H. Schreiber, and O. Steinhauser, *J. Am. Chem. Soc.,* **119,** 4206 (1997). The Temperature-Dependence of Hydrophobic Association in Water. Pair versus Bulk Hydrophobic Interactions.

77. S. Shimizu and H. S. Chan, *J. Chem. Phys.,* **113,** 4683 (2000). Temperature Dependence of Hydrophobic Interactions: A Mean Force Perspective, Effects of Water Density, and Nonadditivity of Thermodynamic Signatures.

78. L. X. Dang, *J. Chem. Phys.,* **100,** 9032 (1994). Potential of Mean Force for the Methane-Methane Pair in Water.

79. S. W. Rick and B. J. Berne, *J. Phys. Chem. B,* **101,** 10488 (1997). Free Energy of the Hydrophobic Interaction from Molecular Dynamics Simulations: The Effects of Solute and Solvent Polarizability.

80. S. W. Rick, *J. Phys. Chem. B,* **104,** 6884 (2000). Free Energy, Entropy and Heat Capacity of the Hydrophobic Interaction as a Function of Pressure.

81. S. Shimizu and H. S. Chan, *J. Am. Chem. Soc.,* **123,** 2083 (2001). Configuration-Dependent Heat Capacity of Pairwise Hydrophobic Interactions.

82. J. W. Arthur and A. D. J. Haymet, *J. Chem. Phys.,* **110,** 5873 (1999). Hydrophobic Hydration: Heat Capacity of Solvation from Computer Simulations and from an Information Theory Approximation.

CHAPTER 3

Born–Oppenheimer Direct Dynamics Classical Trajectory Simulations

Lipeng Sun and William L. Hase

Department of Chemistry and Department of Computer Science, Wayne State University, Detroit, Michigan 48202

INTRODUCTION

Classical Trajectory Simulations

Since the early 1960s[1,2] classical trajectory simulations, with Monte Carlo sampling of initial conditions, have been widely used to study the unimolecular and intramolecular dynamics of molecules and clusters; reactive and nonreactive collisions between atoms, molecules, and clusters; and the collisions of these species with surfaces.[3,4] For a classical trajectory study of a system, the motions of the atoms for the system under study are determined by numerically integrating the system's classical equations of motion. These equations are usually expressed in either Hamilton's form[5]

$$\frac{\partial H}{\partial q_i} = -\frac{dp_i}{dt} \quad \text{and} \quad \frac{\partial H}{\partial p_i} = \frac{dq_i}{dt} \qquad [1]$$

where H, the sum of the system's kinetic $T(\mathbf{p},\mathbf{q})$ and potential $V(\mathbf{q})$ energies, is the system's Hamiltonian

$$H = T(\mathbf{p},\mathbf{q}) + V(\mathbf{q}) \qquad [2]$$

Reviews in Computational Chemistry, Volume 19
edited by Kenny B. Lipkowitz, Raima Larter, and Thomas R. Cundari
ISBN 0-471-23585-7

or Newton's form[5]

$$m_i \frac{d^2 q_i}{dt^2} = -\frac{\partial V(\mathbf{q})}{\partial q_i} \qquad [3]$$

For the most general case (see section on integrating classical equations of motion), T depends on both the momenta $\mathbf{p}$ and coordinates $\mathbf{q}$.[6] The index i in the equations above is the number of coordinates or conjugate momenta for the Hamiltonian. If Cartesian coordinates are used, this number is $3N$, where N is the number of atoms.

An ensemble of trajectories is calculated in a trajectory simulation, with each trajectory in the ensemble specified by the system's initial set of momenta $\mathbf{p}$ and coordinates $\mathbf{q}$. The initial ensemble of $\mathbf{p}$ and $\mathbf{q}$ is chosen to represent the experiment under investigation or chosen so that a particular dynamical attribute of the system may be studied. Distribution functions are usually sampled randomly in choosing the ensemble of initial conditions and the methodology of sampling is often called *Monte Carlo sampling*. Procedures for choosing trajectory initial conditions to represent unimolecular and bimolecular reactions, and gas–surface collisions are described in the section on trajectory initial conditions.

In addition to choosing initial conditions for the ensemble of trajectories, a trajectory computer program requires a potential energy function $V(\mathbf{q})$ for the system under study, an algorithm for numerically integrating the classical equations of motion (i.e., either Hamilton's or Newton's form), and procedures for transforming a trajectory's final values for momenta and coordinates into properties that may be compared with experiment. These properties include vibrational, rotational, and relative translational energies of the products of a chemical reaction, the lifetime of a vibrationally excited molecule, and energies in a molecule's vibrational modes versus time. The above components for a classical trajectory simulation are incorporated in the general chemical dynamics computer program VENUS.[7] A flowchart of the components of a trajectory computer program is given in Figure 1.

Traditional Approach: Analytic Potential Energy Surfaces

The traditional approach for performing classical trajectory simulations is to represent $V(\mathbf{q})$ by either an empirical analytic function, with adjustable parameters, or as an analytic function fit in total or in part to ab initio potential energies. A widely used empirical potential is the London–Eyring–Polanyi–Sato function for triatomic systems.[8] Since the number of independent coordinates is $3N - 6$ for a nonlinear system with N atoms, to fit $V(\mathbf{q})$ with potential energies for each internal coordinate at NP different positions, a total of $(NP)^{3N-6}$ ab initio points are required. Thus, only for reactive systems with a small number of atoms is it practical to derive $V(\mathbf{q})$ completely from

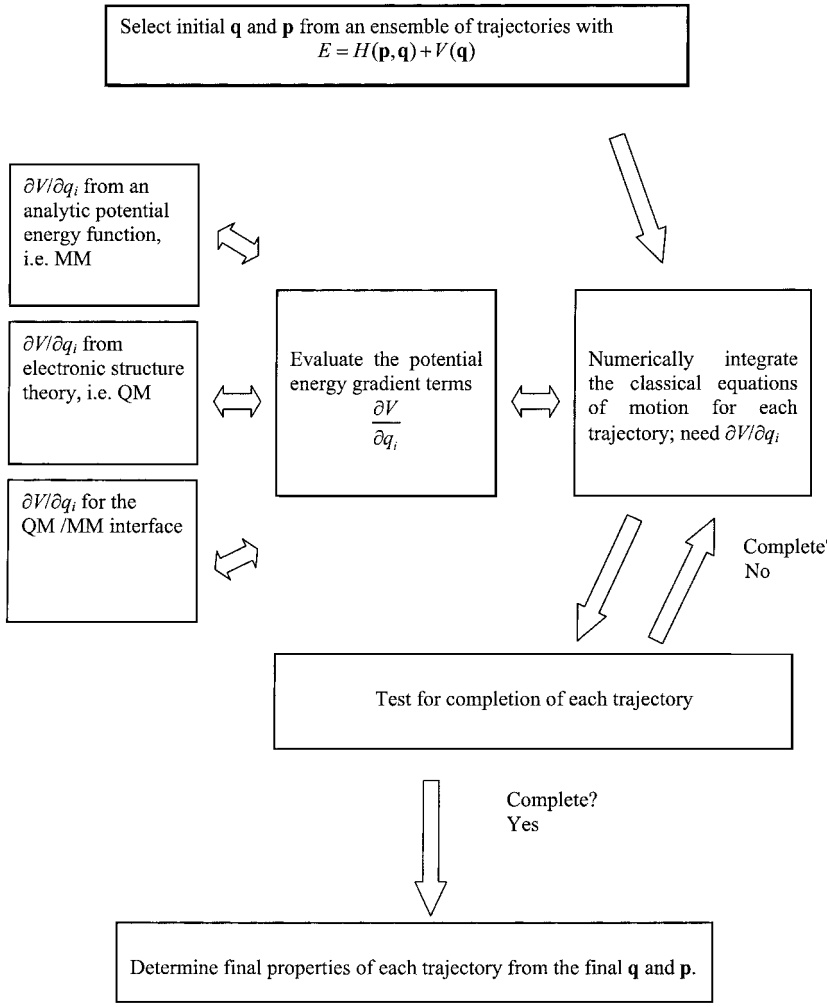

Figure 1 Flowchart for a classical trajectory computer program, in which an ensemble of trajectories is calculated in a parallel/distributed environment. The potential energy function may be analytic (MM), quantum-mechanical (QM), or a QM+MM or QM/MM combination.

high-level ab initio calculations. Potential energy functions derived in this manner include those for $H + H_2 \rightarrow H_2 + H$,[9] $F + H_2 \rightarrow HF + H$,[10] $O + H_2 \rightarrow HO_2 \rightarrow H + O_2$,[11] and $HCO \rightarrow H + CO$.[12]

An approach often used for large polyatomic systems is to derive, from ab initio calculations, an analytic potential energy function for the few degrees of freedom thought to be most critical for the dynamics, and use empirical

analytic potential energy terms for the remaining degrees of freedom.[13] This latter empirical potential is usually fit to experimental data such as force constants, equilibrium geometries, and bond energies. A representative analytic potential energy function of this form is the one developed for S_N2 nucleophilic substitution reactions of the general type[14]

$$X^- + CH_3Y \rightarrow XCH_3 + Y^- \qquad [4]$$

and applied to the specific reactions $Cl^- + CH_3Cl$,[14] $Cl^- + CH_3Br$,[15] and $F^- + CH_3Cl$.[16] The general form of the potential is illustrated here for $Cl^- + CH_3Cl$. The potential is a model chosen to represent global properties of the potential energy surface (PES) and then refined by fitting ab initio and experimental data. A potential energy contour diagram in terms of the two C—Cl distances is shown in Figure 2.

Two particularly important coordinates for the $Cl_a^- + CH_3Cl_b \rightarrow Cl_aCH_3 + Cl_b^-$ potential energy function are the Cl_a—C and C—Cl_b bond distances denoted by r_a and r_b, respectively. The terms $g_a = r_a - r_b$ and $g_b = r_b - r_a$ measure the extent of reaction. They also conveniently reflect the symmetry of the reactions; that is, g_a is $+\infty$ for reactants, 0 for the

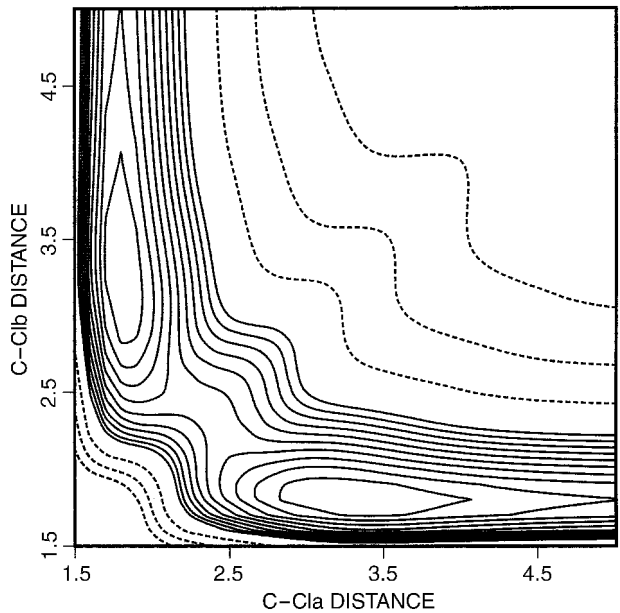

Figure 2 $Cl^- + CH_3Cl$ potential contour plot in terms of the two C–Cl distances. The remaining coordinates are set to optimized values as a function of $g_a = r_a - r_b$. Solid contour lines are at 3-kcal/mol intervals; dashed contour lines are at 15-kcal/mol intervals. (From Ref. 14.)

transition state, and $-\infty$ for products. A general model analytic function for a symmetric S_N2 reaction, $Cl_a^- + CH_3Cl_b$, may be written as

$$\begin{aligned} V_{\text{total}} = {} & V_{\text{Cl}}(r_a, g_a)[1 - S_{\text{LR}}(g_a)] + V_{\text{Cl}}(r_b, g_b)[1 - S_{\text{LR}}(g_b)] \\ & + V_\phi(r_a, g_a)[1 - S_{\text{LR}}(g_a)] + V_\phi(r_b, g_b)[1 - S_{\text{LR}}(g_b)] \\ & + V_{\text{ClCl}}[1 - S_{\text{LR}}(g_a)][1 - S_{\text{LR}}(g_b)] + V_\theta(g_a) \\ & + V_{\text{HC}} + V_{\text{LR}}^a S_{\text{LR}}(g_a) + V_{\text{LR}}^b S_{\text{LR}}(g_b) + D_{\text{MC}} + D_c \end{aligned} \quad [5]$$

where the interaction of Cl^- with CH_3Cl is divided into two regions: the long-range (electrostatic) region outside the cluster area where g_a (or g_b) is greater than the value of g for the cluster denoted by g_c and the short-range (bond-forming) region where g_a (or g_b) $< g_c$. The long-range potential terms are given by V_{LR}^a and V_{LR}^b. For large separations, these terms approach the ion-dipole potential. The $[Cl{-}CH_3{-}Cl]^-$ short-range interaction is described by the V_{Cl} Morse terms for the $Cl_a{-}C$ and $C{-}Cl_b$ stretches, the $Cl_a{-}CH_3$ and $CH_3{-}Cl_b$ angular deformation terms are denoted by V_ϕ, and the Cl—Cl interaction term by V_{ClCl}. The HCH bending potential of the CH_3 moiety is given by V_θ. V_{HC} represents the potential for the three HC stretches. D_{MC} is the ClC bond energy for CH_3Cl (methyl chloride), and D_c is the ClC bond energy for cluster.

The long-range potential terms are smoothly connected to the short-range potential terms by the S_{LR} switching functions. For small g_a, $S_{\text{LR}}(g_a)$ approaches zero, effectively turning off V_{LR}^a and turning on the short-range potential functions for Cl_a. However, for large g_a where $S_{\text{LR}}(g_a) = 1.0$ and $S_{\text{LR}}(g_b) = 0$, the total potential function becomes

$$V_{\text{total}} = V_{\text{Cl}}(r_b, g_b) + V_\phi(r_b, g_b) + V_\theta(g_a) + V_{\text{HC}} + V_{\text{LR}}^a + D_{\text{MC}} + D_c \quad [6]$$

Here, the potential function contains terms for the short-range $CH_3{-}Cl_b$ interactions, long-range $Cl_a^- + CH_3Cl_b$ interactions, V_θ, and V_{HC}.

When g_a and g_b are both less than g_c, the V_{ClCl} term is completely turned on, since both S_{LR} terms equal zero. For this region, the potential becomes

$$\begin{aligned} V_{\text{total}} = {} & V_{\text{Cl}}(r_a, g_a) + V_{\text{Cl}}(r_b, g_b) + V_\phi(r_a, g_a) + V_\phi(r_b, g_b) \\ & + V_{\text{ClCl}} + V_\theta(g_a) + V_{\text{HC}} + D_{\text{MC}} + D_c \end{aligned} \quad [7]$$

In the intermediate range where Cl_a^- is approaching methyl chloride and $S_{\text{LR}}(g_a)$ is changing from 1.0 to 0.0, all terms in the potential function contribute except for V_{LR}^b.

The function in Eq. (5) is also used for $Cl^- + CH_3Br$ and $F^- + CH_3Cl$, except the CH_3Cl_b moiety is replaced by CH_3Br for the former and F^- replaces Cl_a^- for the latter. These two potential functions are unsymmetric with respect

to both the reactant and product asymptotic limits and the strongly interacting central barrier and ion–dipole complex regions.

The abovementioned approach for representing PESs, for large polyatomics, has several ambiguities and difficulties. For many reactions there may be considerable uncertainty in identifying the coordinates most critical for the dynamics and for which an ab initio potential is required. Furthermore, sufficient experimental information is usually lacking to uniquely parameterize the potential for the remaining "noncritical" coordinates. Instead, a "realistic" potential for these coordinates is constructed by combining terms such as Morse functions and valence force field potentials, which span the complete coordinate space, but only require a small number of parameters. There are also uncertainties in representing the potential energy couplings between the critical and noncritical coordinates, and it is hoped that the important couplings for the reaction dynamics are retained in the ab initio potential for the assumed critical degrees of freedom.

Direct Dynamics Simulations

With the increased speed of computers it has become possible to use electronic structure theory directly in classical trajectory simulations, without the need for an empirical or analytic potential energy function or having to distinguish between critical and noncritical degrees of freedom. The trajectories are integrated "on the fly" with the potential energy $V(\mathbf{q})$ and its derivatives $\partial V/\partial q_i$ obtained directly from electronic structure theory. This approach was first used by Wang and Karplus[17] in 1973 to study the $^1CH_2 + H_2 \rightarrow CH_4$ reaction. With direct dynamics, the "unadulterated" classical dynamics is obtained for a particular electronic structure theory. Thus, there is no uncertainty in testing different electronic structure theory methods when comparing the dynamics with experiment, nor is there a need to fit potential energy points for the electronic structure theory to an analytic potential energy function.

Two approaches have been advanced for performing direct dynamics simulations on a potential energy surface for a single electronic state.[18] The Born–Oppenheimer (BO) direct dynamics approach is considered here. It bears a close resemblance to traditional classical trajectory simulations and electronic structure calculations. At each step of the trajectory integration the potential energy $V(\mathbf{q})$ and gradient $\partial V(\mathbf{q})/\partial q_i$ are obtained by optimizing the electronic wavefunction.

For the second approach, called Car–Parrinello (CP) direct dynamics,[19] the electronic wavefunction and nuclear motion are propagated simultaneously. When applying this method within the framework of density functional theory (DFT), the wavefunction is propagated by using fictitious electronic degrees of freedom with arbitrary masses. In ab initio and semiempirical electronic structure theories, the wavefunction is expanded in a set of basis functions and then as a superposition of zeroth-order electronic state

wavefunctions to treat electron correlation. The CP method is applied by propagating the resulting expansion coefficients. A drawback of the CP method is that, unless the CP wavefunction is reoptimized at each integration step, energy may flow from the nuclear coordinates to the fictitious electronic degrees of freedom, thereby leading to CP dynamics that may occur on multiple BO potential energy surfaces.

The remainder of this chapter is organized as follows. Born–Oppenheimer direct dynamics is reviewed in the next (second major) section. Approaches for integrating the classical equations of motion are outlined in the third major section (on integrating classical equations of motion). Algorithms for choosing initial conditions for ensembles of trajectories representing unimolecular and bimolecular reactions are reviewed in the fourth major section. The adequacy of classical mechanics for describing the dynamics of chemical processes, and the possible importance of quantum effects, is reviewed in the fifth major section. The final section surveys several applications of direct dynamics.

BORN–OPPENHEIMER DIRECT DYNAMICS

As discussed above, in Born–Oppenheimer (BO) direct dynamics the potential energy $V(\mathbf{q})$ and derivatives $\partial V/\partial q_i$ for each step of the trajectory integration are obtained by optimizing the electronic wavefunction. For a Born–Oppenheimer electronic structure theory calculation the electronic energy $E_e(\mathbf{q})$ is determined variationally from

$$E_e(\mathbf{q}) = \frac{\langle \psi_e(\mathbf{q}) H_e(\mathbf{q}) \psi_e(\mathbf{q}) \rangle}{\langle \psi_e(\mathbf{q}) \psi_e(\mathbf{q}) \rangle} \qquad [8]$$

Adjustable parameters in the electronic wavefunction $\psi_e(\mathbf{q})$ are varied to minimize $E_e(\mathbf{q})$ for the set of coordinates $\mathbf{q}$. The potential energy for the system is given by

$$V(\mathbf{q}) = E_e(\mathbf{q}) + V_{NN}(\mathbf{q}) \qquad [9]$$

where $V_{NN}(\mathbf{q})$ is the nuclear–nuclear repulsion energy. It is straightforward to show that the derivative $\partial V_{NN}(\mathbf{q})/\partial q_i$ is analytic and, depending on the electronic structure theory and computer program used for the simulations, the derivative $\partial E_e(\mathbf{q})/\partial q_i$ may be determined directly as $E_e(\mathbf{q})$ is calculated without the need for a finite difference. The gradient $\partial V/\partial q_i$ needed to integrate the classical equations, in Eqs. [1] and [3], is the sum of $\partial E_e(\mathbf{q})/\partial q_i$ and $\partial V_{NN}(\mathbf{q})/\partial q_i$.

Direct dynamics was first applied by Wang and Karplus[17] in a study of the $^1CH_2 + H_2 \rightarrow CH_4$ reaction. The CNDO semiempirical electronic structure theory was used for this calculation. Two years later, Warshel and

Karplus[20] employed this level of theory to study the photoisomerization of 2-butene. The first ab initio direct dynamics study is that by Leforestier[21] for the $H^- + CH_4 \rightarrow CH_4 + H^-$ S_N2 nucleophilic substitution reaction.

Because the electronic energy $E_e(\mathbf{q})$ in Eq. [8] and its derivatives must be calculated at each integration step of a classical trajectory, a direct dynamics simulation is usually very computationally intense. A standard numerical integration time step is $\Delta t = 10^{-16}$ s. Thus, if a trajectory is integrated for 10^{-12} s, 10^4 evaluations of Eq. (8) are required for each trajectory. An ensemble for a trajectory simulation may be as small as 100 events, but even with such a small ensemble 10^6 electronic structure calculations are required. Because of such computational demands, it is of interest to determine the lowest level of electronic structure theory and smallest basis set that gives an adequate representation for the system under study. In the following parts of this section, semiempirical and ab initio electronic structure theories and mixed electronic structure theory (quantum mechanical) and molecular mechanical (i.e. QM/MM)[22] approaches for performing direct dynamics are surveyed.

Semiempirical Electronic Structure Theory

The compute time required for a Hartree-Fock calculation scales as the fourth power of the number of basis functions,[23] which arises from the large number of two-electron integrals that must be calculated. In the semiempirical method, the computational cost is decreased by reducing the number of these integrals.[24] This is accomplished in part by explicitly considering only the valence electrons and representing them by a minimal basis set. The computational effort is further reduced by neglecting the products of all basis functions on different atoms. To compensate for these approximations, the remaining integrals are made into parameters, and their values are assigned on the basis of calculation or experimental data.

The above approximations form the basis for the neglect of diatomic differential overlap (NDDO) model, which has been used in BO direct dynamics simulations. The MNDO,[25] AM1,[26] PM3,[27] and MNDO/d[28] methods are parameterizations of the NDDO model. As discussed above, these semiempirical methods require parameters for electron integrals. In the MNDO framework, the parameters are monoatomic and include one-electron integrals (U_{ss} and U_{pp}), two-electron one-center integrals (G_{ss}, G_{sp}, G_{pp}, G_{p2}, and H_{sp}), core–core repulsion range parameters (α), Slater orbital exponents (z_s and z_p), and resonance integral multipliers (β_s and β_p). These terms are described in detail elsewhere.[29] The parameters were optimized in the MNDO method[25] to reproduce observed heats of formation, dipole moments, ionization potentials, and molecular geometries. As this method was unable to correctly describe hydrogen bonding, two to four spherical Gaussian terms were added for each atom in order to correct for the excessive repulsions at van der Waals distances. In this improved model, called AM1,[26] these terms

act as van der Waals attraction and dispersion operators, and therefore mimic long-range correlation effects. For these MNDO and AM1 methods, parameters were derived for one element at a time while keeping the parameters for the remaining atoms constant. In contrast for PM3,[27] a more recently derived NDDO model, all the parameters are treated as adjustable which were derived simultaneously for many elements in order to reproduce large amounts of experimental data. The functional form for PM3 is the same as for AM1, except that only two Gaussians are assigned to each atom.

The principal parameterization of the MNDO, AM1, and PM3 models is for *s* and *p* functions. Though they have parameters for some metals, these are often based on very limited experimental data and, thus, may be very unreliable. Thiel and co-workers[28,30] have developed MNDO/d,[30] which more accurately represents metals. With *s*, *p*, and *d* functions, MNDO/d typically employs 15 parameters per atom. MNDO/d is one of the MNDO methods in the computer program package MNDO97.[28] OM1 and OM2 methods, which go beyond MNDO methods by employing orthogonalization corrections, are also included in MNDO97.

The above NDDO models may be viewed as functionals with parameters for fitting a potential energy surface. This approach was first suggested by Gonzalez-Lafont, Truong, and Truhlar[31] as a means to represent reaction path properties for a specific reaction. This has been called the NDDO-SRP approach, where SRP denotes specific reaction parameters. NDDO-SRP potentials have been derived by either varying only a subset of the previously fitted NDDO parameters or refitting all of the parameters. An example of the former is the original work by Gonzalez-Lafont, Truong, and Truhlar.[31] Here an AM1-SRP potential was derived for the $Cl^- + CH_3Cl$ S_N2 reaction by modifying the one-center, one-electron energies U_{pp}^x, for the p-orbitals, on atom X with X = C and Cl. The remaining AM1 parameters were used without change. The U_{pp}^{Cl} parameter for Cl was readjusted to make the calculated electron affinity for Cl agree with the experimental value. The U_{pp}^{C} parameter for *C* was adjusted to fit the classical barrier height at the $[Cl{-}{-}{-}CH_3{-}{-}{-}Cl]^-$ saddle point.

The strategy of refitting all the NDDO parameters was used to represent the $H_2CO \rightarrow H_2 + CO$ potential energy surface.[32] Eight semiempirical models were derived by introducing SRPs into the AM1 and PM3 Hamiltonians to improve the fit to selected ab initio and experimental properties. Five were obtained by fitting to points distributed over the HF/6-31G** surface for the reaction and a sixth by only fitting to data at the HF/6-31G** stationary points. The HF/6-31G** level of theory was used in an ab initio direct dynamics study of the $H_2 + CO$ product energy distributions in H_2CO dissociation,[33] and these models were constructed to ascertain if they would give the same product energy distribution as the ab initio surface. The final two models were obtained by fitting to experimental data and CCSD(T) results,[34] since calculations at this level of theory are in excellent agreement with experiment. The revised semiempirical parameters are given in Reference 32.

Semiempirical models have also been modified to more accurately represent a potential energy surface (PES) by using SRPs and including additional analytic potential energy functions. This approach was used to develop an accurate PES for trimethylene and its geometric and structural isomerization pathways.[35] The SRPs involved changing original resonance integrals $H_{\mu\nu}$, for atomic orbitals μ, ν located on different atoms, to $H'_{\mu\nu} = \beta_{\mu\nu} H_{\mu\nu}$, where $\beta_{\mu\nu}$ depends only on μ and ν. These $\beta_{\mu\nu}$ parameters were determined for the resonance integrals between H atoms of trimethylene and the terminal C atoms, and for the resonance integrals between the terminal C atoms, by fitting experimental and CASSCF potential energy surface properties.

Semiempirical electronic structure theory will continue to be important in direct dynamics simulations. The compute time for an NDDO method scales according to N^2, which makes these methods attractive for large molecular systems. Since integrals are parameterized in the semiempirical methods, they are much faster than ab initio approaches. For example, the relative compute time required to calculate a single energy for protonated glycine is 1 : 11 : 20 at the AM1, B3LYP/6-31G* and MP2/6-31G* levels of theory. The semiempirical methods may be used in QM/MM models (see discussion below) to represent very large molecular systems. An example of such a direct dynamics study is the $O(^3P)$ reaction with an n-hexylthiolate self-assembled monolayer (SAM).[36]

Ab Initio Electronic Structure Theory

A variety of ab initio methods have been used in Born–Oppenheimer direct dynamics simulations. Since ab initio methods require substantial compute time, a balance must be found in choosing a method that is computationally tractable and also provides meaningful results. In the Hartree–Fock model each electron sees only the average field of the other electrons. In reality, the electrons must explicitly avoid each other because of their mutual Coulombic repulsion; hence their motions are correlated. The difference between the Hartree–Fock energy and the exact energy is called the *correlation energy*. The Hartree–Fock wavefunction can be improved by taking a linear combination of Slater determinants, yielding a configuration interaction (CI) wavefunction:[37]

$$\Psi = a_0 \Psi_0 + \sum_{ia} a_i^a \Psi_i^a + \sum_{i<j, a<b} a_{ij}^{ab} \Psi_{ij}^{ab} + \cdots \qquad [10]$$

where $\Psi_i^a, \Psi_{ij}^{ab}, \ldots$ are Slater determinants in which occupied spin orbitals $\phi_i, \phi_j, \ldots$ in the reference determinant Ψ_0 are replaced by unoccupied or virtual spin orbitals $\phi_a, \phi_b, \ldots$ (i.e., determinants that are singly excited, doubly excited, etc.). In a standard CI calculation Ψ_0 is first determined by a Hartree-Fock calculation. The coefficients $a_i^a, a_{ij}^{ab} \ldots$ for the excited Slater determinants

are then determined variationally. In the multiconfiguration self-consistent field (MCSCF) method,[38,39] a variational calculation is performed by simultaneously minimizing the energy with respect to the coefficients c_{ni} for the molecular orbitals, and the $a_i^a, a_{ij}^{ab}, \ldots$ coefficients, Eq. [10]. An approach for selecting the necessary configurations in the MCSCF method is the complete active space (multiconfiguration) self-consistent field (CASSCF) method,[40–42] in which the molecular orbitals are partitioned into active and inactive spaces. A full CI is performed in the active space with the MCSCF optimization. The molecular orbitals for the active space usually are chosen as some of the highest occupied orbitals and some of the lowest unoccupied orbitals, while in the inactive space, the molecular orbitals are chosen in the way that they are either doubly occupied or empty.

Although the CI energy is variational, it is not size-consistent; that is, E_{CI} for X and Y at large separation is not the sum of the E_{CI} for X and E_{CI} for Y computed individually. This is often a severe problem in computing reaction energies, and it is thus desirable to have a CI-like method that is size-consistent. This role is filled by the coupled-cluster (CC)[43] method and the quadratic configuration interaction (QCI) approach.[44] The MCSCF method is size consistent. Instead of choosing the HF wavefunction as the reference in the CI method, the MCSCF wavefunction can also be chosen as the reference. This method is defined as the multireference configuration interaction (MRCI) method.[45,46] The MRCI method is not size-consistent.

The coefficients $a_i^a, a_{ij}^{ab}, \ldots$ in Eq. [10] can also be determined by perturbation theory. A convenient zeroth-order Hamiltonian operator $\hat{H}_0$ is the Fock operator, since the Hartree–Fock wavefunction is an eigenfunction of the Fock operator, as are excited configurations derived from it by replacing occupied orbitals with virtual orbitals. This choice of $\hat{H}_0$ yields Møller–Plesset (MP) perturbation theory,[47,48] in which the correlated motion of the electrons is the perturbation. A calculation of this type is referred to as MP2, MP3, or MP4 if it is performed through second, third, or fourth order, respectively. The MP*n* methods are size-consistent.

The relative compute times required for different ab initio methods are compared in Table 1 for the $Cl^- + CH_3Cl$ S_N2 reaction.[49] This comparison illustrates the utility of the MP2 method. Though it gives more accurate structures and energies than does HF, the MP2 calculations do not require appreciably more compute time; that is, only approximately a factor of 3 more is needed for $Cl^- + CH_3Cl$. At the present time, a very high-level electronic structure theory such as CCSD(T) is not feasible for direct dynamics. Multiconfiguration ab initio methods are practical for direct dynamics simulations, as illustrated by the use of CASSCF in a recent study of the unimolecular dynamics of the cyclopropyl radical.[50]

In contrast to the wavefunction approach for electronic structure calculations, described above, the density functional theory (DFT) is based on the Hohenberg-Kohn theorem[51] that the complete ground-state properties of the

Table 1 D_{3h} and C_s Barrier Properties for $Cl^- + CH_3Cl$ and CPU Time for Direct Dynamics at Different Levels of Electronic Structure Theory[a]

	D_{3h} Barrier			C_s Barrier			
Theory	Energy[b]	C–Cl	C–H	Energy[c]	C–Cl	Cl–C–Cl	Relative CPU Time
HF/3-21+G*	2.06	2.40	1.06	54.70	2.70	92.8	1.00
HF/6-31G*	3.57	2.38	1.06	56.34	2.73	95.2	1.14
HF/6-31G**	3.42	2.38	1.06	55.30	2.75	96.8	1.49
HF/6-31+G*	6.59	2.39	1.06	57.78	2.79	98.6	1.59
HF/6-311++G**	6.91	2.39	1.06	56.78	2.81	101.2	8.52
MP2/6-31G*	4.54	2.31	1.07	55.56	2.42	85.1	3.05
MP2/6-31G**	4.52	2.30	1.07	55.04	2.41	85.4	4.24
MP2/6-31+G*	7.66	2.32	1.07	56.68	2.44	84.2	4.58
MP2/6-311++G**	7.96	2.30	1.07	56.01	2.40	84.7	23.14
CCSD(T)/367cGTOs	3.16	2.31	1.07				

[a] Energies are in kcal/mol, distances in angstroms, and angles in degrees. The relative direct dynamics CPU time is for calculations using one processor on a SGI/MIPS R10000 workstation.
[b] The classical potential energy barrier. Including harmonic zero-point energies lowers the barrier by 0.3–0.5 kcal/mol.
[c] The classical potential energy barrier. Including harmonic zero-point energies lowers the barrier by ~1–2 kcal/mol.

system are determined by the electronic density. However, the universal energy density functional $E(\rho)$ is not known and approximate models for $E(\rho)$ must be used. Kohn and Sham[52] proposed that the functional for a system of electrons can be written as:

$$E_{KS}[\rho] = T_S[\rho] + E_{es}[\rho] + E_{xc}[\rho] \qquad [11]$$

where the terms on the right-hand side are the kinetic energy of non interacting electrons, the electrostatic energy, and the so-called exchange-correlation energy, respectively. For practical purposes further approximations such as local density approximation (LDA)[53] and gradient corrected or generalized gradient approximations (GGA)[54–57] models are proposed for treating the exchange-correlation term in the above equation. Widely used formulas such as SVWN,[53] B88,[54] B3/ACM,[55] BLYP,[54,56] and PW91[57] are examples of these models.

Due to the delocalized nature of quantum mechanical particles, the abovementioned quantum-mechanical calculations are highly computationally demanding. To apply quantum mechanical calculations to very large molecular systems linear scaling methods have been developed. The key point to achieving linear scaling is the localization of the electronic degrees of freedom. By dividing the system into subsystems determined by local Hamiltonians[58–60] or by using localized orbitals,[61,62] the $O(N^3)$ computational effort for diagonalizing Kohn–Sham/Fock matrices can be reduced to $O(N)$. The time-consuming evaluation of exchange and Coulomb integrals are approximated by using either a hierarchical approach,[63] fast multipole moment (FMM)

method,[64,65] or recursive bisection method (RBM).[66,67] A detailed description of various linear scaling methods for large system calculations can be found in the review article by Yang.[68] Because a large number of energy and gradient evaluations are required for each classical trajectory, the importance of linear scaling in Born–Oppenheimer direct dynamics simulations is obvious.

QM + MM and QM/MM Methods

Many chemical reactions proceed in the condensed phase and involve a large number of atoms. It is not possible to directly simulate such a system with the current computational power. Instead, simplified theoretical models are designed to simulate these reactions. A model system is usually chosen to include at least several thousand atoms in order to correctly represent the physical and chemical properties of the real system. Quantum mechanics provides the exact molecular properties at the microscopic level. However, accurate ab initio methods can only treat mid-sized systems (i.e., $\leq$100 atoms). Semiempirical and DFT methods can extend the system size under study up $\sim$1000 atoms, but that is still not big enough even for simplified model systems. Molecular dynamics or Monte Carlo classical trajectory simulations have been successfully used to study large systems of $\leq 10^6$ atoms.[69] However, their applications are limited to the use of molecular mechanical force fields that do not correctly describe bond cleavage or chemical reaction. Therefore, it is natural to develop methods that combine quantum and molecular mechanics potentials to simulate complex reaction systems. QM + MM and QM/MM methods, in which atoms that are most important to reactions are treated by quantum mechanics (QM) and the rest by molecular mechanics (MM), have proven to be powerful tools for modeling large systems. The QM/MM approach was first developed by Warshel and Karplus.[22] Since the early 1980s there has been a rapid development in the QM/MM and QM + MM methods and these methods have been used to simulate reactions in solution[70] and in enzymes.[71] There are several excellent reviews on the QM/MM method.[72,73] In the following, we give only a brief description of the method.[72–75]

When using a point mass model for the nuclei and electrons, and ignoring spin–orbit coupling, the full Hamiltonian operator with nuclei and electronic degrees of freedom can be written as

$$\hat{H} = -\frac{\hbar^2}{2m_i}\sum \nabla_i^2 - \frac{\hbar^2}{2}\sum \frac{1}{m_\alpha}\nabla_\alpha^2 + \sum_i \sum_{i<j} \frac{e^2}{r_{ij}} + \sum_\alpha \sum_{\alpha<\beta} \frac{Z_\alpha Z_\beta e^2}{R_{\alpha\beta}} - \sum \sum \frac{Z_\alpha e^2}{r_{\alpha i}} \quad [12]$$

where i,j and α, β are indexes for electrons and nuclei, respectively. Making the Born–Oppenheimer approximation, the second term in this equation is

ignored. The electronic Hamiltonian is then

$$\hat{H} = -\frac{\hbar^2}{2m_i}\sum \nabla_i^2 + \sum_i \sum_{i<j} \frac{e^2}{r_{ij}} - \sum \sum \frac{Z_\alpha e^2}{r_{\alpha i}} + \sum_\alpha \sum_{\alpha<\beta} \frac{Z_\alpha Z_\beta e^2}{R_{\alpha\beta}} \qquad [13]$$

For convenience the last term in Eq. [13], which is the nuclear repulsion V_{NN}, is also included in the electronic Hamiltonian operator. This is because, for each nuclear configuration, this term is a constant and does not affect the electronic wavefunction.

By partitioning the system into QM and MM parts, as shown in Figure 3, the above Hamiltonian operator can be expressed as

$$\hat{H} = \hat{H}_{\mathrm{QM}} + \hat{H}_{\mathrm{QM/MM}} + \hat{H}_{\mathrm{MM}} \qquad [14]$$

$\hat{H}_{QM}$ takes the same form as Eq. [13] except that the indexes are only for QM atoms. The total energy of the system is

$$E = \langle \Psi | \hat{H}_{\mathrm{QM}} + \hat{H}_{\mathrm{QM/MM}} | \Psi \rangle + E_{\mathrm{MM}} \qquad [15]$$

where Ψ is the normalized wavefunction, which is a function of electronic coordinates r, QM nuclear coordinates R_{QM} and MM nuclear coordinates R_{MM}. Using the Born–Oppenheimer approximation, the potential energy surface is obtained by integrating the first term on the right hand side of Eq. [15] over all the nuclear configurations of R_{QM} and R_{MM}.

$\hat{H}_{\mathrm{QM/MM}}$ depends on the QM/MM model. If the QM/MM interaction force field is represented by only long-range point charges q_{M} and Lennard-Jones potentials in the MM part, then it can be written as

$$\hat{H}_{\mathrm{QM/MM}} = -\sum \frac{q_M e}{r_{iM}} + \sum \frac{Z_\alpha q_M e^2}{R_{\alpha M}} + \sum \left\{ \frac{a_{\alpha M}}{R_{\alpha M}^{12}} - \frac{b_{\alpha M}}{R_{\alpha M}^{6}} \right\} \qquad [16]$$

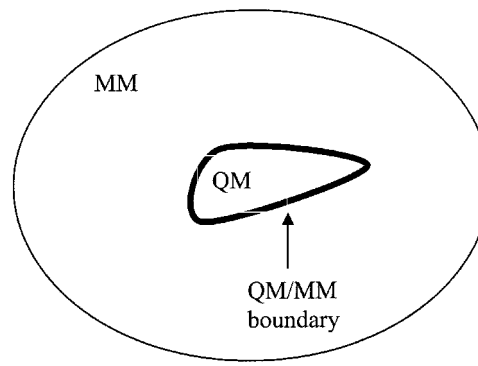

Figure 3 Partition of the QM/MM system.

Furthermore, if there is no charge interaction between the QM and MM parts, then the above QM/MM Hamilton operator is solely determined by nuclear coordinates, so that

$$E = \langle \Psi | \hat{H}_{\mathrm{QM}} | \Psi \rangle + E_{\mathrm{QM/MM}} + E_{\mathrm{MM}} \qquad [17]$$

This is called the *QM + MM model*.

The integrals in Eqs. [15] and [17] are evaluated by solving the time-independent Schrödinger equation. Depending on the system size and accuracy requirement, ab initio, DFT or semiempirical methods can be used to solve the Schrödinger equation and determine the system's potential energy surface. The quantum mechanical methods are described in the previous two sections and are not repeated in this section. The direct dynamics calculation is performed with this potential energy surface.

With the current development of quantum chemistry, it is routine to evaluate Eq. [17] for the QM + MM model and the application of QM + MM direct dynamics is described in the section on trajectory initial conditions. However, in many situations the QM/MM boundary must cut through a chemical bond in a molecule. In such a case, the total electronic Hamiltonian cannot be divided as for the QM + MM model. Different approaches have been developed to treat QM/MM interactions when the boundary cuts through a chemical bond. Gao et al.[76] identified a criterion for treating a covalent bond at the QM/MM boundary. In general, a reasonable boundary method should be able to mimic the real physical properties of the model system as closely as possible. The obtained properties such as vibrational frequencies, energies, and electronegativities, *etc*. should be comparable to experiment or accurate ab initio calculations.

A straightforward boundary method involves the "link atom."[74,77] In order to saturate the valence of the QM atoms at the boundary, an unphysical atom is added to each of the boundary QM atoms. Typically a hydrogen atom is chosen as the link atom, since the broken bond is usually a σ bond, such as a C—C bond in enzymes. These link atoms can be invisible to MM atoms; that is, there are no interactions between the link atoms and MM atoms and constraints may be included to keep the hydrogen atom lying along the direction of the covalent bond. Allowing the link atom to move freely will change the actual dynamics and the QM/MM interaction forces, while adding constraints to the link atom is unphysical and omits forces between the MM and QM regions. The net effect is that the QM fragment does not experience the actual electrostatic environment. An approach to overcome the problem has been proposed by Eichinger et al.[78] They transformed the force exerted on the link H atom to the C atom by the scaled-position link atom method (SPLAM), to mimic the real C—C force field between the QM and MM boundary. Instead of using hydrogen as the link atom, there are other approaches that use halogen like atoms to saturate the valence of the QM part.[79]

In order to overcome the defects arising from adding unphysical link atoms to the system, efforts have been made to search for better approaches. In the spirit of the hybrid orbital approach suggested by Warshel and Levitt,[80] Rivail et al.[81–83] proposed a local self-consistent field (LSCF) approach, in which a frozen hybrid orbital was used to saturate the free valence at the QM/MM boundary. The local frozen density orbitals were obtained by optimizing other smaller model systems and were assumed to be transferable to larger systems. The LSCF method has been implemented with semiempirical, ab initio, and DFT methods.[81,83,84] Gao et al.[76,85] developed a generalized (semiempirical) hybrid orbital (GHO) approach. In their method, the local bond orbitals are made more transferable by optimizing the semiempirical parameters of the boundary atoms. The difference between LSCF and GHO is the partition at the QM/MM boundary. In LSCF the boundary atom is a QM atom with the hybrid local bond orbital pointing toward the MM atom, while the boundary in the GHO approach is treated as both a QM and MM atom. In addition to the hybrid orbital approach, Zhang, Lee, and Yang[86] developed a pseudobond method. Instead of using a hydrogen atom to saturate the free valence of a σ bond, the boundary MM atom was replaced by a pseudobond with its effective core potential optimized to mimic the real QM/MM boundary interaction. Zhang, Lee, and Yang[86] tested their approach by constructing the pseudobond for a carbon boundary atom. Other similar approaches can be found in papers by Antes and Thiel[87,88] and Bersuker et al.[89] Gordon and co-workers[90] have developed the effective fragment potential (EFP) method for developing QM/MM potential models. The method describes solvation as well as QM/MM links across covalent bonds.

Even though the above methods have been successfully applied to some large-scale simulations, additional general theoretical developments are still needed. When the QM/MM boundary bisects the chemical bond, none of the above methods can treat the boundary exactly. Introducing link atoms or predetermined MOs does not reflect the real QM/MM interaction potentials. Unphysical flow of energy between the QM and MM parts may occur at the QM and MM boundary and the effect of such dynamics is not predictable. However, as an approximate method to simulate large chemical systems, the QM/MM and QM + MM approaches can provide valuable information such as energies, structures, reaction rates, and chemical dynamics.

INTEGRATING THE CLASSICAL EQUATIONS OF MOTION

As discussed above in the chapter introduction, either Newton's or Hamiltonian's equations may be numerically integrated for direct dynamics simulations. There is also a choice of coordinate representation, such as Cartesian, internal,[6] or instantaneous normal modes.[91,92] Though potential

energy functions are easily conceptualized in internal coordinates, it is efficient only for small molecular systems to integrate the classical equations of motion in these coordinates. This is because, in internal coordinates, the kinetic energy depends on the coordinates as well as the momenta, and the representation of the kinetic energy is very complex.[6] Thus, either Cartesian or instantaneous normal-mode coordinates are commonly used to integrate the classical equations of motion. Procedures for these numerical integrations have been recently surveyed,[18,93] and only cursory descriptions are given here.

Cartesian Coordinates

A number of different algorithms (for example the Gear and Adams-Moulton methods)[18,93] are commonly used to integrate Hamilton's equations of motion, Eq. [1], in Cartesian coordinates. These are predictor-corrector algorithms requiring two evaluations of the gradient terms $\partial V/\partial q_i$ during each numerical integration step. The integration accuracy of these algorithms is usually at fourth order or higher.

Symplectic integrators are often used to integrate the classical equations of motion.[94] Unlike the above numerical methods, symplectic integrators preserve certain dynamical properties such as the phase-space volume, which the exact trajectories are known to exhibit. The Verlet algorithm[95] is a symplectic integration scheme and is widely used to integrate Newton's equations of motion. Verlet's algorithm for positions is obtained by writing the Taylor series from t forward to $t + \Delta t$, and then the Taylor series from t backward to $t - \Delta t$, and then adding the expressions. The resulting algorithm is

$$q_i(t + \Delta t) = 2q_i(t) - q_i(t - \Delta t) - \frac{1}{m_i}\left(\frac{\partial V}{\partial q_i}\right)\Delta t^2 \qquad [18]$$

The velocities $\dot{q}_i$ are not needed to compute the trajectories, but they are useful for calculating the kinetic energy and may be obtained from

$$\dot{q}_i(t) = \frac{q_i(t + \Delta t) - q_i(t - \Delta t)}{2\Delta t} \qquad [19]$$

Symplectic methods typically give good energy conservation for long time integration of large systems, and are superior to predictor–corrector nonsymplectic schemes that yield a continuous drift in energy. However, symplectic integration typically leads to fluctuations in the energy, which, although small in comparison to the long-term drift observed for nonsymplectic integrators, are large compared to short-term drift. Thus, nonsymplectic algorithms are favored when integrating small systems for short times.

Instantaneous Normal-Mode Coordinates

Classical trajectories may also be calculated using instantaneous normal-mode coordinates.[96,97] The potential in a small region, defined by the trust radius around a point $\mathbf{q}_0$ on the potential energy surface, can be expressed as

$$V = V_0 + \mathbf{G}\Delta\mathbf{q} + \tfrac{1}{2}\Delta\tilde{\mathbf{q}}\mathbf{F}\Delta\mathbf{q} \qquad [20]$$

where V_0, $\mathbf{G}$, and $\mathbf{F}$ are the potential, gradient and force constants at $\mathbf{q}_0$, and $\Delta\mathbf{q} = \mathbf{q} - \mathbf{q}_0$ are the Cartesian displacements. Introducing normal mode coordinates leads to separability of the equations of motions so that

$$\ddot{Q}_i = -g_i - \omega_i^2 Q_i \qquad [21]$$

for each normal mode i. Q_i are the normal-mode displacements and, together with the normal mode momenta P_i are integrated according to

$$\begin{aligned}
Q_i(t) &= \frac{P_i^0}{\omega_i}\sin(\omega_i t) - \frac{g_i}{\omega_i^2}[1 - \cos(\omega_i t)], && \omega_i > 0 \\
&= P_i^0 t - \frac{1}{2}g_i t^2, && \omega_i = 0 \\
&= \frac{P_i^0}{|\omega_i|}\sinh(|\omega_i| t) + \frac{g_i}{|\omega_i|^2}[1 - \cosh(|\omega_i| t)], && \omega_i < 0 \\
P_i^0(t) &= \frac{P_i^0}{\omega_i}\cos(\omega_i t) - \frac{g_i}{\omega_i^2}\sin(\omega_i t), && \omega_i > 0 \\
&= P_i^0 - g_i t, && \omega_i = 0 \\
&= \frac{P_i^0}{|\omega_i|}\cosh(|\omega_i| t) - \frac{g_i}{|\omega_i|}\sinh(|\omega_i| t), && \omega_i < 0
\end{aligned} \qquad [22]$$

where P_i^0 is the momentum at $t = 0$. It is, therefore, a simple procedure to integrate the normal modes once the gradient and force constants are known. The Cartesian coordinates and momenta are obtained from the standard transformation from normal to Cartesian coordinates.[6]

Since the harmonic approximation is, in general, valid for only a small region around $\mathbf{q}_0$ (i.e., the trust radius is small), the integration efficiency is limited by the small step size required to maintain a reasonable accuracy.[96] The efficiency of this technique was improved by introducing a corrector step into the integration scheme.[98] A further enhancement in the algorithm is obtained by not determining the force constant matrix $\mathbf{F}$ at each step, and only accurately updating it after multiple integration steps. The matrix is approximated at the intermediate steps.[99]

TRAJECTORY INITIAL CONDITIONS

Procedures for selecting initial values of coordinates and momenta for an ensemble of trajectories has been described in detail in recent chapters entitled "Monte Carlo Sampling for Classical Trajectory Simulations"[100] and "Classical Trajectory Simulations: Initial Conditions."[101] In this section a brief review is given of methods for selecting initial conditions for trajectory simulations of unimolecular and bimolecular reactions and gas–surface collisions.

Unimolecular Reactions

In a unimolecular reaction a reactant is excited above its unimolecular threshold E_0 so that it may decompose to product(s):

$$A^* \rightarrow \text{product(s)} \qquad [23]$$

where the (*) denotes vibrational–rotational excitation. A question of fundamental interest in unimolecular rate theory is whether the unimolecular dissociation is random during the complete unimolecular decomposition from $t = 0$ to ∞.[102] This will be the case if A^* is initially excited with a microcanonical ensemble and if the intramolecular dynamics of A^* is ergodic[103] within the timescale of the unimolecular reaction, so that the initial microcanonical ensemble is maintained during the decomposition. To prepare a microcanonical ensemble, points are chosen randomly on the energy shell defined by $E = H(\mathbf{p}, \mathbf{q})$, so that there is an initial uniform sampling of A^*'s phase space. Each of these randomly chosen points gives a set of values for the momenta and coordinates.

The unimolecular rate constant $k(E)$, for a microcanonical ensemble of reactant states, is identical with the Rice–Ramsperger–Kassel–Marcus (RRKM) rate constant.[104] If $N(0)$ is the number of reactant molecules excited at $t = 0$ in accord with a microcanonical ensemble, the RRKM rate constant is then defined by

$$-\frac{dN(t)}{dt} = k(E)N(t) \qquad [24]$$

evaluated at $t = 0$. If a microcanonical ensemble is maintained as the reactant decomposes, at any time during the decomposition $k(E)$ is given by Eq. [24]. As a result of the fixed time-independent rate constant $k(E)$, $N(t)$ decays exponentially;

$$N(t) = N(0)e^{-k(E)t} \qquad [25]$$

The fundamental assumption of RRKM theory is that the classical motion of the reactant is sufficiently chaotic to maintain the microcanonical ensemble of

states as the reactant decomposes.[102] This assumption is often referred to as one of a rapid intramolecular vibrational (energy) redistribution (IVR).[105]

A quantity of more utility than $N(t)$, for analyzing the classical dynamics of a microcanonical ensemble, is the *lifetime distribution* $P(t)$, which is defined by[104]

$$P(t) = -\frac{1}{N(0)}\frac{dN(t)}{dt} \qquad [26]$$

According to the above RRKM model

$$P(t) = k(E)e^{-k(E)t} \qquad [27]$$

so that both the intercept and slope of a plot of ln $P(t)$ versus t gives the RRKM rate constant $k(E)$. However, if there are classical "bottlenecks" in an excited molecule's phase space restricting IVR, the unimolecular dissociation will not be random as assumed by RRKM theory and $P(t)$ will not conform to Eq. [27].[102] Such dynamics, for a molecule initially energized in accord with a microcanonical ensemble, is called *intrinsic* non-RRKM behavior.[102] There is much interest in identifying molecules whose unimolecular dynamics is intrinsically non-RRKM.

In the following parts of this section, the selection of two different types of initial conditions for a unimolecular reactant are described. Selecting a microcanonical ensemble of states is described first. These initial conditions are never realized in an actual experiment, but are important for identifying intrinsic non-RRKM behavior and studying a molecule's intramolecular dynamics. The last procedure described is the selection of initial conditions for the nonrandom excitation of initial states for a molecule, as occurs in actual experiments.

Classical Microcanonical Ensemble

Exact sampling Classical exact microcanonical sampling for a system with n degrees of freedom is equivalent to choosing a uniform distribution of points in the $2n$-dimensional molecular phase space bounded by hypersurfaces of constant energy H and $H + dH$.[1] An efficient method consists of choosing all the coordinates and momenta except one that is determined from total energy conservation. However, the remaining variable, for instance, p_n, is not sampled uniformly between H and $H + dH$. The proper weighting for selecting p_n is chosen from the following transformation for the volume element $d\mathbf{q}$ and $d\mathbf{p}$:

$$dq_1 \cdots dq_n dp_1 \cdots dp_n = dq_1 \cdots dq_n dp_1 \cdots dp_{n-1} dH \left|\frac{\partial H}{\partial p_n}\right|^{-1} \qquad [28]$$

This equation is correct for any coordinate system representations, since $d\mathbf{p}\,d\mathbf{q}$ is independent of the coordinate system.[106] The relative weighting factor for selecting p_n is then

$$P(p_n) \propto \left|\frac{\partial H}{\partial p_n}\right|^{-1} \quad [29]$$

which is $|p_n|^{-1}$ for a Hamiltonian with a diagonal kinetic energy term. The sampled points are then selected using rejection techniques, such as the von Neumann technique.[107] If a coordinate q_n was chosen from energy conservation instead of a momentum, its relative probability would naturally be

$$P(q_n) \propto \left|\frac{\partial H}{\partial q_n}\right|^{-1} \quad [30]$$

Algorithms have been developed for speeding up the uniform sampling of phase-space points. For example, the efficient microcanonical sampling (EMS) series of schemes[108] exploits the possibility of sampling independently the spatial coordinates and momenta, simply by weighting the sampled geometries by their associated momentum space density in the overall procedure. The latter density only depends on the total available kinetic energy, found by subtracting out the potential energy of the given geometry from the total energy:

$$\rho(E, \mathbf{q}) \propto [E - V(\mathbf{q})]^{(3N-2)/2} \quad [31]$$

The sampling scheme described above will give a distribution of angular momentum j for the molecule and for the projection of j on any axis, for instance, the symmetry axis z for a symmetric top. To select angular momentum, as well as energy in the sampling scheme above, an initial condition is only accepted if j and its projection j_z are each in narrow intervals; i.e. j to $j + \Delta j$ and j_z to $j_z + \Delta j_z$.[108] Overall translation may be excluded from the initial conditions.[108]

Sampling with the Normal-Mode/Rigid-Rotor Hamiltonian An approximate microcanonical ensemble may be sampled by representing the energized molecule as a symmetric-top rigid rotor with $3N$-6 normal modes. The Hamiltonian for the molecule is then the sum of the energies for separable harmonic oscillators and a rigid rotor and is given by

$$H = E = E_r + E_v \quad [32]$$

$$E_v = \sum_{i=1}^{3N-6} E_i = \sum_{i=1}^{3N-6} \frac{P_i^2 + \omega_i^2 Q_i^2}{2} \quad [33]$$

$$E_r = \frac{J(J+1)\hbar^2}{2I_x} + \frac{K^2\hbar^2(1/I_z - 1/I_x)}{2} \quad [34]$$

where the P_i and Q_i are normal-mode momenta and coordinates and J and K are rotational quantum numbers. To form a microcanonical ensemble, random values for the P_i and Q_i are chosen so that there is a uniform distribution in the classical phase space of $H(\mathbf{P}, \mathbf{Q})$.[106] It has been shown[109] that to accomplish this, the energies for the normal modes are selected according to

$$E_i = \left(\left(E_v - \sum_{j=1}^{i-1} E_j \right) (1 - R_i^{1/(n-i)}) \right) \qquad [35]$$

where R_i is a freshly generated random number between 0 and 1. Random values for the Q_i and P_i are then chosen by giving each normal mode a random phase.[110] The normal-mode coordinates vary versus time according to $Q_i = A_i \cos(\omega_i t)$ and $P_i = -(\omega_i A_i) \sin(\omega_i t)$, where $A_i = (2E_i)^{1/2}/\omega_i$ is the amplitude and the relationship between ω_i and the vibration frequency ν_i is $\omega_i = 2\pi\nu_i$. Since each time has equal probability during a vibrational period, random Q_i and P_i are given by

$$Q_i = \left[\frac{(2E_i^{1/2})}{\omega_i} \right] \cos(2\pi R_i) \qquad [36]$$

$$P_i = -(2E_i)^{1/2} \sin(2\pi R_i) \qquad [37]$$

(The R_i in Eqs. [36] and [37] are different than those used to generate E_i in Eq. [35].) It is useful to note that the probability of a value of Q_i is inversely proportional to the number of Q_i within the time interval dt: probability $(Q_i) \propto |dQ_i/dt|^{-1} = |P_i|^{-1}$.

Given the rotational quantum numbers J and K in Eq. [34], the components of the angular momentum are found from

$$j^0 = \sqrt{J(J+1)}\hbar \qquad [38]$$

$$j_z^0 = K\hbar \qquad [39]$$

$$j_x^0 = (j^0 - j_z^0)^{1/2} \sin 2\pi R \qquad [40]$$

$$j_y^0 = (j^{0^2} - j_z^{0^2}) \cos 2\pi R \qquad [41]$$

where R is a random number. Here, specific values of j and j_z are chosen, with j_x and j_y chosen randomly. One may also fix j, but choose j_z randomly as well as j_x and j_y. For this case the initial conditions will not have a well-defined projection of j on the symmetry axis and, thus, K is not fixed.

The following steps are carried out to transform the normal-mode coordinates $\mathbf{Q}$ and $\mathbf{P}$, and angular momentum $j^0 = j_x^0 + j_y^0 + j_z^0$ to Cartesian coordinates and momenta used in the numerical integrations:[110,111]

1. The **Q** and **P** are transferred to Cartesian coordinates **q** and momenta **p** for N atoms using the normal-mode eigenvector **L**:[6]

$$\mathbf{q} = \mathbf{q}_0 + \mathbf{M}^{-1/2}\mathbf{L}\mathbf{Q} \quad [42]$$

$$\mathbf{p} = \mathbf{M}^{1/2}\mathbf{L}\mathbf{P} \quad [43]$$

   where $\mathbf{q}_0$ is a matrix of the equilibrium coordinates and **M** is a diagonal matrix whose elements are the atomic masses. Since normal modes are approximate for finite displacements,[6] a spurious angular momentum $\mathbf{j}_s$, arises following this transformation.[110,111]

2. The spurious angular momentum is found from

$$\mathbf{j}_s = \sum_{i=1}^{N} \mathbf{r}_i \times m_i \dot{\mathbf{r}}_i \quad [44]$$

   where m_i is the mass of the ith atom and $\mathbf{r}_i$ its position vector. The desired angular momentum $\mathbf{j}^0$ is added to the molecule by forming the vector

$$\mathbf{j} = \mathbf{j}^0 - \mathbf{j}_s \quad [45]$$

   and adding the rotational velocity $\omega \times \mathbf{r}_i$ to each of the atoms, where

$$\omega = \boldsymbol{I}^{-1}\mathbf{j} \quad [46]$$

   and $\boldsymbol{I}^{-1}$ is the inverse of the inertia tensor.[5]

3. The actual internal energy E for the Cartesian coordinates and momenta chosen from steps 1 and 2 is calculated using the correct Hamiltonian and compared with the intended energy E^o. If they do not agree within some acceptance criterion, the Cartesian coordinates and momenta are scaled according to

$$q_i' = q_i^o + (q_i - q_i^o)\left(\frac{E^o}{E}\right)^{1/2} \quad [47]$$

$$p_i' = p_i\left(\frac{E^o}{E}\right)^{1/2} \quad [48]$$

   Any spurious center of mass translational energy is subtracted from the molecule, and the procedure loops back to step 2.

This sampling, with the normal-mode/rigid-rotor Hamiltonian, provides an exact microcanonical ensemble for this Hamiltonian, but an approximate microcanonical ensemble for the actual anharmonic and reactive Hamiltonian with vibrational–rotational coupling.

Orthant sampling Orthant sampling[102] works in the classical phase space of the molecular Hamiltonian $H(\mathbf{p},\mathbf{q})$. For a microcanonical ensemble,

each phase-space point in the volume element $d\mathbf{p}d\mathbf{q}$ has equal probability.[106] The classical density of states is then proportional to the surface integral of the phase space shell with $H(\mathbf{p},\mathbf{q}) = E$ and is given by[105]

$$\rho(E) = \int_{H=E} \cdots \int \frac{d\mathbf{p}\, d\mathbf{q}}{h^n} \qquad [49]$$

where h is Planck's constant. Thus, preparing a microcanonical ensemble involves choosing points at random on the energy shell.

In orthant sampling an initial condition for a microcanical ensemble is chosen by projecting a random unit vector of dimension $2n$, with components x_i, onto the $E = H(\mathbf{p},\mathbf{q})$ energy shell:

$$1 = \sum_{i=1}^{2n} x_i^2 \qquad [50]$$

For the normal-mode Hamiltonian in Eq. [32], orthant sampling is exact, as is the microcanonical normal-mode sampling algorithm presented above. Orthant sampling gives an approximate microcanonical[102] ensemble for the Hamiltonian of an actual molecule. The sampling is performed in the Cartesian coordinate system and the steps are as follows:

1. The semiaxes for the Cartesian coordinates and momenta are found at fixed $H(\mathbf{q},\mathbf{p}) - V_0 = E^0$, where E^0 is the intended energy and V_0 is the minimum potential energy. This is done by varying the coordinates and momenta to find their maximum and minimum values, q_i^- and q_i^+ and $p_i^- = -p_i^+$. For each degree of freedom the magnitudes of the minimum and maximum values of the momentum are the same.
2. To obtain the correct relationship between the average initial potential $\bar{V}$ and the kinetic $\bar{T}$ energies, either p_i^- or p_i^+ (chosen randomly) for each degree of freedom is scaled by a parameter p_{scale}. The $\bar{V}$ and $\bar{T}$ may be determined from a trajectory integrated for a long period of time. Harmonic systems obey the Virial theorem $\bar{V} = \bar{T}$, but this is not necessarily the case for anharmonic systems.
3. The initial momenta and coordinates are then chosen from

$$p_i = x_i(p_i^-, p_i^+)p_{\text{scale}} \qquad [51]$$

$$q_i = q_i^0 + x_{3n+i}\left[(q_i^-, q_i^+) - q_i^0\right] \qquad [52]$$

where the x_i are components of the $2n$ dimensional random unit vector, Eq. [50]. Any center-of-mass translation is subtracted from the atoms of the molecule.

The remaining steps for orthant sampling are the same as steps 2 and 3 described above for microcanonical normal-mode sampling.

Representing Experimental Nonrandom Sampling

The random sampling procedures described above pertain to preparing a classical microcanonical ensemble of states. Simulating the dynamics of the ensemble is important for comparing with classical RRKM theory. However, to compare with experiment, initial conditions must be chosen to represent the nonrandom excitation of the molecule's states by the experimental process. In addition, to compare to experiment a classical state must be sampled that is an analog of the quantum-mechanical state prepared by the experiment. Here, procedures are described for sampling initial conditions for unimolecular reactants prepared by three different experimental procedures: chemical activation, $S_1 \rightarrow S_0$ conversion, and local-mode excitation.

Chemical Activation In chemical activation, the unimolecular reactant is excited by the exothermicity of a chemical reaction, as for

$$F + C_2H_4 \rightarrow C_2H_4F^* \rightarrow H + C_2H_3F \qquad [53]$$

Here, the nonrandom excitation of $C_2H_4F^*$ is described by the dynamics of the $F + C_2H_4$ bimolecular reaction. To simulate chemical activation, proper initial conditions must be chosen for the reactants and for their relative properties. The procedure for choosing initial conditions for the reactant's relative properties is given below in the discussion of bimolecular reactions. The quasiclassical method may be used to select initial conditions for molecular reactants. The energy for a symmetric-top polyatomic molecule in a specific vibrational–rotational state may be approximated by the harmonic oscillator/rigid rotor model

$$E = \sum_{i=1}^{3N-6} E_i + E_r = \sum_{i=1}^{3N-6} \left(n_i + \tfrac{1}{2}\right) h\nu_i + E_r(J, K) \qquad [54]$$

where n_i and ν_i are the quantum numbers and vibrational frequencies for the normal modes of vibration and E_r is the rotational energy. The E_i for the normal modes and the rotational quantum numbers J and K are transformed to Cartesian coordinates and momenta as described above in equations [32]–[48].

For many chemical reactions, the reactants are not in specific vibrational–rotational states and instead have a temperature T, so that the vibrational and rotational energies for a reactant must be chosen from their quantum Boltzmann distributions. The resulting probability that normal mode i in n_i exists is given by

$$P(n_i) = \frac{\exp\left[\frac{-(n_i+1/2)h\nu_i}{kT}\right]}{Q_i} \qquad [55]$$

where Q_i is the normal mode's partition function. This probability distribution may be sampled by the von Neumann rejection method. The angular

momentum j for the molecule and its projection of j_z onto the z axis are sampled from their classical Boltzmann distributions[112]

$$P(j_z) = \exp\left(-\frac{j_z^2}{2I_z kT}\right) \qquad 0 \le j_z \le \infty \qquad [56]$$

$$P(j) = j\exp\left(-\frac{j^2}{2I_z kT}\right) \qquad j_z \le j \le \infty \qquad [57]$$

The rejection method is used to sample j_z from $P(j_z)$, whereas j is sampled by the CDF formula[112]

$$j = [j_z^2 - 2I_x kT\ln(1 - R_i)]^{1/2} \qquad [58]$$

The components j_x and j_y of j are found from Eqs. [40] and [41].

$S_1 \rightarrow S_0$ Internal Conversion Absorption of electromagnetic radiation is another means of preparing vibrationally excited molecules. A widely used approach involves initial electronic excitation by absorption of one photon of visible or ultraviolet radiation. After this excitation, many molecules undergo a rapid internal conversion to the ground electronic S_0 state, a process that converts the energy of the absorbed photon into vibrational energy. Such an energization scheme is depicted in Figure 4, where the complete excitation/decomposition mechanism is

$$(S_0) + h\nu \rightarrow (S_1) \rightarrow (S_0)^*$$

The energy distribution of the unexcited ground-state molecule affects the energy distribution of the vibrationally excited ground-state molecule. If the unexcited reactant is vibrationally–rotationally cold, the energy of the excited reactant is simply that of the photon $h\nu$. On the other hand, if the unexcited reactant has a thermal distribution of energies $P_T(E)$ the energy of the excited reactant is expected to be well approximated by $h\nu$ plus the distribution $P_T(E)$. The average energy of the excited reactant is then $h\nu + \langle E\rangle_T$, where $\langle E\rangle_T$ is the average energy of the unexcited reactant.

The $S_0 \rightarrow S_1$ internal conversion step excites S_0 nonrandomly.[113] A microcanonical ensemble of states is not prepared, although S_0 may relax to this ensemble after efficient and complete IVR. Thus, to accurately simulate the intramolecular and unimolecular dynamics of the excited S_0 molecule, it is necessary to choose correct initial conditions for S_0. The specific vibrational excitations on S_0 have probabilities proportional to $|A_{ij}|^2$, where i is the initial vibrational level on S_1 and j is the vibrational level on S_0.[114] The A_{ij} term includes a Franck–Condon factor so that only certain types of S_0 mode excitations have high probabilities and therefore the excitation of S_0 may be highly

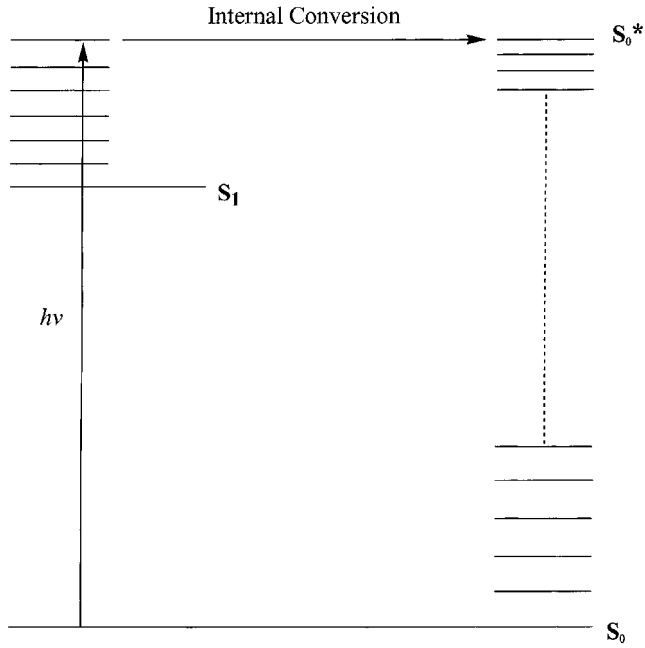

Figure 4 Preparation of a vibrationally excited ground-state molecule $(S_0)^*$ by internal conversion from a vibrational level of S_1.

mode specific. If unexcited S_0 is vibrationally–rotationally cold so that it does not have a high density of states and if the excitation source has a high resolution, it may be possible to excite an individual vibrational–rotational state of S_1. This highly selective initial excitation of S_0 will enhance the mode specificity of the $S_1 \rightarrow S_0$ transitions.

Nonrandom sampling of initial conditions for S_0, following $S_1 \rightarrow S_0$ internal conversion, has been performed for chloroacetylene (H—C≡C—Cl).[115] The rejection method may be used to sample the different $|A_{ij}|^2$ transitions according to their relative probabilities.

Local-Mode Excitation In local-mode sampling an individual local mode such as a CH bond in benzene is excited.[116] This type of trajectory calculation has been performed to determine the population of a local-mode state $|v\rangle$ versus time, from which the absorption linewidth of the overtone state may be determined.[117] Good agreement has been found with both experimental and quantum-mechanically calculated overtone line-widths for benzene[118] and linear alkanes.[119]

The first step in local-mode sampling, to calculate an absorption linewidth, is to choose Cartesian coordinates and momenta, which correspond to the zero-point energy (i.e., $v_i = 0$) in the molecule. The step is the same as

described above for normal-mode sampling. Since the normal-mode zero-point energy is added with random phases, the kinetic and potential energies differ for each bond in the molecule after this step. Similarly, the energy in a particular bond will vary after this step between initial conditions. A particular bond is then excited to a local mode state $|v\rangle$ by adding more energy to the bond so that the Einstein–Brillouin–Keller (EBK)[120] semiclassical quantization condition

$$\oint p_r \, dr = (v + \tfrac{1}{2})h \qquad [59]$$

is realized for a bond energy E_r of

$$E_r = \frac{p_r^2}{2\mu} + V(r) \qquad [60]$$

where p_r is the bond's radial momentum, $V(r)$ the potential energy, and μ the reduced mass for the two atoms constituting the bond. If $V(r)$ is a Morse function,[121] E_v eaquals

$$E_v = (\nu + \tfrac{1}{2})h\nu_e - (v + \tfrac{1}{2})^2 h\nu_e x_e \qquad [61]$$

where ν_e is the harmonic frequency and x_e the anharmonic correction. The energy is added by either extending or compressing (chosen randomly) the bond.

Bimolecular Reactions

In principle the cross section for the reaction between A and B to form products:

$$\mathrm{A} + \mathrm{B} \rightarrow \text{products}$$

may be measured as functions of the A + B relative velocity v_{rel} and the vibrational–rotational energy levels of A and B.[122] These reaction cross sections may then be averaged over the Boltzmann distributions for the v_{rel} and the A and B vibrational–rotational levels to obtain the thermal rate constant $k(T)$. Here, the procedure is described for choosing initial conditions for a collision between an atom B and polyatomic molecule A to calculate their reaction cross section. Sampling of initial conditions for atom + diatom and polyatom + polyatom collisions have been recently described.[100]

For reaction between an atom B and polyatomic molecule A the reactive cross section may be expressed as $\sigma_{\mathrm{r}} = \sigma_{\mathrm{r}}(v_{\mathrm{rel}}, \mathbf{n}_A, J_A, K_A)$, where $\mathbf{n}_{\mathrm{A}}$ are the molecule's vibrational quantum numbers and J_A and K_A its rotational

quantum numbers. If specific values of $\mathbf{n}_A$ and K_A are not selected and, instead, there is a distribution of values, for example, the Boltzmann distribution specified by temperature T_A, the reactive cross section becomes

$$\sigma_r(v_{\text{rel}}; T_A) = \sum_{\mathbf{n}_A} \sum_{J_A} \sigma_r(v_{\text{rel}}, \mathbf{n}_A, J_A) P(\mathbf{n}_A; T_A) P(J_A, K_A; T_A) \qquad [62]$$

where $P(\mathbf{n}_A;T_A)$ and $P(J_A,K_A;T_A)$ are the normalized Boltzmann distributions for $\mathbf{n}_A$ and J_A, K_A at temperature T_A. Multiplying either of the above mentioned cross sections $\sigma_r\,(v_{\text{rel}}, \mathrm{n}_A, J_A)$ or $\sigma_r(v_{\text{rel}}; T_A)$ by v_{rel} gives the bimolecular rate constants for a fixed relative velocity:

$$k(v_{\text{rel}}; T_A) = v_{\text{rel}} \sigma_r(v_{\text{rel}}; T_A) \qquad [63]$$

Integrating the rate constant in Eq. [63] over the Boltzmann relative velocity distribution $P(v_{\text{rel}}; T)$ for temperature $T = T_A$ gives the thermal bimolecular rate constant:

$$k(T) = \int_0^\infty v_{\text{rel}} \sigma_{\text{rel}}(v_{\text{rel}}; T) P(v_{\text{rel}}; T) dv_{\text{rel}} \qquad [64]$$

The classical-mechanical expression for the reaction cross section is

$$\sigma_r = \int_0^{b_{\max}} P_r(b) 2\pi b \, db \qquad [65]$$

where b is the collision impact parameter, $b_{\max}$ is the largest impact parameter that leads to reaction, and $P_r(b)$ is the probability of the reaction as a function of the impact parameter. One may determine σ_r for Eq. [65] by integrating over $P_r(b)$ or from the average $P_r(b)$, which is given by

$$\begin{aligned} \langle P_r(b) \rangle &= \frac{\int_0^{b_{\max}} P_r(b) 2\pi b \, db}{\int_0^{b_{\max}} 2\pi b \, db} \\ &= \frac{\int_0^{b_{\max}} P_r(b) 2\pi b \, db}{\pi b_{\max}^2} \end{aligned} \qquad [66]$$

Comparison of Eqs. [65] and [66] shows that

$$\sigma_r = \langle P_r(b) \rangle \pi b_{\max}^2 \qquad [67]$$

The average reaction probability $\langle P_r(b) \rangle$ is evaluated from trajectories with b chosen randomly according to the distribution function

$$P(b)db = \frac{2\pi b\, db}{\pi b_{\max}^2} \qquad [68]$$

Random values of b between 0 and $b_{\max}$ may be sampled with the CDF

$$R_i = \int_0^{b_{\max}} P(b)db \qquad [69]$$

to give

$$b = (R_i)^{1/2} b_{\max} \qquad [70]$$

With b chosen randomly between 0 and $b_{\max}$, the average reaction probability is $\langle P_r(b) \rangle = N_r/N$, where N is the total number of trajectories and N_r the number of trajectories that are reactive. Thus, the reaction cross section is

$$\sigma_r = \frac{N_r}{N} \pi b_{\max}^2 \qquad [71]$$

The preceding presentation describes how the collision impact parameter is sampled to calculate reaction cross sections. Rate constants as a function of either the reactant relative translational energy E_{rel} or temperature are then determined from the reactive cross sections. In the following, Monte Carlo sampling of the reactant's Cartesian coordinates and momenta is described for atom + polyatom collisions. Initial energies are chosen for the polyatomic, which correspond to quantum-mechanical vibrational–rotational energy levels. This is the quasiclassical model.[4]

For collisions of an atom B with a polyatomic molecule A, the reactive cross section may be determined as a function of relative velocity v_{rel}, and either the vibrational and rotational quantum numbers $\mathbf{n}_A$, J_A, and K_A or temperature T_A of A. For the latter the quantum numbers are chosen from their thermal Boltzmann distributions [i.e., Eqs. [38], [39], [55]–[58]]. These two different samplings of A's vibrational–rotational states give the cross sections $\sigma_r = \sigma_r(v_{\text{rel}}, \mathbf{n}_A, J_A, K_A)$ and $\sigma_r = \sigma_r(v_{\text{rel}}; T_A)$, Eq. [62], respectively. To choose random initial conditions for an ensemble of A + B collisions the vibrational and rotational quantum numbers of A are first transformed to Cartesian coordinates and momenta as described above (in Eqs. [32]–[48]) and [59]. The following steps are then performed to choose random initial conditions for the A + B collision:

1. The preceding Cartesian coordinates and velocities selected for the polyatomic A are randomly rotated though Euler's angles[123] to give a random orientation:

$$q = \mathrm{ROT}(\theta, \phi, \chi)\mathbf{q}^0 \qquad \dot{\mathbf{q}} = \mathrm{ROT}(\theta, \phi, \chi)\dot{\mathbf{q}}^0 \qquad [72]$$

   where $\mathbf{q}^0$ is a vector of the Cartesian coordinates selected above and $\mathrm{ROT}(\theta, \phi, \chi)$ is the Euler rotation matrix.[123] The angles θ, ϕ, χ are chosen randomly according to

$$\cos\theta = 2R_1 - 1 \qquad \phi = 2\pi R_2 \qquad \chi = 2\pi R_3 \qquad [73]$$

   where R_1, R_2, and R_3 are three different random numbers.
2. Since A has a random orientation in a space-fixed coordinate frame, the B atom may be placed in the y, z plane without loss of generality. The x, y, z coordinates of B are then

$$x = 0 \qquad y = b \qquad z = (s^2 - b^2)^{1/2} \qquad [74]$$

   where s is the initial separation between B and the A center of mass, and b is the impact parameter.
3. The A + B relative velocity v_{rel} is now added along the z axis with the restraint that the A + B center of mass remain at rest. The space-fixed Cartesian momenta are then

$$\mathbf{P} = \mathbf{M}(\dot{\mathbf{q}} - \dot{\mathbf{q}}_{\mathrm{rel}}) \qquad [75]$$

   The elements of the relative velocity $\dot{\mathbf{q}}_{\mathrm{rel}}$ are zero for the x and y components and equal $[m_A/(m_A + m_B)]v_{\mathrm{rel}}$ for the z component of atom B and equal to $-[m_B/(m_A + m_B)]v_{\mathrm{rel}}$ for each atom of A.

In selecting initial conditions for bimolecular reactions, it is important that the coordinates and momenta for the atoms have random classical phases as given, for example, by Eqs. [36] and [37]. If this is done the trajectory results will be independent of the initial separation between the reactants.[124]

Exciting the Transition State

Direct dynamics simulations based on a high level of electronic structure theory, may be performed to study chemical events that occur in a short time. Thus, though a large amount of compute time is required for each integration step, only a small number of integration steps are required. High-level direct dynamics is practical for simulating the exit-channel dynamics of a chemical reaction from the transition state to products, since this is usually a direct

short time process. If the populations of the vibrational–rotational levels at the transition state are known, initial conditions for the trajectories may be chosen in accord with these populations and the trajectories then integrated to the product asymptotic limit to determine product properties such as vibrational, rotational, and relative translational energies. An assumption that may be made, regarding the populations of the transition state's vibrational–rotational levels, is that of transition state theory (see discussion below).

If the populations of the transition state's vibrational–rotational levels are assumed to be those of transition state theory, the trajectories may be used to test the fundamental assumption of transition state theory. Both microcanonical and canonical variational transition state theory are based on the assumption that trajectories cross the transition state (TS) only once in forming product(s) or reactant(s).[125,126] The correction κ to the transition-state theory rate constant is determined by initializing trajectories at the TS and sampling their coordinates and momenta from the appropriate statistical distributions.[127–129] The value for κ is the number of trajectories that form product(s) divided by the number of crossings of the TS in the reactant(s) $\rightarrow$ product(s) direction. Transition state theory (TST) assumes this ratio is unity.

Canonical TST assumes there is a Boltzmann distribution of the energy levels at the TS.[70,71] The canonical TST rate constant is given by

$$k(T) = \frac{kT}{h}\frac{Q^{\neq}}{Q}e^{-E_0/kT} \qquad [76]$$

where $Q^{\neq}$ and Q are the partition functions for the transition state and reactants, respectively, and E_0 is the potential energy difference between the TS and reactants. The normal-mode/rigid-rotor quasiclassical model may be used to sample the energy levels at the TS and calculate the correction κ for canonical TST. The energies for the vibrational and rotational modes are sampled from Eqs. [38]–[41] and [55]–[58]. The reaction coordinate translational energy $E_t^{\neq}$ is treated classically and values for $E_t^{\neq}$ are selected in accord with the distribution function

$$P(E_t^{\neq}) = \frac{\exp(-E_t^{\neq}/kT)}{kT} \qquad [77]$$

which may be sampled by the cumulative distribution function

$$E_t^{\neq} = -kT\ln(1-R) \qquad [78]$$

The reaction coordinate momentum is $P_t^{\neq} = 2(E_t^{\neq})^{1/2}$. The procedure for transforming the normal-mode energies, rotational angular momentum, and reaction coordinate momentum into Cartesian coordinates and momenta is the same as described above (in the Eqs. [32]–[48]).

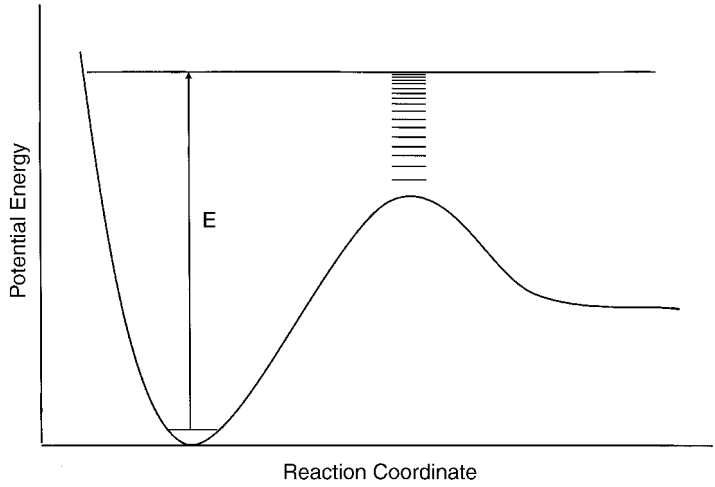

Figure 5 Depiction of vibrational/rotational levels at the transition state for a unimolecular reaction. According to RRKM theory, each level has an equal probability of being populated.

As described (above in the section on unimolecular reactions), RRKM theory assumes that a microcanonical ensemble of states exists during the complete unimolecular decomposition of a molecule from $t = 0$ to ∞. Thus, RRKM theory is the same as microcanonical transition state theory, which assumes that all vibrational–rotational levels for the degrees of freedom orthogonal to the reaction coordinate have equal probabilities of being populated[130,131] (see Figure 5). Whether the levels are actually populated in this manner at the TS depends on the validity of rapid intramolecular vibrational (energy) redistribution (IVR), which maintains the microcanonical ensemble of states for the decomposing molecule. If IVR is efficient so that RRKM theory is valid, it is expected that the TS levels may be selected with equal probability as assumed by microcanonical TST. The quasiclassical normal-mode/rigid-rotor model, discussed above, may be used to choose Cartesian coordinates and momenta for these energy levels. Assuming a symmetric top system, the TS energy $E^{\neq}$ is written as

$$E^{\neq} = E^{\neq}_{\mathbf{n}JK} + E^{\neq}_{t} \qquad [79]$$

where the reaction coordinate translational energy is given by $E^{\neq}_{t} = (P^{\neq}_{t})^2/2$. The first step is to randomly select one of the TS energy levels.[132] The remaining energy $E^{\neq} - E^{\neq}_{\mathbf{n}JK}$ is placed in the reaction coordinate translation. The normal-mode coordinates and momenta and the reaction coordinate momentum are transformed to Cartesian coordinates and momenta as described in the section on normal-mode/rigid-rotor Hamiltonian sampling.

The procedure described above is for sampling a statistical microcanonical distribution at the TS. However, if the unimolecular decomposition of the molecule is non-statistical and not in accord with RRKM theory, a statistical population of the TS's energy levels is not expected. For such a situation it may be impossible to identify how the TS levels are populated and, thus, simulate the experiment. One approach would be to vary the population of the TS levels until the direct dynamics and experimental product energy distributions agree. However, such an approach assumes the level of electronic structure theory used in the simulation is sufficiently accurate. With recent experimental advances in laser spectroscopy and dynamics,[133,134] it may become possible to excite specific vibrational levels at the transition state. It would be straightforward to simulate such experiments.

Gas–Surface Collisions

To simulate collisions between a gaseous molecule and a surface, Cartesian coordinates and momenta are first chosen from the energies for the molecule and surface following procedures described above. The distribution of energies for a surface at temperature T_s may be chosen by either calculating the normal modes of vibration for the surface and then sampling their Boltzmann distributions to form a canonical ensemble or performing a classical molecular dynamics or Monte Carlo simulation to prepare a classical canonical ensemble for the surface. The procedures for these latter two simulation techniques are well-documented,[135–137] and they may be applied to very large surface models. However, calculating the normal modes of vibration is practical only for small surface models. Either classical or quantum sampling may be used to select initial conditions from the Boltzmann distributions for the normal modes. From classical statistical mechanics,[106] the normalized probability that a normal mode of the surface has energy E_i is given by Eq. [77] with E_i replacing $E_t^{\neq}$. This probability distribution may be efficiently sampled by the cumulative distribution function in Eq. [78]. For quasiclassical normal-mode sampling, the energies for the normal modes are sampled from their quantum Boltzmann energy distributions (i.e., Eq. [55]). For both the classical and quasiclassical sampling of the normal-mode Boltzmann distributions, the total surface energy for the initial condition is $\sum E_i$.

Quasiclassical normal-mode sampling may be used to choose initial conditions for the gaseous molecule, which may have a fixed vibrational–rotational energy specified by the quantum numbers $\mathbf{n}, J, K$ or a Boltzmann distribution given by Eqs. [55]–[57]. The procedure for transforming the normal-mode energy of the solid and the normal-mode/rigid rotor energy of the molecule to Cartesian coordinates and momenta is described (in Eqs. [32]–[48]). A random orientation of the gaseous molecule is chosen by randomly rotating its axes through Euler's angles (Eq. [72]).

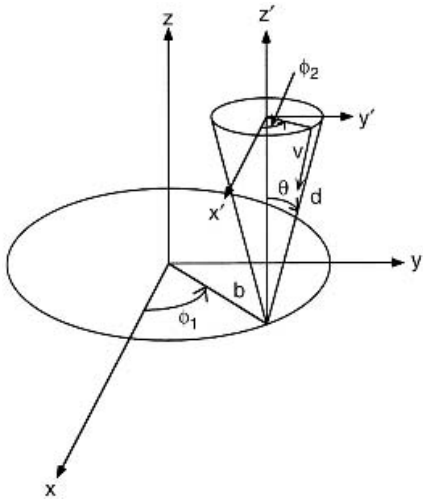

Figure 6 Definition of the coordinates used for sampling trajectory initial conditions to calculate the rate constant for a gas–surface reaction (from Ref. 139).

To calculate a reactive cross section or rate constant for gaseous molecule–surface collisions, the five coordinates b, θ, ϕ_1, ϕ_2, and d, shown in Figure 6, are used to define the position of the center of mass of the gaseous molecule and the orientation of its velocity vector with respect to an aiming point on the surface plane.[138,139] The two coordinates, b and ϕ_1, are used to choose an aiming point on the surface plane. The distance from the surface reactive site b (i.e., the impact parameter) is chosen randomly from between 0 and b_{max} using Eq. [70]. The angle ϕ_1 is chosen from a uniform distribution between 0 and 2π. The angle θ between the incoming projectile's velocity vector and the surface plane is chosen randomly between 0 and θ_{max}. For θ larger than θ_{max}, there are no reactive trajectories. Since the probability of θ is proportional to sin θ, θ may be chosen randomly from its CDF, which gives

$$\theta = \cos^{-1}[1 - R(1 - \cos\theta_{max})] \qquad [80]$$

where R is a fresh random number. The angle ϕ_2, for the gaseous molecule is chosen randomly between 0 and 2π. A sufficiently large initial separation d is chosen so that there is no interaction between the gaseous molecule and the surface.

The reaction cross section for a fixed velocity v of the gaseous molecule, a surface temperature T_s, and a molecular temperature T is given by

$$\sigma(v, T_s, T) = \tfrac{1}{2}\pi b_{max}(1 - \cos\theta_{max})P_r(v, T_s, T) \qquad [81]$$

where $P_r(v, T_s, T)$ is the reaction probability with b, θ, ϕ_1, and ϕ_2 chosen randomly as described above. The factor of $\frac{1}{2}$ accounts for only one-half of the

gaseous molecules in a thermal distribution moving toward the surface. If the velocity of the gaseous molecule is chosen randomly from its Maxwell–Boltzmann distribution,[100] one determines the rate constant

$$k(T, T_s) = \frac{1}{2}\left(\frac{8kT}{m}\right)^{1/2} \pi b_{\max}^2 (1 - \cos\theta_{\max}) P_r(T, T_s) \qquad [82]$$

where m is the mass of the gaseous molecule.

The text above describes the selection of initial conditions when calculating the rate constant for reaction with an isolated site on the surface. For simulating other gas–surface events, such as energy transfer to the surface[140] or to the projectile,[141] initial conditions must be chosen so that the projectile is aimed at a random point on the surface. This is accomplished in the initial conditions, by randomly sampling the points in a unit cell on the surface.[140]

IMPORTANCE OF QUANTUM EFFECTS

Quantum dynamics simulations have allowed detailed comparisons between classical–quantum results for molecular systems.[142] Although there are important limitations in classical trajectory simulations, since they do not include quantum effects such as tunneling and interferences and they allow the unphysical flow and pooling of zero-point energy, there is often quite good agreement between the classical and quantal results.[142]

Bimolecular Reactions

Classical mechanics often gives accurate results for direct bimolecular reactions, even for those that involve significant hydrogen motion as for $H + H_2$ and $F + H_2$ reactions. The agreement between classical and quantum dynamics for these two reactions is striking.[143] The differences between their classical and quantum dynamics arises in part from resonances in the quantum dynamics, which gives more structure in the quantum cross section versus reactant translational energy than found in the classical simulations. For the $F + H_2$ reaction there is a substantial centrifugal barrier arising from the collision's orbital angular momentum. The quantum system can tunnel through this barrier, while the classical system cannot. A comparison between classical and quantum calculations of the differential cross section (DCS) for the $H + D_2 \rightarrow HD + D$ reaction is given in Figure 7.[143]

Polyatomic molecules have large zero-point energies and in classical mechanics simulations of bimolecular reactions this energy may be accessible for surmounting the potential energy barrier for reaction.[144] In the absence of quantum-mechanical tunneling, the threshold for a bimolecular reaction is the vibrationally adiabatic barrier[145–147] with zero-point energy in the vibrational

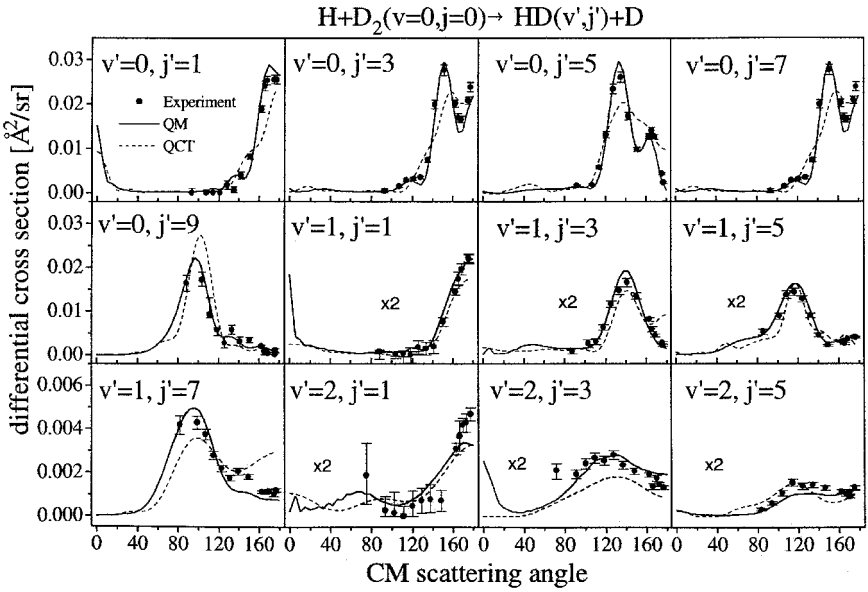

Figure 7 Selected state-resolved DCSs in the CM system for the $H + D_2$ ($v = 0$, $j = 0$) $\rightarrow$ $HD(v', j') + D$ reaction. Solid circles with error bars: experimental results at collision energy of 1.28 eV. Solid line: QM calculations at collision energy of 1.29 eV. Dashed line: QCT calculations at collision energy 1.29 eV. (From Ref. 143.)

modes orthogonal to the reaction coordinate. In a classical-mechanical simulation, the zero-point energy of a polyatomic reactant may transfer to reaction coordinate translational motion allowing reaction to occur for energies lower than the vibrationally adiabatic barrier.[144,147] For some reactions, such as $H + C_2H_4 \rightarrow C_2H_5$,[144] this unphysical effect mimics quantum mechanical tunneling and may give rise to classical low-temperature rate constants in agreement with the quantal prediction. For other reactions, with negligible tunneling probabilities, the effect of this flow of zero-point energy is to give low temperature classical rate constants much larger than the quantum values. Coupling between reaction coordinate motion and vibrational degrees of freedom may be particularly important for bimolecular reactions that proceed through a prereaction potential energy well. The dynamics of such reactive systems is discussed in the next section.

Intramolecular Dynamics and Unimolecular Reactions

Classical dynamics tends to be more accurate for direct short-time dynamical processes, such as the $H + H_2$ and $F + H_2$ reactions, than for processes requiring longer times.[142] The latter may occur if there are potential wells on the potential energy surface giving rise to reaction intermediates. At long times

zero-point energy may flow between vibrational modes of the molecule giving rise to unphysical results.[148] This problem is exemplified by unimolecular dissociation reactions, which are in accord with RRKM theory.[149] If tunneling is unimportant, the quantum threshold for reaction is the classical potential energy at the transition state (TS) plus the TS's zero-point energy. In contrast, since classical mechanics is unaware of zero-point energy, the classical threshold is just the classical potential energy barrier. For large molecules with large zero-point energies, this difference in thresholds can give orders of magnitude difference in the quantal and classical RRKM rate constants.[149] However, the difference in the thresholds is much less for small molecules and their quantal and classical RRKM rate constants are in much better agreement.

Classical mechanics often gives results in excellent agreement with experiment and quantum mechanics for the initial intramolecular and unimolecular dynamics of a non-randomly excited molecule. Two examples of this property are the unimolecular dynamics of the Cl^----CH_3Cl ion–dipole complex formed by $Cl^- + CH_3Cl$ association[150] and the intramolecular relaxation of the $\nu = 3$ C—H local-mode overtone state of benzene.[151] $Cl^- + CH_3Cl$ association excites the three intermolecular modes of the Cl^----CH_3Cl complex (i.e., the Cl^----C stretch and degenerate Cl^----(CH_3)—Cl bend) and the initial unimolecular rate constant for the initial decomposition of this complex is in excellent agreement with experient.[152] At longer times energy transfers nonstatistically to the CH_3Cl intramolecular vibrational modes. The ability of classical mechanics to quantitatively describe this long-time energy transfer is uncertain. However, the classical phase space structures giving rise to this nonstatistical energy transfer are expected to be analogues of the quantum dynamics[153,154] and to provide means to interpret the quantum dynamics.

The initial classical and quantum dynamics of the $\nu = 3$ overtone state of benzene are similar.[151] The classical mechanical population of the $\nu = 3$ state decays exponentially with time giving rise to an adsorption bandwidth of 85 cm^{-1}, nearly identical to the quantum mechanical result[155] (see Figure 8). However, in the quantum dynamics there are long-time recurrences in the population of the $\nu = 3$ overtone state giving rise to structures in the $\nu = 3$ adsorption band, which agree with experiment.[156] These recurrences arise from nonstatistical couplings associated with the $\nu = 3$ intramolecular dynamics and, as described above for the Cl^----CH_3Cl system, there should be signatures of these dynamics in benzene's classical phase-space structure. At this time it is uncertain whether a classical mechanics simulation may be constructed to reproduce the long-time quantum dynamics of the benzene $\nu = 3$ overtone state.

Summary

The accuracy of classical mechanics for simulating classical reaction dynamics may be summarized by considering reaction [53]. At energies in

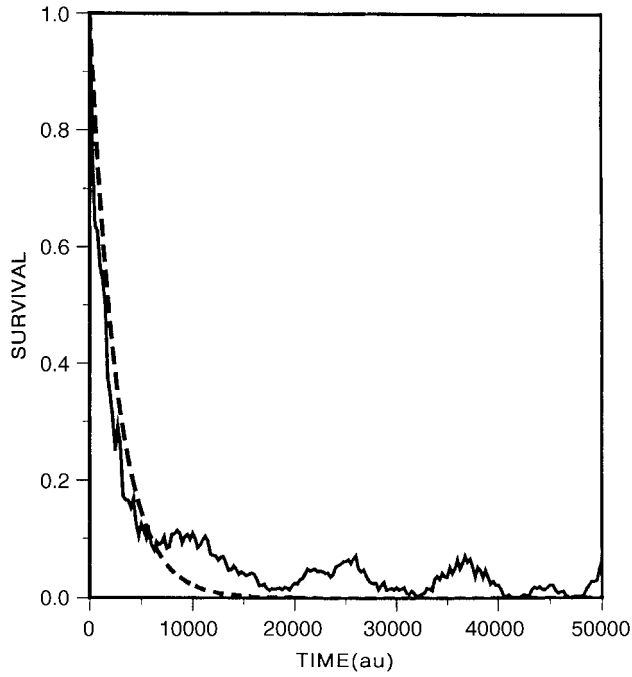

Figure 8 Comparison of quantum (—) and quasiclassical survival probabilities for the $v = 3$ benzene overtone state (from Ref. 155).

excess of the potential energy barrier for $F + C_2H_4 \rightarrow C_2H_4F^*$ association, classical mechanics is expected to give an accurate cross section for this process. However, at energies near and below the potential barrier, the classical cross section may be too large as a result of an enhancement of the reaction rate by the unphysical flow of C_2H_4 zero-point energy to the $F + C_2H_4$ reaction coordinate. Once the $C_2H_4F^*$ intermediate is formed there are strong couplings between the intermediate's vibrational modes[157] and it loses any memory of its zero-point energy. As a result, the threshold for $C_2H_4F^* \rightarrow C_2H_3F + H$ dissociation is the classical barrier, which is substantially lower than the vibrationally adiabatic barrier with zero-point energy in the modes orthogonal to the reaction coordinate. Thus, the classical unimolecular rate constant for $C_2H_4F^*$ decomposition will be substantially larger than the quantum value and only begins to approach this value at high energies.

Since classical mechanics allows $C_2H_4F^*$ dissociation to occur without zero-point energy in the TS's vibrational modes, the energy distribution of the $C_2H_3F + H$ products is expected to agree with experiment only at the high-energy limit. If it is correct to assume the unimolecular decomposition

of $C_2H_4F^*$ is statistical and in accord with RRKM theory, the product energy distribution may be calculated by initializing the trajectories at the TS with quasiclassical sampling and with an equal population of each energy level as assumed by RRKM theory; see the section on TS excitation (above). The trajectories may then be integrated to determine the energy distribution in the product asymptotic limit.[158]

The above description assumes that an intermediate is formed with statistical classical dynamics and pooling of zero-point energy. If the dynamics of the intermediate is nonstatistical (i.e. as for Cl^----CH_3Cl[150]), the intermediate's lifetime and product energy distribution may agree with experiment. A discussion of the applicability of classical mechanics for studying the central barrier dynamics of the $[Cl---CH_3---Cl]^-$ moiety is given below.

APPLICATIONS OF BORN–OPPENHEIMER DIRECT DYNAMICS

An incomplete list of applications of Born–Oppenheimer direct dynamics is given in Table 2. This compilation illustrates the applicability of this simulation technique to a broad range of chemical systems. Here we briefly describe four gas-phase direct dynamics studies of the Hase research group: (1) the structural and geometrical isomerization of trimethylene; (2) the central barrier dynamics of the $Cl^- + CH_3Cl$ S_N2 reaction; (3) the exit-channel dynamics of the $OH^- + CH_3F \rightarrow CH_3OH + F^-$ S_N2 reaction; and (4) the surface-induced dissociation of protonated glycine (gly-H^+).

Cyclopropane Stereomutation

Interest in the decomposition of cyclopropanes and the role of the trimethylene biradical in the decay mechanism has spanned more than three decades and has been fueled by two experiments that give apparently irreconcilable results.[179,180] Experiments of *S*,*S*-trans-cyclopropane-1,2-d_2 at 695 K indicate that isomerization via double-terminal rotation (i.e., con- and disrotation of the terminal methylene groups) is at least 6 times more prevalent than isomerization via single-terminal rotation.[179] Similar experiments with chiral cyclopropanes-[1-^{13}C]1,2,3-d_3 at 680 K yield single and double terminal isomerization rates that are virtually identical.[180]

A kinetic scheme that includes the role of the trimethylene biradical intermediate is required to obtain the relative rates of single- and double-terminal rotations from the experimental observables (i.e., the rate loss of optical activity and the rate of *trans* → *cis* isomerization). Understanding the dynamics of the biradical is thus of pivotal importance. Doubleday has determined an accurate PES for trimethylene from a high level CASSCF ab initio calculation.[181] Trimethylene has a very shallow potential energy minimum

Table 2 Applications of Born–Oppenheimer Direct Dynamics Simulations

Chemical System	Level of theory	Reference
CID and SID of *N*-protonated glycine	AM1	211
1,2,6-Heptatriene rearrangement reaction	CASSCF(8,8)/6-31G(d) and AM1-SRP	159
$OH^- + CH_3F$ S_N2 reaction	MP2/6-31+G(d)	206
Cyclopropyl radical ring opening	CASSCF(3,3)/6-31G(d)	50
Carbene formation from 3H-diazirine or diazomethane	CASSCF(8,7)/6-31G(d)	160
Vinylcyclopropane–cyclopentene rearrangement	AM1-SRP	161,162
HF elimination of 1,1-difluoroethylene	AM1-SRP	163
H_2 elimination of 2,5-dihydrofuran	PM3-SRP	164
Oxidation of a single-wall carbon nanotube	AM1	165
Methodology development	—	166
CO production from $CH_3 + O$ or $CD_3 + O$	B3LYP/6-31G(d)	167
$Cl^- + CH_3Cl$ S_N2 reaction	MP2/6-31G(d)	200
HF elimination from vinyl fluoride	AM1-SRP	168
$F^-(H_2O) + CH_3Cl$ S_N2 reaction	HF/3-21+G(d)	169
Ionization of H_2 clusters	UHF/311G(p)	170
Electron capture by H_3O^+	HF/6-311G(d,p)	171
Methanethiol cation decomposition	AM1	172
$O(^3P)+C_2H_4S(^1A_1)\rightarrow SO(^3\Sigma^-)$ $C_2H_4(^1A_g)$	B3LYP/6-31+G(d)	173
Spin-forbidden dehydrogenation of methoxy cation	HF/6-31G(d,p)	174
Dynamics of hydrogen and muonium atoms trapped in a diamond crystal	PM3	175
$Cl^- + CH_3Cl$ S_N2 reaction	HF/3-21+G(d)	49
$F + C_2H_4 \rightarrow C_2H_3F + H$	UHF/6-31G(d)	158
Trimethylene decomposition in argon bath	AM1-SRP	176
Methodology development	—	177
$F^- + CH_3Cl$ S_N2 reaction	HF/3-21G(d)	178

and lies ~60 kcal/mol above the cyclopropane minimum (see Figure 9). It mediates both the geometric and structural isomerizations of cyclopropane, which result in cyclization and propene formation. The latter process has a barrier of ~7 kcal/mol with respect to the trimethylene potential energy minimum. Cyclopropane may decompose to form trimethylene via three different pathways: conrotation (CON) and disrotation (DIS) paths in which both terminal methylenes rotate and a cis–trans (CT) path with a single methylene rotation.

Semiempirical direct dynamics was used to study trimethylene's unimolecular dynamics and the thermal stereomutation of cyclopropane.[182–184] The semiempirical model used in these simulations is AM1 with specific reaction parameters (SRPs; see discussion of semiempirical electronic structure theory in the section on BO direct dynamics) chosen to fit the CASSCF PES.[181] In choosing the SRPs, the AM1 barrier for propene formation was lowered by

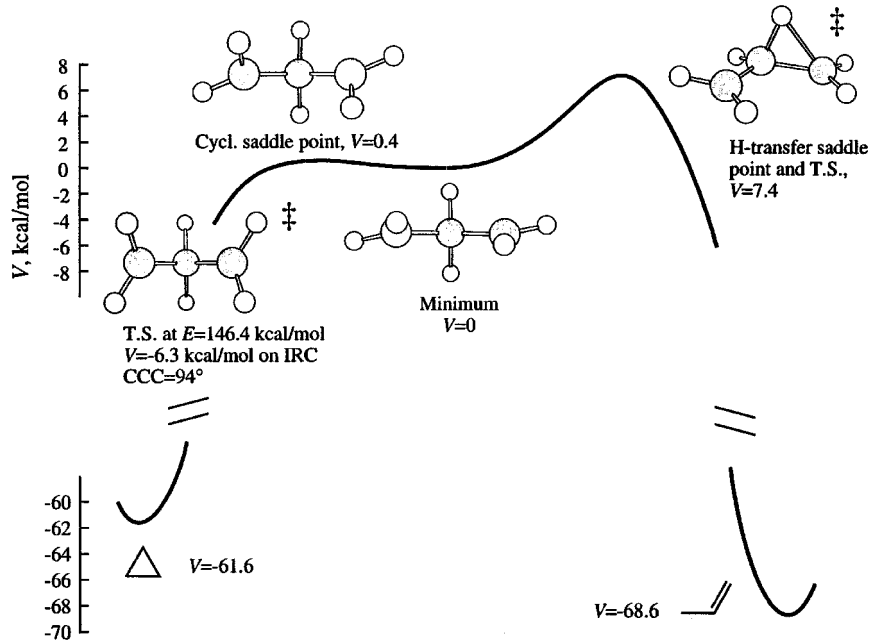

Figure 9 Minimum potential energy along the cyclopropane ↔ propene reaction path; the curve linking the stationary points merely serves to illustrate connectivity (from Ref. 183).

increasing the resonance integrals involving the central hydrogens and terminal carbons, and the energies and geometries of cyclization saddle points were adjusted by scaling the resonance integrals involving both terminal carbons. In addition, the resulting energy differences between trimethylene and the cyclopropane and propene products was corrected by introducing Morse-type energy terms in the product regions of the PES.[182]

To simulate the high-pressure thermal unimolecular decomposition of cyclopropane and its stereomutation, it was assumed that RRKM theory is valid for cyclopropane's unimolecular dynamics, so that Boltzmann distributions of reacting molecules could be sampled at the $CON^{\neq}$, $DIS^{\neq}$, and $CT^{\neq}$ transition states for cyclopropane → trimethylene decomposition.[183] Each trajectory was integrated forward and backward in time until either propene or an isomer of cyclopropane was formed. In this way, the product distribution was obtained by following each cyclopropane isomerization until it completed its journey through the trimethylene biradical region of the PES. To compare with experiment[179,180] the trajectories were further analyzed to determine whether cyclization followed single rotation versus double rotation of trimethylene's terminal methylenes, that is a ratio k_1/k_{12} of single/double rotation rate constants.

The trajectory simulation shows that the unimolecular dynamics of trimethylene is not statistical and non-RRKM.[183,184] If the dynamics were statistical, the ratio of the geometric and isomerization products would depend only on the trimethylene energy and not on which TS is excited (i.e., $CON^{\neq}$, $DIS^{\neq}$, or $CT^{\neq}$) nor how energy is distributed between the degrees of freedom at TS. The trajectory dynamics do not support such a model. For example, initializing the trajectories at the conrotatory TS leads to a strong preference for cyclization through the $CON^{\neq}$ TS.[184] In addition, the ratios of cyclization and propene products are strongly influenced by which modes are excited at each TS. The trimethylene unimolecular dynamics is strongly non-RRKM.[183,184]

The dynamics of the classical trajectories support a mechanistic continuum for trimethylene decomposition encompassing concerted and nonconcerted processes in which nonstatistical effects are paramount.[183] Most double rotation trajectories undergo a single set of 180° rotations and cyclize immediately with an average lifetime of 130 fs. These trajectories could hardly be more direct and it seems appropriate to call them "concerted". On the other hand, the 430 fs average lifetime for the products formed by an overall single methylene rotation is a time scale that accommodates multiple rotations and is more typical of an intermediate. Finally, the k_{12}/k_1 ratio of 2.9–3.5 determined from the trajectories is intermediate of the experimental values of 1.0 ± 0.2[180] and 5–50,[179] and is similar to the value of 4.7 reported by Hrovat et al.[185] from a trajectory simulation on an analytic PES. This trajectory study also exhibits substantial nonstatistical dynamics for trimethylene.

Additional work needs to be done to develop a theoretical model to represent the trimethylene kinetics. The dynamics in the trimethylene region of the potential energy surface is neither statistical nor direct, and instead contains both these elements. Future work on the kinetics of cyclopropane stereomutation will include developing a theoretical model for trimethylene's dynamics, assessing the accuracy of assuming RRKM dynamics for cyclopropane, and determining a more accurate PES for trimethylene.

$Cl^- + CH_3Cl$ Central-Barrier Dynamics

Bimolecular nucleophilic substitution (S_N2) reactions of the type

$$X^- + CH_3Y \rightarrow XCH_3 + Y^- \qquad [83]$$

are of central importance in gas-phase ion chemistry[186,187] and organic reaction mechanisms.[188] In a classic set of experiments, Moylan and Brauman[189] demonstrated that the kinetics of these reactions could be explained by a Walden inversion mechanism with a double-well potential arising from X^----CH_3Y and XCH_3---Y^- ion–dipole complexes and a $[X---CH_3---Y]^-$ central barrier.

Given the prominence of statistical theories in chemical reaction dynamics and kinetics, it was natural to use these theories in modeling studies of S_N2 reactions.[186–189] However, more recent detailed examinations of S_N2 reactions of the type in reaction [83] have discovered a range of important nonstatistical attributes,[186,187,190] arising from weak couplings between the X^----CH_3Y intermolecular modes and CH_3Y intramolecular modes. A particularly important feature of this work has been a close relationship between computational,[186,190] experimental,[191–195] and theoretical studies.[186,187,190,196] The computational studies include quantum-dynamical[197,198] and full-dimensional trajectory calculations.[186,190]

A potentially very significant finding from the trajectory studies is the trapping of trajectories in the central-barrier region of the potential energy surface, with concomitant recrossings of the barrier.[186,190] The former suggests that vibrational states prepared in the central-barrier region may be sufficiently long-lived to resolve their spectra,[134] while the latter indicates that crossing the central barrier may not be a rate-controlling step, as assumed by statistical theories for many S_N2 reactions.[186–189] To illustrate, the $Cl^- + CH_3Cl$ S_N2 reaction has a central barrier with an energy higher than that of the reactants.[192] Transition state theory (TST) assumes crossing this barrier is rate controlling and the rate constant may be determined from the barrier's free energy. However, if barrier recrossing is significant, TST is an invalid model for interpreting the $Cl^- + CH_3Cl$ rate constant.[186,190]

These initial trajectory studies utilized an analytical potential energy surface fit to experimental data and HF/6-31G* calculations.[14] Though this level of theory correctly represents many properties of S_N2 potential energy surface,[14–16] it gives X—C and Y—C bond lengths at the central barrier that are ~0.05–0.1 Å too long.[190] This difference has been discussed in the literature[197–199] and it has been suggested that a HF analytic potential energy function may give dynamics different from those obtained from a potential energy function calculated at higher and more accurate levels of electronic structure theory.[199] In a recent study[200] reviewed here, direct dynamics at the MP2/6-31G* level of theory was used to simulate the $Cl^- + CH_3Cl$ central-barrier dynamics. This theory gives a structure and vibrational frequencies for the $[Cl{-}{-}{-}CH_3{-}{-}{-}Cl]^-$ central barrier in excellent agreement with the values for the much higher CCSD(T) theory;[201] the Cl—C bond lengths of the two theories agree within 0.005 Å and the symmetric Cl—C and C—H stretches differ by only 6 and 65 cm^{-1}, respectively. The MP2 classical potential energy barrier, without zero-point energy, is 4.54 kcal/mol with respect to the reactants. The CCSD(T) value for this barrier is 3.16 kcal/mol, and the HF/6-31G* value, used to derive the analytic potential energy function for the earlier study, is 3.57 kcal/mol.

This MP2 direct dynamics trajectory study was performed with the VENUS96/GAUSSIAN98 package of programs,[7,202] which includes an efficient predictor–corrector integration algorithm[98] and Hessian updating.[99] A

total of 10 trajectories were calculated by sampling 300 K Boltzmann energy distributions at the central barrier for the reaction coordinate, the eleven orthogonal normal modes of vibration, and the three external rotation degrees of freedom. Quasiclassical sampling (discussed above in the section on exciting the transition state) which includes zero-point energy, was used for the vibrations. Each of these trajectories was integrated for 3 ps in both the forward and backward directions off the barrier.

A most striking feature of the direct dynamics trajectories is that they are significantly different from those assumed by RRKM theory, and instead, quite similar to those found in the previous trajectory study.[203] None of the 20 3 ps backward and forward integrations off the central barrier formed $Cl^- + CH_3Cl$ products, while RRKM theory predicts that 50% (i.e., 10) of these integrations should have formed products. Many of the trajectories exhibit a regular type motion, with well-identified frequencies for the Cl—C stretching motions and have extensive recrossing of the central barrier. A trajectory with very regular motion is shown in Figure 10. There are two crossings of the central barrier for the trajectories and, after 3 ps of motion in both forward and backward directions off the central barrier, the trajectory starts and ends in the same Cl^----CH_3Cl complex.

Transition state theory assumes that each crossing of the central barrier leads to reaction. A total of 29 central-barrier crossings occurred for the

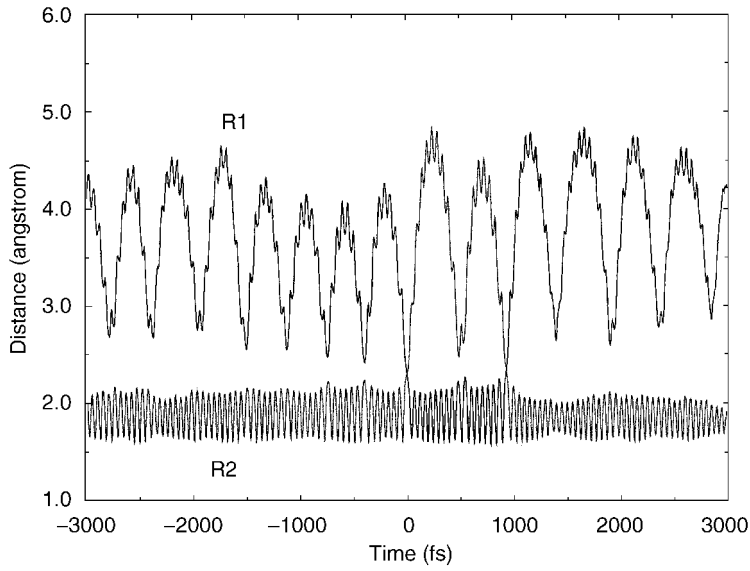

Figure 10 Representative trajectory with regular motion following excitation at the $[Cl{-}{-}{-}CH_3{-}{-}{-}Cl]^-$ central barrier. The trajectory is initiated at time zero and integrated for 3 ps in both the forward and backward dirtections. The top line is R_1, and the bottom line is R_2.

10 trajectories. However, since no S_N2 reactions occurred, it is not possible to determine a definitive correction to TST. An estimate of this correction may be made by assuming that each trajectory that started in one Cl^----CH_3Cl complex and ended in the other will ultimately be a reaction event. With this assumption the TST correction factor is 0.2, which is similar to the 0.1 correction factor estimated from the previous trajectory study,[203] based on an analytic potential energy function. This latter value is an upper limit,[203] as is the former value, since none of the trajectories reached the Cl^----CH_3Cl asymptote and more recrossings of the central barrier are expected before this asymptote is reached for both the backward and forward integrations of the trajectories.

It should be noted that one of the limitations of classical trajectory simulations is that they do not constrain zero-point energy motions and, thus, allow a vibrational mode's energy to fall below the zero-point level during the course of the trajectory (see the section on importance of quantum effects). Although the internal modes are constrained to have at least zero-point energy in the initial conditions, this constraint is not imposed during the classical trajectory. Transfer of energy between the vibrational modes and the reaction coordinate could lead to enhanced recrossing that would not be seen in a more accurate quantum-mechanical study. However, since quantum dynamics is often more regular than classical dynamics,[142] it is also possible that quantum dynamics may have more recrossings. Comparisons of classical and quantum central-barrier dynamics for $Cl^- + CH_3Cl$ reduced-dimensionality models, for which quantum dynamics are feasible, would be of particular interest.

Experimental investigations of the non-RRKM and non-TST dynamics, predicted for the $Cl^- + CH_3Cl$ system by the MP2/6-31G* direct dynamics simulations, are important. A significant amount of barrier recrossing will make the experimental S_N2 thermal rate constant smaller than that predicted by a TST calculation based on an accurate central-barrier energy and structure. Additional experimental measurements of this rate constant, including its temperature dependence, would be very helpful. Barrier recrossing dynamics could also be probed by investigating the central-barrier region with femtochemistry[133] and/or a time-dependent spectroscopic technique.[134] If a wavepacket remains localized in the central-barrier region, it may then be possible to resolve its vibrational dynamics and spectrum. A direct probe of non-RRKM dynamics for the Cl^----CH_3Cl complex would involve measuring the lifetimes of its resonance states.[197,198]

$OH^- + CH_3F$ Exit-Channel Dynamics

Ab initio electronic structure calculations for the reaction

$$OH^- + CH_3F \rightarrow CH_3OH + F^- \qquad [84]$$

show a PES with a double well.[204] However, instead of having a postreaction potential energy well with the traditional S_N2 structure of the halide ion bound to the backside of the CH_3 moiety, there is a global minimum with the halide bound to CH_3OH via a hydrogen bond; that is, $CH_3OH{-}{-}{-}F^-$, with a deep well with respect to the $CH_3OH + F^-$ reaction products.

MP2 and the much higher-level CCSD(T) energies for the stationary points on the PES are in very good agreement.[204] The CCSD(T) and MP2 energies for the largest basis sets-6-311++G(2df,2pd) and aug-cc-pVTZ-predict a central barrier with an energy ~3 kcal/mol less than that of the reactants, a reaction exothermicity of ~20 kcal/mol and a $CH_3OH{-}{-}{-}F^-$ potential minimum ~30 kcal/mol below the product asymptotic limit. The latter well depth is in excellent agreement with the 298 K $F^- + CH_3OH$ association enthalpy of 30 ± 1 kcal/mol.[205] Experimental energies are not available for the other stationary points. The MP2/6-31+G* method was used to perform the direct dynamics simulation.[206] This level of theory gives relative energies for the $[HO{-}{-}{-}CH_3{-}{-}{-}F]^-$, $CH_3OH{-}{-}{-}F^-$, and $CH_3OH + F^-$ stationary points within 3 kcal/mol of the values obtained with the highest levels of theory.

The complete intrinsic reaction coordinate (IRC), connecting the reactants and products was calculated with the MP2/6-31+G* theory, by initializing the IRC calculations at the central barrier and near the reactant and product asymptotic limits. Energies and geometries along the IRC are shown in Figure 11. The initial IRC, from the central barrier toward products, involves F^- dissociation along an approximate O—C—F collinear axis. At *s* of about 5 $amu^{1/2}$-Bohr the IRC enters a flat region, that is apparently a

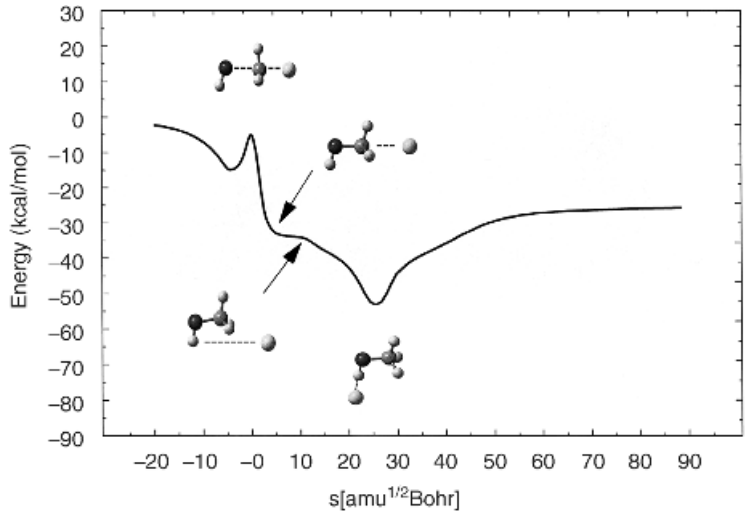

Figure 11 Potential energy along the IRC for $OH^- + CH_3F \rightarrow CH_3OH + F^-$, where *s* is the distance along the IRC (from Ref. 206).

remnant of a backside potential energy minimum which is "lost" by the presence of the much deeper $CH_3OH{-}{-}{-}F^-$ hydrogen-bonded minimum. At s of approximately 12 amu$^{1/2}$-Bohr the IRC leaves the flat region and starts its descent into the $CH_3OH{-}{-}{-}F^-$ minimum.

The MP2/6-31+G* direct dynamics simulations was performed with the VENUS[7] and the GAUSSIAN98[202] program packages. Trajectories were initiated at the central barrier, with conditions chosen from a 300 K Boltzmann distribution for reaction coordinate translation, the 14 vibrational degrees of freedom, and the 3 external rotations (see the section on TS excitation, above). Quasiclassical sampling, which includes zero-point energy, was used to choose initial conditions for the trajectories. The trajectories were integrated with a Hessian-based predictor–corrector algorithm,[98] which includes updating of the Hessian matrix.[99] The trajectory was terminated after 3 ps of motion or when the F^- and CH_3OH product separation exceeded 17 Å. The relative energy and angular momentum were conserved to within 0.01 kcal/mol and 10^{-8} $\hbar$, respectively.

Sixty-four trajectories were initiated at the $[OH{-}{-}{-}CH_3{-}{-}{-}F]^-$ central barrier with the sign of the reaction coordinate momentum chosen randomly, directed toward either reactants or products. Of these trajectories, 33 formed a reaction intermediate in the $OH^-{-}{-}{-}CH_3F$ pre-reaction potential energy well. Two reaction pathways were identified for the remaining 31 trajectories. One follows the IRC and the system becomes trapped in the deep $CH_3OH{-}{-}{-}F^-$ potential energy well and forms a reaction intermediate. Four of the trajectories are of this type, one of which forms the $CH_3OH + F^-$ reaction products during the 3 ps of the trajectory integration. The remaining 27 trajectories follow the second pathway, which is a direct dissociation with departure of the F^- ion approximately along the $O{-}C{-}{-}{-}F^-$ collinear axis. These two pathways are depicted in Figure 12 for two of the trajectories calculated in this study. Only a small fraction ($\sim$10%) of the trajectories actually follow the IRC reaction path. The vast majority of the trajectories follow the non-IRC direct dissociation path, for which $\sim$1 ps is required for the system to move from the central barrier to the F^- and CH_3OH products separated by 17 Å.

The origin of the propensity for the direct reaction path is seen from a PES diagram in which potential energy is plotted versus the $C{-}{-}{-}F^-$ distance and the $O{-}C{-}{-}{-}F^-$ angle.[206] The release of potential energy to the asymmetric $O{-}C{-}{-}{-}F^-$ stretch motion of the reaction coordinate, as the system moves off the central barrier, tends to propel F^- from CH_3OH with the $O{-}C{-}{-}{-}F^-$ angle maintained at nearly 180°. The PES is rather flat for bending of the $O{-}C{-}{-}{-}F^-$ angle, and there is only a very weak force to pull the reactive system from the direct dissociation reaction path into the $CH_3OH{-}{-}{-}F^-$ potential energy well with a $C{-}O{-}{-}{-}F^-$ angle of 102.8°. In the language of IVR, there is very weak coupling between $CH_3OH + F^-$ relative translation and $O{-}C{-}{-}{-}F^-$ bending and other vibrational degrees of freedom of the reactive system. As the system

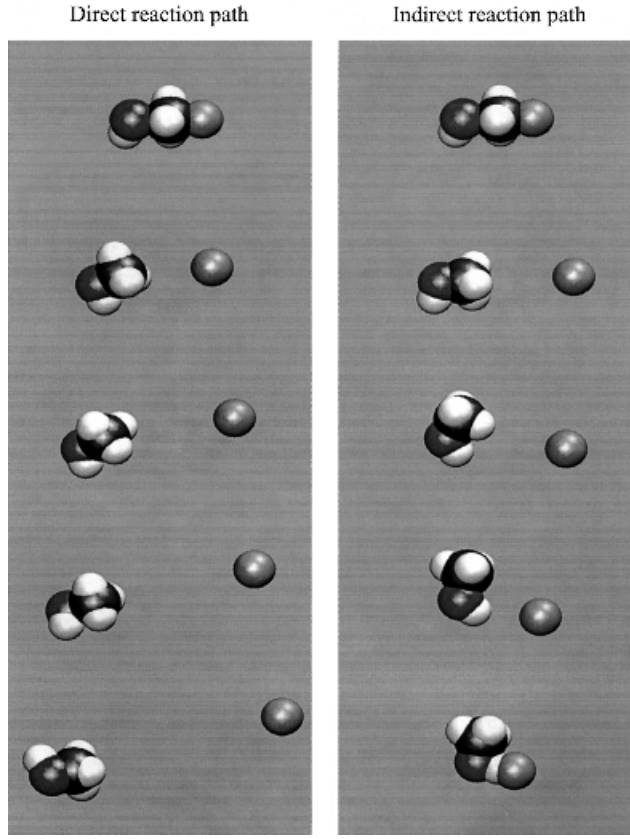

Figure 12 The two pathways for motion from the $[HO{-}{-}{-}CH_3{-}{-}{-}F]^-$ central barrier to the $CH_3OH + F^-$ products. Most of the trajectories follow the direct dissociation path. A small amount, ~10%, form the $CH_3OH{-}{-}{-}F^-$ hydrogen-bonded intermediate and follow a direct path (from Ref. 206).

moves off the central barrier, it moves directly to products without forming an intermediate trapped in the $CH_3OH{-}{-}{-}F^-$ potential energy well.

These simulations show how the efficiency of intramolecular vibrational (energy) redistribution (IVR) and formation of a statistical reaction intermediate are intimately linked to the hierarchy of timescales for intramolecular motions and structural transitions on the PES. Inefficient formation of the $CH_3OH{-}{-}{-}F^-$ reaction intermediate arises from rapid separation of the $CH_3OH + F^-$ products in comparison to the longer timescale for C—O---F^- bending to form the intermediate.

Protonated Glycine Surface-Induced Dissociation

Surface-induced dissociation (SID)[207] is an important experimental tool for determining structural properties of ions and energetic and mechanistic information concerning their dissociation pathways. In SID the ion is energized by collision with a surface. If electronic excitation is unimportant, the collision translational energy E_i is partitioned between the final translational energy E_f, and transfer to the internal vibrational/rotational modes of the ion ΔE_{int} and the vibrations of the surface ΔE_{surf}:

$$E_i = E_f + \Delta E_{\text{int}} + \Delta E_{\text{surf}} \qquad [85]$$

Peptide ion fragmentation has been studied by SID.[208] Glycine is the simplest amino acid and the fragmentation pathways for its protonated form have been extensively studied both theoretically[209] and experimentally.[210] Three major fragmentation pathways have been proposed and are shown in Figure 13. The first involves intramolecular proton transfer from the NH_3 group to the OH group, resulting in loss of water and formation of iminium ion ($NH_2CH_2^+$) and CO. For the second pathway there is proton transfer from the NH_3 group to the carbonyl oxygen, resulting in the loss of dihydroxycarbene, $C(OH)_2$. Formic acid (HCOOH) is formed in the third pathway.

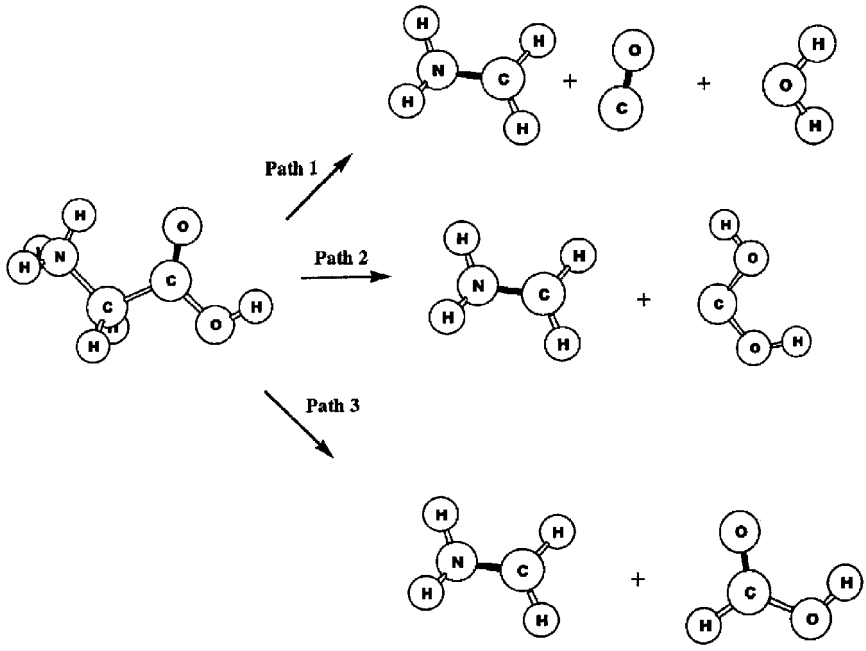

Figure 13 Dissociation pathways for *N*-protonated glycine (from Ref. 211).

A direct dynamics classical trajectory simulation study has been performed to study energy transfer to *N*-protonated glycine, $(gly\text{-}H)^+$, and its fragmentation, when it collides with the diamond {111} surface.[211] In the simulation the AM1 semiempirical electron structure theory is used to represent the $(gly\text{-}H)^+$ intramolecular potential. To examine the accuracy of the AM1 model, its reaction pathways and energetics for $(gly\text{-}H)^+$ fragmentation were compared with those determined previously from experiment[209] and ab initio calculations.[209,212] A summary of the AM1 and ab initio barriers for the $(gly\text{-}H)^+$ fragmentation reaction is given in Table 3. In addition to the barriers for paths 1–3 in Figure 13, barriers are also given for the formation of CO_2 and H_2 as reaction products. The transition state structures for the different reaction pathways are given in Reference 211. Except for the $C(OH)_2$ formation channel, the AM1 and ab initio barriers are in agreement. Also, the AM1 barrier for path 1 to form $CO + H_2O$ is in good agreement with the value of 44 kcal/mol deduced from experiment.[210] The relative amount of the product channel $NH_2CH_2^+ + C(OH)_2$ in the simulations may be too large, since the AM1 barrier for this channel is ~1eV too low as compared to the barrier found at higher levels of theory. However, the effect of this inaccurate barrier on the SID dynamics may be mediated by the high translational energy of the projectile $(gly\text{-}H)^+$.

The potential energy function used for the $(gly\text{-}H)^+$/diamond {111} system is given by

$$V = V_{\text{peptide}} + V_{\text{surface}} + V_{\text{peptide,surface}} \qquad [86]$$

where V_{peptide} is the $(gly\text{-}H)^+$ intramolecular potential, V_{surface} is the potential for the diamond surface, and $V_{\text{peptide,surface}}$ represents the $(gly\text{-}H)^+$/diamond intermolecular potential. As described above, the AM1 semiempirical electronic structure theory model is used for the $(gly\text{-}H)^+$ intramolecular potential. The remaining potentials are analytic functions.[213,214] The potential energy

Table 3 Enthalpy Barriers for $(Gly\text{-}H)^+$ Dissociation[a]

Products	B3LYP[b]	QCISD(T)[c]	MP2[b]	AM1[d]
$NH_2CH_2^+ + CO + H_2$	41.4	35.6	38.5	40.3
$NH_2CH_2^+ + C(OH)_2$	57.2	51.5	63.1	27.2
$NH_2CH_2^+ + HCOOH$	88.5	85.0	92.9	99.5
$NH_3CH_3^+ + CO_2$	74.0	78.4	77.5	78.2
$NH_2CHCOOH^+ + H_2$	80.0[e]	—	—	86.8

[a] The barriers are for 300 K. The ab initio calculations are from Ref. 209, except for the last reaction.
[b] Calculations with 6-31+G* basis.
[c] Calculations with 6-31+G** basis.
[d] From Ref. 211.
[e] Calculations with the 6-31++G* basis from Ref. 212.

function for the diamond {111} model consists of harmonic stretches and bends, with force constants chosen to fit the diamond phonon spectrum.[213] The (gly-H)$^+$/diamond intermolecular potential is modeled by a sum of two-body potentials between the atoms of the peptide and the atoms of diamond. The two-body potential is given by

$$V_{XY} = A_{XY}\exp(-B_{XY}r_{ij}) + \frac{C_{XY}}{r_{ij}^6} \qquad [87]$$

where X corresponds to Ar or the C and H atoms of the diamond and Y corresponds to H, C, O, and N atoms of the peptide. To determine the parameters for the two-body potentials, ab initio potential energy curves were calculated[214] using CH_4, as a model for the C and H atoms of the diamond {111} and CH_4, NH_3, NH_4^+, H_2CO, and H_2O as models for the different types of atoms and functional groups comprising peptides. The ab initio calculations were carried out at the MP2/6-311+G(2df,2pd) level of theory with the frozen-core approximation.[214] Following the discussion in the section on BO direct dynamics, the potential in Eq. [86] is a QM+MM model.

The classical trajectory simulations were carried out with VENUS interfaced with the semiempirical electronic structure theory computer program MOPAC. To simulate experimental conditions for (gly-H)$^+$ + diamond collisions, the center of a beam of (gly-H)$^+$ ion projectiles is aimed at the center of the surface, with fixed incident angle θ_i and fixed initial translational energy, E_i. The radius of the beam was chosen so that the beam overlapped a unit area on the surface. For each trajectory, the projectile was randomly placed in the cross section of this beam and then randomly rotated about its center of mass so that it had an initial random orientation with respect to the surface. The azimuthal angle, χ, between the beam and a fixed plane perpendicular to the surface, was sampled randomly between 0 and 2π. Such a random sampling of χ simulates collisions with different domains of growth on the diamond surface.

The initial conditions for the vibrational modes of the (gly-H)$^+$ were chosen via the quasiclassical normal-mode method,[100] with the energy for each normal mode of vibration selected from the mode's 300 K harmonic oscillator Boltzmann distribution. A 300 K rotational energy of RT/2 was added to each principal axis of rotation of the projectile. Initial conditions for the diamond surface were chosen by first equilibrating the surface to a 300 K Boltzmann distribution with 2 ps of molecular dynamics and scaling the atomic velocities.[135–137] The structure and atomic velocities obtained from this equilibration process are then used as the initial conditions for an equilibration run at the beginning of each trajectory.

One hundred trajectories were calculated to simulate the fragmentation dynamics of (gly-H)$^+$ energized by collision with the diamond {111} surface at $E_i = 70$ eV and $\theta_i = 45°$. Each trajectory was integrated for 1.5 ps or until

$(gly\text{-}H)^+$ fragmentation occurred. The energy transfer probabilities to E_f, E_{int}, and E_{surf}, [i.e., Eq. [85]], for these trajectories with the AM1 potential are statistically the same as those found with AMBER potential for $(gly\text{-}H)^+$.[214] For AMBER, the average percent energy transfer to E_f, E_{int}, and E_{surf} are 11, 37, and 52, respectively. For the simulations with AM1, these percents are 12, 38, and 50. These results show that, to simulate energy transfer in $(gly\text{-}H)^+$ SID, the harmonic AMBER and anharmonic reactive AM1 potentials give the same result.

For 42 of the 100 trajectories, $(gly\text{-}H)^+$ fragmented. The fragmentation products are listed in Table 4, and, of the many product channels, the predominant ones are $NH_3CH^+ + HCOOH$, $NH_2CH_2^+ + H_2O + CO$, $NH_2CH_2^+ + C(OH)_2$, $NHCH_2 + H_2 + COOH^+$, and $NH_3 + CH_2COOH^+$. Thus paths 1 and 2 in Figure 13 are important and formic acid is also formed, but not by path 3. The iminium ion $NH_2CH_2^+$ is formed in 12 of the trajectories and its isomer NH_3CH^+ in 4. One H_2 or two H_2 molecules are products in 14 of the trajectories and NH_3 a product in 8. An important component of the dissociation dynamics is shattering fragmentation, in which $(gly\text{-}H)^+$ dissociates as it either impacts or strongly interacts with the surface. Twenty-three of the dissociations, ~55%, occurred by shattering and their dynamics are discussed in more detail below. Animations of the trajectories are available at the Website http://www.octopus.chem.wayne.edu/hase.

Table 4 Products of $(Gly\text{-}H)^+ + Diamond$ SID[a]

Products	Number[b]
No reaction	58
$NH_3CH_3^+ + CO_2$	1
$NH_3CH_2^+ + COOH$	3(1)
$NH_3CH^+ + HCOOH$	4(4)
$NH_2CH_2^+ + C(OH)_2$	7(3)
$NH_2CH_2^+ + HCOOH$	1(1)
$NH_2CH_2^+ + H_2O + CO$	3
$NH_2CH_2^+ + H_2 + CO_2$	1(1)
$NHCH_2 + H_2 + COOH^+$	6(5)
$NHCH^+ + 2H_2 + CO_2$	1(1)
$NCH + 2H_2 + COOH^+$	1(1)
$NCH + H_2 + H_2O + COH^+$	1(1)
$NH_3 + CH_2COOH^+$	7(1)
$NH_2 + CH_3^+ + CO_2$	1
$NH_3CHCO^+ + H_2O$	1
$NH_2CHCOOH^+ + H_2$	1(1)
$NH_2CHO^+ + H_2 + COH$	1(1)
$NCC(OH)_2^+ + 2H_2$	1(1)
$NCCHOH^+ + H_2 + H_2O$	1(1)

[a] The collision energy and angle are 70 eV and 45°. Of the 100 trajectories, each of 1.5 ps, 42 fragmented to products.

[b] The number of the fragmentations, which are shattering, are given in parentheses.

1. *HCOOH formation.* Formic acid is formed only by shattering. For the four trajectories with NH_3CH^+ as a product, $(gly\text{-}H)^+$ is properly oriented as it impacts the surface, so that one of the H atoms of CH_2 is "driven" into the carbonyl C atom and the products are formed. For the trajectory forming $NH_2CH_2^+$, the dynamics discribed above is the same except $NH_3CH^+ \rightarrow NH_2CH_2^+$ H-atom transfer also occurs.

2. *H_2 formation.* For H_2 formation, shattering dominates, with 13 of the 14 trajectories dissociating this way via four different mechanisms. For 8 of the shattering trajectories, an H_2 molecule is ejected from NH_3 as this end of $(gly\text{-}H)^+$ hits the diamond surface. For another 3 of the shattering trajectories, this H_2 elimination step occurs during the collision and then later

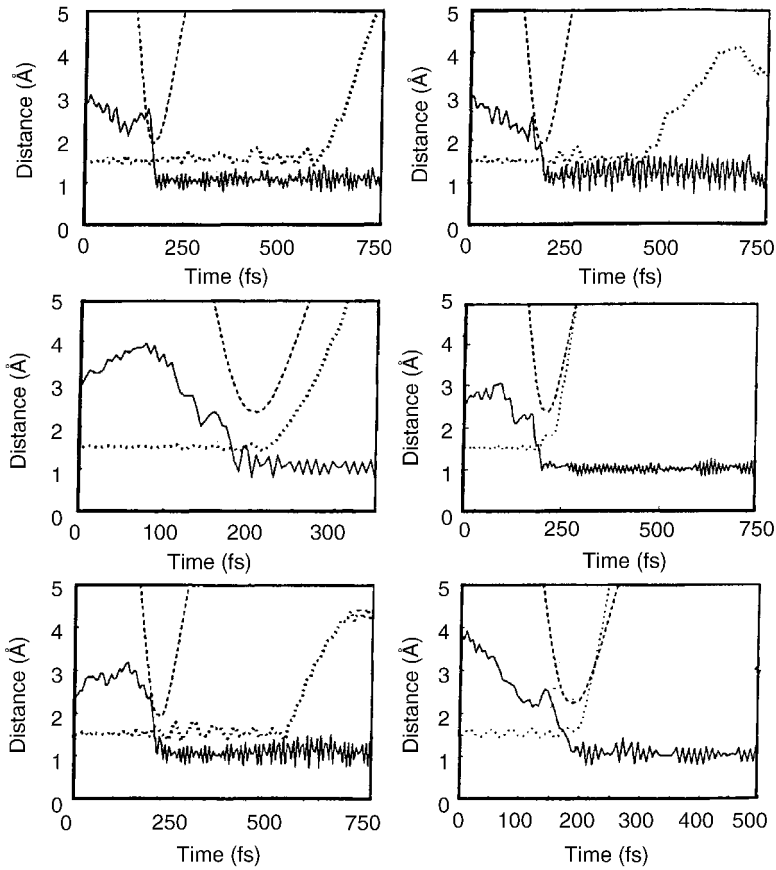

Figure 14 Height of the $(gly\text{-}H)^+$ center of mass from the top carbon layer of the diamond surface (- - -), the C–C distance (····), and the distance between the transferring H atom and the carbonyl O atom (—) versus time for the six trajectories that form $NH_2CH_2^+ + C(OH)_2$, by H-atom transfer to the carbonyl O atom. Three of the dissociations occur by shattering (from Ref. 211).

another H_2 eliminates from CH_2. For the two trajectories forming $NH_2CHCOOH^+$ and $NH_2CHO + COH^+$ as products, the H_2 elimination is four-centered, as proposed previously[209] with one hydrogen coming from nitrogen and the other from carbon. For the one dissociation not occurring by shattering, $(gly\text{-}H)^+$ first fragments to $NH_3CH_2^+$ and COOH and later the ion dissociates into $NHCH_2^+$ and H_2.

3. *$C(OH)_2$ formation.* Seven of the trajectories form the products $NH_2CH_2^+$ and $C(OH)_2$, three of which occur by shattering. For these seven trajectories, the NH_3 moiety of $(gly\text{-}H)^+$ collides with the surface and six of them transfer a H atom from NH_3 to the carbonyl oxygen during the collision. The distances of the $(gly\text{-}H)^+$ center of mass from the diamond surface, the C—C distance, and the distance between the transferring H atom and the carbonyl oxygen are plotted in Figure 14 for these 6 trajectories. Three of the dissociations occur by shattering, for which the C—C bond breaks as the collision promotes transfer of the H atom. For the trajectory not shown in Figure 14, the reaction is nonshattering and the H atom first transfers to the carbonyl carbon.

4. *NH_3 formation.* The product NH_3 is formed in eight, ~20%, of the trajectories. For seven, the other product is CH_2COOH^+, while for one trajectory this species undergoes further dissociation to CH_3^+ and CO. For the single shattering trajectory, the N—C bond ruptured on impact. The primary mechanism, for NH_3 formation, is delayed dissociation, with excitation of $(gly\text{-}H)^+$ by collision with the surface and then energy accumulation in the N—C bond by intramolecular vibrational energy distribution.

These simulations suggest that the collisional activation of protonated amino acids and peptides may directly "drive" the ion to a dissociation transition state structure, resulting in nonstatistical fragmentation dynamics. To consider the generality of this proposition, it will be important to study additional amino acids and larger peptides in the future. It is also important to compare the current AM1 direct dynamics with direct dynamics simulations at higher levels of theory, such as B3LYP and MP2.

CONCLUDING REMARKS

In this chapter, direct dynamics classical trajectory simulations are described for modeling electronic adiabatic reactions that occur on a single Born–Oppenheimer electronic potential energy surface. In concluding, we note that it is possible to extend these simulations to electronically nonadiabatic classical dynamics and to electronically adiabatic semiclassical direct dynamics. Incorporating transitions between electronic states in classical trajectory simulations was first proposed by Tully and Preston in their trajectory surface hopping (TSH) model.[215–217] In the TSH approach a "hopping seam"

is defined and when trajectories evolve into this region the trajectory may be "switched" onto a different electronic state according to the transition probability obtained from solving the electronic Shrödinger equation in the strong coupling region of the two electronic states. This approach has been extended by introducing the fewest switching algorithms in selecting the hopping trajectories. In the same spirit of trajectory hopping, Blais and Truhlar[218] proposed that the trajectory does not hop and stays on its current electronic potential surface if the transition probability is less than 0.5. There are different variants of the TSH method and references can be found in the review by Hack and Truhlar.[219]

Martínez and co-workers have developed the ab initio multiple spawning (AIMS) method,[220,221] for which the system's wavefunction is represented by a linear combination of the product of the nuclei and electronic wavefunctions for the different electronic states. The time-dependent nuclear wavefunctions are approximated by a summation of weighted Gaussians. At each integration step, the propagation of the momenta and coordinates for the nuclei is governed by the classical equations of motion, while the electronic Hamiltonian for the system is solved quantum-mechanically. When the nonadiabatic transition region is entered, new wavefunctions for the nuclei are created, that is, "spawned" onto the excited electronic states. The spawned wavefunctions also have the probability for the transition back to their "parent" electronic state. Therefore, instead of switching the classical trajectories as employed in the trajectory surface hopping method by Tully, the AIMS method expands the wavefunctions of nuclei. By allowing the wavefunctions to spawn on a single electronic state, the method may also be used to include the tunneling effect.[222] Under limiting conditions, this method attains the exact quantum or classical limits. A comprehensive description of the method can be found in the review by Martínez and co-workers.[220]

For some dynamical problems semiclassical wavepacket direct dynamics simulations are possible.[223] A nuclear coordinate wavepacket may be localized in some region of space at a particular time, and it is necessary only to know the potential energy surface in this region to determine the wavepacket's quantum-mechanical motion for a small timestep Δt. Such a situation allows one to use Heller's Gaussian wavepacket dynamics (GWD) algorithm to propagate a multidimensional wavepacket.[224] GWD requires at most (thawed Gaussian approximation) the gradient and second derivative of the potential at the current nuclear configuration,[225] both of which are easily obtained directly from an electronic structure computer program. In some situations the width of the wavepacket may be very small and it may be possible to use the frozen Gaussian approximation,[226] which requires only the gradient of the potential.

The general Gaussian wavefunction for a N-dimensional system at time t with spatial coordinates $\mathbf{q}$ is

$$\phi(\mathbf{q}, t) = \exp\{i[(\mathbf{q} - \mathbf{q}_t) \cdot A_t \cdot (\mathbf{q} - \mathbf{q}_t) + \mathbf{p}_t(\mathbf{q} - \mathbf{q}_t) + \gamma_t]\} \qquad [88]$$

where A_t is a $N \times N$ complex symmetric matrix, $\mathbf{q}_t$ and $\mathbf{p}_t$ are real N-dimensional vectors specifying the position and momenta of the center of the wavepacket, and γ_t is a complex phase normalization factor. In the direct dynamics GWD algorithm, electronic structure information is used to determine the time evolution of the center of the wavepacket. The GWD algorithm remains accurate as long as the wavepacket retains its localized structure. For a general nonquadratic, anharmonic potential, the wavepacket will eventually spread until it no longer has a quadratic form as assumed by Eq. [88]. The time required for this spreading will, of course, depend on the actual potential and the GWD algorithm has been applied successfully for a variety of applications.[223] In particular, absorption and emission spectra may be determined from a time-dependent formalism[224] by simulating the motion of a wavepacket on the electronic excited state potential (absorption) or the ground-state potential (emission). It has been found that GWD dynamics gives sufficient structure in the spectra to compare with experiment.[223–226]

Ohrn and co-workers have developed a direct dynamics approach which incorporates both the electrons and nuclei dynamics (END).[227] The complete electron-nuclear coupling terms are retained in the calculation and, as a result, the dynamics is not constrained to a single Born–Oppenheimer potential energy surface; i.e., electronic non-adiabaticity is explicitly included. A complication in this approach is the computational demand in propagating an electronic wavefunction which is an accurate representation of the ground electronic state as well as multiple excited electronic states. This approach will become more widely used as computation becomes more powerful. In its initial development,[227] Deumens et al. used END and treated the dynamics of the nuclei purely classical as in the above classical direct dynamics. More recently, a semiclassical description of the nuclear motion has been implemented by incorporating Heller's[224–226] Gaussian wave packet dynamics.[228]

ACKNOWLEDGMENTS

W. L. Hase would like to acknowledge financial support from the National Science Foundation for his research in direct dynamics simulations. Animations of the direct dynamics trajectories described in the section on applications of Born-Oppenheimer direct dynamics are available at the Website http://octopus.chem. wayne.edu/hase.

REFERENCES

1. D. L. Bunker, *J. Chem. Phys.*, **37**, 393 (1962). Monte Carlo Calculation of Triatomic Dissociation Rates. I. N_2O and O_3.
2. N. C. Blais and D. L. Bunker, *J. Chem. Phys.*, **37**, 2713 (1962). Monte Carlo Calculation. II. The Reaction of Alkali Atoms with Methyl Iodide.
3. D. L. Bunker, *Meth. Comput. Phys.*, **10**, 287 (1971). Classical Trajectory Methods.
4. L. M. Raff and D. L. Thompson, in *Theory of Chemical Reaction Dynamics*, Vol. III, M. Baer, Ed., Chemical Rubber, Boca Raton, FL, 1985, p. 1.

5. H. Goldstein, *Classical Mechanics,* Addison-Wesley, London, 1950.
6. E. B. Wilson Jr., J. C. Decius, and P. C. Cross, *Molecular Vibrations,* McGraw-Hill, New York, 1955, p. 307.
7. W. L. Hase, R. J. Duchovic, X. Hu, A. Komornicki, K. F. Lim, D.-H. Lu, G. H. Peslherbe, K. N. Swamy, S. R. Vande Linde, A. Varandas, H. Wang, and R. J. Wolf, *Quantum Chem. Program Exchange,* **16,** 671 (1996). Venus.
8. D. M. Hirst, *Potential Energy Surfaces: Molecular Structure and Reaction Dynamics,* Taylor and Francis, London, 1985, p. 112.
9. L. Bañares and M. J. D'Mello, *Chem. Phys. Lett.,* **277,** 465 (1997). Quantum Mechanical Rate Constants for the $D+H_2 \rightarrow HD+H$ Reaction on the BKMP2 Potential Energy Surface; L. Bañares, F. J. Aoiz, V. J. Herrero, M. J. D'Mello, B. Niederjohann, K. Seekamp-Rahn, E. Wrede, and L. Schnieder, *J. Chem. Phys.,* **108,** 6160 (1998). Experimental and Quantum Mechanical Study of the $H+D_2$ Reaction Near 0.5 eV: The Assessment of the H_3 Potential Energy Surfaces; E. Wrede, L. Schnieder, K. H. Welge, F. J. Aoiz, L. Bañares, J. F. Castillo, B. Martínez-Haya, and V. J. Herrero, *J. Chem. Phys.,* **110,** 9971 (1999). The Dynamics of the Hydrogen Exchange Reaction at 2.20 eV Collision Energy: Comparison of Experimental and Theoretical Differential Cross Sections; S. L. Mielke, B. C. Garrett, and K. A. Peterson, *J. Chem. Phys.,* **116,** 4142 (2002). A Hierarchical Family of Global Analytic Born–Oppenheimer Potential Energy Surfaces for the $H + H_2$ Reaction Ranging in Quality from Double-Zeta to the Complete Basis Set Limit.
10. K. Stark and H.-J. Werner, *J. Chem. Phys.,* **104,** 6515 (1996). An Accurate Multireference Configuration Interaction Calculation of the Potential Energy Surface for the $F+H_2 \rightarrow HF+H$ Reaction; F. J. Aoiz, L. Bañares, and J. F. Castillo, *J. Chem. Phys.,* **111,** 4013 (1996). Spin–Orbit Effects in Quantum Mechanical Rate Constant Calculations for the $F + H_2 \rightarrow HF + H$ Reaction; M. H. Alexander, D. E. Manolopoulos, and H.-J. Werner, *J. Chem. Phys.,* **113,** 11084 (2000). An Investigation of the $F + H_2$ Reaction Based on a Full *Ab Initio* Description of the Open-Shell Character of the $F(^2P)$ Atom.
11. M. R. Pastrana, L. A. M. Quintales, J. Brandão, and A. J. C. Varandas, *J. Phys. Chem.,* **94,** 8073 (1990). Recalibration of a Single-Valued Double Many-Body Expansion Potential-Energy Surface of Ground-State HO_2 and Dynamics Calculations for the $O + OH \rightarrow H + O_2$ Reaction; J. Troe and V. G. Ushakov, *J. Chem. Phys.,* **115,** 3621 (2001). Theoretical Studies of the $HO + O \Leftrightarrow HO_2 \Leftrightarrow H + O_2$ Reaction. II. Classical Trajectory Calculations on an *Ab Initio* Potential for Temperatures Between 300 and 5000 K.
12. H. Werner, C. Bauer, P. Rosmus, H. Keller, M. Stumpf, and R. Schinke, *J. Chem. Phys.,* **102,** 3593 (1995). The Unimolecular Dissociation of HCO: I. Oscillations of Pure CO Stretching Resonance Widths.
13. W. L. Hase, G. Mrowka, R. J. Brudzynski, and C. S. Sloane, *J. Chem. Phys.,* **69,** 3548 (1978). An Analytic Function Describing the $H + C_2H_4 \rightleftharpoons C_2H_5$ Potential Energy Surface.
14. S. R. Vande Linde and W. L. Hase, *J. Phys. Chem.,* **94,** 2778 (1990). Complete Multidimensional Analytic Potential-Energy Surface for $Cl^- + CH_3Cl$ S_N2 Nucleophilic Substitution.
15. H. Wang, L. Zhu, and W. L. Hase, *J. Phys. Chem.,* **98,** 1608 (1994). A Model Multidimensional Potential-Energy Function for the $Cl^- + CH_3Br \rightarrow ClCH_3 + Br^-$ Reaction.
16. H. Wang and W. L. Hase, *J. Am. Chem. Soc.,* **119,** 3093 (1997). Kinetics of $F^- + CH_3Cl$ Nucleophilic Substitution.
17. I. S. Y. Wang and M. Karplus, *J. Am. Chem. Soc.,* **95,** 8160 (1973). Dynamics of Organic Reactions.
18. K. Bolton, W. L. Hase, and G. H. Peslherbe, in *Modern Methods for Multidimensional Dynamics Computations in Chemistry,* D. L. Thompson, Ed., World Scientific, London, 1998, p. 143.
19. R. Car and M. Parrinello, *Phys. Rev. Lett.,* **55,** 2471 (1985). Unified Approach for Molecular Dynamics and Density Functional Theory.
20. A. Warshel and M. Karplus, *Chem. Phys. Lett.,* **32,** 11 (1975). Semiclassical Trajectory Approach to Photoisomerization.

21. C. Leforestier, *J. Chem. Phys.*, **68,** 4406 (1978). Classical Trajectories Using the Full *Ab Initio* Potential Energy Surface $H^- + CH_4 \rightarrow CH_4 + H^-$.
22. A. Warshel and M. Karplus, *J. Am. Chem. Soc.*, **94,** 5612 (1972). Calculation of Ground and Excited State Potential Surfaces of Conjugated Molecules. I. Formulation and Parametrization.
23. H. B. Schlegel and M. J. Frisch, in *Theoretical and Computational Models for Organic Chemistry,* J. S. Formosinho, I. G. Csizmadia, and L. G. Arnaut, Eds., Kluwer Academic, the Netherlands, NATO-ASI Series C339, 1991, p. 5
24. M. C. Zerner, in *Reviews in Computational Chemistry,* K. B. Lipkowitz and D. B. Boyd, Eds., Wiley, NY, 1991, 313. Semiempirical Molecular Orbital Methods.
25. M. J. S. Dewar and W. Thiel, *J. Am. Chem. Soc.*, **99,** 4907 (1977). Ground States of Molecules. 39. MNDO Results for Molecules Containing Hydrogen, Carbon, Nitrogen, and Oxygen.
26. M. J. S. Dewar, E. G. Zoebisch, E. F. Healy, and J. J. P. Stewart, *J. Am. Chem. Soc.*, **107,** 3902 (1985). The Development and Use of Quantum-Mechanical Models. 76. AM1—A New General-Purpose Quantum Mechanical Molecular-Model.
27. J. J. P. Stewart, *J. Comput. Chem.*, **12,** 320 (1991). Optimization of Parameters for Semiempirical Methods 3. Extension of PM3 to Be, Mg, Zn, Ga, Ge, As, Se, Cd, In, Sn, Sb, Te, Hg, Tl, Pb and Bi.
28. W. Thiel, Program MNDO97, Univ. Zurich, Zurich, Switzerland, 1997.
29. J. J. P Stewart, *J. Comput. Chem.*, **12,** 320 (1991). Optimization of Parameters for Semiempirical Methods. III. Extension of PM3 to Be, Mg, Zn, Ga, Ge, As, Se, Cd, In, Sn, Sb, Te, Hg, Tl, Pb and Bi.
30. W. Thiel and A. A. Voityuk, *J. Phys. Chem.*, **100,** 616 (1996). Extension of MNDO to d Orbitals: Parameters and Results for the Second-Row Elements and for the Zinc Group.
31. A. Gonzalez-Lafont, T. N. Truong, and D. G. Truhlar, *J. Phys. Chem.*, **95,** 4618 (1991). Direct Dynamics Calculations with NDDO (Neglect of Diatomic Differential Overlap) Molecular Orbital Theory with Specific Reaction Parameters.
32. G. H. Peslherbe and W. L. Hase, *J. Chem. Phys.*, **104,** 7882 (1996). Semiempirical MNDO, AM1, and PM3 Direct Dynamics Trajectory Studies of Formaldehyde Unimolecular Dissociation.
33. W. Chen, W. L. Hase, and H. B. Schlegel, *Chem. Phys. Lett.*, **228,** 436 (1994). *Ab Initio* Classical Trajectory Study of $H_2CO \rightarrow H_2 + CO$ Dissociation.
34. G. E. Scuseria and H. F. Schaefer III, *J. Chem. Phys.*, **90,** 3629 (1989). The Photodissociation of Formaldehyde: A Coupled Cluster Study Including Connected Triple Excitations of the Transition State Barrier Height for $H_2CO \rightarrow H_2 + CO$.
35. C. Doubleday, Jr., K. Bolton, G. H. Peslherbe, and W. L. Hase, *J. Am. Chem. Soc.*, **118,** 9922 (1996). Direct Dynamics Simulation of the Lifetime of Trimethylene.
36. G. Li, S. B. M. Bosio, and W. L. Hase, *J. Molec. Struc.*, **556,** 43 (2000). A QM/MM Model for $O(^3P)$ Reaction with an Alkyl Thiolate Self-Assembled Monolayer.
37. S. F. Boys, *Proc. Roy. Soc. London A,* **201,** 125 (1950). Electronic Wave Functions II. A Calculation for the General State of the Beryllium Atom.
38. H.-J. Werner and W. Meyer, *J. Chem. Phys.*, **74,** 5794 (1981). A Quadratically Convergent MCSCF Method for the Simultaneous-Optimization of Several States.
39. H.-J. Werner and W. Meyer, *J. Chem. Phys.*, **74,** 5802 (1981). MCSCF Study of the Avoided Curve Crossing of the Two Lowest $^1\Sigma^+$ States of LiF.
40. B. Roos, D. Taylor, and P. E. M. Siegbahn, *Chem. Phys.*, **48,** 157 (1980). A Complete Active Space SCF Method (CASSCF) Using a Density Matrix Formulated SUPER-CI Approach.
41. B. Jonsson, B. O. Roos, P. R. Taylor, and P. E. M. Siegbahn, *J. Chem. Phys.*, **74,** 4566 (1981). MCSCF-CI Calculations of Ground-State Potential Curves of LiH, Li_2, and F_2.
42. P. J. Knowles, G. J. Sexton, and N. C. Handy, *Chem. Phys.*, **72,** 337 (1982). Studies Using the CASSCF Wave Function.

43. R. J. Bartlett, *J. Phys. Chem.*, **93,** 1697 (1989). Coupled-Cluster Approach to Molecular Structure and Spectra: A Step Toward Predictive Quantum Chemistry.
44. J. A. Pople, M. Head-Gordon, and K. Raghavachari, *J. Chem. Phys.,* **87,** 5968 (1987). Quadratic Configuration Interaction. A General Technique for Determining Electron Correlation Energies.
45. H. J. Werner and P. J. Knowles, *J. Chem. Phys.,* **89,** 5803 (1988). An Efficient Internally Contracted Multiconfiguration–Reference Configuration Interaction Method.
46. P. J. Knowles and H. J. Werner, *Chem. Phys. Lett.,* **145,** 514 (1988). An Efficient Method for the Evaluation of Coupling Coefficients in Configuration Interaction Calculations.
47. R. J. Bartlett, *J. Chem. Phys.,* **62,** 3258 (1975). Many-Body Perturbation Theory Applied to Electron Pair Correlation Energies. I. Closed-Shell First-Row Diatom Hydrides.
48. R. Krishnan and J. A. Pople, *Int. J. Quantum. Chem.,* **14,** 91 (1978). Approximate Fourth-Order Perturbation Theory of the Electron Correlation Energy.
49. G. Li and W. L. Hase, *J. Am. Chem. Soc.,* **121,** 7124 (1999). *Ab Initio* Direct Dynamics Trajectory Study of the $Cl^- + CH_3Cl$ S_N2 Reaction at High Reagent Translation Energy.
50. D. J. Mann and W. L. Hase, *J. Am. Chem. Soc.,* **124,** 3208 (2002). *Ab Initio* Direct Dynamics Study of Cyclopropyl Radical Ring-Opening.
51. P. Hohenberg and W. Kohn, *Phys. Rev. B,* **136,** 864 (1964). Inhomogeneous Electron Gas.
52. W. Kohn and L. J. Sham, *Phys. Rev. A,* **140,** 1133 (1965). Self-Consistent Equation Including Exchange and Correlation Effects.
53. S. J. Vosko, L. Wilk, and M. Nusair, *Can. J. Phys.,* **58,** 1200 (1980). Accurate Spin-Dependent Electron Liquid Correlation Energies for Local Spin Density Calculations: A Critical Analysis.
54. A. D. Becke, *Phys. Rev. A,* **38,** 3098 (1988). Density Functional Exchange Approximation with Correct Asymptotic Behavior.
55. A. D. Becke, *J. Chem. Phys.,* **98,** 5648 (1993). Density-Functional Thermochemistry. III. The Role of Exact Exchange.
56. C. Lee, W. Yang, and R. G. Parr, *Phys. Rev. B,* **37,** 785 (1988). Development of the Colle-Salvetti Correlation Energy Formula into a Functional of Electron Density.
57. J. P. Perdew, J. A. Chevary, S. H. Vosko, K. A. Jackson, M. R. Pederson, D. J. Singh, and C. Fiolhais, *Phys. Rev. B,* **46,** 6671 (1992). Atoms, Molecules, Solids and Surfaces: Applications of the Generalized Gradient Approximation for Exchange and Correlation.
58. W. Yang, *Phys. Rev. Lett.,* **66,** 1438 (1991); Direct Calculation of Electron Density in Density Functional Theory.
59. S. Baroni and P. Giannozzi, *Europhys. Lett.,* **17,** 547 (1992). Towards Very Large Scale Electronic Structure Calculations.
60. A. F. Voter, J. D. Kress, and R. N. Silver, *Phys. Rev. B,* **53,** 12733 (1996). Linear-Scaling Tight Binding from a Truncated-Moment Approach.
61. F. Mauri, G. Galli, and R. Car, *Phys. Rev. B,* **47,** 9973 (1993). Orbital Formulation for Electronic Structure Calculation with Linear System Size Scaling.
62. P. Ordejón, D. Drabold, M. Grumbach, and R. M. Martin, *Phys. Rev. B,* **48,** 14646 (1993). Unconstrained Minimization Approach for Electronic Calculations that Scales Linearly with System Size.
63. J. M. Pérez-Jordá and W. Yang, *Chem. Phys. Lett.,* **241,** 469 (1995). An Algorithm for 3D Numerical Integration that Scales Linearly with the Size of the Molecule.
64. L. Greengard and V. Rokhlin, *J. Comput. Phys.,* **73,** 325 (1987). A Fast Algorithm for Particle Simulations.
65. H. G. Petersen, D. Soelvason, J. W. Perram, and E. R. Smith, *J. Chem. Phys.,* **101,** 8870 (1994). The Very Fast Multipole Method.
66. D. M. York, T. S. Lee and W. Yang, *J. Chem. Phys.,* **103,** 1003 (1996). Parameterization and Efficient Implimentation of a Solvent Model for Linear-Scaling Semiempirical Quantum Mechanical Calculations of Biological Macromolecules.

67. J. M. Pérez-Jordá and W. Yang, *J. Chem. Phys.,* **104,** 8003 (1996). A Concise Redefinition of the Solid Spherical Harmonics and Its Use in Fast Multipole Methods.

68. W. Yang and J. M. Pérez-Jordá, in *Encyclopedia of Computational Chemistry,* N. L. Allinger, Ed., Wiley, New York, 1998, Vol. 2, p. 1496.

69. B. L. Holian and P. S. Lomdahl, *Science,* **280,** 2085 (1998). Plasticity Induced by Shock Waves in Nonequilibrium Molecular-Dynamics Simulations; Y. Yamaguchi and J. Gspann, *Eur. Phys. J. D,* **16,** 103 (2001). Large-Scale Molecular Dynamics Simulations of High Energy Cluster Impact on Diamond Surface; S. J. Zhou, D. M. Beazly, P. S. Lomdahl, and B. L. Holian, *Phys. Rev. Lett.,* **78,** 479 (1997). Large Scale Molecular Dynamics Simulations of Three-Dimensional Ductile Failure.

70. J.-K. Hwang, G. King, S. Creighton, and A. Warshel, *J. Am. Chem. Soc.,* **110,** 5297 (1988). Simulation of Free Energy Relationships and Dynamics of S_N2 Reactions in Aqueous Solution.

71. A. Warshel, *Proc. Natl. Acad. Sci. (USA),* **81,** 444 (1984). Dynamics of Enzymatic Reactions.

72. J. Gao and D. G. Truhlar, *Annu. Rev. Phys. Chem.,* **53,** 467 (2002). Quantum Mechanical Methods for Enzyme Kinetics.

73. J. Gao and M. A. Thompson, *Combined Quantum Mechanical and Molecular Mechanical Methods,* American Chemical Society, Washington, DC, 1998.

74. M. J. Field, P. A. Bash, and M. Karplus, *J. Comput. Chem.,* **11,** 700 (1990). A Combined Quantum Mechanical and Molecular Mechanical Potential for Molecular Dynamics Simulations.

75. J. Aqvist and A. Warshel, *Chem. Rev.,* **93,** 2523 (1993). Simulation of Enzyme Reactions Using Valence Bond and Other Hybrid Quantum-Classical Approaches.

76. J. Gao, P. Amara, C. Alhambra, and M. J. Field, *J. Phys. Chem. A,* **102,** 4714 (1998). A Generalized Hybrid Orbital (GHO) Method for the Treatment of Boundary Atoms in Combined QM/MM Calculations.

77. U. C. Singh and P. A. Kollman, *J. Comput. Chem.,* **7,** 718 (1986). A Combined *Ab Initio* Quantum Mechanical and Molecular Mechanical Method for Carrying out Simulations on Complex Molecular Systems: Applications to the $CH_3Cl + Cl^-$ Exchange and Gas Phase Protonation of Polyethers.

78. M. Eichinger, P. Tavan, J. Hutter, and M. Parrinello, *J. Chem. Phys.,* **110,** 10452 (1999). A Hybrid Method for Solutes in Complex Solvents: Density Functional Theory Combined with Empirical Force Fields.

79. Hypercube, Inc., Hyperchem *User's Manual, Computational Chemistry,* Hypercube Inc. Waterloo, Ontario, Canada, 1994.

80. A. Warshel and M. Levitt, *J. Molec. Biol.,* **103,** 227 (1976). Theoretical Studies of Enzymic Reactions: Dielectric, Electrostatic and Steric Stabilization of the Carbonium Ion in the Reaction of Lysozyme.

81. V. Thery, D. Rinaldi, and J.-L. Rivail, *J. Comput. Chem.,* **15,** 269 (1994). Quantum Mechanical Calculations on Very Large Molecular System: The Local Self-Consistent-Field Method.

82. G. Monard, M. Loos, V. Thery, K. Baka, and J.-L. Rivail, *Int. J. Quantum Chem.,* **58,** 153 (1996). Hybrid Classical Quantum Force Field for Modeling Very Large Molecules.

83. X. Assfeld and J.-L. Rivail, *Chem. Phys. Lett.,* **263,** 100 (1996). Quantum Chemical Computations on Parts of Large Molecules: The *Ab Initio* Local Self Consistent Field Method.

84. R. B. Murphy, D. M. Philipp, and R. A. Friesner, *Chem. Phys. Lett.,* **321,** 113 (2000). Frozen Orbital QM/MM Methods for Density Functional Theory.

85. P. Amara, M. J. Field, C. Alhambra, and J. Gao, *Theor. Chem. Acc.,* **104,** 336 (2000). The Generalized Hybrid Orbital Method for Combined Quantum Mechanical/Molecular Mechanical Calculations: Formulation and Tests of the Analytical Derivitives.

86. Y. Zhang, T. Lee, and W. Yang, *J. Chem. Phys.,* **110,** 46 (1999). A Pseudobond Approach to Combining Quantum Mechanical and Molecular Mechanical Methods.

87. I. Antes and W. Thiel, in *Combined Quantum Mechanical and Molecular Mechanical Methods,* J. Gao, and M. A. Thompson, Eds., ACS Symp. Series Vol. 712, ACS, Washington, DC, 1998, p. 50.

88. I. Antes and W. Thiel, *J. Phys. Chem.,* **103,** 9290 (1999). Adjusted Connection Atoms for Combined Quantum Mechanical and Molecular Mechanical Methods.

89. I. B. Bersuker, M. K. Leong, J. E. Boggs, and R. S. Pearlman, *Int. J. Quantum Chem.*, **63,** 1051 (1997). A Method of Combined Quantum Mechanical (QM) Molecular Mechanics (MM) Treatment of Large Polyatomic Systems with Charge Transfer between the QM and MM Fragments.

90. M. S. Gordon, M. A. Freitag, P. Bandyopadhyay, J. H. Jensen, V. Kairys, and W. J. Stevens, *J. Phys. Chem. A,* **105,** 293 (2001). The Effective Fragment Potential Method: A QM-Based MM Approach to Modeling Environmental Effects in Chemistry.

91. J. E. Adams and R. M. Stratt, *J. Chem. Phys.*, **93,** 1332 (1990). Instantaneous Normal Mode Analysis as a Probe of Cluster Dynamics.

92. W. H. Miller, W. L. Hase, and C. L. Darling, *J. Chem. Phys.*, **91,** 2863 (1989). A Simple Model for Correcting the Zero Point Energy Problem in Classical Trajectory Simulations of Polyatomic Molecules.

93. K. Bolton and W. L. Hase, in *Encyclopedia of Computational Chemistry,* N. L. Allinger, Ed., Wiley, New York, 1998, p. 1347.

94. S. K. Gray, D. W. Noid, and B. G. Sumpter, *J. Chem. Phys.,* **101,** 4062 (1994). Symplectic Integrators for Large Scale Molecular Dynamics Simulations: A Comparison of Several Explicit Methods.

95. L. Verlet, *Phys. Rev.,* **159,** 98 (1967). Computer "Experiments" on Classical Fluids. I. Thermaldynamical Properties of Lennard-Jones Molecules.

96. T. Helgaker, E. Uggerud, and H. Jensen, *Chem. Phys. Lett.,* **173,** 145 (1990). Integration of the Classical Equations of Motion on *Ab Initio* Molecular Potential Energy Surfaces Using Gradients and Hessians: Application to Translational Energy Release upon Fragmentation; E. Uggerud and T. Helgaker, *J. Am. Chem. Soc.,* **114,** 4265 (1992). Dynamics of the Reaction $CH_2OH^+ \rightarrow CHO^+ + H_2$. Translational Energy Release from *Ab Initio* Trajectory Calculations.

97. G. H. Peslherbe and W. L. Hase, *J. Chem. Phys.,* **104,** 9445 (1996). Comparison of Zero Point Energy Constrained and Quantum Anharmonic Rice-Ramsperger-Kassel-Marcus and Phase Space Theory Rate Constants For Al_3 Dissociation.

98. J. M. Millam, V. Bakken, W. Chen, W. L. Hase, and H. B. Schlegel, *J. Chem. Phys.,* **111,** 3800 (1999). *Ab Initio* Classical Trajectories on the Born–Oppenheimer Surface: Hessian-Based Integrators Using Fifth-Order Polynomial and Rational Function Fits.

99. V. Bakken, J. M. Millam, and H. B. Schlegel, *J. Chem. Phys.,* **111,** 8773 (1999). *Ab Initio* Classical Trajectories on the Born–Oppenheimer Surface: Updating Methods for Hessian-Based Integrators.

100. G. H. Peslherbe, H. Wang, and W. L. Hase, *Adv. Chem. Phys.,* Vol. 105, *Monte Carlo Methods in Chemical Physics,* D. M. Ferguson, J. I. Siepmann, and D. G. Truhlar, Eds., Wiley, New York, 1999, p. 171.

101. W. L. Hase, in *Encyclopedia of Computational Chemistry,* Vol. 1, N. L. Allinger, Ed., Wiley, New York, 1998, p. 402.

102. D. L. Bunker and W. L. Hase, *J. Chem. Phys.,* **54,** 4621 (1973). On Non-RRKM Unimolecular Kinetics: Molecules in General and CH_3NC in Particular.

103. M. C. Gutzwiller, *Chaos in Classical and Quantum Mechanics,* Springer-Verlag, New York, 1990.

104. D. L. Bunker, *J. Chem. Phys.,* **40,** 1946 (1964). Monte Carlo Calculations. IV. Further Studies of Unimolecular Dissociations.

105. T. Uzer and W. H. Miller, *Phys. Rep.,* **199,** 73 (1991). Theories of Intramolecular Vibrational Energy Transfer.

106. D. A. McQuarrie, *Statistical Thermodynamics,* Harper & Row, New York, 1973, p. 117.
107. J. M. Hammersley and D. C. Handscomb, *Monte Carlo Methods,* Metheun, London, 1964, p. 36.
108. H. W. Schranz, S. Nordholm, and G. Nyman, *J. Chem. Phys.,* **94,** 1487 (1991). An Efficient Microcanonical Sampling Procedure for Molecular Systems.
109. W. L. Hase and G. Buckcwski, *Chem. Phys. Lett.,* **74,** 284 (1980). Monte Carlo Sampling of a Microcanonical Ensemble of Classical Harmonic Oscillators.
110. S. Chapman and D. L. Bunker, *J. Chem. Phys.,* **62,** 2890 (1975). An Exploratory Study of Reactant Vibrational Effects in $CH_3 + H_2$ and Its Isotopic Variants.
111. W. L. Hase, D. M. Ludlow, R. J. Wolf, and T. Schlick, *J. Phys. Chem.,* **85,** 958 (1981). Translational and Vibrational Energy Dependence of the Cross Section for $H + C_2H_4 \rightarrow C_2H_5{}^*$.
112. D. L. Bunker and E. A. Goring-Simpson, *Faraday Discuss. Chem. Soc.,* **55,** 93 (1973).
113. E. K. C. Lee, *Acc. Chem. Res.,* **10,** 319 (1977). Laser Photochemistry of Selected Vibronic and Rotational States.
114. D. M. Burland and G. W. Robinson, *J. Chem. Phys.,* **51,** 4548 (1969). Calculated Radiationless Tranistion Rates for Benzene and Deuterobenzene.
115. C. S. Sloane and W. L. Hase, *J. Chem. Phys.,* **66,** 1523 (1977). On the Dynamics of State Selected Unimolecular Reactions: Chloroacetylene Dissociation and Predissociation.
116. M. S. Child and L. Halonen, *Adv. Chem. Phys.,* **57,** 1 (1984). Overtone Frequencies and Intensities in the Local Mode Picture.
117. D.-H. Lu and W. L. Hase, *J. Phys. Chem.,* **92,** 3217 (1988). Classical Calculation of Benzene Overtone Spectra.
118. R. E. Wyatt and C. Iung, *J. Chem. Phys.,* **98,** 5191 (1993). Quantum Dynamics of Overtone Relaxation in Benzene. III. Spectra and Dynamics for Relaxation from $CH(v = 3)$.
119. M. Topaler and N. Makri, *J. Chem. Phys.,* **97,** 9001 (1992). Multidimensional Path Integral Calculations with Quasiadiabatic Propagators: Quantum Dynamics of Vibrational Relaxation in Linear Hydrocarbon Chains.
120. D. W. Noid, M. L. Koszykowski, and R. A. Marcus, *Ann. Rev. Phys. Chem.,* **32,** 267 (1981). Quasi-Periodic and Stochastic-Behavior in Molecules.
121. L. Pauling and E. B. Wilson Jr., *Introduction to Quantum Mechanics,* McGraw-Hill, New York, 1935, p. 271; L. D. Landau and E. M. Lifshitz, *Quantum Mechanics,* 2nd ed., Addison-Wesley, New York, 1965, p. 71.
122. R. D. Levine and R. B. Bernstein, *Molecular Reaction Dynamics and Chemical Reactivity,* Oxford Univ. Press, New York, 1987.
123. E. B. Wilson Jr., J. C. Decius, and P. C. Cross, *Molecular Vibrations,* McGraw-Hill, New York, 1955, p. 285.
124. J. M. Bowman, A. Kupperman, and G. C. Schatz, *Chem. Phys. Lett.,* **19,** 21 (1973). Quantum Initial Conditions in Quasi-Classical Trajectory Calculations.
125. W. H. Miller, *Acc. Chem. Res.,* **9,** 306 (1976). Importance of Nonseparability in Quantum Mechanical Transition State Theory.
126. D. G. Truhlar and B. C. Garrett, *Acc. Chem. Res.,* **13,** 440 (1980). Variational Transition State Theory.
127. J. C. Keck, *Adv. Chem. Phys.,* **13,** 85 (1967). Variational Theory of Reaction Rates; J. B. Anderson, *J. Chem. Phys.,* **58,** 4684 (1973). Statistical Theories of Chemical Reactions. Distributions in the Transition Region.
128. W. H. Miller, *J. Chem. Phys.,* **61,** 1823 (1974). Quantum Mechanical Transition State Theory and a New Semiclassical Model for Reaction Rate Constants.
129. D. G. Truhlar, A. D. Isaacson, and B. C. Garrett, in *Theory of Chemical Reaction Dynamics,* Vol. 4, M. Baer, Ed., CRC Press, Boca Raton, Fl., 1985, p. 65; D. G. Truhlar and B. C. Garrett, *Faraday Discuss. Chem. Soc.,* **84,** 464 (1987).

130. T. Baer and W. L. Hase, *Unimolecular Reaction Dynamics. Theory and Experiment*, Oxford Univ. Press, New York, 1996.

131. W. L. Hase, in *Encyclopedia of Chemical Physics and Physical Chemistry*, Vol. 1, *Fundamentals*, J. H. Moore and N. D. Spencer, Eds., Institute of Physics, Philadelphia, 2001, p. 865.

132. C. Doubleday, Jr., K. Bolton, G. H. Peslherbe, and W. L. Hase, *J. Am. Chem. Soc.*, **118,** 9922 (1996). Direct Dynamics Simulation of the Lifetime of Trimethylene.

133. A. H. Zewail, *Science,* **242,** 1645 (1988). Laser Femtochemistry.

134. D. E. Manolopoulos, K. Stark, H.-J. Werner, D. W. Arnold, S. E. Bradforth, and D. M. Neumark, *Science,* **262,** 1852 (1993). The Transition State of the $F + H_2$ Reaction.

135. J. M. Haile, *Molecular Dynamics Simulation,* Wiley, New York, 1992.

136. D. Frenkel and B. Smit, *Understanding Molecular Simulation,* Academic Press, New York, 1996.

137. M. P. Allen and D. J. Tildesley, *Computer Simulation of Liquids,* Oxford Univ. Press, New York, 1987.

138. M. D. Perry and L. M. Raff, *J. Phys. Chem.,* **98,** 4375 (1994). Theoretical Studies of Elementary Chemisorption Reactions on an Activated Diamond Ledge Surface.

139. K. Song, P. de Sainte Claire, W. L. Hase, and K. C. Hass, *Phys. Rev. B,* **52,** 2949 (1995). Comparison of Molecular Dynamics and Variational Transition State Theory Calculations of the Rate Constant for H-atom Association with the Diamond {111} Surface.

140. T.-Y. Yan and W. L. Hase, *J. Phys. Chem. B,* **106,** 8029 (2002). Comparisons of Models for Simulating Energy Transfer in Ne-Atom Collisions with an Alkyl Thiolate Self-Assembled Monlayer.

141. O. Meroueh and W. L. Hase, *Phys. Chem. Chem. Phys.,* **3,** 2306 (2001). Effect of Surface Stiffness on the Efficiency of Surface-Induced Dissociation.

142. *Advances in Classical Trajectory Methods,* Vol. 3, *Comparisons of Classical and Quantum Dynamics,* W. L. Hase, Ed., JAI Press, London, 1998.

143. F. J. Aoiz, L. Bañares, and V. J. Herrero in Ref. 142, p. 121.

144. K. N. Swamy and W. L. Hase, *J. Phys. Chem.,* **87,** 4715 (1983). A Quasiclassical Trajectory Calculation of the $H + C_2H_4 \rightarrow C_2H_5$ Rate Constant.

145. R. A. Marcus and M. E. Coltrin, *J. Chem. Phys.,* **67,** 2609 (1977). A New Tunneling Path for Reactions Such as $H + H_2 \rightarrow H_2 + H$.

146. D. G. Truhlar, A. D. Isaacson, R. T. Skodje, and B. C. Garrett, *J. Phys. Chem.,* **86,** 2252 (1982). Incorporation of Quantum Effects in Generalized-Transition-State Theory.

147. G. C. Schatz, *J. Chem. Phys.,* **79,** 5386 (1983). The Origin of Cross Section Threshold in $H + H_2$: Why Quantum Dynamics Appears to Be More Vibrationally Adiabatic than Classical Dynamics.

148. D.-H. Lu and W. L. Hase, *Chem. Phys. Lett.,* **142,** 187 (1987). Quasiclassical Trajectory Study of the n=3 Overtone State of Benzene.

149. W. L. Hase and D. G. Buckowski, *J. Comput. Chem.,* **3,** 335 (1982). Dynamics of Ethyl Radical Decomposition. 2. Applicability of Classical Mechanics to Large-Molecule Unimolecular Reaction Dynamics.

150. G. H. Peslherbe, H. Wang, and W. L. Hase, *J. Chem. Phys.,* **102,** 5626 (1995). Unimolecular Dynamics of Cl^----CH_3Cl Intermolecular Complexes Formed by $Cl^- + CH_3Cl$ Cl Association.

151. D.-H. Lu and W. L. Hase, *J. Chem. Phys.,* **91,** 7490 (1989). Classical Mechanics of Intramolecular Vibrational Energy Flow in Benzene. V. Effect of Zero-Point Energy Motion.

152. C. Li, P. Ross, J. E. Szulejko, and T. B. McMahon, *J. Am. Chem. Soc.,* **118,** 9360 (1996). High-Pressure Mass Spectrometric Investigations of the Potential Energy Surfaces of Gas-Phase S_N2 Reactions.

153. R. B. Shirts and W. P. Reinhardt, *J. Chem. Phys.,* **77,** 5204 (1982). Approximate Constant of Motion for Classical Chaotic Viabrational Dynamics. Vague Tori, Semiclassical Quantitization, and Classical Intramolecular Energy Flow.

154. G. Z. Ezra, in *Advances in Classical Trajectory Methods,* Vol. 3, *Comparisons of Classical and Quantum Dynamics,* W. L. Hase, Ed., JAI, Press, London, 1998. p. 35.

155. R. E. Wyatt, C. Iung, and L. Leforestier, *J. Chem. Phys.,* **97,** 3477 (1992). Quantum Dynamics of Overtone Relaxation in Benzene. II. 16-Mode Model for Relaxation from CH($v = 3$).

156. R. H. Page, Y. R. Shen, and Y. T. Lee, *Phys. Rev. Lett.,* **59,** 1293 (1987). Highly Resolve Spectra of Local Modes of Benzene.

157. W. L. Hase and K. C. Bhalla, *J. Chem. Phys.,* **75,** 2807 (1981). A Classical Trajectory Study of the $F + C_2H_4 \rightarrow [C_2H_4F] \rightarrow H + C_2H_3F$ Reaction.

158. K. Bolton, H. B. Schlegel, W. L. Hase, and K. Song, *Phys. Chem. Chem. Phys.,* **1,** 999 (1999). An Ab Initio Quasiclassical Direct Dynamics Investigation of the $F + C_2H_4 \rightarrow C_2H_3F + H$ Product Energy Distributions.

159. S. L. Debbert, B. K. Carpenter, D. A. Hrovat, and W. T. Borden, *J Am. Chem. Soc.,* **124,** 7896 (2002). The Iconoclastic Dynamics of the 1,2,6-Heptatriene Rearrangement.

160. J. F. Arenas, I. López-Tocón, J. C. Otero, and J. Soto, *J. Am. Chem. Soc.,* **124,** 1728 (2002). Carbene Formation in Its Lower Singlet State from Photoexcited 3*H*-Diazirine or Diazomethane. A Combined CASPT2 and *Ab Initio* Direct Dynamics Trajectory Study.

161. C. Doubleday, Jr., G. Li, and W. L. Hase, *Phys. Chem. Chem. Phys.,* **4,** 304 (2002). Dynamics of the Biradical Mediating Vinylcyclopropane–Cyclopentene Rearrangement.

162. C. Doubleday, Jr., *J. Phys. Chem. A.,* **105,** 63333 (2001). Mechanism of the Vinylcyclopropane-Cyclopentene Rearrangement Studied by Quasiclassical Direct Dynamics.

163. E. Martínez-Núñez, C. M. Estévez, J. R. Flores, and S. A. Vázquez, *Chem. Phys. Lett.,* **348,** 81 (2001). Product Energy Distributions for the Four-Center HF Elimination from 1,1-Difluoroethylene. A Direct Dynamics Study.

164. E. Martínez-Núñez, J. M. C. Marques, and S. A. Vázquez, *J. Chem. Phys.,* **115,** 7872 (2001). A Direct Dynamics Study of the H_2 Elimination from 2,5-Dihydrofuran.

165. D. J. Mann and W. L. Hase, *Phys. Chem. Chem. Phys.,* **3,** 4376 (2001). Direct Dynamics Simulations of the Oxidation of a Single Wall Carbon Nanotube.

166. S. Carter, J. M. Bowman, and B. J. Braams, *Chem. Phys. Lett.,* **342,** 636 (2001). On Using Low-Order Hermite Interpolation in 'Direct Dynamics' Calculations of Vibrational Energies Using the Code 'MULTIMODE'.

167. T. P. Marcy, R. R. Díaz, D. Heard, S. R. Leone, L. B. Harding, and S. J. Klippenstein, *J. Phys. Chem.,* **105,** 8361 (2001). Theoretical and Experimental Investigation of the Dynamics of the Production of CO from the $CH_3 + O$ and $CD_3 + O$ Reactions.

168. E. Martínez-Núñez, and S. A. Vázquez, *Chem. Phys. Lett.,* **332,** 583 (2000). Three-Center vs. Four-Center HF Elimination from Vinyl Fluoride: A Direct Dynamics Study.

169. H. Tachikawa, *J. Phys. Chem. A,* **105,** 1260 (2001). Collision Energy Dependence on the Microsolvated S_N2 Reaction of $F^-(H_2O)$ with CH_3Cl: A Full Dimensional *Ab Initio* Direct Dynamics Study.

170. H. Tachikawa, *Phys. Chem. Chem. Phys.,* **2,** 4702 (2000). Full Dimensional *Ab Initio* Direct Dynamics Calculations of the Ionization of H_2 Clusters $(H_2)_n$ ($n = 3$, 4 and 6).

171. H. Tachikawa, *Phys. Chem. Chem. Phys.,* **2,** 4327 (2000). Full Dimensional *Ab-Initio* Dynamics Calculations of Electron Capture Processes by the H_3O^+ Ion.

172. E. Martínez-Núñez, A. Peña-Gallego, R. Rodríguez-Fernández, and S. A. Vázquez, *Chem. Phys. Lett.,* **324,** 88 (2000). Direct Dynamics Simulation of the Methanethiol Cation Decomposition.

173. Y. Ishikawa, Y. Gong, and B. R. Weiner, *Phys. Chem. Chem. Phys.,* **2,** 869 (2000). Gaussian-2 Theoretical and Direct *Ab Initio* Molecular Dynamics Study of the Reaction of $O(^3P)$ with Thiirane, $O(^3P)+C_2H_4S(^1A_1) \rightarrow SO(^3\Sigma^-)+C_2H_4(^1A_g)$.

174. J. N. Harvey and M. Aschi, *Phys. Chem. Chem. Phys.,* **1,** 5555 (1999). Spin-Forbidden Dehydrogenation of Methoxy Cation: A Statistical View.

175. A. Shimizu, H. Tachikawa, and M. Inagaki, *Solid State Ionics,* **127,** 157 (2000). Dynamics of Hydrogen and Muonium Atoms Trapped in Diamond Crystal.

176. K. Bolton, W. L. Hase, and C. Doubleday, Jr., *J. Phys. Chem. B,* **103,** 3691 (1999). A QM/MM Direct Dynamics Trajectory Investigation of Trimethylene Decomposition in an Argon Bath.

177. F. Eckert and H. Werner, *Chem. Phys. Lett.,* **302,** 208 (1999). Local Interpolation of *Ab Initio* Potential Energy Surfaces for Direct Dynamics Studies of Chemical Reactions.

178. H. Tachikawa and M. Igarashi, *Chem. Phys. Lett.,* **303,** 81 (1999). A Direct *Ab Initio* Dynamics Study on a Gas Phase S_N2 Reaction $F^- + CH_3Cl \rightarrow CH_3F + Cl^-$: Dynamics of Near-Collinear Collision.

179. J. A. Berson, L. D. Pederson, and B. K. Carpenter, *J. Am. Chem. Soc.,* **98,** 122 (1976). Thermal Stereomutation of Cyclopropanes.

180. J. E. Baldwin, S. J. Cianciosi, D. A. Glenar, G. J. Hoffman, I. Wu, and D. K. Lewis, *J. Am. Chem. Soc.,* **114** (1992). Kinetics of Thermal Geometric Isomerizations of Three Sets of Isotopically Labeled Cyclopropanes Followed by Tunable Diode Laser Spectroscopy.

181. C. Doubleday, Jr., *J. Phys. Chem.,* **100,** 3520 (1996). Lifetime of Trimethylene Calculated by Variational Unimolecular Rate Theory.

182. C. Doubleday, Jr., K. Bolton, G. H. Peslherbe, and W. L. Hase, *J. Am. Chem. Soc.,* **118,** 9992 (1996). Direct Dynamics Simulation of the Lifetime of Trimetylene.

183. C. Doubleday, Jr., K. Bolton, and W. L. Hase, *J. Am. Chem. Soc.,* **119,** 5251 (1997). Direct Dynamics Simulation of the Stereomutation of Cyclopropane; C. Doubleday, Jr., K. Bolton, and W. L. Hase, *J. Phys. Chem. A,* **102,** 3648 (1998). Direct Dynamics Quasiclassical Trajectory Study of the Thermal Stereomutations of Cyclopropane.

184. K. Bolton, W. L. Hase, and C. Doubleday, Jr., *Ber. Bunsen-Ges. Phys. Chem.,* **101,** 414 (1997). Isomerisation of Deuterated Cyclopropanes—the Possibility for Stereochemical Control.

185. D. A. Hrovat, S. Fang, W. T. Borden, and B. K. Carpenter, *J. Am. Chem. Soc.,* **119,** 5253 (1997). Investigation of Cyclopropane Stereomutation by Quasiclassical Trajectories on an Analytical Potential Energy Surface.

186. W. L. Hase, *Science,* **266,** 998 (1994). Simulations of Gas-Phase Chemical Reactions. Applications to S_N2 Nucleophilic Substitution.

187. M. L. Chabinyc, S. L. Craig, C. K. Regan, and J. I. Brauman, *Science,* **279,** 1882 (1998). Gas-Phase Ionic Reactions: Dynamics and Mechanism of Nucleophilic Displacement.

188. S. S. Shaik, H. B. Schlegel, and S. Wolfe, *Theoretical Aspects of Physical Organic Chemistry. The S_N2 Mechanism,* Wiley, New York, 1992.

189. C. R. Moylan and J. I. Brauman, in *Advances in Classical Trajectory Methods,* Vol. 2, W. L. Hase, Ed., JAI Press, New York, 1994, p. 95.

190. W. L. Hase, H. Wang, and G. H. Peslherbe, in *Advances in Gas-Phase Ion Chemistry,* Vol. 3, N. G. Adams and L. M. Babcock, Eds., JAI Press, New York, 1998, p. 125.

191. A. A. Viggiano, R. A. Morris, J. S. Paschkewitz and J. F. Pauson, *J. Am. Chem. Soc.,* **114,** 10477 (1992). Kinetics of the Gas-Phase Reactions of Chloride Anion, Cl^- with CH_3Br and CD_3Br: Experimental Evidence for Nonstatistical Behavior?

192. V. F. DeTuri, P. A. Hintz, and K. M. Ervin, *J. Phys. Chem. A,* **101,** 5969 (1997). Translational Activation of the S_N2 Nucleophilic Displacement Reactions $Cl^- + CH_3Cl\ (CD_3Cl) \rightarrow ClCH_3\ (ClCD_3) + Cl^-$: A Guided Ion Beam Study.

193. D. S. Tonner and T. B. McMahon, *J. Am. Chem. Soc.,* **122,** 8783 (2000). Non-Statistical Effects in the Gas Phase S_N2 Reaction.

194. S. T. Graul and M. T. Bowers, *J. Am. Chem. Soc.,* **116,** 3875 (1994). Vibrational Excitation in Products of Nucleophilic Substitution: The Dissociation of Metastable $X^-(CH_3Y)$ in the Gas Phase.

195. S. Kato, G. E. Davico, H. S. Lee, C. H. Depuy, and V. M. Bierbaum, *Int. J. Mass Spectrom.,* **210,** 223 (2001). Deuterium Kinetic Isotope Effects in Gas Phase S_N2 Reactions.

196. H. Wang and W. L. Hase, *J. Am. Chem. Soc.,* **119,** 3093 (1997). Kinetics of $F^- + CH_3Cl$ S_N2 Nucleophilic Substitution.

197. S. Schmatz and D. C. Clary, *J. Chem. Phys.,* **110,** 9483 (1999). Quantum Scattering Calculations on the S_N2 Reaction $Cl^- + CH_3Br \rightarrow ClCH_3 + Br^-$.

198. S. Schmatz, P. Botschwina, J. Hauschildt, and R. Schinke, *J. Chem. Phys.,* **114,** 5233 (2001). Symmetry Specificity in the Unimolecular Decay of the $Cl^- \cdots CH_3Cl$ Complex: Two-Mode Quantum Calculations on a Coupled-Cluster [CCSD(T)] Potential Energy Surface.

199. S. C. Tucker and D. G. Truhlar, *J. Phys. Chem.,* **93,** 8138 (1989). Ab Initio Calculations of the Transition-State Geometry and Vibrational Frequencies of the S_N2 Reaction of Chloride with Chloromethane.

200. L. Sun, W. L. Hase, and K. Song, *J. Am. Chem. Soc.,* **123,** 5753 (2001). Trajectory Studies of S_N2 Nucleophilic Substitution. 8. Central Barrier Dynamics for Gas Phase $Cl^- + CH_3Cl$.

201. P. Botschwina, *Theor. Chem. Acc.,* **99,** 436 (1998). The Saddle Point of the Nucleophilic Substitution Reaction $Cl^- + CH_3Cl$: Results of Large-Scale Coupled Cluster Calculations.

202. Frisch, M. J.; Trucks, G. W.; Schlegel, H. B.; Scuseria, G. E.; Robb, M. A.; Cheeseman, J. R.; Zakrzewski, V. G.; Montgomery, J. A., Jr.; Stratmann, R. E.; Burant, J. C.; Dapprich, S.; Millam, J. M.; Daniels, A. D.; Kudin, K. N.; Strain, M. C.; Farkas, O.; Tomasi, J.; Barone, V.; Cossi, M.; Cammi, R.; Mennucci, B.; Pomelli, C.; Adamo, C.; Clifford, S.; Ochterski, J.; Petersson, G. A.; Ayala, P. Y.; Cui, Q.; Morokuma, K.; Malick, D. K.; Rabuck, A. D.; Raghavachari, K.; Foresman, J. B.; Cioslowski, J.; Ortiz, J. V.; Stefanov, B. B.; Liu, G.; Liashenko, A.; Piskorz, P.; Komaromi, I.; Gomperts, R.; Martin, R. L.; Fox, D. J.; Keither, T.; Al-Laham, M. A.; Peng, C. Y.; Nanayakkara, A.; Gonzalez, C.; Challacoombe, M.; Gille, P. M. W.; Johnson, B.; Chen, W.; Wong, M. W.; Andres, J. L.; Gonzalez, C.; Head-Gordon, M.; Replogle, E. S.; Pople, J. A., *Gaussian98,* Gaussian, Inc.: Pittsburgh, PA, 1998.

203. Y. J. Cho, S. R. Vande Linde, L. Zhu, and W. L. Hase, *J. Chem. Phys.,* **96,** 8275 (1992). Trajectory Studies of S_N2 Nucleophilic Substitution. II. Nonstatistical Central Barrier Recrossing in the $Cl^- + CH_3Cl$ System.

204. J. M. Gonzales, R. S. Cox III, S. T. Brown, W. D. Allen, and H. F. Schaefer III, *J. Phys. Chem. A,* **105,** 11327 (2001). Assessment of Density Functional Theory for Model S_N2 Reactions: $CH_3X + F^-$ (X = F, Cl, CN, OH, SH, NH_2, PH_2).

205. J. W. Larson and T. B. McMahon, *J. Am. Chem. Soc.,* **105,** 2944 (1983). Strong Hydrogen Bonding in Gas-Phase Anions. An Ion Cyclotron Resonance Determination of Fluoride Binding Energetics to Broensted Acids from Gas-Phase Fluoride Exchange Equilibrium Measurements.

206. L. Sun, K. Song, and W. L. Hase, *Science,* **296,** 875 (2002). A S_N2 Reaction that Avoids Its Deep Potential Energy Minimum.

207. M. A. Mabud, M. J. Gekrey, and R. G. Cooks, *Int. J. Mass. Spectrom. Ion Process.,* **67,** 285 (1985). Surface-Induced Dissociation of Molecular-Ions.

208. J. Laskin, E. Denisov, and J. Futrell, *J. Phys. Chem. B,* **105,** 1895 (2001). Comparative Study of Collision-Induced and Surface-Induced Dissociation. 2. Fragmentation of Small Alanine-Containing Peptides in FT-ICR MS.

209. R. A. J. O'Hair, P. S. Broughton, M. L. Styles, B. T. Frink, and C. M. Hadad, *J. Am. Mass. Spectrom., Soc.* **11,** 687 (2000). The Fragmentation Pathways of Protonated Glycine: A Computational Study.

210. J. S. Klassen and P. Kebarle, *J. Am. Chem. Soc.,* **119,** 6552 (1997). Collision-Induced Dissociation Threshold Energies of Protonated Glycine, Glycinamide, and Some Small Related Peptides and Peptide Amino Amides.

211. O. Meroueh, Y. Wang, and W. L. Hase, *J. Phys. Chem. A,* **106,** 9983 (2002). Direct Dynamics Simulations of Collision- and Surface-Induced Dissociation of N-Protonated Glycine. Shattering Fragmentation.

212. B. Balta, M. Basma, V. Aviyente, C. Zhu, and C. Lifshitz, *Int. J. Mass Spectrom.,* **201,** 69 (2000). Structures and Reactivity of Gaseous Glycine and Its Derivatives.

213. K. C. Hass, M. A. Tamor, T. R. Anthony, and W. F. Banholzer, *Phys. Rev. B,* **45,** 7171 (1992). Lattice-Dynamics and Raman-Spectra of Isotopically Mixed Diamond.

214. O. Meroueh and W. L. Hase, *J. Am. Chem. Soc.,* **124,** 1524 (2002). Dynamics of Energy Transfer in Peptide-Surface Collisions.

215. J. C. Tully and P. K. Preston, *J. Chem. Phys.,* **55,** 562 (1971). Trajectory Surface Hopping Approach to Nonadiabatic Molecular Collisions.

216. J. C. Tully, in *Dynamics of Molecular Collisions,* Part B, W. H. Miller, Ed., Plenum Press, New York, 1975, p. 217.

217. J. C. Tully, *J. Chem. Phys.,* **93,** 1061 (1990). Molecular Dynamics with Electron Transitions.

218. N. C. Blais and D. G. Truhlar, *J. Chem. Phys.,* **79,** 1334 (1983). Trajectory Surface Hopping Study of $Na(3p\ ^2P) + H_2 \rightarrow Na\ (3s\ ^2S) + H_2(v',j',\theta)$

219. M. D. Hack and D. G. Truhlar, *J. Phys. Chem. A,* **104,** 7917, (2000). Nonadiabatic Trajectories at an Exhibition.

220. M. Ben-Nun and T. J. Martínez, *Adv. Chem. Phys.,* **121,** 439 (2002). *Ab Initio* Quantum Molecular Dynamics.

221. M. Ben-Nun, J. Quenneville, and T. J. Martínez, *J. Phys. Chem.,* **104,** 5161 (2000). *Ab Initio* Multiple Spawning: Photochemistry from First Principles Quantum Molecular Dynamics.

222. M. Ben-Nun and T. J. Martínez, *J. Chem. Phys.,* **112,** 6113 (1999). A Multiple Spawning Approach to Tunneling Dynamics.

223. A. E. Cárdenas, R. Krems, and R. D. Coalson, *J. Phys. Chem. A,* **103,** 9469 (1999). Semiclassical Wave Packet Dynamics with Electronic Structure Computed on the Fly: Application to Photophysics of Electronic Excited States in Condensed Phase.

224. E. J. Heller, *Acc. Chem. Res.,* **14,** 368 (1981). The Semiclassical Way to Molecular Spectroscopy.

225. E. J. Heller, *J. Chem. Phys.,* **62,** 1544 (1975). Time Dependent Approach to Semiclassical Dynamics.

226. E. J. Heller, *J. Chem. Phys.,* **75,** 2923 (1981). Frozen Gaussian: A Very Simple Semiclassical Approximation.

227. E. Deumens, A. Diz, R. Longo, and Y. Öhrn, *Rev. Mod. Phys.,* **66,** 917 (1994). Time-Dependent Theoretical Treatments of the Dynamics of Electrons and Nuclei in Molecular Systems.

228. E. Deumens and Y. Öhrn, *J. Chem. Soc. Faraday Trans.,* **93,** 919 (1997). Wavefunction Phase Space. An Approach to the Dynamics of Molecular Systems.

CHAPTER 4

The Poisson–Boltzmann Equation

Gene Lamm

Department of Chemistry, University of Louisville, Louisville, Kentucky 40292

INTRODUCTION

State of the Field

The classic papers of Gouy[1,2] and Debye and Hückel[3–5] dealt with the statistical mechanics of relatively simple models of strong electrolyte solutions: the former papers concerned the distribution of point ions near a charged planar surface, which is now referred to as the *electric double layer*, while the latter dealt with the distribution of an isotropic and neutral system of charged hard spheres. Both studies were instrumental in providing convincing proof of the validity of Arrhenius' theory of the existence of completely dissociated ions in solution proposed some 30 years earlier, despite Arrhenius' own beliefs.[6] Later improvements and reformulations[7–11] by Chapman, Stern, Grahame, Onsager and Kirkwood increased the significance and usefulness of their ideas. This however does not explain the increasing fascination with the Poisson–Boltzmann equation since the mid/late 1920s, with an almost exponential surge of interest since the early 1990s. This appeal can be attributed to three things: the succinct analytical and physical description on which the method is based, the ease with which it may be extended, both analytically and numerically, to more complex systems, and, most importantly, the breadth and depth of the phenomena to which the equation applies.

Most applications of the Poisson–Boltzmann (PB) equation can be placed into one of two areas: investigations of the chemical physics of ionic or

Reviews in Computational Chemistry, Volume 19
edited by Kenny B. Lipkowitz, Raima Larter, and Thomas R. Cundari
ISBN 0-471-23585-7

colloidal solutions and calculations of the electrostatic energy of large biomolecules. Those involving the former are concerned with the statistical mechanical and thermodynamic description of polyelectrolyte solutions with recent biophysical applications involving, for example, the estimation of the persistence length of DNA, the determination of forces between membranes, and the calculation of the electrostatic potential near charge-regulated micelles and inside cylindrical micropores. A number of articles reviewing this field have appeared over the years.[12–24] For the most part these reviews describe advances in our understanding of electrolyte and colloidal solutions and the electric double layer, with the Poisson–Boltzmann equation serving as a benchmark against which other theories are measured.

When a system becomes too complicated for analytical techniques to provide useful solutions, numerical procedures are invoked. For example, researchers in the second area use general-purpose PB programs to map out the electrostatic potential in and around large protein, membrane and nucleic acid assemblies. This potential map aids our understanding of biomolecular function by predicting free energy and pK_a changes as a function of macromolecular and environmental changes.[25–35] To be sure, large-scale applications of the PB equation first appeared around the early 1980s, but, with a few notable exceptions, the computational enhancements offered by general-purpose programs available today are relatively modest as most algorithms use a brute-force approach to the problem. Recently, however, this has begun to change. Of significance is the extension of PB theory beyond the relatively simple calculations of ion concentrations to include the prediction of protein pK_a values and solvation energies as well as new methods using Poisson–Boltzmann data as input into more detailed molecular dynamics or quantum-mechanical calculations. Still, the two important areas of research mentioned above operate somewhat independently of one another.

The number of publications in which the PB equation has been used has climbed steadily. As seen in Figure 1, the increase from 1970 to 1990 is modest but clear, however a sudden, almost exponential jump occurred in 1990 that now appears to be leveling off. This leap in interest in the PB equation coincides with significant advances in three initially unrelated areas: computers, biotechnology, and renewed studies of basic colloidal systems. Fast and cheap computational power prompted the development of general-purpose programs for applying the PB equation to biological complexes. The need for these programs was driven by the almost assembly-line determination of high-resolution structures of biomolecules whose functions could be explained to a large extent by their electrostatic nature. Today, with the mapping of the human and other genomes proceeding apace and with the proteomics era beginning, the supply of polyelectrolyte systems in need of systematic studies appears endless. Computers have also aided the study of simpler electrolyte systems with Monte Carlo and molecular dynamics simulations providing baseline calculations to test the accuracy of standard Poisson–Boltzmann approaches, highlighting the need for improvements.

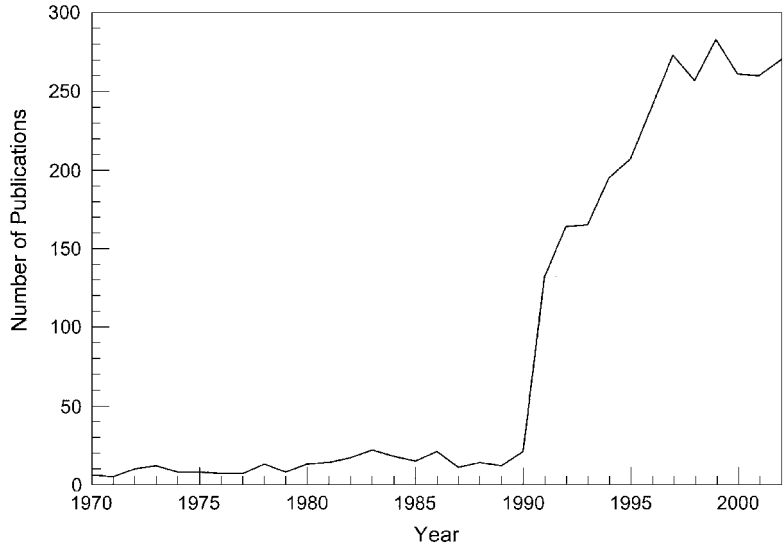

Figure 1 Approximate number of publications per year in which the Gouy–Chapman, Debye–Hückel, or Poisson–Boltzmann equation was used.

While this tutorial primarily emphasizes application of the PB equation to systems of biophysical interest such as proteins, nucleic acids, and membranes, its foundation and development are firmly entrenched in the study of colloidal solutions.[36] Two additional areas in which the PB equation plays major roles and that have purposely been neglected from this study are dusty plasmas[37] and Schottky junctions,[38] contributors of about two dozen articles per year to the field (and that have not been included in Fig. 1). The appearance of an article such as this one usually indicates that a field has reached a certain level of maturity, such as, for example, the area of computational quantum mechanics. However, the increase in the number of publications related to the basic tenets of the PB equation and the independent directions in which different areas are moving suggest that this is a field with significant growth ahead. Somewhat surprisingly, despite the large number of publications relating the analytical solution of the PB equation to physical properties of colloidal and biological systems, no elementary survey has yet appeared that brings together and discusses the wide range of these results. The present tutorial attempts to remedy this situation.

Overview of the Chapter

This review is organized into four parts. We begin with a brief history of the Poisson–Boltzmann equation followed by an abbreviated derivation. In the second part the PB equation is applied to several model systems whose

symmetry allows reduction to a single dimension and for which exact or approximate analytical solutions can be found. This rather extensive, and by far largest, part allows us to bring together many examples for planar and curved systems that are scattered throughout the literature with the aim of demonstrating a coherence of purpose and application within the field. This is aided by the introduction of a simple method, based on the "nonlinear Debye–Hückel" solution, by which approximate potentials for planar and curved one- and two-particle systems may be found. Numerous figures are given in this part of the chapter to illustrate and compare the analytical results among different approximations and different systems. While recent applications of PB theory to large biophysical systems tend to involve the ready application of one of the general-purpose programs, more physical insight can often be gained by working through simplified one-dimensional PB models beforehand, and it is usually the case that numerical methods must be used where limitations of analytical approaches become unduly noticeable. It is also true that the one-dimensional PB equation gives a remarkably accurate description of a wide range of experimental data for many colloidal and biological systems. A major reason for the success of the PB approach is the ease with which the electrolyte properties of planar membranes, cylindrical DNA models and spherical micelles may be calculated, analytically as well as numerically. It is hoped that the results presented here will be of use to anyone who desires a quick estimation of the electrostatic effects of charged surfaces immersed in an electrolyte. Those readers with a more immediate interest in large-scale numerical calculations are encouraged to skip ahead to the third part of this tutorial after reviewing the discussion of the Gouy–Chapman model.

In the third part of this chapter we review numerical methods commonly used in applying the PB equation to more complicated systems than simpler one-dimensional representations. Because two major articles covering most aspects of the numerical solution of the PB equation have recently appeared,[34,39] only an overview of the numerical work is presented, emphasizing those aspects of primary importance or those that have been given less coverage elsewhere. Included is a brief description of finite-difference/finite-element PB algorithms similar to those used in popular programs such as UHBD,[34,40,41] DelPhi,[42,43] MEAD,[29] and APBS;[44-47] alternative approaches such as the boundary element method are also discussed. An introduction to some of the more popular large-scale applications of the PB method is presented, which includes (1) the calculation of the binding energy of two molecules, (2) the calculation of the free energy of macromolecular solvation, (3) the determination of protein pK_a values, and (4) mixed-method procedures in which the PB solution is used in conjunction with other techniques, such as Monte Carlo, molecular dynamics, and Brownian dynamics, to enhance and extend its usefulness.

The fourth and final part introduces topics that are slightly more advanced than those considered in the first two parts. It allows the avid

student or more mature reader to view the field in a broader context. We begin with a discussion of the major assumptions implicit in using the standard Poisson–Boltzmann equation and then elaborate on two of the most commonly used approximations: assumption of a bulk electrolyte and the linearization of the PB equation. This is followed by brief descriptions of several of the more popular alternative approaches including modified PB equations, counterion condensation theory, and the Monte Carlo method. The review concludes with a few final remarks as well as a table summarizing the analytical solutions presented in the second part.

In keeping with the intent of this series, this tutorial is both an introduction to the field as well as a review of past work. In this regard the references, which are quite numerous, fall into three categories. The first of these are textbooks which generally provide only the briefest of overviews of the Poisson–Boltzmann equation, partly because many of the useful results consist of snippets of information here and there and partly because much of this material has only recently (as of 2003) been published. If several textbooks are cited simultaneously it is usually to indicate that any reference will suffice as most presentations follow pretty much the same path, with more specialized texts the exceptions.[36,48,49] The second category of references contains those that appear during a derivation. For these the cited works serve either as the basis for the development, offer an alternative method of approach, or provide an important clarifying point. Finally, we have those references citing work that goes beyond the discussion presented here by way of either complication or application. Most of these are listed under the "Related...Calculations" sections for the appropriate system geometry and constitute the bulk of the reference review, although a large number also appear following derivations if deemed immediately relevant.

A Brief History

The earliest known solution to what is now called the Poisson–Boltzmann equation appears to be due to Liouville who, while investigating surfaces of constant curvature, showed that the solution to the differential equation

$$\frac{d^2 \log \lambda}{du\, dv} \pm \frac{\lambda}{2\, a^2} = 0 \qquad [1]$$

is given by

$$\lambda(u, v) = \frac{4\, a^2\, e^{\varphi(u)+\psi(v)}}{\left[1 \pm e^{\varphi(u)+\psi(v)}\right]^2} \frac{d\varphi(u)}{du} \frac{d\psi(v)}{dv} \qquad [2]$$

where $\varphi(u)$ and $\psi(v)$ are arbitrary functions.[50,51] (Letting $u = v = x$ be a coordinate variable and $\lambda(x)$ represent the local charge density for a system of ions

of charge q, which in turn is related to the local electrostatic potential $q\psi(x)$ through Boltzmann's equation, that is, $\lambda(x) \sim \exp[q\psi(x)/k_BT]$, Eq. [1] is seen to reduce to the Poisson–Boltzmann equation as expressed by Eq. [7].)

The first derivation of the PB equation in the context of electrolyte solutions is due to Gouy, who considered a system of ions in the presence of a surface of fixed charge density.[1,2] By balancing the electrostatic force of ions toward or away from the surface against their osmotic pressure, he obtained a set of simultaneous equations relating the concentration of all ions in solution to the surface charge density. His analysis showed that there would be a "condensation des ions d'un signe" at the charged surface. These ions, whose charge is opposite in sign to that of the surface, are called *counterions*; ions of the same sign as the surface are *coions*. In 1917 Gouy applied the theory to an investigation of electrocapillaries.[52] About the same time, and independently of Gouy, Chapman followed a more modern approach to the problem.[7] Beginning with Poisson's equation for the potential at a given distance from a charged surface, Chapman performed a first integration to find the total charge on a unit surface in an electrolyte solution and a second integration to obtain the total work in charging the surface. The results of Gouy and Chapman gave the unsettling prediction that as the surface charge increased, so would the number of (point) counterions in its immediate neighborhood, without end. This difficulty was resolved by Stern, who, in introducing a finite ion size, imposed a distance (or plane) of closest approach of ions to the surface.[8] While Stern also mentioned that specific absorption of ions on the surface might occur, he did not consider this case explicitly and so did not separate the double layer into what are now called the *inner* (adsorbed) and *outer* (nonadsorbed) *Helmholtz layers*. This was later done by Grahame in his classic review of the electric double layer.[9]

Independent of Gouy and roughly concurrently, Milner developed a theory of electrolyte solutions in which an equal number of cations and anions, interacting via a Coulomb potential, were distributed according to Boltzmann's distribution.[53] A treatment of the osmotic pressure in such a system was presented a year later.[54] While essentially equivalent to the result obtained by Debye and Hückel 10 years later, Milner developed his theory directly from the Coulomb potential rather than from Poisson's equation. Thus, his method of solution bypassed the ease of presentation and insight to be gained in dealing with a differential equation. This had to wait until Debye and Hückel, who were aware of Milner's results, published their celebrated work in two papers in 1923, the first presenting their famous solution and dealing with freezing-point depression and osmotic pressure of electrolyte solutions, and the second treating ionic conductivity. Almost coincident with the first paper (February 1923), Debye, as sole author, submitted a brief treatment of osmotic pressure using kinetic theory, the Brownian motion result of Einstein and the ideas that he and Hückel had developed.[55] Numerous papers were published by Debye and Hückel over the next 5 years, either jointly or with other authors,

extending the theory. In 1927 Fowler presented a more detailed analysis of the Debye–Hückel derivation in which he addressed two primary concerns.[56] The first dealt with the use of a constant dielectric coefficient but conceded that any improvement would be difficult. The second concern was with the implicit neglect of a fluctuation term involving the potential energy. However, Fowler's method was later shown to be overly restrictive by Onsager[10] and again by Kirkwood.[11]

The publication in 1948 of a monograph by Verwey and Overbeek[36] detailing work done by them and others during World War II on the application of the PB equation, and, in particular, the Gouy–Chapman version of it, to the study of colloids has proved to be as important as the initial publications by Gouy and Chapman and Debye and Hückel. This study laid the foundation for the modern study of colloids and has served as the primary guidepost for most of the work described here. Today, the PB equation, and in particular the Debye–Hückel (DH) linearized approximation, forms the foundation for modern descriptions of electrolyte and colloid theory. New theories are compared with and often derived from the nonlinear Poisson–Boltzmann equation and in the appropriate limits reduce to the DH result. As has been shown by modern statistical methods, the Debye–Hückel theory of electrolyte solutions is analogous to the lowest-order harmonic approximation in potential theory.[57]

The Poisson–Boltzmann Equation

The derivation of the Poisson–Boltzmann (PB) equation and its variants are well-known and available in many textbooks.[36,48,49,58–62] Over seventy years of hindsight has shown us that, despite the relative simplicity of the approach, most of the physics and chemistry of polyelectrolyte solutions are well described by the Poisson–Boltzmann equation. To go beyond the PB equation, however, is not as simple as one might think. We therefore include a discussion of the assumptions behind the equation and attempts at improving it in the final part of this review.

Consider a system containing known amounts of ions (fixed as well as mobile) in a solvent treated as a structureless but locally varying dielectric continuum at a given temperature. These ions may be of varying size and charge and subject to any specified short-range, long-range, and external forces. To determine the equilibrium distribution of ions, one generally starts from either the differential or integral form of Maxwell's law describing the variation of the electrostatic potential throughout the system.[63] For a spatially varying dielectric continuum, the differential form defining the potential is more convenient:

$$\nabla \cdot \varepsilon(\underline{r}) \cdot \nabla \bar{\psi}(\underline{r}) = -4\pi \bar{\rho}(\underline{r}) \qquad [3]$$

where $\varepsilon(\underline{r})$ is the value of the local dielectric coefficient at position $\underline{r}$, $\bar{\psi}(\underline{r})$ is the mean electrostatic potential, and $\bar{\rho}(\underline{r})$ is the mean charge density. The

electrostatic Poisson equation [3] is then "closed" by assuming that *the mobile component of the mean charge density is determined through application of the Boltzmann expression*

$$\begin{aligned}\bar{\rho}_{PB}(\underline{r}) &= \bar{\rho}^{\text{fixed}}(\underline{r}) + \bar{\rho}^{\text{mobile}}(\underline{r}) \\ &= \sum_{n=1}^{N} q_n \delta(\underline{r} - \underline{r}_n) + \sum_{i=0}^{I} \frac{e_0 z_i n_i e^{-\beta e_0 z_i \bar{\psi}(\underline{r})}}{\int_{V_i} e^{-\beta e_0 z_i \bar{\psi}(\underline{r})} d\tau} \\ &\equiv \sum_{n=1}^{N} q_n \delta(\underline{r} - \underline{r}_n) + \sum_{i=0}^{I} e_0 z_i c_i^R e^{-\beta e_0 z_i \bar{\psi}(\underline{r})} \end{aligned} \quad [4]$$

where the two summations correspond to N fixed (or source) and I mobile ions in the system, e_0 is the proton charge, z_i and n_i denote the valence and number of ions of species i, $\beta = 1/k_B T$ defines the temperature, $c_i^R \equiv c_i(\underline{R})$ denotes the concentration of species i at some outer boundary $\underline{R}$ where the potential vanishes (which may be at infinity), and $\delta(\underline{r} - \underline{r}_n)$ is the Kronecker delta function, which vanishes everywhere except at the positions $\underline{r}_n$ of the fixed charges (where it is then unity). It is convenient to denote ions of species $i = 0$ as those ions required for electroneutrality in the absence of added salt (e.g., those initially bound to a polyelectrolyte that are released on solvation).

The integral in the denominator of the second term is taken over the system volume V_i accessible to species i and ensures the proper normalization of the number of ions for a system with a finite volume. When this integral is included, Eqs. [3] and [4] constitute what we refer to as the *full* Poisson–Boltzmann equation. For systems with a bulk electrolyte, the number of ions is considered infinite so the Boltzmann expression for mobile ions as written in the third line of Eq. [4] is used and the concentration at the outer boundary c_i^R is replaced by a bulk concentration c_i^B. Also, since ions of species 0 are finite in number (compared to bulk species), they are then neglected from the summation.

The well-known Debye–Hückel equation results from expanding the Boltzmann expression for the mobile ions in Eq. [4] in terms of the (small) potential, that is, using $e^x \approx 1 + x + x^2/2 + \cdots$, where $x = -\beta e_0 z_i \bar{\psi}(\underline{r})$, and keeping only the first two terms:

$$\bar{\rho}_{\text{DH}}(\underline{r}) = \sum_{n=1}^{N} q_n \delta(\underline{r} - \underline{r}_n) + \sum_{i=0}^{I} e_0 z_i c_i^R \left[1 - \beta e_0 z_i \bar{\psi}(\underline{r})\right] \quad [5]$$

(This limit of weak coupling between the charged surface and the electrolyte environment also obtains in the absence of electrolyte, that is, in the Coulomb limit, and one which is most easily found by letting $z \to 0$.) Using this result in Eq. [3] gives a linear second-order differential equation for the mean potential,

which is much easier to solve than the nonlinear PB equation. If a bulk electrolyte solution is assumed, then $c_i^R \rightarrow c_i^B$ (with c_0^B neglected as discussed above) and the first term of the second summation vanishes due to electroneutrality of the dissolved electrolyte:

$$\sum_{i=1}^{I} z_i c_i^B = 0 \qquad [6]$$

[In some publications the "Debye–Hückel equation" is used only in reference to the spherically symmetric bulk electrolyte solution, with the term "linear Poisson–Boltzmann" (or LPB) equation referring to the result of linearizing the Poisson-Boltzmann equation, whatever its application. We follow more common usage and use the two terms interchangeably; thus "DH" = "LPB" in our notation.]

Equations [3] and either [4] or [5] are solved subject to appropriate boundary conditions to obtain the ion distributions through the system. Two boundary conditions (BCs) are required and most often these are chosen from among the following:

BC1. Fixed potential on a surface (Dirichlet condition)
BC2. Fixed charge density (or electric field) on a surface (this includes the electroneutrality condition) (Neumann condition)
BC3. A mixed condition coupling the charge density and potential on a surface (Cauchy condition)
BC4. Finiteness of the potential or field within a specific region or at infinity (one of conditions BC1–BC3 applied at one surface with the other surface removed to infinity)

In addition to these conditions, the continuity of the potential throughout the system requires that further relationships involving the potential and/or electric field at boundaries between regions need to be applied.

ANALYTICAL SOLUTIONS TO THE POISSON–BOLTZMANN EQUATION

Equations [3] and [4] subject to two appropriate boundary conditions constitute the Poisson–Boltzmann equation. A number of important, and at one time misunderstood, assumptions have been used in its "derivation." These are discussed in the last part of this review. Here we apply the PB equation or its DH approximation to three model systems for which analytical solutions are readily found. While only a handful of systems possess (exact) analytical solutions, there exists at least one such solution for each of the three common one-dimensional geometries (planar, cylindrical, and spherical) and a wide range of approximate analytical solutions can be found.

Besides serving to demonstrate the physical principles involved in applying the PB equation as well as checks for the numerical solution of more complicated geometries, these three systems are also excellent models for systems of extreme biophysical importance, modeling flat-cell membranes, extended polyelectrolytes such as DNA, and spherical micelles. For each geometry, we will solve the PB equation and discuss the resulting potential profile. For those cases in which both nonlinear PB as well as linear DH solutions exist, the similarities and differences (particularly near the interface) are emphasized.

Because of its biological relevance, we are concerned solely with surfaces having a fixed charge density. Solutions for these cases are somewhat more difficult to obtain than for those with a fixed surface potential. There are many biological systems in which a mixed boundary (case BC3, listed above) is important whereby the surface charge is regulated by the potential. For example, proteins possess ionizable sites whose charge depends strongly on the local potential. Changes in this potential can lead to protonation or deprotonation of these sites, which, in turn, can affect both the conformation of the protein as well as its recognition by a binding partner. Coupling this ionization process to potential changes due to a particular binding candidate (such as DNA) is a natural way to enhance recognition specificity during binding while maintaining conformational integrity in its absence. The solution for these more complex systems is usually obtained numerically and is not considered here explicitly, although numerous references to charge regulation studies are cited. In most cases, the following PB and DH solutions for surfaces with a fixed charge density may be applied to surfaces held at a fixed potential by inserting the value of this potential into the derived potential profiles.

A number of new approximate, but accurate, analytical results are also presented here; the most significant ones are (1) the extension of Gouy–Chapman theory to mixed electrolyte solutions whereby an effective counterion valence is introduced, (2) two approximate potential profiles for curved surfaces (one of them new) are generalized to include the presence of mixed electrolytes, (3) the apparent surface charge density for curved surfaces for which the Debye–Hückel potential asymptotically matches the Poisson–Boltzmann profile, and (4) a unified treatment of two interacting charged surfaces.

Planar Geometry: The Membrane Model

The simplest polyelectrolyte model of biological relevance is that of a single semiinfinite impenetrable charged plane in equilibrium with a bulk electrolyte solution of known composition. The charged plane also serves as an introduction to the properties of the electric double layer. We simplify the representation of a membrane by assuming that (1) the membrane is impenetrable to ions, (2) the surface charge is uniformly distributed and constant, (3) the electrolyte is modeled as hard-sphere ions of specific size, and (4) the solvent is a structureless continuum described by a uniform dielectric coefficient

(the restricted primitive model electrolyte). While any of the above assumptions can be relaxed to provide a more realistic treatment, the essential features of the physical phenomena displayed by membranes and other large polyelectrolyte surfaces are described by this simple model due to Gouy, Chapman, Stern, and Grahame. Although our analytical solutions to the PB equation usually assume that the surface charge is spread uniformly on a smooth surface, we use the term *polyelectrolyte*, instead of a more appropriate but less descriptive term such as *macroion*. Summaries and more detailed accounts of the PB equation applied to charged planar surfaces may be found in texts or review articles on electrochemistry, colloids, or membranes.[36,48,49,64–72]

General Equations

For our first analytical solution of the PB equation, we consider a semi-infinite (in the y and z directions) charged plane at $x = a$ in the presence of a point ion electrolyte solution ($x > a$; Figure 2). (As discussed at the end of this section, this model also describes a surface at $x = 0$ with primitive model electrolyte ions of equal radius a, but it is common practice to absorb the ion radius into the position of the charged surface.) Equations [3] and [4] yield the Poisson–Boltzmann equation for this system

$$\frac{d^2\bar{\psi}(x)}{dx^2} = -\frac{4\pi e_0}{\varepsilon_0}\sum_{i=0}^{I} c_i^R z_i e^{-\beta e_0 z_i \bar{\psi}(x)} \qquad [7]$$

where ε_0 is the bulk dielectric coefficient of the solvent and z_i and c_i^R are the valence and reference concentration of ion species i (e.g., 0, $1 = Na^+$, $2 = Mg^{2+}$ and $3 = Cl^-$). R is some reference position at which the outer boundary conditions are determined and that may be assumed to be infinity if the plane is in contact with a bulk electrolyte solution. For an impenetrable plane with fixed surface charge density, the charged surface is more conveniently introduced through a boundary condition on the electric field (an inhomogeneous Neumann condition) determined by applying Gauss' law, rather than as a charge (or source) distribution at $x = a$

$$\left.\frac{d\bar{\psi}(x)}{dx}\right|_{x=a} = -\frac{4\pi\sigma_a}{\varepsilon_0} \qquad [8]$$

for constant surface density σ_a. The second boundary condition follows either from the assumed electroneutrality of a finite system ($R < \infty$) or from the finiteness of the electric field far from the surface ($R \to \infty$), both assumptions giving

$$\left.\frac{d\bar{\psi}(x)}{dx}\right|_{R} = 0 \qquad [9]$$

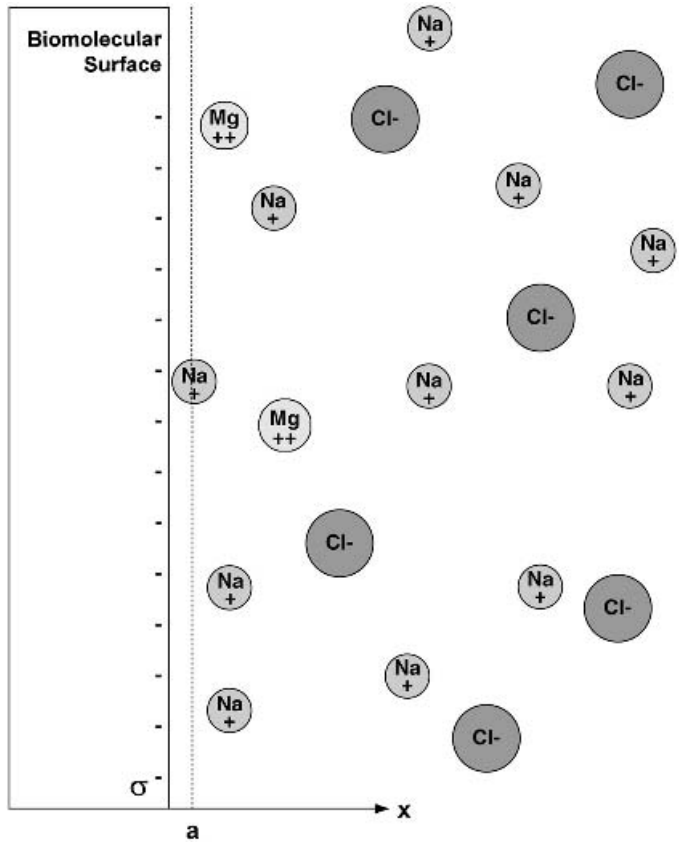

Figure 2 Illustration of a negatively charged biomolecular surface with charge density σ in the presence of a mixed electrolyte. The surface may represent that of a colloidal or biophysical particle such as a membrane (plane), polynucleic acid (cylinder), or micelle (sphere) where the distance of closest approach of ions is designated $x = a$. In the solution of the Gouy–Chapman equation, and of the Poisson–Boltzmann equation in general, the charged surface is usually displaced from its actual position (relative to the solvent) to the plane of closest approach of nonadsorbed ions, also called the *outer Helmholtz plane*.

An additional condition on the solution that is often used is to fix the gauge or reference value of the electrostatic potential by $\bar{\psi}(R) = 0$. That this choice is only one of convenience and not necessity (two boundary conditions suffice in determining the solution to a second-order differential equation) is easily seen by adding a constant to the potential in Eq. [7] and absorbing the leftover factor into the reference concentration c^R.

It is convenient to define three characteristic lengths of the system. The first is a property of the solvent and is called the *Bjerrum length*:

$$L_B = \beta e_0^2/\varepsilon_0 \qquad [10]$$

For water at 298 K, $\varepsilon_0 = 78.5$ gives $L_B = 7.14$ Å. The second length that we introduce is the *Gouy–Chapman length*[68]

$$\lambda_{GC} = \frac{e_0}{2\pi L_B|\sigma_a|} \qquad [11]$$

which is a property of the surface (and solvent through L_B). The final characteristic length is the well-known *Debye length* R_D and is given by the inverse of the (bulk) Debye screening constant

$$R_D \equiv \frac{1}{\kappa_D} = \frac{1}{\sqrt{4\pi L_B A_0 \sum_{i=1}^{I} c_i^B z_i^2}} \qquad [12]$$

and is a property of the electrolyte. In Eq. [12] we have explicitly inserted the conversion factor $A_0 = 6.022 \times 10^{-4} M^{-1}\text{Å}^{-3}$ for concentrations given in molarity and lengths in angstroms. In terms of the ionic strength I of the electrolyte, Eq. [12] reads: $\kappa_D(\text{Å}^{-1}) = 0.33\sqrt{I(M)}$. Rouzina and Bloomfield have used these three lengths to investigate the similarities between competitive mono- and divalent counterion binding to planar and cylindrical charged surfaces.[73,74]

If we now introduce the reduced or scaled potential (in units of $k_BT/e_0 =$ 25 mV at 298 K)

$$\phi(x) = \beta e_0 \bar{\psi}(x) \qquad [13]$$

Eqs. [7]–[9] take the form

$$\phi''(x) = -4\pi L_B A_0 \sum_{i=0}^{I} c_i^R z_i e^{-z_i\phi(x)} \qquad [14]$$

and

$$\begin{aligned} \phi'(a) &= \frac{-2S_a}{\lambda_{GC}}, \qquad & S_a &= \text{sgn}(\sigma_a) \\ \phi'(R) &= 0, & \phi(R) &= 0, \end{aligned} \qquad [15]$$

where S_a is the sign of the surface charge and single or double primes indicate first- or second-order differentiation with respect to the distance coordinate.

Multiplying Eq. [14] by $\phi'(x)$ and integrating from x to R gives the first integral

$$[\phi'(x)]^2 = 8\pi L_B A_0 \sum_{i=0}^{I} c_i^R [e^{-z_i\phi(x)} - 1] \qquad [16]$$

which can be rearranged to reduce the solution to quadrature (i.e., in terms of an integral)

$$\int_{\phi_a}^{\phi} \frac{d\phi}{\sqrt{\sum_{i=0}^{I} c_i^R (e^{-z_i\phi} - 1)}} = -S_a \sqrt{8\pi L_B A_0}\,(x - a) \qquad [17]$$

where ϕ_a is the surface potential. A more convenient form of Eq. [17] for finite systems ($R < \infty$) is

$$\int_{0}^{\phi} \frac{d\phi}{\sqrt{\sum_{i=0}^{I} c_i^R (e^{-z_i\phi} - 1)}} = S_a \sqrt{8\pi L_B A_0}\,(R - x) \qquad [18]$$

Equation [16] can be rearranged to read[75,76]

$$-\frac{[\phi'(x)]^2}{8\pi L_B} + A_0 \sum_{i=0}^{I} c_i^R [e^{-z_i\phi(x)} - 1] = 0 \qquad [19]$$

Equation [19] expresses the condition of equilibrium as a balance between the electrostatic pressure on ions, where the first term is simply the Maxwell electric field stress tensor,[77] and the osmotic pressure with respect to bulk, given by the second term.[78] Only in special cases can the integral in Eq. [17] be evaluated analytically.[2,79–81] Several analytical approximations to the planar PB equation for asymmetric electrolytes have been suggested.[82–84] We now present three examples possessing exact analytical solutions beginning with the classic Gouy–Chapman solution.

Bulk Model: z : z Electrolyte

The prototypical example is that of a charged plane in contact with a bulk $z:z$ symmetric electrolyte ($z > 0$), in which case we let $R \to \infty$ and $c_0^R \to 0$, so Eq. [14] becomes

$$z\phi''(x) = \kappa_D^2 \sinh[z\phi(x)] \qquad [20]$$

where we have simplified the result by introducing the Debye–Hückel screening constant of Eq. [12]. The solution to this equation is most immediately found by evaluating the integral in Eq. [17]:

$$\int_{\phi_a}^{\phi} \frac{d\phi}{\sqrt{2c^B[\cosh(z\phi) - 1]}} = \frac{1}{2\sqrt{c^B}} \int_{\phi_a}^{\phi} \frac{d\phi}{\sinh(z\phi/2)} = \frac{1}{\sqrt{c^B z^2}} \ln\left(\frac{\tanh(z\phi/4)}{\tanh(z\phi_a/4)}\right) \quad [21]$$

where c^B now denotes the bulk electrolyte concentration. Inserting this into the left-hand side of Eq. [17], identifying the screening constant, and denoting the potential by $\phi_{PB}(x)$ (which, because of its monotonicity, has the same sign as the surface value ϕ_a) gives

$$\tanh\frac{z\phi_{\text{PB}}(x)}{4} = \tanh\left(\frac{z\phi_a}{4}\right) e^{-\kappa_D(x-a)} \quad [22]$$

this is then inverted to yield the standard *Gouy–Chapman potential*:

$$z\phi_{\text{PB}}(x) = -2 \ln\left(\frac{1 - \tanh(z\phi_a/4)\, e^{-\kappa_D(x-a)}}{1 + \tanh(z\phi_a/4)\, e^{-\kappa_D(x-a)}}\right) \quad [23]$$

The ion concentrations for valence $\pm z$ are found from Eq. [23] using the Boltzmann expression $c^{\pm}(x) = c^B \exp[\mp z\phi(x)]$:

$$c^{\pm}_{\text{PB}}(x) = c^B \left(\frac{1 \mp \tanh(z\phi_a/4)\, e^{-\kappa_D(x-a)}}{1 \pm \tanh(z\phi_a/4)\, e^{-\kappa_D(x-a)}}\right)^{\pm 2} \quad [24]$$

Equation [23] gives the solution in terms of the surface potential. For application to biophysical macromolecules, an expression involving the surface charge density is usually preferable to one involving the surface potential. The relation between the two can be found from Eqs. [15] and [16]:

$$\frac{z}{\kappa_D \lambda_{\text{GC}}} = S_a \sinh\frac{z\phi_a}{2} \quad [25]$$

This important result relating the surface charge density to the surface potential is often referred to as *Grahame's equation*.[67] A little manipulation allows us to express the potential [23] in the "simpler" form

$$z\phi_{\text{PB}}(x) = -2\, S_a \ln\left(\tanh\frac{\kappa_D(x - a + \delta_{\text{DGC}})}{2}\right) \quad [26]$$

where, for convenience, we have defined the *Debye–Gouy–Chapman length*

$$\delta_{\mathrm{DGC}} = \kappa_D^{-1} \sinh^{-1} \frac{\kappa_D \lambda_{\mathrm{GC}}}{z} \qquad [27]$$

with $\sinh^{-1}(w) = \ln(w + \sqrt{w^2 + 1})$. Because most biological systems have low salt concentrations near a highly charged surface, implying that the Debye length is much larger than the Gouy–Chapman length ($\kappa_D \lambda_{\mathrm{GC}} \ll 1$), the Debye–Gouy–Chapman length usually approaches the Gouy–Chapman length (per counterion charge). The potential profiles corresponding to two systems with identical ionic strengths but different surface charge densities are self-similar in that they differ only in a spatial shift given by the difference in their δ_{DGC} values. Equation [26] may also be obtained directly by noting that $z\phi(x) = -2 \ln(\tanh(\gamma_1 x + \gamma_2))$ is the general solution to Eq. [20].

Evaluating Eq. [26] at $x = a$ yields the surface potential, which is simply

$$z\phi_a = -2 S_a \ln\left(\tanh\frac{\kappa_D \delta_{\mathrm{DGC}}}{2}\right) \qquad [28]$$

The surface potential is shown in Figure 3 as a function of surface charge density for two concentrations of mono- and divalent symmetric electrolytes. The

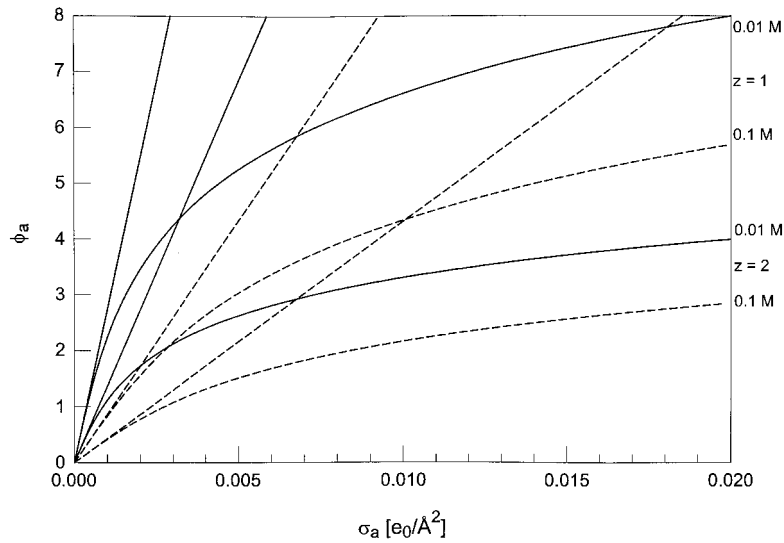

Figure 3 The Gouy–Chapman and Debye–Hückel surface potentials ϕ_a (Eqs. [25] and [32], respectively) for a positively charged plane with a surface charge density σ_a (in $e_0/\text{Å}^2$) in symmetric mono- and divalent electrolytes at concentrations of 0.01 M (solid lines) and 0.1 M (dashed lines); Debye–Hückel potentials are given by straight lines.

electrostatic (Helmholtz) free energy per unit area of the system is easily obtained from Eq. [28] by charging the surface:[36,85,86]

$$\begin{aligned}\frac{e_0\beta A_{\text{el}}}{\text{Area}} &= \int_0^{\sigma_a} \phi_a(\sigma)d\sigma \\ &= \sigma_a\phi_a - \int_0^{\phi_a} \sigma(\phi)d\phi\end{aligned} \qquad [29]$$

where the second line follows from the first by an integration by parts; the choice of integrals to use is determined by whether the surface charge density or potential is the independent variable. The free energy of a double layer system can also be dissected into energetic (U), entropic ($T\Delta S$), and chemical components, where for systems with surfaces held at constant charge density (such as those considered here) the chemical component due to adsorption or desorption of ions is omitted, as in Eq. [29].[86] Using Eqs. [11] and [25], the second line in Eq. [29] gives

$$\begin{aligned}\frac{\beta A_{\text{el}}}{\text{Area}} &= \frac{\kappa_D}{2\pi L_B z^2}\left[z\phi_a \sinh\left(\frac{z\phi_a}{2}\right) - 2\cosh\left(\frac{z\phi_a}{2}\right) + 2\right] \\ &= \frac{\kappa_D}{\pi L_B z^2}[p\ln(p+q) + 1 - q], \qquad p \equiv \frac{z}{\kappa_D\lambda_{\text{GC}}}, \qquad q \equiv \sqrt{1+p^2}\end{aligned} \qquad [30]$$

The electrostatic free energy can be used to investigate bending rigidity[87] and electrostatic pressure[48] of planar membranes. Most calculations are performed at a specific temperature and at known ion concentrations; hence the Helmholtz free energy is the appropriate quantity to use. Experiments, however, are performed at constant temperature and pressure and thus measure the Gibbs free energy. Because condensed phases are almost incompressible, the difference between the two free energies is small and this distinction is usually ignored.[86]

For a small surface potential or charge density, Eqs. [11] and [25] provide a linear relationship between them

$$\frac{\sigma_a}{e_0} = \frac{\kappa_D\phi_a}{4\pi L_B} \qquad [31]$$

and Eq. [22] reduces the potential profile to a simple screened exponential:

$$\phi(x) = \phi(a)\, e^{-\kappa_D(x-a)} = \frac{2\,S_a}{\kappa_D\lambda_{\text{GC}}}\, e^{-\kappa_D(x-a)} \qquad [32]$$

Equation [32] can also be derived by initially linearizing Eq. [14]. This is known as the *Debye–Hückel potential* and is valid for low surface charge

density or high ionic strength (either restriction leads to a small surface potential). The surface potential implicit in Eq. [32] is also shown in Figure 3 and compared with the Gouy–Chapman potential from Eq. [25]. It is seen that the GC surface potential approaches the linear DH dependence for small charge densities.

In the opposite limit of large surface potential we have $|\phi_a| \gg 1$ ($\kappa_D \lambda_{GC} \ll 1$, giving $\delta_{DGC} \approx \lambda_{GC}/z$) so that near the surface Eq. [26] gives

$$z\phi_{near}(x) \approx -2\ S_a\ \ln \frac{\kappa_D(x - a + \lambda_{GC}/z)}{2} \qquad [33]$$

with surface ion concentrations

$$c_i(x) \approx c_i^B \left(\frac{\kappa_D(x - a + \lambda_{GC}/z)}{2} \right)^{\pm 2} \qquad [34]$$

where $\pm$ indicates coions and counterions, respectively. For a large surface potential far from the surface, $\kappa_D(x - a) \gg 1$ and Eq. [26] becomes

$$z\phi_{asymp}(x) \approx -2\ S_a\ \ln \left| \frac{1 - e^{-\kappa_D(x-a+\lambda_{GC}/z)}}{1 + e^{-\kappa_D(x-a+\lambda_{GC}/z)}} \right| \approx 4\ S_a\ e^{-\kappa_D(x-a+\lambda_{GC}/z)} \qquad [35]$$

The decay is again determined by the Debye screening constant, but the high surface potential (or charge density) has little effect on the asymptotic potential profile. Thus, experimental data on a highly charged system, which depend on the (linear) properties of the tail of the potential, are only weakly dependent on the (nonlinear) properties at the surface and extrapolation of asymptotic properties to a highly charged surface is extremely unreliable.

Before we discuss the above results, we note that for a spatially dependent dielectric coefficient, a good approximation can be found by simply replacing the exponential terms in Eq. [22] or [23] with

$$e^{-\kappa_D(x-a)} \rightarrow \exp\left(-\kappa_D \int_a^x \sqrt{\frac{\varepsilon(x)}{\varepsilon_0}}\, dx \right) \qquad [36]$$

and λ_{GC} by $(\varepsilon_a/\varepsilon_0)\lambda_{GC}$ in Eq. [25] to get the surface potential.[88]

Discussion of the Gouy–Chapman (GC) Solution

In Figure 4 the GC potential profile of Eq. [26] is compared to the Debye–Hückel (Eq. [32]) and apparent Debye–Hückel (Eq. [93], discussed later) potentials for two monovalent salt concentrations (0.01 and 0.1 M) for a surface with charge density $\sigma = 0.01\ e_0/\text{Å}^2$. (The value for the surface

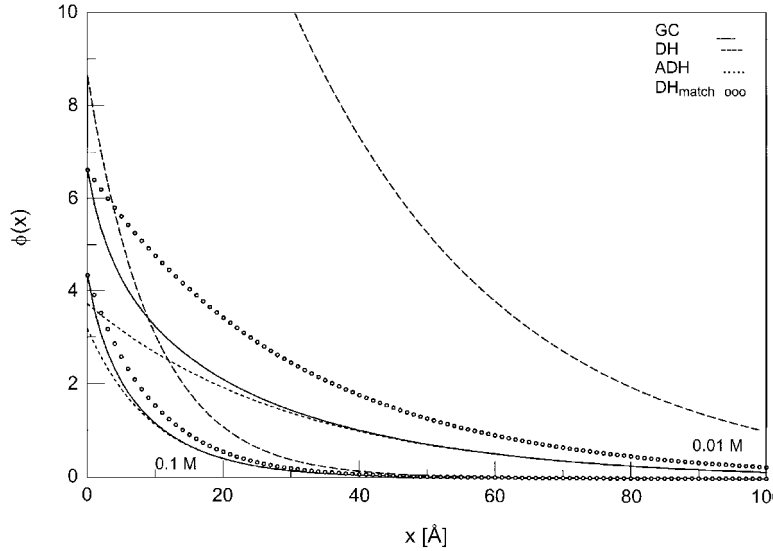

Figure 4 A comparison of the Gouy–Chapman (Eq. [26]), Debye–Hückel (Eq. [32] or Eq. [89]), and apparent Debye–Hückel (Eq. [93]) potentials for a planar surface with charge density $\sigma_a = 0.01\ e_0/\text{Å}^2$ in a monovalent electrolyte of concentrations 0.01 and 0.1 M; also shown are the Debye–Hückel profiles that match the Gouy–Chapman solution at the surface (circles).

charge density chosen here and below is typical of biopolyelectrolytes: for B-DNA, $|\sigma_a| \sim 0.01\ e_0/\text{Å}^2$, for planar membranes, $|\sigma_a| \sim 0.015\ e_0/\text{Å}^2$, and for spherical micelles, $|\sigma_a| \sim 0.01-0.02\ e_0/\text{Å}^2$.) Despite the complicated appearance of Eq. [26], the monotonic decay of the Gouy–Chapman potential away from the surface is a typical feature of one-dimensional solutions of the Poisson–Boltzmann equation. The relative simplicity of the PB potential profile might lead one to assume incorrectly that analytical solutions to the equation could be found readily (the rub lies in the nonlinearity, and to some extent the degree of nonlinearity, of the equation). Small changes in initial or boundary conditions or in system properties lead to large changes in the potential. Many standard analytical and numerical techniques also fail because the most physically meaningful solutions require that the derivative of the potential, rather than the potential itself, be specified at the charged surface. While exact analytical solutions for most models of biophysically interesting systems are not forthcoming, approximate (yet accurate) analytical expressions can be derived; several of these are presented later in the tutorial.

The region next to a charged surface in the presence of an electrolyte is called the *electric double layer*, a term describing what was originally thought to be two separate positively and negatively charged layers. Now it simply

refers to that part of the electrolyte solution that has properties distinct from those of the bulk solution (e.g., clustering of like ions, orientation of solvent molecules, etc.). Because the double layer blends continuously into the bulk (over a distance of several Debye lengths), the adjective *diffuse* is often applied. The charged surface attracts predominantly counterions with these ions serving to partially neutralize or *renormalize* the surface charge, as seen by more distant ions, leading to an apparent lowering of the surface charge density (or potential). Thus the long range Coulomb attraction or repulsion between two charged components (ions and/or surfaces) becomes a much shorter ranged local force when an electrolyte is present. This allows infinite systems to be treated as finite, or, finite systems to be extended to infinity, as convenience dictates. This exponential-like screening is common to all geometries and is a fundamental property of (poly)electrolyte systems. For systems with either low surface charge density or high ionic strength, resulting in a small potential throughout the system, the exact exponential screening of the DH profile is approached; for other systems, the exponential decay is approached only at much larger distances from the surface. The faster decay of the GC potential compared to the DH profile seen in Figure 4 implies a narrower but more concentrated double layer for the GC potential; this is the nonlinear aspect of GC theory. The DH potential clearly overestimates the actual potential, even at relatively large distances from the surface where the potential is small, but improves at higher electrolyte concentrations. Choosing an apparent or effective surface charge density such that the DH form of the potential reproduces the asymptotic decay rate of the GC potential gives the apparent DH (ADH) profile shown in Figure 4 (derived below as Eq. [93]). We also show the Debye–Hückel profiles that match the Gouy–Chapman potentials at the surface. The matched DH profile lies above the GC profile for both electrolyte concentrations emphasizing that the decay rate of the GC profile is faster than that based on the bulk Debye screening constant.

Equation [23] represents the GC solution for point ions. A key development in the theory of electrolytes was the introduction of a finite distance of closest approach of ions to a charged surface by Stern[8] and further elaborated upon by Grahame.[9] The layer of ions directly adsorbed onto the surface constitutes the inner Helmholtz layer; those ions that make contact but do not adsorb define the abovementioned distance of closest approach and constitute the outer Helmholtz or Stern layer. These modifications still admit an analytical solution to the GC equation: Laplace's equation is solved in the Stern layer with the (linear) potential and (constant) field matched at the polyelectrolyte surface and to the outer GC solution.[49] The adsorbed ions serve to reduce the charge density of the surface. Identification of the inner and outer Helmholtz layers has been particularly helpful in improving agreement between GC theory and electrochemical data. If we assign a common radius a to all electrolyte ions, then the identification of the interface at $x = a$ actually

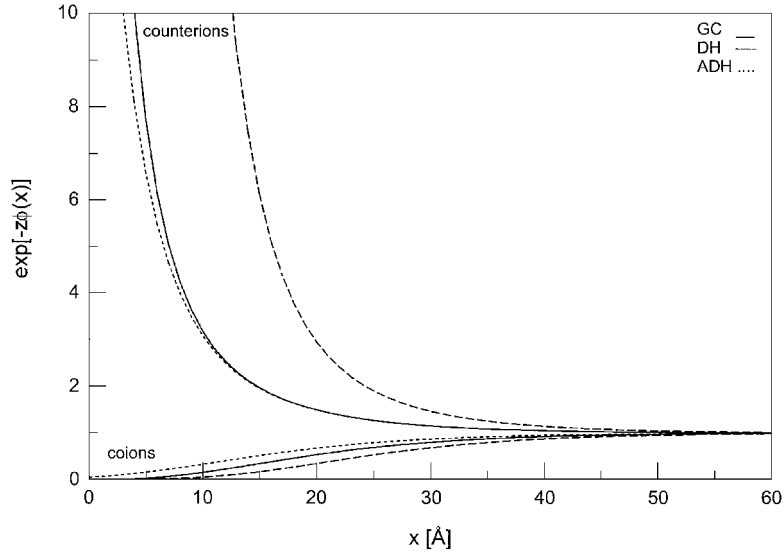

Figure 5 The correlation functions for monovalent counter- and coions according to the Gouy–Chapman, Debye–Hückel, and apparent Debye–Hückel solutions (Eqs. [24], [83], and [93], respectively) for a 0.1 M symmetric electrolyte near a plane with charge density $\sigma_a = 0.01\ e_0/\text{Å}^2$.

corresponds to the outer Helmholtz layer for a charged plane at $x = 0$. The surface charge density should then take into account any charge reduction due to adsorbed ions.

Figure 5 displays the counter- and coion correlation functions (equivalent to the concentration profile per bulk concentration) according to the Gouy–Chapman, Debye–Hückel, and apparent Debye–Hückel solutions (Eqs. [23], [32], and [93]) for a bulk symmetric electrolyte at 0.1 M near a planar surface with charge density $|\sigma_a| = 0.01\ e_0/\text{Å}^2$. Far from the surface, where the potential is small, the correlation functions approach unity and the amounts of counter- and coions are equal; close to the surface the number of counterions increases and the number of coions decreases as a result of the electrostatic attraction to and repulsion from the surface, respectively. The apparent DH counterion correlation function is, as can be seen, a marked improvement over the standard DH result.

The preceding comments concerning the potential and ion profiles for the Gouy–Chapman and Debye–Hückel equations apply equally well to other nonsymmetric and/or mixed electrolytes and geometries, as will be seen in many of the figures which follow. Therefore, rather than repeat the comments above for each of these systems, we simply show the additional potential profiles to illustrate differences between systems and approximations as well as to provide numerical data for those wishing to check their results. We have limited the treatment so far to a symmetric electrolyte as originally discussed by

Gouy. Although Gouy also presented analytical solutions for asymmetric 1 : 2 and 2 : 1 electrolytes,[2] they are less relevant biologically than the simple 1 : 1 case. However, since in most biological systems some amount of divalent cation is usually present, the mixed electrolyte cases of 1 : 1–2 : 1 and 1 : 1–2 : 2 are also important, and we consider them in detail below.

Bulk Model: 1 : 1–2 : 1 Electrolyte

For a negatively charged plane (at $x = a$) in the presence of a bulk 1 : 1–2 : 1 electrolyte (e.g., a mixture of NaCl and $MgCl_2$), the integral in Eq. [17] can be evaluated (species i: $1 = Na^+$, $2 = Mg^{2+}$, $3 = Cl^-$) as follows[89,90]

$$\begin{aligned}\int_{\phi_a}^{\phi} \frac{d\phi}{\sqrt{\sum_{i=1}^{3} c_i^B (e^{-z_i\phi} - 1)}} &= \int_{\phi_a}^{\phi} \frac{d\phi}{\sqrt{c_1^B(e^{\phi} + e^{-\phi} - 2) + c_2^B(2e^{\phi} + e^{-2\phi} - 3)}} \\ &= \frac{1}{\sqrt{c_1^B + 3c_2^B}} \int_{\phi_a}^{\phi} \frac{dW}{W\sqrt{1 + W}}, \quad W = \frac{e^{\phi} - 1}{1 - \alpha_1} \\ &= \frac{1}{2\sqrt{c_1^B + 3c_2^B}} \int_{\phi_a}^{\phi} \frac{d\Phi}{\sinh(\Phi/2)}, \quad \Phi = W + 1 \end{aligned} \tag{37}$$

where $\alpha_1 = c_2^B/(c_1^B + 3c_2^B)$. The final integral in Eq. [37] is identical to that in Eq. [21] and yields the solution

$$\Phi(x) = -2 \ln\left(\frac{1 - \tanh(\Phi_a/4)\, e^{-\kappa_D(x-a)}}{1 + \tanh(\Phi_a/4)\, e^{-\kappa_D(x-a)}}\right), \quad \Phi_a \equiv \Phi_{PB}(a) \tag{38}$$

where the Debye screening constant is $\kappa_D^2 = 8\pi L_B A_0(c_1 + 3c_2)$ and the PB potential profile is given by

$$\phi_{PB}(x) = \ln\left(\frac{\exp[\Phi(x)] - \alpha_1}{1 - \alpha_1}\right) \tag{39}$$

The relation between the surface potential and charge density (i.e., Grahame's equation and the analog of Eq. [25]) is readily found by applying the boundary condition of Eq. [15] to solution [38]:

$$\begin{aligned}\frac{1}{\kappa_D \lambda_{GC}} &= \frac{S_a \sinh(\Phi_a/2)}{1 - \alpha e^{-\Phi_a}} \\ &= S_a \sinh\left(\frac{\phi_a}{2}\right) \sqrt{1 - \alpha_1 + \alpha_1 e^{-\phi_a}} \end{aligned} \tag{40}$$

where λ_{GC} is the Gouy–Chapman length of Eq. [11] and S_a is the sign of the surface charge density. The surface potential as a function of positive and negative surface charge densities obtained from Eq. [40] is shown in Figure 6

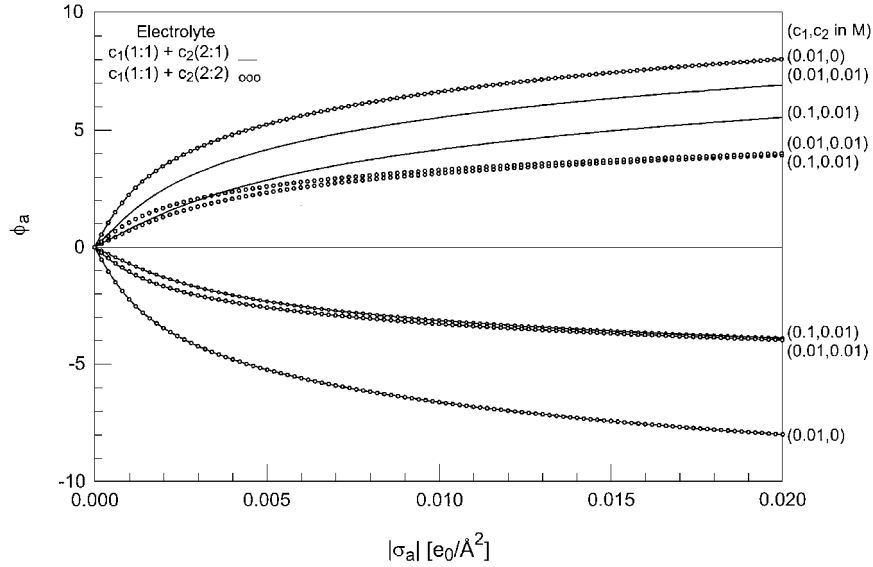

Figure 6 The Gouy–Chapman surface potential for positively and negatively charged planes with a surface charge density σ_a (in $e_0/\text{Å}^2$) in asymmetric (solid line; Eq. [40]) and symmetric (circles; Eq. [48]) mixed electrolytes for different mono- and divalent cation concentrations (c_1 and c_2 in M).

(as solid lines) for several concentrations of a mixture of 1 : 1 and 2 : 1 electrolytes. Also shown in the figure (as circles) is the surface potential for a mixture of symmetric 1 : 1 and 2 : 2 electrolytes according to Eq. [48]. The asymmetry in the surface potential with respect to the sign of the surface charge for the 1 : 1–2 : 1 electrolyte is evident when compared to that of the 1 : 1–2 : 2 electrolyte. Also, for negative surfaces, the difference between having mono- versus divalent anions is negligible as evidenced by the agreement between the curves for the two systems. In Figure 7 we display the potential profile of Eq. [39] for a negatively charged plane in a mixed 1 : 1–2 : 1 electrolyte. Also shown are the high charge density GC, effective-valence GC, and apparent DH approximations (Eqs. [57], [70] and [93], respectively), discussed below following Eqs. [41], [72] and [93].

For low surface charge densities, Eqs. [38]–[40] give the DH potential of Eq. [32]. In the more interesting limit of high surface charge density, the potential near the surface is

$$\begin{aligned}\phi_{\text{near}}(x) &\approx -2\ \ln\left[\sqrt{1-\alpha_1}\kappa_D(x-a+\lambda_{\text{GC}})/2\right], \quad S_a > 0 \\ &\approx \ln[\sqrt{\alpha_1}\kappa_D(x-a+\lambda_{\text{GC}}/2)], \quad S_a < 0 \end{aligned} \qquad [41]$$

where it is assumed that $\alpha_1 > 0$; for $\alpha_1 = 0$, Eq. [33] obtains. Surface ion concentrations (similar to those of Eq. [34]) are readily obtained from these

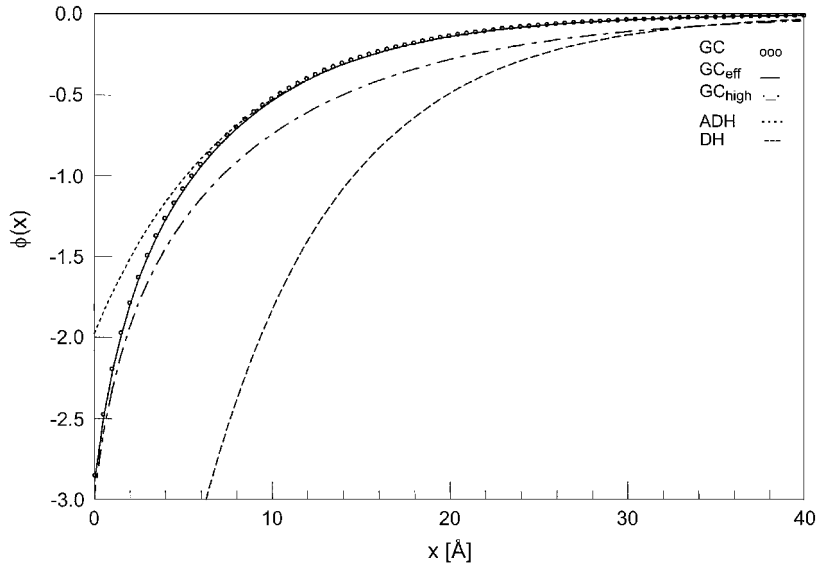

Figure 7 The Gouy–Chapman potential profile for a negatively charged plane with a surface charge density $\sigma_a = -0.01\ e_0/\text{Å}^2$ in a mixed asymmetric 1 : 1–2 : 1 electrolyte (solid line; Eq. [39]) for mono- and divalent salt concentrations $c_1 = 0.1$ M and $c_2 = 0.02$ M, respectively. The exact GC profile (circles) is compared with three approximate profiles based on the effective-valence approximation (solid line; Eq. [70]), the high charge density approximation (dotted–dashed line; Eq. [57]), and the apparent (dotted line; Eq. [93]) and actual (dashed line; Eq. [89]) DH approximations.

results. The appropriate curve (dotted–dashed line) in Figure 7 shows that the high charge density approximation of Eq. [41] agrees fairly well near the surface and provides a reasonable estimate of the surface potential. While Eqs. [41] assume a planar surface, the expressions are also valid for curved surfaces in the limit that the local surface curvature R_c is large compared to the Debye length: $\kappa_D R_c \gg 1$. Far from the surface, the potential decays as

$$\begin{aligned} \phi_{\text{asymp}}(x) &\approx \frac{4}{1-\alpha_1}\ e^{-\kappa_D(x-a+\lambda_{GC})}, && S_a > 0 \\ &\approx \frac{-4}{\left(1+\sqrt{\alpha_1}\right)^2}\ e^{-\kappa_D(x-a+\lambda_{GC}/2)}, && S_a < 0 \end{aligned} \qquad [42]$$

Systems with a negative surface charge density have more biochemical relevance, but equations for the positive case are shown to illustrate the asymmetry in the solution due to inclusion of a 2 : 1 electrolyte. Note that in Eqs. [41] and [42], the Gouy–Chapman length appears with a factor representing the largest counterion valence at the surface, as indicated explicitly in the $z : z$ electrolyte case of Eq. [35].

A simple and accurate approximation of Eq. [39] is easily derived. Because the limiting case of $\alpha_1 = 0$ reduces to the symmetric $z:z$ electrolyte case, an expression based on the Gouy–Chapman solution [26] would seem appropriate. Introducing an effective counterion valence z_e (>0) gives the approximate solution

$$z_e\phi_{\mathrm{PB}}(x) \approx -2\,S_a \ln\left(\tanh\frac{\kappa_D(x-a+\delta_{\mathrm{DGC}})}{2}\right) \qquad [43]$$

where application of the boundary condition at $x = a$ requires that the Debye–Gouy–Chapman length obeys

$$\delta_{\mathrm{DGC}} = \kappa_D^{-1}\sinh^{-1}\frac{\kappa_D\lambda_{\mathrm{GC}}}{z_e} \qquad [44]$$

The actual Debye screening constant must be retained to give the correct decay at large distances from the surface. We determine the effective valence by requiring that the approximate solution give the correct surface potential and, after a little algebra, find that z_e satisfies

$$\frac{\sinh(z_e\phi_a/2)}{z_e\sinh(\phi_a/2)} = \sqrt{1-\alpha_1+\alpha_1 e^{-\phi_a}} \qquad [45]$$

where ϕ_a is given by Eq. [40].

Bulk Model: 1 : 1–2 : 2 Electrolyte

As with the 1 : 1–2 : 1 electrolyte case presented above, we can also obtain the solution for a charged plane in the presence of a 1 : 1–2 : 2 mixed electrolyte. Although this case is not as biologically relevant, its solution will be helpful in deriving an analytical approximation for the potential profile of a moderately charged plane in a general monovalent–divalent mixed electrolyte. With c_1^B and c_2^B denoting bulk concentrations of the 1 : 1 and 2 : 2 electrolytes, respectively, the integral in Eq. [17] for this case gives

$$\begin{aligned}
&\int_{\phi_a}^{\phi}\frac{d\phi}{\sqrt{c_1^B(e^{\phi}+e^{-\phi}-2)+c_2^B(e^{2\phi}+e^{-2\phi}-2)}}\\
&=\frac{1}{2\sqrt{c_1^B+4c_2^B}}\int_{\phi_a}^{\phi}\frac{d\phi}{\sinh(\phi/2)\sqrt{1+\alpha_2\sinh^2(\phi/2)}}\\
&=\frac{1}{2\sqrt{c_1^B+4c_2^B}}\int_{w_a}^{w}\frac{dw}{w\sqrt{\alpha_2 w^2+(\alpha_2+1)w+1}},\quad w=\sinh^2(\phi)\\
&=\frac{1}{\sqrt{c_1^B+4c_2^B}}\ln\left[\frac{\sinh(\phi/2)}{\cosh(\phi/2)+\sqrt{1+\alpha_2\sinh^2(\phi/2)}}\right]_{\phi_a}^{\phi}
\end{aligned} \qquad [46]$$

where $\alpha_2 = 4c_2^B/(c_1^B + 4c_2^B)$. The potential profile therefore satisfies

$$\frac{\sinh(\phi(x)/2)}{\cosh(\phi(x)/2) + \sqrt{1 + \alpha_2 \sinh^2(\phi(x)/2)}} = \frac{\sinh(\phi_a/2)}{\cosh(\phi_a/2) + \sqrt{1 + \alpha_2 \sinh^2(\phi_a/2)}} e^{-\kappa_d(x-a)} \quad [47]$$

where the Debye screening constant is $\kappa_D^2 = 8\pi L_B A_0(c_1 + 4c_2)$. A different set of substitutions in Eqs. [46] can provide an explicit expression for the potential,[91] but Eq. [47] better serves our purposes. The surface potential is readily found from boundary condition [15]:

$$\frac{1}{\kappa_D \lambda_{GC}} = S_a \sinh\left(\frac{\phi_a}{2}\right)\sqrt{1 + \alpha_2 \sinh^2 \phi_a/2} \quad [48]$$

This can be solved to give

$$\phi_a = 2\, S_a \sinh^{-1}\left[\frac{\sqrt{2}/\kappa_D \lambda_{GC}}{\left(\sqrt{1 + \alpha_2(2/\kappa_D \lambda_{GC})^2} + 1\right)^{1/2}}\right] \quad [49]$$

For the limiting cases of $\alpha_2 = 0$ and 1, Eqs. [47] and [49] reduce to the symmetric $z:z$ electrolyte cases of $z = 1$ and 2, respectively, given by Eqs. [22] and [25]. In Figure 6, the surface potential according to Eq. [48] (circles) is compared with that for the asymmetric mixed electrolyte case of Eq. [40] (solid lines) for several different electrolyte compositions. The symmetry of the former with respect to surface sign contrasts clearly with the asymmetry of the latter. Also, as noted above, the effect of mono- versus divalent anions for the second electrolyte is negligible for negatively charged surfaces at the concentrations studied.

In a manner similar to the 1 : 1–2 : 1 electrolyte case, a good approximation to the potential profile of Eq. [47] can be found. As previously, we assume an approximate solution of the Gouy–Chapman form

$$z_e \phi_{PB}(x) \approx -2\, S_a \ln\left(\tanh\frac{\kappa_D(x - a + \delta_{DGC})}{2}\right) \quad [50]$$

where the Debye–Gouy–Chapman length is again used to satisfy the boundary condition ($z_e > 0$)

$$\delta_{DGC} = \kappa_D^{-1} \sinh^{-1} \frac{\kappa_D \lambda_{GC}}{z_e} \quad [51]$$

The effective valence z_e is now given by

$$\frac{\sinh(z_e\phi_a/2)}{z_e\sinh(\phi_a/2)} = \sqrt{1+\alpha_2\sinh^2\frac{\phi_a}{2}} \qquad [52]$$

where ϕ_a is given by Eq. [49].

Bulk Model: Highly Charged Surface

For the case of a highly charged surface, an approximate analytical expression for the potential profile near the surface can be found by considering only the contribution to the charge density of the highest valence counterion. Denoting its concentration by c_c, valence by $z_c = -S_a|z_c|$, and screening constant by $\kappa_c^2 = 4\pi L_B A_0 c_c z_c^2$, the Poisson–Boltzmann equation [14] becomes

$$y''(x) = \kappa_c^2 e^{y(x)} \qquad [53]$$

where $y(x) = -z_c\phi(x) > 0$. The general solution to Eq. [53] is

$$y(x) = -2\ \ln\left[\left(\frac{\kappa_c}{\sqrt{2}\gamma_1}\right)\cos(\gamma_1 x+\gamma_2)\right] \qquad [54]$$

where constants γ_1 and γ_2 are determined from the boundary conditions. The potential near the surface can be obtained from Eq. [54] in either of two ways: (1) we can apply boundary conditions (typically on the field) at the surface and at some finite distance R, and let R go to infinity, or (2) we can take the small-x limit. We could also just "guess" the solution

$$y_{\text{near}}(x) = -2\ \ln\left[\frac{\kappa_c}{\sqrt{2}}(x+\gamma)\right] \qquad [55]$$

which can be verified by substitution to obey Eq. [53]. Equation [55] gives the potential profile near the surface if we apply boundary condition [15], which then provides the final result

$$|z_c|\phi_{\text{near}}(x) \approx -2\,S_a\ \ln\left[\frac{\kappa_c}{\sqrt{2}}\left(x-a+\frac{\lambda_{\text{GC}}}{|z_c|}\right)\right] \qquad [56]$$

Equation [56] is readily shown to reduce to Eqs. [33] and [41] for those cases and can also be obtained by integrating Eq. [17] and applying Eq. [15].

While Eq. [56] describing the potential is useful in predicting its value near a highly charged surface, this result can be extended to give an approximate description everywhere. The assumption of retaining only the contribution

to the charge density of the highest-valence counterion implies that terms corresponding to lower-valence counterions and, in particular, coions are negligible. We may then add a "negligible" term to the right-hand side of Eq. [53] describing "dummy" coions of valence $-z_c$ and concentration c_c (which may, in fact, exist). The resulting solution is then obviously given by the Gouy–Chapman profile [26] for a $z_c : z_c$ electrolyte with the Debye screening constant κ_D replaced by $\sqrt{2}\kappa_c$:

$$|z_c|\phi_{PB}(x) \approx -2\,S_a\,\ln\left(\tanh\frac{\kappa_c(x - a + \delta_{DGC})}{\sqrt{2}}\right) \qquad [57]$$

where

$$\delta_{DGC} = \left(\sqrt{2}\kappa_c\right)^{-1}\sinh^{-1}\frac{\sqrt{2}\kappa_c\lambda_{GC}}{|z_c|} \qquad [58]$$

Equation [57 is an improvement on the limiting result given by Eq. [56] both near the surface and asymptotically and for all values of λ_{GC}. A similar analysis can also be applied to highly charged cylindrical and spherical geometries for which approximate but accurate $z : z$ potential profiles are derived later.

The assumption of considering only the highest-valence counterions provides an estimate of when Eq. [57] adequately represents the potential profile near the surface. To be specific, we consider the surface to be negatively charged and the electrolyte to be a mixture of mono- and divalent cationic salts (e.g., NaCl and $MgCl_2$). Retention of only divalent cations (of concentration c_2) and neglect of monovalent cations (of concentration c_1) implies that, at the surface

$$2c_2e^{-2\phi_a} \gg c_1e^{-\phi_a} \qquad [59]$$

If we assume that the left-hand term is an order of magnitude larger than the right, then we have the condition

$$|\phi_a| > 1.6 - \ln\frac{c_2}{c_1} \qquad [60]$$

or, using Eqs. [11] and [56]

$$\sqrt{c_2} > \frac{0.018\,c_1}{|\sigma_a|} \qquad [61]$$

for concentrations in molar units (M) and the surface charge density in $e_0/\text{Å}^2$. For a typical surface charge density of 0.015 $e_0/\text{Å}^2$ in a 0.1 M monovalent salt,

Eq. [61] gives a divalent salt concentration of $c_2 > 0.015$ M for Eq. [56] to be applicable. As surface potentials near biopolyelectrolytes are typically larger than a few k_BT/e_0 for physiological concentrations of salt, Eq. [60] is usually satisfied.

Bulk Model: Moderately Charged Surface

For a moderately charged surface in the presence of a bulk mixed electrolyte containing both monovalent and divalent counterions, both counterion types must be considered; the simplification used above for a highly charged surface is not applicable. If the stoichiometry of the electrolyte solution coincides with either of the two cases treated above, 1 : 1–2 : 1 or 1 : 1–2 : 2, then the effective-valence profiles corresponding to those cases, Eqs. [43]–[45] or Eqs. [50]–[52], respectively, or indeed the exact profiles, may be used. However, the great similarity in the effective-valence profiles, a similarity that is not apparent in the exact analytical description, suggests that it might be possible to obtain a single approximate analytical solution that describes both.

We begin by noting that the difference in the two effective-valence profiles lies on the right-hand side of Eqs. [45] and [52], a difference that can be traced back to the equations used for obtaining the surface potential: Eqs. [40] and [48], respectively. A solution based on the 1 : 1–2 : 2 case is preferred because the surface potential can be obtained analytically by direct inversion, without recourse to an iterative procedure. The difference in the potential dependence of the right-hand side of Eqs. [45] and [52] is usually negligible; for negative potentials (when this case has divalent counterions), we can put

$$e^{-\phi} - 1 \approx e^{-\phi} - 1 + (e^{\phi} - 1) = 4\sinh^2\frac{\phi}{2} \qquad [62]$$

and the term in parentheses in the middle expression of Eq. [62] is generally either small, if $|\phi| \ll 1$, or much less that the term before it, if $|\phi| \gg 1$. If we also make the identification

$$4\alpha_1 = \alpha_2 = 2\left(\frac{\kappa_2}{\kappa_D}\right)^2 \qquad [63]$$

where κ_2 indicates the Debye screening constant due *only* to divalent counterions, then the expressions for both potential profiles become identical, with Eq. [49] giving the surface potential and Eq. [52] giving the effective valence. Collecting expressions, our approximation to the potential profile is then

$$\phi_{\mathrm{PB}}(x) = \frac{-2S_a}{z_e}\ln\left(\tanh\frac{\kappa_D(x - a + \delta_{\mathrm{DGC}})}{2}\right) \qquad [64]$$

where the Debye–Gouy–Chapman length is ($z_e > 0$)

$$\delta_{\mathrm{DGC}} = \kappa_D^{-1} \sinh^{-1} \frac{\kappa_D \lambda_{\mathrm{GC}}}{z_e} \qquad [65]$$

and ion concentrations are given by

$$c_i(r) = c_i^B \left(\tanh \frac{\kappa_D (x - a + \delta_{\mathrm{DGC}})}{2} \right)^{\frac{2 z_i S_a}{z_e}} \qquad [66]$$

The effective counterion valence z_e obeys

$$\frac{\sinh(z_e \phi_a / 2)}{z_e \sinh(\phi_a / 2)} = \sqrt{1 + 2 \left[\left(\frac{\kappa_2}{\kappa_D} \right) \sinh \left(\frac{\phi_a}{2} \right) \right]^2} \qquad [67]$$

where the solution falls within the limits $\sqrt{1 + 3(\kappa_2/\kappa_D)^2} \leq z_e \leq 2$, and the surface potential is given by

$$\phi_a = 2 S_a \sinh^{-1} \left[\frac{\sqrt{2}/\kappa_D \lambda_{\mathrm{GC}}}{\left(\sqrt{1 + 8(\kappa_2/\kappa_D^2 \lambda_{\mathrm{GC}})^2} + 1 \right)^{1/2}} \right] \qquad [68]$$

As a final, "bare-bones" approximation, we note that the potential is not extremely sensitive to the effective valence and that any reasonable value of the valence that falls between the above limits can be used. We suggest the simple approximation

$$z_e = 1 + \frac{\sqrt{2} \kappa_2}{\kappa_D} \qquad [69]$$

which reduces properly for symmetric mono- and divalent salts, is close to the actual value for surface potentials in the range 2–5 $k_B T / e_0$, and works well outside this range for asymmetric 1 : 1–2 : 1 salt provided $c(1:1) > c(2:1)$. As this expression is independent of the surface potential, the potential profile now reduces to

$$\phi_{\mathrm{PB}}(x) = \frac{-2 S_a}{z_e} \ln \left(\tanh \frac{\kappa_D (x - a + \delta_{\mathrm{DGC}})}{2} \right) \qquad [70]$$

where

$$\delta_{\mathrm{DGC}} = \kappa_D^{-1} \sinh^{-1} \frac{\kappa_D \lambda_{\mathrm{GC}}}{z_e} \qquad [71]$$

Expression [69] for the effective valence is extremely useful in that it allows standard formulas based on symmetric electrolytes to be (approximately)

extended to asymmetric or mixed-salt electrolytes. In later sections we will derive approximations to the potential profile for one or two curved charged surfaces, specifically for cylinders and spheres, in the presence of a $z:z$ electrolyte; these results can then be applied to general electrolytes by introducing an effective valence into those expressions. The surface potential implied by the profile of Eq. [70] is

$$\phi_a = \frac{2\,S_a}{z_e} \ln\left[\sqrt{1+\left(\frac{z_e}{\kappa_D \lambda_{GC}}\right)^2} + \frac{z_e}{\kappa_D \lambda_{GC}}\right] \qquad [72]$$

and represents an approximation to Eq. [67] or [68]. The approximate electrostatic free energies of the double layer follow immediately from Eqs. [30] with z_e substituted for z. For a $1:1$–$2:2$ electrolyte, Eq. [70] is surprisingly accurate; for a $1:1$–$2:1$ electrolyte, the largest error in the potential (typically a few percent and much less than the 25% error common to PB predictions involving divalent cations) occurs at the surface and decreases with increasing surface charge. The primary source of this error is in the use of Eq. [62] and not Eq. [69]. The effective-valence profile of Eq. [70] (solid line) is compared with the exact profile of Eq. [39] (circles) in Figure 7 and is seen to give excellent agreement throughout.

Cell Model: No Added Salt

As a final example of the planar PB equation, consider a finite system bounded by two parallel identically charged planes separated by a distance $2R$ with the electrolyte solution between them consisting of a single neutralizing species of counterions of valence z_0. For a neutral system, the field must vanish midway between the planes, and it is convenient to choose the potential to vanish there as well. Applying boundary conditions at the planar surface and at R amounts to invoking a "cell model" of the system.[92] While the term "cell model" is more often applied to the cylindrical and spherical cases, and is discussed at greater length below, it is also applied to the planar case. In this case the integral in Eq. [18] can be evaluated to give the PB cell (PBC) model potential profile

$$z_0 \phi_{PBC}(x) = \ln\left(\cos^2 \frac{\kappa_R (R-x)}{\sqrt{2}}\right) \qquad [73]$$

where the screening constant

$$\begin{aligned} \kappa_R &= \sqrt{4\pi L_B A_0 \sum_{i=0}^{I} c_i^R z_i^2} \\ &= \sqrt{4\pi L_B A_0 c_0^R z_0^2} \end{aligned} \qquad [74]$$

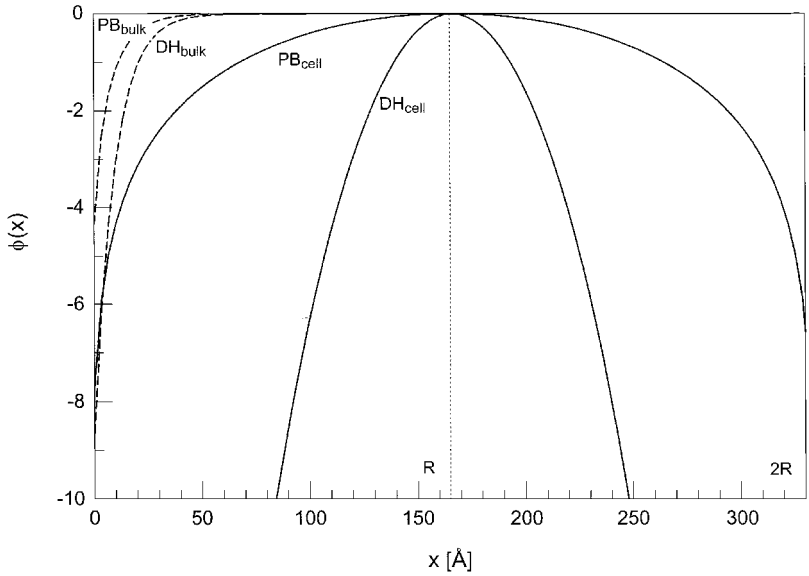

Figure 8 The PB and DH cell (solid lines; Eqs. [73] and [87], respectively) and bulk model (dashed lines; Eqs. [26] and [89], respectively) potential profiles for a negatively charged plane of charge density $\sigma_a = -0.01\ e_0/\text{Å}^2$ in the presence of 0.1 M counterions; the cell model for this system has $R = 166$ Å.

is found by solving the transcendental equation obtained by applying the boundary condition on the potential at the interface:

$$z_0\phi'(a) = \frac{-2z_0S_a}{\lambda_{GC}} = \sqrt{2}\,\kappa_R \tan\frac{\kappa_R R}{\sqrt{2}} \qquad [75]$$

Figure 8 compares the PB cell model potential profile obtained from Eq. [73] with the bulk PB profile of Eq. [26] for a negatively charged plane ($\sigma_a = -0.01e_0/\text{Å}^2$) in the presence of monovalent counterions (the bulk model also contains monovalent coions). The cell model profile is seen to decrease in magnitude from its surface value to zero at the cell boundary ($R = 166$ Å for a monovalent counterion concentration of 0.1 M) and rise to its surface value in the next cell. The bulk PB potential falls toward zero and vanishes at infinity, indicative of its boundary conditions. To see why the bulk model potential decays faster than that of the cell model, consider Figure 9, in which the concentration profile of Na^+ in the cell model (dashed line) is shown to the left (A) of a barrier impermeable to ions (indicated by the vertical dotted line at $x = R$). To the right of this barrier (B) is a bulk solution of 0.1 M NaCl, with the Na^+ concentration also shown by a dashed line. Removing the barrier extends the range of the electrostatic potential, which initially vanished at R, to infinity, thus causing sodium ions to flow down the potential well toward

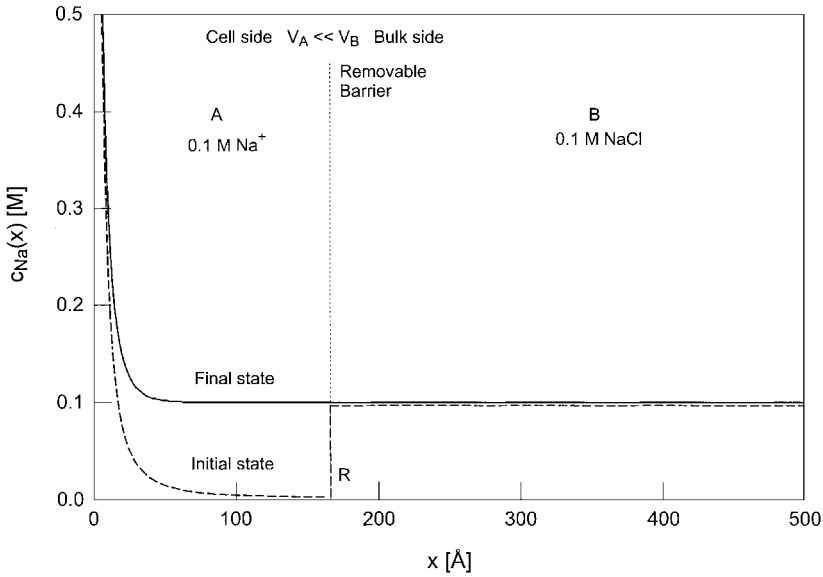

Figure 9 The PB concentration profiles corresponding to the cell and bulk models of Figure 8. Initially there is an ion-impenetrable barrier (vertical dotted line) between the cell system to the left (side A), in which the counterion concentration is 0.1 M, and the bulk model to the right (side B), which contains a solution of 0.1 M monovalent salt (NaCl). The initial state concentration of Na^+ is indicated by the dashed line. Removing the barrier establishes an equilibrium in which the sodium ion distribution is given by the solid line, indicating that sodium ions moved from the bulk side to the cell side.

the charged surface, removing the discontinuity in the ion concentration at the initial cell boundary. An increase in the number of counterions in side A causes the potential to decay more rapidly. In related work, the planar cell model with no added salt has been used to investigate the attraction of planar membranes,[93–95] and Zara et al. have numerically investigated the added salt case for various concentrations of mixed mono- and divalent salt, comparing the results with Monte Carlo simulations.[96] Briscoe and Attard have maximized the contrained entropy to derive free-energy expressions within the no-added-salt planar PB cell model for the case of charge regulated surfaces, which includes the more common conditions of constant surface charge density and constant surface potential.[97] Their work emphasizes the difference between high-salt, bulk model PB solutions and those describing low-salt, cell model solutions, as Figure 8 illustrates.

Cell Model: Debye–Hückel Screening Constant

Before considering a planar geometry, we derive a general expression for the Debye screening constant within the one-dimensional DH cell model. In

d dimensions, the radial Debye–Hückel equation is obtained by expanding the exponential on the right-hand side of Eq. [14] and keeping only the first two terms (this assumes that the surface potential will be small: $|\phi_a| \ll 1$), yielding

$$\frac{1}{r^{d-1}}\frac{d}{dr}\left[r^{d-1}\frac{d\phi_{\mathrm{DH}}(r)}{dr}\right] = \kappa_R^2\phi_{\mathrm{DH}}(r) - 4\pi L_B A_0 \sum_{i=0}^{I} c_i^R z_i \qquad [76]$$

subject to the boundary conditions of Eq. [15]; the first expression of Eq. [74] defines κ_R. The general solution to Eq. [76] can be written as

$$\phi_{\mathrm{DH}}(r) = \phi_H(r) + C \qquad [77]$$

where the first term is the homogeneous solution. Use of Eqs. [76], [77] and the gauge condition $\phi_{\mathrm{DH}}(R) = 0$ gives

$$C = \frac{\sum_{i=0}^{I} c_i^R z_i}{\sum_{i=0}^{I} c_i^R z_i^2} = -\phi_H(R) \qquad [78]$$

Starting from the DH expression for the radial concentration of ions

$$c_i(r) = c_i^R[1 - z_i\phi_{\mathrm{DH}}(r)] \qquad [79]$$

and integrating over the radial coordinate from a to R, we find

$$\int_a^R c_i(r)r^{d-1}dr = \bar{c}_i V_d = c_i^R\left[V_d - z_i\int_a^R \phi_{\mathrm{DH}}(r)r^{d-1}dr\right] \qquad [80]$$

where $\bar{c}_i$ is the average concentration in the cell of ion species i and $V_d = (R^d - a^d)/d$. Integrating Eq. [76] over the radial coordinate and using the boundary conditions gives

$$\langle\phi_{\mathrm{DH}}(\kappa_R)\rangle \equiv \frac{\int_a^R \phi_{\mathrm{DH}}(r)r^{d-1}dr}{\int_a^R r^{d-1}dr} = \frac{4\pi L_B\sigma_a da^{d-1}}{e_0\kappa_R^2(R^d - a^a)} - \phi_H(\kappa_R R) \qquad [81]$$

where the dependence on κ_R has been explicitly indicated. Finally, solving Eq. [80] for c_i^R, multiplying by z_i^2, summing over ion species, and using Eq. [81] gives the general result for the cell boundary screening constant

$$\kappa_R^2 = \sum_{i=0}^{I} \frac{4\pi L_B A_0 \bar{c}_i z_i^2}{1 - z_i\langle\phi_{\mathrm{DH}}(\kappa_R)\rangle} \approx \kappa_D^2\left\{1 + \langle\phi_{\mathrm{DH}}(\kappa_R)\rangle\frac{\sum_{i=0}^{I}\bar{c}_i z_i^3}{\sum_{i=0}^{I}\bar{c}_i z_i^2}\right\} \qquad [82]$$

where the approximation assumes that the correction to κ_D is small. For monovalent salts, the sum in the numerator of the right-hand expression in Eq. [82] reduces to c_0, so the correction is generally small. Equation [82] applies only to what might be called the strict cell model, which is generally used for cylindrical geometries. For a planar system, an approximate cell model is more often considered whereby the two confining surfaces are assumed to be in contact with a bulk electrolyte; the screening constant in this case is equated to the bulk value. Such a system models two large but finite surfaces whose separation is much smaller than the surface dimension.

The use of Eq. [79] in the derivation of Eq. [82] prompts the following comments concerning the Debye–Hückel equation in general. While linearization of the nonlinear PB equation restricts the validity of the DH solution to small surface potentials, the DH result is sometimes used in circumstances when this restriction does not hold. Most often the exponential decay form for the potential is "borrowed" and the surface charge density and/or Debye constant changed to provide a good fit to experimental data. In some cases, however, this presents difficulties in interpretation. For example, consider the ion concentrations corresponding to Eq. [79]. This expression is fine for counterions where $z_i\phi_a < 0$, but resulting coion concentrations are meaningful only for small potentials. To sidestep this problem, ion concentrations within the linear DH approximation are sometimes determined from the nonlinear Boltzmann expression and referred to as the *DHX approximation*:[98]

$$c_i^{\mathrm{DHX}}(r) = c_i^R \exp[-z_i\phi_{\mathrm{DH}}(r)] \qquad [83]$$

which is everywhere positive. The difficulty with this expression is that the DH equation tends to overestimate considerably the surface potential of highly charged systems with the result being that surface concentrations predicted by Eq. [83] are unduly high. While the DHX approximation violates electroneutrality, this in itself is not the cause of any numerical inaccuracies, as Ruff[99] has shown by comparing Eq. [83] to the electroneutral alternative for a bulk $z:z$ electrolyte ($z > 0$)

$$\begin{aligned} c(r) &= c^B \exp[\mp \sinh^{-1}(z\phi_{\mathrm{DH}}(r))] \\ &= c^B \left[z\phi_{\mathrm{DH}}(r) + \sqrt{(z\phi_{\mathrm{DH}}(r))^2 + 1} \right]^{\mp 1} \end{aligned} \qquad [84]$$

where the upper/lower $(-/+)$ sign is chosen for counterions/coions, respectively. The generalization of the first-order expansion of Eq. [84] provides the simpler relations:

$$\begin{aligned} c_i(r) &= c_i^R[1 - z_i\phi_{\mathrm{DH}}(r)] \qquad \text{counterions} \\ c_i(r) &= \frac{c_i^R}{1 + z_i\phi_{\mathrm{DH}}(r)} \qquad \text{coions} \end{aligned} \qquad [85]$$

In addition to always giving a positive coion concentration, and, for small potentials, at the same level of accuracy as Eq. [79], Eqs. [84] and [85] give the product of the anion/cation concentrations for $z:z$ salts as unity, as it is with the nonlinear PB equation. (Of course, use of Eq. [85] violates electroneutrality.)

Cell and Bulk Models: Debye–Hückel Potential

We now solve Eq. [76] for the planar case ($d = 1$). The homogeneous solution is

$$\phi_H(x) = Ae^{-\kappa_R x} + Be^{\kappa_R x} \qquad [86]$$

where A and B are determined from the boundary conditions. The final result for the Debye–Hückel cell (DHC) model potential profile is

$$\phi_{\mathrm{DHC}}(x) = \frac{2S_a}{\kappa_R \lambda_{\mathrm{GC}}} \frac{\cosh[\kappa_R(R-x)] - 1}{\sinh[\kappa_R(R-a)]} \qquad [87]$$

where Eq. [82] gives

$$\kappa_R^2 = \sum_{i=0}^{I} \frac{4\pi L_B A_0 \bar{c}_i z_i^2}{1 - \frac{2S_a z_i}{\kappa_R \lambda_{\mathrm{GC}}} \left(1 - \frac{\kappa_R(R-a)}{\sinh[\kappa_R(R-a)]}\right)} \qquad [88]$$

Ion concentrations can be obtained from Eq. [85]. When the distance $2R$ between two planes becomes infinitely large, we recover the standard (bulk) DH solution from Eq. [87]:

$$\phi_{\mathrm{DH}}(x) = \phi_{\mathrm{DH}}(a)\, e^{-\kappa_D(x-a)} = \frac{2\,S_a}{\kappa_D \lambda_{\mathrm{GC}}} e^{-\kappa_D(x-a)} \qquad [89]$$

in agreement with Eq. [32]. This bulk solution has already been compared with the Gouy–Chapman solution of Eq. [26] for a monovalent electrolyte at two concentrations (0.01 M and 0.1 M) in Figure 4, where we saw that the DH potential overestimates the actual potential. Figure 8 displays the DH cell model surface potential obtained from Eq. [87] for a negatively charged plane in the presence of monovalent counterions and compares it to the corresponding bulk DH potential (Eq. [89]) as well as the cell model and bulk PB potentials (Eqs. [73] and [26]). As in the bulk case noted previously, the cell model DH potential considerably overestimates the actual potential for large surface charge densities.

Bulk Model: Apparent Debye–Hückel Surface Charge Density

For $\kappa_D(x-a) \gg 1$, the right-hand side of Eq. [22] giving the PB potential for a $z:z$ electrolyte becomes small, implying that the left-hand side does

as well. Thus we expand the left-hand side and keep the lowest-order term ($\tanh w \approx w, |w| \ll 1$):

$$z\phi_{\mathrm{PB}}(x) = 4\tanh\left(\frac{z\phi_a}{4}\right)e^{-\kappa_D(x-a)} \quad (\text{for large } x) \qquad [90]$$

Comparison of Eqs. [89] and [90] shows that asymptotically the $z:z$ PB solution behaves like the DH solution but with an "apparent" surface potential given by

$$z\phi_{\mathrm{ADH}}(a) = 4\tanh\frac{z\phi_{\mathrm{PB}}(a)}{4} \qquad [91]$$

Inserting expressions for the surface potential from Eqs. [89] and [28] into Eq. [91] along with the definition of the Debye–Gouy–Chapman length in Eq. [27], we obtain the following relationship between apparent and actual Gouy–Chapman lengths:

$$\frac{\kappa_D\lambda_{\mathrm{AGC}}}{z} = \frac{1}{2}\left(\frac{\kappa_D\lambda_{\mathrm{GC}}}{z} + \sqrt{\left(\frac{\kappa_D\lambda_{\mathrm{GC}}}{z}\right)^2 + 1}\right) \qquad [92]$$

The apparent Debye–Hückel (ADH) potential written in terms of the apparent Gouy–Chapman length is

$$\phi_{\mathrm{ADH}}(x) = \frac{2\,S_a}{\kappa_D\lambda_{\mathrm{AGC}}}e^{-\kappa_D(x-a)} \qquad [93]$$

The adjectives "reduced," "effective," and "renormalized" have also been used to describe the surface potential of Eq. [91] and concomitant surface charge density; we will use the term "apparent" since its usefulness lies in how Debye–Hückel-like the actual potential appears at large distances from the surface and then in extrapolating the potential back to the surface via Eq. [91].[24] We also choose to avoid any confusion with the "effective" valence introduced earlier. It is important to understand that the apparent charge density has meaning only with respect to an assumed DH solution; it is the actual charge density that should be used in the boundary conditions for the nonlinear Poisson–Boltzmann equation. We also point out that alternative definitions of the apparent charge density are possible, for example, one based on matching DH and PB osmotic pressures at the cell boundary. The lucid review by Levin is particularly recommended.[100]

In Figure 4 this apparent DH potential is compared with the Gouy–Chapman and actual Debye–Hückel potentials for a monovalent electrolyte at two concentrations near a charged plane. The ADH solution does much

better than the DH solution over the entire range and gives a much better, albeit significantly low, estimate of the potential at the surface. The counter- and coion correlation functions for these cases are compared in Figure 5, mirroring the results of Figure 4. In Figure 7, the ADH profile of Eq. [93] (dotted line) for a mixed asymmetric electrolyte, in which an effective valence based on Eq. [69] has been used in Eq. [92], is compared with the PB profile of Eq. [39] (solid line). The long-range agreement between the two profiles is evident.

Using Eq. [11] we can convert Eq. [92] into a relationship between apparent and actual surface charge densities:[101,102]

$$\sigma_{\mathrm{ADH}} = \frac{2\sigma_a}{\sqrt{(\sigma_a/\sigma_0)^2 + 1} + 1} \qquad [94]$$

where we have defined a planar reference density $\sigma_0 \equiv e_0\kappa_D/(2\pi L_B z) = e_0\sqrt{2A_0c^B/\pi L_B}$. Thus, far from the charged plane, the $z:z$ PB solution behaves like the DH solution but in response to an apparent charged density that is smaller than the actual one. Note that for high surface charge densities ($|\sigma_a| \gg \sigma_0$), Eq. [94] reduces to $\sigma_{\mathrm{ADH}} \approx 2S_a\sigma_0$, independent of surface properties and consistent with the analysis of Eq. [35]. We will discuss the planar surface charge density of Eq. [94] later in this tutorial after we have derived its extension to charged cylindrical and spherical surfaces.

We can use Eq. [94] to obtain a condition under which the Debye–Hückel equation may be reliably applied to a planar system. As the ratio of the apparent charge density to the actual charge density approaches unity, the ADH surface potential approaches the PB (and DH) value. If we solve Eq. [94] for the ratio σ_a/σ_0 and, using Eqs. [27] and [11], insert this into the value of the surface potential given by Eq. [28], we obtain the expressions

$$\begin{aligned} \frac{\sigma_a}{\sigma_0} &= \frac{2S_a\sqrt{1 - \sigma_{\mathrm{ADH}}/\sigma_a}}{\sigma_{\mathrm{ADH}}/\sigma_a} \\ z\phi_a &= 4S_a \ln\left(\frac{1 + \sqrt{1 - \sigma_{\mathrm{ADH}}/\sigma_a}}{\sqrt{\sigma_{\mathrm{ADH}}/\sigma_a}}\right) \end{aligned} \qquad [95]$$

Figure 10 displays both functions in Eq. [95] - the ratio σ_a/σ_0 (solid line, top frame) and the surface potential (solid line, bottom frame) as a function of the ratio $\sigma_{\mathrm{ADH}}/\sigma_a$. (We assume that the surface potential is positive, although this does not affect the analysis.) As σ_{ADH} approaches σ_a, the ADH potential approaches the PB potential, implying that the DH equation gives an increasingly more accurate description of the system. Let us assume that we are satisfied with the DH representation if we are within a tolerance limit of $\sigma_{\mathrm{ADH}}/\sigma_a > 0.95$, that is, the apparent charge density is less than 5% smaller

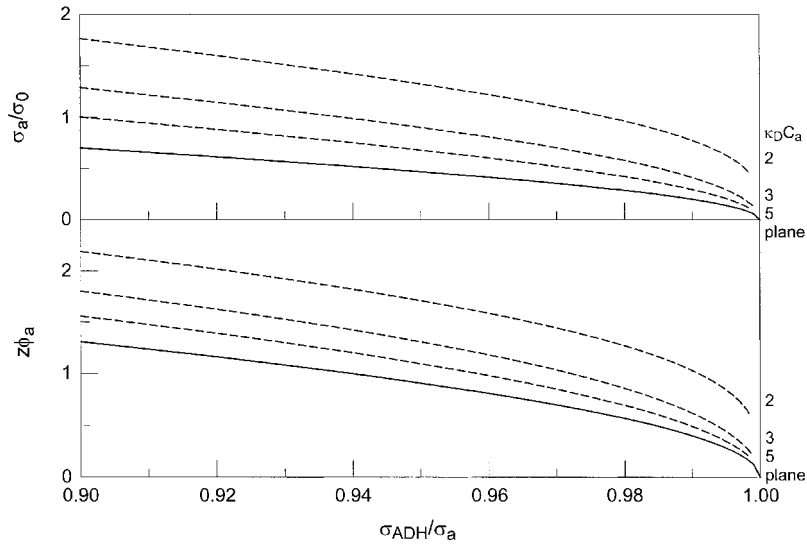

Figure 10 The surface charge density ratio σ_a/σ_0 (top frame) and the surface potential (bottom frame) as a function of the σ_{ADH}/σ_a tolerance limit for planar (solid lines; Eq. [95]) and curved surfaces (dashed lines; numerical inversion of Eq. [322]) for $\kappa_D C_a = 2, 3, 5$.

than the actual charge density. According to Eqs. [95] and Figure 10, we have $z\phi_a < 1$, indicating that for surface potentials less than $k_B T/e_0$, the Debye–Hückel equation is pretty good; we also see that this occurs when $\sigma_a < \sigma_0/2$. The frequently assumed condition $z\phi_a \ll 1$ is therefore much too strict. Thus, assuming that 95% tolerance is adequate, the reliability condition for using the planar ADH profile is the upper bound

$$|\sigma_a| < \frac{\sigma_0}{2} \qquad [96]$$

(Also presented in Figure 10 are results for curved surfaces, discussed later following Eq. [326].)

By comparing the actual charge density to the apparent charge density in Eq. [94], we can define the fraction of surface charge neutralized by counterions, f_{neut}, *according to the apparent Debye–Hückel solution*, as

$$f_{\text{neut}} = 1 - \frac{\sigma_{\text{ADH}}}{\sigma_a} = 1 - \frac{2}{\sqrt{(\sigma_a/\sigma_0)^2 + 1} + 1} \qquad [97]$$

Much more work has been done investigating the relationship between counterion condensation phenomena and the PB equation for charged cylinders

than for planes, so we postpone discussion until later (e.g., see Eqs. [265]–[269] and Figs. 29 and 30).

For planar surfaces in a mixed electrolyte solution, the effective-valence solution of Eqs. [69]–[72] can be used to write the generalization of Eqs. [92] and [94]. In both cases we simply substitute expression [69] for the valence z. The apparent surface charge density is useful since experimental data often describe only the asymptotic environment of a polyelectrolyte. Fitting these data by assuming that the standard Debye–Hückel expression applies may lead to poorer results when extrapolated to the surface; more reasonable results can be obtained by basing this extrapolation instead on the apparent surface charge density. For example, as shown in the following section, the ADH potential can be used to give a quantitative description of the electrostatic interaction energy between two charged plates provided their separation distance is such that Eq. [93] is applicable.

Bulk Model: Two Parallel Charged Surfaces

The case of two charged planar surfaces in equilibrium with a bulk electrolyte is of special interest in biophysics as it represents a model for the interaction of two cellular membranes. Also, the experimental attraction between mica surfaces has been attributed to van der Waals and hydration forces, ion correlations and density fluctuations.[48,49,67] Although it has been shown that the force between any two like-charged particles or surfaces solely within PB theory is necessarily repulsive,[48,75,103–106] the Poisson–Boltzmann equation still serves as the starting point for most investigations into charged surface interactions, including the classic DLVO theory of colloidal stability, identified by the initials of its originators: Derjaguin, Landau, Verwey, and Overbeek.[36,48,49,67] Analytical solutions for the interaction of two charged planar surfaces are available only within Debye–Hückel theory or for the artificial case of no added salt.[93,94] For a single surface, the potential profile and free energy describe the system and are relatively easy to calculate or approximate. For two interacting surfaces it is the force (or pressure) between them that is most often desired. While an adequate approximation to the potential profile can be found simply by adding the individual Gouy–Chapman profiles together (if the surfaces are at least a few Debye lengths apart), this gives no coupling between the individual double layers and the force between the surfaces is zero. The approximations developed below are presented more from a qualitative than a quantitative point of view. The primary purpose for presenting them is to provide some insight into the interaction of two double layers, although for certain systems they should have some practical utility as well.

For two equally charged planar surfaces immersed in a bulk electrolyte and situated in the y–z plane at positions $x = \pm R$, we solve PB equation [14] in the region between the surfaces according to the boundary

conditions

$$\begin{aligned}\phi'(\pm R) &= \pm\frac{2S_R}{\lambda_{GC}}, \quad S_R = \mathrm{sgn}(\sigma_R)\\ \phi'(0) &= 0\end{aligned} \qquad [98]$$

where the normal to each surface is directed into the solution, that is, toward the other surface. In place of Eqs. [16] and [17], we have

$$\phi'(x) = \sqrt{8\pi L_B A_0 \sum_{i=1}^{I} c_i^B [e^{-z_i\phi(x)} - e^{-z_i\phi_0}]} \qquad [99]$$

which gives

$$\int_{\phi_0}^{\phi} \frac{d\phi}{\sqrt{\sum_{i=1}^{I} c_i^B (e^{-z_i\phi} - e^{-z_i\phi_0})}} = -S_R\sqrt{8\pi L_B A_0}\,x \qquad [100]$$

For the standard example of a $z:z$ electrolyte, Eq. [100] becomes

$$\int_{\phi_0}^{\phi} \frac{d\phi}{\sqrt{\cosh(z\phi) - \cosh(z\phi_0)}} = -\frac{S_R\sqrt{2}\kappa_D x}{z} \qquad [101]$$

which can be converted into an incomplete elliptic integral of the first kind.[36,103,107–110] The solution for a mixed 1 : 1–2 : 1 salt was obtained by Ninham and Parsegian[111] and that for dissimilarly charged planes held under either constant potential or constant charge density has been discussed elsewhere.[112–114] The more general and interesting case of charge-regulating surfaces, in which mixed boundary condition BC3 is used, has been the subject of numerous investigations.[115–121] McBroom and McQuarrie have treated the case with different size counter- and coions.[122] Burak and Andelman have incorporated a correction term into the PB equation that accounts for effects due to solvent packing at the surface[123] and Bostrom, Williams and Ninham have shown the importance of including dispersion forces.[124,125]

First, we find the interaction energy between two (unequal) surfaces within the Debye–Hückel approximation. To simplify the notation, consider two surfaces at $x = \pm R$ with charges densities $\sigma(\pm R) \equiv \sigma_\pm$ in equilibrium with a bulk electrolyte. (For the remainder of this section, convenience and correspondence with previous work requires that we work with charge densities instead of Gouy–Chapman lengths.) We solve the DH equation in the region between the surfaces

$$\phi''_{DH}(x) = \kappa_D^2\phi_{DH}(x), \qquad |x| \le R \qquad [102]$$

subject to the boundary conditions

$$\phi'(\pm R) = \frac{\pm 4\pi L_B \sigma_\pm}{e_0} \qquad [103]$$

Assuming a general solution of the form

$$\phi_{\mathrm{DH}}(x) = A_- e^{-\kappa_D x} + A_+ e^{\kappa_D x} \qquad [104]$$

and imposition of the boundary conditions leads to a pair of simultaneous linear equations for coefficients A_- and A_+. Solving these equations gives the DH potential

$$\phi_{\mathrm{DH}}(x) = \frac{4\pi L_B}{e_0 \kappa_D} \frac{\sigma_- \cosh[\kappa_D(R-x)] + \sigma_+ \cosh[\kappa_D(R+x)]}{\sinh(2\kappa_D R)} \qquad [105]$$

with the surface potential

$$\phi_{\mathrm{DH}}(\pm R) = \frac{4\pi L_B}{e_0 \kappa_D} \frac{\sigma_\pm \cosh(2\kappa_D R) + \sigma_\mp}{\sinh(2\kappa_D R)} \qquad [106]$$

Having found the electrostatic potential, we can now obtain the interaction potential per unit area from the electrostatic free energy of charging both surfaces relative to charging the surfaces at infinite separation:

$$V(2R) = A_{\mathrm{el}}(2R) - A_{\mathrm{el}}(\infty) \qquad [107]$$

The electrostatic free energy per unit area is found from Eq. [29]

$$\begin{aligned} \frac{\beta A_{el}(2R)}{\text{Area}} &= \frac{\sigma_- \phi(-R) + \sigma_+ \phi(R)}{2e_0} \\ &= \frac{2\pi L_B}{e_0^2 \kappa_D} \frac{(\sigma_-^2 + \sigma_+^2)\cosh(2\kappa_D R) + 2\sigma_- \sigma_+}{\sinh(2\kappa_D R)} \end{aligned} \qquad [108]$$

with the reference free energy

$$\frac{\beta A_{el}(\infty)}{\text{Area}} = \frac{2\pi L_B}{e_0^2 \kappa_D}(\sigma_-^2 + \sigma_+^2) \qquad [109]$$

With Eqs. [107]–[109] we have the potential per unit area between the surfaces in the low potential limit:[75,113]

$$\frac{\beta V(2R)}{\text{Area}} = \frac{4\pi L_B}{e_0^2 \kappa_D} \frac{e^{-2\kappa_D R}\left(2\sigma_- \sigma_+ + (\sigma_-^2 + \sigma_+^2) e^{-2\kappa_D R}\right)}{1 - e^{-4\kappa_D R}} \qquad [110]$$

Equation [110] shows that the leading term in the potential displays an exponential dependence on surface separation, a result that will appear for other geometries as well. This exponential term combined with a short-range van der Waals attractive term forms the basis for DLVO theory and has considerable experimental support.[36,48,49,67] The (longitudinal) pressure, or force per unit area, between the surfaces can be obtained from Eq. [110] by differentiating the potential with respect to the surface separation $2R$:[75]

$$\begin{aligned}\beta P(R) &= -\beta\frac{dV(2R)}{d(2R)} \\ &= \frac{8\pi L_B}{e_0^2}\frac{e^{-2\kappa_D R}\left(\sigma_-\sigma_+(1+e^{-4\kappa_D R})+(\sigma_-^2+\sigma_+^2)e^{-2\kappa_D R}\right)}{(1-e^{-4\kappa_D R})^2}\end{aligned} \qquad [111]$$

If analytical evaluation of the electrostatic free energy is not possible, an alternative route to the pressure is to add the electric field stress tensor to the osmotic pressure as in Eq. [19] and evaluate their sum (for a bulk $z:z$ electrolyte)[75]

$$\begin{aligned}\beta P(x) &= -\frac{[\phi'(x)]^2}{8\pi L_B}+\frac{\kappa_D^2}{4\pi L_b z^2}[\cosh(z\phi(x))-1] \\ &= \frac{\kappa_D^2}{2\pi L_b z^2}\sinh^2\left(\frac{z\phi(x)}{2}\right)-\frac{[\phi'(x)]^2}{8\pi L_B}\end{aligned} \qquad [112]$$

at one of the surfaces. For our DH case, Eq. [112] simplifies at either boundary to

$$\beta P(\pm R) = \frac{\kappa_D^2}{8\pi L_b}[\phi(\pm R)]^2-\frac{2\pi L_B}{e_0^2}\sigma_\pm^2 \qquad [113]$$

and use of Eq. [106] reproduces Eq. [111].

The exponential term in the denominator of Eq. [110] implies that the energy required to bring the two charged planes together is infinite. In reality, as two charged surfaces approach one another, the initially bound counterions will be adsorbed back on the surfaces. The appropriate boundary condition on each surface is then one of charge regulation rather than constant surface charge density (or constant surface potential)[67] and a different analytical solution follows. At such close distance, however, other factors such as discrete solvent and ion size also come into play. Under the present assumptions ($\kappa_D R > 1$), this term and that within parentheses in the numerator in Eq. [110] make relatively small contributions, thus showing that the potential decreases approximately exponentially with increasing surface separation. The potential is then what one would expect for a single charged plane in the DH-determined electrostatic field of a second surface a distance $2R$ away (a factor

of 2 accounts for the mutual interaction of the surfaces). Note, however, that the restriction is not on the magnitude of the surface potential but on the potential midway between the surfaces; that is, R must be sufficiently large such that the separate potentials effectively add, as implied by the previous statement. This near additivity was noticed by Verwey and Overbeek[36] and explored by Levine and coworkers who termed it the "linear superposition approximation."[126–128] To reiterate what was stated above, use of apparent surface densities reduces the potentials considerably from their Debye–Hückel values (see Figs. 4 and 7) and allows the above estimation of the interaction energy to be used over a much wider separation range. For surfaces with a fixed potential, the effect of ion movement on the electric potential must be taken into account by including the chemical contribution to the free energy.[36] Parsegian and Gingell considered the Debye–Hückel case of two surfaces having different surface charge densities or potentials,[75] and Richmond has discussed systems with arbitrary surface charge densities.[113]

Before displaying the DH potential profile of Eq. [105], let us consider the same system using the PB equation for a bulk $z:z$ electrolyte. In place of Eq. [102] we now want to solve

$$z\phi''(x) = \kappa_D^2 \sinh[z\phi(x)], \qquad |x| \le R \tag{114}$$

subject to Eq. [103]. As mentioned above, even for like surfaces no analytical solution for this coupled Gouy–Chapman system is available except in terms of elliptic integrals. The simplest approximation is to assume that the effect of the surfaces is additive

$$\phi_{\text{add}}(x) = A_-\phi_-(x) + A_+\phi_+(x) \tag{115}$$

where we have defined

$$\frac{z\phi_\pm(x)}{4} = \tanh^{-1}\left(\frac{2\hat{\sigma}_\pm}{\sqrt{4\hat{\sigma}_\pm^2 + 1} + 1} e^{-\kappa_D(R \mp x)}\right) \tag{116}$$

with the *scaled charge densities*

$$\hat{\sigma}_\pm \equiv \frac{\sigma_\pm}{2\sigma_0}, \qquad \sigma_0 \equiv \frac{\kappa_D e_0}{2\pi L_B z} \tag{117}$$

and where each term in Eq. [115] is the individual Gouy–Chapman solution [22] for the appropriate surface (Eqs. [11] and [25] were also used). Determining the coefficients by applying the boundary conditions [103] and retaining

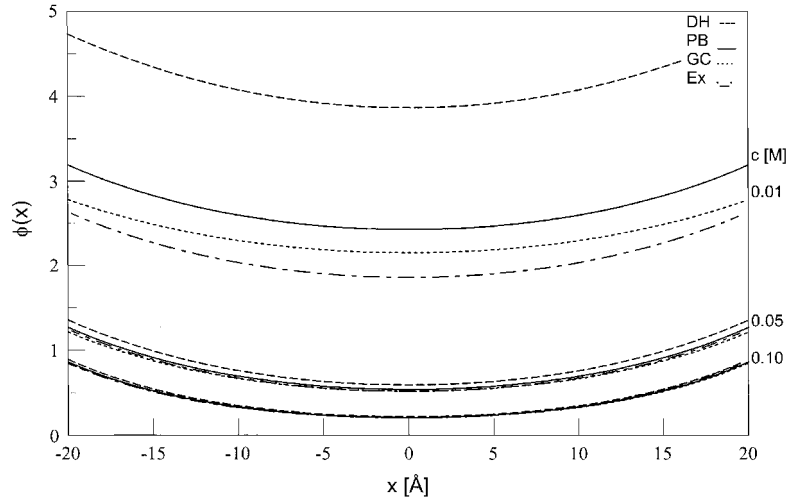

Figure 11 The potential profiles according to the DH (dashed line; Eq. [105]), additive Gouy–Chapman (dotted line; Eq. [115]), and approximate PB (solid line; Eqs. [121] and [125]) expressions are compared with the exact solution (dotted–dashed line; finite-difference method, Eq. [389]) for two charged surfaces with charge densities $\sigma = 0.001$ $e_0/\text{Å}^2$ placed 40 Å apart in a 1 : 1 electrolyte at concentrations of 0.01, 0.05, and 0.1 M.

only the lowest-order terms in $\exp(-\kappa_D R)$ gives

$$A_- = 1 + \frac{2\hat{\sigma}_+/\hat{\sigma}_-}{\sqrt{4\hat{\sigma}_+^2 + 1} + 1} e^{-2\kappa_D R}, \qquad A_+ = 1 + \frac{2\hat{\sigma}_-/\hat{\sigma}_+}{\sqrt{4\hat{\sigma}_-^2 + 1} + 1} e^{-2\kappa_D R} \quad [118]$$

For small charge density and to lowest order in $\exp(-\kappa_D R)$, these coefficients reduce Eq. [115] to the DH potential of Eq. [105]. While this looks promising, coupling the surfaces by letting $A_\pm$ differ from unity does not significantly improve the potential, nor does it allow for a convenient analytical expression for the pressure. However, the additive GC potential is much better than the DH potential of Eq. [105], as can be seen in Figure 11 (a more detailed discussion is presented below). Approximating the pressure by using the potential of Eq. [115] with $A_\pm = 1$, we find that Eq. [112] gives

$$\beta P(x) = \frac{2\kappa_D^2}{\pi L_B z^2} \sinh\frac{z\phi_-(x)}{2} \sinh\frac{z\phi_+(x)}{2} \cosh^2\frac{z\big(\phi_-(x) + \phi_+(x)\big)}{4} \quad [119]$$

The pressure clearly vanishes if the contribution from either surface vanishes, but since Eq. [115] is not the exact solution of PB equation for two surfaces, this expression is not independent of the position x. This can be seen in

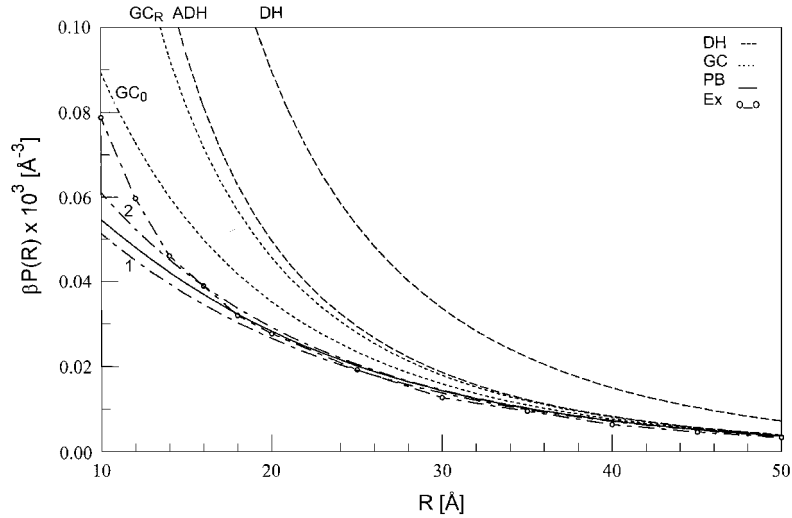

Figure 12 The pressure between two like-charged surfaces for the system shown in Figure 11 with a 0.01 M 1 : 1 electrolyte according to the DH (dashed line; Eq. [111]), additive Gouy–Chapman (dotted lines; Eq. [119]), approximate PB (solid line; Eq. [129]), and exact (finite-difference) solutions (circle–dashed line; Eqs. [112] and [389]); one- and two-term approximate PB results are indicated by dotted–dashed lines.

Figure 12, where a comparison with other results (see below) is presented. For like-charged surfaces, the pressure at the midplane simplifies to

$$\beta P(0) = \frac{\kappa_D^2}{2\pi L_B z^2}\sinh^2(z\phi(0)) = \frac{8\kappa_D^2}{\pi L_B z^2}\left(\frac{2\hat{\sigma}}{\sqrt{4\hat{\sigma}^2+1}+1}\right)^2 e^{-2\kappa_D R} \qquad [120]$$

to lowest order in $\exp(-\kappa_D R)$; this expression is shown below to be correct. We now improve upon the results above.

A similar but better approach to finding an approximate solution to the coupled Gouy–Chapman problem is to compare the single-surface DH solution (Eq. [89]) with Eq. [104] for two surfaces, which suggests that the two-surface Gouy–Chapman solution might be generalized by putting DH solution [104] *inside* the $\tanh^{-1}$ function:

$$\frac{z\phi(x)}{4} = \tanh^{-1}[u(x)] = \tanh^{-1}(A_- e^{-\kappa_D x} + A_+ e^{\kappa_D x}) \qquad [121]$$

where coefficients $A_\pm$ are found by applying boundary conditions [103]. Use of the $\tanh^{-1}$ substitution allows a first-order linearization of the $z:z$ PB equation and will be discussed at length in a later section. Equation [121]

clearly works if the potential is everywhere small since in this case we may replace $\tanh[z\phi(x)/4]$ by $z\phi(x)/4$ and the Debye–Hückel solution of Eq. [105] is obtained. This solution is also expected to be good in the region between the surfaces if the potential there (but not necessarily at the surfaces) is small since now the apparent Debye–Hückel solution holds. The assumption of potential additivity has been used numerous times since Bell, Levine and McCartney applied the "linear superposition approximation" to the calculation of the interaction of two charged spheres.[128] The distinction here is that by applying it *within* the $\tanh^{-1}$ function and applying standard PB boundary conditions (which here are constant surface charge density conditions), we extend the applicability of the potential to smaller plane (or, later, particle) separations and obtain correct expressions for apparent charge densities within the DH approximation at larger separations. This procedure, which we call the "nonlinear Debye–Hückel approximation," is developed more formally in a later section and subsequently applied to interacting cylinders and spheres. It is introduced here to demonstrate its utility with regard to the special case of charged planes. Using $[u(x)]^2 - [u'(x)]^2 = 4A_-A_+$, the approximation potential of Eq. [121] can be shown to satisfy the differential equation

$$z\phi''(x) = \kappa_D^2 \sinh[z\phi(x)] - 4\kappa_D^2 A_- A_+ \left(\sinh[z\phi(x)] + 2\sinh\frac{z\phi(x)}{2} \right) \qquad [122]$$

The solution will therefore be adequate if $|A_-A_+| < 0.01$, say. Since the product $|A_-A_+|$ will be found to behave as $\exp(-2\kappa_D R)$, the leading order term for large $\kappa_D R$ of Eq. [121] can be identified as the asymptotic solution for the interaction of two planar surfaces. Further analysis must await explicit expressions for coefficients $A_\pm$.

Applying boundary conditions [103] to Eq. [121] and using Eqs. [117] leads to the simultaneous equations

$$\hat{\sigma}_- = \frac{A_- e^{\kappa_D R} - A_+ e^{-\kappa_D R}}{1 - (A_- e^{\kappa_D R} + A_+ e^{-\kappa_D R})^2} \qquad [123]$$

and

$$\hat{\sigma}_+ = \frac{-A_- e^{-\kappa_D R} + A_+ e^{\kappa_D R}}{1 - (A_- e^{-\kappa_D R} + A_+ e^{\kappa_D R})^2} \qquad [124]$$

While solving these two equations numerically is trivial, an exact analytical solution in the general case involves the cumbersome task of writing down the roots of two quartic equations. However, for several special cases the solution reduces to two easily solved quadratic equations: $R \to \pm\infty$, $\hat{\sigma}_+ = \pm\hat{\sigma}_-$ and $\hat{\sigma}_- = 0$. Since we already know that the exact solution to

Eqs. [123] and [124] will not give the exact potential profile for the problem at hand (the assumed form of Eq. [121] is not exact), we will be content with an approximation that reduces to the exact solution for the quadratic cases presented above. A little algebra verifies that the following expression satisfies these requirements:

$$A_- = \frac{2(\hat{\sigma}_- + \hat{\sigma}_+ e^{-2\kappa_D R})e^{-\kappa_D R}}{\sqrt{4(\hat{\sigma}_- + 2\hat{\sigma}_+ e^{-2\kappa_D R} + \hat{\sigma}_- e^{-4\kappa_D R})^2 + (1 - e^{-4\kappa_D R})^2} + 1 - e^{-4\kappa_D R}} \quad [125]$$

where A_+ is found by switching $\hat{\sigma}_- \leftrightarrow \hat{\sigma}_+$. (Coefficient A_+ is only approximate for $\hat{\sigma}_- = 0$, but the error in the potential is small.) Using this expression in the error condition $|A_- A_+| < 0.01$ gives a rough range of $\kappa_D R$ for which the predicted potential is close to the actual one:

$$\kappa_D R > \ln\left(\frac{20\sqrt{|\hat{\sigma}_- \hat{\sigma}_+|}}{\sqrt{(2|\hat{\sigma}_-| + 1)(2|\hat{\sigma}_+| + 1)}}\right) \approx \ln\left(\frac{20\,\sigma_{ave}}{2\,\sigma_{ave} + 1}\right) \quad [126]$$

Here the approximate formula holds for surfaces with nearly equal (in magnitude) charge densities and $\sigma_{ave} = \sqrt{|\hat{\sigma}_- \hat{\sigma}_+|}$. The approximate relationship in Eq. [126] is plotted in Figure 13 and shows that the potential profile of Eq. [121] is good for all surfaces separated by at least four Debye lengths.

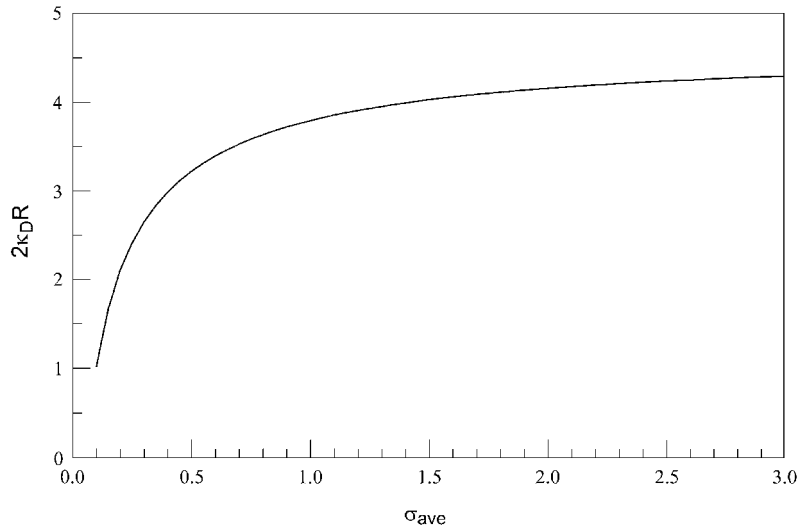

Figure 13 The scaled separation distance $2\kappa_D R$ as a function of the scaled average surface charge density σ_{ave} (Eq. [126]) for which the approximate two-surface potential profile (Eqs. [121] and [125]) is a good solution to the PB equation.

For two highly charged surfaces with $\sigma = 0.01\, e_0/\text{Å}^2$ in a 0.1 M 1 : 1 electrolyte ($\kappa_D = 0.1\,\text{Å}^{-1}$), we have $\sigma_{ave} = 2.16$ giving $2R > 40\,\text{Å}$; for $\sigma = 0.001\, e_0/\text{Å}^2$ we have $2R > 20\,\text{Å}$ or two Debye lengths. At separations much smaller than this, the assumptions of a continuum solvent and point ions are called into question.

In Figure 11, the potential profiles for the DH (Eq. [105]), additive Gouy–Chapman (Eq. [115] with $A_\pm = 1$), approximate PB (Eqs. [121] and [125]) and exact (Eq. [389], below) cases are compared for two surfaces with charge densities $\sigma = 0.001\, e_0/\text{Å}^2$ placed 40 Å apart in a 1 : 1 electrolyte at concentrations of 0.01, 0.05, and 0.1 M (Debye lengths of 30, 14, and 10 Å, respectively). For the separation distance chosen, the approximate PB profile should be good for the latter two electrolyte concentrations according to Eq. [126], in agreement with what is shown. The DH potential lies above the exact potential in all cases and is particularly poor for the lowest concentration. For this case, although the additive GC potential does better than the approximate PB potential, it must be noted that the GC expression predicts zero pressure between the surfaces. The profiles for the same system as Figure 11 but with two oppositely charged surfaces ($\sigma = \pm 0.001\, e_0/\text{Å}^2$) are shown in Figure 14. For the lowest concentration (0.01 M), the additive GC model shows the worst agreement, while the DH profile shows (fortuitously) the best. The approximate PB profile is best for 0.05 M and 0.1 M electrolytes, consistent with the range given by Eq. [126]. For higher charge densities, the analysis still holds, albeit for larger separations.

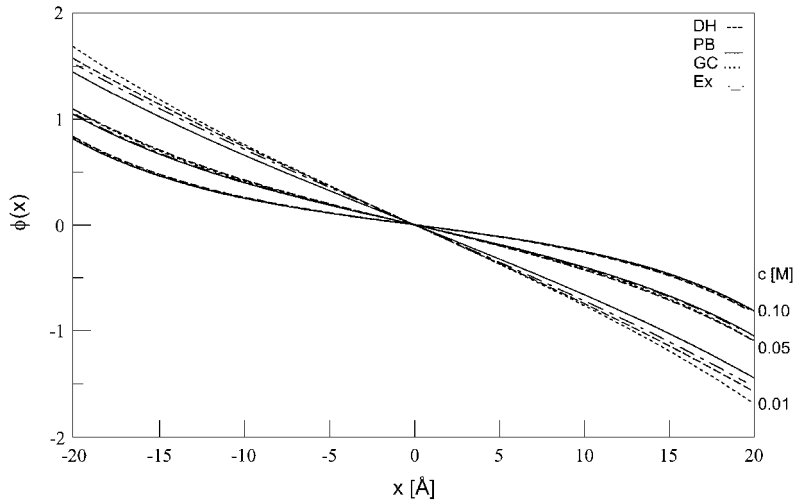

Figure 14 The same potential profile comparison as Figure 11 except for two oppositely charged surfaces with charge densities $\sigma(-R) = 0.001\, e_0/\text{Å}^2$ and $\sigma(R) = -0.001\, e_0/\text{Å}^2$.

For small surface charge densities, Eq. [125] reduces to

$$A_- = \frac{\hat{\sigma}_- + \hat{\sigma}_+ e^{-2\kappa_D R}}{1 - e^{-4\kappa_D R}} \left[1 - \left(\frac{\hat{\sigma}_- + 2\hat{\sigma}_+ e^{-2\kappa_D R} + \hat{\sigma}_- e^{-4\kappa_D R}}{1 - e^{-4\kappa_D R}} \right)^2 + \cdots \right] e^{-\kappa_D R} \quad [127]$$

where inserting the low-order term into Eq. [121] gives the DH profile of Eq. [105]. For large surface separations, we let $R \to \infty$ in Eq. [125] to get the asymptotic (i.e., large R) expansion

$$A_- = \frac{2\hat{\sigma}_- e^{-\kappa_D R}}{\sqrt{4\hat{\sigma}_-^2 + 1} + 1} + \left(3 - \frac{4\hat{\sigma}_-^2 + 3}{\sqrt{4\hat{\sigma}_-^2 + 1}} \right) \frac{\hat{\sigma}_+}{2\hat{\sigma}_-^2} e^{-3\kappa_D R} + \cdots \quad [128]$$

For low charge densities, these two terms reduce to the DH prefactor (without the denominator) of Eq. [127]. We therefore find that not only does the leading term of the coefficients give the correct limiting behavior, but the second-order term does as well. We will thus include it in our analysis of the pressure below, but with the understanding that its specific form will not necessarily match the corresponding term in the exact asymptotic expansion of the correct solution. For large surface separations, the first term of Eq. [128], when combined with Eqs. [11] and [25], reduces Eq. [121] to either the Gouy–Chapman potential of Eq. [22] for a single surface for $x \sim \pm R$ or to the sum of separate ADH potentials (Eq. [93]) where apparent charge densities result from the $\tanh^{-1}$ function chosen for the form of the approximate solution and imposition of the boundary condition. [One can devise an approximate third-order expression that reduces correctly to the DH potential and accounts for the infinite repulsion of like surfaces as $\kappa_D R \to 0$ by dividing the two terms of Eq. [128] by $1 - f(\hat{\sigma}_-)\exp(-4\kappa_D R)$, where $f(\hat{\sigma}_-)$ is the prefactor of $\hat{\sigma}_+ \exp(-3\kappa_D R)$, but $f(\hat{\sigma}_-)$ is generally too large—it is unity in the DH approximation. The same problem occurs if the next-order term in Eq. [128] is used; in this case, $f(\sigma)$ depends on both surface charge densities, which is undoubtedly true.]

The approximate PB profile of Eq. [121] with Eq. [125] is too complicated to allow analytical evaluation of the electrostatic free energy from Eq. [29] (or Eq. [395], below) but calculation of the pressure from Eq. [122] is straightforward. Multiplying Eq. [122] by $\phi'(x)$, integrating from one surface (say, R) to infinity and substituting in Eq. [121], we find

$$\beta P(R) = \frac{8\kappa_D^2}{\pi L_B z^2} A_-(R) A_+(R) \quad [129]$$

where we have indicated an explicit dependence of the coefficients of Eq. [125] on R. The prefactor in Eq. [129] can be simplified to $64A_0c$, where c is the

concentration of electrolyte in M and $A_0 = 6.022 \times 10^{-4} \mathrm{M}^{-1}\,\mathrm{\AA}^{-3}$. Combining this with the error condition on the approximation shows that the profile and pressure are good provided the pressure between the surfaces is small: $|\beta P(R)| < 0.64\, A_0 c$. The pressure is obviously symmetric in the individual surface charge densities, as it must be, and independent of position since we have used Eq. [122] instead of Eq. [114] (or equivalently Eq. [112]). Because our approximate solution holds for surfaces at least a few Debye lengths apart (unless the charge densities are so small that the Debye–Hückel approximation applies), we will consider only the asymptotic form of the coefficients, as given by Eqs. [128]. This gives the following asymptotic form of the pressure

$$\beta P(R) = \frac{8\kappa_D^2}{\pi L_B z^2}\left[\hat{s}_-\hat{s}_+ e^{-2\kappa_D R} + \left(\frac{\hat{s}_-^2(1-3\hat{s}_+^2)(1-\hat{s}_+^2)}{(1-\hat{s}_-^2)(1+\hat{s}_+^2)} + \frac{\hat{s}_+^2(1-3\hat{s}_-^2)(1-\hat{s}_-^2)}{(1-\hat{s}_+^2)(1+\hat{s}_-^2)}\right)e^{-4\kappa_D R}\right] \quad [130]$$

where

$$\hat{s}_\pm \equiv \frac{2\hat{\sigma}_\pm}{\sqrt{4\hat{\sigma}_\pm^2 + 1} + 1} \quad [131]$$

are the *scaled apparent Debye–Hückel surface densities*. The first term is seen to be identical to that of the Debye–Hückel pressure of Eq. [111] with apparent charge densities of Eq. [94] replacing actual charge densities at large surface separations and, for like surfaces, agrees with the previous approximation of Eq. [120]. The second term, however, matches the DH term only for small charge densities, so a simple generalization of the DH pressure obtained by inserting apparent charge densities for actual ones fails beyond the first term.

To make the discussion more explicit, consider Figures 12 and 15, in which the pressure according to the DH (Eq. [111]), additive GC (Eq. [119]) and approximate PB (Eqs. [129] and [130]) expressions are compared with finite-difference values (Eqs. [112] and [389]) for the same systems as Figures 11 and 14. Only data for the 0.01 M electrolyte case with oppositely charged surfaces is shown; agreement is better for the 0.05 M and 0.1 M cases. Focusing first on the data for a 0.01 M electrolyte with like-charged surfaces (Fig. 12), the exact values are shown by the circle–dashed line. The standard DH results (dashed line) give much too high a pressure as expected. Using apparent charge densities in place of actual ones gives the dashed curve marked "ADH" which lies closer to the exact data. The additive GC pressure evaluated either at a surface ("GC_R") or the dividing plane ("GC_0") is better than the DH or ADH pressure but still fails at relatively large separations. The approximate PB pressure shows good agreement except for very small separations and is much better than either the DH or GC pressures. Retaining only the first term of the approximate PB pressure in Eq. [130] produces dotted

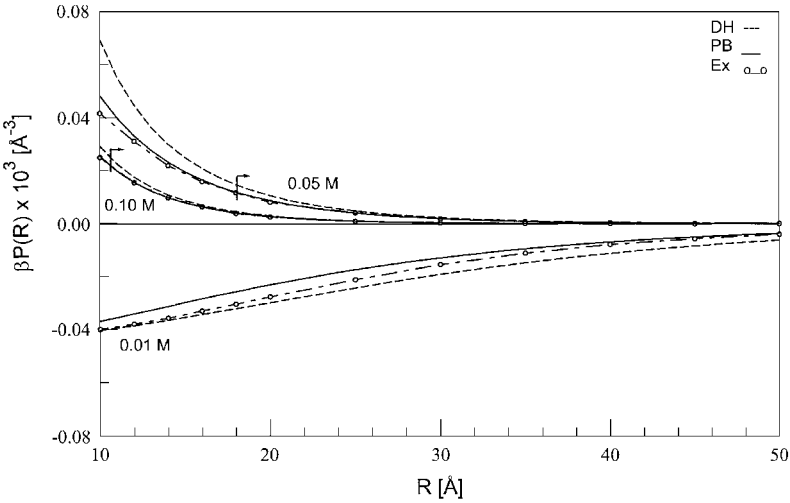

Figure 15 The pressure between two charged surfaces for the same systems as shown in Figures 11 and 14 according to the DH (dashed line; Eq. [111]), approximate PB (solid line; Eq. [129]) and exact (finite-difference) solutions (circle–dashed line; Eqs. [112] and [389]). Only the 0.01 M electrolyte case for oppositely charged surfaces is shown.

curve *1* just below the solid line corresponding to Eq. [129]; retaining two terms in Eq. [130] produces dotted curve *2* just above the solid line. Thus, even the first term of an asymptotic expansion [130] is remarkably accurate. (These remarks also apply to the use of one- and two-term approximations for the coefficients in the potential.) Both the PB and DH pressures are good for oppositely charged surfaces. This is because the double layers of oppositely charged surfaces tend to self-neutralize and hence decrease the magnitude of the potential between the surfaces below the corresponding like-surface values (of Figs. 11 and 14). Thus, conclusions drawn by Parsegian and Gingell using DH theory on the restrictions on the ratio of the charge densities for attraction and repulsion between unlike surfaces are not likely to be significantly affected by the nonlinear PB results derived here.[75]

The range of pressures that are valid according to Eq. [126] is shown in Figure 15 by the arrows for the like-charged 0.05 M and 0.1 M cases ($R > 18\,\text{Å}$ and $R > 10.6\,\text{Å}$). It is seen that the range is overly restrictive and is more appropriate for the validity of the DH pressure; the restriction on the pressure ($|\beta P(R)| < 0.64\,A_0 c$) is a better measure of the approximate PB range. A final comment needs to be made concerning our treatment only of surfaces held at constant charge density. Modifying the boundary conditions to address surfaces at constant potential is straightforward and should also extend the range of applicability since the case of constant charge density provides an upper bound to the charge-regulated case, which,

in turn, lies above the constant potential case.[120] Behrens and Borkovec have suggested a method by which the fixed charge density and fixed surface potential results can be used to estimate the pressure between charge-regulated surfaces.[120]

Having obtained the pressure (force per unit area), we may now work backward using the first of Eqs. [111] to find the potential per unit area via quadrature:

$$\begin{aligned}\frac{\beta V(2R)}{\text{Area}} &= 2\beta \int_R^\infty P(R^*)dR^* \\ &= \frac{16\kappa_D^2}{\pi L_B z^2}\int_R^\infty A_-(R^*)A_+(R^*)dR^*\end{aligned} \quad [132]$$

While the integral in Eq. [132] is easily evaluated numerically using Eq. [125] for the coefficients, the asymptotic form [128] should be almost as accurate and provides an analytical expression for the interaction potential:

$$\begin{aligned}\frac{\beta V(2R)}{\text{Area}} = \frac{4\kappa_D}{\pi L_B z^2}\Bigg[&2\hat{s}_-\hat{s}_+ e^{-2\kappa_D R} \\ &+ \left(\frac{\hat{s}_-^2(1-3\hat{s}_+^2)(1-\hat{s}_+^2)}{(1-\hat{s}_-^2)(1+\hat{s}_+^2)} + \frac{\hat{s}_+^2(1-3\hat{s}_-^2)(1-\hat{s}_-^2)}{(1-\hat{s}_+^2)(1+\hat{s}_-^2)}\right)e^{-4\kappa_D R}\Bigg]\end{aligned} \quad [133]$$

The first term in Eq. [133] is also what one would find from classical electrostatics for the energy of a plane with charge density $\hat{s}_-$ in the presence of the Debye–Hückel potential due to a second plane with charge density $\hat{s}_+$ at a distance $2R$. The electrostatic free energy is now found from the interaction potential and Eq. [107]

$$A_{\text{el}}(2R) = V(2R) + A_{\text{el}}(\sigma_-) + A_{\text{el}}(\sigma_+) \quad [134]$$

where all quantities are per unit area and the single-surface free energies $A_{\text{el}}(\sigma_\pm)$ are given by (see Eq. [30])

$$\frac{\beta A_{\text{el}}(\sigma_\pm)}{\text{Area}} = \frac{\kappa_D}{\pi L_B z^2}[p\ln(p+q)+1-q], \quad p \equiv 2\hat{\sigma}_\pm, \quad q \equiv \sqrt{1+p^2} \quad [135]$$

As with the case of a single surface immersed in a mixed electrolyte, one may apply these expressions to two surfaces in a bulk mixed electrolyte by using the effective valence of Eq. [69] but with the proviso that Eq. [69] was derived based on the analytical solutions for single surfaces.

Related Planar Calculations

The above-derived analytical solutions are based on a number of simplifying assumptions that are required in order to obtain simple expressions for

the potential profile. Some of these assumptions have to do with the derivation of the Poisson–Boltzmann equation in general and will be discussed later, but other assumptions are made merely for analytical simplicity; the most relevant are (1) all ions have the same radius a, (2) the charge surface is perfectly planar, and (3) the surface charge is distributed uniformly. Counterions of different size may be treated by introducing a different Stern layer for each ion and solving the Poisson–Boltzmann equation within each region, matching the potential and its slope at each boundary.[81,129] Alternatively, competition between mono- and divalent counterions[130] may be studied by assuming that divalent counterions condense onto the surface while monovalent ions remain solvated.[131] Borukhov, Andelman and Orland have derived a modified Gouy–Chapman equation that accounts for steric packing of large counterions at highly charged surfaces.[132,133] If the average surface curvature is planar but with an undulating height to describe surface roughness, the Debye–Hückel equation may be used to determine the effect of roughness on the potential profile and the electrostatic free energy.[134] One effect of surface roughness is to give the appearance of local variations in the surface charge density.[135]

In addition to adding surface roughness, a more accurate model of membranes would be to replace the constant surface charge density assumption with an array of discrete surface charges. Close to the surface (within a Debye length), the electrostatic potential due to discrete charges may deviate considerably from that based on a constant surface charge density.[136–140] It may also be necessary to account for charge regulation whereby the magnitude of the surface potential affects the degree of dissociation of charged surface groups. The boundary condition appropriate under these circumstances is the mixed condition BC3.[111,141,142] The GC model applied to one side of a charged surface may also be extended to treat both sides of a planar bilayer system.[143–145] This leads naturally to the case of ion-penetrable membranes in which some or all species may diffuse across a uniformly charged surface.[146–153]

In other work on planar interactions, Trizac and Hansen have used the DH cell model to study the free-energy and counterion/coion distributions for square platelets.[154,155] Ettelaie and Buscall[119] and Ohshima[156] have obtained an analytical solution for the interaction of two charged surfaces using the Poisson–Boltzmann equation when the surfaces are close, and Chan has devised a simple algorithm for a system in an asymmetric electrolyte.[157]

Curved Surfaces: Cylinders and Spheres

The analytical solution to the Gouy–Chapman equation has proved to be particularly useful in understanding the behavior of ions at charged planar surfaces. Although most biological surfaces are not planar, they can be treated as such if both the Debye length and the distance from the surface are much smaller than the local radius of curvature. Unfortunately, two especially relevant biological systems, micelles and extended lengths of DNA, rarely behave as

planar surfaces. To understand clearly how the surface curvature of charged spheres and cylinders alter predictions of the Gouy-Chapman equation, an analytical solution to the PB equation for these geometries is needed. Some qualitative insight can be obtained by solving the Debye–Hückel equation for these systems, but a detailed investigation requires knowledge of the nonlinear potential. While no exact analytical solution to the (one-dimensional) cylindrical and spherical PB equations has been found, two accurate approximate expressions for a $z:z$ electrolyte can be derived: one based on a perturbation expansion of the planar GC solution and a second obtained by "nonlinearizing" the Debye–Hückel potential.

Bulk Model: Perturbed Gouy–Chapman Approximation

Initial work on solving the PB equation for curved surfaces in the presence of an electrolyte primarily dealt with matching "inner" and "outer" region solutions[158,159] or by defining upper and lower bounds.[160–164] Despite the lack of "clean" analyticity, these approaches give accurate results for a wide range of system parameters such as radius of curvature and electrolyte concentration. An alternative asymptotic expansion procedure has been applied more often since it provides a single expression for the PB potential and its range of applicability includes model representations of DNA. In this method the planar Gouy–Chapman solution is used as a first-order approximation to systems with a slightly curved boundary.[165–171]

Consider now the one-dimensional bulk PB equation (in d dimensions) that corresponds to the Debye–Hückel equation [76]:[165,166]

$$\phi''_{\mathrm{PB}}(r) + \frac{d-1}{r}\phi'_{\mathrm{PB}}(r) = C(\phi_{\mathrm{PB}}) \equiv -4\pi L_B A_0 \sum_{i=1}^{I} c_i^B z_i e^{-z_i \phi_{\mathrm{PB}}(r)} \qquad [136]$$

Designating the known planar ($d = 1$) solution to Eq. [136] (e.g., Eq. [26]) by $\phi_0(r)$, we can express an approximate first-order solution for $d > 1$ as a perturbation expansion in $1/r$

$$\phi_{\mathrm{PB}}(r) = \phi_0(r) + \frac{\phi_1(r)}{r} \qquad [137]$$

where the first-order correction $\phi_1(r)$ is subject to the conditions

$$\phi_1(a) = 0 \quad \text{and} \quad \phi_1(\infty) = 0 \qquad [138]$$

Inserting this assumed solution into Eq. [136] and retaining terms of order lower than $1/r$, we find

$$\phi''_1(r) = \frac{dC(\phi_0)}{d\phi_0}\phi_1(r) - (d-1)\phi'_0(r) \qquad [139]$$

where the assumption that $\phi_1(r)/\kappa_D r$ is small compared to $\phi_0(r)$ allows the approximation

$$\begin{aligned} C(\phi_{PB}) - C(\phi_0) &= C(\phi_0 + \phi_1/r) - C(\phi_0) \\ &\approx \frac{dC(\phi_0)}{d\phi_0}\frac{\phi_1}{r} \end{aligned} \qquad [140]$$

We note that for the spherical case of $d = 3$, the only approximation in Eq. [139] is use of Eq. [140]. Thus, the solution developed below will be "almost exact" for a sphere, numerically as well as analytically, and we will see that the asymptotic form of the solution exactly matches the spherical Debye–Hückel potential. For the cylindrical case, however, Eq. [139] can be justified only on numerical grounds since the asymptotic solution should behave as a sum of modified Bessel functions.[172] To put Eq. [139] into a form more amenable to solution, we temporarily change variables from r to ϕ_0 and introduce the following substitutions

$$\begin{aligned} D_0(\phi_0) &\equiv \kappa_D^{-2}\frac{dC(\phi_0)}{d\phi_0},\ E_0(\phi_0) \equiv \kappa_D^{-1}\phi_0'(r) \\ \frac{d}{dr} &= \kappa_D E_0(\phi_0)\frac{d}{d\phi_0} \\ \phi_1(r) &= \kappa_D^{-1}E_0(\phi_0)f(\phi_0) \end{aligned} \qquad [141]$$

to find

$$E_0^2\frac{d^2f(\phi_0)}{d\phi_0^2} + 3E_0E_0'\frac{df(\phi_0)}{d\phi_0} + \left(E_0E_0'' + E_0'^2\right)f(\phi_0) = D_0f(\phi_0) - (d-1) \qquad [142]$$

Specializing to a $z:z$ electrolyte, we have $C(\phi_0) = \kappa_D^2\sinh(z\phi_0)/z$ and

$$\begin{aligned} D_0(\phi_0) &= \cosh(z\phi_0), \\ E_0(\phi_0) &= -2\,z^{-1}\sinh\frac{z\phi_0}{2} \end{aligned} \qquad [143]$$

so that Eq. [142] becomes

$$\sinh^2(y)\frac{d^2f(y)}{dy^2} + 3\sinh(y)\cosh(y)\frac{df(y)}{dy} + (d-1) = 0 \qquad [144]$$

where we have introduced $y(r) = z\phi_0(r)/2$. Equation [144] is a first-order linear differential equation in $f'(y)$ and has the solution

$$\begin{aligned} f'(y) &= c_1 e^{\psi(y)} - (d-1)e^{\psi(y)} \int e^{-\psi(y)} \mathrm{csch}^2(y) dy \\ \psi(y) &= -3 \int \coth(y) dy \end{aligned} \quad [145]$$

where c_1 is an integration constant. After performing the integrations in Eq. [145], followed by a second integration to get $f(y)$, we have

$$f(y) = -(c_1/2)\left(\ln\left[\tanh\left(\frac{y}{2}\right)\right] + \frac{\cosh(y)}{\sinh^2(y)} \right) + \left(\frac{d-1}{2}\right)\coth^2(y) + c_2 \quad [146]$$

where c_2 is a second integration constant. To evaluate c_1 and c_2, we apply conditions [138]; this gives $c_1 = d - 1$ and, after some algebra, the following expression for the potential:

$$\phi_{\mathrm{PB}}(r) = \phi_0(r) + \frac{2a}{z\kappa_D C_a r}\left(\frac{u(r)}{1-[u(r)]^2}\right)\left[2\ln(u(r)/u_a) - [u(r)]^2 + u_a^2\right] \quad [147]$$

where

$$u(r) \equiv \tanh\frac{z\phi_0(r)}{4}, \quad u_a = u(a) \quad [148]$$

$\phi_0(r)$ is given by Eq. [23] or [26], and we have introduced the radius of curvature C_a (which defines either the radius of a sphere or the diameter of a cylinder). We have used the identity $2\cosh(y)[\cosh(y) - 1] = [\cosh(y) - 1]^2 + \sinh^2(y)$.

The surface potential is found using a generalization of Grahame's equation [25] obtained by applying Eq. [15]:

$$\frac{z S_a}{\kappa_D \lambda_{\mathrm{GC}}} = \sinh\left(\frac{z\phi_a}{2}\right) + \frac{2}{\kappa_D C_a}\tanh\left(\frac{z\phi_a}{4}\right) \quad [149]$$

Additional expressions for the surface potential correct up to second- and higher-orders in $\kappa_D C_a$ for cylinders[171,173] and spheres[168,171,173] have also been derived and detailed discussions of the error in truncating the asymptotic expansion have been given.[168,173,174] Ohshima has obtained a relation similar to Eq. [149] but more complicated and specifically for cylinders.[175] Equation [149] is accurate if the correction term (the second) is small compared to the

first; for small surface potentials, we have $\kappa_D C_a \gg 1$, while for large surface potentials, $\kappa_D C_a > 1$ suffices. For charged spheres (owing to the cancellation of terms in arriving at Eq. [139]), the latter condition is quite good even for moderate surface potentials. Using Eq. [149] in Eq. [29], we have the electrostatic component of the free energy for a curved surface:

$$\frac{\beta A_{\text{el}}}{\text{Area}} = \frac{\kappa_D}{\pi L_B z^2}\left[y_a\left(\sinh(y_a) + \frac{2}{\kappa_D C_a}\tanh\frac{y_a}{2}\right) + 1 - \cosh(y_a) - \frac{4}{\kappa_D C_a}\ln\left(\cosh\frac{y_a}{2}\right)\right] \quad [150]$$

where $y_a \equiv z\phi_a/2$. Defining as before $p \equiv z/\kappa_D\lambda_{\text{GC}}$ and $q \equiv \sqrt{1+p^2} = \cosh(y_a)$, where the latter equality holds to first-order in $1/\kappa_D C_a$ since $\cosh(y)$ is an even function of y, Eq. [150] reduces to

$$\frac{\beta A_{\text{el}}}{\text{Area}} = \frac{\kappa_D}{\pi L_B z^2}\left[p\ln(p+q) + 1 - q - \frac{2}{\kappa_D C_a}\ln\left(\frac{q+1}{2}\right)\right] \quad [151]$$

Higher-order corrections to Eq. [151] have also been derived[168,171,174] and used to investigate the elasticity of curved membranes[171] and the adsorption of monovalent ions in thin, curved double layers.[174]

Inserting Eq. [26] for the planar solution into Eq. [147] gives the final result for the potential profile in the presence of a slightly curved charged surface with a bulk $z:z$ electrolyte:

$$z\phi_{\text{PGC}}(r) = -2S_a\ln\left(\tanh\frac{\kappa_D(r-a+\delta_{\text{DGC}})}{2}\right) + \frac{S_a a}{2\kappa_D C_a r}\frac{\exp(-2\kappa_D\delta_{\text{DGC}}) - \exp(-2\kappa_D(r-a+\delta_{\text{DGC}})) - 2\kappa_D(r-a)}{\sinh(\kappa_D(r-a+\delta_{\text{DGC}}))} \quad [152]$$

with the value at the surface given by

$$z\phi_a = -2S_a\ln\left(\tanh\frac{\kappa_D\delta_{\text{DGC}}}{2}\right) \quad [153]$$

Because the Gouy–Chapman potential was used as the low-order term in a perturbative expansion, Eq. [152] will be referred to as the *perturbed Gouy–Chapman* (PGC) solution for a curved surface. [Loeb, Overbeek and Wiersma refer to approximations using the Gouy–Chapman solution as a reference as "flat-plate" approximations.[176] While both the PGC and the nonlinear Debye–Hückel (NLDH) approximation of the following section are exact for flat plates, their range of applicability is quite different. In fact, the NLDH solution also becomes good for surfaces with vanishingly small radii of curvature. We thus apply more distinctive names to reflect this.]

The PGC expression for the Debye-Gouy-Chapman length follows from Eqs. [149] and [153]:

$$\sinh(\kappa_D \delta_{\mathrm{DGC}}) = \frac{\kappa_D \lambda_{\mathrm{GC}}}{z}\left[1 + \frac{1}{\kappa_D C_a}\left(1 - e^{-2\kappa_D \delta_{\mathrm{DGC}}}\right)\right] \qquad [154]$$

Thus, for a fixed surface charge density, a sphere of radius 20 Å and a cylinder of radius 10 Å have the same surface potential according to Eq. [154]. This was observed numerically by Guéron and Weisbuch in their PB investigation comparing counterion condensation around a sphere and a cylinder.[177] Considering the non-planar term on the right-hand side of Eq. [154] to be a correction, which will often suffice, we can replace δ_{DGC} in it by the planar value given in Eq. [27] to obtain the approximate expression

$$\kappa_D \delta_{\mathrm{DGC}} \approx \sinh^{-1}\left(\frac{\kappa_D \lambda_{\mathrm{GC}}(1+f)}{z}\right) \qquad [155]$$

where f represents the correction due to surface curvature

$$f = \frac{2}{\kappa_D C_a\left(1 + \sqrt{1 + (z/\kappa_D \lambda_{\mathrm{GC}})^2}\right)} \qquad [156]$$

The range of accuracy given in Eq. [155] is found by requiring that f be small. Equations [152]–[155] represent a good approximation to the actual potential profile provided the correction terms to the planar solution are small.

Equation [154] will be a good approximation to the actual surface potential, provided the term accounting for surface curvature is small; this implies $\pi L_B z C_a |\sigma_a| \gg 1$. Combining this with the restriction that f also be small ($\kappa_D C_a > 1$) gives a rough indication of the conditions under which Eq. [152], when used with Eq. [155], is reliable:

$$\kappa_D C_a > \sqrt{2\pi\left|\frac{\sigma_0}{\sigma_a}\right|}, \qquad \sigma_0 \equiv \frac{e_0 \kappa_D}{2\pi L_B z} \qquad [157]$$

Although Eq. [157] has not been derived on strict mathematical grounds, we will find that it is, in fact, a good measure of reliability. In Figure 16 we give the minimum values of the radius of curvature as a function of surface charge density for several $z:z$ electrolyte concentrations for which the PGC potential profile of Eqs. [152] and [155] is accurate to within a few percent. Equation [157] will be consulted periodically to verify the range of applicability of results based on Eq. [152].

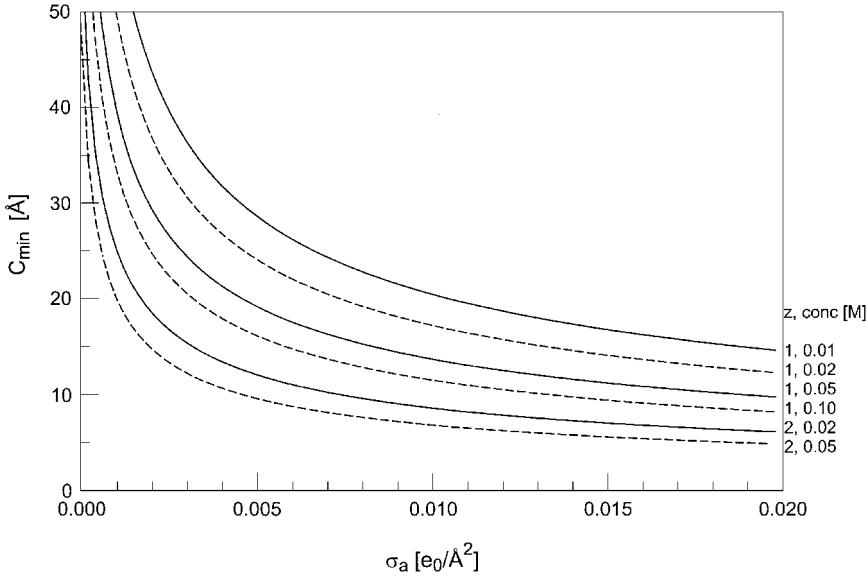

Figure 16 The minimum radius of curvature (in Å) for which the potential profile given by Eq. [152] may be considered reliable is shown as a function of the surface charge density (in $e_0/\text{Å}^2$) for several concentrations of mono- and divalent $z:z$ electrolytes according to Eq. [157]; the electrolyte valence and concentrations for each curve are listed at the right.

An alternative error estimate describing the entire potential profile can be found by multiplying both sides of Eq. [136] by r^{d-1} and integrating from the charged boundary to infinity. The left-hand side reduces to the electrostatic field at the surface and the right-hand side gives the total integrated ion density, that is, the total charge. For the exact solution this expression is simply a reflection of Gauss' law; for an approximate solution, there is some deviation. We may thus define an error value by

$$\text{Error} = \left|\frac{\sigma_0}{2\sigma_a}\right| \int_{X_a}^{\infty} (x/X_a)^{d-1} \sinh[z\phi(x)]dx - 1 \qquad [158]$$

where we have specialized to a $z:z$ electrolyte and introduced the scaled variables $x = \kappa_D r, X_a = \kappa_D a$, and $|\sigma_a/\sigma_0| = z/\kappa_D\lambda_{GC}$. For a planar surface, Eq. [158] can be evaluated analytically to give Error $= 0$; any deviation from zero is a measure of the accumulated difference between the approximate potential and the exact potential. Figures 17 and 18 show Error for a charged cylinder and sphere, respectively, as a function of $\kappa_D a$ for several values of σ_a/σ_0 for the approximate (Eqs. [152] and [155]) and exact (Eqs. [152] and [154]) PGC potential. The maximum value chosen for $\kappa_D a (= 3)$ corresponds

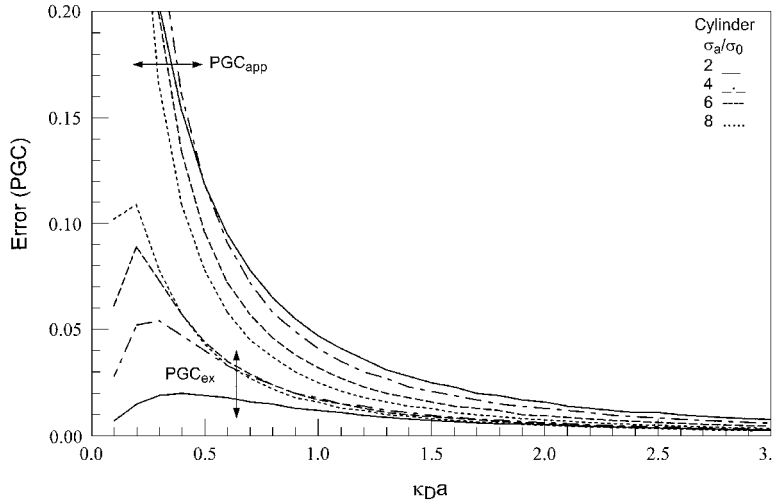

Figure 17 The error in the PGC solution of Eq. [152] according to Eq. [158] for a cylinder as a function of the scaled radius $\kappa_D a$ for several values of the scaled surface charge density σ_a/σ_0; curves obtained using the exact (Eq. [154]) and approximate (Eq. [155]) Debye–Gouy–Chapman lengths are grouped by arrows.

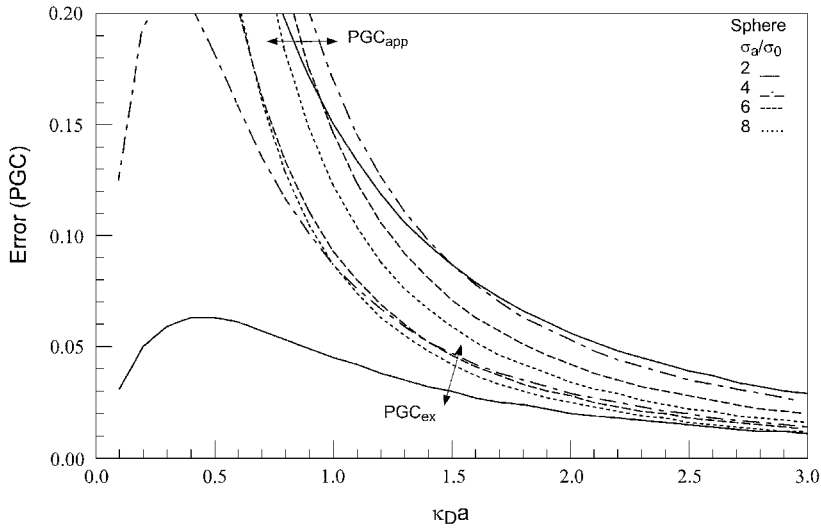

Figure 18 The error in the PGC solution of Eq. [152] according to Eq. [158] for a sphere as a function of the scaled radius $\kappa_D a$ for several values of the scaled surface charge density σ_a/σ_0; curves obtained using the exact (Eq. [154]) and approximate (Eq. [155]) Debye–Gouy–Chapman lengths are grouped by arrows.

to a cylinder of radius 30 Å in a 0.1 M monovalent salt or a 15 Å cylinder in mixed 1:1-2:1 salts of 0.1 M each. The maximum range on σ_a/σ_0 (= 8) corresponds to the same salt conditions for a surface with charge density $\sigma_a = 0.02e_0/\text{Å}^2$. The data for the approximate and exact PGC potentials are grouped by double-ended arrows; multiplication by 100 would indicate the error on a percentage scale, with 5% (Error < 0.05) being good agreement between the approximate and exact potentials. For the same parameter values, the error for each potential for a cylinder is less than that for a sphere in part because a cylinder is more "planelike" than a sphere. Figure 17 shows that a 5% error for the approximate PGC potential obtains for $\kappa_D a > 1$; the error for the exact potential is only ~2% or less. For $\kappa_D a < 1$, the error in the approximate potential grows without bound owing to the inappropriateness of replacing Eq. [154] with Eq. [155]. The exact potential does better for cylinders with small radius (or low ionic strength) but the error in this region increases dramatically for low surface charge densities. The picture for charged spheres, shown in Figure 18, offers the same analysis, but at larger radii ($\kappa_D a > 2$). The relatively slow improvement toward larger $\kappa_D a$ values is indicative of solutions based on an asymptotic expansion.

Bulk Model: Nonlinearizing the Debye–Hückel Solution

The preceding perturbation solution to the PB equation for curved surfaces, although exact up to the specified power of the expansion parameter $1/\kappa_D r$, becomes increasingly unreliable as this parameter approaches unity. It is also difficult to extend to many-particle systems, so an alternative method of solution is desirable. As shown above for a charged plane, the Debye–Hückel solution can be obtained in one of two ways: by solving the linear DH equation or by linearizing the PB solution. We might therefore ask: Since we can't find an exact solution to the nonlinear PB equation for a curved surface, might we be able to find a useful approximation by "nonlinearizing" the easily obtainable linear solution? We would also want the approximation to reduce to the exact planar solution in the appropriate limit. A clue to our approach is to be found by noticing that the decay dependence on the right-hand side of the Gouy–Chapman solution (Eq. [22]) is identical to that of the DH potential (Eq. [32]). Thus, taking the $\tanh^{-1}$ of both sides of Eq. [22] (to obtain the PB potential) performs a "nonlinearization" of the linear solution and is analogous to the approach used previously for two interacting charged planes (e.g., Eq. [121]). We expect that this nonlinearization, while exact in the limit of a charged plane or small surface charge density, will only approximate the effect for a general curved surface. This justification is merely the other side of the coin presented earlier, that is, use of the $\tanh^{-1}$ function performs a partial linearization of the $z:z$ PB equation.

While some progress can be made for a general electrolyte, we expedite matters by starting with Eq. [136] for a $z:z$ salt and rely on an effective valence for other cases. We first consider the PB equation for an isolated

charged particle in contact with a bulk electrolyte:

$$\phi''_{\mathrm{PB}}(r) + \frac{d-1}{r}\phi'_{\mathrm{PB}}(r) = z^{-1}\kappa_D^2 \sinh[z\phi_{\mathrm{PB}}(r)] \qquad [159]$$

subject to the usual conditions

$$\phi'_{\mathrm{PB}}(a) = \frac{-2S_a}{\lambda_{\mathrm{GC}}}, \quad \phi'_{\mathrm{PB}}(\infty) = 0 \qquad [160]$$

We assume a solution of the form

$$\frac{z\phi_{\mathrm{PB}}(r)}{4} = \tanh^{-1}[u(r)] \qquad [161]$$

which, when put into Eq. [159], gives

$$u''(r) + \frac{d-1}{r}u'(r) = \kappa_D^2 u(r) + \frac{2u(r)}{1-[u(r)]^2}\left(\kappa_D^2[u(r)]^2 - [u'(r)]^2\right) \qquad [162]$$

subject to

$$\frac{u'(a)}{1-[u(a)]^2} = \frac{-zS_a}{2\lambda_{\mathrm{GC}}}, \quad u'(\infty) = 0 \qquad [163]$$

Noticing that the terms in Eq. [162] linear in $u(r)$ correspond exactly to the DH equation, we further specify that the solution takes the form

$$u(r) = u_0(r) + v(r) \qquad [164]$$

where $u_0(r)$ and $v(r)$ obey

$$\begin{aligned} u_0''(r) + \frac{d-1}{r}u_0'(r) &= \kappa_D^2 u_0(r) \\ \frac{u_0'(a)}{1-[u_0(a)]^2} &= \frac{-zS_a}{2\lambda_{\mathrm{GC}}}, \quad u_0'(\infty) = 0 \end{aligned} \qquad [165]$$

and

$$\begin{aligned} v''(r) + \frac{d-1}{r}v'(r) &= \kappa_D^2 v(r) + \frac{2u(r)}{1-[u(r)]^2}\left(\kappa_D^2[u(r)]^2 - [u'(r)]^2\right) \\ v'(a) &= \frac{-(2u_0(a)+v(a))u_0'(a)v(a)}{1-[u_0(a)]^2}, \; v'(\infty) = 0 \end{aligned} \qquad [166]$$

So far we have made no approximations. Because of the presence of the Debye–Hückel solution within the argument of the $\tanh^{-1}$ function and the comments made at the beginning of this section, we refer to this method as the *nonlinear Debye–Hückel* (NLDH) approach. The DH equation [165] subject to its nonstandard boundary condition (that is, the presence of the denominator) is relatively easy to solve for a wide variety of systems. Equation [166], however, is more difficult. Under what conditions can we simply neglect $v(r)$ compared to $u_0(r)$? For one-dimensional single-particle systems, Eq. [165] shows that $u_0(r) \sim \exp(-\kappa_D r)$ and then Eq. [166] implies $v(r) \sim \exp(-3\kappa_D r)$. Thus for $\kappa_D r$ large enough, we may consider $v(r)$ to be small, and we see that our solution essentially represents an asymptotic expansion, where $u_0(r)$ is the first term. But it is more than this for two reasons, the first being that for a single charged plane, $\kappa_D u(r) = u'(r)$, where the second term on the right-hand side of Eq. [166] vanishes identically, thus yielding the solution $v(r) = 0$. This implies that the resulting solution of Eq. [165] inserted into Eq. [161] is valid for *all* r and not just asymptotically. (This is verified by carrying out the calculation.) The second reason our solution is useful is that for small surface potentials or charge densities, neglecting all terms of order $[u(r)]^2$ reduces Eq. [165] and its boundary condition to the standard DH result, and Eq. [166] again gives $v(r) \approx 0$; we thus recover the radial Debye–Hückel potential in d dimensions for all r. The presence of curvature effects in the low-order solution distinguishes this approach from that of the PGC approximation presented previously.

In the following section we present a particularly simple approximation to Eq. [162] that bypasses the need for $v(r)$. However, for those cases in which greater accuracy is required, Eq. [166] could be solved for $v(r)$. One might think it possible to ignore the denominator of the second term in Eq. [166] and/or replace $u(r)$ by $u_0(r)$, further simplifying the equation, but this procedure will lead to considerable error since any errors in obtaining $v(r)$ are magnified through the (nonlinear) $\tanh^{-1}$ function of Eq. [161]. We note that the above procedure is *not* based on a perturbative expansion in which $v(r)$ is assumed to be much less than some zeroth-order solution ($u_0(r)$, $\phi_{\mathrm{DH}}(r)$ or the planar GC solution) at the outset. Doing so, typically by introducing an expansion parameter ε and collecting terms, as was implicit in the PGC procedure of the previous section, would remove higher-order terms from inside the $\tanh^{-1}$ function, resulting in some degree of linearization. It is particularly important to retain nonlinearity in the boundary condition. We will show in the following section that because of this $u_0(r)$ is actually the generalization of the planar ADH potential given in Eq. [93]. The nonlinear boundary condition does not complicate the solution but does increase considerably the accuracy of the final potential, as can be seen by comparing the DH and ADH potentials for a charged plane in Figure 4. One might argue that, since this NLDH solution is not based on a perturbative method, neglect of $v(r)$ may lead to large errors in the potential near the particle surface. This is, of course, true but for

many systems, particularly those involving more than a single polyelectrolyte, thermodynamic properties are determined by asymptotic features of the potential and these are well reproduced by $u_0(r)$. Finally, although we have specified typical single-particle bulk electrolyte boundary conditions in Eq. [165], the NLDH can be used with other boundary conditions. A number of two-particle systems are treated within the NLDH approach in later sections.

Bulk Model: Single-Particle NLDH Potential

One of the most important yet simplest systems is that of a single-charged surface immersed in a bulk $z:z$ electrolyte because it serves as a reference model for colloidal and biomolecular systems. In this section we will obtain a general expression for the asymptotic form of the Poisson–Boltzmann potential for a radially-symmetric particle (a cylinder or sphere) and show that it reduces to that for a plane in the limit of large particle radius. We then show how the asymptotic result can be modified slightly to correct the value of the potential at the particle surface.

Returning to Eq. [165], let us write the general solution to the radial d-dimensional Debye–Hückel equation as

$$u_0(r) = Aw(r) \tag{167}$$

where $w(r)$ denotes the radial component $e^{-\kappa_D r}$, $K_0(\kappa_D r)$ or $e^{-\kappa_D r}/r$, for $d = 1$, 2 or 3, respectively. [It is not necessary to explicitly know $w(r)$ at this point, only that it satisfies the appropriate DH equation.] The boundary condition at $r = a$ can be written as

$$\frac{A|w'(a)|}{1 - A^2[w(a)]^2} = \frac{zS_a}{2\lambda_{GC}} \tag{168}$$

which is solved to give the coefficient

$$A = \frac{zS_a}{\sqrt{[zw(a)]^2 + [w'(a)\lambda_{GC}]^2} + |w'(a)|\lambda_{GC}} \tag{169}$$

Comparison with the standard Debye–Hückel solution obtained by neglecting the denominator on the left-hand side of Eq. [168]:

$$\phi_{DH}(r) = \frac{2S_a}{\lambda_{GC}}\left|\frac{w(r)}{w'(a)}\right| \tag{170}$$

shows that the $u_0(r)$ may be written in the form of the DH solution by replacing λ_{GC} with a curvature-dependent apparent Gouy–Chapman length

$$\lambda_{AGC} = \frac{1}{2}\left(\lambda_{GC} + \sqrt{\lambda_{GC}^2 + \left(\frac{zw(a)}{w'(a)}\right)^2}\right) \qquad [171]$$

and thus represents the generalization of the planar ADH potential of Eq. [93].[176] Using Eq. [11], we collect the additional curvature factor δ_a into the reference density σ_0 and express Eqs. [171] in terms of charge densities and the DH potential:

$$\begin{aligned} \sigma_{ADH} &= \frac{2\sigma_a}{\sqrt{(\sigma_a/\sigma_0)^2 + 1} + 1} \\ \sigma_0 &= \frac{e_0\kappa_D}{2\pi L_B z \delta_a}, \quad \delta_a = \left|\frac{\kappa_D \phi_{DH}(a)}{\phi'_{DH}(a)}\right| \end{aligned} \qquad [172]$$

so that Eq. [167] now gives the equivalent expressions

$$u_0(r) = \frac{z}{4}\phi_{ADH}(r) = \frac{z\sigma_{ADH}}{4\sigma_a}\phi_{DH}(r) = \frac{\sigma_{ADH}}{2\sigma_0}\frac{\phi_{DH}(r)}{\phi_{DH}(a)} \qquad [173]$$

We note that, as with $\phi_{DH}(r)$, $\phi_{ADH}(r)$ does not depend on the electrolyte valence. With $v(r) \approx 0$, the NLDH solution to the single-surface radial d-dimensional PB equation is simply

$$\frac{z\phi_{NLDH}(r)}{4} = \tanh^{-1}\frac{z\phi_{ADH}(r)}{4} \qquad [174]$$

Far from the surface the ADH potential is small, and only the first term in the series expansion of $\tanh^{-1}$ need be retained. The NLDH potential then reduces to the Debye–Hückel solution but with a reduced charge density given by Eq. [172]. It is convenient to write Eq. [174] in an alternative form equivalent to Eq. [22] for a charged plane:

$$\frac{z\phi_{NLDH}(r)}{4} = \tanh^{-1}\left[\tanh\left(\frac{z\phi_a}{4}\right)f(r)\right], \quad f(r) = \frac{\phi_{DH}(r)}{\phi_{DH}(a)} \qquad [175]$$

where the actual surface potential is related to the Debye–Hückel surface potential by

$$\sinh\frac{z\phi_a}{2} = \frac{z}{2}\phi_{DH}(a) \qquad [176]$$

Having laid the groundwork for the NLDH approach, we now improve on this result but in a way that avoids having to deal with the equation for $v(r)$. We recall that the ADH potential does not depend explicitly on the electrolyte valence and see, from Eq. [174], that for large distances from the surface the valence cancels; the electrolyte valence is thus a factor only near the surface, much as $v(r)$ is. This suggests that we might be able to multiply the valence by a parameter chosen in such a way as to optimize the potential at the surface. This is most easily done by introducing a parameter ζ into Eq. [175]:

$$\begin{aligned}\phi_{\mathrm{NLDH}}(r) &= \frac{4}{\zeta z}\tanh^{-1}(u(r)) \\ &= \frac{4}{\zeta z}\tanh^{-1}\left(\tanh\left(\frac{\zeta z\phi_a}{4}\right)f(r)\right)\end{aligned} \qquad [177]$$

Note that this expression for the solution essentially replaces the valence z (or effective valence if Eq. [69] used for asymmetric or mixed salts) by a "new effective valence" ζz, where ζ takes surface curvature into account. Inserting $\phi_{\mathrm{NLDH}}(r)$ into Eq. [159] gives

$$\frac{\kappa_D^2[u(r)]^2}{1-[u(r)]^2} + 2u(r)\left(\frac{u'(r)}{1-[u(r)]^2}\right)^2 = \frac{\kappa_D^2}{4}\sinh[z\phi_{\mathrm{NLDH}}(r)] \qquad [178]$$

Because the presence of nonintegral ζ does not allow simplification of the right-hand side of Eq. [178] in terms of $u(r)$ as was done in Eq. [162], it is simpler to work with $\phi(r)$ than $u(r)$. We "minimize" the error in our solution by choosing ζ such that Eq. [178] vanishes at the surface. The result is

$$1 + \frac{2}{\delta_a^2}\sinh^2\frac{\zeta z\phi_a}{4} = \frac{\zeta\sinh(z\phi_a)}{2\sinh(\zeta z\phi_a/2)} \qquad [179]$$

which may be rewritten in the more symmetric form

$$\frac{1+(2/\delta_a^2)\sinh^2(\zeta z\phi_a/4)}{1+2\sinh^2(\zeta z\phi_a/4)} = \frac{\zeta\sinh(z\phi_a)}{\sinh(\zeta z\phi_a)} \qquad [180]$$

where δ_a is easily seen to be a function only of $\kappa_D a$ and less than one for finite a, while ζ is bounded between a small positive value (given by Eq. [182]) and unity, approaching the latter for high surface potentials. If the value of the surface potential is known, Eq. [180] immediately provides ζ. Here we generally assume that the charge density is known. We thus follow the procedure used in the planar system (Eq. [25]) whereby the boundary condition at the surface

leads to Grahame's equation relating the surface potential to the charge density, which in this case can be expressed as

$$\sinh\frac{\zeta z\phi_a}{2} = \frac{\zeta z}{2}\phi_{\mathrm{DH}}(a) \qquad [181]$$

Equations [180] and [181] are solved simultaneously to give parameter ζ and the surface potential, which formally completes the one-particle NLDH solution.

An approximate value for ζ may be obtained by expanding Eq. [180] in powers of the surface potential and, up to second order in ϕ_a, we find

$$\zeta_a^2 = \frac{4\delta_a^2}{3+\delta_a^2} \qquad [182]$$

which is useful when taking the DH or point-particle limit ($\kappa_D a \to 0$). A better approximation based on the large surface potential expansion

$$\lim_{|\phi_a|\to\infty}\zeta = 1 + \frac{\ln(\delta_a^2)}{z|\phi_a|} \approx 1 + \frac{\ln(\delta_a)}{\ln(z|\phi_{\mathrm{DH}}(a)|)} \qquad [183]$$

where the second equality follows from Eq. [181], is given by

$$\zeta^2 = \zeta_a^2 + (1-\zeta_a^2)\exp\left(\frac{2\ln(\delta_a^2)}{z|\phi_a|}\right) \approx \zeta_a^2 + (1-\zeta_a^2)\exp\left(\frac{1-\ln(\delta_a^2)}{1+\ln(z|\phi_{\mathrm{DH}}(a)|)}\right) \qquad [184]$$

These expressions may be used in conjunction with the following limits for curvature function δ_a: for small surface curvature

$$\lim_{\kappa_D a\to 0}\delta_a = \begin{cases} -\kappa_D a\ln(\kappa_D a) & \text{(approximate for a cylinder)} \\ \dfrac{\kappa_D a}{1+\kappa_D a} & \text{(exact for a sphere)} \end{cases} \qquad [185]$$

and for large surface curvature

$$\lim_{\kappa_D a\to\infty}\delta_a = \begin{cases} \dfrac{2\kappa_D a}{2\kappa_D a+1} & \text{(approximate for a cylinder)} \\ \dfrac{\kappa_D a}{\kappa_D a+1} & \text{(exact for a sphere)} \end{cases} \qquad [186]$$

To summarize the NLDH procedure up to this point, the approximate analytical solution to PB equation [159] subject to conditions [160] is given

by Eq. [177], where $f(r)$ is the normalized Debye–Hückel solution; the surface potential and parameter ζ are found from Eqs. [180] and [181]. For a charged plane, the DH solution shows that $f(r) = \exp[-\kappa_D(r-a)]$ so that $\delta_a = 1$ and, from Eq. [180], $\zeta = 1$, as required. The form chosen for the approximate solution, Eq. [177], is correct in two limits: for all ϕ_a when $\zeta \sim 1$ and for all ζ when $\phi_a \ll 1$. We thus expect our solution to be more accurate for smaller surface potentials than larger as ζ deviates from unity, which also implies that the solution would be accurate at moderate to long distances from the surface. One advantage of the NLDH solution over the PGC solution of the previous section is that we are not limited by the magnitude of the radius of curvature, that is, the cylinder or sphere radius may be small compared to the Debye length. A second advantage is its ability to treat more than a single surface. Finally, the NLDH approximation naturally leads to the asymptotic ADH potential for curved surfaces, as we now show.

The result of introducing parameter ζ is to retain the expressions of Eq. [173]

$$u_0(r) = \frac{z}{4}\phi_{\mathrm{ADH}}(r) = \frac{z\sigma_{\mathrm{ADH}}}{4\sigma_a}\phi_{\mathrm{DH}}(r) \tag{187}$$

but modify the apparent Gouy–Chapman length

$$\lambda_{\mathrm{AGC}} = \frac{1}{2}\left(\lambda_{\mathrm{GC}} + \sqrt{\lambda_{\mathrm{GC}}^2 + \left(\frac{\zeta z \delta_a}{\kappa_D}\right)^2}\right) \tag{188}$$

and apparent charge density

$$\sigma_{\mathrm{ADH}} = \frac{2\sigma_a}{\sqrt{(\sigma_a/\sigma_0)^2 + 1} + 1}, \quad \sigma_0 = \frac{e_0\kappa_D}{2\pi L_B \zeta z \delta_a} \tag{189}$$

where once again we group the new parameter ζ in σ_0. As with the two-plane solution, the appearance of an apparent charge density is a natural consequence of using the $\tanh^{-1}$ function in our approximate solution coupled with the charge density boundary condition. Equation [189] has the limits

$$\lim_{|\sigma_a| \ll \sigma_0} \sigma_{\mathrm{ADH}} = \sigma_a\left(1 - \left(\frac{\sigma_a}{2\sigma_0}\right)^2\right) \tag{190}$$

and

$$\lim_{|\sigma_a| \gg \sigma_0} \sigma_{\mathrm{ADH}} = 2S_a\sigma_0\left(1 + \frac{\ln(\delta_a)}{\ln(\sigma_0/2|\sigma_a|)} - \frac{\sigma_0}{|\sigma_a|}\right) \tag{191}$$

where Eq. [183] has been used. Equation [185] or [186] may be used in these expressions for cases of small or large surface curvature. As with the ADH planar solution and Eq. [97], Eq. [189] allows us to define the fraction of surface charge neutralized by counterions as

$$f_{\text{neut}} = 1 - \frac{\sigma_{\text{ADH}}}{\sigma_a} = 1 - \frac{2}{\sqrt{(\sigma_a/\sigma_0)^2 + 1} + 1} \qquad [192]$$

with the limits

$$\begin{aligned} \lim_{|\sigma_a| \ll \sigma_0} f_{\text{neut}} &= \left(\frac{\sigma_a}{2\sigma_0}\right)^2 \\ \lim_{|\sigma_a| \gg \sigma_0} f_{\text{neut}} &= 1 - \frac{2\sigma_0}{|\sigma_a|} \end{aligned} \qquad [193]$$

The fraction of surface charge neutralized according to Eq. [192] corresponds to what one would find by fitting the asymptotic form of the potential to the standard Debye–Hückel form and comparing it to the standard DH solution. Of course, to do this, one must know the actual surface charge density as well as the particle radius for a cylinder or sphere, properties that cannot be separately determined from the potential alone (Gauss' law); it is generally assumed, as we do here, that these properties are known. Equation [192] clearly predicts that at least some surface charge will be neutralized under all conditions for charged planes, cylinders, and spheres and thus is at odds with the interpretation by Le Bret and Zimm[178] based on the no-added-salt cylinder cell model. A more detailed analysis is presented below in connection with specific geometries.

For small (or even moderate) surface potentials such that ζ can be approximated by Eq. [182], we can use Eq. [181] to find the electrostatic free energy of the charged surface according to Eq. [29]. Since the approximate solution [177] has the same form as the Gouy–Chapman solution for a plane and δ_a, and hence ζ_a, is independent of the surface potential, the evaluation of the free energy follows that leading to the planar result of Eq. [30] in all details, and we can immediately write

$$\frac{\beta A_{\text{el}}}{\text{Area}} = \frac{\kappa_D}{\pi L_B \zeta_a^2 z^2 \delta_a}[p \ln(p+q) + 1 - q], \quad p \equiv \frac{\zeta_a z \delta_a}{\kappa_D \lambda_{\text{GC}}}, \quad q \equiv \sqrt{1+p^2} \qquad [194]$$

To proceed further, specific expressions for δ_a must be given, which requires that the DH equation be solved for the geometry of interest; these will be given below in the appropriate sections. We simply note that an expression for δ_a

that is exact for a sphere (and a plane) and asymptotically correct (in $\kappa_D C_a$) for a cylinder is (see Eqs. [252] and [300])

$$\delta_a = \frac{\kappa_D C_a}{\kappa_D C_a + 1}, \quad C_d = 2a/(d-1) \qquad [195]$$

Use of Eq. [195] implies that a sphere of radius 20 Å and a cylinder of radius 10 Å at a given surface charge density will have the same surface potential (if ζ can be approximated by the low-potential formula [182]). This observation agrees with the PGC approximation of the previous section. Equations [194] and [195] can be used to find the approximate electrostatic free energy of a convex body (*i.e.*, positive local radius of curvature) by integrating the free energy per area over the surface. For simple shapes (rod, disk), the free energy can be written as an analytic sum of the free energies for each type of geometric surface (plane, cylinder or sphere).

Figures 19 and 20 display the error according to Eq. [158] for the approximate (Eqs. [177], [181] and [182]) and exact (Eqs. [177], [180] and [181]) NLDH potentials. (The analytical NLDH solution for a charged cylinder or charged sphere is displayed in later sections.) An analysis similar to the PGC potential of Figures 17 and 18 applies here with the exact NLDH error being about twice that of the exact PGC error at large $\kappa_D a$. The unbounded error for the approximate NLDH potential for a cylinder at small $\kappa_D a$

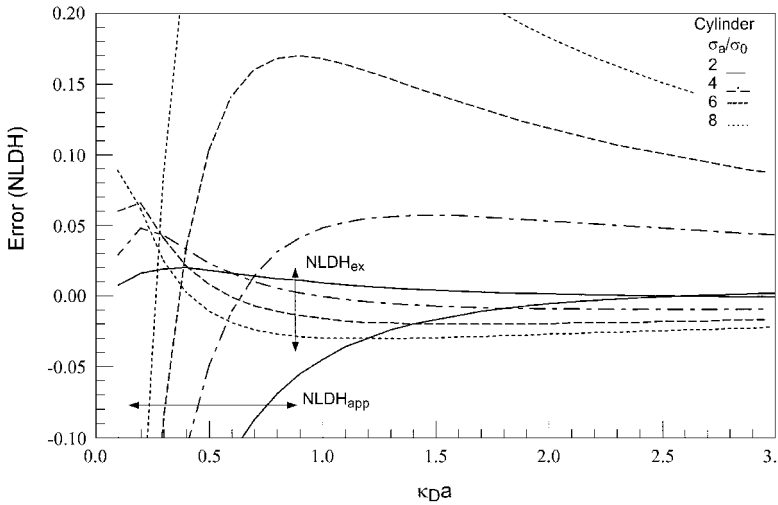

Figure 19 The error in the NLDH solution of Eq. [177] according to Eq. [158] for a cylinder as a function of the scaled radius $\kappa_D a$ for several values of the scaled surface charge density σ_a/σ_0; curves obtained using exact (Eq. [180]) and approximate (Eq. [182]) values for ζ are grouped by arrows.

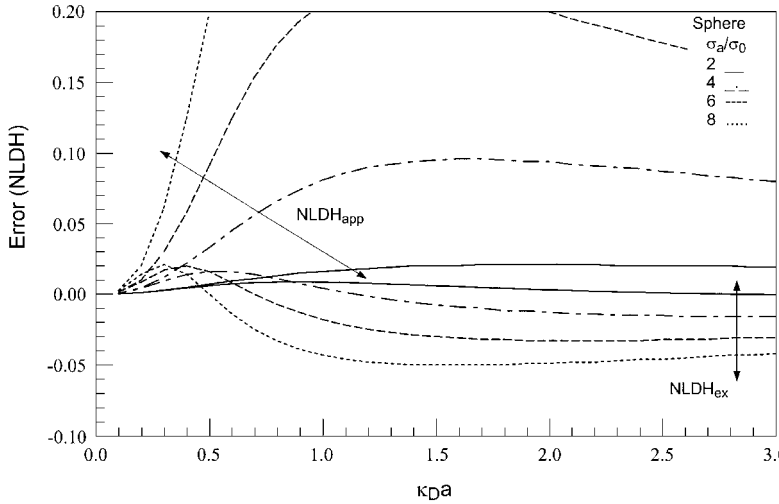

Figure 20 The error in the NLDH solution of Eq. [177] according to Eq. [158] for a sphere as a function of the scaled radius $\kappa_D a$ for several values of the scaled surface charge density σ_a/σ_0; curves obtained using exact (Eq. [180]) and approximate (Eq. [182]) values for ζ are grouped by arrows.

(Figure 19) is due to the replacement of Bessel functions with their asymptotic expressions (see text below). One important distinction between the exact PGC and NLDH potentials is that the NLDH potential is more accurate for surfaces with small radii of curvature. For cylinders, the (exact) NLDH error is lower than the (exact) PGC error for roughly $\kappa_D a < 1$; for spheres, the NLDH error is lower for $\kappa_D a < 1.5$-3, depending on the surface charge density. In general, the approximate NLDH potential is adequate only for spherical systems with $\kappa_D a < 0.03$–0.05 unless the sphere has a low charge density.

We note that the NLDH approximation is similar to, and in a sense a special case of, that of Martynov,[179–181] who assumed a solution in terms of a series expansion involving the potential at the outset. After several approximations in which the series solution is resummed, he arrives at an expression that is equivalent to Eq. [177] for the spherical case. We also note that his expression for ζ (actually his $4/\sqrt{3B}$) involves exponential integrals but can be well approximated by the much simpler formula $\zeta^2 \approx 2/(3/\delta_a - 1)$, which, when used with Eq. [195], is easily shown to agree with Eq. [182] to lowest order in C_a. His higher-order approximations, which we could designate an "extended NLDH approximation," go beyond the solution developed here but also lose some of the analytical simplicity. There is also a superficial similarity of our ADH profile with the linearized PB potentials of Fogolari et al.[182] and Bocquet, Trizac and Aubony.[183,184] Finally, we mention that Wang et al.

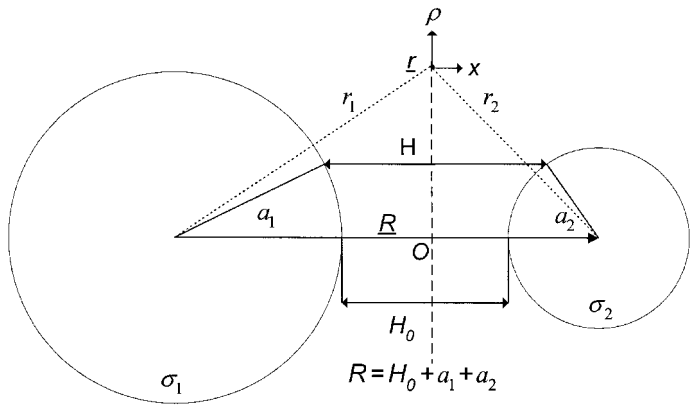

Figure 21 Diagram defining the parameters used to calculate the interaction of two charged particles (planes, cylinders, or spheres) of radii a_1 and a_2; a plane is treated by the limiting case of infinite radius. The dividing plane at $H_0/2$ (or R/z) used to evaluate the potential (or pressure) is indicated by the dotted vertical line placed at the origin of the 2D cylindrical (ρ, x) coordinate system; any point $\underline{r}$ on this plane lies an equal distance from the respective particle centers. R is the distance between particle centers, H_0 is the closest distance between surfaces (the separation distance) and H denotes the distance between any two points on the particles that lie the same distance ρ above the inter-center axis (and in the plane of the paper).

have presented a simple and elegant functional iterative method for analytically nonlinearizing the spherical DH solution.[185]

Bulk Model: Two-Particle NLDH Potential

Now that we have obtained single-particle NLDH potentials, we extend the treatment by generalizing the plane–plane interaction discussed previously to any two, possibly dissimilar, charged particles of simple geometry (planes, cylinders, or spheres), oriented as depicted in Figure 21; for planes and spheres, the coordinate system is cylindrically symmetric. We let $\underline{R}$ be the separation vector between the centers of the two particles (from 1 to 2) with σ_1 and a_1 denoting the surface charge density and radius, respectively, of one of the particles (a plane is treated as the limiting case of infinite radius); $H_0 = R - a_1 - a_2$ is the closest distance between the surfaces. In this (ρ, x) coordinate system, ρ defines the perpendicular distance from $\underline{R}$ and x is the distance projected along $\underline{R}$ with respect to the origin at a point O situated between the particle centers (at $H_0/2$ or $R/2$, depending on whether the potential or pressure is being calculated). In this section we will first obtain an approximate solution for the two-particle potential and then use it to find the pressure on the dividing plane, again explicitly considering only a $z:z$ electrolyte.

From Eqs. [121] and [175] we assume a potential of the form

$$\begin{aligned} z\phi(r)/4 &= \tanh^{-1}[u(r)] \\ &= \tanh^{-1}[A_1 f_1(r_1) + A_2 f_2(r_2)] \end{aligned} \quad [196]$$

where

$$f_1(r_1) = \frac{\phi_1(r_1)}{\phi_1(a_1)}, \quad f_2(r_2) = \frac{\phi_2(r_2)}{\phi_2(a_2)} \quad [197]$$

are the individual DH potentials scaled to the values at the surface. At this point we need not explicitly give the DH solutions—this will be done in later sections—but $f(r)$ is in fact $w(r)/w(a)$, where $w(r)$ for the appropriate particle geometry is given immediately following Eq. [167]. To determine coefficients A_1 and A_2 it is simplest if the origin of the coordinate system is placed halfway between the particle surfaces at $H_0/2$. From Figure 21 we have

$$\begin{aligned} r_1^2 &= (h_1 + x)^2 + \rho^2, \quad h_1 = a_1 + \frac{H_0}{2} \\ \frac{\partial r_1}{\partial \rho} &= \frac{\rho}{r_1}, \quad \frac{\partial r_1}{\partial x} = \frac{h_1 + x}{r_1} \end{aligned} \quad [198]$$

with similar expressions for r_2. Although complete boundary conditions would have angular contributions, we apply them only at the point on each surface closest to the other particle, that is, along $\underline{R}$ ($\rho = 0$) with $x = \pm H_0/2$. This great simplification corresponds to considering only the lowest-order term in an angular expansion of the potential and thus correctly describes the leading order term in the solution. For interacting cylinders and interacting spheres, McQuarrie and co-workers have shown that for separation distances of a few Debye lengths, this approximation is entirely adequate.[186,187] For separations large compared to the particle radii, the potential will not vary greatly across each surface, while for separations small compared to the particle radii, the interaction should approach that of two planes (for which there is no angular dependence); in both cases the correct boundary condition is being applied. Applying the boundary conditions

$$\begin{aligned} \phi'\left(\frac{-H_0}{2}\right) &= \frac{-4\pi L_B \sigma_1}{e_0} \\ \phi'\left(\frac{H_0}{2}\right) &= \frac{4\pi L_B \sigma_2}{e_0} \end{aligned} \quad [199]$$

to the potential of Eq. [196] leads to the coupled equations

$$\begin{aligned}\hat{\sigma}_1 &= \frac{A_1 - (\varepsilon_2\delta_1/\delta_2)A_2}{1-(A_1+\gamma_2 A_2)^2}\\ \hat{\sigma}_2 &= \frac{-(\varepsilon_1\delta_2/\delta_1)A_1 + A_2}{1-(\gamma_1 A_1 + A_2)^2}\end{aligned} \qquad [200]$$

where several variable assignments have been made (those with index 2 follow by symmetry):

$$\begin{aligned}&\hat{\sigma}_1 = \frac{\sigma_1}{2\sigma_{01}}, \qquad \sigma_{01} = \frac{e_0\kappa_D}{2\pi L_B z \delta_1}\\ &\gamma_1 = f_1(H_0+a_1), \quad \delta_1 = \frac{-\kappa_D}{f_1'(a_1)}, \quad \varepsilon_1 = \frac{f_1'(H_0+a_1)}{f_1'(a_1)}\end{aligned} \qquad [201]$$

Note that γ, δ, and ε all range between zero and one; also, γ and ε decrease exponentially as the surface separation H_0 increases. As with Eqs. [123] and [124] for the planar case, Eqs. [200] can be solved exactly for two particles of identical ($A_1 = A_2$) or opposite ($A_1 = -A_2$) charge density or for one uncharged particle ($A_2 = 0$) so we need only generalize our solution for two planes (Eq. [125])

$$A_1 = \frac{2(\hat{\sigma}_1 + \varepsilon_1\hat{\sigma}_2)}{\sqrt{4((1+\varepsilon_1\gamma_2\delta_2/\delta_1)\hat{\sigma}_1 + (\varepsilon_1+\gamma_2\delta_1/\delta_2)\hat{\sigma}_2)^2 + (1-\varepsilon_1\varepsilon_2)^2} + (1-\varepsilon_1\varepsilon_2)} \qquad [202]$$

where A_2 is found by switching indices $1 \leftrightarrow 2$. Equation [202] provides the low charge density expansion

$$A_1 = \frac{\hat{\sigma}_1 + \varepsilon_1\hat{\sigma}_2}{(1-\varepsilon_1\varepsilon_2)}\left[1 - \left(\frac{(1+\varepsilon_1\gamma_2\delta_2/\delta_1)\hat{\sigma}_1 + (\varepsilon_1+\gamma_2\delta_1/\delta_2)\hat{\sigma}_2}{(1-\varepsilon_1\varepsilon_2)^2}\right)^2 + \cdots\right] \qquad [203]$$

where the first term is the Debye–Hückel limit, and the large-separation expansion

$$A_1 = \hat{s}_1 + \frac{(1-\hat{s}_1^2)\hat{s}_2}{(1+\hat{s}_1^2)(1-\hat{s}_2^2)}((1-\hat{s}_1^2)\varepsilon_1 - (2\hat{s}_1^2\delta_1/\delta_2)\gamma_2) + \cdots \qquad [204]$$

where the scaled apparent charge density $\hat{s}_1$ is defined as

$$\hat{s}_1 = \frac{2\hat{\sigma}_1}{\sqrt{4\hat{\sigma}_1^2 + 1} + 1} \qquad [205]$$

Setting $\gamma = 1$ and $\delta = \varepsilon = \exp(-\kappa_D H_0)$ in Eqs. [203] and [204] reproduces the planar expression of Eqs. [127] and [128]. Equation [204] shows that the leading term in the coefficient is independent of particle separation and weakly dependent on particle radius (through δ). Equation [205] agrees with Eq. [189] for $\zeta = 1$; we can improve the potential by including separate ζ values in σ_{01} and σ_{02} based on the individual particle potentials and letting $z \to \zeta_{\text{ave}} z$ on the left-hand side of Eq. [196], where, for example, ζ_{ave} is determined by:

$$\zeta_{\text{ave}} = \sqrt{\zeta_1 \zeta_2} \qquad [206]$$

but this can be introduced later by inspection (see Eqs. [282], [332] and [377]). Equation [196] with the coefficients of Eq. [202], or the limits given by Eqs. [203] and [204], constitutes the two-particle potential within the NLDH approximation.

As a prelude to finding the two-particle interaction potential, we now turn to the evaluation of the pressure on the dividing plane, which, for convenience, we place midway between the particle centers at $R/2$. The pressure at $\underline{r}(\rho, x)$ is given by[128,188]

$$\beta P(R, \rho, x) = \frac{\kappa_D^2}{2\pi L_B z^2} \sinh^2\left(\frac{z\phi(R, \rho, x)}{2}\right) + \frac{1}{8\pi L_B} \times \left[\left(\frac{\partial \phi(R, \rho, x)}{\partial \rho}\right)^2 - \left(\frac{\partial \phi(R, \rho, x)}{\partial x}\right)^2\right] \qquad [207]$$

For a planar system, the potential is independent of ρ and Eq. [207] reduces to Eq. [112]. Substitution of $u(r)$ according to Eq. [196] gives the following expression for the pressure at the dividing plane ($x = 0$):

$$\beta P(R, \rho, 0) = \frac{2}{\pi L_B z^2} \left[\frac{\kappa_D^2 u^2 + (\partial u/\partial \rho)^2 - (\partial u/\partial x)^2}{(1 - u^2)^2}\right]_{x=0} \qquad [208]$$

Use of Eqs. [198] with $r_1 = r_2 = r$ (hence our choice of origin) gives

$$\beta P(R, r) = \frac{2}{\pi L_B z^2 (1 - u^2)^2} \left\{\kappa_D^2 (A_1(R) f_1(r) + A_2(R) f_2(r))^2 + (A_1(R) f_1'(r) + A_2(R) f_2'(r))^2 - 2\left(\frac{R}{2r}\right)^2 \left[(A_1(R) f_1'(r))^2 + (A_2(R) f_2'(r))^2\right]\right\} \qquad [209]$$

where the dependence of the coefficients on the separation distance R has been explicitly indicated. With the function substitution $f_1(r) = f_2(r) = \exp[-\kappa_D (r - a)]$, application of the appropriate limits ($a_1 = a_2 = a \to \infty$ with $r - a =$ constant), and ignoring the higher-order term in the denominator, Eq. [209] reduces to the pressure between two charged planes given by Eq. [130]. The pressure is used to find the force and, from the force, the interaction potential between the two charged particles. Evaluation of the force requires knowledge of the particle geometry, so this is treated later in the appropriate sections.

Bulk Model: Upper/Lower-Bound Variational Solution

The NLDH approximation of the previous section assumes a relatively simple form for the approximate potential profile. It is based on the Gouy-Chapman solution for a plane and the Debye–Hückel solution for a curved surface, with a single-variable parameter introduced to allow the approximate solution to satisfy the differential equation at the surface. One problem with this solution is that it is difficult to improve upon unless one follows Martynov[179] and develops a solution based on a series expansion in powers of the potential. An alternative method is to introduce more parameters and require them to satisfy some variational principle. We demonstrate this more simply by retaining the one-parameter solution of Eq. [177] but determine ζ using the calculus of variations[189] instead of through Eq. [179]. Upper and lower variational bounds for a general set of differential equations, including the Poisson–Boltzmann equation, have been derived by Arthurs and coworkers;[190–192] we rely on the last reference in which a change in notation from the previous two has been introduced. We also note that Olivares and McQuarrie used the same variational method in obtaining their solution to the PB equation for a sphere.[193] We first introduce the upper-bound problem, which is applicable to a wide variety of systems, followed by a simultaneous consideration of the upper and lower bounds.

Consider the bulk model PB equation for a 1 : 1–2 : α electrolyte, where $\alpha = 1$ or 2:

$$\phi''(x) + \frac{d-1}{x}\phi'(x) = \frac{c_1 \sinh(\phi) + c_2(e^{\alpha\phi} - e^{-2\phi})}{c_1 + (2+\alpha)c_2} \qquad [210]$$

where $x = \kappa_D r$ is the scaled distance and the solution is subject to the usual boundary conditions

$$\phi'(\kappa_D a) = \frac{-2S_a}{\kappa_D \lambda_{GC}}, \quad \phi'(\infty) = 0 \qquad [211]$$

The results that follow are readily generalizable to any electrolyte, but a 1 : 1–2 : α salt is sufficiently variable for most purposes. The upper-bound variational

integral for this problem can be written as[192,193]

$$J(\eta) = \int_{\kappa_D a}^{\infty} \left[\frac{\bar{z}^2}{2} (\phi'(\eta, x))^2 + \frac{c_1 \cosh(\phi(\eta, x)) + c_2 \left(e^{-2\phi(\eta,x)} + \frac{2}{\alpha} e^{\alpha \phi(\eta,x)} \right)}{c_1 + (2+\alpha)c_2} - 1 \right] \times \left(\frac{x}{\kappa_D a} \right)^{d-1} dx - \frac{2\bar{z}^2}{\kappa_D \lambda_{GC}} \phi(\eta, \kappa_D a) \quad [212]$$

where we have defined

$$\bar{z}^2 \equiv \frac{c_1 + (2+\alpha)c_2}{c_1 + (2+\alpha)c_2/2\alpha} \quad [213]$$

and η is chosen such that $J'(\eta) = 0$. Arthurs[192] treats only the case of Dirichlet boundary conditions but Neumann conditions, which result in the second term in Eq. [212], may be obtained from his results and were in fact used by Olivares and McQuarrie.[193] To find an approximate solution to Eq. [210], we use the form of Eq. [177] but replace ζz by the variational parameter η since it is not necessary here to separate out the valence

$$\phi(\eta, x) = \frac{4}{\eta} \tanh^{-1}[\tanh(\eta\, \phi(\eta, \kappa_D a)/4) f(x)] \quad [214]$$

where $f(x) = \phi_{DH}(x)/\phi_{DH}(\kappa_D a)$ and the surface potential is determined by the boundary condition at the surface:

$$\phi(\eta, \kappa_D a) = \frac{2}{\eta} \sinh^{-1} \frac{\eta \phi_{DH}(\kappa_D a)}{2} \quad [215]$$

From Eq. [214] we find

$$\phi'(\eta, x) = \left(\frac{2}{\eta \delta(x)} \right) \sinh(\eta\, \phi(\eta, x)/2), \quad \delta(x) \equiv \left| \frac{f(x)}{f'(x)} \right| \quad [216]$$

The Poisson–Boltzmann equation with our form for the solution will not allow the analytical solution to $J'(\eta) = 0$, but η is readily found via computer by inserting Eqs. [214]–[216] into Eq. [212], with $f(x)$ determined for the appropriate geometry, and using a root solver. An illustrative example will be given below.

If the functional dependence of the charge density on the potential is simple enough to allow inversion, then a lower bound integral can also be obtained,[192,193] often putting strict limits on the variable parameter. The general electrolyte of Eq. [210] is too complicated for this approach, but if we

restrict ourselves to a symmetric $z:z$ electrolyte or, better yet, use the effective valence of Eq. [69] to approximate the charge density of a 1 : 1–2 : α electrolyte by a sinh function and set

$$z_e = 1 + \sqrt{\frac{4c_2}{c_1 + (2+\alpha)c_2}} \qquad [217]$$

then we replace Eq. [210] by

$$\nabla^2\phi(x) = \phi''(x) + \frac{d-1}{x}\phi'(x) = z_e^{-1}\sinh(z_e\phi(x)) \qquad [218]$$

We can then write an expression for the lower bound integral. Olivares and McQuarrie[193] give such an integral obtained from Arthurs,[192] but rather than individually minimizing and maximizing the upper and lower bound integrals, we minimize the difference between the two.[193] Performing an integration by parts on the upper-bound integral $J(\eta)$ and combining this with the lower bound integral $G(\eta)$, we rearrange to get

$$H(\zeta) \equiv \tfrac{1}{2}|J(\zeta) - G(\zeta)| = \int_{\kappa_D a}^{\infty} |h(\zeta,x)|\left(\frac{x}{\kappa_D a}\right)^{d-1} dx \qquad [219]$$

where ζ is now the variational parameter (since z_e is considered fixed) and the function in the integrand is given by

$$h(\zeta,x) = \sinh\left[\frac{z_e}{2}(\phi(\zeta,x) - \Phi(\zeta,x))\right]\sinh\left[\frac{z_e}{2}(\phi(\zeta,x) + \Phi(\zeta,x))\right] - \frac{z_e^2}{2}(\phi(\zeta,x) - \Phi(\zeta,x))\nabla^2\phi(\zeta,x) \qquad [220]$$

with

$$\Phi(\gamma,x) = z_e^{-1}\sinh^{-1}(z_e\nabla^2\phi(\gamma,x)) \qquad [221]$$

and

$$\phi(\gamma,x) = \frac{4}{\gamma z_e}\tanh^{-1}\left[\tanh\left(\frac{\gamma z_e\,\phi(\gamma,\kappa_D a)}{4}\right)f(x)\right] \qquad [222]$$

[Inversion of the charge density is the necessary step in defining $\Phi(\zeta,x)$.] This form for $H(\zeta)$ converges much faster than evaluating $J(\eta)$ and $G(\eta)$ separately, and this particular factorization (which also reduces errors in the

evaluation of the integrand) shows that if $\phi(\zeta, x)$ is the exact solution to Eq. [218], then $\phi(\zeta, x) = \phi(x) = \Phi(\zeta, x)$ and $h(\zeta, x)$ vanishes identically. For $\phi(\zeta, x)$ given by Eq. [214], after some algebra, we find

$$\nabla^2\phi(\zeta, x) = \left(\frac{2}{\zeta z_e}\right)\sinh\left(\frac{\zeta z_e \phi(\zeta, x)}{2}\right)\left[1 + \frac{2}{(\delta(x))^2}\sinh^2\frac{\zeta z_e \phi(\gamma, x)}{4}\right] \quad [223]$$

As with the upper-bound integral of Eq. [212], we find ζ such that $H'(\zeta) = 0$.

We now treat a specific example. Consider a charged sphere of radius 20 Å in a bulk 1 : 1–2 : 1 electrolyte ($\alpha = 1$ in Eq. [210]) with salt concentrations $c_1 = 0.1$ M and $c_2 = 0.02$ M ($\kappa_D = 0.132$ Å^{-1} and $z_e = 1.707$) and surface charge density $\sigma_a = -0.01\ e_0/\text{Å}^2$. With $\delta(x) = x/(x+1)$, minimizing the upper-bound integral [212] gives the parameter $\eta_J = 1.467$; minimizing the upper/lower integral [219] gives $\zeta_H = 0.854$ or $\eta_H = \zeta_H z_e = 1.458$, and use of Eqs. [180] and [181] gives $\zeta = 0.858$ or $\eta = 1.464$. The resulting potentials are practically indistinguishable from each other and from the exact result (as will be shown in Fig. 34 later in this chapter). As a note, the upper and lower bound integrals contributing to Eq. [219] give $\eta_J = 0.844$ and $\eta_G = 0.855$, showing that, as is often the case, the closer bound is also the more difficult to obtain. Although we have treated a charged sphere in a bulk electrolyte as an example, the expressions apply to charged planes ($d = 1$) and cylinders ($d = 2$) and the cell model as well. One can also improve on the solution above by adding more variational parameters.

Prior to the work of Olivares and McQuarrie,[193] Brenner and Roberts[194] used the variational principle to obtain a simple yet accurate expression for the PB potential around a charged sphere. More recently, Reiner and Radke, in a clear and thorough analysis, applied the method to the calculation of the free energy of single- and double-plate systems.[195]

Cylindrical Geometry: The Polymer Model

One of the most fruitful applications of the PB equation is in the description of long cylindrical polyelectrolytes, of which DNA is the prototypical example.[12,196,197] The same simplifications used in the planar case with a uniform and constant surface charge density and a restricted primitive model of the electrolyte are assumed here.

General Equations

We now consider the case of an infinitely long cylinder of fixed radius a (which also includes a common electrolyte ion radius) and surface charge density σ_a surrounded by an electrolyte solution. The corresponding one-dimensional PB equation and boundary conditions, in a cylindrical coordinate

system whose origin lies on the axis of the cylinder with coordinate r perpendicular to this axis, are

$$\frac{1}{r}\frac{d}{dr}\left[r\frac{d\phi(r)}{dr}\right] = -4\pi L_B A_0 \sum_{i=0}^{I} c_i^R z_i e^{-z_i\phi(r)} \qquad [224]$$

and

$$\begin{aligned} \phi'(a) &= \frac{-4\pi L_B \sigma_a}{e_0} = \frac{-2S_a}{\lambda_{GC}} \\ \phi'(R) &= 0, \quad \phi(R) = 0 \end{aligned} \qquad [225]$$

While at first sight Eq. [224] looks relatively benign, it is actually a nonlinear integrodifferential equation since the concentration of ions at the reference position R involves an integral over the potential profile (see Eq. [4]) and must be determined self-consistently with the potential. The system we are modeling is that of a given concentration of cylindrical polyelectrolytes such as DNA. Although any real molecule is finite in length and has irregularly spaced charges, we can represent it as an infinite cylinder with a uniform surface charge density if the Debye length is both shorter than the cylinder length and longer than the individual charge spacing. In this case ions at the center of the molecule can be considered unaffected by end effects and discrete surface charges appear to be smeared out. For a 0.1 M monovalent salt solution, the Debye length at 298 K is about 10 Å; since the linear charge spacing of B-form DNA is about 1.7 Å, the simplified model applies to molecules ~20 base pairs or larger. These same considerations also pertain to the planar membrane case but were not explicitly discussed earlier.

For applications to DNA or other linear polyelectrolytes, two particular points not always emphasized when dealing with planar system must be mentioned. For concentrations of DNA such that the intermolecular separation is on the order of a few Debye lengths or less, we imagine that each molecule acts independently of every other molecule and lies at the center of a cylindrical region mirroring its shape of radius R to be determined (Figure 22). The second point concerns the fact that an individual unsolvated DNA molecule must be electrically neutral. Upon solvation initially bound counterions are released into solution from ionizable sites; for DNA and other biomolecules, the sodium salt is often assumed so that initially bound counterions (species 0 in Eq. [224]) are usually thought of as being sodium ions. Now, let b be the average axial distance between ionizable sites. We then only need to consider ions in a slice of the cylindrical region that is of height b since by symmetry what happens in this slice is repeated in all other slices. Thus the system has been reduced to a cylindrical disk of height b and radius R in which

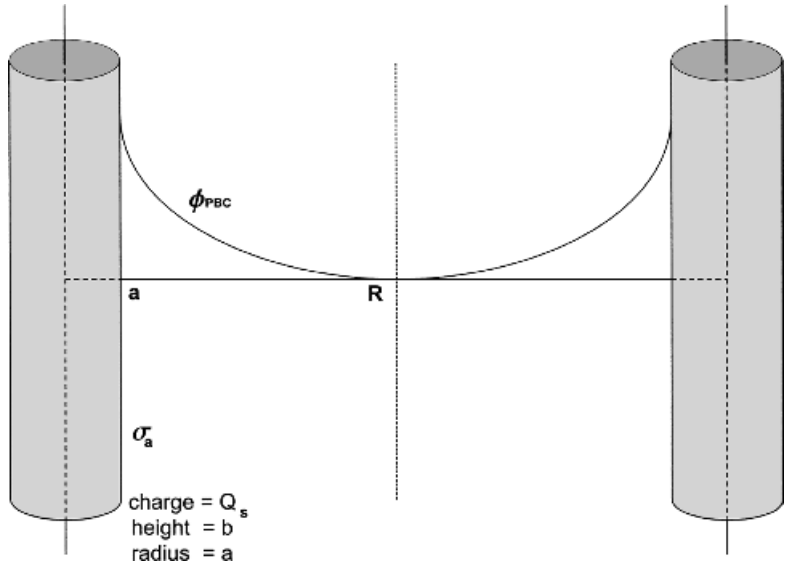

Figure 22 A diagram of the cylindrical cell model in which an infinite cylinder of radius a has a surface charge density $\sigma_a = e_0 Q_s/(2\pi ab)$, where charged sites of valence Q_s are spaced a distance b apart along the cylindrical axis; the concentration of charged sites defines a cell with radius R and volume πbR^2 within which each cylinder determines the ionic distribution. The Poisson–Boltzmann cell model potential ϕ_{PBC} is subject to conditions on its derivative at the cylinder surface ($r = a$) and at the cell boundary ($r = R$) and is typically assigned the gauge $\phi_{PBC}(R) = 0$; ions beyond the cell radius are considered as belonging to the neighboring cell. In the Debye–Hückel cell model, the DH equation is solved subject to the same boundary conditions and gauge.

lies a single ionization site of valence Q_s. The surface charge density of this disk is

$$\sigma_a = \frac{e_0 Q_s}{2\pi ab} \tag{226}$$

DNA and linear polyelectrolyte concentrations usually refer to the concentration of the ionizable sites (for DNA these are the phosphate groups) along the backbone. Denoting this concentration by C_s, the volume of our cylindrical disk is just $1/C_s$:

$$C_s^{-1} = \pi A_0 bR^2 \tag{227}$$

This equation gives the radius of our slice in terms of the ionizable site spacing and polyelectrolyte concentration. Note that there is no "correction" for the finite size of the cylinder (i.e., $R^2 - a^2$) since the total volume of all slices must

equal the volume accessible to the entire molecule. This cylindrical slice is termed the *cell* and is sometimes called a *Wigner–Seitz cell*[198] in reference to its close relation to crystal cells; this model of our system is called the *Poisson–Boltzmann cell model*.[92] The two boundary conditions in Eq. [30] define the electric field at the cylinder surface due to the surface charge density and at the cell boundary due to electroneutrality of the system; the third condition is the potential gauge.

Before solving Eq. [224], we need to specify the concentration of initially bound counterions (added salt concentrations are assumed known). While the definition of the cell model assigns one initially bound counterion to the cell, the magnitude of the charge of the ionizable site is not required to be (although it often is) equal to that of the counterion. With Q_s and z_0 denoting the site and counterion valences, respectively, the number of counterions n_0 that neutralize N_s sites is

$$n_0 = \frac{-Q_s N_s}{z_0} \qquad [228]$$

The average counterion concentration is found by converting the numbers n_0 and N_s to concentrations keeping in mind that the volume accessible to the site ($1/C_s$) is larger than that accessible to the counterion:

$$\bar{c}_0 = -\left(\frac{Q_s}{z_0}\right)\left(1 - \frac{a^2}{R^2}\right) C_s \qquad (229)$$

While we have implicitly assumed that counterions are represented as point charges, any finite radius may simply be incorporated into the cylinder radius a, which then describes the distance of closest approach to the cylindrical axis.

Equation [224] for no added salt can be solved in a manner similar to that for the planar case,[12,178,199–202] but to offer another perspective we choose an alternative procedure. As both boundary conditions of Eq. [225] involve the field, rather than the potential, let us introduce a variable related to the field

$$\xi(r) = \frac{r}{2}\frac{d\phi(r)}{dr}, \quad \phi[\xi(r)] = -2\int_r^R \frac{\xi(r)}{r} dr \qquad [230]$$

which is subject to the boundary conditions ($S_a = -1$, as for DNA)

$$\begin{aligned} \xi(a) &= \frac{-2\pi L_B a \sigma_a}{e_0} = \frac{a}{\lambda_{GC}} = \frac{L_B}{b} \\ \xi(R) &= 0 \end{aligned} \qquad [231]$$

Using this in Eq. [224] gives the integrodifferential equation for $\xi(r)$:

$$\frac{d\xi(r)}{dr} = -2\pi L_B A_0 r \sum_{i=0}^{I} c_i^R z_i \mathrm{e}^{-z_i\phi[\xi(r)]} \qquad [232]$$

We now differentiate both sides of Eq. [232] and rearrange to get the differential equation

$$r\xi''(r) = \xi'(r) - 2\bar{z}[\xi(r)]\xi(r)\xi'(r) \qquad [233]$$

where we have defined the quantity

$$\bar{z}[\xi(r)] = \frac{\sum_{i=0}^{I} c_i^R z_i^2 e^{-z_i\phi[\xi(\underline{r})]}}{\sum_{i=0}^{I} c_i^R z_i e^{-z_i\phi[\xi(\underline{r})]}} \qquad [234]$$

To see the physical meaning of $\xi(r)$, integrate both sides of Eq. [232]

$$\begin{aligned}\xi(r) &= 2\pi L_B A_0 \sum_{i=0}^{I} c_i^R z_i \int_r^R \mathrm{e}^{-z_i\phi(r)} r\, dr \\ &= 2\pi b \xi_a e_0^{-1} \int_r^R \rho(r) r\, dr \\ &= \xi_a[1 - Q(r)] \end{aligned} \qquad [235]$$

where $Q(r)$ is the amount of total ionic charge (per surface site charge) between the cylinder surface and r. Since ξ_a is proportional to the linear surface charge density, $\xi(r)$ is the effective linear charge density of the total charge (including the surface charge) enclosed by a cylinder of radius r. $\xi(r)$ plays a major role in the counterion condensation theory of Manning, and we thus refer to it as the *radial Manning parameter* (RMP). Manning's theory is discussed briefly below.

Cell Model: No Added Salt

At this point, although Eq. [233] is exact, an analytical solution for the RMP can be obtained only for no added salt, in which case the summations in Eq. [234] reduce to single terms giving $\bar{z}(r) = z_0$ (independent of r). Restricting our system to no added salt, Eq. [233] can be integrated twice [using $r\xi'' = (r\xi')' - \xi'$] to give

$$\int_0^{\xi} \frac{d\xi}{z_0\xi^2 - 2\xi - R\xi'(R)} = \ln\frac{R}{r} \qquad [236]$$

where the constant of integration from the first integral is easily found by inspection of Eq. [232]

$$\xi'(R) = -2\pi L_B A_0 R c_0^R z_0 \qquad [237]$$

The final integral in Eq. [236] is standard

$$\int \frac{dx}{ax^2 + 2bx + c} = \frac{1}{\delta}\tan^{-1}\left(\frac{ax+b}{\delta}\right) \qquad [238]$$

where we are restricted to

$$\delta^2 \equiv ac - b^2 > 0 \qquad [239]$$

For $\delta = 0$, we need only take the limit $\delta \to 0$ in Eq. [238]; for $\delta^2 < 0$ (the low surface charge density case), we put $\delta \to i\delta$ and by analytic continuation obtain the $\tanh^{-1}$ function. The form of the integral chosen is appropriate for highly charged cylindrical polyelectrolytes such as DNA. We then have the solution for the RMP within the PB cell model with no added salt

$$z_0\xi_{\mathrm{PBC}}(r) - 1 = \delta\,\frac{\delta\,\tan[\delta\,\ln(R/r)] - 1}{\tan[\delta\,\ln(R/r)] + \delta} \qquad [240]$$

where δ contains the integration constant and, using Eq. [74], is explicitly given by

$$\delta^2 + 1 = 2\pi L_B A_0 R^2 c_0^R z_0^2 = \tfrac{1}{2}(\kappa_R R)^2 \qquad [241]$$

Equation [240] is easily seen to obey the correct boundary condition at $r = R$. Recalling that c_0^R and hence κ_R are initially unknown, they can be determined from Eq. [241] by using the remaining boundary condition in Eq. [240] for $\xi(a) = \xi_a$ at the cylinder surface. This condition leads to the transcendental equation fixing δ:

$$\tan[\delta\,\ln(R/a)] = \frac{z_0\xi_a\delta}{\delta^2 + 1 - z_0\xi_a} \qquad [242]$$

With δ now given by Eq. [242], Eq. [240] represents the completed solution for $\xi(r)$ as a function of distance from the cylinder surface.

Before we obtain the potential, we notice that for systems with a linear charge density such that $\xi_a > 1$ (DNA and most other biopolyelectrolytes fall into this category), there is a specific distance at which $\xi(r) = 1$. This distance we denote by R_M (the Manning radius) and is found from Eq. [240]:[178]

$$R_M = R\,\exp[-\delta^{-1}\arctan(\delta^{-1})] \qquad [243]$$

We can now express our solution [240] a little more succinctly as

$$z_0\xi_{\mathrm{PBC}}(r) = \delta \tan\left(\delta \ln\frac{R_M}{r}\right) + 1 \qquad [244]$$

This form is readily integrated to yield the potential

$$z_0\phi_{\mathrm{PBC}}(r) = 2 \ln\left[\frac{r \cos(\delta \ln(r/R_M))}{R \cos(\delta \ln(R/R_M))}\right] \qquad [245]$$

Using Eq. [245] for the potential, one can verify that Eq. [241] is satisfied by c_0^R where

$$c_0^R = \frac{n_0}{2\pi b A_0 \int_a^R e^{-z_0\phi(r)} r \, dr} \qquad [246]$$

with $n_0 = 1/z_0$ (*i.e.*, z_0 counterions per DNA site; see Eq. [228]). The relevance in determining the concentration of counterions at the cell boundary is seen by finding the osmotic pressure of our system of cylindrical charged rods in an electrolyte solution. Using Eq. [241], the osmotic pressure is found to be[78,92,203]

$$\pi = \beta^{-1} \sum_{i=0}^{I} c_i^R = \frac{\delta^2 + 1}{2\pi\beta L_B A_0 R^2 z_0^2} \qquad [247]$$

Note that since the polyelectrolyte attracts counterions to its surface, thus reducing their concentration at the cell boundary, the osmotic pressure of the solution in the presence of a polyelectrolyte will be less than that in its absence.

The Poisson–Boltzmann RMP and potential profiles given by Eqs. [244] and [245] are displayed in Figure 23. Note that no special feature appears in the RMP near $\xi(R_M) = 1$. Manning's counterion condensation (CC) theory is discussed in some detail later, but we reveal here that it essentially describes counterions near a charged surface as a two-state system. Those ions within the Manning radius are considered condensed or less mobile than ions further out that are representative of the bulk electrolyte. The absence of any immediate connection between CC and PB theories (other than certain mathematical properties for the cylindrical model[178,204,205]) along with the belief that CC theory does have a physical basis suggests that the PB equation is somewhat limited in its description of counterion behavior at a charged surface. Comparisons between MC simulations and PB theory of hard sphere ionic solutions bear this out. One difficulty is in defining what constitutes a condensed counterion, whether the model used is a cell model or a bulk model. Within

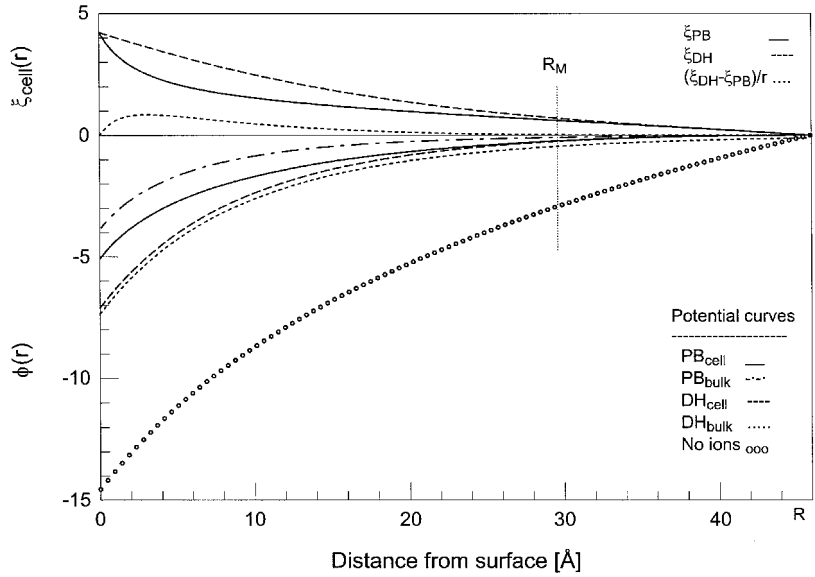

Figure 23 The radial Manning parameter $\xi(r)$ (top frame, cell model only; Eq. [244]) and potential $\phi(r)$ (bottom frame; Eq. [245]) in the PB cell and bulk models for a charged cylinder of radius $a = 10$ Å and surface charge density $\sigma_a = -0.094\ e_0/\text{Å}^2$ (corresponding to an average charge spacing of $b = 1.69$ Å as in B-DNA). A site concentration (corresponding to a phosphate concentration in DNA) of 0.1 M has been chosen, giving a Manning radius of $R_M = 29.6$ Å and a cell radius of $R = 56$ Å. The PB cell model potential profile (solid lines) is compared to the bulk PB (dotted–dashed line; Eq. [389]), DH cell model (dashed lines; Eq. [256]), DH bulk model (dotted line; Eq. [259]), and no-ion (circles; Eq. [362]) values.

Manning's theory, one often uses the Manning radius but other definitions are possible,[12,206,207] and a measure of condensation was suggested earlier in connection with the NLDH approximation (e.g., Eqs. [265]–[269]). It has also been found useful to consider counterions at a potential more negative than $-k_BT/e_0$ as being condensed in the CC sense, thus allowing at least an indirect comparison between CC and PB (and MC) predictions and experiment.[208,209] For the system considered, the potential in the lower frame of Figure 23 equals $-k_BT/e_0$ at 25.8 Å, in approximate agreement with a Manning radius of 29.6 Å. Also shown for comparison are the bulk PB, bulk and cell DH, and no-electrolyte potential profiles. No exact solution exists for the bulk model cylindrical PB equation so a numerical finite-difference method (to be discussed later; see Eq. [389]) was used to obtain the potential. The DH equations for the RMP and potential in the cell and bulk models are derived below (Eqs. [256] and [259]), but it is interesting to point out that despite having the same surface and cell values, the PB and DH RMP profiles are quite different.

The potential can be obtained from the $\xi(r)$ profile through a simple integration (Eq. [230]). The difference in $\xi(r)/r$ between the DH and PB values is also shown in Figure 23 (top frame, dotted line) with most of the difference occurring within one Debye length of the surface ($\kappa_D^{-1} = 13.6$ Å). Of particular relevance to biophysical systems is the competition between mono- and divalent counterions at the cylindrical surface,[210] the discussion of which we defer until later, and that between monovalent counterions with different radii.[202] Also, Deserno and Holm have compared molecular dynamics simulations with the prediction of PB cell model theory for the calculation of osmotic coefficients and the quantification of counterion condensation.[211]

Cell Model: Added Salt

If the ionic strength of added salt is much smaller than that of initially bound counterions, that is, if

$$\sum_{i=1}^{I} \bar{c}_i z_i^2 \ll \bar{c}_0 z_0^2 \qquad [248]$$

then the added salt is not expected to substantially change the potential from the no-added-salt case.[78] Under these circumstances, Eq. [245] can be used for the potential, with ion concentrations given by

$$c_i(r) = c_i^R \exp(-z_i \phi_{\mathrm{PBC}}(r)) \qquad [249]$$

Ion concentrations at the cell boundary are found from the analogue of Eq. [246] with the osmotic pressure π given by the middle expression in Eq. [247]. Unfortunately, no exact analytical solution has been found for the important case of the cylindrical cell model with larger amounts of added salt, but good approximations are available.[212]

Bulk Model: Highly Charged Cylinder

For a highly charged cylinder in the presence of a general bulk electrolyte, an analytical approximation to the potential profile can be obtained by using the $z:z$ result of Eq. [152] and applying the argument leading to Eq. [57] for a highly charged plane. This leads to Eqs. [147] and [149] or Eqs. [152] and [154] with z replaced by $|z_c|$, the highest counterion valence, and κ_D replaced by $\sqrt{2}\kappa_c$. The PGC potential at the cylinder surface, Eq. [153], reduces to

$$|z_c|\phi_{\mathrm{high}}(a) \approx -2\, S_a \ln\left[\tanh\left(\frac{\kappa_c \lambda_{\mathrm{GC}}}{\sqrt{2}|z_c|}\left(1 + \frac{\lambda_{\mathrm{GC}}}{|z_c|a}\right)\right)\right] \qquad [250]$$

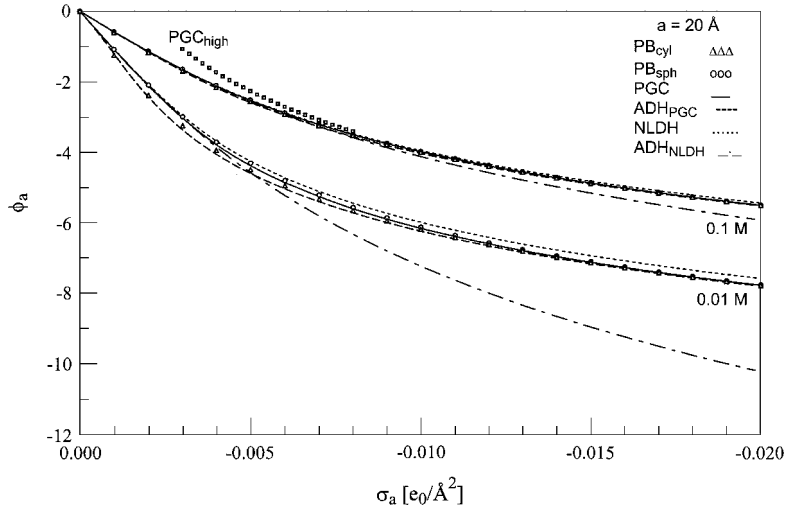

Figure 24 The surface potential of a negatively charged sphere of radius 20 Å (or cylinder of radius 10 Å) in 0.01 and 0.1 M 1 : 1 electrolytes ($\kappa_D C_a = 0.7$ and 2.0, respectively) as a function of surface charge density obtained from the PGC solution of Eq. [153] based on the Debye–Gouy–Chapman length of Eq. [154] (solid lines) and Eq. [155] (dashed lines) as well as from the NLDH expression of Eq. [181] in which exact (dotted lines; Eq. [180]) and approximate (dotted–dashed lines; Eq. [182]) values for parameter ζ were used. The exact potential values obtained using a finite-difference method (Eq. [389]) are shown as circles; values from Eq. [250] are shown as squares.

Provided that the curvature correction term is small, this result is valid for symmetric salts and for mixed-salt divalent counterion concentrations satisfying

$$\sqrt{c_2} > \frac{1.64a\,c_1}{2|\xi_a| - 1} \qquad [251]$$

in which a is the cylinder radius in Å, and concentrations are in M. For double-stranded B-DNA in a solution of 0.1 M monovalent salt, Eq. [251] gives $c_2 > 0.05$ M. The values given by Eq. [250] start to deviate from the exact values when the predicted surface potential drops to less than $\sim$3–4 k_BT/e_0 in magnitude. A definition of "high surface charge density" would depend on the concentration as well as stoichiometry of the electrolyte (e.g., $|\sigma_a| \gg \sigma_0$), but for DNA, where the surface charge density is about -0.01 e_0/Å^2 ($\sigma_0 = 0.002$ e_0/Å^2 for 0.1 M monovalent salt), approximation [250] is quite good. Values of the surface potential according to Eq. [250] is shown in Figure 24 (squares) for σ_a between -0.003 e_0/Å^2 and -0.008 e_0/Å^2 in 0.1 M monovalent salt.

Bulk Model: Moderately Charged Cylinder

An approximate potential profile for a moderately charged cylinder in the presence of a mixed electrolyte can be found by using the effective-valence planar solution of Eq. [69] in either the PGC approximation of Eq. [152] or the NLDH approximation of Eq. [177]. Application of Eq. [152] is straightforward, but the NLDH potential of Eqs. [177]–[181] still requires development in terms of the cylindrical geometry. The solution to DH equation [165] for $d = 2$ subject to conditions [160] is given in terms of Bessel functions and is derived in the following section. This solution is given by Eq. [259] below and leads to

$$\begin{aligned} \phi_{\mathrm{DH}}(a) &= \frac{2S_a\delta_a}{\kappa_D\lambda_{\mathrm{GC}}} \\ f(r) &= \frac{K_0(\kappa_D r)}{K_0(\kappa_D a)} \approx \frac{e^{-\kappa_D(r-a)}}{\sqrt{r/a}} \\ \delta_a &= \frac{K_0(\kappa_D a)}{K_1(\kappa_D a)} \approx \frac{2\kappa_D a}{2\kappa_D a + 1} \end{aligned} \qquad [252]$$

where the right-hand equalities obtain for $\kappa_D a \gg 1$. The NLDH solution [177] is then

$$\begin{aligned} \phi_{\mathrm{NLDH}}(r) &= \frac{4}{\zeta z}\tanh^{-1}\left[\tanh\left(\frac{\zeta z\phi_a}{4}\right)\frac{K_0(\kappa_D r)}{K_0(\kappa_D a)}\right] \\ &= \frac{4}{\zeta z}\tanh^{-1}\left[\frac{\sigma_{\mathrm{ADH}}}{2\sigma_0}\frac{K_0(\kappa_D r)}{K_0(\kappa_D a)}\right] \\ &\approx \frac{4}{\zeta z}\tanh^{-1}\left[\frac{\sigma_{\mathrm{ADH}}}{2\sigma_0}\frac{e^{-\kappa_D(r-a)}}{\sqrt{r/a}}\right] \end{aligned} \qquad [253]$$

where ζ and ϕ_a are determined from Eqs. [180] and [181] (or approximately from Eqs. [182] and [181]) and σ_{ADH} and σ_0 are given by Eq. [189]. The approximate electrostatic free energy is given by Eq. [194].

Figure 24 displays the PGC and NLDH surface potentials as a function of charge density for a negatively charged cylinder of radius 10 Å (and a sphere of radius 20 Å) in a 1 : 1 electrolyte at 0.1 M and 0.01 M; the exact (finite-difference approach of Eq. [389]) results are also shown. According to Eq. [157], the PGC values are valid if $C_a > 8$ Å for 0.1 M and $C_a > 14$ Å for 0.01 M, for $|\sigma_a| = 0.02\ e_0/\text{Å}^2$, which is consistent with the data. Other potentials shown were calculated using the exact results of Eq. [389] and the NLDH values of Eq. [177] (using Eq. [181] with ζ given by either Eq. [180] or [182]; only data for a sphere are shown). The predicted surface potentials using the value of ζ according to Eqs. [180] and [181] (dotted lines)

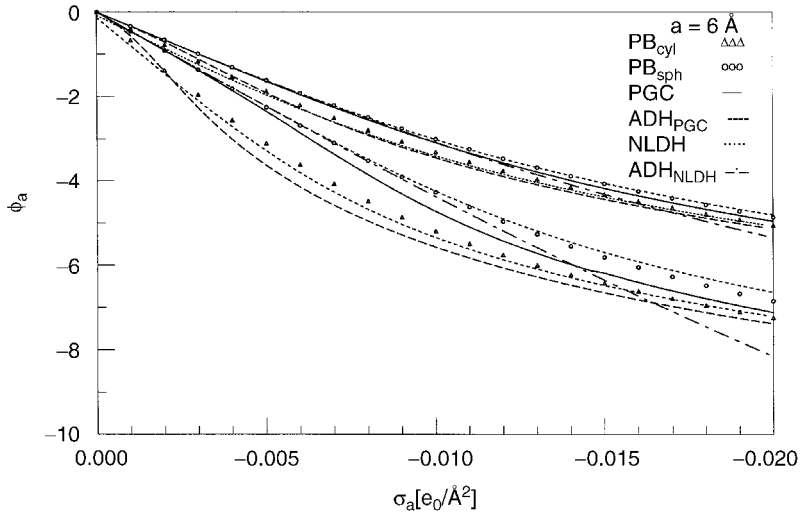

Figure 25 The same conditions as in Figure 24 except for a sphere radius of 6 Å (or cylinder radius of 3 Å); 0.1 M (0.01 M) electrolyte is the upper (lower) set of curves.

are slightly above the exact profile, and although the agreement is good, it is not as good as that found using the PGC results of Eq. [153] (solid or dashed lines). The potentials using the small-potential expression for ζ (Eq. [182]) are good up to $|\phi_a| \sim 4k_BT$.

Similar data are shown in Figure 25 for a cylinder of radius 3 Å (and a sphere of radius 6 Å). It is seen that in this case the difference between the cylinder (triangles) and sphere (circles) data is clearly noticeable and that the PGC potential predicted from Eqs. [153] and [154] lies in between, yet fitting neither well for the 0.01 M salt, indicative of the much smaller $\kappa_D C_a$ value (0.2) in this case. Improving the potential by including terms up to second order in $\kappa_D C_a$ would help considerably. The potential utilizing the first-order approximation of Eq. [155] (dashed line) for the Debye–Gouy–Chapman length does well for the 0.1 M salt, falling just below the cylinder data, but it does less well for 0.01 M, although the general trend of the data is followed. Both the PGC and NLDH potential predictions improve considerably for 0.1 M electrolyte and the NLDH results using the exact ζ (for which both the cylinder and sphere potentials are shown as dotted lines) are in fact better than the (first-order in $\kappa_D C_a$) PGC potential. (Equation [184] gives results only slightly different from those using the exact ζ for these systems.)

Figure 26 displays the potential profile for a charged cylinder of radius 10 Å according to the exact (Eq. [389]), PGC (Eq. [152]), and NLDH (Eq. [177]) solutions for a mixed 1 : 1–2 : 1 electrolyte using the effective-valence approximation of Eq. [69] for the latter two. The DH (Eq. [259]),

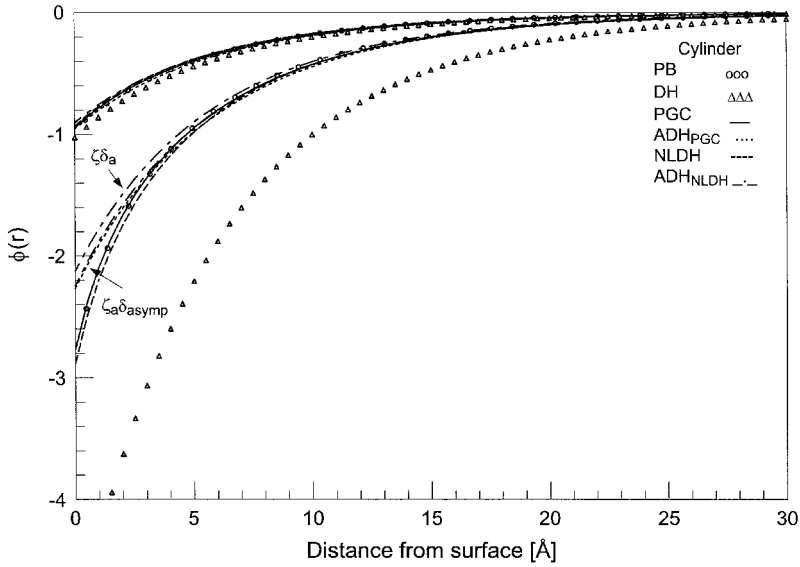

Figure 26 Various potential profiles as a function of distance from the surface for a charged cylinder of radius 10 Å with surface charge densities of $-0.002\ e_0/\text{Å}^2$ and $-0.01\ e_0/\text{Å}^2$ in a mixed 1 : 1–2 : 1 electrolyte with concentration of 0.1–0.02 M. Exact PB (circles; according to Eq. [389]) and DH (triangles; Eq. [259]) solutions are compared with the PGC (solid lines; Eqs. [152] and [155]) and NLDH (dashed lines; Eq. [253] with approximate $\zeta_a\delta_{\text{asymp}}$ values) solutions and their ADH//PCG (dotted lines; Eq. [366]) and ADH//NLDH (dotted–dashed lines; Eq. [261] with either exact $\zeta\delta_a$ or approximate $\zeta_a\delta_{\text{asymp}}$ values) potentials.

ADH//PGC (Eq. [366]), and ADH//NLDH (Eqs. [187]) profiles are also shown for comparison. For the two surface charge densities considered ($-0.002\ e_0/\text{Å}^2$ and $-0.01\ e_0/\text{Å}^2$), the PGC profile agrees very well with the exact (finite-difference) solution. The NLDH profile was determined using the simple approximation of Eq. [182] for ζ; use of Eq. [180] gives values intermediate between those shown and the PGC values and is necessary for more highly charged systems. Thus, the much simpler NLDH expression also works quite well. The ADH profiles are discussed below.

Cell and Bulk Models: Debye–Hückel Potential

Taking the weak-field limit of Eq. [224] results in the cylindrical version of Eq. [76]:

$$\frac{1}{r}\frac{d}{dr}\left[r\frac{d\phi(r)}{dr}\right] = \kappa_R^2\phi(r) - 4\pi L_B A_0 \sum_{i=0}^{I} c_i^R z_i \qquad [254]$$

Analogous to the planar case, the solution to Eq. [254] is given by Eq. [77], and the homogeneous solutions corresponding to Eq. [86] are

$$\phi_H(r) = AK_0(\kappa_R r) + BI_0(\kappa_R r) \qquad [255]$$

where K_0 and I_0 denote modified Bessel functions of the second kind.[213] Using the properties of the Bessel functions, the solution subject to the boundary conditions in Eq. [255] is readily shown to be

$$\begin{aligned}\xi_{\mathrm{DHC}}(r) &= \frac{r\xi_a}{aD(\kappa_R)}[I_1(\kappa_R R)K_1(\kappa_R r) - K_1(\kappa_R R)I_1(\kappa_R r)] \\ \phi_{\mathrm{DHC}}(r) &= \frac{-2\xi_a}{\kappa_R aD(\kappa_R)}[I_1(\kappa_R R)K_0(\kappa_R r) + K_1(\kappa_R R)I_0(\kappa_R r) - (\kappa_R R)^{-1}]\end{aligned} \qquad [256]$$

where

$$D(\kappa_R) = I_1(\kappa_R R)K_1(\kappa_R a) - K_1(\kappa_R R)I_1(\kappa_R a) \qquad [257]$$

and $\xi_a = L_B/b$. Use of the Wronskian verifies that $\phi(R) = 0$. From Eq. [256], the value of $\phi_H(R)$ can be identified as the negative of the constant term (Eq. [78]), so Eq. [82] for κ_R becomes

$$\kappa_R^2 = \sum_{i=0}^{I} \frac{4\pi L_B A_0 \bar{c}_i z_i^2}{1 + \frac{2z_i\xi_a}{\kappa_R^2}\left[\frac{2}{R^2-a^2} - \frac{1}{aRD(\kappa_R)}\right]} \qquad [258]$$

In the limit of low polyelectrolyte concentration, we let $R \to \infty$ in Eq. [256] to find

$$\begin{aligned}\xi_{\mathrm{DH}}(r) &= \frac{r\xi_a}{a}\frac{K_1(\kappa_D r)}{K_1(\kappa_D a)} \\ \phi_{\mathrm{DH}}(r) &= \frac{-2\xi_a}{\kappa_D a}\frac{K_0(\kappa_D r)}{K_1(\kappa_D a)}\end{aligned} \qquad [259]$$

This potential is compared to the exact PB potential in Figure 26. For $\kappa_D a \gg 1$, these results reduce to the asymptotic expressions

$$\begin{aligned}\xi_{\mathrm{DH}}(r) &= \xi_a\sqrt{\frac{r}{a}}e^{-\kappa_D(r-a)} \\ \phi_{\mathrm{DH}}(r) &= \frac{-2\xi_a}{\kappa_D\sqrt{ar}}e^{-\kappa_D(r-a)}\end{aligned} \qquad [260]$$

The exact and asymptotic solutions apply to a single polyelectrolyte cylinder immersed in a bulk electrolyte with screening constant κ_D determined by Eq. [12]. The cell (Eq. [256]) and bulk (Eq. [259]) model DH potentials are compared with the corresponding PB potentials in Figure 23.

Bulk Model: Apparent DH Linear Charge Density and Counterion Condensation

The identification of an apparent surface charge density may also be interpreted as support for the concept of counterion condensation within PB theory in the sense that altering the amount of bulk electrolyte does little to affect ionic properties near the surface, thus implying some sort of two-state model for ions. As mentioned earlier and discussed again in its own section near the end of this chapter, the counterion condensation theory of Manning[214] has provided simple, yet elegant, explanations for a wide variety of physical phenomena involving linear polyelectrolytes. A continuing issue is the extent to which the Poisson–Boltzmann theory supports the hypothesis of counterion condensation. In this section we restrict the generalized expressions for the apparent Debye–Hückel charge density and potential to a cylindrical geometry and view it in light of counterion condensation.

The apparent Debye–Hückel potential for a cylinder within the NLDH approximation is determined from Eqs. [188], [187], and [252]. We then have

$$\phi_{\mathrm{ADH}}(r) = \frac{2S_a}{\kappa_D \lambda_{\mathrm{AGC}}} \frac{K_0(\kappa_D r)}{K_1(\kappa_D a)} \qquad [261]$$

where the apparent Gouy–Chapman length is given by

$$\lambda_{\mathrm{AGC}} = \frac{1}{2}\left(\lambda_{\mathrm{GC}} + \sqrt{\lambda_{\mathrm{GC}}^2 + \left(\frac{\zeta z K_0(\kappa_D a)}{\kappa_D K_1(\kappa_D a)}\right)^2}\right) \qquad [262]$$

and ζ is found using Eqs. [180] and [181]; the apparent charge density is given by Eq. [189] with $\delta_a = K_0(\kappa_D a)/K_1(\kappa_D a)$. If $\kappa_D a \gg 1$, asymptotic expressions for the Bessel functions may be introduced and, for low surface charge density, Eq. [182] may be used for ζ. It is important to emphasize that Eqs. [261] and [262] accurately describe the asymptotic Debye–Hückel tail of the potential even under circumstances when the NLDH approximation fails, provided, of course, that the charge density of the surface is known (and not charge-regulated). Reliance on the validity of the NLDH approximation is only necessary if one wishes to use the apparent Gouy–Chapman length (which determines ζ through Eq. [262]) to determine the potential at or near the surface from Eq. [181] [$\phi_{\mathrm{DH}}(a)$ is found from Eq. [261]]. In analogy with

Eqs. [189]–[191], Eq. [262] may be rewritten in terms of apparent and actual linear charge densities:

$$\xi_{\mathrm{ADH}} = \frac{2\xi_a}{\sqrt{(\xi_a/\xi_0)^2 + 1} + 1}, \quad \xi_0 = \frac{\kappa_D a}{\zeta z \delta_a} \qquad [263]$$

with the low and high charge density limits

$$\begin{aligned} \lim_{|\xi_a| \ll \xi_0} \xi_{\mathrm{ADH}} &= \xi_a \left[1 - \left(\frac{\xi_a}{2\xi_0} \right)^2 \right], \\ \lim_{|\xi_a| \gg \xi_0} \xi_{\mathrm{ADH}} &= 2S_a \xi_0 \left(1 + \frac{\ln(\delta_a)}{\ln(\xi_0/2|\xi_a|)} - \frac{\xi_0}{|\xi_a|} \right) \end{aligned} \qquad [264]$$

The perturbed Gouy–Chapman potential of Eq. [152] can also be used to obtain an (approximate) ADH potential. This procedure requires integrating the asymptotic spherical potential derived from Eq. [152] along a line charge and is discussed in a later section on the additivity of the spherical DH solution; the result is given by Eq. [366]. In light of the asymptotically exact ADH potential obtained from the NLDH approximation, that based on the PGC potential is only necessary if one wishes to predict the surface potential from the apparent charge density, which requires that the PGC potential be accurate. This is elaborated on below in connection with charged spheres.

The apparent DH profiles based on the PGC and NLDH solutions to the Poisson–Boltzmann equation are shown in Figure 26 for a charged cylinder of radius 10 Å for two surface charge densities (-0.002 and -0.01 $e_0/\text{Å}^2$) and compared with the exact (Eq. [389]), DH (Eq. [259]), and nonlinear approximations (Eqs. [152] and [253]). Both approximations (PGC and NLDH) also give good ADH potentials, particularly in comparison to the actual DH profile. The best fit asymptotically for distances greater than 10 Å from the surface is that of the "accurate" ADH//NLDH profile (indicated by $\zeta\delta_a$ in Fig. 26). The "simple" ADH//NLDH profile (indicated by $\zeta_a\delta_{\mathrm{asymp}}$) obtained by using ζ_a of Eq. [182] and the asymptotic expansion in Eq. [252] for ζ_a is almost as good and closely matches the ADH//PGC profile. This supports the well-reasoned contention that for the ADH profile one may use the low-potential approximation for ζ as well as the asymptotic expansion for δ_a. Although not particularly noticeable in the figure, the ADH//PGC profile lies below (is more negative than) the exact curve for a wide range of intermediate distances (5–15 Å). This stems from assuming that the apparent surface charge density for a cylinder can be obtained by integrating the ADH potential for a sphere along a line charge.

In Figure 27 the apparent linear charge density as a function of the actual linear charge density is shown for the NLDH (Eq. [263]) and PGC (Eq. [365])

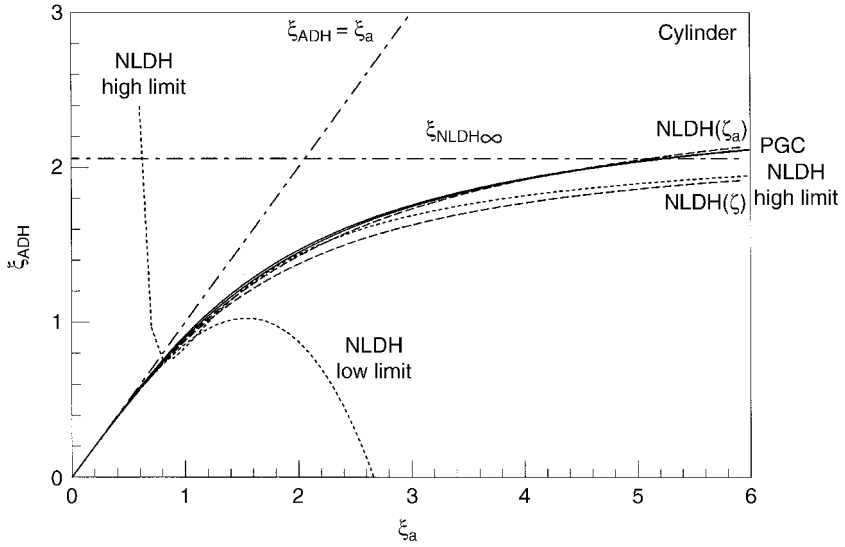

Figure 27 The apparent linear charge density as a function of actual linear charge density for a cylinder of radius 10 Å in a mixed 1 : 1–2 : 1 electrolyte with concentration 0.1–0.02 M within the NLDH (dashed lines; Eq. [263] with the exact ζ or approximate ζ_a values) and PGC (solid lines; Eq. [365] with exact and approximate δ_{DGC} values) approximations. The NLDH low and high charge density approximations (Eqs. [264]) are shown by dotted lines; the infinite-charge density limit is shown by the horizontal dotted–dashed line.

approximations for a 10-Å-radius cylinder in the presence of a mixed 1 : 1–2 : 1 mixed electrolyte with concentrations of 0.1 M and 0.02 M, respectively. The NLDH high and low charge density limits of Eqs. [264] are also shown and the effective-valence approximation of Eq. [69] was used in all cases. The exact NLDH curve, designated by ζ to indicate that Eq. [180] was used, has the limiting value $\xi_\infty = 2.06$ and falls about 10% below the curve calculated using the surface potential approximation of Eq. [182]; the exact value for δ_a from Eq. [252] was used in both cases, although here the asymptotic value also gives good results. The result of this 10% difference is the 10% difference seen in the NLDH surface potentials of Figure 26. The PGC curve follows the approximate NLDH data closely. Note the dramatic reduction in the apparent linear charge density for actual charge densities greater than the limiting value ($\xi_\infty = 2.06$ and 2.53 for the NLDH and PGC approximations, respectively). This implies that system properties near the surface, such as the potential or ion concentration, are well screened from being accurately observed asymptotically. Thus, the difficulty in obtaining an accurate fit to the asymptotic potential results in considerable uncertainty in predicted surface potentials or other surface properties and this extrapolation becomes increasingly more difficult

as the surface charge density is increased. The extraction of an apparent linear charge density from experimental data was pioneered by Stigter, who also gives tables of correction factors that have been widely used.[215–219] Stigter's numerical procedure, although similar in spirit to the analytical approach adopted here, is based on a line charge model while the ADH//NLDH method retains a finite cylinder radius.

The fact that the apparent linear charge density is lower than the actual charge density can be seen as confirmation that PB theory does predict some sort of counterion condensation. We mention that because the ADH method results from a (linear) DH interpretation of the (nonlinear) PB equation, it also has a (rather tenuous) mathematical connection to Manning's counterion condensation theory, which also makes use of the DH solution.[214] From either Eq. [192] or Eq. [263], the fraction of linear charge density neutralized can be written as (ignoring a contribution from ζ)

$$f_{\text{neut}} = 1 - \frac{\xi_{\text{ADH}}}{\xi_a} = 1 - \frac{2}{\sqrt{(z\xi_a K_0(\kappa_D a)/[\kappa_D a K_1(\kappa_D a)])^2 + 1} + 1} \qquad [265]$$

which is a function of $\kappa_D a$. To see that this might be a promising result, for $\xi_a/\xi_0 \gg 1$, we have

$$\lim_{|\xi_a| \gg \xi_0} f_{\text{neut}} = 1 - \frac{2\kappa_D a K_1(\kappa_D a)}{z\xi_a K_0(\kappa_D a)} \qquad [266]$$

Manning's counterion condensation theory,[214] developed for a line charge in a dilute electrolyte ($\kappa_D a \sim 0$), predicts

$$f_M = 1 - \frac{1}{z\xi_a} \qquad [267]$$

which agrees with Eq. [266] for the relatively small value $\kappa_D a \sim 0.17$ and that corresponds to a cylinder of 10 Å radius (DNA) in a 2.6 mM 1 : 1 electrolyte. To see how sensitive the neutralized fraction is to changes in $\kappa_D a$, in Figure 28 we plot Eq. [265] as a function of the linear charge density (actually $z\xi_a$) for several values of $\kappa_D a$ and compare it with Manning's formula. We see that despite some discrepancies, the form of the curves roughly follows Manning's result and for large linear charge density and small $\kappa_D a$ Eq. [265] does quite well; for large values of $\kappa_D a$, Eq. [267] is not expected to hold.[214] Also, we note that the neutralized fraction is relatively insensitive to ionic strength for high linear charge density: for $z\xi_a = 4$, a 100-fold increase in electrolyte concentration (from $\kappa_D a = 0.01$ to 0.1) results in only a 10% decrease in f_{neut}.

Given the neutralization fraction, one can then find the radius that encloses the appropriate number of neutralizing counterions. Stated another

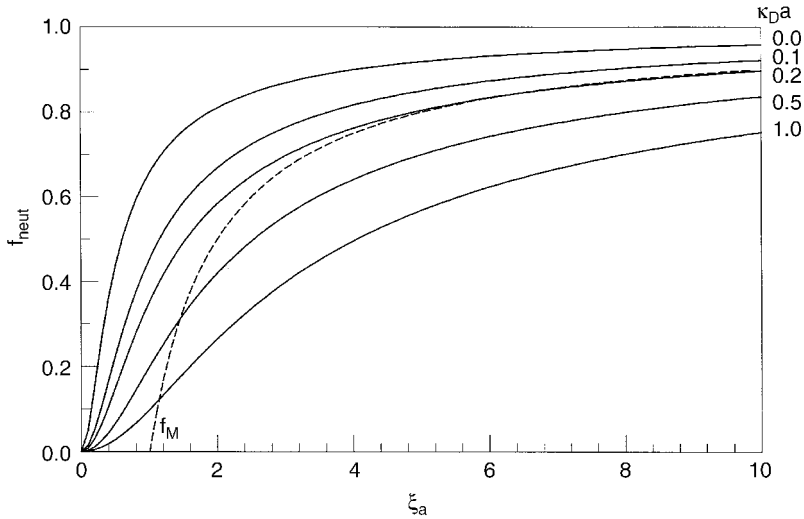

Figure 28 A plot of the ADH//NLDH fraction of surface charge neutralized by a bulk 1 : 1 electrolyte according to Eq. [265] for a charged cylinder as a function of the linear charge density $z\xi_a$ for several values of the variable $\kappa_D a$ given at right. The prediction of Manning's counterion condensation theory (f_M) for a line charge is shown by the dashed line.

way, at what radius is the PB electric field such that the apparent charge density is σ_{ADH}? In a two-state model, counterions within this radius are considered condensed while those outside are free. One would normally introduce a distance- or potential-dependent, two-state model specifically to determine the fraction of neutralized charge, not the other way around, but we do so to see how consistent the PB equation (or at least the NLDH approximation) is with the assumption of a two-state distance-dependent model. By applying Gauss' law for the d-dimensional radial PB equation, we find

$$f_{neut} = \frac{\int_a^r \rho(r) r^{d-1} dr}{\int_a^\infty \rho(r) r^{d-1} dr} = \frac{r^{d-1}\phi'_{\mathrm{PB}}(r)}{a^{d-1}\phi'_{\mathrm{PB}}(a)} \qquad [268]$$

This leads to the following expression for the "condensation radius" r_c

$$\left(\frac{r_c}{a}\right)^{d-1}\left(\frac{\phi'_{\mathrm{DH}}(r_c)}{\phi'_{\mathrm{DH}}(a)}\right) + \left(\frac{\sigma_{\mathrm{ADH}}}{2\sigma_0}\frac{\phi_{\mathrm{DH}}(r_c)}{\phi_{\mathrm{DH}}(a)}\right)^2 = 1 \qquad [269]$$

where

$$\frac{\sigma_{\mathrm{ADH}}}{2\sigma_0} = \frac{\sigma_a/\sigma_0}{\sqrt{(\delta_a\sigma_a/\sigma_0)^2 + 1} + 1}, \quad \sigma_0 = \frac{e_0\kappa_D}{2\pi L_B z}, \quad \delta_a = \frac{-\kappa_D\phi_{\mathrm{DH}}(a)}{\phi'_{\mathrm{DH}}(a)} \qquad [270]$$

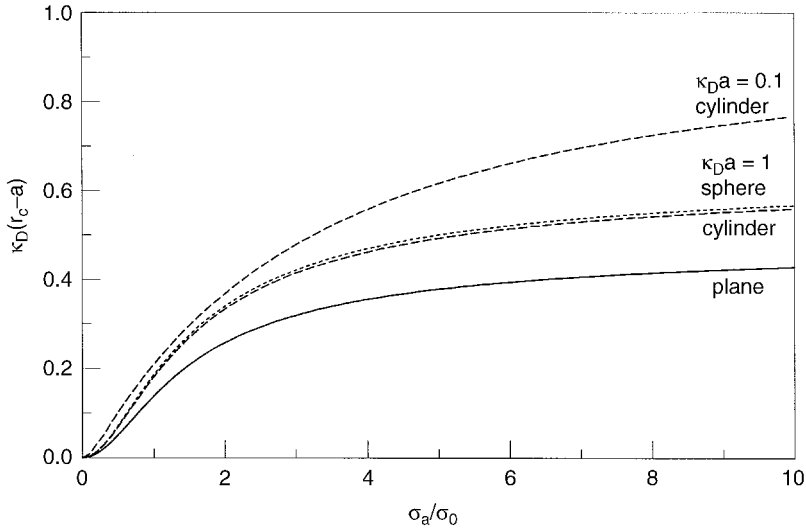

Figure 29 The scaled condensation radius determined from Eq. [269] as a function of the scaled surface charge density σ_a/σ_0 for a plane (solid line), cylinder (dashed lines; $\kappa_D a = 1$ and $\kappa_D a = 0.1$) and sphere (dotted line; $\kappa_D a = 2$).

Equation [269] can be solved analytically for r_c only for a charged plane. In Figure 29 we compare the condensation radius $\kappa_D r_c$ as a function of the scaled surface charge density σ_a/σ_0 for planar, cylindrical, and spherical systems. We have explicitly included the geometric factor δ_a so that the abscissa corresponds to identical surface charge densities for the three systems. Little difference is seen between the cylinder and sphere curves, which predict noticeably, although perhaps not significantly, larger condensation radii than for a plane with the same charge density. The important feature of all three systems is the limiting value of the condensation radius at higher charge densities demonstrating that there is at least the semiquantitative suggestion that PB theory supports a distance-dependent two-state model of counterion condensation. To see how well a potential-dependent model is supported, the value of the NLDH potential at the condensation radius is shown in Figure 30 as a function of the scaled charge density for the same systems as shown in Figure 29. A limiting value of the potential is apparent as all curves are very much closer. Also shown in Figures 29 and 30 are the cylinder curves for a 100-fold decrease in electrolyte concentration ($\kappa_D a = 0.1$ vs. 1 previously).

Bulk Model: Two Charged Cylinders

Solutions containing linear colloidal particles, such as DNA segments or tobacco mosaic virus, are systems which may be modeled by interacting cylindrical polyelectrolytes.[220] We may apply the results derived earlier for

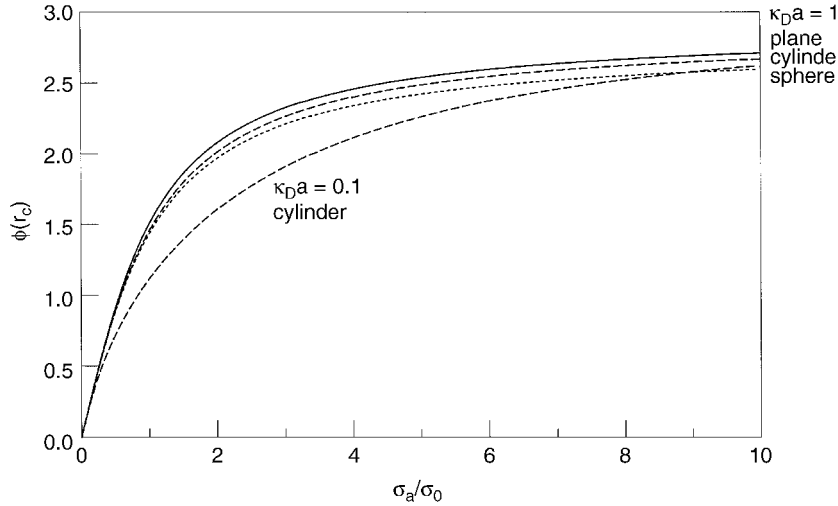

Figure 30 The NLDH potential at the condensation radius for the systems of Figure 29.

two charged particles by specializing them to charged cylinders. We first consider the cylinders to be parallel, as shown in Figure 21, and use the expressions given in Eqs. [196], [197], [201], [202], and [209]. To adopt these equations to the situation of two interacting cylinders, we use the Debye–Hückel solution [259] to assign

$$\begin{aligned} f_1(r) &= \frac{K_0(\kappa_D r)}{K_0(\kappa_D a_1)}, \quad \gamma_1 = \frac{K_0(\kappa_D(H_0 + a_1))}{K_0(\kappa_D a_1)} \\ \delta_1 &= \frac{K_0(\kappa_D a_1)}{K_1(\kappa_D a_1)}, \quad \varepsilon_1 = \frac{K_1(\kappa_D(H_0 + a_1))}{K_1(\kappa_D a_1)} \end{aligned} \qquad [271]$$

The force per unit length between the particles is found by integrating the pressure over lengthwise strips of width $d\rho$ in the dividing plane:

$$\frac{F(R)}{\text{Length}} = \int_0^\infty P(R, \rho, 0) d\rho = \frac{R}{2} \int_0^\infty P\left(R, \frac{R}{2}\cosh(\theta)\right) \cosh(\theta) d\theta \qquad [272]$$

where the right-hand integral follows from making the variable substitution

$$\rho = \sqrt{\left(\frac{R}{2}\right)^2 - r^2} = \frac{R}{2}\sinh(\theta) \qquad [273]$$

To obtain the force from the pressure, we ignore the term in the denominator of Eq. [209] and use Eqs. [271] to find

$$\beta F(R) = \frac{\kappa_D^2 R}{\pi L_B z^2}\left(\frac{A_1(R)}{K_0(\kappa_D a_1)} + \frac{A_2(R)}{K_0(\kappa_D a_2)}\right)^2 \int_0^\infty \left[K_0^2\left(\frac{\kappa_D R}{2}\cosh\theta\right) + K_1^2\left(\frac{\kappa_D R}{2}\cosh\theta\right)\right]\cosh\theta\, d\theta - \frac{2\kappa_D^2 R}{\pi L_B z^2}\left[\left(\frac{A_1(R)}{K_0(\kappa_D a_1)}\right)^2 + \left(\frac{A_2(R)}{K_0(\kappa_D a_2)}\right)^2\right]\int_0^\infty K_1^2\left(\frac{\kappa_D R}{2}\cosh\theta\right)\operatorname{sech}\theta\, d\theta \quad [274]$$

The first integral can be evaluated with the help of the identities[221,222]

$$K_\mu(x)K_\nu(x) = 2\int_0^\infty K_{\mu\pm\nu}(2x\cosh\theta)\cosh[(\mu \mp \nu)\theta]d\theta \quad [275]$$

and

$$K_\mu(x) = \int_0^\infty e^{-x\cosh\theta}\cosh(\mu\,\theta)d\theta \quad [276]$$

to give

$$\int_0^\infty \left[K_0^2\left(\frac{\kappa_D R}{2}\cosh\theta\right) + K_1^2\left(\frac{\kappa_D R}{2}\cosh\theta\right)\right]\cosh\theta\, d\theta = \frac{2\pi}{\kappa_D R}K_1(\kappa_D R) \quad [277]$$

The second integral is

$$\int_0^\infty K_1^2\left(\frac{\kappa_D R}{2}\cosh\theta\right)\operatorname{sech}\theta\, d\theta = \frac{\pi}{\kappa_D R}K_1(\kappa_D R) \quad [278]$$

Written as expressions of a single variable, Eqs. [277] and [278] are easily verified numerically. Use of these results yields the force per unit length:

$$\frac{\beta F(R)}{\text{Length}} = \frac{4A_1(R)A_2(R)K_1(\kappa_D a R)}{L_B z^2 K_0(\kappa_D a_1)K_0(\kappa_D a_2)} \quad [279]$$

For large $\kappa_D R$, the coefficients are independent of separation distance H_0 and only weakly dependent on the cylinder radii (through geometric factor δ), an observation noted previously by Brenner and McQuarrie.[186] Keeping only

the first term in the asymptotic expansion of the coefficients (Eq. [204]) gives

$$\frac{\beta F(R)}{\text{Length}} = \frac{4\hat{s}_1\hat{s}_2 K_1(\kappa_D R)}{L_B z^2 K_0(\kappa_D a_1) K_0(\kappa_D a_2)} \qquad [280]$$

where $\hat{s}_1$ is the scaled apparent charge density of Eq. [205] (including the geometric factor δ_1 of Eq. [271]). Equation [280] agrees exactly with the expression derived by Brenner and Parsegian[223] but has the advantage of assigning a specific value to their "effective charge" (our apparent charge density). Equation [280] also reduces to the results of Brenner and McQuarrie[186] in the limit of large $\kappa_D R$ by simply using the asymptotic expression for the Bessel function. Integration of the force according to

$$V(R) = \int_R^\infty F(R^*) dR^* \qquad [281]$$

provides the interaction potential per unit length (including the ζ parameters):

$$\frac{\beta V(R)}{\text{Length}} = \frac{4\hat{s}_1\hat{s}_2 K_0(\kappa_D R)}{L_B \zeta_1 \zeta_2 z^2 K_0(\kappa_D a_1) K_0(\kappa_D a_2)} \qquad [282]$$

Brenner and McQuarrie have combined the asymptotic form of the potential with an attractive van der Waals term and calculated the total interaction energy as a function of ionic strength and pH for identical interacting cylinders.[220] We have kept only the leading term in the asymptotic expansion of the interaction energy based on the coefficients of Eq. [204]. (Retention of the next-order term is discussed in a later section on interacting spheres in an analysis that applies here as well; see the paragraph following Eq. [353].)

We now obtain the total interaction energy for two skewed but nontouching cylinders.[223] With R representing the distance of closest approach and φ the crossing angle between the cylinders (see Fig. 31), the distance between closest segments is

$$R^{*2} = R^2 + \ell^2 \sin^2 \varphi \qquad [283]$$

Integrating the interaction potential along one cylinder length gives the total interaction potential between cylinders:

$$\begin{aligned} \beta V(R) &= 2\int_0^\infty \left[\frac{\beta V(R^*)}{\text{Length}}\right] d\ell \\ &= \frac{2}{\sin\varphi}\int_0^\infty \frac{\beta V(R^*)/\text{Length}}{\sqrt{R^{*2} - R^2}}\, R^* dR^* \\ &= \frac{2R}{\sin\varphi}\int_0^\infty [\beta V(R\cosh\theta)/\text{Length}]\cosh\theta\, d\theta \end{aligned} \qquad [284]$$

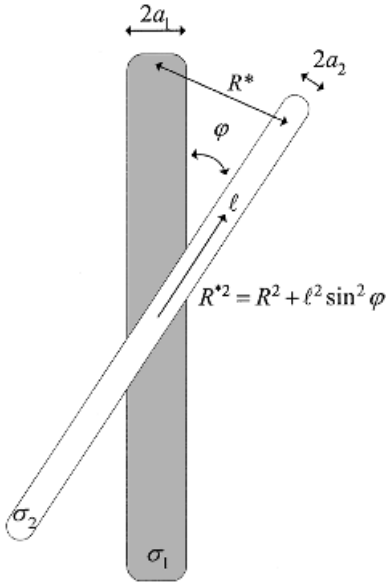

Figure 31 Diagram defining the parameters used to calculate the interaction of two charged, skewed cylinders of charge density σ_1, σ_2 and radii a_1, a_2. The cylinders make an angle φ with respect to one another, where R is the closest interaxial distance; R^* defines the interaxial distance between segments $d\ell$.

where we have used the substitution $R^* = R\cosh\theta$. Inserting Eq. [282] and using Eq. [275] gives (with ζ included in σ_0 as well)

$$\beta V(R) = \frac{4\pi\hat{s}_1\hat{s}_2 e^{-\kappa_D R}}{L_B\zeta_1\zeta_2 z^2 K_0(\kappa_D a_1)K_0(\kappa_D a_2)\sin\varphi} \qquad [285]$$

In the low-charge-density Debye–Hückel limit, the scaled apparent charge density $\hat{s}_1$ (and $\hat{s}_2$) reduces to the scaled charge density $\hat{\sigma}_1$ of Eq. [201].

Cell Model: Capillaries and Nanopores

Turning the no-added-salt cylindrical cell model inside-out and applying the charged surface boundary condition at R with a zero field condition at $a = 0$ gives a model for capillaries and nanopores in which the (inside) charged cylindrical wall is neutralized by counterions.[224–227] Of course, at some point in a complete description of the model the length L of the cylinder must be made finite to allow entry and exit of ions, but if the cylinder is long enough ($\kappa_D L > 3$, say), then end effects are negligible near the middle and need not concern us here. Because Eq. [245] gives the potential profile within the cylinder cell for $a < r < R$, most of the work in finding the solution for $a = 0$ has already been done. The potential inside a charged cylinder clearly has the form of Eq. [245] but with δ and R_M being two constants of integration that need to be determined anew based on the different boundary conditions. Replacing R with a in Eq. [245] satisfies the gauge condition $\phi(a) = 0$, where we will

take the limit $a \to 0$ later. The first constant δ may be determined in a number of ways. The quickest is to temporarily replace R with a Eq. [241] and then set $a = 0$; this implies that $\delta = \pm i$. With this substitution in Eq. [245] and letting $\gamma = 1/R_M$ be the second integration constant, we have

$$z_0\phi_{\mathrm{PBC}}(r) = \lim_{a\to 0} \ln\left[\frac{r\,\cosh(\ln(\gamma r))}{a\,\cosh(\ln(\gamma a))}\right]^2 = 2\ln(1+\gamma^2 r^2) \qquad [286]$$

Following this same procedure, but with variable δ, also shows that $\delta = \pm i$ if the potential is to remain finite at $r = 0$. We now find γ by applying the boundary condition on the electric field at $r = R$ but first note that electroneutrality requires that the average counterion concentration be related to the surface charge density by

$$\frac{z_0\sigma_R}{e_0} = \frac{-A_0 c_0 z_0^2 R}{2} \equiv \frac{-\kappa_D^2 R}{8\pi L_B} \qquad [287]$$

where we have introduced the "average" Debye screening constant κ_D. The boundary condition at R can now be written as

$$z_0\phi'_{\mathrm{PBC}}(R) = \left.\frac{4\gamma^2 r}{(1+\gamma^2 r^2)}\right|_{r=R} = \frac{-\kappa_D^2 R}{2} \qquad [288]$$

which determines γ. From Eq. [286] the counterion concentration is

$$\frac{c_{\mathrm{PBC}}(r)}{c_0} = \frac{e^{-z_0\phi(r)}\int_0^R r\,dr}{\int_0^R e^{-z_0\phi(r)} r\,dr} = \frac{(1+\gamma^2 R^2)}{(1+\gamma^2 r^2)^2} \qquad [289]$$

Equations [286]–[289] represent the PB solution for a cylindrical capillary without added salt. The case of added salt is more interesting but has no analytical solution. For a capillary in equilibrium with a bulk electrolyte, setting the potential to zero at the center of the capillary would not be appropriate; for this system it would be necessary to consider the finiteness of the capillary. The potential should then vanish far from capillary where the ion distribution is the same as bulk.

The Debye–Hückel solution for a cylindrical capillary follows along lines similar to those of the previous section except that we again extract the solution valid at $r = 0$. For this system, Eq. [258], which gives the Debye constant κ_0 at the position of the potential gauge ($r = 0$), simplifies to

$$2\kappa_0 I_1(\kappa_0 R) = \kappa_D^2 R \qquad [290]$$

where Eq. [287] defines κ_D. Equation [290] shows that for a small capillary radius or low surface charge density ($\kappa_D R < 0.5$) $\kappa_0 \sim \kappa_D$. The DH potential, its derivative and counterion concentration are then

$$\begin{aligned} z_0\phi_{\mathrm{DHC}}(r) &= \frac{-R\kappa_D^2}{2\kappa_0}\frac{I_0(\kappa_0 r) - 1}{I_1(\kappa_0 R)} \\ z_0\phi'_{\mathrm{DHC}}(r) &= \frac{-R\kappa_D^2}{2}\frac{I_1(\kappa_0 r)}{I_1(\kappa_0 R)} \\ \frac{c_{\mathrm{DHC}}(r)}{c_0} &= \frac{\kappa_0^2}{\kappa_D^2}(1 - z_0\phi_{\mathrm{DHC}}(r)) \end{aligned} \qquad [291]$$

These expressions are readily generalized to the case when added salt is present (only Eq. [290] changes).

In Figure 32 we compare the electrostatic potential (lower frame) and field (upper frame) calculated according to the PB (Eqs. [286] and [288], solid lines) and DH (Eq. [291], dashed lines) equations for a charged capillary of radius 20 Å with a surface charge density of $\sigma = -0.01\ e_0/\text{Å}^2$ for monovalent counterions ($z_0 = 1$) and no added salt; also shown are the DH values given in Eq. [291] using the average Debye constant κ_D in place of κ_0 (dotted lines). As usual, the DH potential considerably overestimates the magnitude of the

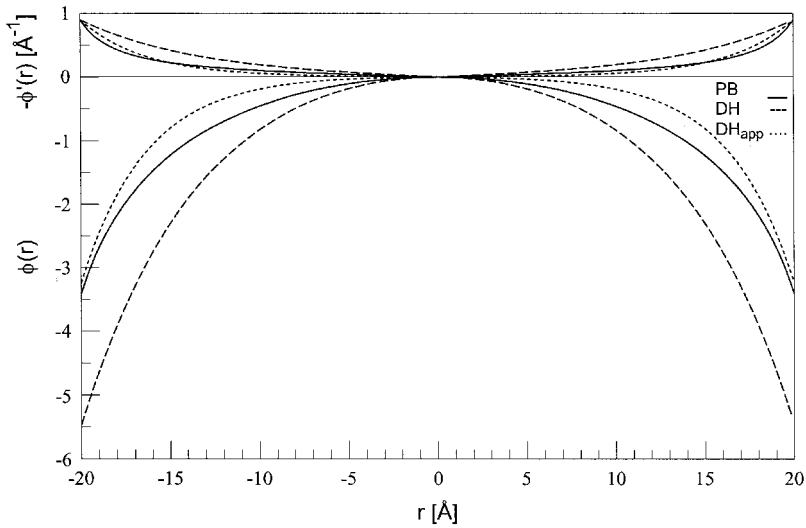

Figure 32 The PB (solid lines) and DH (dashed lines) potential and field profiles as a function of the distance from the center of a charged capillary of radius 20 Å with surface charge density $\sigma_a = -0.01\ e_0/\text{Å}^2$ in the absence of added salt (only counterions are present) according to Eqs. [286], [288], and [291]; the effect of using an average Debye screening constant in the DH expressions is shown by dotted lines.

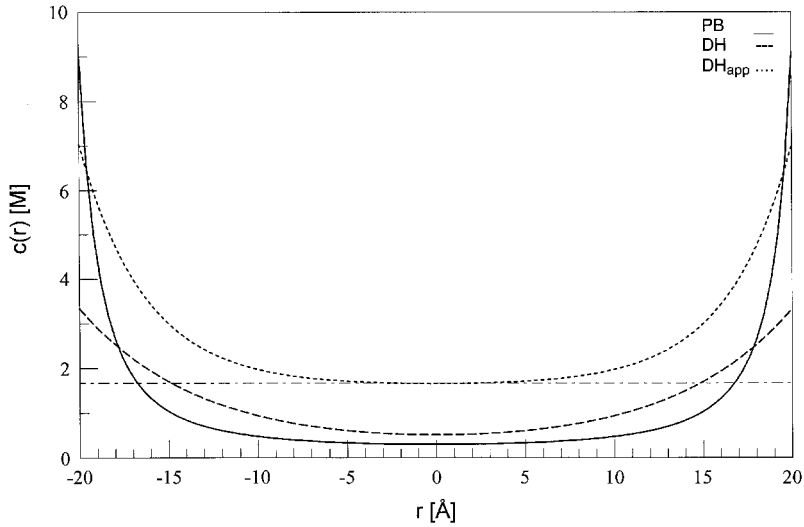

Figure 33 The PB (solid line) and DH (dashed line) concentration profiles for the same conditions as in Figure 32 according to Eqs. [289] and [291]; the approximate DH concentration profile using an average screening constant is shown by the dotted line.

surface potential, while use of the average Debye constant for the DH potential and field would seem to offer a considerable improvement. However, comparison of the counterion concentrations in Figure 33 shows that although this gives some agreement in the value of the counterion concentration at the surface, the value in the center of the capillary is much too high in comparison to the PB result. For the system considered we have $\kappa_0 R = 3.3$ with the average Debye constant being determined from Eq. [290].

Related Cylindrical Calculations

While the above solutions assume a constant surface potential or constant charge density, a cylinder with a regulated charge, that is, one in which the surface charge density is dependent upon the surface potential (boundary condition BC3 applies), is also of interest. Rice and Whitehead used the DH equation to determine corrections to classical electrokinetic flow within a cylindrical capillary[228] and Levine et al. have extended this to higher surface potentials using the PB equation.[229] Brenner and McQuarrie have presented a similar self-consistent calculation within the Debye–Hückel approximation.[230] Bentz has derived an approximate analytical expression for the potential between charged concentric cylindrical surfaces for a general electrolyte.[231] Martynov and Avdeev have applied their "extended NLDH approximation" (our terminology) to capillaries.[180] Several investigators[232–237] have compared Monte Carlo and PB predictions of ion distributions and Donnan exclusion

coefficients inside cylindrical pores. Martinez et al.[238] and van Keulen and Smit[239] have developed variational expressions for the potential profile in cylindrical micropores. Rice and Horne give an analytical solution to the DH equation inside a capillary of finite height.[240,241] Sharif, Tabatabaian and Bowen have studied multivalent counterion effects between charged spheres inside charged cylindrical pores.[242] Gil Montoro and Abascal have looked at the effect of helical charge symmetry on the PB potential[243,244] and Ouroushev has derived a solution to the PB equation for a set of line charges distributed on the surface of a finite cylinder,[245] both investigations approximating the discrete charge effects of a more realistic model of DNA. Nishio and Minakata have relaxed the common assumption of equal-size counterions in looking at competition between mono- and divalent ions.[246] Mokady, Mestel and Winlove have studied fluid flow through a layer composed of periodically spaced charged cylinders.[247]

We have assumed above that the charged cylinder is infinite and straight; neither of these assumptions apply exactly to biomolecules such as DNA. Thus, Stigter and Dill have used the Debye–Hückel equation to investigate end effects between finite-charged rods, comparing data on the second virial coefficient with experiment.[219] Allison has characterized the end effects of finite-length cylinders using the PB approach[248] and Nyquist, Ha and Liu have combined an extended DH theory with a two-state counterion description to investigate counterion condensation around finite-length cylinders.[249] Many investigations into the bending of long cylinders rely on the DH equation and begin with the solution for a charged sphere (this approach is discussed in a later section on additivity of the Debye–Hückel solution). However, progress has been made in solving the PB equation for a slightly curved cylinder.[250–254] Bowen and co-workers have developed two alternative iterative algorithms, one based on the differential Debye–Hückel equation[255] and the other using the integral nonlinear PB equation,[256] to investigate electroviscous flow in charged capillaries in the presence of added monovalent salt. Trizac and Hansen have published several studies in which the DH and PB cell models with and without added salt were used to determine the thermodynamic properties of finite cylindrical disks.[154,155,257–260]

The most common application of the cylindrical PB equation (by far) is to investigate the thermodynamic properties of polyelectrolyte such as DNA.[58,78,196,197,202,261–263] Within the PB cell model, the counterion concentration at the outer boundary gives the osmotic pressure, which is a measure of the electrostatic repulsion between neighboring biomolecules. This pressure can also be experimentally determined.[264–266] The Donnan coefficient, on the other hand, is strongly influenced by conditions at the macromolecular surface and can be used to provide key insight into the nature of polyelectrolyte–counterion interaction.[197,267–270] This interaction is important because of the salt-induced conformational changes DNA undergoes.[271–273] The nature of this behavior is believed to arise from the partial collapse, or condensation,

of the counterion cloud around the polyelectrolyte, thus weakening the phosphate–phosphate repulsion enough to allow for changes in the internal structure of DNA. This counterion condensation has thus been the focus of much work.[202,204,207,214,274–285] Within a hybrid PB-DH cell model, Löwen has defined an apparent linear charge density by integrating the density profile and finds a relationship between apparent and actual densities that is similar in form to our bulk NLDH approximation.[286] Of particular interest in this regard is the competition between mono- and divalent counterions.[73,74,209,287–294] Divalent counterions play a crucial role in the conformation of both single- and double-stranded nucleic acids[295–305] and may also be a key feature in DNA–protein recognition involving endonucleases.[306–312] Guéron, Demaret and Filoche have used a planar approximation to study the change in free energy for the B–Z transition in DNA.[313] Their work could easily be extended using either the PGC or NLDH approximation applied to a cylinder model of DNA.

Sparnaay has applied the Derjaguin approximation (which we discuss below in connection with two interacting spheres) to two parallel and to two crossed cylinders.[314] In an investigation of interacting parallel cylinders with different radii, Harries has numerically solved the PB equation in bi-cylindrical coordinates to obtain the force per unit length and the free energy as a function of separation distance.[315] Kuo and Hsu have used a perturbation approach to derive PB expressions for the free energy, entropy, and surface excess of coions of interacting cylinders or spheres in a general electrolyte.[316]

Spherical Geometry: The Micelle Model

The final system we consider in this tutorial is that of a spherical charged polyelectrolyte which serves as a model for a colloidal particle, micelle, or globular protein.[22] The primary characteristic that differs between modeling a micelle and a protein at this level of representation is the much greater surface charge density associated with a micelle. A secondary, but still important, consideration, is the pK_a values of the protein ionization sites, which might require use of boundary condition BC3 instead of BC2 as assumed below.[230]

General Equations

In a spherical coordinate system whose origin is at the center of a charged sphere of radius a (including a common electrolyte ion radius) and total charge $Q_a e_0$, the cell model PB equation and boundary conditions are

$$\frac{1}{r^2}\frac{d}{dr}\left[r^2\frac{d\phi(r)}{dr}\right] = -4\pi L_B A_0 \sum_{i=0}^{I} c_i^R z_i e^{-z_i\phi(r)} \qquad [292]$$

and

$$\phi'(a) = \frac{-L_B Q_a}{a^2} = \frac{-2S_a}{\lambda_{GC}} \qquad \phi'(R) = 0, \quad \phi(R) = 0 \qquad [293]$$

While no exact analytical solution to Eq. [292] is available, approximate nonlinear expressions corresponding to the PGC and NLDH solutions as well as the weak-field Debye-Hückel solution are given below.

Bulk Model: Grahame's Equation

In many cases it is unnecessary to obtain the entire potential profile for a system because the surface potential often suffices to describe the quantity of interest. In modeling catalytic hydrolysis near a micellar surface, the hydrolysis rate is related to the surface potential;[317,318] when investigating globular protein function the surface potential describes the pK_a of ionizable sites on the surface.[25,26] As shown previously, to determine the electrostatic free energy of a charged surface in an electrolyte requires knowing only the surface potential as a function of the charge density, or vice versa (Eq. [29]).[36] Several investigators have therefore derived approximate relationships between the surface charge density and the surface potential, known as *Grahame's equation*,[67] thus obviating the need for solving the PB equation explicitly. Abraham-Shrauner used a perturbation expansion of the nonlinear PB equation for a uniformly charged sphere of radius a in a 1 : 1 electrolyte to obtain the following expression for the surface potential:[167]

$$\phi_a \approx 2 \ln\left(\frac{1 + \sqrt{(\kappa_D \lambda_{GC})^2 + 1}}{\kappa_D \lambda_{GC}}\right) + \frac{4\lambda_{GC}}{a}\left(\frac{\kappa_D \lambda_{GC}}{\sqrt{(\kappa_D \lambda_{GC})^2 + 1}} - 1\right) \qquad [294]$$

where $\kappa_D a \gg 1$. For $a \to \infty$, Eq. [294] clearly reduces to the planar result of Eq. [25] for a monovalent electrolyte. A number of people have derived the (inverse) first- and second-order results, respectively, for a charged sphere (of sign S_a) in a 1 : 1 electrolyte:[168,171,319]

$$\frac{1}{\kappa_D \lambda_{GC}} \approx S_a \left(\sinh\frac{\phi_a}{2} + \frac{2}{\kappa_D a}\tanh\frac{\phi_a}{4}\right) \qquad [295]$$

and

$$\frac{1}{\kappa_D \lambda_{GC}} \approx S_a \sinh\frac{\phi_a}{4}\sqrt{1 + \frac{2}{\kappa_D a \cosh^2(\phi_a/4)} + \frac{8\ln(\cosh(\phi_a/4))}{(\kappa_D a)^2 \sinh^2(\phi_a/2)}} \qquad [296]$$

Equation [149], or equivalently Eq. [153], is a generalization of Eq. [295] to include cylinders and, with the use of an effective valence (Eq. [69]), to systems in an asymmetric or mixed electrolyte. Figures 24 and 25 display Grahame's equation within the PGC approximation for a negatively charged sphere of radius in a 1 : 1 electrolyte according to Eq. [153]. Similar expressions have also been derived for a charged sphere in a $z:z$ or 2 : 1 electrolyte[168,320] and Zhou has obtained a second-order relation for a general electrolyte.[321] Ohshima has derived approximate expressions for Grahame's equation for a spheroid within the Debye–Hückel approximation[322] and for a charged sphere in the absence of added salt within the PB cell model (counterions only).[323] Finally, we note that Eqs. [180] and [181], when specified for a spherical geometry, provides a relationship between the surface potential and charge density within the NLDH approximation. For low surface potentials, Eq. [182] may be used for parameter ζ, which then leads to the generalization of Eq. [25]:

$$\frac{z}{\kappa_D \lambda_{GC}} = \frac{S_a \sqrt{3+\delta_a^2}}{2\delta_a^2} \sinh\left(\frac{z\phi_a \delta_a}{\sqrt{3+\delta_a^2}}\right) \qquad [297]$$

where $\delta_a = \kappa_D a/(\kappa_D a + 1)$. This result is easily inverted to give an expression for the surface potential in terms of the charge density. Figures 24 and 25 display the surface potential for a charged sphere as a function of charge density according to Eq. [297] as well as that obtained by using the exact expression [180] for ζ.

Bulk Model: Highly Charged Sphere

The analytical approximation for the potential profile near a highly charged surface obtained earlier, given by Eqs. [147] and [149] or Eqs. [152] and [154], is applicable to a spherical micelle with z_c again representing the highest counterion valence and κ_c the screening constant. The potential at the surface, Eq. [153], then becomes

$$|z_c|\phi_{high}(a) \approx -2\, S_a \ln\left[\tanh\left(\frac{\kappa_c \lambda_{GC}}{\sqrt{2}|z_c|}\left(1 + \frac{2\lambda_{GC}}{|z_c|a}\right)\right)\right] \qquad [298]$$

Provided that the curvature correction term is small, this result is valid for symmetric salts and for mixed-salt divalent counterion concentrations satisfying

$$\sqrt{c_2} > \frac{0.82\, a c_1}{3.6\, Q_a/a - 1} \qquad [299]$$

in which a is the sphere radius in Å (angstroms), $Q_a e_0$ is the micellar charge, and concentrations are in M (molar units). For a spherical micelle of radius

20 Å and charge 60 e_0 in a solution of 0.1 M monovalent salt, Eq. [299] gives $c_2 > 0.06$ M.

Bulk Model: Moderately Charged Sphere

As with the moderately charged cylinder, an approximate potential profile for a moderately charged sphere in the presence of a mixed electrolyte can be found by using the effective-valence planar solution of Eq. [69] in either the asymptotic approximation of Eq. [147] or the NLDH approximation of Eq. [177]. For the latter we need the DH solution to Eq. [165] for $d = 3$ subject to boundary conditions [160]. The result is given by Eq. [307] and provides

$$\begin{aligned} \phi_{\mathrm{DH}}(a) &= \frac{2S_a\delta_a}{\kappa_D\lambda_{\mathrm{GC}}} \\ f(r) &= \frac{a}{r}e^{-\kappa_D(r-a)} \\ \delta_a &= \frac{\kappa_D a}{\kappa_D a + 1} \end{aligned} \qquad [300]$$

This then gives the NLDH potential

$$\begin{aligned} \phi_{\mathrm{NLDH}}(r) &= \frac{4}{\zeta z}\tanh^{-1}\left[\tanh(\zeta z\phi_a/4)\frac{e^{-\kappa_D(r-a)}}{r/a}\right] \\ &= \frac{4}{\zeta z}\tanh^{-1}\left[\frac{\sigma_{\mathrm{ADH}}}{2\sigma_0}\frac{e^{-\kappa_D(r-a)}}{r/a}\right] \end{aligned} \qquad [301]$$

where ζ and ϕ_a are determined from Eqs. [180] and [181] and σ_{ADH} and σ_0 are given by Eq. [189]. The approximate electrostatic free energy is given by Eq. [194]. Note that the NLDH potential is similar to an expression obtained by Levine:[324]

$$\phi_{\mathrm{Levine}}(r) = \frac{4a}{zr}\tanh^{-1}\left(\tanh\left(\frac{z\phi_a}{4}\right)e^{-\kappa_D(r-a)}\right) \qquad [302]$$

which is a lower bound for a $z:z$ electrolyte. The PGC and NLDH surface potentials as functions of surface charge density for a sphere are compared in Figures 24 and 25 and were discussed above in connection with the moderately charged cylinder.

Figure 34 displays the potential profile for a charged sphere of radius 20 Å according to the exact (Eq. [389]), PGC (Eq. [152]), and NLDH (Eq. [301]) solutions for a mixed 1 : 1–2 : 1 electrolyte (0.1–0.02 M) using the effective-valence approximation of Eq. [69] for the latter two. The DH (Eq. [259]), ADH//PGC (Eq. [366]), simple ADH//NLDH (Eqs. [308] and [182]), and

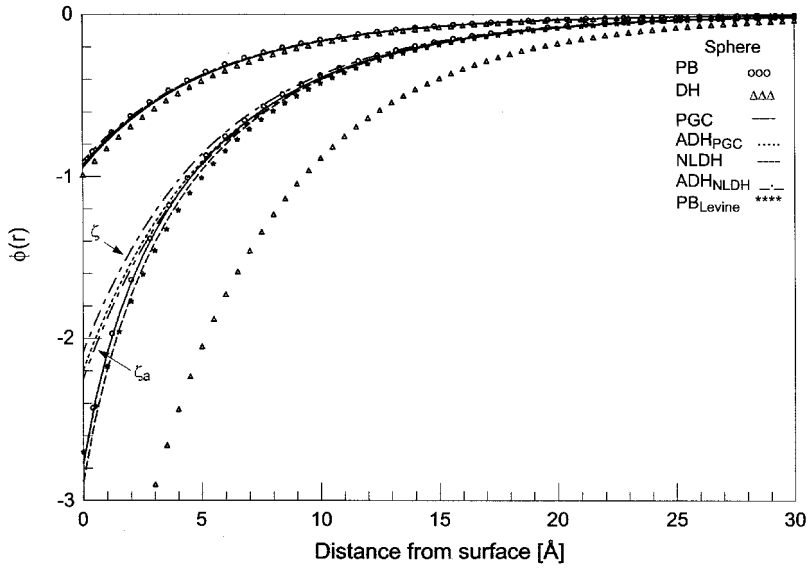

Figure 34 Various potential profiles as a function of distance from the surface for a charged sphere of radius 20 Å with surface charge densities of $-0.002\ e_0/\text{Å}^2$ and $-0.01\ e_0/\text{Å}^2$ in a mixed 1 : 1–2 : 1 electrolyte with concentration 0.1–0.02 M. Exact PB (circles; according to Eq. [389]), DH (triangles; Eq. [307]), and Levine (stars; Eq. [302]) solutions are compared with the PGC (solid lines; Eqs. [152]) and NLDH (dashed lines; Eqs. [253] with approximate ζ_a values) solutions and their ADH//PCG (dotted lines; Eq. [315]) and ADH//NLDH (dotted–dashed lines; Eq. [308] with either exact ζ or approximate ζ_a values) potentials.

Levine (Eq. [302]) profiles are also shown for comparison. For the two surface charge densities ($-0.002\ e_0/\text{Å}^2$ and $-0.01\ e_0/\text{Å}^2$), the PGC and NLDH (not shown but following the PGC curve) profiles agree very well with the exact solution. As with the cylindrical case shown in Figure 26, the simple NLDH expression (using Eq. [182] instead of Eq. [180]) also works very well, although it predicts a surface potential about 5% too large (the accurate NLDH and PGC surface potentials are too large by $\sim$1%). This overall agreement of the spherical case mirrors closely that found for the cylinder since both systems have an equivalent radius of curvature and the charge densities investigated were the same; indeed, the potential profiles for the two systems are almost identical. The ADH potentials are discussed below, but note that the exact DH potential is satisfactory only for the smaller charge density but agrees quite well in that case. Finally, condition [157] for the two charge densities (and using an effective valence) imposes restrictions on the radius of the sphere under which the results are reliable: $a > 18$ Å and $a > 8$ Å, respectively, in agreement with the observed accuracy.

Cell and Bulk Models: Debye–Hückel Potential

The homogeneous solution to the weak-field limit of Eq. [292] (or equivalently Eq. [76] with $d = 3$) can be written as

$$\phi_H(r) = A\frac{e^{-\kappa_R r}}{r} + B\frac{e^{\kappa_R r}}{r} \qquad [303]$$

The explicit form of Eq. [303] subject to the boundary conditions of Eq. [293] gives the Debye–Hückel cell model solution

$$\phi_{\mathrm{DHC}}(r) = \frac{L_B Q_a}{D(\kappa_R)}\left[\frac{(1-\kappa_R R)e^{\kappa_R(R-r)} - (1+\kappa_R R)e^{-\kappa_R(R-r)}}{r} + 2\kappa_R\right] \qquad [304]$$

where

$$D(\kappa_R) = (1+\kappa_R a)(1-\kappa_R R)e^{\kappa_R(R-a)} - (1-\kappa_R a)(1+\kappa_R R)e^{-\kappa_R(R-a)} \qquad [305]$$

With the value of $\phi_H(R)$ identified from Eq. [304], Eq. [82] for κ_R becomes

$$\kappa_R^2 = \sum_{i=0}^{I} \frac{4\pi L_B A_0 \bar{c}_i z_i^2}{1 - \frac{z_i L_B Q_a}{\kappa_R^2}\left[\frac{3}{R^3-a^3} + \frac{2\kappa_R^3}{D(\kappa_R)}\right]} \qquad [306]$$

For low-polyelectrolyte concentrations, $R \to \infty$ and Eqs. [304] and [305] give the standard bulk Debye–Hückel solution for the potential near an ion of radius a

$$\phi_{\mathrm{DH}}(r) = \frac{L_B Q_a e^{-\kappa_D(r-a)}}{(1+\kappa_D a)r} = \frac{2\,S_a a^2 e^{-\kappa_D(r-a)}}{(1+\kappa_D a)\lambda_{\mathrm{GC}} r} \qquad [307]$$

which is the original Debye–Hückel expression.[61]

Bulk Model: Apparent Debye–Hückel Charge and Surface Charge Density

Equation [93] gives the Debye–Hückel potential, based on an apparent surface charge density, which matches the nonlinear Gouy–Chapman solution far from a charged planar surface. The ADH//NLDH potential for a sphere is easily found from Eqs. [188], [187], and [300]:

$$\phi_{\mathrm{ADH}}(r) = \frac{2S_a\delta_a}{\kappa_D\lambda_{\mathrm{AGC}}}\frac{e^{-\kappa_D(r-a)}}{r/a}, \quad \delta_a = \frac{\kappa_D a}{\kappa_D a + 1} \qquad [308]$$

where

$$\lambda_{\mathrm{AGC}} = \frac{1}{2}\left(\lambda_{\mathrm{GC}} + \sqrt{\lambda_{\mathrm{GC}}^2 + \left(\frac{\zeta z \delta_a}{\kappa_D}\right)^2}\right) \qquad [309]$$

and ζ is found using Eqs. [180] and [181]; for low surface charge density, Eq. [182] may be used for ζ. As was pointed out for the charged cylinder, the ADH potential based on the NLDH approximation for a sphere is the correct asymptotic description of the PB potential, even for systems for which the NLDH approximation is poor. The limitation of the NLDH approximation lies in "inverting" the apparent Gouy–Chapman length to obtain the surface potential based on Eq. [181]:

$$\phi_a = \frac{2S_a}{\zeta z}\sinh^{-1}\left(\frac{2\zeta z}{\kappa_D \lambda_{\mathrm{AGC}}}\right) \qquad [310]$$

where ζ is determined by Eq. [309] (λ_{GC} is assumed to be known). For systems to which the NLDH approximation applies (see Fig. 20), Eq. [310] can be used to estimate the surface potential given the asymptotic potential tail.

For a sphere with charge $Q_a e_0$, the apparent charge for which the Debye–Hückel potential asymptotically fits the Poisson–Boltzmann profile is simply

$$Q_a = \frac{2a^2}{L_B \lambda_{\mathrm{GC}}}, \quad Q_{\mathrm{ADH}} = \frac{2a^2}{L_B \lambda_{\mathrm{AGC}}} \qquad [311]$$

The usefulness in identifying an apparent charge for micelles was recognized early on by Langmuir.[107] This can be viewed as the spherical extension of Manning's cylindrical counterion condensation theory[214] whereby counterions reduce the apparent surface charge to a level and within a region where the linear DH equation may be applied.[282] Expressing Eq. [309] in terms of apparent and actual charges (in units of e_0), we find

$$Q_{\mathrm{ADH}} = \frac{2Q_a}{\sqrt{(Q_a/Q_0)^2 + 1} + 1}, \quad Q_0 \equiv \frac{2\kappa_D a^2}{L_B \zeta z \delta_a} \qquad [312]$$

with the low and high charge limits

$$\begin{aligned} \lim_{|Q_a| \ll Q_0} Q_{\mathrm{ADH}} &= Q_a\left[1 - \left(\frac{Q_a}{2Q_0}\right)^2\right] \\ \lim_{|Q_a| \gg Q_0} Q_{\mathrm{ADH}} &= 2S_a Q_0\left(1 + \frac{\ln(\delta_a)}{\ln(Q_0/2|Q_a|)} - \frac{Q_0}{|Q_a|}\right) \end{aligned} \qquad [313]$$

The perturbed Gouy–Chapman expression of Eq. [152] may also be used to derive an apparent Debye–Hückel potential similar to Eq. [308]. Using the approximate solution for a $z:z$ electrolyte given by either Eqs. [147] and [149] or Eqs. [152] and [154], we can obtain an apparent DH potential far from a slightly curved charged surface. The two leading terms in the asymptotic expansion of Eq. [152] are

$$\phi(r) = \left(\frac{3-d}{2} + \frac{a}{2\kappa_D C_a r}(e^{-2\kappa_D \delta_{\mathrm{DGC}}} + 2\kappa_D a)\right)\frac{4S_a}{z} e^{-\kappa_D(r-a+\delta_{\mathrm{DGC}})} \qquad [314]$$

For the cylindrical case ($d = 2$), the radial dependence of the leading term in Eq. [314] does not agree with the Debye–Hückel potential of Eq. [260]. (See, however, the discussion leading to Eq. [366].) For the spherical case ($d = 3$, $C_a = a$), the radial dependence of the leading term *does* agree with the Debye–Hückel expression [307], which allows us to extend the earlier planar results for an apparent surface charge density to a sphere. This gives an apparent Debye–Hückel potential for a charged sphere in a $z:z$ electrolyte within the PGC approximation

$$\phi_{\mathrm{ADH}}(r) = w(w^2 + 2\kappa_D a)\frac{2S_a e^{-\kappa_D(r-a)}}{z\kappa_D r} \qquad [315]$$

where Eq. [153] gives

$$w \equiv e^{-\kappa_D \delta_{\mathrm{DGC}}} = \tanh\left|\frac{z\phi_a}{4}\right| \qquad [316]$$

In terms of the Gouy–Chapman length, Eq. [155] yields

$$w^{-1} = \sqrt{1 + \left(\frac{\kappa_D \lambda_{\mathrm{GC}}(1+f)}{z}\right)^2} + \frac{\kappa_D \lambda_{\mathrm{GC}}(1+f)}{z} \qquad [317]$$

where f is given by Eq. [156] with $d = 3$; Eq. [154] gives the exact result for the Debye–Gouy–Chapman length and hence w. For $|z\phi_a| \ll 4\kappa_D a$, Eq. [315] reduces to the standard Debye–Hückel result of Eq. [307]. Comparison of Eq. [315] with Eq. [307] allows identification of the apparent PGC charge

$$Q_{\mathrm{ADH}} = \frac{2(1+\kappa_D a)}{L_B z \kappa_D} w(w^2 + 2\kappa_D a) \qquad [318]$$

where low and high charge limits within the PGC approximation may be obtained from Eqs. [324] below.

The ADH//NLDH and ADH//PGC profiles for a charged sphere are shown in Figure 34, where the good agreement between the general NLDH and PGC potentials has already been discussed. As with the cylindrical case of Figure 26, both methods give equally good ADH potentials with the PGC profile again bracketed by those of the simple NLDH (indicated by ζ_a) and accurate NLDH (indicated by ζ) profiles. However, the accurate ADH// NLDH profile is again a slightly better fit to the exact curve for distances greater than 10 Å from the surface.

Figure 35 displays the apparent charge as a function of the actual charge within the NLDH and PGC approximations (Eqs. [312] and [318], respectively) for a sphere of radius 20 Å under the same electrolyte conditions as Figure 26, including use of an effective valence; the PGC low and high charge limits (obtained from Eqs. [324]) are also shown. The analysis is similar to Figure 27 for the cylindrical case discussed earlier with the exact (ζ) and approximate (ζ_a) NLDH curves bracketing the PGC values and with the NLDH limiting value (23.8) falling below the PGC value shown (28.0). Groot[325] and Chen and Lu[326] have observed this relationship between apparent and actual charges by numerically solving the PB equation or by performing Monte Carlo simulations.

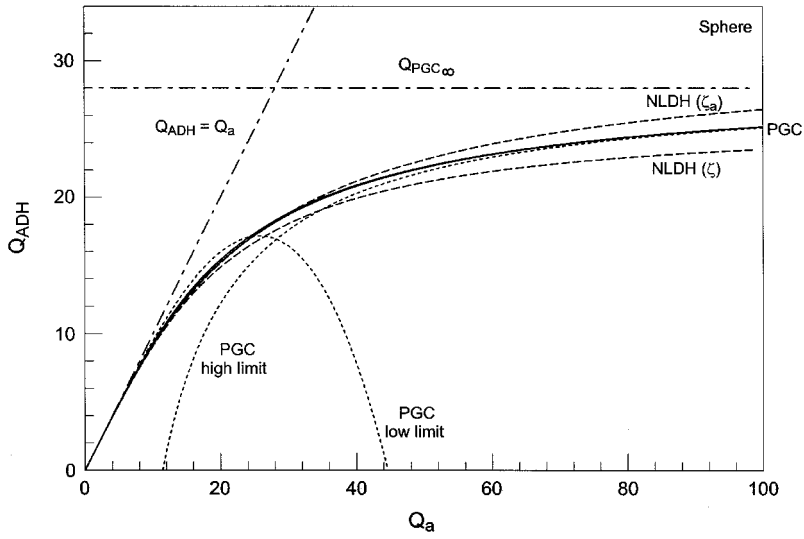

Figure 35 The apparent charge density as a function of actual linear charge density for a sphere of radius 20 Å in a mixed 1 : 1–2 : 1 electrolyte with concentration 0.1–0.02 M within the NLDH (dashed lines; Eq. [312] with the exact ζ or approximate ζ_a values) and PGC (solid lines; Eq. [365] with exact and approximate δ_{DGC} values) approximations. The PGC low and high charge density approximations (obtained from Eqs. [324]) are shown by dotted lines; the infinite-charge density limit is shown by the horizontal dotted–dashed line.

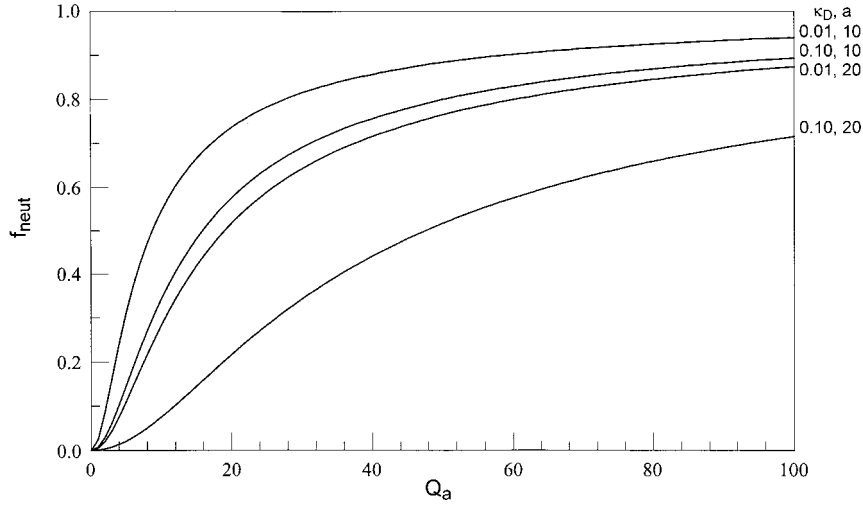

Figure 36 A plot of the ADH//NLDH fraction of surface charge neutralized by a bulk 1 : 1 electrolyte according to Eq. [319] for a charged sphere as a function of the surface charge Q_a for two values of the Debye constant κ_D (0.01 and 0.1 Å^{-1}) and for two different sphere radii a (10 and 20 Å) as listed at right.

Equation [192] or [312] gives the fraction of neutralized surface charge within the ADH//NLDH approximation

$$f_{\text{neut}} = 1 - \frac{Q_{\text{ADH}}}{Q_a} = 1 - \frac{2}{\sqrt{(zQ_aL_B/[2a(1+\kappa_D a)])^2+1}+1} \qquad [319]$$

Unlike the cylindrical case of Eq. [265], this expression is not a function of $\kappa_D a$ alone. We have plotted this fraction in Figure 36 for two values of the Debye constant (0.01 and 0.1 Å^{-1}) and for two different sphere radii (10 and 20 Å). For micelles of radius 20 Å, there is a noticeable difference between $\kappa_D = 0.01$ and 0.1 Å^{-1} in the rate at which the limiting fraction plateau is reached. The condensation radius determined from Eq. [269] and the corresponding potential as a function of the scaled charge density are displayed in Figures 29 and 30, respectively, and compared with those for the plane and cylinder. Comments follow those given earlier for a charged cylinder.

Bulk Model: Reliability of the ADH//PGC Approximation

While the NLDH approximation is not particularly amenable to improvement, the PGC approximation, which is based on a perturbation expansion, is. It is therefore possible and useful to delineate an approximate range of reliability of the ADH//PGC potential, something that is easier to

do than with the ADH//NLDH potential, thus providing some insight into the applicability of both approximations and of the DH-PB relationship as well.

The apparent Gouy–Chapman length for which the Debye–Hückel potential asymptotically matches the PB profile, subject to the accuracy of Eq. [152], as shown for a sphere in Figure 18, is

$$\lambda_{\mathrm{AGC}} = \frac{z\kappa_D a C_a}{w(w^2 + 2\kappa_D a)(1 + \kappa_D a)} \qquad [320]$$

where the radius of curvature has been appropriately inserted into the numerator. Although the dimension of the space is partly accounted for by explicitly including C_a, the explicit form of Eq. [320] is correct only for the spherical case, as mentioned above in the discussion following Eq. [140]. We would like to generalize Eq. [320] to the cylindrical case in a way that retains the analytical form of the expression (since we have no other obvious alternative) but in a way that better accounts for the change in the dimensionality of the space. (That Eq. [320] does poorly when applied to a charged cylinder of radius a is easily seen numerically.) It was noted in connection with Eq. [154] that the surface potential obtained from Eq. [152] is dependent on C_a rather than on a, a fact noted by Guéron and Weisbuch.[177] If we explain this observation by reasoning that the apparent Gouy–Chapman length, or equivalently the surface charge density, is actually a measure of the curvature of a surface within the context of the dimensionality of space, then the radius a of the sphere in Eq. [320] should be replaced by the radius of curvature C_a. This replacement is also justified by the fact that the resulting expression correctly reduces to the apparent Gouy–Chapman length for a plane ($C_a \to \infty$; Eq. [92]) as well as for a sphere. We thus have

$$\lambda_{\mathrm{AGC}} = \frac{z\kappa_D C_a^2}{w(w^2 + 2\kappa_D C_a)(1 + \kappa_D C_a)} \qquad [321]$$

We will see that this generalization works well for charged cylinders. To estimate the surface potential from the apparent Gouy–Chapman length within the PGC approximation, we simply solve Eq. [321] for w and use Eq. [316].

The apparent PGC surface charge density is obtained from the analog of Eq. [11], so we have

$$\sigma_{\mathrm{ADH}} = S_a \sigma_0 \frac{w(w^2 + 2\kappa_D C_a)(1 + \kappa_D C_a)}{(\kappa_D C_a)^2}, \quad \sigma_0 = \frac{e_0 \kappa_D}{2\pi L_B z} \qquad [322]$$

where Eq. [317] becomes

$$w^{-1} = \sqrt{1 + \left((1+f)\frac{\sigma_0}{\sigma_a}\right)^2} + (1+f)\frac{\sigma_0}{|\sigma_a|}, \quad f = \frac{(2/\kappa_D C_a)}{1 + \sqrt{1 + (\sigma_a/\sigma_0)^2}} \qquad [323]$$

It is useful to give the following expansions obtained by combining Eqs. [11], [321], and [322]:

$$\begin{aligned}\lim_{|\sigma_a|\ll\sigma_0}\sigma_{\mathrm{ADH}} &= \sigma_a\left[1+\frac{(2-\kappa_D C_a)(1+2\kappa_D C_a)}{8(1+\kappa_D C_a)^2}\left(\frac{\sigma_a}{\sigma_0}\right)^2\right]\\ \lim_{|\sigma_a|\gg\sigma_0}\sigma_{\mathrm{ADH}} &= S_a\sigma_0\frac{(1+\kappa_D C_a)(1+2\kappa_D C_a)}{(\kappa_D C_a)^2}\left[1-\frac{3+2\kappa_D C_a}{1+2\kappa_D C_a}\left(\frac{\sigma_0}{|\sigma_a|}\right)\right]\end{aligned} \qquad [324]$$

Equations [322]–[324] within the PGC approximation are analogous to Eqs. [189]–[191] within the NLDH approximation. The reliability of the PGC expressions is determined by condition [157], which we now write as a lower "bound" on the surface charge density:

$$|\sigma_a| > \frac{2\pi\sigma_0}{(\kappa_D C_a)^2} \qquad [325]$$

Use of the word "bound" is not intended here to indicate a strict bound in the mathematical sense, but rather to delineate an approximate range of conditions under which use of an ADH-based charge density is valid for a given specified tolerance (see discussion below). As always, for a mixed electrolyte, z in Eqs. [322]–[325] should be replaced by the effective valence of Eq. [69].

The condition of applying the ADH//PGC potential to a curved surface can be found by analyzing Eq. [322] in a manner similar to that done earlier in connection with the planar expression of Eq. [94] and that resulted in Eq. [96]. Analytical inversion of Eq. [322] to obtain σ_a/σ_0 is not possible, but for $\kappa_D C_a > 5$, one has the *approximate* relations

$$\begin{aligned}\frac{\sigma_a}{\sigma_0} &= \frac{2S_a\sqrt{1-\sigma_{\mathrm{ADH}}/\sigma_a}}{\sigma_{\mathrm{ADH}}/\sigma_a}\left(1+\frac{2}{\kappa_D C_a}\right)\\ z\phi_a &= 2S_a\ln\left(\left|\frac{\sigma_a}{\sigma_0}\right|+\sqrt{1+\left(\frac{\sigma_a}{\sigma_0}\right)^2}\right)\end{aligned} \qquad [326]$$

(The second of Eqs. [326] is exact but becomes approximate when used with the first. Also, for $\kappa_D C_a < 5$, Eq. [326] yields a "bound," as determined below, that is slightly too strict.) Figure 10 displays the numerical inversion of Eqs. [322] for several values of the product $\kappa_D C_a$ (2, 3, and 5) as well as the planar limit given by Eq. [95]. While there is a relatively weak dependence on $\kappa_D C_a$ for $\kappa_D C_a > 2$, the presence of surface curvature relaxes the planar condition [96] (by a factor of <3) and the magnitude of the surface potential (by a factor of <2) for which the DH equation is valid (i.e., according to the

choice for σ_{ADH}/σ_a). For a tolerance of $\sigma_{ADH}/\sigma_a = 0.95$, Eqs. [326] give the following (approximate) upper bound on the surface charge density for which the ADH//PGC equation is reliable:

$$|\sigma_a| < \sigma_0 \left(\frac{1}{2} + \frac{1}{\kappa_D C_a} \right) \qquad [327]$$

The upper (Eq. [327]) and lower (Eq. [325]) bounds coalesce at $\kappa_D C_a = 2.7$, so for any value greater than this, the Debye–Hückel profile will be accurate everywhere. According to Eq. [326], the surface potential at coalescence is $|z\phi_a| = 1.6\ k_B T/e_0$. The upper and lower bounds of Eqs. [325] and [327], along with the surface potential predicted by Eq. [326], are shown in Figure 37 as a function of $\kappa_D C_a$ assuming a 95% tolerance limit. We display only the bound curves for $\kappa_D C_a > 1$ since the potential on which our asymptotic solution is based is valid only in this domain. The region in which the ADH//PGC solution applies lies below the upper bound and is confined to surface potentials less than $\sim 1.6\ k_B T/e_0$, a value slightly more restrictive than that ($2.2\ k_B T/e_0$) found by Lampert and Crandall[327] using a more analytical approach. The potential of Eq. [315] is valid asymptotically in the region greater than the lower-bound curve. These delineations on the figure are only approximate, but they serve to point out that there exists a wide range of conditions for

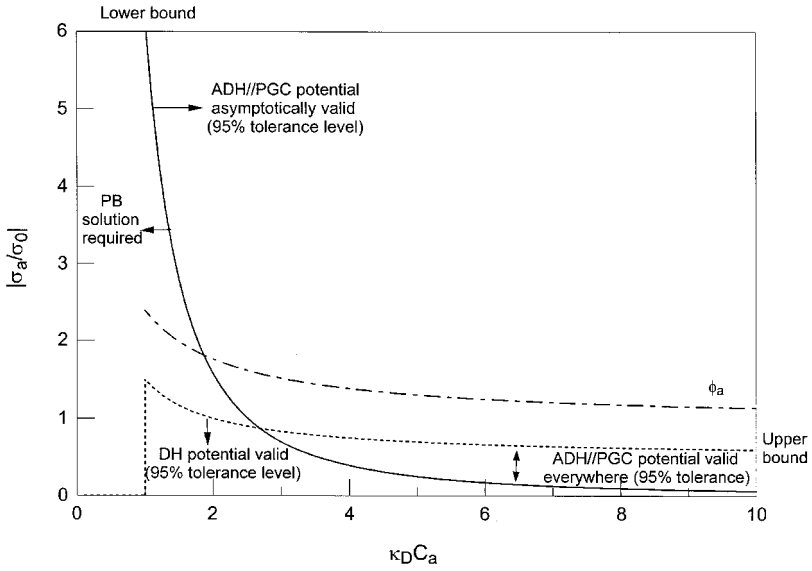

Figure 37 The upper (dotted line, Eq. [327]) and lower (solid line, Eq. [325]) bounds of the ratio $|\sigma_a/\sigma_0|$ defining regions of applicability of the DH and ADH//PGC potential profiles as a function of $\kappa_D C_a$ assuming a 95% tolerance level; the surface potential according to Eq. [326] is shown by the dotted–dashed line.

which the apparent DH potential gives a good description of the asymptotic potential while the linear DH potential fails. Returning to Figure 34, for this system $\sigma_0 = 0.0017\ e_0/\text{Å}^2$ and $\kappa_D C_a = 2.6$, so according to Eqs. [325] and [327] (or Fig. 37), the ADH//PGC potential for the low charge density curve ($|\sigma_a| = 0.002\ e_0/\text{Å}^2$) should be accurate everywhere, and the data demonstrate this. In Figure 35, Eq. [327] gives the reliable range for the ADH//PGC potential to be $|Q_a| < 8$, which agrees very well with the linear region of the curves.

Figure 38 shows the ratio of the apparent charge density to the actual charge density (Eq. [322]) for which the ADH//PGC potential of Eq. [315] asymptotically matches the (approximate) Poisson–Boltzmann profile Eq. [152] as a function of the actual charge density on the sphere scaled to the quantity σ_0. Solid lines indicate use of an approximate Debye–Gouy–Chapman length according to Eq. [155], while circles indicate use of the "exact" value given by Eq. [154] (with an effective valence). (By "exact," we mean the solution of Eq. [154], which, of course is not the exact solution to the PB equation, but rather a very good approximation.) Consider first the

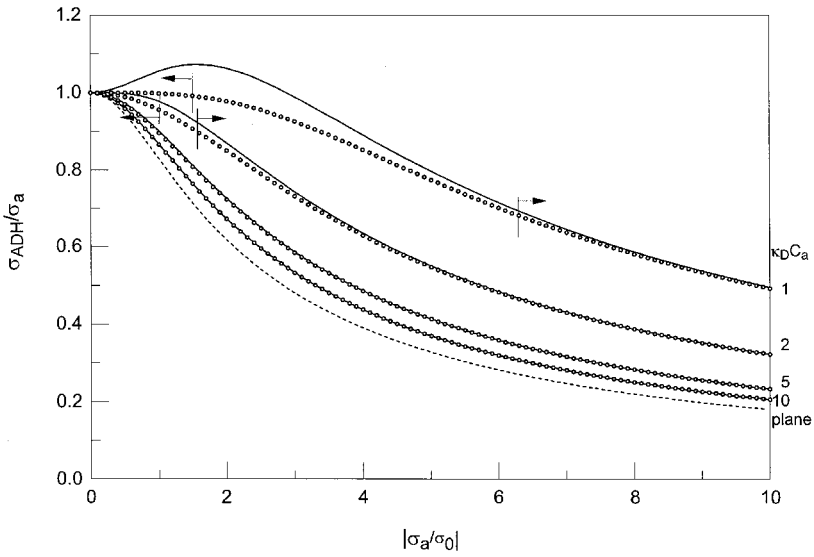

Figure 38 The ratio σ_{ADH}/σ_a of Eqs. [322] and [323] for the Debye–Hückel potential of Eq. [315] that asymptotically matches the PB profile given by Eq. [152] as a function of the ratio $|\sigma_a/\sigma_0|$, where σ_a is the surface charge density and σ_0 is defined by Eq. [322]; values of $\kappa_D C_a$ for each curve are given at right with the planar surface indicated by the dotted line. Reliability bounds according to Eqs. [325] and [327] are indicated by arrows. To get a feel for the variable ranges, a mixed 1 : 1–2 : 1 electrolyte with concentration 0.1–0.02 M has $\kappa_D = 0.132\ \text{Å}^{-1}$ and $\sigma_0 = 0.0017\ e_0/\text{Å}^2$; for this case, the ordinate ranges from $\sigma_a = 0$ to $0.017\ e_0/\text{Å}^2$ and the curvature radii at the right correspond to spheres of radius $a = 8, 15, 38$ and 123 Å (or cylinders of diameter a).

exact curves (circles): for $\kappa_D C_a = 1$ and 2, the lower and upper bounds [325] and [327] are indicated in the figure and show the range of reliability of the ADH//PGC solution. As discussed above, the ranges coalesce for $\kappa_D C_a > 2.7$ so the entire curve is accurate. For the approximate curves (solid lines), bound [327] fails since $|\sigma_a/\sigma_0| (= z/\kappa_D \lambda_{GC})$ is small and the approximation used in going from Eq. [154] to Eq. [155] is not valid. This explains why the approximate curve for $\kappa_D C_a = 1$ indicates an apparent charge density larger than the actual density. However, the lower bound of Eq. [325] is still valid, and the close agreement with the exact curves in the region supports this.

In Figure 39 we present the same results as shown in Figure 38 but as a function of the product $\kappa_D C_a$. The lower bound reliability regions for the exact curves (circles) according to Eq. [325], which also roughly match those for the approximate curves (solid lines), are shown by arrows. The upper bound regions of Eq. [327] are not indicated since as $\kappa_D C_a$ approaches unity, data based on Eq. [152] become invalid.

Bulk Model: Two Charged Spheres in the NLDH and Derjaguin/mHHF Approximations

In this section we adapt our earlier results on the interaction of two particles to the treatment of two interacting charged spheres. This system was

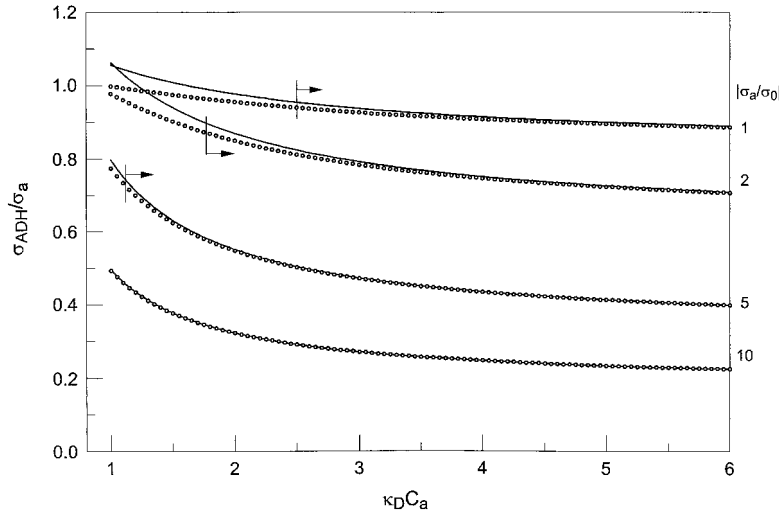

Figure 39 The ratio σ_{ADH}/σ_a in Eq. [322] and [323] for the Debye–Hückel potential of Eq. [315], which asymptotically matches the PB profile given by Eq. [152] as a function of $\kappa_D C_a$; values of the ratio $|\sigma_a/\sigma_0|$ are given at right. Reliability bounds according to Eqs. [325] are indicated by arrows. For a mixed 1 : 1–2 : 1 electrolyte with concentration 0.1–0.02 M, $\kappa_D = 0.132$ Å^{-1}, and $\sigma_a = 0.0017\ e_0/$Å^2; for this case, the ordinate ranges from $a = 8$ to 123 Å, where a is the sphere radius (or cylinder diameter), and the surface charge density at the right corresponds to $\sigma_a = 0.0017, 0.003, 0.009$, and $0.017\ e_0/$Å^2.

used initially to investigate the stability of colloidal solutions,[36] but it also serves as a model for interacting biomolecules such as proteins and micelles. The standard method is that due originally to Derjaguin[328] and later modified by Hogg, Healy, and Furstenau[112] (HHF) and is applicable to low charge density (or potential) spheres nearly in contact. In the opposite limit at which the spheres are separated by several Debye lengths, one can use the procedure of Bell, Levine and McCartney[128] called the "linear superposition approximation," of which the NLDH method presented is a generalization. The ranges of validity for which the Derjaguin and linear superposition approximations hold were compared by Glendinning and Russel for constant potential and constant charge density boundary conditions.[329] The interaction potential obtained in these two distinct limits were combined by Sader, Carnie and Chan[330] to provide a single analytical approximation over the entire separation range. We begin by specializing the two-particle NLDH approximation to two spheres.

Figure 21 represents the interaction of two charged particles. The appropriate equations for the NLDH potential and pressure were derived previously and are given by Eqs. [196], [197], [201], [202], and [209]. The development here is similar to that used previously for two interacting cylinders. To implement the general expressions to treat two interacting spheres, we use the Debye–Hückel solution [307] to put

$$f_1(r) = \frac{e^{-\kappa_D(r-a_1)}}{r/a_1}, \quad \gamma_1 = \frac{a_1 e^{-\kappa_D H_0}}{H_0 + a_1}$$
$$\delta_1 = \frac{\kappa_D a_1}{1+\kappa_D a_1}, \quad \varepsilon_1 = \left(\frac{a_1}{H_0+a_1}\right)^2 \left(\frac{1+\kappa_D(H_0+a_1)}{1+\kappa_D a_1}\right) e^{-\kappa_D H_0} \qquad [328]$$

Cylindrical symmetry allows the force between the spheres to be found by integrating the pressure over rings of width $d\rho$ in a dividing plane placed midway between the sphere centers

$$F(R) = 2\pi \int_0^\infty P(R,\rho,0)\rho d\rho = 2\pi \int_{R/2}^\infty P(R,r) r\, dr \qquad [329]$$

where the right-hand integral follows from changing the integration variable to r. To obtain the force using the pressure, we ignore the term in the denominator of Eq. [209] and use Eqs. [328] to get

$$\beta F(R) = \frac{4\kappa_D^2}{L_B z^2}(A_1(R)a_1 e^{-\kappa_D a_1} + A_2(R)a_2 e^{-\kappa_D a_2})^2 \int_{R/2}^\infty \left(\frac{2}{r} + \frac{2}{\kappa_D r^2} + \frac{1}{\kappa_D^2 r^3}\right) e^{-2\kappa_D r} dr$$
$$- \frac{2\kappa_D^2 R^2}{L_B z^2}[(A_1(R)a_1 e^{-\kappa_D a_1})^2 + (A_2(R)a_2 e^{-\kappa_D a_2})^2] \int_{R/2}^\infty \left(\frac{1}{r^3} + \frac{2}{\kappa_D r^4} + \frac{1}{\kappa_D^2 r^5}\right) e^{-2\kappa_D r} dr \qquad [330]$$

The integrals can be evaluated to give

$$\beta F(R) = \frac{16 a_1 a_2 e^{\kappa_D (a_1 + a_2)}}{L_B z^2} \frac{A_1(R) A_2(R)(1 + \kappa_D R)}{R^2} e^{-\kappa_D R} \qquad [331]$$

As observed for two interacting cylinders, for large $\kappa_D R$, the coefficients are independent of separation distance and approximately independent of the sphere radii.[331] Force curves predicted by Eq. [331] are in good agreement with those obtained by Ledbetter, Croxton and McQuarrie who solved the PB equation numerically.[331] Finally, we integrate the force according to Eq. [281] and, as for the planar and cylindrical cases, analytical evaluation of the integral requires that we restrict ourselves to separations of at least two to three Debye lengths. Using Eq. [204], the leading terms in the interaction potential between two charged spheres are found to be

$$\beta V_{\mathrm{PB}}(R) = \frac{8 a_1 a_2 e^{-\kappa_D H_0}}{L_B \zeta_1 \zeta_2 z^2 R} \left[\begin{array}{c} 2\hat{s}_1 \hat{s}_2 + \frac{(1-\hat{s}_2^2)\hat{s}_1^2}{(1+\hat{s}_2^2)(1-\hat{s}_1^2)} \left((1 - \hat{s}_2^2)\varepsilon_2 - \left(\frac{2\hat{s}_2^2 \delta_2}{\delta_1} \right) \gamma_1 \right) \\ + \frac{(1-\hat{s}_1^2)\hat{s}_2^2}{(1+\hat{s}_1^2)(1-\hat{s}_2^2)} \left((1 - \hat{s}_1^2)\varepsilon_1 - \left(\frac{2\hat{s}_1^2 \delta_1}{\delta_2} \right) \gamma_2 \right) \end{array} \right] \qquad [332]$$

where ε and γ vary as $\exp(-\kappa_D H_0)$. As done previously for two interacting cylinders, we have introduced the ζ parameters of Eq. [206] (and in the definition of σ_0 as well) that are useful for taking the $\kappa_D a \to 0$ limit. This potential in the low-charge-density (DH) limit is

$$\beta V_{\mathrm{DH}}(R) = \frac{8 a_1 a_2}{L_B \zeta_1 \zeta_2 z^2 R} (2\hat{\sigma}_1 \hat{\sigma}_2 + \hat{\sigma}_1^2 \varepsilon_2 + \hat{\sigma}_2^2 \varepsilon_1) e^{-\kappa_D H_0} \qquad [333]$$

Equations [332] and [333] represent the leading terms in an asymptotic expansion of the interaction potential and as such become increasingly inaccurate as the separation distance between the spheres decreases. To evaluate the potential in the opposite limit in which the spheres are almost touching, we combine Eqs. [281] and [329] and change the order of integration to write

$$V(R) = 2\pi \int_0^\infty \left[\int_R^\infty P(R^*, \rho, 0) dR^* \right] \rho \, d\rho \qquad [334]$$

Note that the term in brackets represents the interaction potential per unit area as determined by the pressure due to two charged rings of radius ρ and width $d\rho$ at the dividing plane. The inner integral in Eq. [334] can be evaluated by following the generalization of Derjaguin's method[328] by Hogg, Healy, and Fuerstenau.[112] For values of ρ less than the radius of the smaller sphere ($= a_{\min}$), this pressure and the resulting interaction potential can be approximated by that due to two opposing and parallel planar rings *if the spheres are*

sufficiently close; what "sufficiently close" means will be determined below. Thus, in place of the bracketed term we can insert the interaction potential per unit area between two planes with charge densities σ_1 and σ_2 separated by a distance

$$H(R,\rho) = R - \sqrt{a_1^2 - \rho^2} - \sqrt{a_2^2 - \rho^2} \quad \text{for} \quad \rho \le a_{\min} \qquad [335]$$

This allows us to write Eq. [334] as

$$V_{\mathrm{HHF}}(R) = 2\pi \int_0^{a_{\min}} V_{\mathrm{pl}}[\sigma_1, \sigma_2, H(R,\rho)]\rho \, d\rho \qquad [336]$$

where the planar interaction potential V_{pl} is given by Eq. [110]. Equation [335] may be inverted analytically for $[\rho(H)]^2$

$$[\rho(H)]^2 = \frac{(2a_1 + H_0 - H)(2a_2 + H_0 - H)(2a_1 + 2a_2 + H_0 - H)(H - H_0)}{4(a_1 + a_2 + H_0 - H)^2} \qquad [337]$$

which lets us write Eq. [336] as

$$V_{\mathrm{HHF}}(R) = \frac{\pi}{2} \int_{H_0}^{H_{\max}} V_{\mathrm{pl}}(\sigma_1, \sigma_2, H) \left(R - H - \frac{(a_1^2 - a_2^2)^2}{(R-H)^3} \right) dH,$$
$$H_{\max} = R - \sqrt{|a_1^2 - a_2^2|} \qquad [338]$$

Clearly, Eq. [338] represents an approximation to the actual interaction energy since (1) the rings become progressively less parallel as ρ and hence H increases, (2) this ignores contributions from that part of the larger sphere beyond the smaller sphere radius as well as those from the backsides of both spheres, and (3) there are pressure contributions on the dividing plane beyond $a_{\min}$ not considered at all. These concerns are minimized if the system meets two conditions:[332] (1) the closest spacing between spheres is much less than the smaller radius, and (2) the thickness of both spherical double layers is small:

$$\frac{H_0}{a_{\min}} \ll 1 \ll \kappa_D a_{\min} \qquad [339]$$

The first condition guarantees that most field lines contributing to the interaction are parallel, satisfying point (1), while the second condition implies that the interaction falls off quickly with curvature, satisfying point (2). The second

condition also allows us to extend the upper integration limit from $H_{\max}$ to infinity since there are then no significant contributions beyond this value, thus rendering point (3) moot. Although we apply the Derjaguin approximation only to spheres in this chapter, it is equally applicable to any two curved surfaces provided a_1 and a_2 are interpreted as the radii of curvature of the surfaces at their points of closest approach.[332] We noted earlier that Sparnaay has obtained expressions for the interaction for two parallel and for two crossed cylinders within the Derjaguin approximation for low and moderate surface potentials.[314]

Consider the interaction potential according to Eq. [338] for two spheres of equal radius a:

$$V(H_0 + 2a) = \frac{\pi}{2}\int_0^{2a} V_{\mathrm{pl}}(\sigma_1, \sigma_2, H^*)(2a - H^*)dH^*, \quad H^* = H - H_0 \qquad [340]$$

Let us first compare the potential between two identical spheres to that between two planes. We see below that the distance dependence of the leading term in the potential between two spheres is the same as that between two planes, $\exp(-\kappa_D H)$, so the ratio of potentials is approximately

$$\frac{V_{\mathrm{sp}}(H^*)}{V_{\mathrm{pl}}(0)} = \frac{\int_0^{2a} e^{-\kappa_D H^*}(2a - H^*)dH^*}{\int_0^{2a}(2a)dH^*} = \frac{2\kappa_D a + e^{-2\kappa_D a} - 1}{(2\kappa_D a)^2} < 1 \qquad [341]$$

For small $\kappa_D a$, the limit is one-half; for large $\kappa_D a$, the ratio is smaller: $1/(2\kappa_D a)$. Thus, even in the limit of large sphere radii, the potential will not approach that for a plane. A second point concerns the common practice of simplifying the integral by setting $H^* = 0$ in Eq. [340] (or $H = H_0$ in Eq. [338]). This leads to the ratio

$$\frac{V_{\mathrm{sp}}(0)}{V_{\mathrm{sp}}(H^*)} = \frac{2\kappa_D a(1 - e^{-2\kappa_D a})}{2\kappa_D a + e^{-2\kappa_D a} - 1} > 1 \qquad [342]$$

with limit 2 for small $\kappa_D a$ and $1 + 1/(2\kappa_D a)$ for large $\kappa_D a$; hence, the simplification leads to an overestimation of the potential. Instead of setting $H^* = 0$, one could put $H^* \approx \int e^{-\kappa_D H} H\, dH / \int e^{-\kappa_D H} dH = 1/\kappa_D$ to correct for this. In a similar vein, Overbeek[333] reasoned that the largest contribution to the integral Eq. [338] occurs within a Debye length of each sphere: $H^* = H - H_0 \approx 2/\kappa_D$. Thus, he suggested

$$R - H \approx a_1 + a_2 - \frac{2}{\kappa_D} \qquad [343]$$

and simplified the interaction energy between two spheres to

$$V_{\mathrm{HHF}}(H_0) = \frac{\pi}{2} F(a_1, a_2, \kappa_D) \int_{H_0}^{\infty} V_{\mathrm{pl}}[\sigma_1, \sigma_2, H] dH \qquad [344]$$

where

$$F(a_1, a_2, \kappa_D) = a_1 + a_2 - \frac{2}{\kappa_D} - \frac{(a_1^2 - a_2^2)^2}{(a_1 + a_2 - 2/\kappa_D)^3} \qquad [345]$$

Expanding F in terms of large $\kappa_D a$ according to the right-hand inequality of Eq. [339] (the assumption of a thin double layer), we find

$$F(a_1, a_2, \kappa_D) \approx \frac{4a_1 a_2}{a_1 + a_2} \left(1 - \frac{2(a_1^2 - a_1 a_2 + a_2^2)}{a_1 a_2 (a_1 + a_2)\kappa_D} - \cdots\right) \qquad [346]$$

The lowest-order term agrees with that derived by HHF,[112] and the next-order term, on putting $a_1 = a_2 = a_{\min}$, matches Overbeek's correction.[333] All in all, the curvature of the spheres has been taken into account in a relatively minor, but not insignificant, way through the integration over ρ (or H).

For the Debye–Hückel case consistent with large charge radii and low charge densities, we use Eq. [110] for the planar interaction potential and integrate Eq. [344] to find[334,335]

$$\beta V_{\mathrm{HHF}}(H_0) = \frac{\pi^2 L_B}{e_0^2 \kappa_D^2} F(a_1, a_2, \kappa_D) \left[2\sigma_1\sigma_2 \ln\left(\frac{1 + e^{-\kappa_D H_0}}{1 - e^{-\kappa_D H_0}}\right) - (\sigma_1^2 + \sigma_2^2) \ln\left(1 - e^{-2\kappa_D H_0}\right)\right] \qquad [347]$$

This result may be written in terms of surface potentials using Eq. [31] but it must be remembered that the final expression will not agree with derivations in which the constancy of the surface potential was used as a boundary condition,[112,333] owing to neglect of the chemical free energy in Eq. [108] for the electrostatic free energy of a charged plane. For like spheres ($a_1 = a_2 = a$, $\sigma_1 = \sigma_2 = \sigma$), Eq. [347] gives

$$\beta V_{\mathrm{HHF}}(H_0) \approx -\frac{8\pi^2 L_B a \sigma^2}{e_0^2 \kappa_D^2} \ln(1 - e^{-\kappa_D H_0}) \qquad [348]$$

Note that the distance decay for large separations of Eq. [348] is that of a screened exponential function rather than the faster (and correct) decay of a screened Coulomb. Our derivation is clearly limited to small $\kappa_D H_0$; for large separations the effect of surface curvature becomes apparent as nonparallel deviations of the field lines for two spheres leads to a faster decay than does

that for two planes. Papadopoulos and Cheh[336] proposed a method for including the effects of surface curvature by defining the distance H between rings based on a connecting circular arc rather than a straight line, thus mapping the surface of each sphere onto the dividing plane by essentially following the electric field lines. Sader, Carnie, and Chan[330] have extended the above-mentioned near-planar DH results by modifying earlier work by Bell, Levine, and McCartney[128] and obtained an expression for the interaction potential that reduces properly for both small and large values of $\kappa_D H_0$. Their modified HHF result consists of simply replacing Eq. [346] with

$$F(a_1, a_2, \kappa_D) \approx \frac{4a_1 a_2}{H_0 + a_1 + a_2} \equiv \frac{4a_1 a_2}{R} \qquad [349]$$

Their result has also been derived independently by Ohshima by expanding the potential for the two-sphere Debye–Hückel equation in terms of Bessel functions centered on each sphere.[337–339] While the addition of H_0 in the denominator has its origin in an integration over the sphere surfaces,[36] its absence in our expression for F can be shown to be consistent with conditions [339] as follows. These conditions require that the interaction between the spheres approximates that between two planes. Because the total width of two planes' double layers is about two Debye lengths, we put $H_0 \sim 2\kappa_D$ in Eq. [343] to write $R - H \sim a_1 + a_2 - H_0$. Furthermore, because one of our conditions is $H_0 \ll a_{\min}$, we first let $R - H \sim (a_1 + a_2)/[1 + H_0/(a_1 + a_2)] \sim (a_1 + a_2)^2/R$ and then relax the condition that H_0 be small; the result is essentially Eq. [349]. Thus, the modification by Sader, Carnie and Chan[330] not only allows Derjaguin theory to be applied at larger separations, but at short separations it corrects for the overestimation noted above. A slightly more obtuse version of this argument has been given by Haoping, Jun, and Blum.[340] Finally, we can extend the DH potential to higher charge densities by inserting scaled apparent charge densities, giving a final modified HHF (mHHF) expression

$$\beta V_{\mathrm{mHHF}}(H_0) = \frac{4a_1 a_2}{L_B \zeta_1 \zeta_2 z^2 R}\left[2\hat{s}_1\hat{s}_2 \ln\left(\frac{1 + e^{-\kappa_D H_0}}{1 - e^{-\kappa_D H_0}}\right) - (\hat{s}_1^2 + \hat{s}_2^2)\ln(1 - e^{-2\kappa_D H_0})\right] \qquad [350]$$

where

$$\hat{s}_1 = \frac{\sigma_1/\sigma_{01}}{\sqrt{(\sigma_1/\sigma_{01})^2 + 1} + 1}, \quad \sigma_{01} = \frac{\kappa_D e_0}{2\pi L_B \zeta_1 z \delta_1} \qquad [351]$$

Comparing this expression with the NLDH low-charge-density limit of Eq. [333] suggests that the low-order asymptotic NLDH result of Eq. [332]

may be extended to smaller separations by writing[330]

$$\beta V_{\mathrm{PB}}(R) \approx \frac{8a_1a_2\hat{s}_1\hat{s}_2}{L_B\zeta_1\zeta_2 z^2 R}\ln\left(\frac{1+e^{-\kappa_D H_0}}{1-e^{-\kappa_D H_0}}\right), \quad R = H_0 + a_1 + a_2,\ \kappa_D a_{\min} \gtrsim 3 \qquad [352]$$

For $\kappa_D a_{\min} < 3$, Eq. [332] or [333] should be used. The electrostatic free energy may now be found from Eqs. [352] and [107]:

$$A_{\mathrm{el}}(R) = V(R) + A_{\mathrm{el}}(\sigma_1) + A_{\mathrm{el}}(\sigma_2) \qquad [353]$$

where the single-sphere free energies $A_{\mathrm{el}}(\sigma_{1,2})$ are found by adapting either Eq. [151] or [194] to the spherical case. Note that in the limit $z \to 0$, Eq. [194] properly reduces to the Coulomb self energy of a charged sphere.

The curvature factors δ_1 and δ_2 contained in $\hat{s}_1$ and $\hat{s}_2$ in Eq. [352] result from applying the boundary conditions at the surface of each sphere. Those factors correspond to the same factors appearing in the standard DH solution for an isolated sphere (e.g., Eq. [307]). They do not appear in the mHHF solution where both a planar solution and planar boundary conditions are used (the $\delta \to 1$ limit). Equation [352] agrees with both the small-separation mHHF result and the large-separation PB limit. It is, however, correct only in the appropriate limits because one would expect the *ln* term in Eq. [352] to contain charge-dependent factors of order $\hat{s}^2$, which disappear in the DH limit, and curvature-dependent factors involving δ, which disappear in the mHHF limit. (See also the discussion following Eq. [128].) In fact, had we used the planar asymptotic PB potential of Eq. [133] in the mHHF procedure (which is of dubious validity in view of the requirement of small sphere separations), the low-order result would be identical to that of Eq. [332] with $\delta_1 = \delta_2 = 1$. Unfortunately, the correctness of the next-order term in Eq. [332] is questionable, owing in part to retention of just the leading term in the force (Eq. [331]). The mHHF/PB procedure just mentioned would yield a term half as large as that in Eq. [332]. These two approaches, the asymptotic PB derivation versus that of mHHF, work in distinct regions of separation with the next-order term attempting to extend applicability of the result into the region of the other method. Although the asymptotic expression accounts for surface curvature (via δ), something that the mHHF approach lacks, and reproduces the correct second-order DH term for the planar case, terms of order $\exp(-2\kappa_D H_0)/R^2$ and higher (resulting from an exponential integral function) have been neglected in Eq. [332] and the angular dependence of the boundary conditions ignored. In most cases, it is expected that higher-order terms are of little consequence, particularly since their contribution to the pressure between two charged planes is small, as pointed out in regard to discussion of Figure 12.

As a purely illustrative example, the interaction potential between two spheres with radii $(a_1, a_2) = (20\ \text{Å}, 10\ \text{Å})$ and charge density $(\sigma_1, \sigma_2) = (0.01\ e_0/\text{Å}^2, 0.001\ e_0/\text{Å}^2)$ in a 0.1 M 1 : 1 electrolyte as a function of the

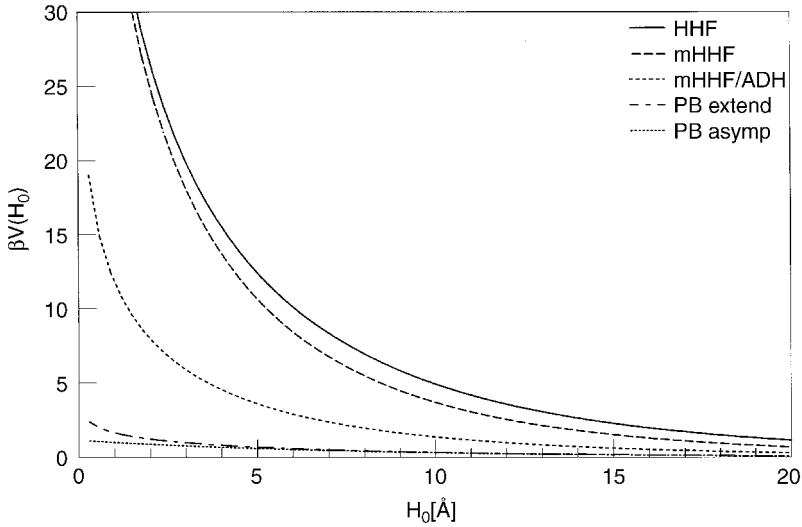

Figure 40 The interaction potential for two spheres with radii 20 and 10 Å and charge densities of 0.01 and 0.001 $e_0/Å^2$, respectively, in a 0.1 M 1 : 1 electrolyte as a function of surface separation according to the HHF (solid line; Eqs. [347] and [345] without the Overbeek correction), mHHF (long dashed line; Eqs. [347] and [349]), mHHF with apparent charge densities (short dashed line; Eq. [350]), lowest-order asymptotic PB (dotted-dashed line; first term in Eq. [332]), and extended PB (dotted line; Eq. [352]) expressions.

surface–surface separation distance H_0 is shown in Figure 40 for the following expressions: HHF (Eqs. [347] and [345] without the Overbeek correction), mHHF (Eqs. [347] and [349]), mHHF with apparent Debye–Hückel charge densities (Eq. [350]), lowest-order PB (first asymptotic term in Eq. [332]), and extended PB (Eq. [352]). The HHF and mHHF data approach each other for close separations but at larger separations the HHF expression gives a significantly larger potential than the mHHF result. The difference between the mHHF and mHHF/ADH potentials is due to the use of apparent charge densities in the latter, and the improved agreement with the PB results at larger separations is noticeable. However, the HHF and mHHF potentials are significantly larger than the PB potentials, essentially mirroring the discrepancy observed between DH and PB potentials for isolated spheres (Fig. 34). The difference between the mHHF/ADH and PB-extended potentials is due solely to the inclusion of curvature factors (δ) which become unity within the HHF/mHHF conditions of Eq. [339]. Finally, the modification introduced into the PB potential of Eq. [352], which corrects the potential for nearly touching spheres, raises the potential above the unmodified value for separations within $\sim$2–3 Å. Since this modification has no significant effect elsewhere, and, as it

forces the potential for touching spheres to become infinite, it seems particularly useful,[341] although its specific form is somewhat suspect, as noted above. Moreover, despite the "PB" designation, Eq. [352] is essentially an extended Debye–Hückel result, modifying the Derjaguin expression through the inclusion of apparent charge density, curvature, and long-range corrections. Combined with short-range van der Waals–like terms, Eq. [352] could therefore be used in an additive fashion for the interaction potential for low concentrations of like-charged spheres immersed in a bulk electrolyte. For mixtures of oppositely charged spheres, cancellation of terms, and higher concentrations will tend to emphasize any errors incurred by the additivity assumption so results are likely to be only qualitatively useful.[342] In related work, Glendinning and Russel[329] and Carnie, Chan, and Stankovich[341] have solved the two-sphere PB equation numerically under constant surface potential and constant charge density conditions in their thorough investigations of the accuracy of the Derjaguin, HHF and superposition (asymptotic) approximations.

Bulk Model: Dressed-Ion Theory

Consider the potential of mean force between one ion (labeled j with valence z_j and radius a_j) and another (labeled k):[61]

$$\beta w_{jk} = z_k \phi_j(r_{jk}) = \frac{L_B z_j z_k e^{-\kappa_D (r_{jk} - a_j)}}{(1 + \kappa_D a_j) r_{jk}} \qquad [354]$$

This result displays an inherent asymmetry in the way in which the two ions are treated. To better see this, we group together the properties specific to ion j in order to express the potential of mean force in a form identical to the point solution

$$\beta w_{jk} = \frac{L_B z_j^* z_k e^{-\kappa_D r_{jk}}}{r_{jk}} \qquad [355]$$

where we have defined the "dressed" valence of ion a by

$$z_j^* = \frac{z_j e^{\kappa_D a_j}}{1 + \kappa_D a_j} \qquad [356]$$

This shows that although the jth ion is treated with a finite radius, all others are considered as point ions. The "obvious" remedy, which can also be justified on statistical mechanical grounds according to "dressed-ion theory" (DIT),[343–345] is to replace Eq. [355] with the symmetric relation

$$\beta w_{jk} = \frac{L_B z_j^* z_k^* e^{-\kappa_D r_{jk}}}{r_{jk}} \qquad [357]$$

where now all ions are represented by their apparent charges given by the analog of Eq. [356]. To be consistent, the Debye screening constant in Eq. [357] should be replaced by one determined by these dressed valences. The appropriate relationship is actually[343–345]

$$\kappa_{\mathrm{DIT}}^2 = 4\pi L_B A_0 \sum_{i=1}^{I} c_i^B z_i z_i^* \qquad [358]$$

which can be shown to lead to a self-consistent equation for κ_{DIT} in terms of the Debye screening constant and a common ion radius a:

$$\frac{\kappa_{\mathrm{DIT}}^2}{\kappa_D^2} = \frac{e^{\kappa_{\mathrm{DIT}} a}}{1 + \kappa_{\mathrm{DIT}} a} \qquad [359]$$

For particles of different radii, Eqs. [357] and [358] still hold but with κ_{DIT} determined self-consistently from[346]

$$\kappa_{\mathrm{DIT}}^2 = 4\pi L_B A_0 \sum_{i=1}^{I} \frac{c_i^B z_i^2 e^{\kappa_{\mathrm{DIT}} a_i}}{1 + \kappa_{\mathrm{DIT}} a_i} \qquad [360]$$

The DIT potential near an ion with radius a is thus given by

$$\phi_{\mathrm{DIT}}(r) = \frac{2 S_a a^2 e^{-\kappa_{\mathrm{DIT}}(r-a)}}{\lambda_{\mathrm{GC}}(1 + \kappa_{\mathrm{DIT}} a) r} \qquad [361]$$

where κ_{DIT} is determined from Eq. [360], and represents a slight improvement over the DH expression [307] for ions of finite size.

Bulk Model: Debye–Hückel Additivity

The point charge Debye–Hückel solution given by Eq. [307] has utility beyond a description of the interaction of two charges in an electrolyte solution. This is demonstrated by the following examples. Equation [307] (with $a = 0$) represents the Green function for the modified Helmholtz equation,[189] which we have been referring to as the Debye–Hückel equation, and so it can also be used to obtain the potential for more extended charge distributions.[189,347] In this section we treat three problems on the basis of the additivity of the DH solution: the potential due to a charged cylinder, the potential due to a charged arc of finite length, and the persistence length of a charged cylinder.

An Infinite Charged Cylinder Consider first an infinite, straight-line charge in a bulk dielectric extended along the z axis. The potential at a radial

distance r is related to the integral obtained by integrating the point charge Coulomb solution along the cylindrical axis:

$$\begin{aligned}\phi(r) &= L_B\left[\int \frac{dq}{\sqrt{r^2+z^2}} - \int \frac{dq}{\sqrt{R^2+z^2}}\right] \\ &= \xi\left[\int_{-\infty}^{\infty} \frac{dz}{\sqrt{r^2+z^2}} - \int_{-\infty}^{\infty} \frac{dz}{\sqrt{R^2+z^2}}\right] = 2\xi \ln\frac{r}{R}\end{aligned} \quad [362]$$

where ξ is the (unitless) linear charge density. Now treat the same line charge in a bulk electrolyte solution by replacing the Coulomb point charge potential with the point charge DH solution of Eq. [307]:

$$\phi(r) = \xi \int_{-\infty}^{\infty} \frac{e^{-\kappa_D\sqrt{r^2+z^2}}dz}{\sqrt{r^2+z^2}} \quad [363]$$

The variable substitution $z = r \sinh\theta$ leads to

$$\phi(r) = 2\xi \int_0^{\infty} e^{\kappa_D r\cosh\theta} d\theta = 2\xi K_0(\kappa_D r) \quad [364]$$

where Eq. [276] has been used; this result is just the Debye–Hückel potential due to a line charge, as given by Eq. [259] in the limit of vanishing cylinder radius a. To extend Eq. [364] to a cylinder of finite radius, we note that the solution to the Debye–Hückel equation involves two constants of integration: one multiplicative and one additive. We determine the multiplicative constant (ξ) from the boundary condition at the cylinder surface; the (zero) additive constant is determined by requiring that the potential vanish asymptotically. This again gives Eq. [259] but for a nonzero cylinder radius.

To obtain the apparent DH potential within the PGC approximation that asymptotically matches the cylindrical PB profile, we simply replace ξ_a in Eq. [259] with an apparent linear charge density ξ_{ADH} obtained from Eq. [322]:

$$\xi_{\mathrm{ADH}} = \frac{2\pi L_B a \sigma_{\mathrm{ADH}}}{e_0} \quad [365]$$

The ADH//PGC potential is then simply

$$\phi_{\mathrm{ADH}}(r) = \frac{2\,\xi_{\mathrm{ADH}}}{\kappa_D a}\frac{K_0(\kappa_D r)}{K_1(\kappa_D a)} \quad [366]$$

We note that this apparent potential should not be expected to agree perfectly with the asymptotic cylindrical PB potential due to the approximations

involved in solving Eq. [315] and, more importantly, because the additivity of nonlinear spherical corrections will not reproduce exact nonlinear cylindrical behavior. The reliability limit on the linear charge density is, from Eq. [325], equivalent to the lower bound:

$$|\xi_a| > \frac{\pi}{2z\kappa_D a} \qquad [367]$$

In cases where Eq. [367] fails to hold, the inequality can be inverted to provide a distance $r = \pi/|2z\kappa_D\xi_a|$ beyond which the ADH potential would be expected to be a good approximation to the actual PB profile. The apparent linear charge density of Eqs. [322] and [365] can be combined with the asymptotic DH potential of Eq. [366] to give the electrostatic interaction energy per unit length between two charged cylinders.[348] In Figure 26, the surface charge densities studied ($-0.002\ e_0/\text{Å}^2$ and $-0.01\ e_0/\text{Å}^2$) correspond to linear charge densities of $|\xi_a| = 0.9$ and 4.5, respectively. The reliability of the asymptotic fit according to Eq. [367] is assured for both since $|\xi_a| > 0.7$, while the upper-bound condition [327] implies that the ADH//PGC equation is justified for $|\xi_a| < 0.8$. The latter range defines the linear region of the curves (as it did for the spherical case shown in Fig. 35). The joining of the upper and lower bounds occurs because, as with the charged sphere, we have $\kappa_D C_a = 2.6$ (see Fig. 37).

As shown here, the DH potential for an extended charge distribution can be obtained by integrating over a point charge representation of the extended distribution and applying the appropriate boundary conditions.[348–352] The DH solution can then be modified to provide an approximate nonlinear result by introducing apparent charges or charge densities, a procedure that can be applied to existing analytical expressions such as those describing the interaction of two charged cylinders[348] or disks.[260] This "first-order approximation" to the PB solution, which is often quite accurate, can also serve as a useful guess in general-purpose programs. In simulations of supercoiled DNA, the polyelectrolyte is often modeled as a linear array of charged beads in which the spherical DH potential with modified charges is combined with a contact or excluded volume term.[353–356] Most of these investigations determine the modified charges by a fitting procedure that in essence reproduces the apparent charge densities of the NLDH approximation. The ADH potential can also be used in Monte Carlo or molecular dynamics simulations to model the interaction between charged polymer segments in an electrolyte[353,357–360] and in the interaction between a long polymer and a charged spherical macroion.[361]

A Finite Arc of Charge As a second example of using the point ion DH solution as a Green function, consider a finite, curved line (arc) of charge of length L and radius of curvature C, as shown in Fig. 41. With appropriately chosen parameters, this models a small piece of extended, but slightly curved,

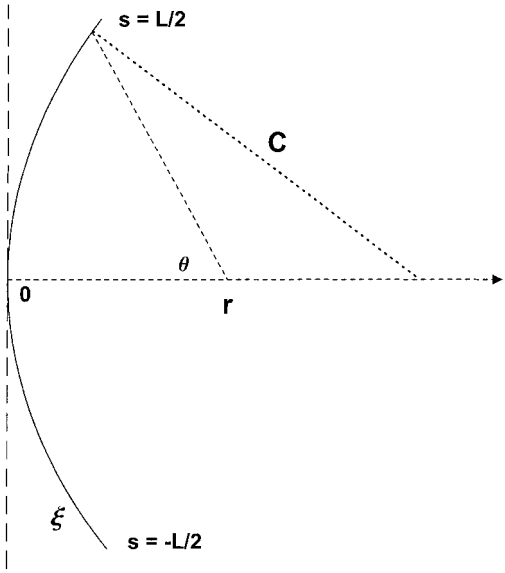

Figure 41 Diagram indicating a line arc of charge of length L with linear charge density ξ with a radius of curvature C whose center is placed at the origin; r is the perpendicular distance from the center of the arc and is positive to the right (or concave) side and negative to the left, s indicates a point on the arc measured from the origin along the arc, and θ is the angle between a vector from r to the origin and one from r to a point s on the arc.

DNA. Choosing r as the perpendicular distance from the center *and in the plane* of the arc and integrating over the length of charge using Eq. [307], with r defined as positive for the concave side (to the right in Fig. 41) and negative for the convex side (to the left), we obtain the following integral for the potential

$$\phi(r) = 4\xi_{\mathrm{ADH}} C \int_0^{L/2C} \frac{\exp\left(-\kappa_D \sqrt{r^2 + 4C|C - r|\sin^2\theta}\right)}{\sqrt{r^2 + 4C|C - r|\sin^2\theta}} d\theta \qquad [368]$$

after inserting the apparent linear charge density for the actual charge density. For a straight-line charge we take the limit $C \to \infty$ in Eq. [368]. In the absence of ions ($\kappa_D \to 0$), Eq. [368] expresses the Coulomb potential of a charged arc as an elliptic integral of the first kind. Figure 42 shows the ratio of the DH potential of Eq. [368] for a finite, straight ($C = \infty$) line charge to that of the infinite line charge of Eq. [364] for several different lengths ($L = 5$, 10, 20, 50 Å) as a function of the perpendicular distance from the center of the line charge; a Debye length of $R_D = 7.6$ Å was chosen to mimic typical electrolyte conditions (0.1 M monovalent and 0.02 M divalent salts). As seen in the figure, a line charge of 50 Å in length is essentially indistinguishable from an infinite line charge since end effects are screened by the salt. A simple condition on when end (or boundary) effects may be ignored is given below (see the discussion following Eq. [434]) and is very nearly satisfied in this case

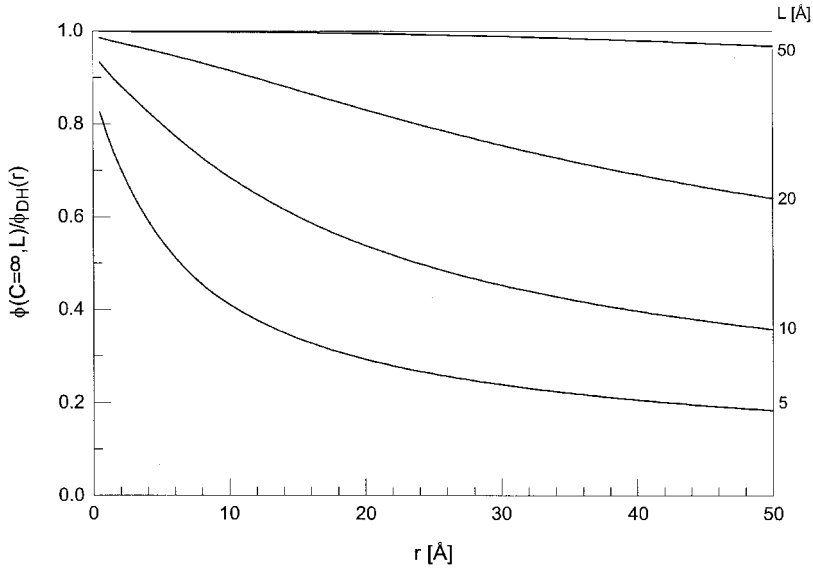

Figure 42 The ratio of the Debye–Hückel potential due to a finite straight line charge (Eq. [368], $C = \infty$) to that of an infinite line charge (Eq. [364]) as a function of the perpendicular distance (in Å) from the center of the finite line charge for several different lengths ($L = 5, 10, 20, 50$ Å) listed at the right; a Debye screening constant of $\kappa_D = 0.132$ Å^{-1} was used, corresponding to 0.1 M monovalent salt and 0.02 M divalent salt.

($\kappa_D L/2 = 3.3$). The influence of end effects is much more obvious for smaller line segments.

The effect of a curved arc is shown in Figure 43 where the same ratio as in Figure 42 is plotted. In this case the line segment is fixed at a length of $L = 50$ Å but the radius of curvature of the charged segment is varied ($C = 20$, 50, 100 Å). Potential ratios as a function of the distance from the arc center to the concave (+) and convex (−) side are shown. The potential on the convex side of the arc (to the left in Fig. 41) shows a simple monotonic decrease as a function of distance from the arc relative to the infinite DH line charge potential. The potential on the concave side (to the right in Fig. 41) is more interesting. For the relatively high curvature radius of $C = 20$ Å, the potential relative to the infinite line charge value goes through a maximum as the distance approaches the radius of curvature, falling off quickly as the point is passed; this is true as well for the straighter arcs with $C = 50$ Å and 100 Å. These maxima, however, do not show up in a plot of the potential since the infinite DH potential falls off faster than the rise in the ratio. The infinite line potential for a linear charge density corresponding to the double-stranded B-form DNA ($\xi = 4.2$) is also displayed in the figure (dotted–dashed line) and

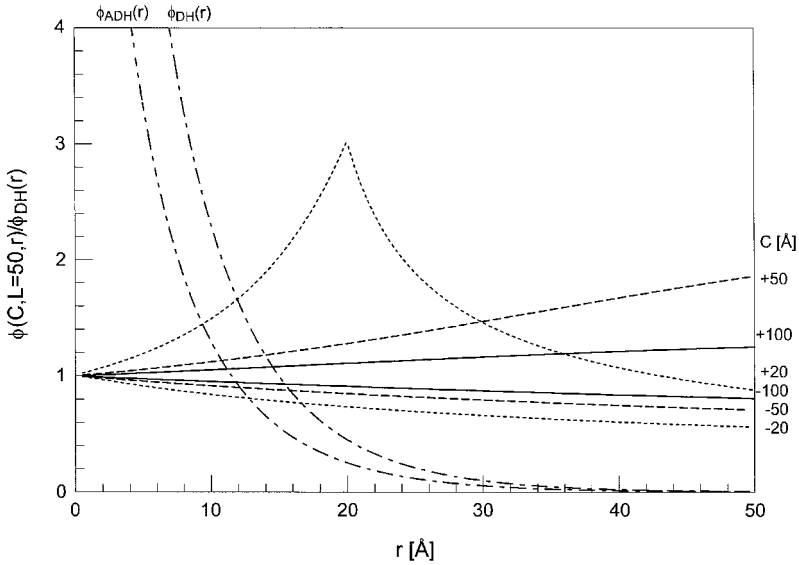

Figure 43 The ratio of the Debye–Hückel potential due to a charged arc (Eq. [368], $L = 50$ Å) to that of an infinite line charge (Eq. [364]) as a function of the perpendicular distance (in Å) from the center of the arc for several different radii of curvature ($C = 20, 50, 100$ Å) listed at the right. The plus and minus signs on the curvature radii indicate whether the distance is measured to the concave (+) or convex (−) side of the arc. For comparison the Debye–Hückel potential for an infinite line charge with linear charge density $\xi = 4.2$ corresponding to double-stranded B-DNA is shown along with the corresponding ADH//NLDH potential for a 10 Å radius cylinder (dotted–dashed lines); a Debye screening constant of $\kappa_D = 0.132$ Å^{-1} was used, corresponding to 0.1 M monovalent salt and 0.02 M divalent salt.

shows that, for distances from the surface greater than 30 Å, the potential of the charged arc is negligible. Equation [368], with the appropriate limits and distance restrictions, also applies to a circular ring of charge modeling a bacterial plasmid of DNA. Note, however, that we have treated only a line of charge and in reality a cylinder of finite radius, if only due to the Stern layer, should be used. One can then approximate the nonlinear PB solution by replacing the actual linear charge density ξ by the ADH charge density given by Eq. [263] or [365]. This potential is also shown in Figure 43, where the apparent charge density is 2.36.

Persistence Length of a Finite Line Charge As a final example using the additivity of the DH potential, consider again the finite curved arc of charge in Figure 41. One property of biophysical interest is the flexibility of a snippet of DNA. Although we are treating the molecule as a line of charge (roughly based on Gauss' law), we can imagine this line to follow the axis of a charged

cylinder of radius ~10 Å. One would expect the low-energy state of this cylinder to be straight, with the potential energy costs of bending due to the mechanical analogies of flexion and torsion and with the inclusion of electrostatic repulsion between charged line segments. Let s be a coordinate measuring the distance from the center of the arc *along the contour* and $\boldsymbol{u}(s)$ be a unit vector tangent to the arc at s. Because a straight line corresponds to a constant value of $\boldsymbol{u}(s)$, or $\boldsymbol{u}'(s) = 0$ and hence $\boldsymbol{u} \cdot \boldsymbol{u}' = 0$, an expansion of the bending energy (in units of $k_B T$) in $\boldsymbol{u}(s)$ must be quadratic in $\boldsymbol{u}'(s)$. Thus we write[362]

$$\begin{aligned} U_{\text{bend}} &= \frac{P}{2}\int_{-L/2}^{L/2}\left(\frac{\partial \mathbf{u}(s)}{\partial s}\right)^2 ds + \cdots \\ &= \frac{PL}{2C^2} + \cdots \end{aligned} \qquad [369]$$

where P is the persistence length and $C = |\boldsymbol{u}'(s)|^{-1}$ is the (constant) radius of curvature. The persistence length is a measure of the stiffness of a cylinder; for double-stranded DNA, experimental data give $P \sim 500$ Å.[363] The total persistence length can be expressed as the sum of mechanical and electrostatic persistence lengths ($P = P_m + P_e$);[364] here we estimate the (static) coulombic contribution based on a Debye–Hückel interaction between charged line segments. The electrostatic energy of a charged arc is given by[63]

$$\beta W_{\text{el}} \sim \frac{1}{2}\int \rho(\underline{x})\phi(\underline{x})d\underline{x} = \frac{\xi_{\text{ADH}}}{2}\int_{-L/2}^{L/2}\phi(C,s)ds \qquad [370]$$

again using the apparent linear charge density. The factor of $\frac{1}{2}$ corrects for double counting and the same expression can also be obtained through a charging procedure.[365] Calculating the change in electrostatic energy on bending and setting this equal to the bending energy of Eq. [369] gives the formula for the electrostatic persistence length:

$$P_e = \frac{\xi_{\text{ADH}}}{L}\lim_{C\to\infty}\left[C^2\int_{-L/2}^{L/2}(\phi(C,s) - \phi(\infty,s))ds\right] \qquad [371]$$

For a cylinder of finite radius, $\phi(C,s)$ denotes the average potential over the surface at constant s.[366,367] If no analytical expression for the potential is available, the persistence length must be determined from Eq. [371] numerically.[368] We calculate the potential at any point s along the arc due to the remainder of the arc by integrating the Debye–Hückel potential for a point charge:

$$\phi(C,s) = \frac{\xi_{\text{ADH}}}{L_B}\int_{-L/2}^{L/2}\frac{\exp\left[-2\kappa_D C\sin\left(\frac{|s'-s|}{2C}\right)\right]}{2C\sin\left(\frac{|s'-s|}{2C}\right)}ds' \qquad [372]$$

Inserting this potential into Eq. [371], expanding in inverse powers of C, and evaluating the integrals gives the electrostatic persistence length of a charged rod (of negligible radius):[364,369]

$$P_e = \frac{\xi_{\mathrm{ADH}}^2}{4\kappa_D^2 L_B}\left[1 - \frac{8}{3\kappa_D L} + \frac{e^{-\kappa_D L}}{3\kappa_D L}(8 + 5\kappa_D L + \kappa_D^2 L^2)\right] \qquad [373]$$

For most systems with high ionic strength, which are also the conditions under which the Debye–Hückel potential is applicable, the limiting value for long rods holds:[364,370]

$$\lim_{\kappa_D L \to \infty} P_e = \frac{\xi_{\mathrm{ADH}}^2}{4\kappa_D^2 L_B} \qquad [374]$$

Nguyen and Shklovskii have compared Monte Carlo calculations of the persistence length of long polyelectrolytes in ionic solution and found that the theory described above works well.[371]

In Figure 44, the ratio of the electrostatic persistence length for a finite line charge (Eq. [373]) to that of an infinite line charge (Eq. [374]) is shown as a function of the Debye screening constant for several values of the line length L.

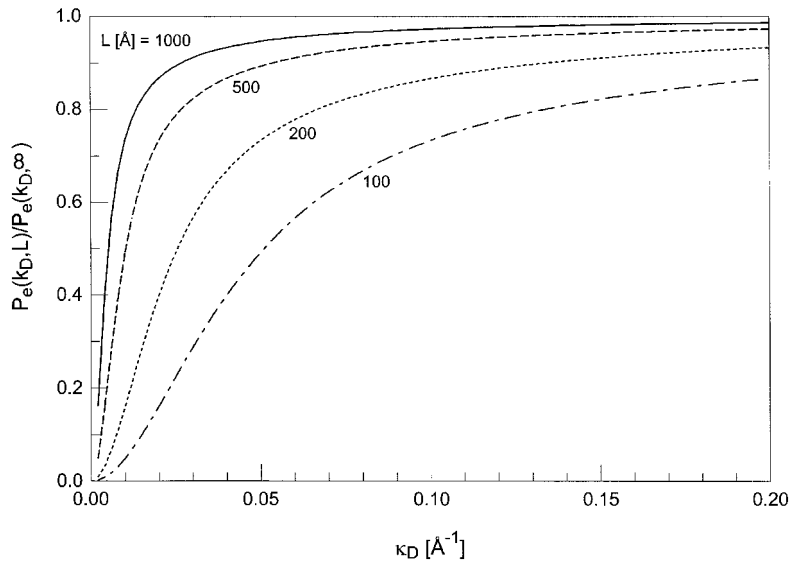

Figure 44 The ratio of the electrostatic persistence length of a finite line of charge (Eq. [373]) to that of an infinite line charge (Eq. [374]) as a function of the Debye screening constant κ_D (in Å^{-1}); the curves correspond to difference values of the length of the line ($L = 100, 200, 500, 1000$ Å).

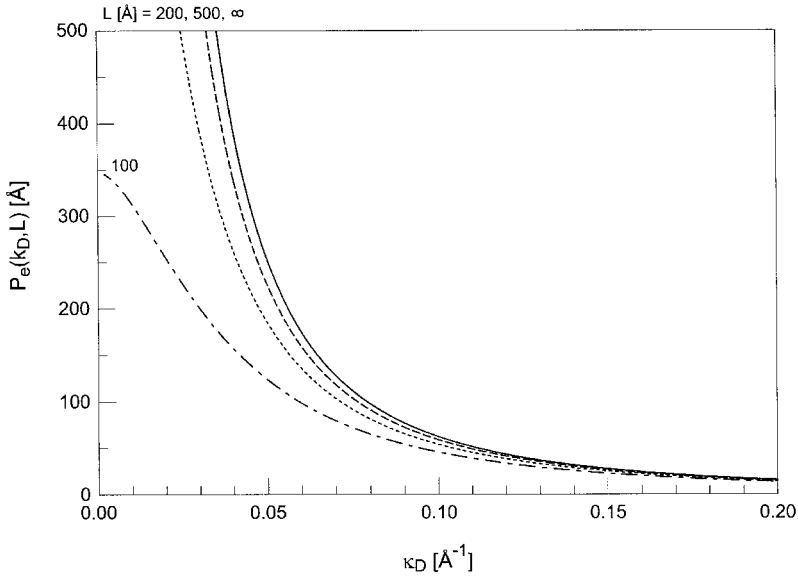

Figure 45 The electrostatic persistence length (in Å) of a finite line of charge (Eq. [373]) with linear charge density $\xi = 4.2$ (B-DNA) as a function of the Debye screening constant κ_D (in Å^{-1}); the curves correspond to different values of the length of the line ($L = 100, 200, 500, \infty$ Å).

The decrease in the persistence length for shorter line segments is obvious and more pronounced for lower ionic strengths where end effects are larger. Figure 45 displays the electrostatic persistence length for a charged line with linear charge density $\xi = 4.2$ of different lengths as a function of the Debye screening constant according to Eq. [373]. The persistence length of an infinite line charge is shown by the solid line and corresponds to the prefactor in Eq. [373], or equivalently by Eq. [374]. The end effects due to a finite line charge, while particularly noticeable for $L = 100$ Å, as shown in Figure 44, are not important for the common ionic strength range corresponding to $\kappa_D > 0.1$ Å^{-1}. In typical biological systems, electrostatic persistence lengths of $\sim$50 Å for DNA are found to represent a small, but nonnegligible, contribution to an overall persistence length of $\sim$500 Å. Again, as with the previous example, the actual linear charge density ξ can be replaced by the ADH value given by Eq. [263] or [365] to approximate the nonlinear PB result.

Numerically, the evaluation of the electrostatic energy of a collection of charges immersed in a high ionic strength solution (so that the Debye–Hückel approximation applies) is a relatively straightforward sum of all the pairwise interactions.[349] Unfortunately, this $O(N^2)$ approach may become computationally unwieldy when applied to specific large biophysical systems such as supercoiled DNA. To reduce the problem to $O(N)$, Fenley et al. have devised

a fast adaptive multipole algorithm for treating such systems.[372–374] Also, Sun and Walz have described a boundary element method for calculating the electrostatic interaction between two arbitrarily rough charged surfaces or particles subject to Debye–Hückel interactions.[375] Edwards and co-workers have used the DH solution as a Green function in obtaining the electrostatic potential for a model of double-stranded B-DNA in which the phosphate charges of each strand are helically wrapped along a cylinder.[376,377] Beard and Schlick have developed a procedure for asymptotically reproducing nonlinear PB potential distributions by fitting apparent Debye–Hückel charges[378] and represents the numerical generalization of relating apparent and actual charge densities given by Eq. [312] or [318]. Tsao has used DH additivity to study the interaction of an arbitrary distribution of fixed charges with a linearly regulated charged plate.[379]

Related Spherical Calculations

In a very early application of the DH equation to a system with biophysical significance, Kirkwood represented a molecule as a collection of point charges embedded in a dielectric sphere surrounded by mobile electrolyte ions and then calculated the electrostatic energy of the molecule by summing over the DH contribution of each embedded charge.[380] That work prompted Lenhoff to apply the DH equation to obtain the potential inside and outside a rippled sphere with a charge at its center.[381] Alexander et al.,[382] Gisler et al.,[383] and Stevens et al.[384] have investigated the relationship between the apparent charge and added salt concentration. In extensions of Kirkwood's approach, Phillies[385] and McClurg and Zukoski[386] have used the DH equation to analytically estimate the electrostatic energy for two interacting arbitrary distributions of point charges. Reiner and Radke have investigated the effect of charge regulation at the surface of spherical particles on the interaction energy.[387] Several studies by Hsu and Kuo on the double layer of ion-penetrable membranes apply to spherical particles.[146–149] Hsu and Liu have obtained series solutions for a charged spheroidal surface assuming the Debye–Hückel equation in the presence of an electrolyte with a mixed boundary condition (BC3)[388] and assuming the Poisson–Boltzmann equation in the presence of a $z:z$ electrolyte with either a fixed surface potential or charge density.[389] Yoon has presented an elegant iterative integral equation approach for solving the spherical PB equation.[390]

Evans and Ninham have compared the electrostatic free energy of spherical micelles calculated using Eq. [151] with experiment and found good agreement.[170] Knott and Ford have solved the DH equation for a system of charged spherical macroions in the presence of point counterions but with no added salt.[391] Zydney[392] has used the DH equation to investigate the electrophoretic motion of a charged sphere inside a charged spherical cavity, and Tsao and Sheng[393] have investigated the electrostatic free energy for a similar system. Lopez-Garcia, Horno and Grosse have solved the PB equation inside a

spherical cavity for a general electrolyte.[394] Yuet and Blankschtein have used the PB equation to derive approximate potentials for the inner and outer surfaces of charged spherical vesicles in a $z:z$ electrolyte,[395] and von Grünberg has solved the PB equation in the "eccentric cell model" in which a macroion is placed off-center in a spherical cell containing point counterions.[396] Neto et al. have used the spherical PB equation to estimate the pK_a of monoprotonic acid as a function of ionic strength.[397]

Hsu and co-workers have investigated the interaction between ion-penetrable spheres,[398,399] ion-penetrable spheroids,[400] and charge-regulated spheres[401] within the Debye–Hückel approximation. Ohshima has also studied ion-penetrable spheres[337] as well as the effect of including polarization terms on induced surface charges for interacting DH spheres.[402] Lopez-Garcia, Grosse and Horno have solved the PB equation for a spherical charge-permeable membrane surrounding an impermeable charged core.[403] Numerical calculations of the two-sphere PB equation are usually performed in bispherical coordinates.[347] In early work, Hoskin[404] and later McCartney and Levine[405] and Ledbetter, Croxton and McQuarrie[331] investigated the interaction of identical spheres, while more recently Ring[406] and Stankovich and Carnie[407] studied nonidentical spheres. Others[408–410] have presented numerical procedures applicable to interacting spheres with different radii and surface potentials, and Sengupta and Papadopoulos have numerically solved the PB equation for a sphere within a spherical cavity.[411] If only the interaction force and/or interaction potential are needed, and not the PB potential, boundary-based methods can be more efficient. Stankovich and Carnie have used the boundary Galerkin method to study the effect of nonuniform surface potentials on interacting DH spheres and, in particular, the torque involved, a question of considerable relevance to the mutual docking of macromolecules.[412]

Mixed-Geometry Studies

More complicated than studies of like–like particle interactions are investigations of the interaction between particles with dissimilar geometries. These have several purposes: to compare results with simpler systems in order to determine what physical principles guide both, to discover differences between the two that might illustrate new phenomena, and to serve as substitutes for interactions among even more complex biological systems. The forces involved in complicated biological systems can now be measured with atomic force microscopy and used to decipher the nature of polyelectrolyte interactions.[413–419]

Bulk Model: Sphere–Plane Interactions

The Gouy–Chapman equation treating the interaction between point electrolyte ions and a charged planar surface is inherently a mean-field approach. If we let one of the counterions assume a finite radius much larger than its neighbors, we now have a three-body interaction involving the

surface, the finite charged sphere, and the electrolyte. This system not only mimics biological interactions involving extended bodies such as proteins near a cell membrane but also can be used to investigate the approximations assumed by the mean-field approach. While much of the work in this area is of a statistical-mechanical nature and outside the range of this review, some of it has led to modified versions of standard Poisson–Boltzmann theory,[420] relying on Monte Carlo calculations to test and compare suggested theories, as discussed briefly in a later section.

Following the derivation of the sphere–sphere interaction, we sketch that for a sphere interacting with a charged plane. Putting the dividing plane at $H_0/2$, where H_0 is the closest sphere–plane distance, and with the charged plane situated at $x = 0$, we assume a potential of the form

$$\phi_{\mathrm{PB}}(\underline{r}) = \frac{4}{z}\tanh^{-1}\left[A_1 e^{-\kappa_D x} + A_2 \frac{e^{-\kappa_D(r_2-a)}}{r_2/a}\right] \qquad [375]$$

As in the sphere–sphere case, we may obtain the coefficients from the general expression of Eq. [202] or, more simply, proceed from the sphere–sphere case and set $\gamma_1 = 1$ and $\delta_1 = \varepsilon_1 = \exp(-\kappa_D H_0)$. This gives the leading term of the force

$$\beta F(H_0) = \frac{16\kappa_D a}{L_B z^2} A_1(H_0) A_2(H_0) e^{-\kappa_D H_0} \qquad [376]$$

where the leading term of the interaction potential is

$$\beta V_{\mathrm{PB}}(H_0) = \begin{cases} \dfrac{16a}{L_B \zeta_2 z^2}\hat{s}_1\hat{s}_2 e^{-\kappa_D H_0}, & \kappa_D a < 3 \\ \dfrac{8a}{L_B \zeta_2 z^2}\hat{s}_1\hat{s}_2 \ln\left(\dfrac{1+e^{-\kappa_D H_0}}{1-e^{-\kappa_D H_0}}\right), & \kappa_D a > 3 \end{cases} \qquad [377]$$

where $\hat{s}_1$ (for $\delta_1 = \zeta_1 = 1$) and $\hat{s}_2$ are given by Eq. [205] and we have used the small-separation extension suggested by the corresponding HHF solution for large $\kappa_D a$ (found by letting $a_1 \to \infty$ in Eq. [347]).

Sphere–plane interactions are often treated as a special case of sphere–sphere interactions in which the radius of one sphere is allowed to approach infinity with image charges induced in the planar dielectric boundary being a primary concern. Ohshima has extended sphere–sphere studies to look at the interaction of spheres with an ion-penetrable membrane within the Debye–Hückel approximation.[337,421] Carnie and co-workers have used both DH and PB sphere–plane calculations to test the validity of the Derjaguin/HHF approximation for these systems.[407,422] Stahlberg, Appelgren and Jönsson have performed a detailed analysis of sphere–plane interactions within the DH approximation to assess the importance of neglect of ion correlation in Gouy–Chapman theory.[423] Jönsson and Stahlberg have also applied Derjaguin

theory to model ion-exchange chromatography of proteins.[424] Grant and Saville used a boundary element method to investigate the Debye–Hückel interaction between a nonuniformly charged sphere and a plane.[425] Bhattacharjee and Elimelech have extended Derjaguin's analytical ideas to propose a surface element integration algorithm for calculating the interaction between particles of arbitrary shape and a charged plane.[426] Hsu and Liu have proposed a numerical boundary integral procedure that can be applied to any type of interacting geometries and explicitly considered sphere–sphere, sphere–plane, sphere–planar slit, sphere–spherical pore, and sphere–cylindrical pore systems.[427,428] Von Grünberg and Mbamala have used the PB cylindrical cell model to confine a charged sphere near a dielectric boundary and compared the results with Monte Carlo calculations.[429] More recently, sphere-plane investigations have been extended to systems with two or more spheres. Within the DH approximation, Goulding and Hansen have derived an effective pair potential between two charged spheres in the presence of a neutral or charged wall,[430,431] and Sader and Chan have considered the interaction of two spheres confined between two parallel charged plates.[432]

Bulk Model: Other Mixed-Geometry Interactions

In the tutorial presented in this chapter, we have given expressions for the interaction potential between two planes (Eq. [133]), two cylinders (Eq. [285]), and two spheres (Eq. [352]) as well as that between a plane and a sphere (Eq. [347]). The two remaining cases, those for a plane and a cylinder and for a sphere and a cylinder, are easily found by following the same procedure involving the NLDH approximation used in the cases described above.

In related work, Mark, Kaplan and Williams Jr. calculated the interaction energy between an ion-penetrable sphere and an ion-penetrable rod within the DH approximation.[433] Gu used the Derjaguin/HHF approach to find the interaction potential for sphere–plate and sphere–cylinder systems.[434] Hsu and Kao calculated the free energy for a spheroidal particle within a spherical cavity.[435] Ospeck and Fraden solved the PB equation numerically for two parallel like-charged cylinders confined between two parallel charged plates.[436] Schiessel studied the bending of charged flexible planes due to nearby charged cylindrical macroions,[437] and Menes, Gronbech-Jensen, and Pincus have used the Debye–Hückel equation to calculate the interaction between two charged cylinders adsorbed onto a surface.[352]

NUMERICAL SOLUTIONS TO THE POISSON–BOLTZMANN EQUATION

One-Dimensional Geometries

For more general applications involving electrolyte ions of various charges and sizes or for mixed boundary conditions in which the surface

potential and charge density are coupled, the one-dimensional PB equation must be solved numerically. The method of choice is usually the Runge–Kutta procedure,[438] but a simple finite-element approach is discussed later. For a fixed surface potential, one guesses an initial slope (field), typically based on a known nonlinear or Debye–Hückel solution, and steps out to some predetermined distance from the surface that can be considered to represent the bulk electrolyte solution (i.e., several Debye lengths). If the potential diverges before this distance is reached or if the potential changes sign (the solution must be monotonic for a single surface), one starts again with a slightly different guess for the initial slope. For most biopolyelectrolytes the surface charge density is known, so the abovementioned procedure is still followed but with an initial guess for the surface potential and iterated until convergence. Under some circumstances, neither the surface charge density nor the surface potential are known, only a coupled relation. A procedure similar to the above would be used in conjunction with this relation.[230]

Finite-Difference/Finite-Element Algorithms

While simple one-dimensional models often suffice for qualitative and sometimes semiquantitative prediction, more accurate results require that an all-atom model of the polyelectrolyte be used. One might also want to use more realistic representations of the electrolyte ions and solvent by including (at least) finite ion radii and a spatially dependent dielectric coefficient. Modern computational approaches to solving the PB equation, which have been summarized by Beck[39] and to which the reader is referred for more detail, can incorporate all of these imporvements. Most general-purpose programs constructed to solve the Poisson–Boltzmann equation for an arbitrary polyelectrolyte are based on a discrete representation of Eqs. [3] and [4]. Whether the method is termed *finite-difference* or *finite-element* basically depends on the particular technique used to solve the discretized equations and the interpretation as to whether the equations are solved "at points" or "within elements," a distinction that can be traced to using either a differential or an integral (i.e., variational) equation.[39] Finite-difference methods usually write the discretized (differential) equation in terms of matrices and use linear algebra algorithms for convergence, a procedure that takes advantage of multilevel grids with constant (usually cubic) spacing.[34,41,43,439–442] Since iteration in finite-difference algorithms necessarily involves only nearest-neighbor gridpoints, long-range deviations, and particularly oscillations, from the final solution tend to persist. The method around this convergence problem is to alternate iterations between coarse and fine grids. A disadvantage to fixed spacing, multigrid finite-difference methods is that a very large number of gridpoints are required to accurately discretize the region where most of the "action" takes place, that is, at the biomolecular surface.

Finite-element approaches, often based on Galerkin's method of finding an extremum of a variational integral, can take advantage of nonuniform, adaptive meshes that conform to physical boundaries and have long been popular in hydrodynamic and structural engineering applications.[443–449] Unfortunately, the use of variable grid spacing tends to lead to large meshes without the advantage of multilevel convergence optimization. This situation led naturally to a combination of the two methods: adaptive finite-element gridding within a multilevel approach that can take advantage of the most recent developments in parallel computing.[44,45,446] This technique has been used to obtain the solution of the Debye–Hückel equation for several extremely large biomolecular systems (up to one million atoms).[46,47]

As with the analytical solutions presented above, we consider in detail the PB cell model and take the bulk model limit at the end. We begin the derivation of the finite-element PB algorithm by writing the mobile charge density of Eq. [4] as an explicit functional of the potential:

$$\rho^{\text{mobile}}[\phi(\underline{r})] = e_0 A_0 \sum_{i=0}^{I} c_i^R z_i e^{-z_i \phi(\underline{r}) + \Delta\gamma(\underline{r})} \qquad [378]$$

For further reference below, we have also included any nonelectrostatic contributions to the potential of mean force in the form of an activity coefficient: $\Delta\gamma(\underline{r}) = \gamma(\underline{r}) - \gamma(\underline{R})$. Using Eq. [378] with Eq. [3] gives

$$\nabla \cdot \eta(\underline{r}) \cdot \nabla\phi(\underline{r}) = -4\pi L_B e_0^{-1} [\rho^{\text{fixed}}(\underline{r}) + \rho^{\text{mobile}}[\phi(\underline{r})]] \qquad [379]$$

where $\eta(\underline{r}) = \varepsilon(\underline{r})/\varepsilon_0$ is the ratio of the local dielectric coefficient to a reference value.

Discretization

To solve Eq. [379] for a general polyelectrolyte–electrolyte system, we discretize the system into a grid consisting of either a lattice of points or a set of small volume elements. It is assumed that any nonmobile system charges are contained within the grid and are not external to it; this condition may be relaxed as illustrated in the one-dimensional version of the algorithm presented below. Any method of subdivision may be used, resulting, for example, in either an array of periodically spaced points[41,43] or a higher density of Voronoi polyhedral elements near the polyelectrolyte surface.[39,44,45,445,446,450–452] Each lattice point or finite element in the system must be assigned to represent either part of the polyelectrolyte or its ionic environment. To account for a finite distance of closest approach to the polyelectrolyte surface by ions of varying size, a rolling-sphere algorithm may be

used to lay down successive layers of environmental points or elements, keeping track of which layers are accessible by which ions.[453,454]

Initialization

After the system has been discretized, an initial assignment of charges, dielectric coefficient, and potential for each grid position must be made. In an all-atom representation, the polyelectrolyte is represented by a collection of fixed point charges within a region of constant, but possibly spatially dependent, dielectric coefficient from which mobile electrolyte ions in the environment are excluded. The polyelectrolyte charge is usually mapped, on an atom-by-atom basis, onto the grid using the van der Waals radius of each atom.[455] Dielectric coefficients in the range 4–20 are often chosen for grid elements partitioning the polyelectrolyte,[456] while the bulk water value of 78–80 is used for the ionic environment, although the best method for assigning dielectric coefficients to the interior of a biomolecule is still being debated,[34,457–461] and, indeed, an accurate procedure for all cases may not be possible.[462–464] An initial guess for the potential at each grid position is made. Basing this guess on additivity of the point charge Debye–Hückel solution is a convenient and qualitative one that is often used. (Results presented in this tutorial suggest using the apparent DH potential instead.) For grid positions labeled by index j and fixed polyelectrolyte charges by index n, Eq. [307] gives

$$\phi_{\text{init}}(\underline{r}_j) = L_B \sum_{n=1}^{N} \frac{q_n e^{-\kappa_D |\underline{r}_j - \underline{r}_n|}}{\eta_j |\underline{r}_j - \underline{r}_n|} \qquad [380]$$

where one could substitute apparent charges for the actual charges.

Iteration

Differential equation [379] can be converted into an integral representation by integrating over the jth volume element (with volume v_j) to get

$$\int_{v_j} dS \cdot \eta(\underline{r}) \cdot \nabla\phi(\underline{r}) = -4\pi L_B e_0^{-1} v_j [\rho^{\text{fixed}}(r_j) + \rho^{\text{mobile}}[\phi(\underline{r})]] \qquad [381]$$

The surface integral in Eq. [381] has contributions from only those grid positions $k(j)$ sharing a common boundary with element j. Denoting $\phi(r_j)$ by ϕ_j, $|\underline{r}_j - \underline{r}_k|$ by r_{jk}, the common surface area between elements j and k by S_{jk}, and an average dielectric coefficient (to be defined later) by η_{jk}, Eq. [381] can be written

$$\sum_{k(j)} \frac{\eta_{jk} S_{jk} (\phi_k - \phi_j)}{r_{jk}} = -4\pi L_B e_0^{-1} v_j \left(\rho^{\text{fixed}}(r_j) + \rho^{\text{mobile}}[\phi_j] \right) \qquad [382]$$

Solving Eq. [382] for ϕ_j gives the discretized version of the full Poisson–Boltzmann equation (Eqs. [378] and [379]) applicable to non-Cartesian grids:

$$\phi_j = \frac{4\pi L_B v_j e_0^{-1}(\rho^{\text{fixed}}(r_j) + \rho^{\text{mobile}}[\phi_j]) + \sum_{k(j)} \frac{\eta_{jk} S_{jk} \phi_k}{r_{jk}}}{\sum_{k(j)} \frac{\eta_{jk} S_{jk}}{r_{jk}}} \qquad [383]$$

Initial versions of the general-purpose PB programs treated only the Debye–Hückel equation,[40,42,43,465,466] but shortly thereafter algorithms for solving the nonlinear PB equation in a bulk 1 : 1 electrolyte were developed.[41,467] While this limits the representation of the mobile charge distribution to a $\sinh(\varphi)$ term, use of an effective valence according to Eq. [69] allows more general electrolytes to be treated (or at least approximated) within these programs. Some later releases now allow inclusion of a mixed 2 : 1 salt.[468] The development of Eq. [383] contains an inherent inaccuracy due to the self-energy of the fixed charge distribution, which approaches infinity as a gridpoint approaches a fixed charge. However, Zhou et al. have shown how a minor modification in the derivation of Eq. [383] can be used to remove this self energy, thus improving the accuracy of the method.[469] Finally, we point out that these programs assume a bulk electrolyte so that concentrations entering into the mobile charge densities are bulk concentrations; cell model calculations, in which ion concentrations at the outer cell boundary must either be known or continually updated (which is equivalent to setting the potential gauge), may not be accurate without explicitly modifying the code.

Using an initial guess for the potentials such as that given by Eq. [380], we can iterate Eq. [383] until convergence based on some appropriate criterion; the average of the potential at positions closest to the polyelectrolyte surface would be one such choice. For the cell model, the ion concentrations at the outer boundary c_i^R in Eq. [383] must be updated during each iteration. This is done by calculating the concentration of each species i at each position j according to

$$c_i(r_j) = \frac{n_i e^{-z_i \phi_j}}{A_0 \sum_k v_k e^{-z_i \phi_k}} \qquad [384]$$

where the summation in the denominator "renormalizes" the initially assigned concentrations (in the numerator) to the correct number of ions. The three terms in the numerator of Eq. [383] propagate information about fixed polyelectrolyte charges, mobile electrolyte charges in the environment, and the gauge condition on the potential, respectively. Since each grid position is designated as either polyelectrolyte or environment, only one term of the first two applies in any given element.

The finite difference approach of direct iteration of Eq. [383] was first used by Warwicker and Watson to study the electrostatic potential inside the active site of the enzyme phosphoglycerate mutase.[465] Shortly thereafter, Pack and co-workers applied the method to study the relationship between counterion distributions and different conformations of double-stranded DNA.[453,470–473] Convergence in this standard approach can be accelerated in one of two ways: (1) by updating the potential array immediately (Gauss–Seidel iteration), rather than storing the potential values and updating the array only after the entire space has been iterated (Jacobi iteration); and (2) by estimating the potential change during an iteration based on previous changes (successive overrelaxation).[39,438] Unfortunately, the convergence rate for direct iteration increases as the number of gridpoints and so is impractical for all except the simplest systems. It is, however, one of the easiest methods to program and for one-dimensional systems is entirely adequate (see discussion below). More recent finite-difference techniques for solving the PB equation take advantage of modern multigrid methods in which the PB equation is first solved on a fine grid, then solved on a coarser grid, and finally the coarse-grid solution is used to improve the fine-grid solution.[39,438] This technique is particularly amenable to treatment using a cubic grid.[474] Combining the multigrid method with a coarse/fine-grid predictor–corrector scheme based on the conjugate gradient method provides a robust and efficient algorithm for solving the nonlinear PB equation under a variety of conditions. Similar routines have also been introduced into newer finite-element approaches.[44–46,446]

Variable-Solvent Dielectric Coefficient

In Eq. [383] the average dielectric coefficient between two neighboring elements is often taken as the inverse of the arithmetic mean of the inverses:[475]

$$\eta_{jk} = \frac{\eta_j \eta_k}{\alpha \eta_j + (1 - \alpha)\eta_k} \qquad [385]$$

for an element boundary offset by a fraction α with respect to the element centers, implying that adjacent elements act as capacitors in series. Other methods of mapping the dielectric coefficient have also been presented.[476,477] If one wants to include solvent dielectric changes due to the electric field of the polyelectrolyte and/or local ion concentration, the approach of Lamm and Pack[478] can be used (see also Warwicker[466]). On the basis of Booth's work,[479,480] the field-dependent dielectric coefficient can be written as[88]

$$\eta_j = 0.023 + (1 - 0.023)L(2.26\,\phi'_j) \qquad [386]$$

where ϕ'_j indicates the reduced electric field strength at the jth grid element (in units of Å^{-1}), and $L(x) = 3[\coth(x) - 1/x]/x$. A larger effect on the solvent

dielectric coefficient is due to local ion concentrations, which, for sodium cations, can be calculated from[88]

$$\eta_j = \frac{1 - \theta_j + 3\theta_j \eta_{\text{cat}}/2}{1 + \theta_j/2} \qquad [387]$$

where

$$\theta_j = \frac{c_{\text{Na}}(r_j)}{c_{\text{Na}}(r_j) + c_{\max}} \qquad [388]$$

$\eta_{\text{cat}} \sim 0.051$, and $c_{\max} \sim 11.2$ M is the maximum concentration for sodium ions modeled as 1.4-Å spheres and solvated by 4.6 water molecules. Equation [387] is a special case, for $\eta_{\text{cat}} \ll 1$, of Maxwell's formula for a heterogeneous mixture of dielectric spheres;[481] Maxwell's result was later extended by Rayleigh,[482] who sometimes gets the credit.[483,484] If magnesium counterions are also present, then $c_{\max} \sim 9.2$ M for this contribution, with the two separate Na^+ and Mg^{2+} η values multiplied together to give the total decrement. The anion (i.e., coion) contribution can also be calculated, but near a positively charged surface it is generally small enough to be neglected. If both Eqs. [386] and [387] are used, they can be multiplied together to yield the combined effect. (It is actually more legitimate to replace the bulk factor represented by unity in Eq. [386] by the value obtained in Eq. [387], but the effect is small.) One can also include a small geometric contribution that takes into account the restricted rotational motion of water molecules in contact with a surface.[88] Except for narrow cavities, this effect is much smaller than those due to a local electric field and to ions.

The effect of a variable local dielectric coefficient based on Eqs. [385]–[388] is shown in Figures 46–48. In Figure 46, the self-consistently determined dielectric coefficient profiles for a charged plane, cylinder, and sphere of surface charge density $\sigma_a = -0.01\ e_0/\text{Å}^2$ in the presence of a bulk 0.05 M monovalent electrolyte are shown. In all cases the bulk dielectric value is reached within about three water layers of the surface (~5 Å) but the dielectric decrement close to the surface is large. The effect is more pronounced for a charged plane owing to a higher electric field and greater ion concentration at the surface. The standard PB (constant ε) potential profiles as well as those obtained by including a variable dielectric coefficient for these same systems are shown in Figure 47. It is seen that little difference exists between the two profiles (in all cases, the value of the surface potential for the variable dielectric coefficient case is slightly more negative). The reason for this is seen in the resulting concentration profiles shown in Figure 48. For the charged plane, the inclusion of a variable dielectric coefficient leads to a considerable increase in the surface counterion concentration, which in turn reduces the potential to near its standard PB value. Thus, if one is interested only in the surface potential, the effect

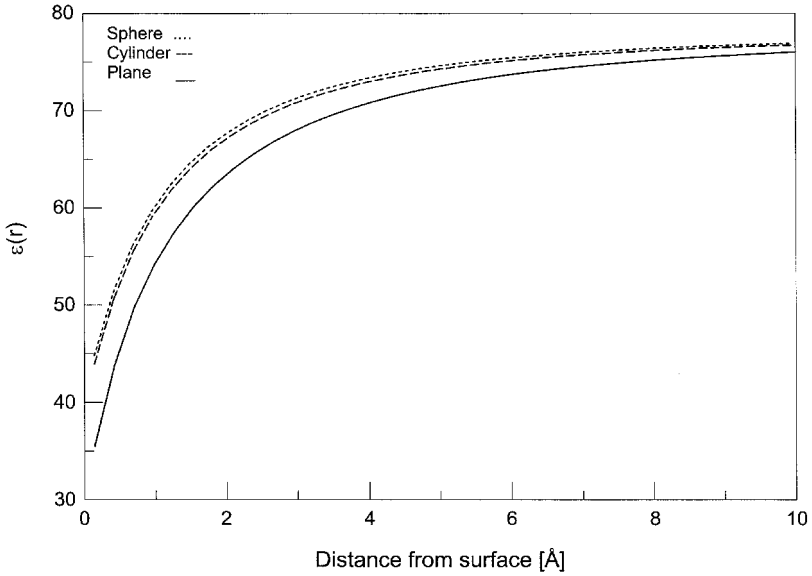

Figure 46 The dielectric coefficient profiles calculated from Eqs. [385]–[388] for a plane (solid line), cylinder of radius 10 Å (dashed line), and sphere of radius 20 Å (dotted line) with a surface charge density of $\sigma_a = -0.01\ e_0/\text{Å}^2$ in the presence of a bulk 0.05 M 1 : 1 electrolyte.

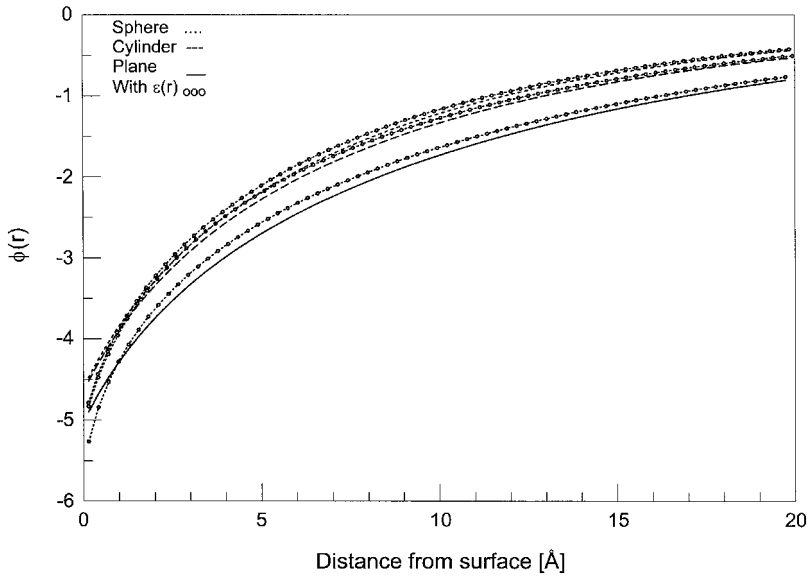

Figure 47 The potential profiles for the systems of Figure 46 with (circles) and without (no circles) the local dielectric coefficient correction.

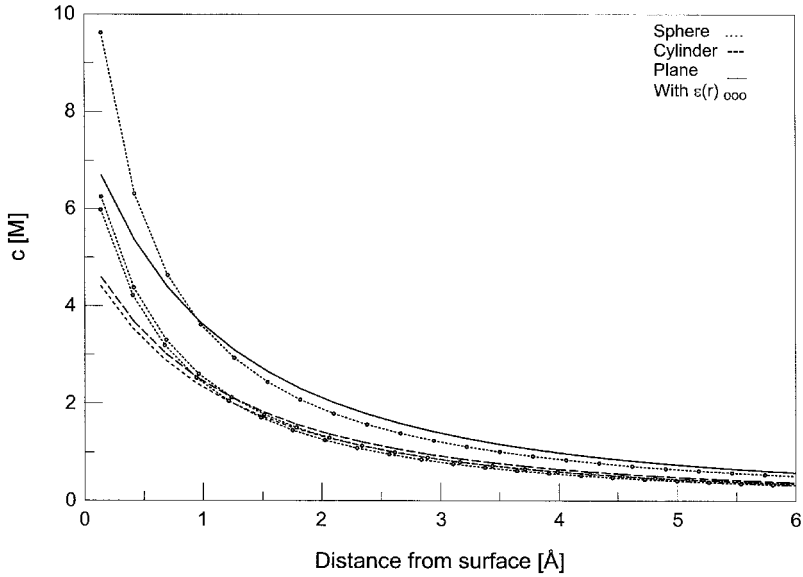

Figure 48 The cation concentration profiles for the systems of Figure 46 with (circles) and without (no circles) the local dielectric coefficient correction.

of a variable dielectric coefficient is not large;[466] however, if one requires a measure of surface counterion concentrations, then the effect can be quite noticeable.

One-Dimensional Finite-Difference Algorithm

As a simple example, we repeat the steps leading to Eq. [383] but with three changes: (1) we treat the radial d-dimensional PB equation, (2) we consider the cell model with the derivative of the potential specified at the boundaries, and (3) there are no fixed charges. Dividing the region $a < R$ into N equal segments with a gridpoint placed at the center of each segment, we obtain three equations:

$$\phi_1 = \frac{-\eta_1 \phi_a' a^{d-1}\Delta + \eta_{12}(r_1 + \Delta/2)^{d-1}\phi_2 + 4\pi L_B e_0^{-1}\rho[\phi_1] r_1^{d-1}\Delta^2}{\eta_{12}(r_1 + \Delta/2)^{d-1}}$$

$$\phi_j = \frac{\eta_{j-1,j}(r_j - \Delta/2)^{d-1}\phi_{j-1} + \eta_{j,j+1}(r_j + \Delta/2)^{d-1}\phi_{j+1} + 4\pi L_B e_0^{-1}\rho[\phi_j] r_j^{d-1}\Delta^2}{\eta_{j-1,j}(r_j - \Delta/2)^{d-1} + \eta_{j,j+1}(r_j + \Delta/2)^{d-1}}$$

$$\phi_N = \frac{\eta_N \phi_R' R^{d-1}\Delta + \eta_{N-1,N}(r_N - \Delta/2)^{d-1}\phi_{N-1} + 4\pi L_B e_0^{-1}\rho[\phi_N] r_N^{d-1}\Delta^2}{\eta_{N-1,N}(r_N - \Delta/2)^{d-1}} \qquad [389]$$

where

$$\Delta = \frac{R-a}{N}, \qquad \rho[\phi_j] = e_0 A_0 \sum_{i=0}^{I} c_i^R z_i e^{-z_i\phi_j+\Delta\gamma_j}$$
$$\eta_{j,j+1} = \frac{2\eta_j\eta_{j+1}}{\eta_j+\eta_{j+1}}, \quad c_i^R = \frac{n_i e^{-z_i\phi_N}}{A_0\Delta\sum_{j=1}^{N} r_j^{d-1}e^{-z_i\phi_j}} \qquad [390]$$

and ϕ'_a, ϕ'_R are known potential derivatives (electrostatic fields) at the cell boundaries. Although a fixed stepsize has been found sufficient for all examples in this tutorial, one could easily incorporate a variable stepsize into Eq. [389] based on the known exponential decay of the potential,[485] and one might speed up the algorithm somewhat by introducing an iterative scheme based on the linearized solution.[486] For most biological systems, the potential (and hence η_j and ρ_j) can be initialized using Eq. [57] for the planar case or Eq. [152] for the cylindrical ($d = 2$) and spherical ($d = 3$) cases, where $z = z_e$ is the effective valence. For the cell model, ion concentrations c_i^R at the outer boundary must be updated. For a single biomolecule in a bulk electrolyte, these concentrations are replaced by bulk ion concentrations c_i^B and an outer-boundary distance R is chosen sufficiently far from the inner boundary at a such that the field at R is negligible. As discussed below (see Eq. [434]), it is sufficient to choose R such that $\kappa_D(R-a) > 5$.

The one-dimensional algorithm of Eq. [389] has been used throughout this tutorial to obtain "exact" data for comparison with approximate results. We illustrate its utility here in a different way. In Figure 49, the potential (lower frame) and counterion concentration (upper frame) for a spherical micelle of radius $a = 20$ Å and surface charge density $\sigma_a = -0.01\ e_0/\text{Å}^2$ in the presence of a 0.1 M 1 : 1 electrolyte are shown by the solid lines. We can model a vesicle with an ion-penetrable membrane by (1) extending the system to $r = 0$, (2) removing the field boundary condition at $r = a$ (now $\phi'(0) = 0$ by symmetry), and (3) adding a source term to the mobile charge density in Eq. [389]

$$\rho[\phi_j] = e_0 A_0 \sum_{i=0}^{I} c_i^R z_i e^{-z_i\phi_j+\Delta\gamma_j} + \frac{e_0 Q_a \delta(r_j-a)}{(4\pi a^{d-1}\Delta^2)}$$

where $Q_a = -50.265$ (corresponding to the charge density presented above). The resulting potential and counterion concentration are shown in Figure 49 by the dashed lines where extrema occur at the position of the (infinitely thin) membrane layer. A membrane of finite width can be treated by defining a region of lower dielectric constant inside the position of the source charge.[487] If the system is once again restricted to the $r > a$ and the zero-field condition

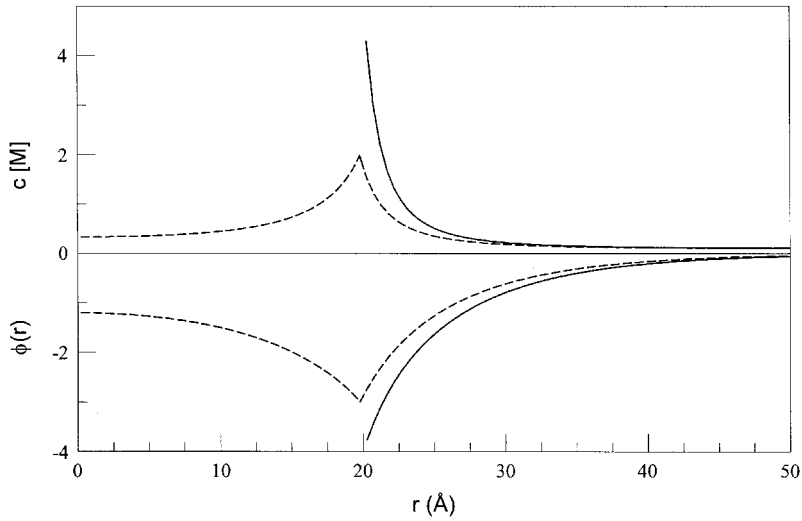

Figure 49 The potential (lower frame) and counterion concentration (upper frame) profiles for a spherical micelle of radius $a = 20$ Å and surface charge density $\sigma_a = -0.01$ $e_0/\text{Å}^2$ in the presence of a 0.1 M 1 : 1 electrolyte. The solid lines show data for a solid (ion-impenetrable) sphere, and the dashed lines show data for an ion-penetrable sphere.

$\phi'(a) = 0$ is imposed (still in the presence of the charge at $r = a$), we numerically recover the original (solid line) case, thus showing the equivalence of a field boundary condition and a source charge term, as implied by Gauss' law.

Cubic Grid–Bulk Model Finite-Difference Algorithm

The algorithm used in most general-purpose programs assumes a cubic grid and treats a single polyelectrolyte in a bulk electrolyte solution. In this case, Eq. [383] simplifies to

$$\phi_j = \frac{\sum\limits_{k(j)} \eta_{jk}\phi_k + 4\pi L_B s^2(\rho^{\text{fixed}}(r_j) + \rho^{\text{mobile}}[\phi_j])}{\sum\limits_{k(j)} \eta_{jk}} \qquad [391]$$

for cubic elements of dimensions $s \times s \times s$. This method has the advantages of not requiring the intermediate calculation of ion concentrations at the boundary and allowing a simple and computationally efficient refocusing procedure to be implemented. As a useful exercise, the PB equation can be solved analytically on a cubic grid in terms of Fourier series with the series coefficients determined by the boundary conditions on the grid.[488]

Alternative General-Purpose Methods

Closely related to the finite-element approach is the boundary element method.[374,489–506] In this procedure the surface of a macromolecule, which serves to partition space into two regions with different dielectric coefficients, is divided into small surface elements, typically using triangulation. The electrostatic potential at any point in space is then written as an integral of the induced charge density on the surface with the charge density obtained by solving a system of linear equations. The advantage of this method is that discretization of the surface involves far fewer points than does discretization of space. Although the boundary element approach is usually restricted to a single surface and generalization of the method to a spatially variable dielectric coefficient is likely to be difficult, the method is well suited for investigating the hydration of biomolecules.[491,495,497–499,507]

A number of algorithms have been devised for solving the PB equation by introducing a fictitious time and, through correspondence with the diffusion equation, finding a solution by simulating a stochastic process. Ettelaie has used a random walk method to solve the linearized PB equation[508] and Hwang and Mascagni have suggested an improved version of the method.[509] In a similar vein, Zaloj and Agmon have applied a Brownian dynamics algorithm to obtain a solution[510] and Alvarez-Ramirez, Martinez and Diaz-Herrera, viewing the problem as one of reaction–diffusion, have extended this type of treatment to the nonlinear PB equation.[511]

Large-Scale Applications

In the second section of this chapter, a survey of representative calculations pertinent to the particular one-dimensional system (planar, cylindrical, or spherical) was presented. We now do the same for several topics of research in which the systems studied are too complex to categorize as one-dimensional, thus requiring that the calculations be performed using one of the general-purpose algorithms discussed above. Historically, initial applications were aimed at accurately determining the electrostatic potential map around a macromolecule and, in conjunction with this, the ion distributions. Following this, free-energy calculations, which rely on the potential in a more complicated way than ion concentrations, were performed. Presently, free energies are, in turn, used to obtain binding energies and solvation energies of large macromolecules and to determine the pK_a values of ionizable sites on proteins. Also, Poisson–Boltzmann calculations are being coupled with other techniques such as Brownian dynamics, Monte Carlo and molecular dynamics simulations, or quantum mechanics in an effort to reach beyond "simple" equilibrium electrostatics of biomolecules.

Binding Energy

In addition to standard applications involving the calculation of electrostatic potentials and ion distributions around a single macromolecule, the finite-difference/finite-element (FDFE) approach to solving the PB equation can be used to determine the free energy of a single macromolecule or, more importantly, the binding free energy of two molecules by subtracting out the individual energies from the total. Traditionally, the free energy of a macromolecule was determined through a charging mechanism such as that implied by Eq. [29], but this method is too computationally time-consuming for FDFE approaches. Overbeek derived an expression for the total free energy that avoids the charging process, thus making it more suitable for computations.[86,494,512] Considering separately the energetic, entropic and chemical terms, he showed that (in our notation) the total Helmholtz free energy can be written as

$$\beta A_{\text{tot}} = -\frac{1}{4\pi L_B}\int_V \left(\frac{\eta(\underline{r})}{2}(\nabla\phi)^2 + \int_0^{\phi}(\nabla^2\phi^*)d\phi^*\right)d\tau \qquad [392]$$

where the outer integral is over the system volume and $\eta(\underline{r}) = \varepsilon(\underline{r})/\varepsilon_0$ is the ratio of the local dielectric coefficient to the reference value used in defining L_B (and κ_D). The first term of the volume integrand in Eq. [392] represents the energy density of the electric field (the Maxwell stress tensor[77]), while the second term gives the osmotic contribution to the free energy.[78] As noted previously, for systems in which the charged surfaces are held at constant charge density, the chemical component of the free energy is omitted. Removing this contribution from Eq. [392], we can express the electrostatic component of the free energy as

$$\begin{aligned}\beta A_{\text{el}} &= \frac{1}{4\pi L_B}\int_V \left(\frac{\eta(\underline{r})}{2}(\nabla\phi)^2 + \phi\,(\nabla\eta(\underline{r})\nabla\phi) - \int_0^{\phi}(\nabla\eta(\underline{r})\nabla\phi^*)d\phi^*\right)d\tau \\ &= \frac{1}{4\pi L_B}\int_V \left(\frac{1}{2}\phi\,(\nabla\eta(\underline{r})\nabla\phi) - \int_0^{\phi}(\nabla\eta(\underline{r})\nabla\phi^*)d\phi^*\right)d\tau \\ &\quad + \frac{1}{8\pi L_B}\int_S \eta(\underline{r})\phi\,\nabla\phi\,dS \end{aligned} \qquad [393]$$

where the surface integral is over the system boundaries. For a bulk $z:z$ electrolyte with fixed charges, we obtain

$$z\nabla\eta(\underline{r})\nabla\phi = \kappa_D^2\sinh(z\phi) \qquad [394]$$

so the second of Eqs. [393] becomes

$$\beta A_{\text{el}} = \frac{1}{4\pi L_B}\int_V \left[\frac{2\pi L_B}{e_0}\rho^{\text{fixed}}\phi(\underline{r}) + \frac{\kappa_D^2}{2z^2}[z\phi(\underline{r})\sinh(z\phi(\underline{r})) + 2 - 2\cosh(z\phi(\underline{r}))]\right]d\tau + \frac{1}{8\pi L_B}\int_S \eta(\underline{r})\phi\,\nabla\phi\,dS \qquad [395]$$

where the integrals can be evaluated numerically by obtaining the potential at each gridpoint and summing the integrands.[86] Note that the variable dielectric coefficient appears explicitly only in the surface integral. Also, for an isolated macromolecule in the absence of boundaries or external fields, the surface integral vanishes, while for a system with no fixed (source) charges, the first term in the volume integral vanishes. Within linear DH theory without source charges or dielectric variation, only the surface integrand is nonzero, leading to $\beta A_{\text{el}} = \sigma_a\phi_a/2$ for a planar surface and in agreement with Eq. [29]. To check Eq. [395] for PB theory, we apply it to a planar surface represented as a source charge (in place of boundary conditions) by using the Gouy–Chapman solution of Eq. [22] to make the substitutions

$$\begin{aligned}\int d\tau &\rightarrow \text{Area}\int_a^\infty dx \\ \rho^{\text{fixed}} &= \sigma_a\delta(x-a) = \frac{\kappa_D e_0}{2\pi L_B z}\sinh\left(\frac{z\phi_a}{2}\right)\delta(x-a) \qquad [396] \\ \sinh\frac{z\phi(x)}{2}dx &= \frac{-z}{2\kappa_D}\phi'(x)dx = \frac{-z}{2\kappa_D}d\phi\end{aligned}$$

Using two hyperbolic identities, Eq. [395] is readily integrated to yield the free energy per unit area

$$\frac{\beta A_{\text{el}}}{\text{Area}} = \left(\frac{\kappa_D}{\pi L_B z^2}\right)\left(\frac{z}{2}\phi_a\sinh\frac{z\phi_a}{2} + 1 - \cosh\frac{z\phi_a}{2}\right) \qquad [397]$$

a result identical to Eq. [30]. We may also represent the surface as a boundary condition rather than as a source charge:

$$\frac{1}{8\pi L_B}\int_S \phi\,\nabla\phi dS = -\frac{1}{2e_0}\int_a^\infty \phi\,\sigma dS = \frac{\phi_a\sigma_a}{2e_0} = \frac{\kappa_D}{4\pi L_B z}\phi_a\sinh\frac{z\phi_a}{2} \qquad [398]$$

which leads to the same result, as it must. Equation [393] is easily evaluated for other electrolytes but for most purposes, particularly if an effective valence is used for z, Eq. [397] will suffice.

The free energy expression of Eq. [393] can also be justified (although not strictly derived) using the upper bound variational integral of Eq. [212].

For a $z:z$ electrolyte ($c_2 = 0$) in the absence of a surface charge density condition but in the presence of fixed charges and treating the potential as variable, we have

$$J[\phi] = \int \left[\frac{z^2}{2}(\phi')^2 + \cosh(z\phi) - 1 - z\rho^{\text{fixed}}\phi\right] d\tau \qquad [399]$$

where the integration is over the system volume. $J[\phi]$ is now considered a functional of the electrostatic potential, which is found subject to the integral being an extremum; the resulting potential is easily shown to satisfy the appropriate Poisson–Boltzmann equation.[195] Because the system free energy is also an extremum (actually the free energy is a minimum, while $J[\phi]$ yields a maximum [195,513]), Sharp and Honig identified a Poisson–Boltzmann free energy by incorporating additive and multiplicative constants into Eq. [399].[494,514]

The electrostatic free energy of binding for two macromolecules A and B can be found simply by using Eq. [393] for the separated and bound systems:[30,35]

$$\Delta G_{\text{el}} = G_{\text{el}}(A + B) - G_{\text{el}}(A) - G_{\text{el}}(B) \qquad [400]$$

where we have switched to the common practice of referring to Gibbs free energies. This method is illustrated at the bottom of Figure 50. A more accurate approach can be used if the dielectric coefficients throughout the solvent

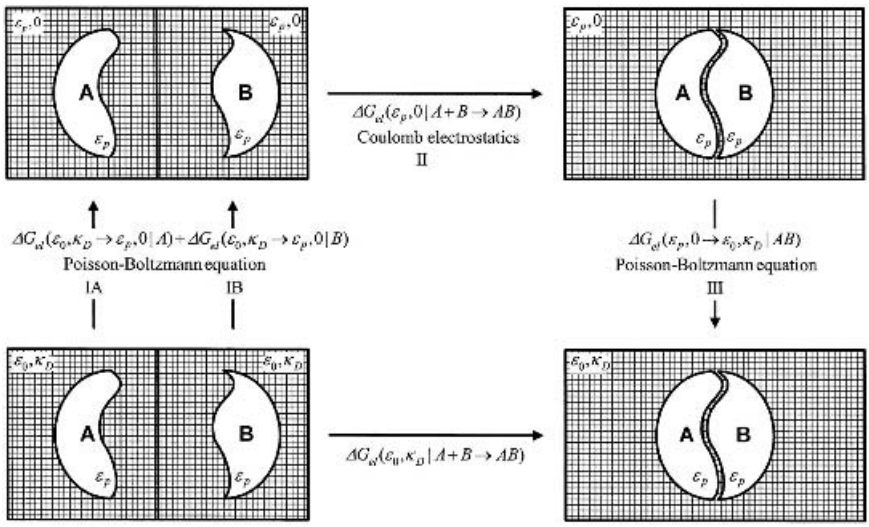

Figure 50 Diagram illustrating the thermodynamic cycle for the determination of the binding energy of two macromolecules using the numerical solution to the Poisson–Boltzmann equation.

(ε_0) and within each macromolecule (ε_M) can be treated as uniform (but different). In this case we resort to a thermodynamic cycle indicated by steps I, II, and III in the figure. In step I the PB approach is used to separately calculate the free energies for molecules A and B going from a solvent with dielectric constant ε_0 and Debye constant κ_D to a solvent with dielectric constant ε_M and no electrolyte ions. In step II, since dielectric and ionic boundaries have been removed, one can evaluate the interaction energy between A and B in a uniform dielectric constant ε_M as a straightforward sum of Coulombic terms. In step III, the AB complex is now solvated with water and ions in a single PB calculation analogous to the reverse of step I. The choice for ε_M is crucial as the free energy for steps I and III are particularly sensitive to this. The thermodynamic cycle has the advantage that PB-induced errors such as discretization tend to cancel when the free energies from steps I and III are combined. However, as with all PB-based calculations, the solvent is treated as a continuum so the effect of individual solvent molecules, whether due to reorganization at or expulsion from the A–B interface, is neglected. This may be particularly important for interactions involving highly charged macromolecules such as nucleic acids or micelles whose strong electric fields polarize water in their first solvation shell.

A sampling of the diverse investigations based on calculating the PB free energy are the arabinose and sulfate binding proteins,[515] subtilisin–chymotrypsin inhibitor and chymotrypsin–ovomucoid docking,[516] DAPI-DNA and λcI repressor–DNA complexes,[517–520] the B–Z transition of DNA,[521] drug-induced DNA unwinding,[522] conformational analysis of DNA fragments,[523,524] electron transfer reorganization in proteins,[525] heat capacity of DNA–ligand complexes,[526] binding of HIV-1 reverse transcriptase inhibitors,[527] Mg^{2+}–nucleic acid binding,[528,529] hydration of neuraminidase inhibitors,[530] and cyclic urea–HIV protease binding.[531] A general review of binding has been presented by Gilson et al.[33]

Solvation Energy

The calculation of macromolecular solvation energy can be traced back to a simple expression by Born for the electrostatic contribution from a single charge. In the absence of electrolyte, the surface potential of a charge of radius a and valence Q_a in water is $\phi_a = L_B Q_a/a$. From standard electrostatics, or from Eq. [29], the energy of the ion is then $\beta W_{\text{water}} = L_B Q_a^2/2a$, and its energy in water with respect to its energy in vacuum is therefore $\beta\Delta G_{\text{el}} = \beta W_{\text{water}} - \beta W_{\text{vacuum}}$. This gives Born's formula for the solvation energy of an ion:[532]

$$\beta\Delta G_{\text{Born}} = \frac{-L_1 Q_a^2}{2a}\left(1 - \frac{1}{\varepsilon_0}\right), \quad L_1 \equiv \beta e_0^2 \qquad [401]$$

This result has been extended to a variable dielectric coefficient by Bucher[533,534] and Ehrenson.[535] In the presence of a point-ion electrolyte, the Debye–

Hückel solution [307] gives the surface potential $\phi_{DH}(a) = L_B Q_a/(1 + \kappa_D a)a$, leading to the solvation energy

$$\beta\Delta G_{DH} = \frac{-L_1 Q_a^2}{2a}\left(1 - \frac{1}{\varepsilon_0(1 + \kappa_D a)}\right) \qquad [402]$$

This result is readily extended to electrolyte ions of finite radius b by solving Laplace's equation in the region between a and $a + b$ (which contains no ions) subject to Eq. [402] holding at $a + b$.[25,380] If we also use either the NLDH or PGC-ADH approximation (Eq. [312] or [318], respectively), we obtain an expression that also partially corrects for nonlinear (i.e., PB) effects:

$$\beta\Delta G_{\text{Kirkwood}-\text{ADH}} = \frac{-L_1 Q_a^2}{2a}\left[1 - \frac{Q_a}{\varepsilon_0 Q_{\text{ADH}}}\frac{1 + \kappa_D b}{1 + \kappa_D(a + b)}\right] \qquad [403]$$

Alternatively, one may use the full NLDH or PGC free-energy expression (Eq. [194] or [151]) when the DH or ADH approximation is not appropriate.

The expressions above give the solvation energy of a single ion. To apply them to a collection of charges, we could sum over all the individual (Born) and pairwise contributions to the free energy, but we would be restricted to charges that are far enough apart to be treated as individually solvated. This poses a problem for macromolecules in which the charge distribution is not confined to individual spherical centers. We must then resort to use of a general Poisson–Boltzmann program to calculate the difference in free energies between the solvated and gas phases of the macroion based on Eq. [393]. An alternative to the PB procedure would be a generalized Born (GB) model in which empirically determined "effective Born radii" are used within the simple analytical descriptions given above to provide a computationally fast yet reasonably reliable means for estimating the hydration energy of ions and molecules.[536–540] One could also use a combination of PB and GB methods.[541]

In addition to the electrostatic contribution to the free energy, there are also components from van der Waals and hydrogen bonding interactions with the solvent as well as the energy necessary to create the solvent cavity occupied by the macromolecule. These free-energy terms are often estimated on the basis of molecular surface area:[536,542]

$$\Delta G_{\text{vdW}+\text{cavity}} = \sum_{\text{atoms}} \sigma_i SA_i \qquad [404]$$

where SA_i is the surface area exposed to the solvent and σ_i is an empirical "atomic solvation parameter" (typically 5–7 cal mol^{-1} Å^{-2}) for the ith atom.[543]

pK_a Calculations

The one-dimensional analytical results derived in earlier sections assumed a constant and known surface charge density. While this condition often holds for strongly charged surfaces like membranes and cylindrical representations of double-stranded DNA, this is not the case for many systems such as weakly charged proteins, and proteins are the most common systems investigated with PB techniques. Many amino acid side chains possess atoms or groups whose charge depends strongly on the local electrostatic potential. These atoms or groups change their charge by donating or accepting electrons or protons with a solvent molecule (water). Alteration of the local charge on the surface of a protein can be a critical component in the recognition energetics between the protein and a ligand, another protein, or a segment of DNA,[544,545] both in the pairing of salt bridges as well as in inducing required conformational changes. Single strands of nucleic acids also have bases in which an atom (typically a nitrogen) can act as a proton acceptor and thus change the charge of the strand. This process allows a single strand to form hydrogen bonds with one side of a double-stranded segment in a mechanism known as *Hoogsteen pairing*.[546] It is thus important to be able to predict the specific charges of ionizable groups of biomolecules as a function of molecular conformation and environmental conditions. An excellent review[34] of the calculation of biomolecular pK_a changes and other pH-dependent properties has recently (as of 2003) been published, so only the salient features of pK_a calculations are presented here.

If macromolecules were to possess only a single titratable site, protonation would be akin to "simple" ligand binding, and the free-energy change on protonation could be calculated from Eq. [400]. However, the presence of multiple, often hundreds, of simultaneously protonating and deprotonating sites changes the nature of the problem. The classic work in this field is that of Tanford and Kirkwood[25,26] in which a protein is modeled as a dielectric sphere with embedded titratable sites.[380] Since analytical restrictions do not allow generalization of this method to arbitrary shapes, Bashford, Karplus and others have developed a computational procedure based on the numerical solution to the Poisson–Boltzmann equation that is applicable to all-atom models of macromolecules.[27–29,34,547–550] Their method is diagrammed in Figure 51 as a thermodynamic cycle where the desired free-energy step for deprotonation of a particular site in a protein, which is proportional to the pK_a value of that site (in the protein), is at the bottom. (The reverse step gives the free energy for protonation.) A titratable site consists of those charges that change values when *one* of the charges undergoes protonation, which may be a single charge or a group of charges depending on the chemistry involved or the approximation used. Identification of titratable sites assumes that all charges within a site may be uniquely defined as belonging to that particular site, that is, the value of the charge changes only when its site is protonated. To calculate the pK_a for a site, a "model compound" is identified in

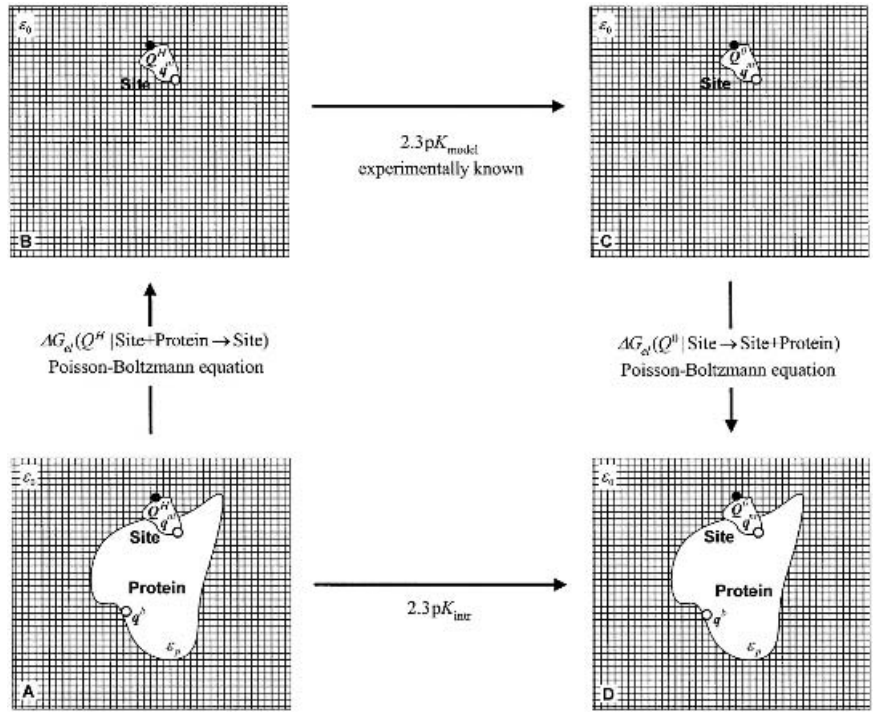

Figure 51 Diagram illustrating the thermodynamic cycle for the determination of the pK_a of protonation sites on a macromolecule using the numerical solution to the Poisson–Boltzmann equation.

which this site Q as well as other non-titratable charges q^{nt} appear and for which the pK_a *in solution* is known:

$$2.3\,\mathrm{p}K_{\mathrm{model}} = \beta\,\Delta\,G_{\mathrm{el}}(Q^H \rightarrow Q^0 \mid \mathrm{site}) \qquad [405]$$

where Q^H and Q^0 denote the titratable charge (or charges) of the site when protonated and unprotonated, respectively, and we have ignored the free energy of the proton disappearing into the solvent bath. Were one to choose the gas-phase pK_a for the model compound, the free energy of transferring a proton from the gas phase into solution would also have to be taken into account; note as well that no particular distinction need be made between acidic or basic sites. Other background protein charges not part of the site under consideration are designated q^b. We now assume that the local electrostatic potential is small and that we can apply Debye–Hückel theory. (At this point, due to the intimate relationship the following expressions have with programming code, the reader is offered a warning: *Proceed with caution—notation ahead.*)

Referring to Figure 51, the electrostatic free energy for state **A** is found by starting with all *titrating* charges Q set to zero and charging them to their protonated values Q^H in the presence of other nontitratable charges q^{nt} and q^b:

$$\begin{aligned}\beta G_{\text{el}}^{A}(Q^H \mid \text{site} + \text{protein}) = \frac{1}{2}\sum_{i}^{\text{titrating}} Q_i^H \phi_p(Q^H \mid r_i) \\ + \sum_{j}^{\text{nontitrating}} q_j^{nt}[\phi_p(Q^H \mid r_j) - \phi_p(0 \mid r_j)] \\ + \sum_{k}^{\text{background}} q_k^{b}[\phi_p(Q^H \mid r_k) - \phi_p(0 \mid r_k)] \qquad [406]\end{aligned}$$

The notation $\phi_p(Q^H \mid r_i)$ indicates the value of the potential in the protein (vs. that in the model compound) at position r_i when the set of titrating charges are held at their value Q^H; this can be calculated using a standard PB program. The first term in Eq. [406] follows from the integral expression for the self-energy of a charge distribution[63] represented by delta functions, the second and third terms give the change in energy of a set of charges ($q^{nt} + q^b$, which are sometimes grouped together) when an external set ($Q^0 \rightarrow Q^H$) is charged, and assumption of the validity of the linear PB equation implies additivity of all energy terms. It will not be necessary to explicitly determine the uncharged potential values $\phi(0 \mid r_i)$ since these terms will be seen to cancel. Similarly, the free energies of the other three states in Figure 51 are

$$\begin{aligned}\beta G_{\text{el}}^{C}(Q^H \mid \text{site}) = \frac{1}{2}\sum_{i}^{\text{titrating}} Q_i^H \phi_m(Q^H \mid r_i) \\ + \sum_{j}^{\text{nontitrating}} q_j^{nt}[\phi_m(Q^H \mid r_j) - \phi_m(0 \mid r_j)] \\ \beta G_{\text{el}}^{B}(Q^0 \mid \text{site}) = \frac{1}{2}\sum_{i}^{\text{titrating}} Q_i^0 \phi_m(Q^0 \mid r_i) \\ + \sum_{j}^{\text{nontitrating}} q_j^{nt}[\phi_m(Q^0 \mid r_j) - \phi_m(0 \mid r_j)] \qquad [407] \\ \beta G_{\text{el}}^{D}(Q^0 \mid \text{site} + \text{protein}) = \frac{1}{2}\sum_{i}^{\text{titrating}} Q_i^0 \phi_p(Q^0 \mid r_i) \\ + \sum_{j}^{\text{nontitrating}} q_j^{nt}[\phi_p(Q^0 \mid r_j) - \phi_p(0 \mid r_j)] \\ + \sum_{k}^{\text{background}} q_k^{b}[\phi_p(Q^0 \mid r_k) - \phi_p(0 \mid r_k)]\end{aligned}$$

The thermodynamic cycle of Figure 51 gives

$$\begin{aligned} 2.3\,\mathrm{p}K_{\mathrm{intr}} = {} & 2.3\,\mathrm{p}K_{\mathrm{model}} + \beta\,\Delta\,G_{\mathrm{el}}(Q^H \mid \mathrm{site} + \mathrm{protein} \rightarrow \mathrm{site}) \\ & + \beta\,\Delta\,G_{\mathrm{el}}(Q^0 \mid \mathrm{site} \rightarrow \mathrm{site} + \mathrm{protein}) \end{aligned} \quad [408]$$

where

$$\begin{aligned} \Delta\,G_{\mathrm{el}}(Q^H \mid \mathrm{site} + \mathrm{protein} \rightarrow \mathrm{site}) &= G^B_{\mathrm{el}}(Q^H \mid \mathrm{site}) - G^A_{\mathrm{el}}(Q^H \mid \mathrm{site} + \mathrm{protein}) \\ \Delta\,G_{\mathrm{el}}(Q^0 \mid \mathrm{site} \rightarrow \mathrm{site} + \mathrm{Protein}) &= G^D_{\mathrm{el}}(Q^0 \mid \mathrm{site} + \mathrm{protein}) - G^C_{\mathrm{el}}(Q^0 \mid \mathrm{site}) \end{aligned} \quad [409]$$

Inserting Eqs. [406] and [407] into Eq. [409] and thence into Eq. [408] and regrouping gives the intrinsic (see below) pK_a for the titratable protein site under consideration:

$$\begin{aligned} 2.3\,\mathrm{p}K_{\mathrm{intr}} &\equiv -\beta\Delta\,G_{\mathrm{intr}} \\ &= 2.3\,\mathrm{p}K_{\mathrm{model}} - \beta(\Delta\,\Delta\,G_{\mathrm{Born}} + \Delta\,\Delta\,G_{\mathrm{back}}) \end{aligned} \quad [410]$$

where we have identified the free-energy change contributions

$$\begin{aligned} \beta\,\Delta\,\Delta\,G_{\mathrm{Born}} = {} & \frac{1}{2}\sum_i^{\text{titrating}} Q_i^H[\phi_p(Q^H \mid r_i) - \phi_m(Q^H \mid r_i)] \\ & - \frac{1}{2}\sum_i^{\text{titrating}} Q_i^0[\phi_p(Q^0 \mid r_i) - \phi_m(Q^0 \mid r_i)] \end{aligned} \quad [411]$$

and

$$\begin{aligned} \beta\,\Delta\,\Delta\,G_{\mathrm{back}} = {} & \sum_j^{\text{nontitrating}} q_j^{nt}[\phi_p(Q^H \mid r_j) - \phi_p(Q^0 \mid r_j)] \\ & - \sum_j^{\text{nontitrating}} q_j^{nt}[\phi_m(Q^H \mid r_j) - \phi_m(Q^0 \mid r_j)] \\ & - \sum_k^{\text{background}} q_k^{b}[\phi_p(Q^H \mid r_k) - \phi_p(Q^0 \mid r_k)] \end{aligned} \quad [412]$$

Equation [411] represents the free energy or pK_a change due to (partially) solvating the model compound in the protein, while Eq. [412] represents the change effected by nontitrating and background charges on protonation of the site. Each summation in Eqs. [411] and [412] is evaluated using the two

potential maps, protonated and unprotonated, calculated with the same grid and placement of model compound charges to minimize errors.

Equation [410] gives the equilibrium constant for the reaction

$$\text{siteH} \overset{K_{\text{intr}}}{\rightleftharpoons} \text{site} + \text{H}, \quad K_{\text{intr}} = \frac{[\text{site}][\text{H}]}{[\text{siteH}]} \tag{413}$$

The probability of the site being protonated is

$$\langle x \rangle = \frac{[\text{siteH}]}{[\text{site}] + [\text{siteH}]} = \frac{e^{2.3(\text{p}K_{\text{intr}} - \text{pH})}}{1 + e^{2.3(\text{p}K_{\text{intr}} - \text{pH})}} \tag{414}$$

where Eq. [413] has been used, and the average site charge is

$$\langle Q \rangle = Q^0 + \langle x \rangle \tag{415}$$

Equation [414] solved for $\text{p}K_{\text{intr}}$ (actually $\text{p}K_a$ for a single site) gives the standard Henderson–Hasselbach titration curve.[34,551]

In the discussion above we considered only a single titratable site. To extend the procedure to multiple sites first requires that the $\text{p}K_a$ be calculated for each site according to Eqs. [410]–[412]. The $\text{p}K_a$ of a site determined while all other sites are *unprotonated* is called the *intrinsic* $\text{p}K_a$ of the site.[25] We now define a protonation vector $\underline{x} = \{x_1, x_2, \ldots, x_N\}$ for N sites where each x_μ is either 1 or 0 depending on whether the site is protonated; $\underline{x}$ thus spans a space of $2N$ vectors and $\underline{x}^n$ denotes one of them. The charge on site μ corresponding to state n is then

$$Q_\mu^n = Q_\mu^0 + x_\mu^n \tag{416}$$

which, for sites in which protonation changes the value of multiple charges, can be linearly apportioned among the site atoms:

$$Q_{\mu,i}^n = Q_{\mu,i}^0 + x_\mu^n (Q_{\mu,i}^H - Q_{\mu,i}^0) \tag{417}$$

The average protonation state for site μ is found by performing a thermodynamic average over all $2N$ possible vectors

$$\langle x_\mu \rangle = \frac{\sum_{n=1}^{2N} x_\mu^n \exp\left[2.3\left(\sum_\nu^{\text{sites}} x_\nu^n \text{p}K_{\text{intr},\nu} - \text{pH}\right)\right]}{\sum_{n=1}^{2N} \exp\left[2.3\left(\sum_\nu^{\text{sites}} x_\nu^n \text{p}K_{\text{intr},\nu} - \text{pH}\right)\right]} \tag{418}$$

which represents the generalization of Eq. [414], and the average charge of site μ is then

$$\langle Q_\mu \rangle = Q_\mu^0 + \langle x_\mu \rangle \qquad [419]$$

To go beyond the Tanford–Kirkwood model, we must take into account the interaction of one site with other sites *as they are mutually protonated*. One straightforward, although computationally tedious, method is to insert the average charges obtained from Eq. [419], or its extension to Eq. [417], back into the Poisson–Boltzmann equation and iterate the process until self-consistency. This mean-field approach results in a set of partial charges for the protonation vector, incorrectly implying that each site is partially protonated. An improvement would be to use the pK_{intr} values from the first iteration to fix the charges of certain sites at their protonated or unprotonated values if $\langle x_\mu \rangle$ for these sites is, say, greater than 0.95 or less than 0.05, respectively, as in the reduced site model[27] (see below).

An alternative and popular mean-field approach was proposed by Tanford and Roxby.[552] They first considered the interaction energy between two protonated sites μ and ν as the difference in free energy between protonating site μ while site ν is protonated and protonating site μ while site ν is unprotonated

$$\begin{aligned} W_{\mu\nu} &= \sum_i^{\text{titrating}} (Q_{\mu,i}^H - Q_{\mu,i}^0)\phi_{p,\nu}(Q^H \mid r_i) - \sum_i^{\text{titrating}} (Q_{\mu,i}^H - Q_{\mu,i}^0)\phi_{p,\nu}(Q^0 \mid r_i) \\ &= \sum_i^{\text{titrating}} (Q_{\mu,i}^H - Q_{\mu,i}^0)[\phi_{p,\nu}(Q^H \mid r_i) - \phi_{p,\nu}(Q^0 \mid r_i)] \end{aligned} \qquad [420]$$

where $W_{\mu\mu}$ is defined to be zero. With this interaction energy included, the average protonation state of site μ becomes

$$\langle x_\mu \rangle = \frac{\sum_{n=1}^{2N} x_\mu^n \exp\left[2.3\left(\sum_\nu^{\text{sites}} x_\nu^n \, pK_{\text{intr},\nu} - \text{pH}\right) - \frac{1}{2}\sum_{\nu,\lambda}^{\text{sites}} Q_\nu^n \, W_{\nu\lambda} Q_\lambda^n\right]}{\sum_{n=1}^{2N} \exp\left[2.3\left(\sum_\nu^{\text{sites}} x_\nu^n \, pK_{\text{intr},\nu} - \text{pH}\right) - \frac{1}{2}\sum_{\nu,\lambda}^{\text{sites}} Q_\nu^n \, W_{\nu\lambda} Q_\lambda^n\right]} \qquad [421]$$

where the far-right summation in each exponential term is the free-energy contribution due to the interaction among protonated sites. Titration of the entire molecule is described by a summation of $\langle x_\mu \rangle$ over all sites. For a small number of titratable sites, all protonation states can be explicitly, although perhaps tediously, enumerated and all interaction energies determined.[27,553] For

regularly repeating structures like triple-stranded DNA, periodic approximations may be used.[554] For most cases, however, an approximation to the sum over states is necessary. Tanford and Roxby assumed that the shift in the pK_a of a particular site from its intrinsic value is approximately equal to the sum of all interaction energies with other sites, assuming that those sites have a charge based on their average protonation state [419]:[552]

$$2.3\,\mathrm{p}K_\mu = 2.3\,\mathrm{p}K_{\mathrm{intr},\mu} - \beta \sum_{\nu}^{\text{sites}} \langle Q_\mu \rangle W_{\mu\nu} \langle Q_\nu \rangle \qquad [422]$$

This strategy decouples interacting sites and the sum over protonation states is avoided with the result that Eq. [421] is replaced by Eq. [414]:

$$\langle x_\mu \rangle = \frac{e^{2.3(\mathrm{p}K_\mu - \mathrm{pH})}}{1 + e^{2.3(\mathrm{p}K_\mu - \mathrm{pH})}} \qquad [423]$$

Equations [422] and [423] are then solved to self-consistency. The Tanford–Roxby approach works well provided that sites with similar pK_a values do not interact strongly.[28] We emphasize that the preceding expressions are valid only within linear PB theory. The extension to the nonlinear case means that the free energy expressions of Eqs. [406], [407], and [420], obtained by charging the site of interest, must be found instead from a nonlinear formula such as Eq. [393]. As mentioned elsewhere in this chapter, it is also important to assign a ''reasonable'' value to the internal protein dielectric coefficient. Unfortunately the particular value depends in part on what system property is being calculated.[462] Although a value of $\varepsilon_p \sim 2$–4 is physically reasonable on the basis of the high-frequency coefficient for organic compounds, values in the 10–20 range often work better (but see Warwicker[459]). It appears that a higher dielectric coefficient accounts in part for some assumptions implicit in the usual PB approach, such as rigidity of protein side chains, single-site charge assignments,[456,457] and simplified solvent dielectric modeling.[34,555,556]

An intermediate approach that lies between the Tanford–Roxby mean-field approximation, and explicit enumeration of all protonation states was introduced by Bashford and Karplus[27] and is called the ''reduced-site approximation.'' After an initial iteration, this method selects sites that are likely to remain fully protonated or unprotonated at the pH of interest and fixes them as such, as described above. This generally removes a large number of protonation states from consideration, reducing the total to a manageable number that can then be treated explicitly. Alternative and similar approaches are those of Gilson,[31] Yang et al.,[32] and Karshikoff,[557] who partition site–site interactions into exact and mean-field categories based on distance or energy. An

alternative technique is to use a Monte Carlo algorithm to energetically sample different protonation states.[34,558–560]

The importance of accurately determining pK_a values of titratable sites of proteins is supported by the large number of studies pertaining to their calculation. In addition to method development[31,32,439,456–458,548,561–567] and review articles,[34,549,550] some of the systems most recently studied are noted here: α-chymotrypsin,[558] bacteriorhodopsin,[29,566] myoglobin,[31,566,568–570] ribonuclease T_1,[571] ribonuclease A,[458,561] protein G,[572] BPTI,[561,563] lysozyme,[31,439,559,561–563,566] calbindin,[563,566] third-domain ovomucoid,[563,565] calcium binding protein,[564] β-lactamase,[573] papain and caricain,[574] and β-lactoglobulin.[575] The next important step after the reliable determination of pK_a is to apply the method to macromolecule stability and conformational change and some work in this area has begun.[34,547,576–579]

Mixed-Method Procedures

The electrostatic free energy, while important, is only one component in the total free energy of a system. As two molecules approach one another, the long-range electrostatic interaction energy increases, causing forces that induce shifts in the positions of individual atoms relative to those at infinite separation. This situtation cannot be handled by electrostatics alone since covalent bonding potentials now come into play. The computational treatment of covalent interactions actually has a longer history than the relatively recent development of Poisson–Boltzmann techniques. Monte Carlo and molecular dynamics (MD) methods for treating molecular systems classically, that is, according to Newtonian mechanics, in a sense began with the introduction of the Metropolis Monte Carlo algorithm (discussed in greater detail below)[580] in the early 1950s and has continued with the development of the molecular force field.[581] Biophysical investigations using molecular dynamics simulations have proliferated even more than those in which PB calculations are performed. However, these explicit ball-and-stick methods all have one serious limitation: an operationally efficient treatment of the solvent. Treating the solvent on the same footing as the biomolecule makes it difficult to handle large systems effectively because most of the computational power is then spent handling the dynamics of the solvent rather than the biomolecule. Explicit solvent also makes it difficult to obtain good free-energy estimates, although much work is presently being done in this area. The way around this problem is essentially to invoke McMillan–Mayer theory and average over the solvent degrees of freedom.[60,582] That is, treat the solvent, and its ions, as a dielectric continuum with the Poisson–Boltzmann equation solved according to boundary conditions set up by the biomolecule, which, in turn, obeys classical Newtonian mechanics in response to the PB-determined electrostatic field. (Strictly speaking, hydrophobic forces are not exactly the purview of PB theory and one is certainly not limited to classical mechanics.)

The simplest marriage between PB theory and the classical force-field approach is illustrated by the works of Caflisch and Karplus, in which structures from several MD trajectories of barnase were used in PB calculations to determine the electrostatic interaction energy between various groups,[583] and that of Archontis, Simonson and Karplus, who compared the binding of aspartate and asparagine to aspartyl-tRNA synthetase.[584] Other studies are those of Cheatham et al., on the stability of DNA duplexes;[585] Srinivasan et al., on the stability of RNA hairpins;[586] Reyes and Kollman,[587] on RNA–protein binding; Cubero et al.,[588] on triple-stranded DNA formation; and Tsui and Case,[589] on trivalent cobalt binding to RNA.

A more entwined relationship is to couple the PB electrostatic potential to a molecular dynamics simulation by periodically updating the potential during the course of a trajectory. In a relatively early work, Sharp used this approach to investigate solvent-induced conformational changes of alanine dipeptide, the prototypical "protein" often studied during method development.[590] Later articles are those by Niedermeier and Schulten,[591] on BPTI, Gilson et al.,[592] on dichloroethane and alanine dipeptide; and Grychuk,[593] on lysozyme and ovomucoid third domain. In 1995, Tironi et al. proposed a novel method, somewhat akin to the original Tanford–Kirkwood model, in which the Debye–Hückel equation is solved analytically within a sphere encompassing a system of point charges (representing a protein) and used to provide the reaction field component to a standard molecular dynamics force field.[594] Similar to these combined MD-PB studies are the Monte Carlo–based docking schemes in which PB-calculated electrostatic energies are fed into a Metropolis Monte Carlo algorithm that samples the internal molecular degrees of freedom. Zacharias et al. used this procedure to evaluate how λ repressor binds to DNA,[595] and Caflisch, Fischer and Karplus studied the interaction of a tetrapeptide with FK506 binding protein.[596] PB theory may also be coupled to MD simulations by using the results of pK_a calculations to determine when protonation of charged sites occurs during folding, as would occur, for example, during the formation of triple helical nucleic acid structures.[553]

Progress has also been made in the area of incorporating PB potential calculations into quantum-mechanical structure calculations. This work is similar to the way in which (other) polarized continuum models have been included but with the advantage of including irregular dielectric boundaries and ionic strength effects. Chen et al. have used a PB-DFT (density function theory) approach,[597] and Wilson, Schaldach and Bourcier have proposed a Green function/MP2 procedure[598] to study the effect of solvation on the internal geometries of several small molecules. Gogonea and Merz have developed a combined semiempirical-PB linear scaling algorithm to calculate the solvation free energies and charge transfer of a wide range of molecules,[599–602] and Park and Goddard have used HF plus PB calculations to investigate the conformational surface of short polypeptides.[603,604]

Finally, we mention efforts to extend the usefulness of the Poisson–Boltzmann equation into the time domain. This is at its most natural in coupling the PB-determined electrostatic potential to a Brownian dynamics algorithm whereby one molecule, immersed in a dielectric continuum, diffuses in the electrostatic field of a second. Diffusion is simulated by numerically propagating the molecule according to the Smoluchowski equation, typically using the Ermak–McCammon algorithm,[605] and using the PB equation to update the electrostatic potential map due to the relative motion of the two molecules.[606] The technique is typically used to calculate time-dependent rate coefficients for diffusion-controlled bimolecular association and reaction,[607–609] such as the binding of superoxide to superoxide dismutase[606] and the barnase–barstar[610] and Fab-antigen complexes.[611] The review by Gabdouline and Wade is particularly recommended.[612]

BEYOND THE POISSON–BOLTZMANN EQUATION

In this section we present in more detail the key assumptions behind the use of the Poisson–Boltzmann equation and discuss some of the ways in which these assumptions have been relaxed. We also give brief introductions to several of the popular alternative approaches to standard PB theory.

Assumptions of the Poisson–Boltzmann Equation

The simplicity of the Poisson–Boltzmann approach to electrolyte solutions belies several approximations used in the derivation of Eqs. [3] and [4]. The first of two parts of the derivation begins with Maxwell's equation for the electric displacement $D(\underline{r})$:

$$\underline{\nabla} \cdot \underline{D}(\underline{r}) = -4\pi\rho(\underline{r}) \qquad [424]$$

where $\rho(\underline{r})$ is the local (not mean) charge density. One then performs a spatial averaging over a macroscopically sized volume element of the system centered at $\underline{r}$ to determine the local electric polarization (i.e., the local dipole moment density).[63] It is also assumed that the polarization is linearly related to the local electric field, which is assumed to be small and constant over the volume element.[613] If this volume element contains polar molecules with rotational degrees of freedom, then a further canonical averaging over the temperature-dependent orientation between these molecules and the local electric field is necessary. If the solvent is water, then the averaging needs to include at most three solvation layers around a central water molecule.[478] This procedure results in the macroscopic Maxwell equation [3] but with the adjective "mean" not yet applied to the potential and charge density.

The second part of the derivation requires that a particular ion (i.e., a single fixed or mobile charge) be chosen and its position fixed.[3,59–61] The distribution of ions of type i at position $\underline{r}$ with respect to the chosen ion is

$$c_i(\underline{r}) = c_i^R e^{-\beta[w_i(\underline{r})-w_i(\underline{R})]} \qquad [425]$$

where $w_i(\underline{r})$ is the potential of mean force relative to that at some position $\underline{R}$ (typically either the outer cell boundary or in the bulk). The leading term in the potential of mean force is expected to be the mean electrostatic potential:

$$\beta w_i(\underline{r}) = z_i\phi(\underline{r}) + \gamma_i(\underline{r}) \qquad [426]$$

where all other contributions are contained in $\gamma_i(\underline{R})$ that can be related to an activity coefficient.[60] Neglecting this latter term, which in general is not known exactly, removing the contribution of the chosen ion from the electrostatic potential energy of the system, and canonically averaging over the coordinates of all other mobile ions gives the Poisson–Boltzmann result of Eq. [4]. One inconsistency that results from truncating Eq. [426] after the first term is that the symmetry condition for two ions i and j is no longer obeyed

$$z_i\phi_j(\underline{r}_i) \neq z_j\phi_i(\underline{r}_j) \qquad [427]$$

where the subscript on ϕ indicates which ion has been specifically chosen. While this lack of symmetry is sometimes a cause of concern when dealing with standard electrolyte solutions where one would want to treat all ions on an equivalent basis, a system in which a large central polyelectrolyte is surrounded by many much smaller counter- and coions is already highly asymmetric, so the lack of symmetry among the smaller ions is a minor problem.

We mention that to lowest order and at the same level of approximation, the dielectric coefficient in Eq. [3] does not enter into the canonical averaging if it is determined (in a self-consistent manner) by the local *mean* electric field and thus is already an averaged quantity. We also note that the canonical average over mobile ions occurs over a volume much larger than that used in determining $\varepsilon(\underline{r})$ so the use of a local dielectric coefficient determined by a locally constant electric field retains some validity. Maeda and Oosawa have shown that the mean-field Boltzmann approximation applies in the presence of a variable dielectric coefficient.[614] If one is concerned about performing spatial averages over regions too small to be accurately characterized by a continuum model, one can then adopt the point of view that one is really performing time averages, as suggested by Fowler and others.[615–617]

Debye and Hückel were concerned with treating a system of hard-sphere cations and anions of identical size and opposite charge in an isotropic environment without explicit boundaries. By linearizing the charge density with

respect to the mean potential, an analytical solution for finite ions could be obtained. An additional benefit is that symmetry condition [427] is obeyed by their solution. Today most applications of the PB equation involve mobile ions in the presence of a fixed polyelectrolyte (colloid, protein, micelle, nucleic acid, or membrane) so we are concerned primarily with the accurate description of the electric double layer near a colloid or biomolecule that is large compared to the solvated salt ions. The ionic radial distribution function used in expressing the charge density in terms of the mean potential describes the interaction of (point) mobile ions only with the polyelectrolyte (which necessarily becomes the fixed charge in the standard derivation of the PB equation), not with one another; the former are treated as continuous interpenetrating charge densities. Membranes may be viewed as a spherical macroion in the limits of infinite radius and zero concentration.

Having outlined the derivation of the Poisson–Boltzmann equation, we now turn to a discussion of the main assumptions used, under which circumstances they become invalid, and how these problems might be remedied. A comprehensive treatment of the PB equation in which most of the approximations are addressed in a detailed manner was given by Bell and Levine.[420] In their work they derived a modified PB equation which provided corrections for most of the deficiencies in the original theory. Their results have been further extended by Outhwaite and co-workers in an attempt to place the PB equation on par with other more elaborate theories. We discuss here only the generalities of the basic DH assumptions; for specific details the reader is referred to the Bell–Levine paper[420] and others cited below.

Uniqueness of the Solution

Garrett and Poladian[15] demonstrate the uniqueness of the nonlinear PB equation for the case of a constant dielectric coefficient. The extension for a variable (and positive) dielectric coefficient is readily shown by a suitable modification of Green's theorem based on Eq. [3]. However, care must be taken in the numerical solution of some modified PB theories as nonuniqueness has been observed.[618]

Continuum Solvent

The main tenet of the McMillan–Mayer theory of nonelectrolytes is that if one is interested in the equilibrium properties of a dilute solution of solute molecules in which their mutual interaction is through short-range forces, then specific interactions between the solute and solvent can be "removed" by integrating over the solvent degrees of freedom.[60,582,617,619] In this continuum solvent picture there is a direct correspondence between the thermodynamic equations describing this system and that of an imperfect gas. For example, the pressure of an imperfect gas translates into the osmotic pressure of the solvated system. The theory can be extended to electrolyte solutions provided the long-range interaction between ions falls off faster than the Coulomb

interaction. For finite (nonzero) concentrations of ions, the interaction between two charges falls off exponentially with distance (the Debye–Hückel solution) so McMillan–Mayer theory can be applied. The great success of the Poisson–Boltzmann approach reflects this. Unfortunately, the increasingly popular application of the method to large biomolecular polyelectrolytes also has the inherent side effect of pointing out inadequacies when invoking the McMillan–Mayer approximation. Investigations of highly or multiply charged systems such as nucleic acids, lipid membranes, and proteins in which ions are necessarily clustered near charged surfaces highlight the need for better representations of specific solvent-mediated ion–surface interactions. This is particularly important when distinct polyelectrolyte regions are involved, as in DNA–protein recognition, protein–membrane interactions, or protein folding. One way to treat such systems is to include only part of the solvation shell explicitly in an all-atom representation of the polyelectrolyte.[620] In fact, the treatment of ion solvation based on the Poisson–Boltzmann equation is one of the more promising areas of development and is discussed in more detail below. By incorporating an empirical parameter into classic DH theory that apparently accounts for some of the structural changes in the solvent induced by an ion, Pailthorpe, Mitchel and Ninham reproduced a wide range of activity coefficient data.[621] Kralg-Iglic and co-workers have derived particularly simple expressions for the free energy of planar and cylindrical double layers that incorporates the excluded volume effect due to ion-displaced solvent molecules.[622,623] Burak and Andelman[123,624] have addressed discrete solvent effects by adding a nonlocal hydration–correction term to the standard PB mean-field energy expression.

Small Local Electric Field and Constant Dielectric Coefficient

It was realized early on that solvated ions tend to orient the individual molecules of a polar solvent such as water,[10,56,625,626] leading to a decrease in the dielectric coefficient relative to the bulk value. Poisson's equation can still be applied if an isotropic dielectric coefficient representing an average of spatially varying values is used provided the average local field is not so large such that dielectric saturation occurs.[626] The standard derivation of the dielectric coefficient from Maxwell's laws assumes that the local polarization is linearly related to the electric field.[613] While this condition holds for most systems in which highly charged surfaces and hence large electric fields are absent, this is not the case near highly charged polyelectrolyte surfaces nor for highly concentrated ionic solutions. Several exact higher-order extensions of the Kirkwood–Fröhlich approach for pure solutions have been developed,[627] while the approximations of Booth[479] and Grahame[79,628] apply in the limit of complete saturation. Conway, Desnoyers and Smith have used the PB and Booth equations to investigate the local dielectric coefficient near charged spheres and cylinders,[629] and Gur, Ravina and Babchin[630] and Maeda and Oosawa[614,631] have approximated the Booth–Grahame formula to treat

dielectric saturation near a planar charged surface. Bahe has shown that polarization created by the dielectric coefficient gradient near an ion leads to a repulsive force between ions.[632] Bucher[533,534] and Ehrenson[535] have extended classical Born theory to study the effect of a variable dielectric coefficient on the hydration of ions.

Chernenko has investigated the effect of a counterion-induced dielectric decrement on the solution of the Gouy–Chapman equation.[21,633–635] Sansom et al. have studied the effect of a local dielectric coefficient in an ion channel pore (in the absence of ions),[636] and others have analyzed cylindrical models of DNA.[637–639] Kozak and co-workers [640–642] and Frahm and Diekmann[643] have investigated how this effect alters the solution of the spherically symmetric PB equation and the subsequent calculation of thermodynamic properties of electrolytes. Because inclusion of a local dielectric coefficient increases the surface concentration of ions near an all-atom model of DNA by about 15%, the effect can be significant.[88] A more extensive treatment of a local dielectric coefficient has been given by Bell and Levine[420] in their derivation of a modified PB equation. Finally, in an interesting example of reverse engineering, Vasilyev has shown how the PB method can be used to obtain distance-dependent dielectric functions applicable in molecular dynamics simulations.[644]

Point Mobile Ions

In addition to neglecting ion correlation, using the mean electrostatic potential results in the replacement of discrete mobile ions with a continuous, smeared-out charge density, subsuming any description of finite ion size. This limitation is felt in two ways: in ionic interactions with any polyelectrolyte surface and in the interaction of mobile ions among themselves. Surface interactions may partly be taken into account by introducing a distance of closest approach to the surface for each ion type. Although somewhat crude in appearance, calculations show that this simple modification yields results that are quantitatively in agreement with more sophisticated approaches, as the original finite-ion-size extension by Debye and Hückel demonstrates.

The second limitation mentioned above concerns the representation of specific ion–ion interactions, which should include at least a hard-sphere component to the interaction potential as well as having the Coulomb potential, with the latter based on two continuous charge distributions. The presence of a hard sphere interion potential would limit the maximum local ion concentration to that of close packing. The effect of this hard-sphere interaction is independent of charge and can be accounted for approximately by introducing a hard-sphere-based activity coefficient into Eq. [426] for the potential of mean force. The (log of the) activity coefficient at position $\underline{r}$ for ion species i with a hard-sphere radius a_i is[60,645]

$$\gamma_i^{hs}(\underline{r}) = -\frac{4\pi}{3} A_0 \sum_{j=1}^{I} (a_i + a_j)^3 \, c_j(\underline{r}) \qquad [428]$$

and can be included in a general-purpose algorithm via the exponential term in Eq. [378]. The obvious effect of including an activity coefficient to account for hard-sphere repulsion is to further reduce the already low correlation-free ion concentrations at the surface of polyelectrolytes. Thus, without accounting for the effect of ion correlation discussed in the following section, it is better to ignore the hard-sphere activity coefficient correction.[646] Another effect of the close packing of finite-size ions, and one that depends strongly on the specific ion sizes, charges and concentrations, is a region of charge reversal observed in Monte Carlo simulations and also in more detailed statistical-mechanical studies.[647–649] This packing effect shows up as an oscillation in the potential profile in contrast to the strictly monotonic potential of the standard PB equation.

Use of the Mean Electrostatic Potential

The replacement of the potential of mean force with the mean electrostatic potential by Debye and Hückel (and implicit in the Gouy–Chapman approach) has caused the greatest amount of concern for those applying the PB equation. Fowler severely criticized use of the PB equation on this basis, but his investigation was soon shown to be overly restrictive.[10,11,56] Still, the effect of neglecting ion–ion correlation, which this mean-field approximation implies, is a continual source of study. Hence there have been published numerous comparisons between PB theory and more detailed statistical-mechanical theories or calculations that do include correlation. While the size of the effect depends on the particular system studied, calculations on the cylindrical and all-atom models of DNA show that PB calculations tend to underestimate ion concentrations at the surface by 15–25% for mono- or divalent ions, respectively.[178,209,650–652]

In addition to neglecting ion correlation, using the mean electrostatic potential has the undesirable consequence that the (nonlinear) PB equation no longer satisfies a reciprocity condition that use of the potential of mean force would obey.[61] Linearization of the equation by Debye and Hückel regained this condition. These considerations led Outhwaite[653–655] and others[656,657] to propose modifications of the PB equation to treat these problems. Within this modified Poisson–Boltzmann (MPB) theory, the effect of ion correlation is expressed in terms of a fluctuation potential for which a first-order (local) expression, written as an activity coefficient, can be derived.[658] Their result for bulk hard-sphere electrolyte ions of valence z_i and common radius a gives the formula[659,660]

$$\gamma_i^{\text{hs-fluc}}(\underline{r}) = \delta(\underline{r}) + \frac{z_i^2 L_B \kappa(\underline{r})}{2[1 + 2a\kappa(\underline{r})]} + \left[\frac{3 + 2a\kappa(\underline{r})}{1 + 2a\kappa(\underline{r})}\right] \frac{z_i \mu(\underline{r})}{6} \qquad [429]$$

where we have defined the local (i.e., position-dependent) variables

$$\delta(\underline{r}) = -\frac{4\pi}{3}(2a)^3 A_0 \sum_{i=1}^{I} c_i(\underline{r})$$

$$\kappa(\underline{r}) = \sqrt{4\pi L_B A_0 \sum_{i=1}^{I} c_i(\underline{r}) z_i^2} \qquad [430]$$

$$\mu(\underline{r}) = 4\pi L_B A_0 (2a)^2 \sum_{i=1}^{I} c_i(\underline{r}) z_i$$

The first term in Eq. [429] is the hard-sphere exclusion volume term, which decreases the counterion concentration at the surface; the second and third terms respectively represent the fluctuation potential and increase the surface concentration of ions. These terms can be included as an activity coefficient in a general-purpose algorithm through the exponential term in Eq. [378]. For ion distances Δr closer to the surface than three ion radii, Bratko and Vlachy[658] multiply the ion concentrations in Eqs. [430] by an excluded volume correction factor $B(\underline{r}) = (\Delta r + a)/4a$; for distances $\Delta r < a$, ion concentrations are, of course, zero because of hard-sphere exclusion.

If the activity corrections of Eq. [429] are relatively small, we may calculate the uncorrected PB potential $\phi_0(\underline{r})$, for example, according to Eq. [26] for a planar surface or Eq. [152] for a curved one, determine the uncorrected concentrations from it according to

$$c_i^{\text{uncorr}}(\underline{r}) = c_i^B e^{-z_i \phi_0(\underline{r})} \qquad [431]$$

and use these concentrations in Eqs. [429] and [430] to obtain corrected concentrations:

$$c_i^{\text{corr}}(\underline{r}) = c_i^B e^{-z_i \phi_0(\underline{r}) - \gamma_i^{\text{hs-fluc}}(\underline{r})} \qquad [432]$$

If the activity terms are relatively large, the PB equation must be solved numerically with the activity terms determined self-consistently. For accurate calculations, one often resorts to an evaluation of thermodynamic properties using Monte Carlo techniques.[661–663]

Figure 52 compares the counterion concentration profile for a bulk 0.05 M 1 : 1 electrolyte with 1- or 2-Å hard-sphere ions near a charged cylinder of radius 10 Å with surface charge density $\sigma_a = -0.01\ e_0/\text{Å}^2$. Surface concentrations obtained from Metropolis Monte Carlo simulations (circles) are seen to be about 15% larger than those predicted by the PB equation without including activity corrections. Using the hard-sphere activities of Eqs. [429] and [430] results in much better agreement for 1-Å ions; the improvement for 2-Å ions is less impressive but still noticeable. Similar results for a bulk 0.05

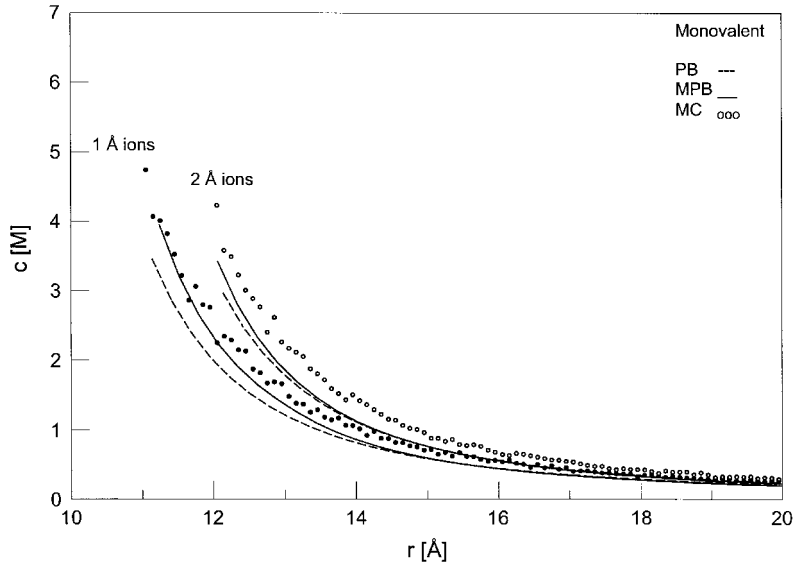

Figure 52 A comparison of cation concentration profiles for a bulk 0.05 M 1 : 1 electrolyte with 1 and 2-Å radius hard-sphere ions in the presence of a charged cylinder of radius 10 Å with surface charge density $\sigma_a = -0.01\, e_0/\text{Å}^2$ calculated according to the PB equation (Eq. [389]) without activity corrections (dashed line), the PB equation with MPB activity corrections of Eqs. [429] and [430] (solid line), and Metropolis Monte Carlo simulations (filled circles −1 Å; open circles −2 Å).

M 2 : 2 electrolyte are seen in Figure 53, except that the error at the surface is much larger (∼25%).

Other Neglected Effects

We consider the above assumptions to be the most significant. In addition to these, we list a few more, some of which are discussed by Bell and Levine:[420]

1. Polarization of the electronic charge distribution around an ion including its hydration shell near a polyelectrolyte surface,
2. The presence of an ion that creates a correlation hole in the double layer,
3. Discrete solvent effects,
4. Compressibility of the solvent near a polyelectrolyte surface,
5. Discrete surface charges.

Common Approximations to the Poisson–Boltzmann Equation

The two most common approximations used in applying the PB equation are the assumption of a bulk electrolyte and linearization of the equation.

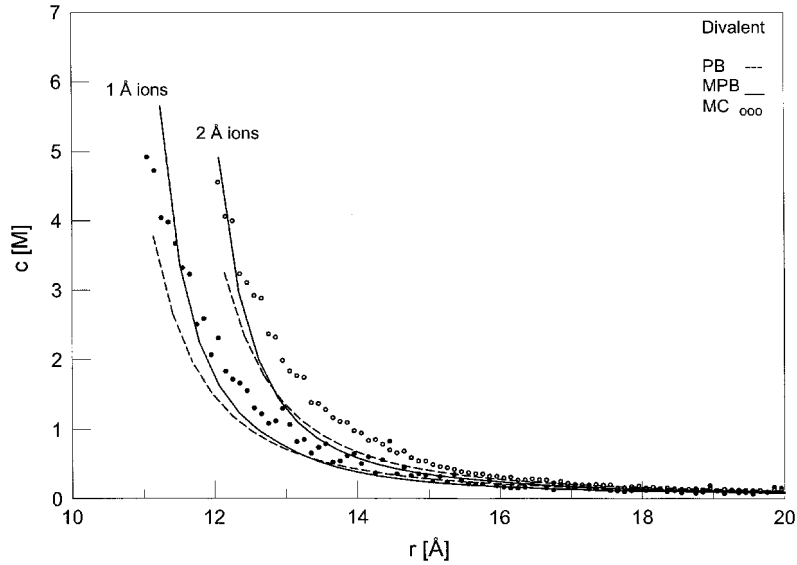

Figure 53 The cation concentration profile comparison as shown in Figure 52 except for a 0.05 M 2 : 2 electrolyte.

Together these essentially replace the Poisson–Boltzmann cell model with the Debye–Hückel bulk model, allowing many more systems to be treated analytically, although not necessarily accurately, and providing considerable insight into the physical characteristics of electrolyte solutions.

The Bulk Model

The most commonly used simplification when applying the PB equation to a polyelectrolyte is to assume that the solvent environment of the macroion extends to infinity. Doing so allows one to ignore any counterions initially bound to the polyelectrolyte ($c_0 \rightarrow 0$) and to replace concentrations at the outer boundary by bulk concentrations ($c_i^R \rightarrow c_i^B$). This simplification increases the rate at which the iterative solution to the PB equation converges since ion normalization is no longer a constraint. It is readily shown that the condition under which a finite system may be treated as infinite is[664]

$$z_0^2 c_0^B \ll \sum_{i=0}^{I} z_i^2 c_i^B \qquad [433]$$

For a system in which R defines the distance to the closest outer boundary enclosing a single central polyelectrolyte, and if the dielectric coefficient is constant or increases toward some bulk value ε^B at R, Eq. [433] can be recast into the more expressive form

$$\kappa_D R \gg 1 \qquad [434]$$

Because κ_D describes the length scale over which the potential decays away from the polyelectrolyte, Eq. [434] essentially says that if the potential distal from the polyelectrolyte falls to zero before the outer boundary is reached, this boundary may then be removed to infinity without affecting the solution to the PB equation. In practice, the restriction $\kappa_D R > 5$ seems sufficient for invoking an infinite model of a finite system containing mono- and divalent ions.[664]

Linearization of the Equation

The second most frequent simplification of the PB equation is linearization of the charge density with respect to the potential. The resulting Debye–Hückel equation may also be applied independently of, though usually in conjunction with, the preceding approximation of Eq. [433]. If the dielectric coefficient of the environment is constant, analytical solutions under a wide variety of boundary conditions may be obtained for systems with sufficient symmetry, as shown above. The obvious condition under which linearization is valid is that where the quadratic term in the expansion of the exponential is small compared to the linear term, that is,

$$|z_i \phi_a| \ll 1 \qquad [435]$$

for all ion species in the system. For most applications, however, Eq. [435] is overly restrictive and, as shown previously, values of $|z\phi_a|$ near unity admit accurate Debye–Hückel solutions (e.g., see Fig. 37). The calculation of thermodynamic properties usually requires the evaluation of a free-energy integral. Thus, Eq. [435] may fail to hold over a relatively small region of the system, yet the Debye–Hückel result would be accurate. Whether a less restrictive condition than Eq. [435] applies obviously depends on the quantity being calculated and how sensitive this quantity is to regions where the potential is large. The DH equation has also been shown to give the exact limiting law for the activity coefficient for solutions with low electrolyte concentrations,[61] thus placing it on a firmer foundation than the nonlinear PB equation. Despite this, under circumstances in which Eq. [435] fails to hold, the PB equation provides better agreement with more accurate calculations than the DH equation.

Alternatives to the Poisson–Boltzmann Equation

The usefulness in applying the Poisson–Boltzmann equation to a wide range of physical, chemical, and biological situations has led to numerous detailed studies of its range of applicability as well as ways to extend it. Most investigations into its deficiencies begin with the simple systems treated by Gouy and Chapman and Debye and Hückel. To determine the extent of error introduced by describing the statistical mechanics of hard-sphere models using the PB equation, results (e.g., ion distributions, osmotic pressure) are compared with those derived from more detailed calculations.[665,666] The models considered are termed the *primitive model* (PM), in which electrolyte ions are treated as hard spheres and the solvent is a constant dielectric continuum,

and the *restricted primitive model* (RPM), in which all ions have the same radius and cations and anions have equal but opposite charge (as in the Debye–Hückel model). Some of the more promising avenues of research are highlighted below. As an extensive discussion of these works is beyond the scope of this review, the original papers should be consulted for specific details.

Modified Poisson–Boltzmann Theories

Kirkwood[11] gave the first detailed derivation of the nonlinear PB equation, including corrections due to correlation (fluctuation) and finite ion size. These were elaborated on by Levine, culminating in a paper with Bell[420] dealing with the electric double layer near a polyelectrolyte surface. The leading terms in the Bell–Levine treatment were kept and some restrictions and approximations were applied to obtain a modified Poisson–Boltzmann (MPB) equation in the form of an integrodifference/differential equation[618,667,668] that took into account the fluctuation potential of Kirkwood. Later work included several expressions for Kirkwood's finite-size volume effect,[669,670] the extension to ions of different size,[660] symmetrization of the radial distribution function,[653 671,672] the extension to systems with cylindrical shape,[673] and multiple component mixtures.[655,674–677] Modified PB theory has also been used to help interpret neutron structure factors in polyamine–DNA interactions. The theory is presently the most comprehensive extension of the standard PB equation and compares favorably with more time-consuming Monte Carlo and hypernetted chain (HNC) calculations.[618,669,670,678,679] The simplification used by Bratko and Vlachy[658,680,681] for the fluctuation term (Eqs. [429] and [430]) is applicable to general PB treatments in the same manner that the hard-sphere volume effect was introduced.[645] Gavryushov and Zielenkiewicz have applied MPB theory to investigate ionic correlation[682] and local dielectric coefficients near models of DNA.[639] Tomac and Graslund have combined Kirkwood's corrections with the multigrid method of UHBD to gauge the importance of fluctuation corrections on mono- and divalent ions near a large spherical macroion.[683]

When investigating the critical behavior of electrolyte solutions, Fisher and Levin[281,684–687] derived a generalized Debye–Hückel equation that incorporated the ideas of Bjerrum[688] concerning ion association. A later modification by Lee and Fisher[689,690] replaced the Debye screening factor defined in Eq. [12] with one determined by the local charge density. In an earlier but related investigation, Attard[691] showed that the Stillinger-Lovett second-moment condition,[692–694] which is disobeyed by the normal analytical finite-ion DH solution, can be satisfied if the Debye screening factor of Eq. [12] is replaced by

$$\kappa = \frac{\kappa_D}{\sqrt{1 - (\kappa_D d)^2/2 + (\kappa_D d)^3/6}} \qquad [436]$$

for ions of diameter d.

Borukhov, Andelman and Orland[132,133] have included the finite-ion-size contribution to the entropic term of the free energy and derived a modified Gouy–Chapman equation. Analytical results for a planar surface of charge density σ_0 have been presented for $1:z$ and $z:z$ electrolytes. For ions of diameter d, a measure of the size of excluded volume effects can be described by the single parameter

$$\varsigma = \frac{2\pi L_B d^3 \sigma_0^2}{e_0^2} \qquad [437]$$

Integral Equation and Field–Theoretic Approaches

In addition to theories based on the direct analytical extension of the PB or DH equation, PB results are often compared with statistical-mechanical approaches based on integral equation or density functional methods. We mention only a few of the most recent theoretical developments. Among the more popular are the mean spherical approximation (MSA) and the hypernetted chain (HNC) equation.[61,695,696] Kjellander and Marčelja have developed an anisotropic HNC approximation that treats the double layer near a flat charged surface as a series of discrete layers.[697–699] Attard, Mitchell and Ninham have used a Debye–Hückel closure for the direct correlation function to obtain an analytical extension (in terms of elliptic integrals) to the PB equation for the planar double layer.[101,700] Both of these approaches, which do not include finite volume corrections, treat the fluctuation potential in a manner similar to the MPB theory of Outhwaite.

Kjellander and Marčelja[701] have also used their results to show that the traditional PB approach can describe ion distributions quite well if an apparent rather than actual surface charge is used.[102,646,702] This prompted Kjellander and co-workers to propose the dressed-ion theory (DIT) model, discussed briefly above, in which each primitive model ion is represented as a bare ion "dressed" in part of its surrounding ion cloud.[343–346,703–705]

Netz and co-workers treat electrolyte systems within a field-theoretic framework that reduces to the Debye–Hückel description at the Gaussian level of approximation.[57,706–709] Of particular interest is the application of the model to ions of valence z_0 (with no added salt) near a planar surface of charge density σ_a where the size of correlation effects can be described by a single parameter:[708]

$$\Sigma = \frac{2\pi z^3 L_B^2 \sigma_a}{e_0} \qquad [438]$$

Moreira and Netz have also obtained the weak- and strong-coupling limits of the counterion charge density profile as a function of the distance x from the surface[710]

$$\rho(x) = \frac{2\pi L_B z_0 e_0^{-1} \sigma_a^2}{(1 + x/\lambda_{GC})^2}, \qquad \Sigma \ll 1 \text{ (weak coupling)} \qquad [439]$$

and

$$\rho(x) = 2\pi L_B z_0 e_0^{-1} \sigma_a^2 e^{-x/\lambda_{GC}}, \ \Sigma \gg 1 \text{ (strong coupling)} \qquad [440]$$

where λ_{GC} is the Gouy–Chapman length of Eq. [11].

Without elaboration, we mention that one of the most promising avenues of work is in the application of density functional methods to electrolyte solutions.[711–716]

The Metropolis Monte Carlo Method

The most popular alternative to the PB equation in evaluating thermodynamic properties of electrolyte solutions is the Metropolis Monte Carlo (MMC) method.[580,717] Numerous reviews of this and similar techniques have appeared,[663] so we present only a short list comparing the primary advantages and disadvantages of the Poisson–Boltzmann and Monte Carlo methods:

- PB advantages
  Analytical approximations can be developed
  Physical insight can guide and/or result from the solution
  Computationally fast for large systems
  Variable dielectric coefficient can be included
- MC advantages
  Easily programmed
  Applicable to most systems and potentials
  Solvent molecules can be treated explicitly
  Finite ion size and correlation effects are included

While the Poisson–Boltzmann and Monte Carlo approaches are usually considered as alternative methods with their own advantages and disadvantages as listed above, we briefly point out one procedure that combines the advantages of both. Consider, as an example, the use of the MC method to determine the ion distribution around a negatively charged micelle. If the solvent is represented by a structureless continuum (i.e., McMillan–Mayer theory is invoked), the resulting cation distribution will appear similar to, but not identical with, that obtained from the corresponding PB calculation. If the PB calculation is based on the same constant solvent dielectric coefficient assumed in the MC calculation, then the MC distribution will be somewhat higher at the surface (~15% for monovalent cations and ~25% for divalent cations; see Figs. 52 and 53) owing to inclusion of correlation effects.[208,209,718–720] If explicit solvent molecules are included in the MC calculation, two additional effects are automatically included: oscillations in the cation distribution due to structured ion solvation and a spatially variable dielectric coefficient caused by local solvent polarization. While accurate MC calculations require that explicit solvent molecules be included, this will increase the size of a system

consisting of only a hundred or fewer cations to one that also contains many thousands of additional water molecules. The resulting increase in computation time can drastically limit the applicability of the procedure. If the effect of solvent-induced oscillations in the ion correlation function with respect to the micellar surface can be ignored, the PB method can be used to provide a correction to the original (continuum solvent) MC calculation that takes into account the local variation in the dielectric coefficient to approximately first order.

Let $\phi_B(\underline{r})$ denote the potential obtained from a standard PB calculation assuming a constant bulk dielectric coefficient and $\phi_{\text{var}}(\underline{r})$ denote that obtained by assuming a variable dielectric coefficient (i.e., Eqs. [385]–[388]). Now let $V_B(\underline{r})$ be the MC potential (a sum of Lennard-Jones and electrostatic terms) that a cation in the system would experience in a bulk dielectric continuum. The approximate effect of including a variable dielectric coefficient in the Monte Carlo simulation can be found by replacing the bulk MC potential $V_B(\underline{r})$ with the "PB-corrected" potential $V_B(\underline{r}) + \phi_{\text{var}}(\underline{r}) - \phi_B(\underline{r})$. Of course the resulting ion distribution will not be self-consistent with the assumed (PB-derived) dielectric coefficient map, but it will be a noticeable improvement on the original MC distribution using a bulk dielectric.

Counterion Condensation Theory

Application of the PB equation to a charged cylinder was found particularly useful in describing the thermodynamic properties of polymers which dissociate upon solvation into an extended polyelectrolyte and many small ions. Intermolecular forces, including electrostatic repulsion between ionized sites on the surface of the polymer, stretch the molecule along its axis, leading to remarkable colligative properties.[78,196,206,261] An observation by Onsager concerning the divergence of the phase integral for an infinite line charge prompted Manning to propose a model of cylindrical polyelectrolytes that succinctly and quantitatively accounts for many of the observed thermodynamic properties of these molecules.[214,279,280,721,722] Expressing the total free energy of a line charge with its counterions as the sum of a Debye–Hückel-like electrostatic term and an entropic mixing component and minimizing the result led Manning to his counterion condensation (CC) theory. It says, in essence, that given a cylindrical polyelectrolyte with linear charge density e_0/b in the presence of counterions of valence z, then if the "Manning parameter" $\xi = L_B/b$ times the valence is greater than unity, enough counterions will "condense" on the line charge to effectively reduce this product to unity.

The success of Manning's simple two-state model in predicting many of the properties of cylindrical polyelectrolytes like DNA ($\xi \sim 4$) has spawned a mini-industry in investigating counterion condensation phenomena within the context of the PB equation.[177,178,205,208,209,218,276,685,723–735] More recent work with Manning's theory has dealt with applying the analytical and numerical[736] versions of the theory to finite,[737] multiple,[738–740] or bent[741,742] polyelectrolytes, helical charge distributions,[743] polarization

effects,[744] and a potential of mean force for counter- and coions.[745] Recently, an alternative view of counterion condensation theory has been presented that includes the effect of dielectric saturation.[746] With Manning's two-state theory[747] being an overestimation of the nonlinearity involved in the interaction of counterions at a highly charged surface,[748,749] Poisson–Boltzmann theory is an underestimation of the effect. Monte Carlo and molecular dynamics[750] simulations, subject to the assumptions involved in using a two-particle potential and the inclusion or neglect of the solvent, appear to most accurately describe the complex and subtle interactions among the various species involved.

CONCLUDING REMARKS

The aim of the tutorial review presented in this chapter is to serve as a useful introduction to the varied methods of solution and application of the Poisson–Boltzmann equation and in so doing relate a little of its relevance to modern colloidal and biophysical research. It is somewhat easier to detail the importance of some biochemical reaction to our health or the knowledge gained in understanding an aspect of colloidal behavior than in demonstrating the immediate usefulness of a specific equation, but progress in science requires moving from the concrete to the abstract and back again. As mentioned in the introduction, the increasing interest in the Poisson–Boltzmann equation lies in its applications—in the wide range of physical phenomena it helps us describe—and finding an adequate solution, either analytically or numerically, for the problem at hand is the first and often most difficult step. Most textbooks on statistical mechanics tend to give the Poisson–Boltzmann equation short shrift so obtaining its solution is often an exercise akin to reinventing the wheel. It is hoped that this review will fill a much-needed gap by serving three purposes: as a compendium of solutions, as an introduction to present-day numerical techniques, and as a guide to some of the literature.

Because the large array of analytical results presented in the second part of this review may at first seem daunting, and perhaps confusing, they are summarized in Table 1 for easier reference. The unifying thread we have woven through the fabric of this tutorial is the NLDH approximation, which, despite its faults, guides us from the Gouy–Chapman potential for a plane, through the asymptotic PB solution for cylinders and spheres, to the apparent Debye–Hückel potential for a particle, with its suggestion of counterion condensation and its additivity property, and back via two-particle interactions. Because the focus of most calculations has been on determining the electrostatic potential and free energy with the interaction potential or binding energy important for two-particle systems, we have discussed their relationships only sparingly with respect to the interpretation of experimental data. It is difficult to observe forces and potentials directly, particularly at the colloidal and

Table 1 Applicability of the Various Analytical Potential Expressions Derived in This Chapter

Equation(s)	Abbreviation[a]	Additive[b]	Range[c]	Charge Density[d]	Surfaces[e]	Model	Electrolyte[f]	Geometry[g]
[22], [23], [26]	GC (PB)	No	Exact	Any	1	Bulk	$z:z$	P
[33]	PB	No	Near	High	1	Bulk	$z:z$	P
[35]	PB	No	Asymptotic	High	1	Bulk	$z:z$	P
[39]	PB	No	Exact	Any	1	Bulk	1 : 1–2 : 1	P
[41]	PB	No	Near	High	1	Bulk	1 : 1–2 : 1	P
[42]	PB	No	Asymptotic	High	1	Bulk	1 : 1–2 : 1	P
[43]	PB	No	Approximate	Any	1	Bulk	1 : 1–2 : 1	P
[47]	PB	No	Exact	Any	1	Bulk	1 : 1–2 : 2	P
[50]	PB	No	Approximate	Any	1	Bulk	1 : 1–2 : 2	P
[56]	PB	No	Near	High	1	Bulk	Any	P
[57]	PB	No	Approximate	High	1	Bulk	Any	P
[64]	PB	No	Approximate	Any	1	Bulk	1 : 1–2 : α, $\alpha = 1,2$	P
[70]	PB	No	Approximate	Any	1	Bulk	Any	P
[73]	PB	No	Exact	Any	1	Cell	No added salt	P
[87]	DH	No	Exact	Low	1	Cell	Any	P
[89]	DH	Yes	Exact	Low	1	Bulk	Any	P
[93]	ADH	Yes	Asymptotic	Any	1	Bulk	Any	P
[105]	DH	No	Exact	Low	2	Bulk	Any	P
[115]	PB	Yes	Asymptotic	Any	2	Bulk	$z:z$	P
[121]	NLDH	No	Asymptotic	Any	2	Bulk	$z:z$	P
[152]	PGC	No	Approximate	Any	1	Bulk	$z:z$	C or S
[174], [175]	NLDH	No	Approximate	Any	1	Bulk	$z:z$	C or S
[177]	NLDH	No	Approximate	Any	1	Bulk	$z:z$	C or S
[196]	NLDH	No	Asymptotic	Any	2	Bulk	$z:z$	Any two
[196] + [271]	NLDH	No	Asymptotic	Any	2	Bulk	$z:z$	C
[196] + [328]	NLDH	No	Asymptotic	Any	2	Bulk	$z:z$	S
[214]	Variational	No	Upper bound	Any	1	Bulk	$z:z$	C or S
[222]	Variational	No	Upper/Lower	Any	1	Bulk	$z:z$	C or S
[245]	PB	No	Exact	Any	1	Cell	No added salt	C
[253]	NLDH	No	Approximate	Any	1	Bulk	$z:z$	C

Table 1 (*Continued*)

Equation(s)	Abbreviation[a]	Additive[b]	Range[c]	Charge Density[d]	Surfaces[e]	Model	Electrolyte[f]	Geometry[g]
[256]	DH	No	Exact	Low	1	Cell	Any	C
[259]	DH	Yes	Exact	Low	1	Bulk	Any	C
[260]	DH	Yes	Asymptotic	Low	1	Bulk	Any	C
[261]	ADH//NLDH	Yes	Asymptotic	Any	1	Bulk	Any	C
[286]	PB	No	Exact	Any	1	Cell	No added salt	Capillary
[291]	DH	No	Exact	Low	1	Cell	Any	Capillary
[301]	NLDH	No	Approximate	Any	1	Bulk	$z:z$	S
[304]	DH	No	Exact	Low	1	Cell	Any	S
[307]	DH	Yes	Exact	Low	1	Bulk	Any	S
[308]	ADH//NLDH	Yes	Asymptotic	Any	1	Bulk	Any	S
[315]	ADH//PGC	Yes	Asymptotic	Any	1	Bulk	$z:z$	S
[361]	DIT	Yes	Exact	Low	Many	Bulk	Any	S
[364]	DH	Yes	Exact	Low	1	Bulk	Any	Line
[366]	ADH//PGC	Yes	Asymptotic	Any	1	Bulk	$z:z$	C
[368]	DH	Yes	Exact	Low	1	Bulk	Any	Arc
[375]	NLDH	No	Asymptotic	Any	2	Bulk	$z:z$	P-S

[a]GC; Gouy–Chapman; PB, Poisson–Boltzmann; DH, Debye–Hückel; ADH, apparent Debye–Hückel; NLDH, nonlinear Debye–Hückel; PGC, perturbed Gouy–Chapman; DIT, dressed-ion theory

[b]Indicates whether the solution may be combined additively to treat multiple surfaces (particles) or an extended charge distribution.

[c]Indicates range and accuracy of solution (range is limited to the electrolyte); exact—solution applicable everywhere; approximate—solution applicable everywhere but only approximates exact solution; near—solution applicable only near the surface (within a Debye length); asymptotic—solution accurate only far from the surface (a few Debye lengths away). The Debye–Hückel solution is considered exact within the low surface density requirement but could also be equivalent to an approximate PB solution.

[d]Restrictions on the surface charge density (or surface potential).

[e]Number of surfaces (particles) to which the solution applies.

[f]Electrolyte stoichiometry used in the solution; an approximate solution may be found for any asymmetric or mixed electrolyte by using the $z:z$ solution with an effective valence given by Eq. [69].

[g]Geometry of surface: P, planar; C, cylindrical; S, spherical.

biochemical level, so connections must be made with more easily obtained properties such as osmotic pressure, Donnan or activity coefficients, and electrokinetic or diffusion data. Several articles are available that describe how this is done, and some of these have been cited above, but with the recent surge of interest in the PB equation, perhaps a more timely review of this material is also in order, particularly in light of the work discussed here.

ACKNOWLEDGMENTS

The author wishes to thank George Pack for demonstrating the relevance of the Poisson–Boltzmann equation to biophysical systems in the mid-1980s and gratefully acknowledges Professor C. W. Outhwaite for his helpful correspondence. Anton Rakitin kindly provided the Monte Carlo data, and Anton Petrov is thanked for numerous discussions. The editors of this series are also appreciated for the numerous suggestions that have improved the presentation of this work and for their restrained persistence. This work was supported in part by a grant (to G. R. Pack) from the National Institutes of Health (GM29079).

REFERENCES

1. G. Gouy, *Compt. Rend. Hebd. Seances Acad. Sci.*, **149,** 654 (1910). Sur la Constitution de la Charge Electrique a la Surface d'un Electrolyte.
2. G. Gouy, *J. Phys. Theoretique Applique,* **9,** 457 (1910). Sur la Constitution de la Charge Electrique a la Surface d'un Electrolyte.
3. P. Debye and E. Hückel, *Phys. Z.,* **24,** 185 (1923). Zur Theorie der Elektrolyte. I. Gefrierpunkts-Erniedrigung und Vewandte Erscheinungen.
4. P. Debye and E. Hückel, *Phys. Z.,* **24,** 305 (1923). Zur Theorie der Elektrolyte. II. Das Grenzgesetz fur die Elektrische Leitfahigkeit.
5. P. Debye, *The Collected Papers of Peter J. W. Debye,* Interscience, New York, 1954.
6. K. J. Laidler, *The World of Physical Chemistry*, Oxford, New York, 1993, pp. 215–217.
7. D. C. Chapman, *Phil. Mag.,* **25,** 475 (1913). A Contribution to the Theory of Electrocapillarity.
8. O. Stern, *Z. Elektrochem.*, **30,** 508 (1924). Zur Theorie der Electrolytischen Doppelschicht.
9. D. C. Grahame, *Chem. Rev.*, **41,** 441 (1947). The Electrical Double Layer and the Theory of Electrocapillarity.
10. L. Onsager, *Chem. Rev.*, **13,** 73 (1933). Theories of Concentrated Electrolytes.
11. J. G. Kirkwood, *J. Chem. Phys.,* **2,** 767 (1934). On the Theory of Strong Electrolyte Solutions.
12. A. Katchalsky, *Pure Appl. Chem.,* **26,** 327 (1971). Polyelectrolytes.
13. J. T. G. Overbeek, *Pure Appl. Chem.,* **46,** 91 (1976). Polyelectrolytes: Past, Present and Future.
14. D. Henderson, *Prog. Surf. Sci.,* **13,** 197 (1983). Recent Progress in the Theory of the Electric Double Layer.
15. A. J. M. Garrett and L. Poladian, *Ann. Phys.,* **188,** 386 (1988). Refined Derivation, Exact Solutions, and Singular Limits of the Poisson-Boltzmann Equation.
16. V. Vlachy, *Annu. Rev. Phys. Chem.,* **50,** 145 (1999). Ionic Theory beyond Poisson-Boltzmann Theory.
17. P. Attard, *Adv. Chem. Phys.,* **92,** 159 (1996). Electrolytes and the Electric Double Layer.

18. S. L. Carnie and G. M. Torrie, *Adv. Chem. Phys.,* **56,** 141 (1984). The Statistical Mechanics of the Electrical Double Layer.
19. J. R. Loehe and M. D. Donohue, *Aiche J.,* **43,** 180 (1997). Recent Advances in Modeling Thermodynamic Properties of Aqueous Strong Electrolyte Systems.
20. J.-L. Barrat and J.-F. Joanny, *Adv. Chem. Phys.,* **94,** 1 (1996). Theory of Polyelectrolyte Solutions.
21. A. G. Volkov, D. W. Deamer, D. L. Tanelian, and V. S. Markin, *Prog. Surf. Sci.,* **53,** 1 (1996). Electrical Double Layers at the Oil/Water Interface.
22. L. Belloni, *J. Phys. Condensed Matter,* **12,** R549 (2000). Colloidal Interactions.
23. J. C. Hansen and H. Lowen, *Annu. Rev. Phys. Chem.,* **51,** 209 (2000). Effective Interactions between Electric Double Layers.
24. P. Attard, *Curr. Opin. Colloid Interface Sci.,* **6,** 366 (2001). Recent Advances in the Electric Double Layer in Colloid Science.
25. C. Tanford and J. G. Kirkwood, *J. Am. Chem. Soc.,* **79,** 5333 (1957). Theory of Protein Titration Curves. I. General Equations for Impenetrable Spheres.
26. C. Tanford, *J. Am. Chem. Soc.,* **79,** 5340 (1957). Theory of Protein Titration Curves. II. Calculation for Simple Models at Low Ionic Strength.
27. D. Bashford and M. Karplus, *Biochemistry,* **29,** 10219 (1990). pK_a's of Ionizable Groups in Proteins: Atomic Detail from a Continuum Electrostatic Model.
28. D. Bashford and M. Karplus, *J. Phys. Chem. B,* **95,** 9556 (1991). Multiple-Site Titration Curves of Proteins: An Analysis of Exact and Approximate Methods for Their Calculation.
29. D. Bashford and K. Gerwert, *J. Molec. Biol.,* **224,** 473 (1992). Electrostatic Calculations of the pK_a Values of Ionizable Groups in Bacteriorhodopsin.
30. P. Kollman, *Chem. Rev.,* **93,** 2395 (1993). Free Energy Calculations: Applications to Chemical and Biochemical Phenomena.
31. M. K. Gilson, *Proteins Struct. Funct. Genet.,* **15,** 266 (1993). Multiple-Site Titration and Molecular Modeling: Two Rapid Methods for Computing Energies and Forces for Ionizable Groups in Proteins.
32. A. S. Yang, M. R. Gunner, R. Sampogna, K. Sharp, and B. Honig, *Proteins Struct. Funct. Genet.,* **15,** 252 (1993). On the Calculation of pK_as in Proteins.
33. M. K. Gilson, J. A. Given, B. L. Bush, and J. A. McCammon, *Biophys. J.,* **72,** 1047 (1997). The Statistical-Thermodynamic Basis for Computation of Binding Affinities: A Critical Review.
34. J. M. Briggs and J. Antosiewicz, in *Reviews in Computational Chemistry,* K. B. Lipkowitz and D. B. Boyd, Eds., Wiley, New York, 1999, pp. 249–311. Simulation of pH-Dependent Properties of Proteins Using Mesoscopic Models.
35. A. H. Elcock, D. Sept, and J. A. McCammon, *J. Phys. Chem. B,* **105,** 1504 (2001). Computer Simulation of Protein-Protein Interactions.
36. E. J. W. Verwey and J. T. G. Overbeek, *Theory of the Stability of Lyophobic Colloids. The Interaction of Sol Particles Having an Electric Double Layer*, Elsevier, New York, 1948 (reprinted by Dover, New York, 1999).
37. G. E. Morfill, H. M. Thomas, U. Konopka, and M. Zuzic, *Phys. Plasmas,* **6,** 1769 (1999). The Plasma Condensation: Liquid and Crystalline Plasmas.
38. J. N. Chazalviel, *Coulomb Screening by Mobile Charges*, Birkhäuser, Boston, 1999.
39. T. L. Beck, *Rev. Modern Phys.,* **72,** 1041 (2000). Real-Space Mesh Techniques in Density-Functional Theory.
40. M. E. Davis, J. D. Madura, B. A. Luty, and J. A. McCammon, *Comput. Phys. Commun.,* **62,** 187 (1991). Electrostatics and Diffusion of Molecules in Solution: Simulations with the University of Houston Brownian Dynamics Program.
41. J. D. Madura, J. M. Briggs, R. C. Wade, M. E. Davis, B. A. Luty, A. Ilin, J. Antosiewicz, M. K. Gilson, B. Bagheri, L. R. Scott, and J. A. McCammon, *Comput. Phys. Commun.,* **91,**

57 (1995). Electrostatics and Diffusion of Molecules in Solution: Simulations with the University of Houston Brownian Dynamics Program.

42. M. K. Gilson, K. A. Sharp, and B. H. Honig, *J. Comput. Chem.,* **9,** 327 (1987). Calculating the Electrostatic Potential of Molecules in Solution: Method and Error Assessment.
43. A. Nicholls and B. Honig, *J. Comput. Chem.,* **12,** 435 (1991). A Rapid Finite-Difference Algorithm, Utilizing Successive Over-Relaxation to Solve the Poisson-Boltzmann Equation.
44. M. Holst, N. Baker, and F. Wang, *J. Comput. Chem.,* **21,** 1319 (2000). Adaptive Multilevel Finite Element Solution of the Poisson-Boltzmann Equation I. Algorithms and Examples.
45. N. Baker, M. Holst, and F. Wang, *J. Comput. Chem.,* **21,** 1343 (2000). Adaptive Multilevel Finite Element Solution of the Poisson-Boltzmann Equation II. Refinement at Solvent-Accessible Surfaces in Biomolecular Systems.
46. N. A. Baker, D. Sept, M. Holst, and J. A. McCammon, *IBM J. Res. Devel.,* **45,** 427 (2001). The Adaptive Finite Element Solution of the Poisson-Boltzmann Equation on Massively Parallel Computers.
47. N. A. Baker, D. Sept, S. Joseph, M. J. Holst, and J. A. McCammon, *Proc. Natl. Acad. Sci. (USA),* **98,** 10037 (2001). Electrostatics of Nanosystems: Application to Microtubules and the Ribosome.
48. D. F. Evans and H. Wennerström, *The Colloidal Domain*, Wiley, New York, 1999.
49. R. J. Hunter, *Foundations of Colloid Science*, Oxford Univ. Press, New York, 2001.
50. J. Liouville, *J. Math. Pures Appliquees,* **18,** 71 (1853). Sur L'Equation aux Differences Partielles.
51. J. Liouville, *Compt. Rend. Hebd. Seances Acad. Sci.,* **36,** 371 (1853). Sur L'equation aux Differences Partielles.
52. G. Gouy, *Annal. Phys.,* **7,** 129 (1917). Sur la Fonction Electrocapillare.
53. S. R. Milner, *Philos. Mag.,* **23,** 551 (1912). XLIX. The Virial of a Mixture of Ions.
54. S. R. Milner, *Phil. Mag.,* **25,** 742 (1913). LXXIX. The Effect of Interionic Forces on the Osmotic Pressure of Electrolytes.
55. P. Debye, *Recueil Travaux Chim. Pays-Bas,* **42,** 597 (1923). Theorie Cinetique des Lois de la Pression Osmotique des Electrolytes Forts.
56. R. H. Fowler, *Trans. Faraday Soc.*, 434 (1927). Strong Electrolytes in Relation to Statistical Theory, in Particular the Phase Integral of Gibbs.
57. R. R. Netz and H. Orland, *Europhys. Lett.,* **45,** 726 (1999). Field Theory for Charged Fluids and Colloids.
58. S. A. Rice and M. Nagasawa, *Polyelectrolyte Solution*, Academic Press, New York, 1961.
59. N. Davidson, *Statistical Mechanics*, McGraw-Hill, New York, 1962.
60. T. L. Hill, *An Introduction to Statistical Thermodynamics,* Dover, New York, 1986.
61. D. A. McQuarrie, *Statistical Mechanics*, Harper & Row, New York, 1976.
62. J. O. Bockris and A. K. N. Reddy, *Modern Electrochemistry*, Plenum Press, New York, 1998.
63. J. D. Jackson, *Classical Electrodynamics*,Wiley, New York, 1999.
64. S. McLaughlin, in *Current Topics in Membranes and Transport,* F. Bronner and A. Kleinzeller, Eds., Academic Press, New York, 1977, pp. 71–144. Electrostatic Potentials at Membrane-Solution Interfaces.
65. S. McLaughlin, *Annu. Rev. Biophys. Biophys. Chem.,* **18,** 113 (1989). The Electrostatic Properties of Membranes.
66. G. Cevc, *Biochim. Biophys. Acta,* **1031,** 311 (1990). Membrane Electrostatics.
67. J. N. Israelachvili, *Intermolecular and Surface Forces,* Academic Press, New York, 1992.
68. D. Andelman, in *Structure and Dynamics of Membranes,* R. Lipowsky and E. Sackmann, Eds., Elsevier, Amsterdam, 1995, pp. 603–642. Electrostatic Properties of Membranes: The Poisson-Boltzmann Theory.

69. M. Langner and K. Kubica, *Chem. Phys. Lipids,* **101,** 3 (1999). The Electrostatics of Lipid Surfaces.
70. A. J. Bard and L. R. Faulkner, *Electrochemical Methods,* Wiley, New York, 2001.
71. P. M. Biesheuvel, *J. Colloid Interface Sci.,* **238,** 362 (2001). Simplifications of the Poisson-Boltzmann Equation for the Electrostatic Interaction of Close Hydrophilic Surfaces in Water.
72. H. H. von Grünberg and E. C. Mbamala, *J. Physics Condensed Matter,* **13,** 4801 (2001). Charged Colloids Near Interfaces.
73. I. Rouzina and V. A. Bloomfield, *J. Phys. Chem. B* (1996). Competitive Electrostatic Binding of Charged Ligands to Polyelectrolytes: Planar and Cylindrical Geometries.
74. I. Rouzina and V. A. Bloomfield, *J. Phys. Chem. B,* **100,** 4305 (1996). Influence of Ligand Spatial Organization on Competitive Electrostatic Binding to DNA.
75. V. A. Parsegian and D. Gingell, *Biophys. J.,* **12,** 1192 (1972). On the Electrostatic Interaction across a Salt Solution between Two Bodies Bearing Unequal Charges.
76. W. Olivares and D. A. McQuarrie, *J. Phys. Chem.,* **84,** 863 (1980). Interaction between Electrical Double Layers.
77. L. D. Landau and E. M. Lifshitz, *Electrodynamics of Continuous Media*, Pergamon Press, Oxford, 1960.
78. R. A. Marcus, *J. Chem. Phys.,* **23,** 1057 (1955). Calculation of Thermodynamic Properties of Polyelectrolytes.
79. D. C. Grahame, *J. Chem. Phys.,* **21,** 1054 (1953). Diffuse Double Layer Theory for Electrolytes of Unsymmetrical Valence Types.
80. F. Andrietti, A. Peres, and R. Pezzotta, *Biophys. J.,* **16,** 1121 (1976). Exact Solution of the Unidimensional Poisson-Boltzmann Equation for a 1:2 (2:1) Electrolyte.
81. L. B. Bhuiyan, L. Blum, and D. Henderson, *J. Chem. Phys.,* **78,** 442 (1983). The Application of the Modified Gouy-Chapman Theory to an Electrical Double Layer Containing Asymmetric Ions.
82. R. De Levie, *J. Electroanal. Chem.,* **278,** 17 (1990). Notes on Gouy Diffuse-Layer Theory.
83. J.-P. Hsu and Y.-C. Kuo, *J. Chem. Soc. Faraday Trans.,* **89,** 1229 (1993). Approximate Analytical Expressions for the Properties of an Electrical Double Layer with Asymmetric Electrolytes.
84. Z. Chen and R. K. Singh, *J. Colloid Interface Sci.,* **245,** 301 (2002). General Solution for Poisson-Boltzmann Equation in Semiinfinite Planar Symmetry.
85. D. Y. C. Chan and D. J. Mitchell, *J. Colloid Interface Sci.,* **95,** 193 (1983). The Free Energy of an Electrical Double Layer.
86. J. T. G. Overbeek, *Colloids Surf.,* **51,** 61 (1990). The Role of Energy and Entropy in the Electrical Double Layer.
87. S. May, *J. Chem. Phys.,* **105,** 8314 (1996). Curvature Elasticity and Thermodynamic Stability of Electrically Charged Membranes.
88. G. Lamm and G. R. Pack, *J. Phys. Chem. B,* **101,** 959 (1997). Calculation of Dielectric Constants Near Polyelectrolytes in Solution.
89. B. Abraham-Shrauner, *J. Math. Biol.,* **2,** 333 (1975). Generalized Gouy-Chapman Potential of Charged Phospholipid Membranes with Divalent Cations.
90. B. Abraham-Shrauner, *J. Math. Biol.,* **4,** 201 (1977). Erratum for "Generalized Gouy-Chapman Potential of Charged Phospholipid Membranes with Divalent Cations."
91. A. Teso, E. D. Filho, and A. A. Neto, *J. Math. Biol.,* **35,** 814 (1997). Solution of the Poisson-Boltzmann Equation for a System with Four Ionic Species.
92. H. Wennerström, B. Jönsson, and P. Linse, *J. Chem. Phys.,* **76,** 4665 (1982). The Cell Model for Polyelectrolyte Systems. Exact Statistical Mechanical Relations, Monte Carlo Simulations, and the Poisson-Boltzmann Approximation.

93. S. Levine and D. G. Hall, *Langmuir,* **8,** 1090 (1992). Electric Double Layer Interactions of Highly Charged Platelike Colloidal Plates.

94. A. W. C. Lau, and P. Pincus, *Eur. Phys. J. B,* **10,** 175 (1999). Binding of Oppositely Charged Membranes and Membrane Reorganization.

95. A. Diehl, M. N. Tamashiro, M. C. Barbosa, and Y. Levin, *Physica A,* **274,** 433 (1999). Density-Functional Theory for Attraction between like-Charged Plates.

96. S. J. Zara, D. Nicholson, N. G. Parsonage, and J. Barber, *J. Colloid Interface Sci.,* **129,** 297 (1989). Mixed Valency Counterions between Charged Walls: An Investigation Using Monte Carlo Simulation and Comparison with Poisson-Boltzmann Theory.

97. W. H. Briscoe and P. Attard, *J. Chem. Phys.,* **117,** 5452 (2002). Counterion-Only Electrical Double Layer: A Constrained Entropy Approach.

98. D. N. Card and J. P. Valleau, *J. Chem. Phys.,* **52,** 6232 (1970). Monte Carlo Study of the Thermodynamics of Electrolyte Solutions.

99. I. Ruff, *Chem. Phys. Lett.,* **93,** 553 (2002). A Formal Mathematical Legalization of the "Exponential" Debye-Hückel Theory.

100. Y. Levin, *Reports Prog. Phys.,* **65,** 1577 (2002). Electrostatic Correlations: From Plasma and Biology.

101. P. Attard, D. J. Mitchell, and B. W. Ninham, *J. Chem. Phys.,* **89,** 4358 (1988). Beyond Poisson-Boltzmann: Images and Correlations in the Electric Double Layer. II. Symmetric Electrolyte.

102. R. Kjellander, *Ber. Bunsenges. Phys. Chem.,* **100,** 894 (1996). Ion-Ion Correlations and Effective Charges in Electrolyte and Macroion Systems.

103. J. T. G. Overbeek, *Molec. Phys.,* **80,** 685 (1993). On the Interaction of Highly Charged Plates in an Electrolyte: A Correction.

104. J. C. Neu, *Phys. Rev. Lett.,* **82,** 1072 (1999). Wall-Mediated Forces between Like-Charged Bodies in an Electrolyte.

105. J. E. Sader and D. Y. C. Chan, *J. Colloid Interface Sci.,* **213,** 268 (1999). Long-Range Electrostatic Attractions between Identically Charged Particles in Confined Geometries: An Unresolved Problem.

106. J. E. Sader and D. Y. C. Chan, *Langmuir,* **16,** 324 (2000). Long-Range Electrostatic Attractions between Identically Charged Particles in Confined Geometries and the Poisson-Boltzmann Theory.

107. I. Langmuir, *J. Chem. Phys.,* **6,** 873 (1938). The Role of Attractive and Repulsive Forces in the Formation of Tactoids, Thixotropic Gels, Protein Crystals and Coacervates.

108. E. A. Marshall, *J. Theor. Biol.,* **81,** 613 (1979). On the Exact Analytical Solution of the Poisson-Boltzmann Equation.

109. N. Martinov, D. Ouroushev, and M. Georgiev, *J. Phys. C,* **17,** 5175 (1984). Energy Bands Induced by Self-Consistent Coulomb Structures.

110. D. Ouroushev, *J. Phys. A,* **21,** 2587 (1988). Localisation of Charges According to the Non-Linear Self-Consistent Electrostatic (Poisson-Boltzmann) Theory.

111. B. W. Ninham and V. A. Parsegian, *J. Theor. Biol.,* **31,** 405 (1971). Electrostatic Potential between Surfaces Bearing Ionizable Groups in Ionic Equilibrium with Physiologic Saline Solution.

112. R. Hogg, T. W. Healy, and D. W. Fuerstenau, *Trans. Faraday Soc.,* **62,** 1638 (1966). Mutual Coagulation of Colloidal Dispersions.

113. P. Richmond, *J. Chem. Soc. Faraday Trans. 2,* **70,** 1066 (1973). Electrical Forces between Particles with Arbitrary Fixed Surface Charge Distributions in Ionic Solution.

114. D. McCormack, S. Carnie, and D. Y. C. Chan, *J. Colloid Interface Sci.,* **169,** 177 (1995). Calculations of Electric Double-Layer Force and Interaction Free Energy between Dissimilar Surfaces.

115. D. Chan, J. W. Perram, L. R. White, and T. W. Healy, *J. Chem. Soc. Faraday Trans.,* **71,** 1046 (1975). Regulation of Surface Potential at Amphoteric Surfaces during Particle-Particle Interaction.

116. D. Chan, T. W. Healy, and L. R. White, *J. Chem. Soc. Faraday Trans.,* **72,** 2844 (1976). Electrical Double Layer Interactions Under Regulation by Surface Ionization Equilibria—Dissimilar Amphoteric Surfaces.

117. T. W. Healy, D. Chan, and L. R. White, *Pure Appl. Chem.,* **52,** 1207 (1980). Colloidal Behaviour of Materials with Ionizable Group Surfaces.

118. S. Carnie and D. Y. C. Chan, *J. Colloid Interface Sci.,* **161,** 260 (1993). Interaction Free Energy between Plates with Charge Regulation: A Linearized Model.

119. R. Ettelaie and R. Buscall, *Adv. Colloid Interface Sci.,* **61,** 131 (1995). Electrical Double Layer Interactions for Spherical Charge Regulating Colloidal Particles.

120. S. H. Behrens and M. Borkovec, *J. Chem. Phys.,* **111,** 382 (1999). Electric Double Layer Interaction of Ionizable Surfaces: Charge Regulation for Arbitrary Potential.

121. S. H. Behrens and M. Borkovec, *Phys. Rev. E,* **60,** 7040 (1999). Exact Poisson-Boltzmann Solution for the Interaction of Dissimilar Charge-Regulating Surfaces.

122. R. B. McBroom and D. A. McQuarrie, *Cell Biophys.,* **11,** 65 (1987). Interaction of Planar Double Layers in the Modified Gouy-Chapman Approximation.

123. Y. Burak and D. Andelman, *Phys. Rev. E,* **62,** 5296 (2000). Hydration Interactions: Aqueous Solvent Effects in Electric Double Layers.

124. M. Bostrom, D. R. M. Williams, and B. W. Ninham, *Phys. Rev. Lett.,* **87,** 168103 (2001). Specific Ion Effects: Why DLVO Theory Fails for Biology and Colloid Systems.

125. M. Bostrom, D. R. M. Williams, and B. W. Ninham, *J. Phys. Chem. B,* **106,** 7908 (2002). The Influence of Ionic Dispersion Potentials on Counterion Condensation on Polyelectrolytes.

126. S. Levine and A. Suddaby, *Proc. Roy. Soc. Lond.,* **64,** 287 (1951). Simplified Forms for Free Energy of the Double Layers of Two Plates in a Symmetrical Electrolyte.

127. S. Levine and J. E. Jones, *Kolloid Z.,* **230,** 306 (1969). Interaction of Two Parallel Colloidal Plates in an Electrolyte Mixture of Univalent and Divalent Ions.

128. G. M. Bell, S. Levine, and L. N. McCartney, *J. Colloid Interface Sci.,* **33,** 335 (1970). Approximate Methods of Determining the Double-Layer Free Energy of Interaction between Two Charged Colloidal Spheres.

129. J. P. Valleau and G. M. Torrie, *J. Chem. Phys.,* **76,** 4623 (1982). The Electrical Double Layer. III. Modified Gouy-Chapman Theory with Unequal Ion Sizes.

130. J. Bentz and S. Nir, *Bull. Math. Biol.,* **42,** 191 (1980). Cation Binding to Membranes: Competition between Mono-, Di- and Trivalent Cations.

131. J. M. Bloch and W. Yun, *Phys. Rev. A,* **41,** 844 (1990). Condensation of Monovalent and Divalent Metal Ions on a Langmuir Monolayer.

132. I. Borukhov, D. Andelman, and H. Orland, *Phys. Rev. Lett.,* **79,** 435 (1997). Steric Effects in Electrolytes: A Modified Poisson-Boltzmann Equation.

133. I. Borukhov, D. Andelman, and H. Orland, *Electrochim. Acta,* **46,** 221 (2000). Adsorption of Large Ions from an Electrolyte Solution: A Modified Poisson-Boltzmann Equation.

134. R. E. Goldstein, A. I. Pesci, and V. Romero-Rochin, *Phys. Rev. A,* **41,** 5504 (1990). Electric Double Layers Near Modulated Surfaces.

135. E. Evans and J. Ipsen, *Electrochim. Acta,* **36,** 1735 (1991). Entropy-Driven Expansion of Electric Dipole Layer Repulsion between Highly Flexible Membranes.

136. A. P. Nelson and D. A. McQuarrie, *J. Theor. Biol.,* **55,** 13 (1975). The Effect of Discrete Charges on the Electrical Properties of a Membrane. I.

137. R. Sauve and S. Ohki, *J. Theor. Biol.,* **81,** 157 (1979). Interaction of Divalent Cations with Negatively Charged Membrane Surfaces. I. Discrete Charge Potential.

138. S. J. Miklavic, *J. Colloid Interface Sci.,* **171,** 446 (1995). Mean-Field Potential for Heterogeneous Electrical Double Layers, with Application to the Surface Pressure of Charged Monolayers.

139. R. M. Peitzsch, M. Eisenberg, K. A. Sharp, and S. Mclaughlin, *Biophys. J.,* **68,** 729 (1995). Calculations of the Electrostatic Potential Adjacent to Model Phospholipid Bilayers.

140. S. Kirchner, *Biochem. Biophys. Acta,* **1279,** 181 (1996). Direct Measurement of Ion Distributions between Lipid Membranes with X-Ray Diffraction.

141. J.-P. Hsu and M. T. Tseng, *J. Chem. Phys.,* **104,** 242 (1995). Solution to Linearized Poisson-Boltzmann Equation with Mixed Boundary Condition.

142. V. M. Aguilella, S. Mafe, and J. A. Manzanares, *Chem. Phys. Lipids,* **105,** 225 (2000). Double Layer Potential and Degree of Dissociation in Charged Lipid Monolayers.

143. D. A. McQuarrie and P. Mulas, *Biophys. J.,* **17,** 103 (1977). Asymmetric Charge Distributions in Planar Bilayer Systems.

144. H. Ohshima and S. Ohki, *Biophys. J.,* **47,** 673 (1985). Donnan Potential and Surface Potential of a Charged Membrane.

145. S. Genet, R. Costalat, and J. Burger, *Acta BioTheor.,* **48,** 273 (2000). A Few Comments on Electrostatic Interactions in Cell Physiology.

146. J.-P. Hsu and Y.-C. Kuo, *J. Chem. Soc. Faraday Trans.,* **91,** 1223 (1995). Solution to the Poisson-Boltzmann Equation for Particles Covered by an Ion-Penetrable Charged Membrane.

147. J.-P. Hsu and Y.-C. Kuo, *J. Colloid Interface Sci.,* **171,** 331 (1995). Properties of a Double Layer with Asymmetric Electrolytes: Cylindrical and Spherical Particles with an Ion-Penetrable Membrane.

148. Y.-C. Kuo and J.-P. Hsu, *J. Chem. Phys.,* **102,** 1806 (1995). Exact Solution to Linearized Poisson-Boltzmann Equation: Ion-Penetrable Membranes Bearing Nonuniformly Distributed Fixed Charges.

149. J.-P. Hsu and Y.-C. Kuo, *J. Colloid Interface Sci.,* **176,** 256 (1995). Net Penetration Charges of an Ion-Penetrable Membrane in a General Electrolyte Solution.

150. Y.-C. Kuo and J.-P. Hsu, *J. Phys. Chem. B,* **103,** 9743 (1999). Double-Layer Properties of an Ion-Penetrable Charged Membrane: Effect of Sizes of Charged Species.

151. J.-P. Hsu and Y.-C. Kuo, *J. Chem. Phys.,* **111,** 4807 (1999). Modified Gouy-Chapman Theory for an Ion-Penetrable Charged Membrane.

152. Y.-C. Kuo, *J. Chem. Phys.,* **118,** 398 (2003). Effects of Sizes of Charged Species on the Flocculation of Biocolloids: Absorption of Cations in Membrane Layer.

153. J.-P. Hsu and S.-W. Huang, *J. Phys. Chem. B,* **107,** 265 (2003). Effect of Ionic Sizes on the Electrokinetic Flow in a Planar Slit Covered by an Ion-Penetrable Charged Membrane.

154. E. Trizac and J.-P. Hansen, *J. Phys. Condensed Matter,* **9,** 2683 (1997). The Wigner-Seitz Model for Concentrated Clay Suspensions.

155. E. Trizac and J.-P. Hansen, *Phys. Rev. E,* **56,** 3137 (1997). Wigner-Seitz Model of Charged Lamellar Colloidal Dispersion.

156. H. Ohshima, *Colloids Surf. A,* **146,** 213 (1999). Approximate Expression for the Potential Energy of Double-Layer Interaction between Two Parallel Similar Plates with Constant Surface Potential.

157. D. Y. C. Chan, *J. Colloid Interface Sci.,* **245,** 307 (2002). A Simple Algorithm for Calculating Electrical Double Layer Interactions in Asymmetric Electrolytes—Poisson-Boltzmann Theory.

158. J. R. Philip and R. A. Wooding, *J. Chem. Phys.,* **52,** 953 (1970). Solution of the Poisson-Boltzmann Equation about a Cylindrical Particle.

159. J.-Y. Parlange, *J. Chem. Phys.,* **57,** 376 (1972). Note on the Poisson-Boltzmann Equation.

160. A. D. MacGillivray, *J. Chem. Phys.,* **57,** 4071 (1972). Lower Bounds on Solutions of the Poisson-Boltzmann Equation Near the Limit of Infinite Dilution.

161. A. D. MacGillivray, *J. Chem. Phys.,* **56,** 80 (1972). Upper Bounds on Solutions of the Poisson-Boltzmann Equation Near the Limit of Infinite Dilution.
162. N. Anderson and A. M. Arthurs, *J. Math. Anal. Appl.,* **103,** 148 (1984). Bounds for the Solution of the Poisson-Boltzmann Equation about a Cylindrical Particle.
163. G. V. Ramanathan and C. P. Woodbury, Jr., *J. Chem. Phys.,* **82,** 1482 (1985). The Cell Model for Polyelectrolytes with Added Salt.
164. R. Natarajan and R. S. Schechter, *J. Colloid Interface Sci.,* **113,** 241 (1986). The Solution of the Nonlinear Poisson-Boltzmann Equation for Thick, Spherical Double Layers.
165. S. S. Dukhin, N. M. Semenichin, and L. M. Shapinskaya, *Doklady Akademii Nauk SSR,* **193,** 540 (1970). Distribution of Potential in the Diffuse Part of the Double Layer of a Spherical Colloidal Particle.
166. V. L. Sigal and N. M. Semenikhin, *J. Chem. Phys.,* **61,** 2170 (1974). On Solution of the Unidimensional Nonlinear Poisson-Boltzmann Equation.
167. B. Abraham-Shrauner, *J. Colloid Interface Sci.,* **44,** 79 (1973). Nonlinear Poisson-Boltzmann Potential for a Uniformly Charged Dielectric Sphere in an Electrolyte.
168. A. N. Stokes, *J. Chem. Phys.,* **65,** 261 (1976). Asymptotic Relations for Solutions of the Poisson-Boltzmann Equation for a Spherical Particle.
169. D. J. Mitchell and B. W. Ninham, *J. Phys. Chem.,* **87,** 2996 (1983). Electrostatic Curvature Contributions to Interfacial Tension of Micellar and Microemulsion Phases.
170. D. F. Evans and B. W. Ninham, *J. Phys. Chem.,* **87,** 5025 (1983). Ion Binding and the Hydrophobic Effect.
171. H. N. W. Lekkerkerker, *Physica A,* **159,** 319 (1989). Contribution of the Electric Double Layer to the Curvature Elasticity of Charged Amphiphilic Monolayers.
172. C. J. Benham, *J. Chem. Phys.,* **79,** 1969 (1983). The Cylindrical Poisson-Boltzmann Equation. I. Transformations and General Solutions.
173. V. V. Panjukov, *J. Colloid Interface Sci.,* **110,** 556 (1986). The Surface Charge Density/Surface Potential Relationship and the Poisson-Boltzmann Equation.
174. G. A. Van Aken, H. N. W. Lekkerkerker, J. T. G. Overbeek, and P. L. De Bruyn, *J. Phys. Chem.,* **94,** 8468 (1990). Adsorption of Monovalent Ions in Thin Sherical and Cylindrical Diffuse Electrical Double Layers.
175. H. Ohshima, *J. Colloid Interface Sci.,* **200,** 291 (1998). Surface Charge Density/Surface Potential Relationship for a Cylindrical Particle in an Electrolyte Solution.
176. A. L. Loeb, J. T. G. Overbeek, and P. H. Wiersma, *The Electrical Double Layer Around a Spherical Colloid Particle,* MIT Press, Cambridge, MA, 1961.
177. M. Guéron and G. Weisbuch, *Biopolymers,* **19,** 353 (1980). Polyelectrolyte Theory. I. Counterion Accumulation, Site-Binding, and Their Insensitivity to Polyelectrolyte Shape in Solutions Containing Finite Salt Concentrations.
178. M. Le Bret and B. H. Zimm, *Biopolymers,* **23,** 287 (1984). Distribution of Counterions around a Cylindrical Polyelectrolyte and Manning's Condensation Theory.
179. G. A. Martynov, *Colloid J.,* **38,** 995 (1976). Solution of the Nonlinear Poisson-Boltzmann Equation for a Sphere.
180. G. A. Martynov and S. M. Avdeev, *Colloid J.,* **44,** 626 (1983). Solution of the Nonlinear Poisson-Boltzmann Equation. I. Outer and Inner Problems for a Cylinder.
181. G. A. Martynov and S. M. Avdeev, *Colloid J.,* **45,** 200 (1983). Solution of the Nonlinear Poisson-Boltzmann Equation. 2. Potential Inside a Flat Slit and Inside or Around a Sphere.
182. F. Fogolari, P. Zuccato, G. Esposito, and P. Viglino, *Biophys. J.,* **76,** 1 (1999). Biomolecular Electrostatics with the Linearized Poisson-Boltzmann Equation.
183. L. Bocquet, E. Trizac, and M. Aubony, *J. Chem. Phys.,* **117,** 8138 (2002). Effective Charge Saturation in Colloidal Suspensions.
184. E. Trizac, L. Bocquet, and M. Aubony, *Phys. Rev. Lett.,* **89,** 248301-1 (2002). Simple Approach for Charge Renormalization in Highly Charged Macroions.

185. Z.-W. Wang, G.-Z. Li, D.-R. Guan, X.-Z. Yi, and A.-J. Lou, *J. Colloid Interface Sci.,* **246,** 302 (2002). The Surface Potential of a Spherical Colloid Particle: Functional Theoretical Approach.

186. S. L. Brenner and D. A. McQuarrie, *J. Colloid Interface Sci.,* **44,** 298 (1973). On the Theory of the Electrostatic Interaction between Parallel Cylindrical Polyelectrolytes.

187. B. Enos, D. A. McQuarrie, and P. Colonomos, *J. Colloid Interface Sci.,* **52,** 289 (1975). Force Balance in Systems of Spherical Polyelectrolytes.

188. N. E. Hoskin and S. Levine, *Phil. Trans. Roy. Soc. Lond. A,* **248,** 449 (1956). The Interaction of Two Identical Spherical Colloidal Particles. II. The Free Energy.

189. G. B. Arfken and H. J. Weber, *Mathematical Methods for Physicists,* Academic Press, New York, 1995.

190. N. Anderson and A. M. Arthurs, *J. Math. Phys.,* **9,** 2037 (1968). Variational Solutions of Nonlinear Poisson-Boltzmann Boundary-Value Problems.

191. A. M. Arthurs and P. D. Robinson, *Proc. Cambridge Phil. Soc.,* **65,** 535 (1969). Complementary Variational Principles for $\Delta^2\phi = F(\phi)$ with Applications to the Thomas-Fermi and Liouville Equations.

192. A. M. Arthurs, *Complementary Variational Principles,* Clarendon Press, Oxford, 1970.

193. W. Olivares and D. A. McQuarrie, *Biophys. J.,* **15,** 143 (1975). On the Theory of Ionic Solutions.

194. S. L. Brenner and R. E. Roberts, *J. Phys. Chem.,* **77,** 2367 (1973). A Variational Solution of the Poisson-Boltzmann Equation for a Spherical Colloidal Particle.

195. E. S. Reiner and C. J. Radke, *J. Chem. Soc. Faraday Trans.,* **86,** 3901 (1990). Variational Approach to the Electrostatic Free Energy in Charged Colloidal Suspensions: General Theory for Open Systems.

196. C. F. Anderson and M. T. Record, Jr., *Annu. Rev. Biophys. Biophys. Chem.,* **19,** 423 (1990). Ion Distributions around DNA and Other Cylindrical Polyions: Theoretical Descriptions and Physical Implications.

197. C. F. Anderson and M. T. Record, Jr., *Annu. Rev. Phys. Chem.,* **46,** 657 (1995). Salt-Nucleic Acid Interactions.

198. J. M. Ziman, *Principles of the Theory of Solids,* Cambridge Univ. Press, London, 1972.

199. G. W. Walker, *Proc. Roy. Soc.,* **A91,** 410 (1915). Some Problems Illustrating the Forms of Nebula.

200. R. M. Fuoss, A. Katchalsky, and S. Lifson, *Proc. Natl. Acad. Sci. (USA),* **37,** 579 (1951). The Potential of an Infinite Rod-Like Molecule and the Distribution of the Counterions.

201. T. Alfrey, Jr., P. W. Berg, and H. Morawetz, *J. Polym. Sci.,* **VII,** 543 (1951). The Counterion Distribution in Solution of Rod-Shaped Polyelectrolytes.

202. D. Dolar and J. Skerjanc, *J. Polym. Sci. Polym. Phys.,* **14,** 1005 (1976). Osmotic Coefficient of a Polyelectrolyte Solution with a Mixture of Monovalent Counterions.

203. T. Akesson and B. Jönsson, *Electrochim. Acta,* **36,** 1723 (1991). Monte Carlo Simulations of Colloidal Stability—beyond the Poisson-Boltzmann Approximation.

204. J. S. McCaskill and E. D. Fackerell, *J. Chem. Soc. Faraday Trans. 2,* **84,** 161 (1988). Painléve Solution of the Poisson-Boltzmann Equation for a Cylindrical Poly-Electrolyte in Excess Salt Solution.

205. C. A. Tracy and H. Widom, *Physica A,* **244,** 402 (1997). On Exact Solutions to the Cylindrical Poisson-Boltzmann Equation with Applications to Polyelectrolytes.

206. A. Katchalsky, Z. Alexandrowicz, and O. Kedem, in *Chemical Physics of Ionic Solutions; a Selection of Invited Papers and Discussions*, B. E. Conway, Ed., Wiley, New York, 1966, pp. 295–346. Polyelectrolyte Solutions.

207. L. Belloni, M. Drifford, and P. Turq, *Chem. Phys.,* **83,** 147 (1984). Counterion Diffusion in Polyelectrolyte Solutions.

208. G. Lamm, L. Wong, and G. R. Pack, *Biopolymers,* **34,** 227 (1994). Monte Carlo and Poisson-Boltzmann Calculations of the Fraction of Counterions Bound to DNA.

209. G. R. Pack, L. Wong and G. Lamm, *Biopolymers,* **49,** 575 (1999). Divalent Cations and the Electrostatic Potential around DNA: Monte Carlo and Poisson-Boltzmann Calculations.

210. D. Dolar and A. Peterlin, *J. Chem. Phys.,* **50,** 3011 (1969). Rodlike Model for a Polyelectrolyte Solution with Mono- and Divalent Counterions.

211. M. Deserno and C. Holm, *Molec. Phys.,* **100,** 2941 (2002). Theory and Simulations of Rigid Polyelectrolytes.

212. H. Van Keulen and J. A. M. Smit, *J. Colloid Interface Sci.,* **170,** 134 (1995). Approximate Analytical Solutions of the Poisson-Boltzmann Equation for Charged Rods in the Presence of Salt: An Analysis of the Cylindrical Cell Model.

213. M. Abramowitz and I. A. Stegun, *Handbook of Mathematical Functions,* Dover, New York, 1972.

214. G. S. Manning, *Quart. Rev. Biophys.,* **2,** 179 (1978). The Molecular Theory of Polyelectrolyte Solutions with Applications to the Electrostatic Properties of Polynucleotides.

215. D. Stigter, *J. Colloid Interface Sci.,* **53,** 296 (1975). The Charged Colloidal Cylinder with a Gouy Double Layer.

216. J. A. Schellman and D. Stigter, *Biopolymers,* **16,** 1415 (1977). Electrical Double Layer, Zeta Potential, and Electrophoretic Charge of Double-Stranded DNA.

217. D. Stigter, *Biopolymers,* **16,** 1435 (1977). Interactions of Highly Charged Colloidal Cylinders with Applications to Double-Stranded DNA.

218. D. Stigter, *J. Phys. Chem.,* **82,** 1603 (1978). A Comparison of Manning's Polyelectrolyte Theory with the Cylindrical Gouy Model.

219. D. Stigter and K. A. Dill, *J. Phys. Chem.,* **97,** 12995 (1993). Theory for Second Virial Coefficients of Short DNA.

220. S. L. Brenner and D. A. McQuarrie, *Biophys. J.,* **13,** 301 (1973). Force Balances in Systems of Cylindrical Polyelectrolytes.

221. I. S. Gradshteyn and I. M. Ryzhik, *Tables of Integrals, Series, and Products*, Academic Press, New York, 1994.

222. G. N. Watson, *A Treatise on the Theory of Bessel Functions,* Cambridge Univ. Press, Cambridge, UK, 1995.

223. S. L. Brenner and V. A. Parsegian, *Biophys. J.,* **14,** 327 (1974). A Physical Method for Deriving the Electrostatic Interaction Between Rod-Like Polyions at All Mutual Values.

224. L. Dresner and K. A. Kraus, *J. Phys. Chem.,* **67,** 990 (1963). Ion Exclusion and Salt Filtering with Porous Ion-Exchange Materials.

225. W. Olivares, T. L. Croxton, and D. A. McQuarrie, *J. Phys. Chem.,* **84,** 867 (1980). Electrokinetic Flow in a Narrow Cylindrical Capillary.

226. M. A. Lampert and R. U. Martinelli, *Chem. Phys.,* **88,** 399 (1984). Solution of the Non-Linear Poisson-Boltzmann Equation in the Interior of Charged, Spherical and Cylindrical Vesicles. I. The High-Charge Limit.

227. H.-K. Tsao, *J. Phys. Chem. B,* **102,** 10243 (1998). Counterion Distribution Enclosed in a Cylinder and a Sphere.

228. C. L. Rice and R. Whitehead, *J. Phys. Chem.,* **69,** 4017 (1965). Electrokinetic Flow in a Narrow Cylindrical Capillary.

229. S. Levine, J. R. Marriott, G. Neale and E. Epstein, *J. Colloid Interface Sci.,* **52,** 136 (1975). Theory of Electrokinetic Flow in Fine Cylindrical Capillaries at High Zeta-Potentials.

230. S. L. Brenner and D. A. McQuarrie, *J. Theor. Biol.,* **39,** 343 (1973). A Self-Consistent Calculation of the Free Energy and Electrostatic Potential for a Cylindrical Polyion.

231. J. Bentz, *J. Colloid Interface Sci.,* **90,** 164 (1982). Electrostatic Potential between Concentric Surfaces: Spherical, Cylindrical, and Planar.

232. V. Vlachy and A. D. J. Haymet, *J. Am. Chem. Soc.,* **111,** 477 (1989). Electrolytes in Charged Micropores.

233. V. Vlachy and A. D. J. Haymet, *J. Electroanal. Chem.,* **283,** 77 (1990). Salt Exclusion from Charged and Uncharged Micropores.

234. V. Vlachy and A. D. J. Haymet, *Austral. J. Chem.,* **43,** 1961 (1990). Electrolytes in Micropores.

235. B. Jamnik and V. Vlachy, *J. Am. Chem. Soc.,* **115,** 660 (1993). Monte Carlo and Poisson-Boltzmann Study of Electrolyte Exclusion from Charged Cyindrical Micropores.

236. B. Jamnik and V. Vlachy, *J. Am. Chem. Soc.,* **117,** 8010 (1995). Ion Partitioning between Charged Micropores and Bulk Electrolyte Solution. Mixtures of Mono- and Divalent Counterions and Monovalent Co-Ions.

237. L. Yeomans, S. E. Feller, E. Sanchez, and M. Lozada-Cassou, *J. Chem. Phys.,* **98,** 1436 (1993). The Structure of Electrolytes in Cylindrical Pores.

238. L. Martinez, A. Hernandez, A. Gonzalez, and F. Tejerina, *J. Colloid Interface Sci.,* **152,** 325 (1992). Use of Variational Methods to Establish and Increase the Ranges of Application of Analytic Solutions of the Poisson-Boltzmann Equation for a Charged Microcapillary.

239. H. Van Keulen and J. A. M. Smit, *J. Colloid Interface Sci.,* **151,** 546 (1992). Analytical Approximations for Potential Profiles in Charged Micropores Originating from the Poisson-Boltzmann Equation.

240. R. E. Rice and F. H. Horne, *J. Chem. Phys.,* **75,** 5582 (1981). Analytical Solution of the Linearized Poisson-Boltzmann Equation in Cylindrical Coordinates.

241. R. E. Rice and F. H. Horne, *J. Colloid Interface Sci.,* **105,** 172 (1985). Analytical Solutions to the Linearized Poisson-Boltzmann Equation in Cylindrical Coordinates for Different Ionic-Strength Distributions.

242. A. O. Sharif, Z. Tabatabaian, and W. R. Bowen, *J. Colloid Interface Sci.,* **255,** 138 (2002). The Wall and Multivalent Counterion Effects on the Electrostatic Force Between Like-Charged Spherical Particles Confined in a Charged Pore.

243. J. C. Gil Montoro and J. L. F. Abascal, *Molec. Phys.,* **89,** 1071 (1996). Discrete Charge Effects on the Structure of Ions around Polyelectrolyte Models.

244. J. C. Gil Montoro and J. L. F. Abascal, *J. Chem. Phys.,* **109,** 6200 (1998). Ionic Distribution around Simple B-DNA Models. II. Deviations Form Cylindrical Symmetry.

245. D. Ouroushev, *Phil. Mag. B,* **80,** 1473 (2000). Electric Field of a Charged Dielectric Cylinder with Counterions: Application to B-DNA.

246. T. Nishio and A. Minakata, *J. Chem. Phys.,* **113,** 10784 (2000). Effects of Ion Size and Valence on Ion Distribution in Mixed Counterion Systems of Rodlike Polyelectrolyte Solution. I. Mixed-Size Counterion Systems with Same Valence.

247. A. J. Mokady, A. J. Mestel, and C. P. Winlove, *J. Fluid Mech.,* **383,** 353 (1999). Flow through a Charged Biopolymer Layer.

248. S. A. Allison, *J. Phys. Chem.,* **98,** 12091 (1994). End Effects in Electrostatic Potentials of Cylinders: Models for DNA Fragments.

249. R. M. Nyquist, B.-Y. Ha, and A. J. Liu, *Macromolecules,* **32,** 3481 (1999). Counterion Condensation in Solutions of Rigid Polyelectrolytes.

250. A. Fogden, J. Daicic, D. J. Mitchell, and B. W. Ninham, *Physica A,* **234,** 167 (1996). Electrostatic Rigidity of Charged Membranes in Systems without Added Salt.

251. J. Daicic, A. Fogden, I. Carlsson, H. Wennerström, and B. Jönsson, *Phys. Rev. E,* **54,** 3984 (1996). Bending of Ionic Surfactant Monolayers.

252. T. Chou, M. V. Jaric, and E. D. Siggia, *Biophys. J.,* **72,** 2042 (1997). Electrostatics of Lipid Bilayer Bending.

253. A. Fogden, I. Carlsson, and J. Daicic, *Phys. Rev. E,* **57,** 5694 (1998). Beyond the Harmonic Bending Theory of Ionic Surfactant Interfaces.

254. A. Fogden and B. W. Ninham, *Adv. Colloid Interface Sci.*, **83,** 85 (1999). Electrostatics of Curved Fluid Membranes: The Interplay of Direct Interactions and Fluctuations in Charged Lamellar Phases.

255. W. R. Bowen and F. Jenner, *J. Colloid Interface Sci.*, **173,** 388 (1995). Electroviscous Effects in Charged Capillaries.

256. Y. Qian, G. Yang, and W. R. Bowen, *J. Colloid Interface Sci.*, **190,** 55 (1997). An Algorithm for the Calculation of the Electrical Potential Distribution in a Charged Capillary with General Electrolytes.

257. E. Trizac and J.-P. Hansen, *J. Physics Condensed Matter,* **8,** 9191 (1996). Free Energy of Electric Double Layers around Finite Particles.

258. J.-P. Hansen and E. Trizac, *Physica A,* **235,** 257 (1997). Electric Double Layers around Finite-Size Clay Particles.

259. R. J. F. Leote De Carvalho, E. Trizac, and J.-P. Hansen, *Phys. Rev. E,* **61,** 1634 (2000). Nonlinear Poisson-Boltzmann Theory of a Wigner-Seitz Model for Swollen Clays.

260. D. G. Rowan, J.-P. Hansen, and E. Trizac, *Molec. Phys.,* **98,** 1369 (2000). Screened Electrostatic Interactions between Clay Platelets.

261. F. Oosawa, *Polyelectrolytes,* Marcel Dekker, New York, 1971.

262. M. D. Frank-Kamenetskii, V. V. Anshellevich, and A. V. Lukashin, *Sov. Phys. Usp.,* **30,** 317 (1987). Polyelectrolyte Model of DNA.

263. A. N. Lane and T. C. Jenkins, *Quart. Rev. Biophys.,* **33,** 255 (2000). Thermodynamics of Nucleic Acids and Their Interactions with Ligands.

264. E. Raspaud, M. Da Conceicao, and F. Livolant, *Phys. Rev. Lett.,* **84,** 2533 (2000). Do Free DNA Counterions Control the Osmotic Pressure?

265. J. Blaul, M. Witteman, M. Ballauff, and M. Rehahn, *J. Phys. Chem. B,* **104,** 7077 (2000). Osmotic Coefficient of a Synthetic Rodlike Polyelectrolyte in Salt-Free Solution as a Test of the Poisson-Boltzmann Cell Model.

266. E. K. Zholkovskij, J. Czarnecki, and J. H. Masliyah, *J. Colloid Interface Sci.,* **234,** 293 (2001). Electrostatic Repulsion in Concentrated Disperse Systems. I. Contribution of Electrostatic Interaction to Osmotic Pressure.

267. L. M. Gross and U. P. Strauss, *Chem. Phys. Ionic Solut.*, 361 (1964). Interactions of Polyelectrolytes with Simple Electrolytes. I. Theory of Electrostatic Potential with Donnan Equilibrium for a Cylinder Rod Model: The Effect of Site Binding.

268. C. F. Anderson and M. T. Record, Jr., *Biophys. Chem.,* **11,** 353 (1980). The Relationship between the Poisson-Boltzmann Model and the Condensation Hypothesis: An Analysis Based on the Low Salt Form of the Donnan Coefficient.

269. B. K. Klein, C. F. Anderson, and M. T. Record, Jr., *Biopolymers,* **20,** 2263 (1981). Comparison of Poisson-Boltzmann and Condensation Model Expressions for the Colligative Properties of Cylindrical Polyions.

270. M. T. Record, Jr., M. Olmsted, and C. F. Anderson, *Theor. Biochem. Molec. Biophys.*, 285 (1990). Theoretical Studies of the Thermodynamic Consequences of Interaction of Ions with Polymeric and Oligomeric DNA: The Preferential Interaction Coefficient and Its Application to the Thermodynamic Analysis of Electrolyte Effects on Conformational Stability and Ligand Binding.

271. D. M. Soumpasis, *J. Biomolec. Struct. Dynam.,* **6,** 563 (1988). Salt Dependence of DNA Structural Stabilities in Solution. Theoretical Predictions Versus Experiments.

272. J. G. Duguid and V. A. Bloomfield, *Biophys. J.,* **70,** 2838 (1996). Electrostatic Effects on the Stability of Condensed DNA in the Presence of Divalent Cations.

273. N. Korolev, A. P. Lyubartsev, and L. Nordenskiöld, *Biophys. J.,* **75,** 3041 (1998). Application of Polyelectrolyte Theories for Analysis of DNA Melting in the Presence of Na^+ and Mg^{2+} Ions.

274. V. A. Bloomfield, R. W. Wilson, and D. C. Rau, *Biophys. Chem.,* **11,** 339 (1980). Polyelectrolyte Effects in DNA Condensation by Polyamines.

275. R. W. Wilson, D. C. Rau, and V. A. Bloomfield, *Biophys. J.,* **30,** 317 (1980). Comparison of Polyelectrolyte Theories of the Binding of Cations to DNA.

276. C. Cametti and A. Di Biasio, *Ber. Bunsenges. Phys. Chem.,* **92,** 1089 (1988). Cylindrical Poisson-Boltzmann Equation for Polyelectrolyte Systems and Counterion Condensation Theory.

277. W. F. Moss, S. G. Lagu, D. W. Bearden, G. B. Savitsky, and H. G. Spencer, *Polymer,* **35,** 3268 (1994). Numerical and Experimental Studies of Territorial Binding of Counterions in Polyelectrolyte Solutions Including the Added Salt Case.

278. K. A. Sharp, R. A. Friedman, V. Misra, J. Hecht, and B. Honig, *Biopolymers,* **36,** 245 (1995). Salt Effects on Polyelectrolyte-Ligand Binding: Comparison of Poisson-Boltzmann, and Limiting Law/Counterion Binding Models.

279. G. S. Manning, *Physica A,* **231,** 236 (1996). Counterion Condensation Theory Constructed from Different Models.

280. G. S. Manning, *Ber. Bunsenges. Phys. Chem.,* **100,** 909 (1996). The Critical Onset of Counterion Condensation: A Survey of Its Experimental and Theoretical Basis.

281. P. S. Kuhn, Y. Levin, and M. C. Barbosa, *Macromolecules,* **31,** 8347 (1998). Rodlike Polyelectrolytes in the Presence of Monovalent Salt.

282. L. Belloni, *Colloids Surf. A,* **140,** 227 (1998). Ionic Condensation and Charge Renormalization in Colloidal Suspensions.

283. M. Deserno, C. Holm, and S. May, *Macromolecules,* **33,** 199 (2000). Fraction of Condensed Counterions around a Charged Rod: Comparison of Poisson-Boltzmann Theory and Computer Simulations.

284. H. Qian and J. A. Schellman, *J. Phys. Chem. B,* **104,** 11528 (2000). Transformed Poisson-Boltzmann Relations and Ionic Distributions.

285. A. Deshkovski, S. Obukhov, and M. Rubinstein, *Phys. Rev. Lett.,* **86,** 2341 (2001). Counterion Phase Transitions in Dilute Polyelectrolyte Solutions.

286. H. Löwen, *J. Chem. Phys.,* **100,** 6738 (1994). Charged Rodlike Colloidal Suspensions: An *Ab Initio* Approach.

287. M. T. Record, Jr., C. F. Anderson, and T. M. Lohman, *Quart. Rev. Biophys.,* **2,** 103 (1978). Thermodynamic Analysis of Ion Effects on the Binding and Conformational Equilibria of Proteins and Nucleic Acids: The Roles of Ion Association or Release, and Ion Effects on Water Activity.

288. J. Granot, *Biopolymers,* **22,** 1831 (1983). Effect of Finite Ionic Size on the Solution of the Poisson-Boltzmann Equation: Application to the Binding of Divalent Metal Ions to DNA.

289. M. D. Paulsen, C. F. Anderson, and M. T. Record, Jr., *Biopolymers,* **27,** 1249 (1988). Counterion Exchange Reactions on DNA: Monte Carlo and Poisson-Boltzmann Analysis.

290. J. Skerjanc and D. Dolar, *J. Chem. Phys.,* **91,** 6290 (1989). Thermodynamic Properties of a Polyelectrolyte Solution Containing a Mixture of Counterions Differing in Charge.

291. W. F. Moss, H. G. Spencer, G. B. Savitsky, and C. M. Riedl, *Polymer,* **32,** 1504 (1991). Improved Numerical Modeling of Competitive Counterion Binding in Polyelectrolyte Solutions.

292. F. Fogolari, G. Manzini, and F. Quadrifoglio, *Biophys. Chem.,* **43,** 213 (1992). Polyelectrolytes in Mixed Salts: Scatchard Plots Obtained by Means of Poisson-Boltzmann Calculations.

293. C. Cametti and A. Di Biasio, *Ber. Bunsenges. Phys. Chem.,* **96,** 1877 (1992). Selective Counterion Binding to Linear Polyelectrolytes in Aqueous Solutions.

294. A. Z. Li, H. Huang, X. Re, L. J. Qi, and K. A. Marx, *Biophys. J.,* **74,** 964 (1998). A Gel Electrophoresis Study of the Competitive Effects of Monovalent Counterion on the Extent of Divalent Counterions Binding to DNA.

295. C. C. Correll, B. Freeborn, P. B. Moore, and T. A. Steitz, *Cell,* **91,** 705 (1997). Metals, Motifs, and Recognition in the Crystal Structure of a 5S RNA Domain.

296. F. Eckstein and B. Bramlage, *Biopolymers,* **52,** 147 (1999). The Hammerhead Ribozyme.

297. L. Jovine, S. Djordjevic, and D. Rhodes, *J. Molec. Biol.,* **301,** 401 (2000). The Crystal Structure of Yeast Phenylalanine tRNA at 2.0 Å Resolution: Cleavage by Mg^{2+} in 15-Year Old Crystals.

298. D. Thirumalai, N. Lee, S. Woodson, and D. K. Klimov, *Annu. Rev. Phys. Chem.,* **52,** 751 (2001). Early Events in RNA Folding.

299. S. L. Heilman-Miller, D. Thirumalai, and S. A. Woodson, *J. Molec. Biol.,* **306,** 1157 (2001). Role of Counterion Condensation in Folding of the Tetrahymena Ribozyme. I. Equilibrium Stabilization by Cations.

300. Y. Tanaka, C. Kojima, E. H. Morita, Y. Kasai, K. Yamazaki, A. Ono, M. Kainosho, and K. Taira, *J. Am. Chem. Soc.,* **124,** 4595 (2002). Identification of the Metal Ion Binding Site on an RNA Motif from Hammerhead Ribozymes Using ^{15}N NMR Spectroscopy.

301. I. Rouzina and V. A. Bloomfield, *Biophys. J.,* **74,** 3152 (1998). DNA Bending by Small, Mobile Multivalent Cations.

302. B. I. Kankia and L. A. Marky, *J. Phys. Chem. B,* **103,** 8759 (1999). DNA, RNA, and DNA/RNA Oligomer Duplexes: A Comparative Study of their Stability, Heat, Hydration, and Mg^{2+} Binding Properties.

303. H. Robinson, Y.-G. Gao, R. Sanishvili, A. Joachimiak, and A. H. J. Wang, *Nucleic Acids Res.,* **28,** 1760 (2000). Hexahydrated Magnesium Ions Bind in the Deep Major Groove and at the Outer Mouth of A-Form Nucleic Acid Duplexes.

304. T. K. Chiu and R. E. Dickerson, *J. Molec. Biol.,* **301,** 915 (2000). 1 Å Crystal Structures of B-DNA Reveal Sequence-Specific Binding and Groove-Specific Bending of DNA by Magnesium and Calcium.

305. B. Jerkovic and P. H. Bolton, *Biochemistry,* **40,** 9406 (2001). Magnesium Increases the Curvature of Duplex DNA that Contains dA Tracts.

306. S. P. Bennett and S. E. Halford, *Curr. Top. Cell. Recogn.,* **30,** 57 (1989). Recognition of DNA by Type II Restriction Enzymes.

307. J. D. Taylor, I. G. Badcoe, A. R. Clarke, and S. E. Halford, *Biochemistry,* **30,** 8743 (1991). EcoRV Restriction Endonuclease Binds All DNA Sequences with Equal Affinity.

308. A. Jeltsch, J. Alves, H. Wolfes, G. Maass, and A. Pingoud, *Proc. Natl. Acad. Sci. (USA),* **90,** 8499 (1993). Substrate-Assisted Catalysis in the Cleavage of DNA by the EcoRI and EcoRV Restriction Enzymes.

309. I. B. Vipond and S. E. Halford, *Molec. Microbiol.,* **9,** 225 (1993). Structure-Function Correlation for the EcoRV Restriction Enzyme: From Non-Specific Binding to Specific DNA Cleavage.

310. I. B. Vipond, G. S. Baldwin, and S. E. Halford, *Biochemistry,* **34,** 697 (1995). Divalent Metal Ions at the Active Sites of the EcoRV and EcoRI Restriction Endonucleases.

311. A. Pingoud and A. Jeltsch, *Eur. J. Biochem.,* **246,** 1 (1997). Recognition and Cleavage of DNA by Type-II Restriction Endonucleases.

312. H. Viadiu and A. K. Aggarwal, *Nature Struct. Biol.,* **5,** 910 (1998). The Role of Metals in Catalysis by the Restriction Endonuclease BamHI.

313. M. Guéron, J.-P. Demaret, and M. Filoche, *Biophys. J.,* **78,** 1070 (2000). A Unified Theory of the B-Z Transition of DNA in High and Low Concentrations of Multivalent Ions.

314. M. J. Sparnaay, *Recueil Travaux Chim. Pays-Bas,* **78,** 680 (1959). The Interaction between Two Cylinder Shaped Colloidal Particles.

315. D. Harries, *Langmuir,* **14,** 3149 (1998). Solving the Poisson-Boltzmann Equation for Two Parallel Cylinders.

316. Y.-C. Kuo and J.-P. Hsu, *Langmuir,* **15,** 6244 (1999). Electrical Properties of Charged Cylindrical and Spherical Surfaces in a General Electrolyte Solution.

317. C. A. Bunton and J. R. Moffatt, *J. Phys. Chem.,* **89,** 4166 (1985). Micellar Reactions of Hydrophilic Ions—a Coulombic Model.

318. C. A. Bunton and J. R. Moffatt, *J. Phys. Chem.,* **90,** 538 (1986). Ionic Competition in Micellar Reactions—a Quantitative Treatment.

319. H. Ohshima, T. W. Healy, and L. R. White, *J. Colloid Interface Sci.,* **90,** 17 (1982). Accurate Analytic Expressions for the Surface Charge Density/Surface Potential Relationship and Double-Layer Potential Distribution for a Spherical Colloidal Particle.

320. J.-P. Hsu and Y.-C. Kuo, *J. Colloid Interface Sci.,* **170,** 220 (1995). Approximate Analytical Expression for Surface Potential as a Function of Surface Charge Density.

321. S. Zhou, *J. Colloid Interface Sci.,* **208,** 347 (1998). An Approximate Analytic Expression for the Surface Charge Density/Surface Potential Relationship for a Spherical Colloidal Particle.

322. H. Ohshima, *Colloids Surf. A,* **169,** 13 (2000). Double-Layer Potential Distribution and Surface Charge Density/Surface Potential Relationship for a Nearly Spherical Spheroid in an Electrolyte Solution.

323. H. Ohshima, *J. Colloid Interface Sci.,* **247,** 18 (2002). Surface Charge Density/Surface Potential Relationship for a Spherical Colloidal Particle in a Salt-Free Medium.

324. S. Levine, *Proc. Roy. Soc. Lond. A,* **146,** 597 (1934). Problem of the Sedimentation Equilibrium in Colloidal Suspensions.

325. R. D. Groot, *J. Chem. Phys.,* **95,** 9191 (1991). Ion Condensation on Solid Particles: Theory and Simulations.

326. P. Chen and C.-Y. D. Lu, *Phys. Rev. E,* **61,** 824 (2000). Force between Charged Particles with Ion Condensation.

327. M. A. Lampert and R. S. Crandall, *Chem. Phys. Lett.,* **68,** 473 (1979). Spherical, Nonlinear Poisson-Boltzmann Theory and Its Debye-Hückel Linearization.

328. B. Derjaguin, *Kolloid Z.,* **69,** 155 (1934). Untersuchungen über die Reibung und Adhäsion, IV.

329. A. B. Glendinning and W. B. Russel, *J. Colloid Interface Sci.,* **93,** 95 (1983). The Electrostatic Repulsion between Charged Spheres from Exact Solutions to the Linearized Poisson-Boltzmann Equation.

330. J. E. Sader, S. Carnie, and D. Y. C. Chan, *J. Colloid Interface Sci.,* **171,** 46 (1995). Accurate Analytic Formulas for the Double-Layer Interaction between Spheres.

331. J. E. Ledbetter, T. L. Croxton, and D. A. McQuarrie, *Can. J. Chem.,* **59,** 1860 (1981). The Interaction of Two Charged Spheres in the Poisson-Boltzmann Equation.

332. L. R. White, *J. Colloid Interface Sci.,* **95,** 286 (1983). On the Derjaguin Approximation for the Interaction of Macrobodies.

333. J. T. G. Overbeek, *J. Chem. Soc. Faraday Trans.,* **84,** 3079 (1988). Double-Layer Interaction between Spheres with Unequal Surface Potentials.

334. G. R. Wiese and T. W. Healy, *Trans. Faraday Soc.,* **66,** 490 (1970). Effect of Particle Size on Colloid Stability.

335. S. Usui, *J. Colloid Interface Sci.,* **44,** 107 (1973). Interaction of Electrical Double Layers at Constant Surface Charge.

336. K. D. Papadopoulos and H. Y. Cheh, *AICHE J.,* **30,** 7 (1984). Theory of Colloidal Double-Layer Interactions.

337. H. Ohshima and T. Kondo, *J. Colloid Interface Sci.,* **155,** 499 (1993). Electrostatic Double-Layer Interaction between Two Charged Ion-Penetrable Spheres: An Exactly Solvable Model.

338. H. Ohshima, *J. Colloid Interface Sci.,* **162,** 487 (1994). Electrostatic Interaction between Two Dissimilar Spheres: An Explicit Analytic Expression.

339. H. Ohshima, *J. Colloid Interface Sci.,* **170,** 432 (1995). Electrostatic Interaction between Two Dissimilar Spheres with Constant Surface Charge Density.

340. W. Haoping, J. Jun, and L. Blum, *Colloid Polym. Sci.,* **273,** 359 (1995). Improvement on the Derjaguin's Method for the Interaction of Spherical Particles.

341. S. L. Carnie, D. Y. C. Chan, and J. Stankovich, *J. Colloid Interface Sci.,* **165,** 116 (1994). Computation of Forces between Spherical Colloidal Particles: Nonlinear Poisson-Boltzmann Theory.

342. R. J. Phillips, *J. Colloid Interface Sci.,* **175,** 386 (1995). Calculation of Multisphere Linearized Poisson-Boltzmann Interactions Near Cylindrical Fibers and Planar Surfaces.

343. R. Kjellander and D. J. Mitchell, *Chem. Phys. Lett.,* **200,** 76 (1992). An Exact but Linear and Poisson-Boltzmann-Like Theory for Electrolytes and Colloid Dispersions in the Primitive Model.

344. J. Ennis, R. Kjellander, and D. J. Mitchell, *J. Chem. Phys.,* **102,** 975 (1995). Dressed Ion Theory for Bulk Symmetric Electrolytes in the Restricted Primitive Model.

345. R. Kjellander, *J. Phys. Chem.,* **99,** 10392 (1995). Modified Debye-Hückel Approximation with Effective Charges—an Application of Dressed Ion Theory for Electrolyte Solutions.

346. R. Kjellander and D. J. Mitchell, *Molec. Phys.,* **91,** 173 (1997). Dressed Ion Theory for Electric Double Layer Structure and Interactions: An Exact Analysis.

347. P. M. Morse and H. Feshbach, *Methods of Theoretical Physics,* McGraw-Hill, New York, 1953.

348. B. Halle, *J. Chem. Phys.,* **102,** 7238 (1995). Orientation-Dependent Electrical Double-Layer Interactions. I. Rodlike Macroions of Finite Length.

349. D. Soumpasis, *J. Chem. Phys.,* **69,** 3190 (1978). Debye-Hückel Theory of Model Polyelectrolytes.

350. H.-K. Tsao, *J. Colloid Interface Sci.,* **202,** 527 (1998). Electrostatic Interactions of a String-Like Particle with a Charged Plate.

351. G. A. Carri and M. Muthukumar, *J. Chem. Phys.,* **111,** 1765 (1999). Attractive Interactions and Phase Transitions in Solutions of Similarly Charged Rod-Like Polyelectrolytes.

352. R. Menes, N. Gronbech-Jensen, and P. Pincus, *Eur. Phys. J. E,* **1,** 345 (2000). Interactions between Charged Rods Near Salty Surfaces.

353. A. Vologodskii and N. Cozzarelli, *Biopolymers,* **35,** 289 (1995). Modeling of Long-Range Electrostatic Interactions in DNA.

354. T. Schlick, B. Li and W. K. Olson, *Biophys. J.,* **67,** 2146 (1994). The Influence of Salt on the Structure and Energetics of Supercoiled DNA.

355. T. P. Westcott, I. Tobias, and W. K. Olson, *J. Chem. Phys.,* **107,** 3967 (1997). Modeling Self-Contact Forces in the Elastic Theory of DNA Supercoiling.

356. J. J. Delrow, J. A. Gebe, and J. M. Schurr, *Biopolymers,* **42,** 455 (1997). Comparison of Hard-Cylinder and Screened Coulomb Interactions in the Modeling of Supercoiled DNAs.

357. M. Severin, *Phys. Rev. B,* **52,** 4104 (1995). Monte Carlo Studies of the Temperature-Dependent Size of Polyelectrolyte Chains.

358. M. J. Stevens and K. Kremer, *J. Phys.,* **6,** 1607 (1996). Structure of Salt-Free Linear Polyelectrolytes in the Debye-Hückel Approximation.

359. Th. M. A. O. M. Barenbrug, J. A. M. Smit, and D. Bedeaux, *Macromolecules,* **30,** 605 (1997). Conformational Free Energy of Lattice Polyelectrolytes with Fixed Endpoints. I. Single-Chain Simulation and Theory.

360. M. J. Stevens and S. J. Plimpton, *Eur. Phys. J. B,* **2,** 341 (1998). The Effect of Added Salt on Polyelectrolyte Structure.

361. P. Chodanowski and S. Stoll, *J. Chem. Phys.,* **115,** 4951 (2001). Polyelectrolyte Adsorption on Charged Particles: Ionic Concentration and Particle Size Effects—a Monte Carlo Approach.

362. L. D. Landau and E. M. Lifshitz, *Statistical Physics,* Pergamon Press, Oxford, 1969.

363. J. Bednar, P. Furrer, V. Katritch, A. Z. Stasiak, J. Dubochet, and A. Stasiak, *J. Molec. Biol.,* **254,** 579 (1995). Determination of DNA Persistence Length by Cryo-Electron Microscopy. Separation of the Static and Dynamic Contributions to the Apparent Persistence Length of DNA.

364. T. Odijk, *J. Polym. Sci. Polym. Phys.,* **15,** 477 (1977). Polyelectrolytes Near the Rod Limit.

365. N. Tralli, *Classical Electromagnetic Theory,* McGraw-Hill, New York, 1963.

366. M. Le Bret, *J. Chem. Phys.,* **76,** 6243 (1982). Electrostatic Contribution to the Persistence Length of a Polyelectrolyte.

367. M. Fixman, *J. Chem. Phys.,* **76,** 6346 (1982). The Flexibility of Polyelectrolyte Molecules.

368. M. O. Fenley, G. S. Manning, and W. K. Olson, *J. Phys. Chem.,* **96,** 3963 (1992). Electrostatic Persistence Length of a Smoothly Bending Polyion Computed by Numerical Counterion Condensation Theory.

369. P. J. Hagerman, *Biopolymers,* **22,** 811 (1983). Electrostatic Contribution to the Stiffness of DNA. Molecules of Finite Length.

370. J. Skolnick and M. Fixman, *Macromolecules,* **10,** 944 (1977). Electrostatic Persistence Length of a Wormlike Polyelectrolyte.

371. T. T. Nguyen and B. I. Shklovskii, *Phys. Rev. E,* **66,** 021801 (2002). Persistence Length of a Polyelectrolyte in Salty Water: Monte Carlo Study.

372. M. O. Fenley, W. K. Olson, K. Chua, and A. Boschitsch, *J. Comput. Chem.,* **17,** 976 (1996). Fast Adaptive Multipole Method for Computation of Electrostatic Energy in Simulations of Polyelectrolyte DNA.

373. A. Boschitsch, M. O. Fenley, and W. K. Olson, *J. Comput. Phys.,* **151,** 212 (1999). A Fast Adaptive Multipole Algorithm for Calculating Screened Coulomb (Yukawa) Interactions.

374. A. Boschitsch, M. O. Fenley, and H.-X. Zhou, *J. Phys. Chem. B,* **106,** 2741 (2002). Fast Boundary Element Method for the Linear Poisson-Boltzmann Equation.

375. N. Sun and J. Y. Walz, *J. Colloid Interface Sci.,* **234,** 90 (2001). A Model for Calculating Electrostatic Interactions between Colloidal Particles of Arbitrary Surface Topology.

376. G. Edwards, D. Hochberg, and T. W. Kephart, *Phys. Rev. E,* **50,** R698 (1994). Structure in the Electric Potential Emanating from DNA.

377. K. Wagner, E. Keyes, T. W. Kephart, and G. Edwards, *Biophys. J.,* **73,** 21 (1997). Analytical Debye-Hückel Model for Electrostatic Potentials around Dissolved DNA.

378. D. A. Beard and T. Schlick, *Biopolymers,* **58,** 106 (2001). Modeling Salt-Mediated Electrostatics of Macromolecules: The Discrete Surface Charge Optimization Algorithm and Its Application to the Nucleosome.

379. H.-K. Tsao, *Langmuir,* **16,** 7200 (2000). The Electrostatic Interaction of an Assemblage of Charges with a Charged Surface: The Charge-Regulation Effect.

380. J. G. Kirkwood, *J. Chem. Phys.,* **2,** 351 (1934). Theory of Solutions of Molecules Containing Widely Separated Charges with Special Application to Zwitterions.

381. A. M. Lenhoff, *Colloids Surf. A,* **87,** 49 (1994). Contributions of Surface Features to the Electrostatic Properties of Rough Colloidal Particles.

382. S. Alexander, P. M. Chaikin, P. Grant, G. J. Morales, and P. Pincus, *J. Chem. Phys.,* **80,** 5776 (1984). Charge Renormalization, Osmotic Pressure, and Bulk Modulus of Colloidal Crystals: Theory.

383. T. Gisler, S. F. Schulz, M. Borkovec, and H. Sticher, *J. Chem. Phys.,* **101,** 9924 (1994). Understanding Colloidal Charge Renormalization from Surface Chemistry: Experiment and Theory.

384. M. J. Stevens, M. L. Falk, and M. O. Robbins, *J. Chem. Phys.,* **104,** 5209 (1995). Interactions between Charged Spherical Macroions.

385. G. D. J. Phillies, *J. Chem. Phys.,* **60,** 2721 (1974). Excess Chemical Potential of Dilute Solutions of Spherical Polyelectrolytes.

386. R. B. McClurg and C. F. Zukoski, *J. Colloid Interface Sci.,* **208,** 529 (1998). The Electrostatic Interaction of Rigid, Globular Proteins with Arbitrary Charge Distributions.

387. E. S. Reiner and C. J. Radke, *Adv. Colloid Interface Sci.,* **47,** 59 (1993). Double Layer Interactions between Charge-Regulated Colloidal Surfaces.

388. J.-P. Hsu and B.-T. Liu, *J. Colloid Interface Sci.,* **183,** 214 (1996). Solution to the Linearized Poisson-Boltzmann Equation for a Spheroidal Surface under a General Surface Condition.

389. J.-P. Hsu and B.-T. Liu, *J. Colloid Interface Sci.,* **192,** 481 (1997). Electrostatic Potential Distribution for Spheroidal Surfaces in Symmetric Electrolye Surfaces.

390. B. J. Yoon, *J. Colloid Interface Sci.,* **192,** 503 (1997). Integral Equation Approach for Solving the Nonlinear Poisson-Boltzmann Equation.

391. M. Knott and I. J. Ford, *Phys. Rev. E,* **63,** 1 (2001). Phase Coexistence in Colloidal Suspensions: An Analytical Poisson-Boltzmann Treatment.

392. A. Zydney, *J. Colloid Interface Sci.,* **169,** 476 (1995). Boundary Effects on the Electrophoretic Motion of a Charged Particle in a Spherical Cavity.

393. H.-K. Tsao and Y.-J. Sheng, *J. Colloid Interface Sci.,* **202,** 477 (1998). Electrostatic Interactions for a Particle-Containing Shell-and-Core System.

394. J. J. Lopez-Garcia, J. Horno, and C. Grosse, *J. Colloid Interface Sci.,* **251,** 85 (2002). Numerical Solution of the Poisson-Boltzmann Equation for a Spherical Cavity.

395. P. K. Yuet and D. Blankschtein, *Langmuir,* **11,** 1925 (1995). Approximate Expressions for the Surface Potentials of Charged Vesicles.

396. H. H. von Grünberg and L. Belloni, *Phys. Rev. E,* **62,** 2493 (2000). Eccentric Poisson-Boltzmann Cell Model.

397. A. A. Neto, E. D. Filho, M. A. Fossey, and J. R. Neto, *J. Phys. Chem. B,* **103,** 6809 (1999). p*K* Determination. A Mean Field Poisson-Boltzmann Approach.

398. J.-P. Hsu, W.-C. Hsu, and Y.-I. Chang, *J. Colloid Interface Sci.,* **165,** 1 (1994). Electrostatic Interactions between Two Spherical Particles with a Charged Surface Layer.

399. J.-P. Hsu, *J. Chem. Phys.,* **103,** 465 (1995). Electrostatic Interactions between Particles with an Ion-Penetrable Charged Membrane.

400. J.-P. Hsu and B.-T. Liu, *J. Colloid Interface Sci.,* **190,** 371 (1997). Electrostatic Interaction between Two Ion-Penetrable Charged Spheroids.

401. J.-P. Hsu and M.-T. Tseng, *J. Colloid Interface Sci.,* **184,** 289 (1996). Electrical Potential Distribution for Multiple Charge Surfaces under a General Boundary Condition.

402. H. Ohshima, E. Mishonova, and E. Alexov, *Biophys. Chem.,* **57,** 189 (1996). Electrostatic Interaction between Two Charged Spherical Molecules.

403. J. J. Lopez-Garcia, C. Grosse, and J. Horno, *J. Colloid Interface Sci.,* **254,** 287 (2002). Numerical Study of the Equilibrium Properties of Suspended Particles Surrounded by a Permeable Membrane with Adsorbed Charges.

404. N. E. Hoskin, *Phil. Trans. Roy. Soc. Lond. A,* **248,** 433 (1956). The Interaction of Two Identical Spherical Colloidal Particles. I. Potential Distribution.

405. L. N. McCartney and S. Levine, *J. Colloid Interface Sci.,* **30,** 345 (1969). An Improvement on Derjaguin's Expression at Small Potentials for the Double Layer Interaction Energy of Two Spherical Colloidal Particles.

406. T. A. Ring, *J. Chem. Soc. Faraday Trans. 2,* **78,** 1513 (1982). Double-Layer Interaction Energy for Two Unequal Spheres.

407. J. Stankovich and S. L. Carnie, *Langmuir,* **12,** 1453 (1996). Electrical Double Layer Interaction between Dissimilar Spherical Colloidal Particles and between a Sphere and a Plate: Nonlinear Poisson-Boltzmann Theory.

408. A. J. Jerri and R. L. Herman, *J. Sci. Comput.,* **11,** 127 (1996). The Solution of the Poisson-Boltzmann Equation between Two Spheres: Modified Iterative Method.

409. E. Barouch and S. Kulkarni, *J. Colloid Interface Sci.,* **112,** 396 (1986). Exact Solution of the Poisson-Boltzmann Equation for Two Spheres with Fixed Surface Potentials.

410. S. A. Palkar and A. M. Lenhoff, *J. Colloid Interface Sci.,* **165,** 177 (1994). Energetic and Entropic Contributions to the Interaction of Unequal Spherical Double Layers.

411. A. K. Sengupta and K. D. Papadopoulos, *J. Colloid Interface Sci.,* **149,** 135 (1992). Electrical Double-Layer Interaction between Two Eccentric Spherical Surfaces.

412. J. Stankovich and S. L. Carnie, *J. Colloid Interface Sci.,* **216,** 329 (1999). Interactions between Two Spherical Particles with Nonuniform Surface Potentials: The Linearized Poisson-Boltzmann Theory.

413. G. Binnig, C. F. Quate, and C. Cherber, *Phys. Rev. Lett.,* **56,** 930 (1986). Atomic Force Microscope.

414. W. A. Ducker, T. J. Senden, and R. M. Pashley, *Nature*, 239 (1991). Direct Measurement of Colloidal Forces Using an Atomic Force Microscope.

415. W. A. Ducker, T. J. Senden, and R. M. Pashley, *Langmuir,* **8,** 1831 (1992). Measurement of Forces in Liquids Using a Force Microscope.

416. I. Larson, C. J. Drummond, D. Y. C. Chan, and F. Grieser, *J. Am. Chem. Soc.,* **115,** 11885 (1993). Direct Force Measurements between TiO_2 Surfaces.

417. C. Rotsch and M. Radmacher, *Langmuir,* **13,** 2825 (1997). Mapping Local Electrostatic Forces with the Atomic Force Microscope.

418. W. R. Bowen and T. A. Doneva, *J. Colloid Interface Sci.,* **229,** 544 (2000). Atomic Force Microscopy Studies of Membranes: Effect of Surface Roughness on Double-Layer Interactions and Particle Adhesion.

419. W. R. Bowen, T. A. Doneva, and J. A. G. Stoton, *Colloids Surf. A,* **201,** 73 (2002). The Use of Atomic Force Microscopy to Quantify Membrane Surface Electrical Properties.

420. G. M. Bell and S. Levine, in *Chemical Physics of Ionic Solutions,* B. E. Conway and R. G. Barradas, Eds., Wiley, New York, 1966, pp. 409–454. A Modified Poisson-Boltzmann Equation in Electric Double-Layer Theory.

421. H. Ohshima, *J. Colloid Interface Sci.,* **198,** 42 (1998). Electrostatic Interaction between a Sphere and a Planar Surface: Generalization of Point-Charge/Surface Image Interaction to Particle/Surface Image Interaction.

422. S. L. Carnie, D. Y. C. Chan, and J. S. Gunning, *Langmuir,* **10,** 2993 (1994). Electrical Double Layer Interaction between Dissimilar Spherical Colloidal Particles and between a Sphere and a Plate: The Linearized Poisson-Boltzmann Theory.

423. J. Stahlberg, U. Appelgren, and B. Jönsson, *J. Colloid Interface Sci.,* **176,** 397 (1995). Electrostatic Interactions between a Charged Sphere and a Charged Planar Surface in an Electrolyte Solution.

424. B. Jönsson and J. Stahlberg, *Colloids Surfaces B,* **14,** 67 (1999). The Electrostatic Interaction between a Charged Sphere and an Oppositely Charged Planar Surface and Its Application to Protein Adsorption.

425. M. L. Grant and D. A. Saville, *J. Colloid Interface Sci.,* **171,** 35 (1995). Electrostatic Interactions between a Nonuniformly Charged Sphere and a Charged Surface.

426. S. Bhattacharjee and M. Elimelech, *J. Colloid Interface Sci.,* **193,** 273 (1997). Surface Element Integration: A Novel Technique for Evaluation of DLVO Interaction between a Particle and a Flat Plate.

427. J.-P. Hsu and B.-T. Liu, *J. Chem. Phys.,* **110,** 25 (1999). Electrical Interaction Energy between Two Charged Entities.

428. J.-P. Hsu and B.-T. Liu, *J. Colloid Interface Sci.,* **217,** 219 (1999). Electrical Interaction Energy between Two Charged Entities in an Electrolyte Solution.

429. H. H. von Grünberg and E. C. Mbamala, *J. Phys. Condensed Matter,* **12,** 10349 (2000). Colloidal Suspensions at Dielectric Interfaces.

430. D. Goulding and J.-P. Hansen, *Molec. Phys.,* **95,** 649 (1998). Effective Interaction between Charged Colloidal Particles Near a Surface.

431. D. Goulding and J.-P. Hansen, *Europhys. Lett.,* **46,** 407 (1999). Attraction between Like-Charged Colloidal Particles Induced by a Surface: A Density-Functional Analysis.

432. J. E. Sader and D. Y. C. Chan, *J. Colloid Interface Sci.,* **218,** 423 (1999). Electrical Double-Layer Interaction between Charged Particles Near Surfaces and in Confined Geometries.

433. L. A. Mark, J. L. Kaplan, and J. C. Williams, Jr., *J. Colloid Interface Sci.,* **229,** 102 (2000). An Exact Solution to the Electrostatic Interaction between an Ion-Penetrable Sphere and an Ion-Penetrable Rod.

434. Y. Gu, *J. Colloid Interface Sci.,* **231,** 199 (2000). The Electrical Double-Layer Interaction between a Spherical Particle and a Cylinder.

435. J.-P. Hsu and C.-Y. Kao, *Langmuir,* **18,** 2743 (2002). Electrical Interaction between a Spheroid and a Spherical Cavity.

436. M. Ospeck and S. Fraden, *J. Chem. Phys.,* **109,** 9166 (1998). Solving the Poisson-Boltzmann Equation to Obtain Interaction Energies between Confined, Like-Charged Cylinders.

437. H. Schiessel, *Eur. Phys. J. B,* **6,** 373 (1998). Bending of Charged Flexible Membranes Due to the Presence of Macroions.

438. W. H. Press, S. A. Teukolsky, W. T. Vetterling, and B. P. Flannery, *Numerical Recipes in Fortran 77*, Cambridge Univ. Press, Cambridge, UK, 1992.

439. H. Oberoi and N. M. Allewell, *Biophys. J.,* **65,** 48 (1993). Multigrid Solution of the Nonlinear Poisson-Boltzmann Equation and Calculation of Titration Curves.

440. M. Holst and F. Saied, *J. Comput. Chem.,* **14,** 105 (1993). Multigrid Solution of the Poisson-Boltzmann Equation.

441. M. J. Holst and F. Saied, *J. Comput. Chem.,* **16,** 337 (1995). Numerical Solution of the Nonlinear Poisson-Boltzmann Equation: Developing More Robust and Efficient Methods.

442. R. Luo, L. David, and M. K. Gilson, *J. Comput. Chem.,* **23,** 1244 (2002). Accelerated Poisson-Boltzmann Calculation for Static Dynamic Systems.

443. E. E. David and C. W. David, *J. Chem. Phys.,* **76,** 4611 (1982). Voronoi Polyhedra as a Tool for Studying Solvation Structure.

444. T. J. You and S. C. Harvey, *J. Comput. Chem.,* **14,** 484 (1993). Finite Element Approach to the Electrostatics of Macromolecules with Arbitrary Geometries.

445. C. M. Cortis and R. A. Friesner, *J. Comput. Chem.,* **18,** 1570 (1997). An Automatic Three-Dimensional Finite Element Mesh Generation System for the Poisson-Boltzmann Equation.

446. C. M. Cortis and R. A. Friesner, *J. Comput. Chem.,* **18,** 1591 (1997). Numerical Solution of the Poisson-Boltzmann Equation Using Tetrahedral Finite-Element Meshes.

447. R. E. Bank and M. Holst, *SIAM J. Sci. Comput.,* **22,** 1411 (2000). A New Paradigm for Parallel Adaptive Meshing Algorithms.

448. P. Dyshlovenko, *J. Comput. Phys.,* **172,** 198 (2001). Adaptive Mesh Enrichment for the Poisson-Boltzmann Equation.

449. P. E. Dyshlovenko, *Comput. Phys. Commun.,* **147,** 335 (2002). Adaptive Numerical Method for Poisson-Boltzmann Equation and Its Application.

450. A. E. James and D. J. A. Williams, *J. Colloid Interface Sci.,* **107,** 44 (1985). Numerical Solution of the Poisson-Boltzmann Equation.

451. C. M. Cortis, J.-M. Langlois, M. D. Beachy, and R. A. Friesner, *J. Chem. Phys.,* **105,** 5472 (1996). Quantum Mechanical Geometry Optimization in Solution Using a Finite Element Continuum Electrostatics Method.

452. T. L. Beck, *Int. J. Quantum Chem.,* **65,** 477 (1997). Real-Space Multigrid Solution of Electrostatics Problems and the Kohn-Sham Equations.

453. G. R. Pack and B. J. Klein, *Biopolymers,* **23,** 2801 (1984). Generalized Poisson-Boltzmann Calculation of the Distribution of Electrolyte Ions around the B- and Z-Conformers of DNA.

454. G. R. Pack, G. A. Garrett, L. Wong, and G. Lamm, *Biophys. J.,* **65,** 1363 (1993). The Effect of a Variable Dielectric Coefficient and Finite Ion Size on Poisson-Boltzmann Calculations of DNA-Electrolyte Systems.

455. D. T. Edmonds, N. K. Rogers, and M. J. E. Sternberg, *Molec. Phys.,* **52,** 1487 (1984). Regular Representation of Irregular Charge Distributions. Application to the Electrostatic Potentials of Globular Proteins.

456. J. Antosiewicz, J. A. McCammon, and M. K. Gilson, *J. Molec. Biol.,* **238,** 415 (1994). Prediction of pH-Dependent Properties of Proteins.

457. J. Antosiewicz, J. M. Briggs, A. H. Elcock, M. K. Gilson, and J. A. McCammon, *J. Comput. Chem.,* **17,** 1633 (1996). Computing Ionization States of Proteins with a Detailed Charge Model.

458. J. Antosiewicz, J. A. McCammon, and M. K. Gilson, *Biochemistry,* **35,** 7819 (1996). The Determinants of pK_as in Proteins.

459. J. Warwicker, *Protein Sci.,* **8,** 418 (1999). Simplified Methods for pK_a and Acid pH-Dependent Stability Estimation in Proteins: Removing Dielectric and Counterion Boundaries.

460. T. Simonson, G. Archontis, and M. Karplus, *J. Phys. Chem. B,* **103,** 6142 (1999). A Poisson-Boltzmann Study of Charge Insertion in an Enzyme Active Site: The Effect of Dielectric Relaxation.

461. B. Z. Lu, W. Z. Chen, C. X. Wang, and X. Xu, *Proteins Struct. Funct. Genet.,* **48,** 497 (2002). Protein Molecular Dynamics with Electrostatic Force Entirely Determined by a Single Poisson-Boltzmann Calculation.

462. A. Warshel and J. Aqvist, *Annu. Rev. Biophys. Biophys. Chem.,* **20,** 267 (1991). Electrostatic Energy and Macromolecular Function.

463. Y. Y. Sham, I. Muegge, and A. Warshel, *Biophys. J.,* **74,** 1744 (1998). The Effect of Protein Relaxation on Charge-Charge Interactions and Dielectric Constants of Proteins.

464. J. W. Pitera, M. Falta, and W. F. van Gunsteren, *Biophys. J.,* **80,** 2546 (2001). Dielectric Properties of Proteins from Simulation: The Effects of Solvent, Ligands, pH, and Temperature.

465. J. Warwicker and H. C. Watson, *J. Molec. Biol.,* **157,** 671 (1982). Calculation of the Electric Potential in the Active Site Cleft Due to α-Helix Dipoles.

466. J. Warwicker, *J. Theor. Biol.,* **121,** 199 (1986). Continuum Dielectric Modelling of the Protein-Solvent System and Calculation of the Long-Range Electrostatic Field of the Enzyme Phosphoglycerate Mutase.

467. B. A. Luty, M. E. Davis, and J. A. McCammon, *J. Comput. Chem.,* **13,** 1114 (1992). Solving the Finite-Difference Non-Linear Poisson-Boltzmann Equation.

468. W. Rocchia, E. Alexov, and B. Honig, *J. Phys. Chem. B,* **105,** 6507 (2002). Extending the Applicability of the Nonlinear Poisson-Boltzmann Equation: Multiple Dielectric Constants and Multivalent Ions.

469. Z. Zhou, P. Payne, M. Vasquez, N. Kuhn, and M. Levitt, *J. Comput. Chem.,* **11,** 1344 (1996). Finite-Difference Solution of the Poisson-Boltzmann Equation: Complete Elimination of Self-Energy.

470. B. J. Klein and G. R. Pack, *Biopolymers,* **22,** 2331 (1983). Calculations of the Spatial Distribution of Charge Density in the Environment of DNA.

471. B. J. Klein and G. R. Pack, *J. Biol. Phys.,* **11,** 23 (1983). Theoretical Studies of the Electrostatic Stability of A, B, C, and Z-DNA Conformers as a Function of Monovalent Ion Concentration and Ion Type.

472. G. R. Pack, C. V. Prasad, J. S. Salafsky, and L. Wong, *Biopolymers,* **25,** 1697 (1986). Calculations on the Effect of Methylation on the Electrostatic Stability of the B- and Z-Conformers of DNA.

473. G. R. Pack, L. Wong, and C. V. Prasad, *Nucleic Acids Res.,* **14,** 1479 (1986). Counterion Distribution around DNA: Variation with Conformation and Sequence.

474. P. MacNeice, K. M. Olson, C. Mobarry, R. de Fainchtein, and C. Packer, *Comput. Phys. Commun.,* **126,** 330 (2000). PARAMESH: A Parallel Adaptive Mesh Refinement Community Toolkit.

475. M. E. Davis and J. A. McCammon, *J. Comput. Chem.,* **12,** 909 (1991). Dielectric Boundary Smoothing in Finite Difference Solutions of the Poisson Equation: An Approach to Improve Accuracy and Convergence.

476. R. E. Bruccoleri, J. Novotny, M. E. Davis, and K. A. Sharp, *J. Comput. Chem.,* **18,** 268 (1997). Finite Difference Poisson-Boltzmann Electrostatic Calculations: Increased Accuracy Achieved by Harmonic Dielectric Smoothing and Charge Antialiasing.

477. J. A. Grant, B. T. Pickup, and A. Nicholls, *J. Comput. Chem.,* **22,** 608 (2001). A Smooth Permittivity Function for Poisson-Botlzmann Solvation Methods.

478. G. Lamm and G. R. Pack, *Int. J. Quantum Chem.,* **65,** 1087 (1997). Local Dielectric Constants and Poisson-Boltzmann Calculations of DNA Counterion Distributions.

479. F. Booth, *J. Chem. Phys.,* **19,** 391 (1951). The Dielectric Constant of Water and the Saturation Effect.

480. F. Booth, *J. Chem. Phys.,* **19,** 1327 (1951). Errata: The Dielectric Constant of Water and the Saturation Effect.

481. J. C. Maxwell, *A Treatise on Electricity and Magnetism,* Dover, New York, 1954, Vol. 1, p. 440.

482. J. W. Rayleigh, *Phil. Mag.,* **34,** 481 (1892). On the Influence of Obstacles Arranged in Rectangular Order upon the Properties of a Medium.

483. L. K. H. van Beek, *Prog. Dielectrics,* **7,** 69 (1967). Dielectric Behaviour of Heterogeneous Systems.

484. J. B. Hasted, *Aqueous Dielectrics,* Chapman & Hall, London, 1973.

485. Y. Gur, I. Ravina, and A. J. Babchin, *J. Colloid Interface Sci.,* **64,** 326 (1978). On the Electrical Double Layer Theory. I. A Numerical Method for Solving a Generalized Poisson-Boltzmann Equation.

486. X. Zhexin, S. Yunyu, and X. Yinhu, *J. Comput. Chem.,* **16,** 200 (1995). Solving the Finite-Difference, Nonlinear, Poisson-Boltzmann Equation Under a Linear Approach.

487. E. Feitosa, A. A. Neto, and H. Chaimovich, *Langmuir,* **9,** 702 (1993). Integration of the Nonlinear Poisson-Boltzmann Equation for Charged Vesicles in Electrolytic Solutions.

488. H. F. Weinberger, *A First Course in Partial Differential Equations*, Dover, New York, 1995.

489. R. J. Zauhar and R. S. Morgan, *J. Molec. Biol.,* **186,** 815 (1985). A New Method for Computing the Macromolecular Electric Potential.

490. R. J. Zauhar and R. S. Morgan, *J. Comput. Chem.,* **9,** 171 (1988). The Rigorous Computation of the Molecular Electrostatic Potential.

491. R. J. Zauhar and R. S. Morgan, *J. Comput. Chem.,* **11,** 603 (1990). Computing the Electric Potential of Biomolecules: Application of a New Method of Molecular Surface Triangulation.

492. B. J. Yoon and A. M. Lenhoff, *J. Comput. Chem.,* **11,** 1080 (1990). A Boundary Element Method for Molecular Electrostatics with Electrolyte Effects.

493. H.-X. Zhou, *Biophys. J.,* **65,** 955 (1993). Boundary Element Solution of Macromolecular Electrostatics: Interaction Energy between Two Proteins.

494. H.-X. Zhou, *J. Chem. Phys.,* **100,** 3152 (1994). Macromolecular Electrostatic Energy within the Nonlinear Poisson Boltzmann Equation.

495. R. Bharadwaj, A. Windemuth, S. Sridharan, B. Honig, and A. Nicholls, *J. Comput. Chem.,* **16,** 898 (1995). The Fast Multipole Boundary Element Method for Molecular Electrostatics: An Optimal Approach for Large Systems.

496. S. A. Allison and V. T. Tran, *Biophys. J.,* **68,** 2261 (1995). Modeling the Electrophoresis of Rigid Polyions: Application to Lysozyme.

497. D. Horvath, D. Van Belle, G. Lippens, and S. J. Wodak, *J. Chem. Phys.,* **104,** 6679 (1996). Development and Parametrization of Continuum Solvent Models. I. Models Based on the Boundary Element Method.

498. D. Horvath, G. Lippens, and D. Van Belle, *J. Chem. Phys.,* **105,** 4197 (1996). Development and Parametrization of Continuum Solvent Models. II. A Unified Approach to the Solvation Problem.

499. R. J. Zauhar and A. Varnek, *J. Comput. Chem.,* **17,** 864 (1996). A Fast and Space-Efficient Boundary Element Method for Computing Electrostatic and Hydration Effects in Large Molecules.

500. S. A. Allison, M. Potter, and J. A. McCammon, *Biophys. J.,* **73,** 133 (1997). Modeling the Electrophoresis of Lysozyme. II. Inclusion of Ion Relaxation.

501. D. Asthagiri and A. M. Lenhoff, *Langmuir,* **13,** 6761 (1997). Influence of Structural Details in Modeling Electrostatically Driven Protein Adsorption.

502. J. Liang and S. Subramaniam, *Biophys. J.,* **73,** 1830 (1997). Computation of Molecular Electrostatics with Boundary Element Methods.

503. G. W. Kwon, Y. S. Won, and B. J. Yoon, *J. Colloid Interface Sci.,* **205,** 423 (1998). Electrical Double-Layer Interactions of Regular Arrays of Spheres.

504. A. Ghosh, C. S. Rapp, and R. A. Freisner, *J. Phys. Chem. B,* **102,** 10983 (1998). Generalized Born Model Based on a Surface Integral Formulation.

505. Q. Fulian and A. C. Fisher, *J. Phys. Chem. B,* **102,** 9647 (1998). Computational Electrochemistry: The Boundary Element Method.

506. M. L. Grant, *J. Phys. Chem. B,* **105,** 2858 (2001). Nonuniform Charge Effects in Protein-Protein Interactions.

507. S. L. Chan and E. O. Purisima, *J. Comput. Chem.,* **19,** 1268 (1998). Molecular Surface Generation Using Marching Tetrahedra.

508. R. Ettelaie, *J. Chem. Phys.,* **103,** 3657 (1995). Solutions of the Linearized Poisson–Boltzmann Equation Through the Use of Random Walk Simulation Method.

509. C.-O. Hwang and M. Mascagni, *Appl. Phys. Lett.,* **78,** 787 (2001). Efficient Modified "Walk on Spheres" Algorithm for the Linearized Poisson-Boltzmann Equation.

510. V. Zaloj and N. Agmon, *Chem. Phys. Lett.,* **284,** 78 (1998). Diffusion Approach to the Linear Poisson-Boltzmann Equation.

511. J. Alvarez-Ramirez, R. Martinez, and E. Diaz-Herrera, *Chem. Phys. Lett.,* **266,** 375 (1997). Solution of the Poisson-Boltzmann Equation through the Use of Pseudo-Dynamic Simulation Method.

512. A. M. Micu, B. Bagheri, A. Ilin, L. R. Scott, and B. M. Pettitt, *J. Comput. Phys.,* **136,** 263 (1997). Numerical Considerations in the Computation of the Electrostatic Free Energy of Interaction with the Poisson-Boltzmann Theory.

513. F. Fogolari and J. M. Briggs, *Chem. Phys. Lett.,* **281,** 135 (1997). On the Variational Approach to Poisson-Boltzmann Free Energies.

514. K. A. Sharp and B. Honig, *J. Phys. Chem. B,* **94,** 7684 (1990). Calculating Total Electrostatic Energies with the Nonlinear Poisson-Boltzmann Equation.

515. J. Shen and F. A. Quiocho, *J. Comput. Chem.,* **16,** 445 (1995). Calculation of Binding Energy Differences for Receptor-Ligand Systems Using the Poisson-Boltzmann Method.

516. R. M. Jackson and M. J. E. Sternberg, *J. Molec. Biol.,* **250,** 258 (1995). A Continuum Model for Protein-Protein Interactions: Application to the Docking Problem.

517. V. K. Misra, K. A. Sharp, R. A. Friedman, and B. Honig, *J. Molec. Biol.,* **238,** 245 (1994). Salt Effects on Ligand-DNA Binding. Minor Groove Binding Antibiotics.

518. V. K. Misra, J. L. Hecht, K. A. Sharp, R. A. Friedman, and B. Honig, *J. Molec. Biol.,* **238,** 264 (1994). Salt Effects on Protein-DNA Interactions. The Lambda cI Repressor and EcoRI Endonuclease.

519. S. W. Chen and B. Honig, *J. Phys. Chem. B,* **101,** 9113 (1997). Monovalent and Divalent Salt Effects on Electrostatic Free Energies Defined by the Nonlinear Poisson-Boltzmann Equation: Application to DNA Binding Reactions.

520. V. K. Misra, J. L. Hecht, A. S. Yang, and B. Honig, *Biophys. J.,* **75,** 2262 (1998). Electrostatic Contributions to the Binding Free Energy of the λcI Repressor to DNA.

521. V. K. Misra and B. Honig, *Biochemistry,* **35,** 1115 (1996). The Electrostatic Contribution to the B to Z Transition of DNA.

522. M. Baginski, F. Fogolari, and J. M. Briggs, *J. Molec. Biol.,* **274,** 253 (1997). Electrostatic and Non-Electrostatic Contributions to the Binding Free Energies of Anthracycline Antibiotics to DNA.

523. M. Zacharias and H. Sklenar, *Biophys. J.,* **73,** 2990 (1997). Analysis of the Stability of Looped-Out and Stacked-in Conformations of an Adenine Bulge in DNA Using a Continuum Model for Solvent and Ions.

524. M. Zacharias, *Biophys. J.,* **80,** 2350 (2001). Conformational Analysis of DNA-Trinucleotide-Hairpin-Loop Structures Using a Continuum Solvent Model.

525. K. A. Sharp, *Biophys. J.,* **73,** 1241 (1998). Calculation of Electron Transfer Reorganization Energies Using the Finite Difference Poisson-Boltzmann Model.

526. K. Gallagher and K. A. Sharp, *Biophys. J.,* **75,** 769 (1998). Electrostatic Contributions to Heat Capacity Changes of DNA-Ligand Binding.

527. M. A. L. Eriksson, J. Pitera, and P. A. Kollman, *J. Med. Chem.,* **42,** 868 (1999). Prediction of the Binding Free Energies of New TIBO-Like HIV-1 Reverse Transcriptase Inhibitors Using a Combination of PROFEC, PB/SA, CMC/MD, and Free Energy Calculations.

528. V. K. Misra and D. E. Draper, *J. Molec. Biol.,* **294,** 1135 (1999). The Interpretation of Mg^{2+} Binding Isotherms for Nucleic Acids Using Poisson-Boltzmann Theory.

529. V. K. Misra and D. E. Draper, *J. Molec. Biol.,* **299,** 813 (2000). Mg^{2+} Binding to tRNA Revisited: The Nonlinear Poisson-Boltzmann Model.

530. C. J. Woods, M. A. King, and J. W. Essex, *J. Comput. Aided Molec. Design,* **15,** 129 (2001). The Configurational Dependence of Binding Free Energies: A Poisson-Boltzmann Study of Neuraminidase Inhibitors.

531. K. L. Mardis, R. Luo, and M. K. Gilson, *J. Molec. Biol.,* **309,** 507 (2001). Interpreting Trends in the Binding of Cyclic Ureas to HIV-1 Protease.

532. M. Born, *Z. Phys. Chem.,* **1,** 45 (1920). Volumen und Hydrationswärme der Ionen.

533. M. Bucher and T. L. Porter, *J. Phys. Chem.,* **90,** 3406 (1986). Analysis of the Born Model for Hydration of Ions.

534. M. Bucher, *J. Phys. Chem.,* **90,** 3411 (1986). Core Electron Spectroscopy of Hydrated Ions.

535. S. Ehrenson, *J. Comput. Chem.,* **10,** 77 (1988). Continuum Radial Dielectric Functions for Ion and Dipole Solution Systems.

536. W. C. Still, A. Tempczyk, R. C. Hawley, and T. Hendrickson, *J. Am. Chem. Soc.,* **112,** 6127 (1990). Semianalytical Treatment of Solvation for Molecular Mechanics and Dynamics.

537. M. Scarsi, J. Apostolakis, and A. Caflisch, *J. Phys. Chem. A,* **101,** 8098 (1997). Continuum Electrostatic Energies of Macromolecules in Aqueous Solutions.

538. D. Bashford and D. A. Case, *Annu. Rev. Phys. Chem.,* **51,** 129 (2000). Generalized Born Models of Macromolecular Solvation Effects.

539. M. S. Lee, F. R. Salsbury, Jr., and C. L. Brooks, III, *J. Chem. Phys.,* **116,** 10606 (2002). Novel Generalized Born Methods.

540. A. Onufriev, D. A. Case, and D. Bashford, *J. Comput. Chem.,* **23,** 1297 (2002). Effective Born Radii in the Generalized Born Approximation: The Importance of Being Perfect.

541. N. Arora and D. Bashford, *Proteins Struct. Funct. Genet.,* **43,** 12 (2001). Solvation Energy Density Occlusion Approximation for Evaluation of Desolvation Penalties in Biomolecular Interactions.

542. D. Eisenberg and A. D. Mclachlan, *Nature,* **319,** 199 (1986). Solvation Energy in Protein Folding and Binding.

543. D. Sitkoff, K. A. Sharp, and B. Honig, *J. Phys. Chem.,* **98,** 1978 (1994). Accurate Calculation of Hydration Free Energies Using Macroscopic Solvent Models.

544. J. G. Kirkwood and J. B. Shumaker, *Proc. Natl. Acad. Sci. (USA),* **38,** 863 (1952). Forces between Protein Molecules in Solution Arising from Fluctuations in Proton Charge and Configuration.

545. T. L. Hill, *J. Am. Chem. Soc.,* **78,** 3330 (1956). On Intermolecular and Intramolecular Interactions between Independent Pair Binding Sites in Proteins and Other Molecules.

546. R. R. Sinden, *DNA Structure and Function,* Academic Press, New York, 1994.

547. T. J. You and D. Bashford, *Biophys. J.,* **69,** 1721 (1995). Conformation and Hydrogen Ion Titration of Proteins: A Continuum Electrostatic Model with Conformational Flexibility.

548. P. Beroza and D. R. Fredkin, *J. Comput. Chem.,* **17,** 1229 (1996). Calculation of Amino Acid pK_as in a Protein from a Continuum Electrostatic Model: Method and Sensitivity Analysis.

549. G. M. Ullmann and E.-W. Knapp, *Eur. Biophys. J.,* **28,** 533 (1999). Electrostatic Models for Computing Protonation and Redox Equilibria in Proteins.

550. C. J. Gibas, P. Jambeck, and S. Subramaniam, *Methods,* **20,** 292 (2000). Continuum Electrostatic Methods Applied to pH-Dependent Properties of Antibody-Antigen Association.

551. H. R. Horton, L. A. Moran, R. S. Ochs, J. D. Rawn, and K. G. Scrimgeour, *Principles of Biochemistry,* Upper Saddle River, NJ, 2002.

552. C. Tanford and R. Roxby, *Biochemistry,* **11,** 2192 (1972). Interpretation of Protein Titration Curves. Application to Lysozyme.

553. A. S. Petrov, G. R. Pack, and G. Lamm (to be published).

554. G. R. Pack, L. Wong, and G. Lamm, *Int. J. Quantum Chem.,* **70,** 1177 (1998). pK_a of Cytosine on the Third Strand of Triplex DNA: Preliminary Poisson-Boltzmann Calculations.

555. J. Warwicker, *J. Molec. Biol.,* **236,** 887 (1994). Improved Continuum Electrostatic Modelling in Proteins with Comparison to Experiment.

556. J. Warwicker, *Protein Eng.,* **10,** 809 (1997). Improving pK_a Calculations with Consideration of Hydration Entropy.

557. A. Karshikoff, *Protein Eng.,* **8,** 243 (1995). A Simple Algorithm for the Calculation of Multiple Site Titration Curves.

558. J. Antosiewicz and D. Porschke, *Biochemistry,* **28,** 10072 (1989). The Nature of Protein Dipole Moments: Experimental and Calculated Permanent Dipole of α-Chymotrypsin.

559. P. Beroza, D. R. Fredkin, M. Y. Okamura, and G. Feher, *Proc. Natl. Acad. Sci. (USA),* **88,** 5804 (1991). Protonation of Interacting Residues in a Protein by a Monte Carlo Method: Application to Lysozyme and the Photoreaction Center of *Rhodobacter Sphaeroides.*

560. J. Antosiewicz and D. Porschke, *Biophys. J.,* **68,** 655 (1995). Electrostatics of Hemoglobins from Measurements of the Electric Dichroism and Computer Simulations.

561. E. Demchuk and R. C. Wade, *J. Phys. Chem. B,* **100,** 17373 (1996). Improving the Continuum Dielectric Approach to Calculating pK_as of Ionizable Groups in Proteins.

562. R. A. Dimitrov and R. R. Crichton, *Proteins Struct. Funct. Genet.,* **27,** 576 (1997). Self-Consistent Field Approach to Protein Structure and Stabiity. I: pH Dependence of Electrostatic Contribution.

563. A. H. Juffer, P. Argos, and H. J. Vogel, *J. Phys. Chem. B,* **101,** 7664 (1997). Calculating Acid-Dissociation Constant of Proteins Using the Boundary Element Method.

564. R. Penfold, J. Warwicker, and B. Jönsson, *J. Phys. Chem. B,* **102,** 8599 (1998). Electrostatic Models for Calcium Binding Proteins.

565. J. J. Havranek and P. B. Harbury, *Proc. Natl. Acad. Sci. (USA),* **96,** 11145 (1999). Tanford-Kirkwood Electrostatics for Protein Modeling.

566. L. Sandberg and O. Edholm, *Proteins Struct. Funct. Genet.,* **36,** 474 (1999). A Fast and Simple Method to Calculate Protonation States in Proteins.

567. J. E. Nielsen and G. Vriend, *Proteins Struct. Funct. Genet.,* **43,** 403 (2001). Optimizing the Hydrogen-Bond Network in Poisson-Boltzmann Equation-Based pK_a Calculations.

568. D. Bashford, D. A. Case, C. Dalvit, L. Tennant, and P. E. Wright, *Biochemistry,* **32,** 8045 (1993). Electrostatic Calculations of Side-Chain pK_a Values in Myoglobin and Comparison with NMR Data for Histidines.

569. A. S. Yang and B. Honig, *J. Molec. Biol.,* **237,** 602 (1994). Structural Origins of pH and Ionic Strength Effects on Protein Stability. Acid Denaturation of Sperm Whale Apomyoglobin.

570. Y.-H. Kao, C. A. Fitch, S. Bhattacharya, C. J. Sarkisian, J. T. Lecomte, and B. Garcia-Moreno E., *Biophys. J.,* **79,** 1637 (2000). Salt Effects on Ionization Equilibria of Histidines in Myoglobin.

571. A. D. MacKerell, Jr., M. S. Sommer, and M. Karplus, *J. Molec. Biol.,* **247,** 774 (1995). pH Dependence of Binding Reactions from Free Energy Simulations and Macroscopic Continuum Electrostatic Calculations: Application to 2′GMP/3′GMP Binding to Ribonuclease T1 and Implications for Catalysis.

572. D. Khare, P. Alexander, J. Antosiewicz, P. Bryan, M. Gilson, and J. Orban, *Biochemistry,* **36,** 3580 (1997). pK_a Measurements from Nuclear Magnetic Resonance for the B1 and B2 Immunoglobin G-Binding Domains of Protein G: Comparison with Calculated Values for Nuclear Magnetic Resonance and X-Ray Structures.

573. J. Lamotte-Brasseur, V. Lounnas, X. Raquet, and R. C. Wade, *Protein Sci.,* **8,** 404 (1999). pK_a Calculations for Class a β-Lactamases: Influence of Substrate Binding.

574. M. A. Noble, S. Gul, C. S. Verma, and K. Brocklehurst, *Biochem. J.,* **351,** 732 (2000). Ionization Characteristics and Chemical Influences of Aspartic Acid Residue 158 of Papain and Caricain Determined by Structure-Related Kinetic and Computational Techniques: Multiple Electrostatic Modulators and Active-Centre Chemistry.

575. F. Fogolari, L. Ragona, S. Licciardi, S. Romagnoli, R. Michelutti, R. Ugolini, and H. Molinari, *Proteins Struct. Funct. Genet.,* **39,** 317 (2000). Electrostatic Properties of Bovine β-Lactoglobulin.

576. A. S. Yang and B. Honig, *J. Molec. Biol.,* **231,** 459 (1993). On the pH Dependence of Protein Stability.

577. D. R. Ripoll, Y. N. Vorobjev, A. Kiwo, J. A. Vila, and H. A. Scheraga, *J. Molec. Biol.,* **264,** 770 (1996). Coupling between Folding and Ionization Equilibria: Effects of pH on the Conformational Preferences of Polypeptides.

578. H.-X. Zhou and M. Vijayakumar, *J. Molec. Biol.,* **267,** 1002 (1997). Modeling of Protein Conformational Fluctuations in pK_a Predictions.

579. W. R. Cannon, B. J. Garrison, and S. J. Benkovic, *J. Molec. Biol.,* **271,** 656 (1997). Consideration of the pH-Dependent Inhibition of Dihydrofolate Reductase by Methotrexate.

580. N. Metropolis, A. W. Rosenbluth, M. N. Rosenbluth, A. H. Teller, and E. Teller, *J. Chem. Phys.,* **21,** 1087 (1953). Equation of State Calculations by Fast Computing Machines.

581. M. Levitt, *Nature Struct. Biol.,* **8,** 392 (2001). The Birth of Computational Structural Biology.

582. W. G. McMillan, Jr., and J. E. Mayer, *J. Chem. Phys.,* **13,** 276 (1945). The Statistical Thermodynamics of Multicomponent Systems.

583. A. Caflisch and M. Karplus, *J. Molec. Biol.,* **252,** 672 (1995). Acid and Thermal Denaturation of Barnase Investigated by Molecular Dynamics Simulations.

584. G. Archontis, T. Simonson, and M. Karplus, *J. Molec. Biol.,* **306,** 307 (2001). Binding Free Energies and Free Energy Components from Molecular Dynamics and Poisson-Boltzmann Calculations. Application to Amino Acid Recognition by Aspartyl-tRNA Synthetase.

585. T. E. Cheatham, III, J. L. Miller, T. Fox, T. A. Darden, and P. A. Kollman, *J. Am. Chem. Soc.,* **117,** 4193 (1995). Molecular Dynamics Simulations on Solvated Biomolecular Systems: The Particle Mesh Ewald Method Leads to Stable Trajectories of DNA, RNA, and Proteins.

586. J. Srinivasan, J. Miller, P. A. Kollman, and D. A. Case, *J. Biomolec. Struct. Dynam.,* **16,** 671 (1998). Continuum Solvent Studies of the Stability of RNA Hairpin Loops and Helices.

587. C. M. Reyes and P. A. Kollman, *J. Molec. Biol.,* **297,** 1145 (2000). Structure and Thermodynamics of RNA-Protein Binding: Using Molecular Dynamics and Free Energy Analyses to Calculate the Free Energies of Binding and Conformational Change.

588. E. Cubero, F. J. Luque, and M. Orozco, *J. Am. Chem. Soc.,* **123,** 12018 (2001). Theoretical Studies of d(A:T)-Based Parallel-Stranded DNA Duplexes.

589. V. Tsui and D. A. Case, *J. Phys. Chem. B,* **105,** 11314 (2001). Calculations of the Absolute Free Energies of Binding between RNA and Metal Ions Using Molecular Dynamics Simulations and Continuum Electrostatics.

590. K. Sharp, *J. Comput. Chem.,* **12,** 454 (1991). Incorporating Solvent and Ion Screening into Molecular Dynamics Using the Finite-Difference Poisson-Boltzmann Method.

591. C. Niedermeier and K. Schulten, *Molec. Simul.,* **8,** 361 (1992). Molecular Dynamics Simulations in Heterogeneous Dielectrics and Debye-Hückel Media—Application to the Protein Bovine Pancreatic Trypsin Inhibitor.

592. M. K. Gilson, J. A. McCammon, and J. D. Madura, *J. Comput. Chem.,* **16,** 1081 (1995). Molecular Dynamics Simulation with a Continuum Electrostatic Model of the Solvent.

593. T. Grycuk, *J. Phys. Chem. B,* **106,** 1434 (2002). Revision of the Model System Concept for the Prediction of pK_as in Proteins.

594. I. G. Tironi, R. Sperb, P. E. Smith, and W. F. van Gunsteren, *J.Chem. Phys.,* **102,** 5451 (1995). A Generalized Reaction Field Method for Molecular Dynamics Simulations.

595. M. Zacharias, B. A. Luty, M. E. Davis, and J. A. McCammon, *J. Molec. Biol.,* **238,** 455 (1994). Combined Conformational Search and Finite-Difference Poisson-Boltzmann Approach for Flexible Docking. Application to an Operator Mutation in the Lambda Repressor-Operator Complex.

596. A. Caflisch, S. Fischer, and M. Karplus, *J. Comput. Chem.,* **18,** 723 (1997). Docking by Monte Carlo Minimization with a Solvation Correction: Application to an FKBP-Substrate Complex.

597. J. L. Chen, L. Noodleman, D. A. Case, and D. Bashford, *J. Phys. Chem.,* **98,** 11059 (1994). Incorporating Solvation Effects into Density Functional Electronic Structure Calculations.

598. W. D. Wilson, C. M. Schaldach, and W. L. Bourcier, *Chem. Phys. Lett.,* **267,** 431 (1997). Single- and Double-Layer Coupling of Schrodinger and Poisson-Boltzmann Equations.

599. V. Gogonea and K. M. Merz, Jr., *J. Phys. Chem. A,* **103,** 5171 (1999). Fully Quantum Mechanical Description of Proteins in Solution. Combining Linear Scaling Quantum Mechanical Methodologies with the Poisson-Boltzmann Equation.

600. V. Gogonea and K. M. Merz, Jr., *J. Chem. Phys.,* **112,** 3227 (2000). A Quantum Mechanical-Poisson–Boltzmann Equation Approach for Studying Charge Flow between Ions and a Dielectric Continuum.

601. V. Gogonea and K. M. Merz, Jr., *J. Phys. Chem. B,* **104,** 2117 (2000). Charge Flow between Ions and a Dielectric Continuum. 2. Variational Method for Distributing Charge into the Dielectric.

602. A. van der Vaart, V. Gogonea, S. L. Dixon, and K. M. Merz, Jr., *J. Comput. Chem.,* **21,** 1494 (2000). Linear Scaling Molecular Orbital Calculations of Biological Systems Using the Semiempirical Divide and Conquer Method.

603. C. Park, M. J. Carlson, and W. A. Goddard, III, *J. Phys. Chem. A,* **104,** 2498 (2000). Solvent Effects on the Secondary Structures of Proteins.

604. C. Park and W. A. Goddard, III, *J. Phys. Chem. B,* **104,** 7784 (2000). Stabilization of α-Helices by Dipole-Dipole Interactions within α-Helices.

605. D. L. Ermak and J. A. McCammon, *J. Chem. Phys.,* **69,** 1352 (1978). Brownian Dynamics with Hydrodynamic Interactions.

606. M. J. Potter, B. Luty, H.-X. Zhou, and J. A. McCammon, *J. Phys. Chem.,* **100,** 5149 (1996). Time-Dependent Rate Coefficients from Brownian Dynamics Simulations.

607. S. H. Northrup, S. A. Allison, and J. A. McCammon, *J. Chem. Phys.,* **80,** 1517 (1984). Brownian Dynamics Simulation of Diffusion-Influenced Biomolecular Reactions.

608. S. H. Northrup, J. O. Boles, and J. C. L. Reynolds, *Science,* **241,** 67 (1988). Brownian Dynamics of Cytochrome C and Cytochrome C Peroxidase Association.

609. H.-X. Zhou, *J. Phys. Chem.,* **94,** 8794 (1990). Kinetics of Diffusion-Influenced Reactions Studied by Brownian Dynamics.

610. R. R. Gabdouline and R. C. Wade, *Biophys. J.,* **72,** 1917 (1997). Simulation of the Diffusional Association of Barnase and Barstar.

611. F. Fogolari, R. Ugolini, H. Molinari, P. Viglino, and G. Esposito, *Eur. J. Biochem.,* **267,** 4861 (2000). Simulation of Electrostatic Effects in Fab-Antigen Complex Formation.

612. R. R. Gabdouline and R. C. Wade, *Curr. Opinion Struct. Biol.,* **12,** 204 (2002). Biomolecular Diffusional Association.

613. J. G. Kirkwood, *J. Chem. Phys.,* **7,** 911 (1939). The Dielectric Polarization of Polar Liquids.

614. H. Maeda and F. Oosawa, *J. Phys. Chem.,* **83,** 2911 (1979). Effects of Dielectric Saturation on Planar Double Layer Interactions for No Added Salt.

615. R. H. Fowler, *Statistical Mechanics*, Cambridge Univ Press, Cambridge, UK, 1966.

616. I. Langmuir, *Phys. Rev.,* **43,** 224 (1933). The Nature of Adsorbed Films of Caesium on Tungsten. Part I. The Space Charge Sheath and the Image Force.

617. T. L. Hill, *Statistical Mechanics*, McGraw-Hill, New York, 1956.

618. C. W. Outhwaite and L. B. Bhuiyan, *J. Chem. Soc. Faraday Trans. 2,* **79,** 707 (1983). An Improved Modified Poisson-Boltzmann Equation in Electric-Double-Layer Theory.

619. J. E. Mayer, *J. Chem. Phys.,* **18,** 1426 (1950). The Theory of Ionic Solutions.

620. A. K. Mazur, *J. Comput. Chem.,* **22,** 457 (2002). Molecular Dynamics of Minimal B-DNA.

621. B. A. Pailthorpe, D. J. Mitchell, and B. W. Ninham, *J. Chem. Soc. Faraday Trans. 2,* **80,** 115 (1984). Ion-Solvent Interactions and the Activity Coefficients of Real Electrolyte Solutions.

622. V. Kralg-Iglic and A. Iglic, *J. Phys.,* **6,** 477 (1996). A Simple Statistical Mechanical Approach to the Free Energy of the Electric Double Layer Including the Excluded Volume Effect.

623. K. Bohinc, A. Iglic, T. Slivnik, and V. Kralg-Iglic, *Bioelectrochemistry,* **57,** 73 (2002). Charged Cylindrical Surfaces: Effect of Finite Ion Size.

624. Y. Burak and D. Andelman, *J. Chem. Phys.,* **114,** 3271 (2001). Discrete Aqueous Solvent Effects and Possible Attractive Forces.

625. E. Hückel, *Physikal. Z.,* **26,** 93 (1925). Zur Theorie Konzentrierterer Wassiger Losungen Starker Elektrolyte.

626. P. Debye and L. Pauling, *J. Am. Chem. Soc.,* **47,** 2129 (1925). The Inter-Ionic Attraction Theory of Ionized Solutes. IV. The Influence of Variation of Dielectric Constant on the Limiting Law for Small Concentrations.

627. A. D. Buckingham, *J. Chem. Phys.,* **25,** 428 (1956). Theory of the Dielectric Constant at High Field Strengths.

628. D. C. Grahame, *J. Chem. Phys.,* **18,** 903 (1950). Effects of Dielectric Saturation upon the Diffuse Double Layer and the Free Energy of Hydration of Ions.

629. B. E. Conway, J. E. Desnoyers, and A. C. Smith, *Phil. Trans. Roy. Soc. Lond. A,* **256,** 389 (1964). On the Hydration of Simple Ions and Polyions.

630. Y. Gur, I. Ravina, and A. J. Babchin, *J. Colloid Interface Sci.,* **64,** 333 (1978). On the Electrical Double Layer Theory. II. The Poisson-Boltzmann Equation Including Hydration Forces.

631. H. Maeda and F. Oosawa, *Biophys. Chem.,* **12,** 215 (1980). Effects of Dielectric Saturation on Planar Electric Double Layers in Salt Solutions.

632. L. W. Bahe, *J. Phys. Chem.,* **76,** 1062 (1972). Structure in Concentrated Solutions of Electrolytes. Field-Dependent-Gradient Forces and Energies.

633. A. A. Chernenko, *Soviet Electrochem.,* **15,** 1201 (1979). Dielectric Structure of the Diffuse Part of the Double Layer.

634. A. A. Chernenko, *Soviet Electrochem.,* **17,** 511 (1981). Diffuse Layer in the Model of Hydrated Ions.

635. A. A. Chernenko, *Soviet Electrochem.,* **17,** 1005 (1981). Structure of the Diffuse Double-Layer Part in the Model of Hydrated Ions.

636. M. S. P. Sansom, G. R. Smith, C. Adcock, and P. C. Biggin, *Biophys. J.,* **73,** 2404 (1997). The Dielectric Properties of Water within Model Transbilayer Pores.

637. A. V. Lukashin, D. B. Beglov, and M. D. Frank-Kamenetskii, *J. Biomolec. Struct. Dynam.,* **9,** 517 (1991). Allowance for Spatial Dispersion of Dielectric Permittivity in Polyelectrolyte Model of DNA.

638. J. R. C. van der Maarel, *Biophys. J.,* **76,** 2673 (1999). Effect of Spatial Inhomogeneity in Dielectric Permittivity on DNA Double Layer Formation.

639. S. Gavryushov and P. Zielenkiewicz, *J. Phys. Chem. B,* **103,** 5860 (1999). Electrostatics of a DNA-Like Polyelectrolyte: Effects of Solvent Dielectric Saturation and Polarization of Ion Hydration Shells.

640. R. A. Goldstein and J. J. Kozak, *J. Chem. Phys.,* **62,** 276 (1975). Relaxation of the Continuum Approximation in the Theory of Electrolytes. I. Formal Results.

641. R. A. Goldstein, P. F. Hay, and J. J. Kozak, *J. Chem. Phys.,* **62,** 285 (1975). On the Relaxation of the Continuum Approximation in the Theory of Electrolytes. II. Ion Distributions.

642. D. G. Knox and J. J. Kozak, *Molec. Phys.,* **33,** 811 (1977). Effect of Relaxing the Continuum Dielectric Approximation on Poisson-Boltzmann Thermodynamics.

643. J. Frahm and S. Diekmann, *J. Colloid Interface Sci.,* **70,** 440 (1979). Numerical Calculation of Diffuse Double Layer Properties for Spherical Colloidal Particles by Means of a Modified Nonlinearized Poisson-Boltzmann Equation.

644. V. Vasilyev, *J. Comput. Chem.,* **23,** 1254 (2002). Determination of the Effective Dielectric Constant from the Accurate Solution of the Poisson Equation.

645. G. Lamm and G. R. Pack, *Proc. Natl. Acad. Sci. (USA),* **87,** 9033 (1990). Acidic Domains around Nucleic Acids.

646. R. Kjellander and S. Marcelja, *J. Phys. Chem.,* **90,** 1230 (1986). Double-Layer Interaction on the Primative Model and the Corresponding Poisson-Boltzmann Description.

647. G. M. Torrie and J. P. Valleau, *Chem. Phys. Lett.,* **73,** 5807 (1980). Electrical Double Layers. I. Monte Carlo Study of a Uniformly Charged Surface.

648. P. Attard, *J. Phys. Chem.,* **99,** 14174 (1995). Ion Condensation in the Electric Double Layer and the Corresponding Poisson-Boltzmann Effective Surface Charge.

649. L. Sjostrom, T. Akesson, and B. Jönsson, *Ber. Bunsenges. Phys. Chem.,* **100,** 898 (1996). Charge Reversal in Electrical Double Layers—a Balance between Energy and Entropy.

650. P. Mills, C. F. Anderson, and M. T. Record, Jr., *J. Phys. Chem. B,* **89,** 3984 (1985). Monte Carlo Studies of Counterion-DNA Interactions. Comparison of the Radial Distribution of Counterions with Predictions of Other Polyelectrolyte Theories.

651. C. S. Murthy, R. J. Bacquet, and P. J. Rossky, *J. Phys. Chem. B,* **89,** 701 (1985). Ionic Distributions Near Polyelectrolytes. A Comparison of Theoretical Approaches.

652. G. R. Pack, G. Lamm, L. Wong, and D. Clifton, in *Theoretical Biochemistry and Molecular Biophysics*, D. L. Beveridge, Ed., Adenine, New York, 1990, pp. 237–246. The Structure of the Electrolyte Environment of DNA.

653. C. W. Outhwaite, *Chem. Phys. Lett.,* **53,** 599 (1978). Symmetrical Radial Distribution Functions in the Potential Theory of Electrolyte Solutions.

654. M. M. Martinez, L. B. Bhuiyan, and C. W. Outhwaite, *J. Chem. Soc. Faraday Trans.,* **86,** 3383 (1990). Thermodynamic Consistency in the Symmetric Poisson-Boltzmann Equation for Primitive Model Electrolytes.

655. J. Rescic, V. Vlachy, C. W. Outhwaite, L. B. Bhuiyan, and A. K. Mukherjee, *J. Chem. Phys.,* **111,** 5514 (1999). A Monte Carlo Simulation and Symmetric Poisson-Boltzmann Study of a Four-Component Electrolyte Mixture.

656. G. Feat and S. Levine, *J. Chem. Soc. Faraday Trans. 2,* **73,** 1345 (1977). Ion-Pair Correlation Function in Electric Double Layer Theory. Part 1.

657. S. Levine and G. Feat, *J. Chem. Soc. Faraday Trans. 2,* **73,** 1359 (1977). Ion-Pair Correlation Function in Electric Double Layer Theory. Part 2.

658. D. Bratko and V. Vlachy, *Colloid Polymer Sci.,* **263,** 417 (1985). An Application of the Modified Poisson-Boltzmann Equation in Studies of Osmotic Properties of Micellar Solution.

659. G. M. Bell and P. D. Rangecroft, *Molec. Phys.,* **24,** 255 (1972). A Linearized Potential Equation for the Interfacial Region in an Unsymmetrical Electrolyte.

660. C. W. Outhwaite and L. B. Bhuiyan, *J. Chem. Phys.,* **84,** 3461 (1986). A Modified Poisson-Boltzmann Equation in Electric Double Layer Theory for a Primitive Model Electrolyte with Size-Asymmetric Ions.

661. J. P. Valleau and S. G. Whittington, in *Statistical Mechanics A: Equilibrium Techniques*, B. J. Berne, Ed., Plenum Press, New York, 1977, pp. 137–168.

662. M. P. Allen and D. J. Tildesley, *Computer Simulation of Liquids*, Clarendon Press, Oxford, 1987.

663. D. M. Ferguson, J. I. Siepman, and D. G. Truhlar, *Monte Carlo Methods in Chemical Physics*, Wiley, New York, 1999.

664. A. S. Petrov, personal communication.

665. J. P. Valleau and L. K. Cohen, *J. Chem. Phys.,* **72,** 5935 (1980). Primitive Model Electrolytes. I. Grand Canonical Monte Carlo Computations.

666. J. P. Valleau, L. K. Cohen, and D. N. Card, *J. Chem. Phys.,* **72,** 5942 (1980). Primitive Model Electrolytes. II. The Symmetrical Electrolyte.

667. C. W. Outhwaite, *J. Chem. Phys.,* **50,** 2277 (1969). Extension of the Debye-Hückel Theory of Electrolyte Solutions.

668. C. W. Outhwaite, *Chem. Phys. Lett.,* **7,** 636 (1970). A Modified Poisson-Boltzmann Equation in the Double Layer.

669. D. M. Burley, V. C. L. Hutson, and C. W. Outhwaite, *Molec. Phys.,* **27,** 225 (1974). A Treatment of the Volume and Fluctuation Term in Poisson's Equation in the Debye-Hückel Theory of Strong Electrolyte Solutions.

670. C. W. Outhwaite, L. B. Bhuiyan, and S. Levine, *J. Chem. Soc. Faraday Trans. 2,* **76,** 1388 (1980). Theory of the Electric Double Layer Using a Modified Poisson-Boltzmann Equation.

671. C. W. Outhwaite, *J. Chem. Soc. Faraday Trans. 2,* **83,** 949 (1987). Numerical Solution of a Poisson-Boltzmann Theory for a Primitive Model Electrolyte with Size and Charge Asymmetric Ions.

672. C. W. Outhwaite, M. Molero, and L. B. Bhuiyan, *J. Chem. Soc. Faraday Trans. 2,* **87,** 3227 (1991). Symmetrical Poisson-Boltzmann and Modified Poisson-Boltzmann Theories.

673. T. Das, D. Bratko, L. B. Bhuiyan, and C. W. Outhwaite, *J. Phys. Chem. B,* **99,** 410 (1995). Modified Poisson-Boltzmann Theory Applied to Linear Polyelectrolyte Solutions.

674. L. B. Bhuiyan and C. W. Outhwaite, *Molec. Phys.,* **87,** 625 (1996). Polyelectrolyte Solutions Using a Three Component Mixture.

675. V. Vlachy, L. B. Bhuiyan, and C. W. Outhwaite, *Molec. Phys.,* **90,** 553 (1997). Asymmetric Electrolyte in Mixture with a Neutral Component: Effects of Counterion Charge.

676. J. Rescic, V. Vlachy, L. B. Bhuiyan, and C. W. Outhwaite, *Molec. Phys.,* **95,** 233 (1998). Monte Carlo Simulations of a Mixture of an Asymmetric Electrolyte and a Neutral Species.

677. S. S. Zakharova, S. U. Egelhaaf, L. B. Bhuiyan, C. W. Outhwaite, D. Bratko, and J. R. C. van der Maarel, *J. Chem. Phys.,* **111,** 10706 (1999). Multivalent Ion-DNA Interaction: Neutron Scattering Estimates of Polyamine Distribution.

678. C. W. Outhwaite, M. Molero, and L. B. Bhuiyan, *J. Chem. Soc. Faraday Trans.,* **89,** 1315 (1993). Primitive Model Electrolytes in the Modified Poisson-Boltzmann Theory.

679. C. W. Outhwaite, M. Molero, and L. B. Bhuiyan, *J. Chem. Soc. Faraday Trans.,* **90,** 2002 (1994). Corrigendum to Primitive Model Electrolytes in the Modified Poisson-Boltzmann Theory.

680. D. Bratko and V. Vlachy, *Chem. Phys. Lett.,* **90,** 434 (1982). Distribution of Counterions in the Double Layer around a Cylindrical Polyion.

681. D. Bratko and V. Vlachy, *Chem. Phys. Lett.,* **115,** 294 (1985). Monte Carlo Studies of Polyelectrolyte Solutions. Effect of Polyelectrolyte Charge Density.

682. S. Gavryushov and P. Zielenkiewicz, *Biophys. J.,* **75,** 2732 (1998). Electrostatic Potential of B-DNA: Effect of Interionic Correlations.

683. S. Tomac and A. Graslund, *J. Comput. Chem.,* **19,** 893 (1998). Multi-Multigrid Solution of Modified Poisson-Boltzmann Equation for Arbitrarily Shaped Molecules.

684. M. E. Fisher and Y. Levin, *Phys. Rev. Lett.,* **71,** 3826 (1993). Criticality in Ionic Fluids: Debye-Hückel Theory, Bjerrum, and Beyond.

685. M. E. Fisher, *J. Stat. Phys.,* **75,** 1 (1994). The Story of Coulombic Criticality.

686. M. E. Fisher, *J. Phys. Condensed Matter,* **8,** 9103 (1996). The Nature of Criticality in Ionic Fluids.

687. M. N. Tamashiro, Y. Levin, and M. C. Barbosa, *Physica A,* **268,** 24 (1999). The One-Component Plasma: A Conceptual Approach.

688. N. Bjerrum, *Kgl. Danske Videnskabernes Selskab. Mathematisk-Fysiske Meddelelser,* **7,** 1 (1926). Untersuchungen uber Ionenassoziation. I. Der Einfluss der Ioneneassoziation auf die Aktivitat der Ionen bei Mittleren Assoziationsgraden.

689. B. P. Lee and M. E. Fisher, *Phys. Rev. Lett.,* **76,** 2906 (1996). Density Fluctuations in an Electrolyte from Generalized Debye-Hückel Theory.

690. B. P. Lee and M. E. Fisher, *Europhys. Lett.,* **39,** 611 (1997). Charge Oscillations in Debye-Hückel Theory.

691. P. Attard, *Phys. Rev. E,* **48,** 3604 (1993). Asymptotic Analysis of Primitive Model Electrolytes and the Electrical Double Layer.

692. F. H. Stillinger, Jr. and R. Lovett, *J. Chem. Phys.,* **48,** 3858 (1968). Ion-Pair Theory of Concentrated Electrolytes. I. Basic Concepts.

693. F. H. Stillinger, Jr. and R. Lovett, *J. Chem. Phys.,* **49,** 1991 (1968). General Restriction on the Distribution of Ions in Electrolytes.

694. D. J. Mitchell, D. A. McQuarrie, A. Szabo, and J. Groeneveld, *J. Statistical Phys.,* **17,** 15 (1977). On the Second-Moment Condition of Stillinger and Lovett.

695. L. Blum, *J. Phys. Chem.,* **81,** 136 (1977). Theory of Electrified Interfaces.

696. J. M. G. Barthel, H. Krienke, and W. Kunz, *Physical Chemistry of Electrolyte Solutions,* Steinkopff, New York, 1998.

697. R. Kjellander and S. Marcelja, *J. Chem. Phys.,* **82,** 2122 (1985). Inhomogeneous Coulomb Fluids with Image Interactions between Planar Surfaces. I.

698. R. Kjellander, *J. Chem. Phys.,* **88,** 7129 (1988). Inhomogeneous Coulomb Fluids with Image Interactions between Planar Surfaces. II. On the Anisotropic Hypernetted Chain Approximation.

699. R. Kjellander and S. Marcelja, *J. Chem. Phys.,* **88,** 7138 (1988). Inhomogeneous Coulomb Fluids with Image Interactions between Planar Surfaces. III. Distribution Functions.

700. P. Attard, D. J. Mitchell, and B. W. Ninham, *J. Chem. Phys.,* **88,** 4987 (1988). Beyond Poisson-Boltzmann: Images and Correlations in the Electric Double Layer. I. Counterions Only.

701. R. Kjellander and S. Marcelja, *J. Phys. Chem.,* **90,** 1230 (1986). Double-Layer Interaction in the Primitive Model and the Corresponding Poisson-Boltzmann Description.

702. H. Löwen and G. Kramposthuber, *Europhys. Lett.,* **23,** 673 (1993). Optimal Effective Pair Potential for Charged Colloids.

703. R. Kjellander and D. J. Mitchell, *J. Chem. Phys.,* **101,** 603 (1994). Dressed-Ion Theory for Electrolyte Solutions—a Debye-Hückel-Like Reformulation of the Exact Theory for the Primitive Model.

704. J. Ennis, S. Marcelja, and R. Kjellander, *Electrochim. Acta,* **41,** 2115 (1996). Effective Surface Charge for Symmetric Electrolytes in the Primitive Model Double Layer.

705. H. Greberg and R. Kjellander, *J. Chem. Phys.,* **108,** 2940 (1998). Charge Inversion in Electric Double Layers and Effects of Different Sizes for Counterions and Coions.

706. R. R. Netz, *Phys. Rev. E,* **60,** 3174 (1999). Debye-Hückel Theory for Interfacial Geometries.

707. R. R. Netz, *Eur. Phys. J. E,* **3,** 131 (2000). Debye-Hückel Theory for Slab Geometries.

708. R. R. Netz and H. Orland, *Eur. Phys. J. E,* **1,** 203 (2000). Beyond Poisson-Boltzmann: Fluctuation Effects and Correlation Functions.

709. A. G. Moreira and R. R. Netz, *Eur. Phys. J. D,* **8,** 145 (2000). One-Component-Plasma: Going beyond Debye-Hückel.

710. A. G. Moreira and R. R. Netz, *Europhys. Lett.,* **52,** 705 (2000). Strong-Coupling Theory for Counter-Ion Distributions.

711. T. Alts, P. Nielaba, B. D'Aguanno, and F. Forstmann, *Chem. Phys.,* **111,** 223 (1987). A Local Density Functional Approximation for the Ion Distribution Near a Charged Electrode in the Restricted Primitive Model Electrolyte.

712. C. N. Patra and S. K. Ghosh, *J. Chem. Phys.,* **100,** 5219 (1994). A Nonlocal Density Functional Theory of Electric Double Layer: Symmetric Electrolytes.

713. C. N. Patra and A. Yethiraj, *J. Phys. Chem. B,* **103,** 6080 (1999). Density Functional Theory for the Distribution of Small Ions around Polyions.

714. R. van Roij, M. Dijkstra, and J.-P. Hansen, *Phys. Rev. E,* **59,** 2010 (1999). Phase Diagram of Charge-Stabilized Colloidal Suspensions: Van der Waals Instability without Attractive Forces.

715. C. N. Patra and A. Yethiraj, *Biophys. J.,* **78,** 699 (2000). Density Functional Theory for the Nonspecific Binding of Salt to Polyelectrolytes: Thermodynamic Properties.

716. D. Y. C. Chan, *Phys. Rev. E,* **63,** 061806-1 (2002). Density Functional Theory of Charged Colloidal Systems.

717. M. A. Miller, L. M. Amon, and W. P. Reinhardt, *Chem. Phys. Lett.,* **331,** 278 (2000). Should One Adjust the Maximum Step Size in a Metropolis Monte Carlo Simulation?

718. M. Le Bret and B. H. Zimm, *Biopolymers,* **23,** 271 (1984). Monte Carlo Determination of the Distribution of Ions about a Cylindrical Polyelectrolyte.

719. G. R. Pack, L. Wong, and G. Lamm, *Int. J. Quantum Chem.,* **16,** 1 (1989). Model Systems for DNA and Its Environment: Suitability and Accuracy in Theoretical Calculations.

720. G. R. Pack and G. Lamm, *Int. J. Quantum Chem.,* **20,** 213 (1993). Counterion Condensation Theory Revisited: Limits on Its Applicability.

721. G. S. Manning, *J. Phys. Chem. B,* **51,** 924 (1969). Limiting Laws and Counterion Condensation in Polyelectrolyte Solutions. I. Colligative Properties.

722. G. S. Manning and J. Ray, *J. Biomolec. Struct. Dynam.,* **16,** 461 (1998). Counterion Condensation Revisited.

723. A. D. MacGillivray, *J. Chem. Phys.,* **56,** 83 (1971). Analytic Description of the Condensation Phenomenon Near the Limit of Infinite Dilution Based on the Poisson-Boltzmann Equation.

724. M. A. Lampert and R. S. Crandall, *Chem. Phys. Lett.,* **72,** 481 (1980). Nonlinear Poisson–Boltzmann Theory for Polyelectrolyte Solutions: The Counterion Condensate around a Line Charge as a δ-Function.

725. G. Weisbuch and M. Guéron, *J. Phys. Chem. B,* **85,** 517 (1981). Polyelectrolyte Theory. 3. The Surface Potential in Mixed-Salt Solutions.

726. M. A. Lampert, *Biopolymers,* **21,** 159 (1982). The δ-Function Counterion Condensate around a Line Charge Derived from the Fuoss, Katchalsky, and Lifson Polyelectrolyte Theory.

727. W. B. Russel, *J. Polym. Sci. Polym. Phys.,* **20,** 1233 (1982). Polyelectrolyte Solutions: Counterion Condensation and Intermolecular Interactions.

728. G. V. Ramanathan and C. P. Woodbury, Jr., *J. Chem. Phys.,* **77,** 4133 (2002). Statistical Mechanics of Electrolytes and Polyelectrolytes. II. Counterion Condensation on a Line Charge.

729. G. V. Ramanathan, *J. Chem. Phys.,* **78,** 3223 (1980). Statistical Mechanics of Electrolytes and Polyelectrolytes. III. The Cylindrical Poisson-Boltzmann Equation.

730. C. P. Woodbury, Jr. and G. V. Ramanathan, *Macromolecules,* **15,** 82 (1982). End Effects in Polyelectrolytes by the Mayer Cluster Integral Approach.

731. B. H. Zimm and M. Le Bret, *J. Biomolec. Struct. Dynam.,* **1,** 461 (1983). Counter-Ion Condensation and System Dimensionality.

732. M. A. Lampert and R. U. Martinelli, *Chem. Phys. Lett.,* **121,** 121 (1985). Buffering of Charge by the Coulomb Condensate in Non-Linear Poisson-Boltzmann Theory.

733. I. Rubinstein, *SIAM J. Appl. Math.,* **46,** 1024 (1986). Counterion Condensation As an Exact Limiting Property of Solutions of the Poisson-Boltzmann Equation.

734. D. Stigter, *Biophys. J.,* **69,** 380 (1995). Evaluation of the Counterion Condensation Theory of Polyelectrolytes.

735. A. L. Kholodenko and A. L. Beyerlein, *Phys. Rev. Lett.,* **74,** 4679 (1995). Painleve III and Manning's Counterion Condensation.

736. M. O. Fenley, G. S. Manning, and W. K. Olson, *Biopolymers,* **30,** 1191 (1990). Approach to the Limit of Counterion Condensation.

737. G. S. Manning and U. Mohanty, *Physica A,* **247,** 196 (1997). Counterion Condensation on Ionic Oligomers.

738. J. Ray and G. S. Manning, *Langmuir,* **10,** 2450 (1994). An Attractive Force between Two Rodlike Polyions Mediated by the Sharing of Condensed Counterions.

739. J. Ray and G. S. Manning, *Macromolecules,* **30,** 5739 (1997). Effect of Counterion Valence and Polymer Charge Density on the Pair Potential of Two Polyions.

740. J. Ray and G. S. Manning, *Macromolecules,* **33,** 2901 (2000). Formation of Loose Clusters in Polyelectrolyte Solutions.

741. P. J. Heath and J. M. Schurr, *Macromolecules,* **25,** 4149 (1992). Counterion Condensation. Effects of Site Binding, Fluctuations in Nearest-Neighbors Interactions, and Bending.

742. M. O. Fenley, W. K. Olson, and G. S. Manning, *Macromolecules,* **33,** 1899 (2001). Dependence of Counterion Binding on DNA Shape as Determined by Counterion Condensation Theory.

743. G. S. Manning, *Macromolecules,* **34,** 4650 (2001). Counterion Condensation on a Helical Charge Lattice.

744. G. S. Manning, *J. Chem. Phys.,* **99,** 477 (1993). A Condensed Counterion Theory for Polarization of Polyelectrolyte Solutions in High Fields.

745. G. S. Manning and J. Ray, *Macromolecules,* **32,** 4588 (1999). Counterion and Coion Distribution Functions in the Counterion Condensation Theory of Polyelectrolytes.

746. M. Rodenbeck, M. Muller, D. Huster, and K. Arnold, *Biophys. Chem.,* **90,** 255 (2001). Counterion Condensation as Saturation Effect under the Influence of Ion Hydration.

747. J. Ray and G. S. Manning, in *Physical Chemistry of Polyelectrolytes*, T. Radeva, Ed., Marcel Dekker, New York, 2001, pp. 111–133. Inverted Forces in Counterion Condensation Theory.

748. J. M. Schurr and B. S. Fujimoto, *Biophys. Chem.*, **101–102**, 425 (2002). Extensions of Counterion Condensation Theory. I. Alternative Geometries and Finite Salt Concentration.

749. J. M. Schurr and B. S. Fujimoto, *J. Phys. Chem. B*, **107**, 4451 (2003). Extensions of Counterion Condensation Theory. 2. Cell Model and Osmotic Pressure of DNA.

750. M. Deserno, C. Holm, and K. Kremer, in *Physical Chemistry of Polyelectrolytes*, T. Radeva, Ed., Marcel Dekker, New York, 2001, pp. 59–110. Molecular Dynamics Simulations of the Cylindrical Cell Model.

Author Index

Reviews in Computational Chemistry, Volume 19
edited by Kenny B. Lipkowitz, Raima Larter, and Thomas R. Cundari
ISBN 0-471-23585-7

Subject Index

Computer programs are denoted in boldface; databases and journals are in italics.

Reviews in Computational Chemistry, Volume 19
edited by Kenny B. Lipkowitz, Raima Larter, and Thomas R. Cundari
ISBN 0-471-23585-7